IAU COLLOQUIUM 145

Supernovae and Supernova Remnants

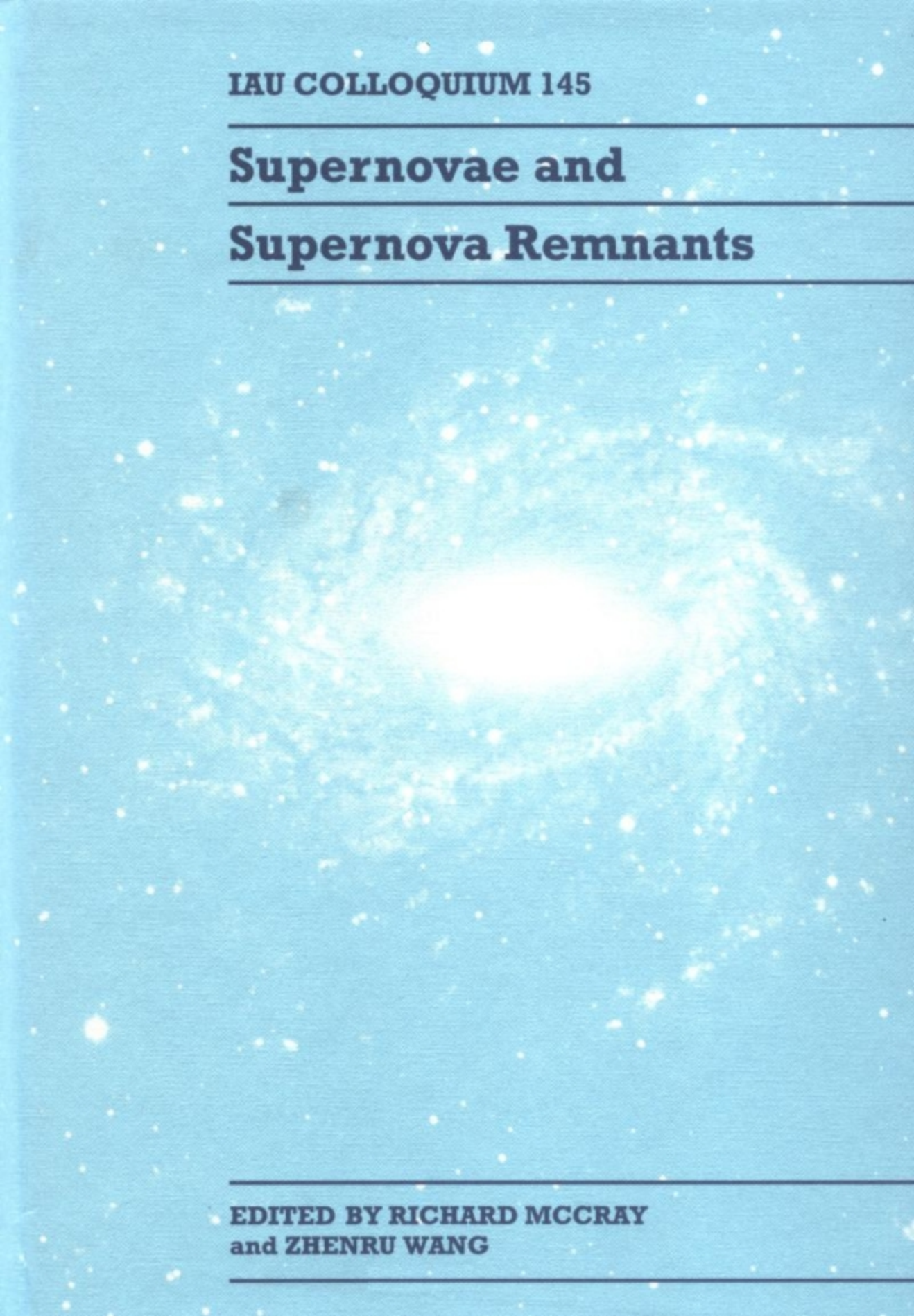

EDITED BY RICHARD MCCRAY
and ZHENRU WANG

Dramatic advances in ground-based and space astronomy, together with observations of the serendipitous supernova 1987A, have led to the study of supernovae and supernova remnants becoming one of the most active and rewarding fields in today's astrophysics. To take stock of these exciting developments and to give focus to future research, the International Astronomical Union held a colloquium in Xian, China, for the world's leading experts and this volume gathers together their articles.

The articles summarise our knowledge of supernova 1987A and give the first results on supernova 1993J. They not only demonstrate the latest techniques for interpreting spectra and light curves of supernovae, but show how they can be applied to measuring the cosmic distance scale. They also cover recent advances in theories for type I and type II supernovae, and observations and interpretations of supernova remnants. Two appendices provide a unique reference of newly discovered supernovae and supernova remnants.

Together these forty review articles provide an up-to-date and wide-ranging review of our understanding of supernovae and supernova remnants for graduate students and researchers.

Supernovae and Supernova Remnants

Supernovae and Supernova Remnants

Proceedings International Astronomical Union
Colloquium 145,
held in Xian, China
May 24–29, 1993

Edited by
RICHARD McCRAY
JILA, University of Colorado, Boulder

ZHENRU WANG
Center for Astrophysics, Nanjing University

CAMBRIDGE
UNIVERSITY PRESS

Published by the Press Syndicate of the University of Cambridge
The Pitt Building, Trumpington Street, Cambridge CB2 1RP
40 West 20th Street, New York, NY 10011- 4211, USA
10 Stamford Road, Oakleigh, Melbourne 3166, Australia

First published 1996

Printed in Great Britain at the University Press, Cambridge

A catalogue record for this book is available from the British Library

Library of Congress cataloguing in publication data available

ISBN 0 521 46080 8 hardback

Contents

SN 1987A, SN 1993J, and Other Supernovae

Supernovae and Circumstellar Matter

Supernova Remnants

Catalogues

Participants

Andronova, Anna	Pulkovo Observatory (Russia)
Arnett, David	U. of Arizona (USA)
Aschenbach, Bernd	Max-Planck-Inst. f. Extraterr. Physik (Germany)
Ball, Lewis Timothy	U. Sydney (Australia)
Bandiera, Rino	Osservatorio Astrofisico di Arcetri (Italy)
Bao, Gang	U. Trondheim (Norway)
Baron, Edward	U. Oklahoma (USA)
Blair, William	Johns Hopkins U. (USA)
Blinnikov, Sergej Ivanovich	Inst. Theor. Expt. Phys., Moscow (Russia)
Bouchet, Patrice	European Southern Observatory (Chile)
Bragaglia, Angela	Osservatorio Astronomico di Bologna (Italy)
Bravo Guil, Eduardo	U. Politecnica Catalunya, Barcelona (Spain)
Burrows, Adam	U. of Arizona (USA)
Canal, Ramon	U. Barcelona (Spain)
Cappellaro, Enrico	Osservatorio Astronomico di Padova (Italy)
Chen, Jun	Nanjing U. (China)
Chen, Xueshi	Atomic and Nucl. Inst. Shanghai (China)
Chen, Yang	Nanjing U. (China)
Cheng Linxiang	Inst. High Energy Physics, Beijing (China)
Chevalier, Roger	U. Virginia (USA)
Choe, Seung-Urn	Seoul National U. (Korea)
Crotts, Arlin	Columbia U. (USA)
Decourchelle, Anne	CEN Saclay Service d'Astrophysique (France)
Eastman, Ronald	U. Calif. Santa Cruz (USA)
Felten, James	NASA - Goddard Space Flight Ctr. (USA)
Fesen, Robert	Dartmouth College (USA)
Filippenko, Alexei	U. California Berkeley (USA)
Fisher, Adam	U. Oklahoma (USA)
Fransson, Claes	Stockholm Observatory (Sweden)
Fuerst, Ernst	Max-Planck-Inst. f. Radioastronomie (Germany)
Gomez, Gabriel	Inst. Astrofisica de Canarias, Tenerife (Spain)
Green, David	Mullard Radio Astronomy Obs. (UK)
Guo, Zhiyu	Pennsylvania State U. (USA)
Han, Jinlin	Beijing Observatory (China)
Hashimoto, Masaaki	Kyushu U. (Japan)
He, Zehui	Inst. High Energy Physics, Beijing (China)
Higgs, Lloyd	DRAO, Penticton (Canada)
Höflich, Peter	U. of Munich (Germany)
Holt, Anne	U. Oslo (Norway)
Hu, Jingyao	Beijing Observatory (China)
Imshennik, Vladimir Sergeevich	Inst. Theor. Expt. Phys., Moscow (Russia)
Isern-Vilaboy, Jorge	Centre Estudis Avancats Blanes (Spain)
Janka, Hans-Thomas	Max-Planck-Inst. f. Astrophysik (Germany)
Kirshner, Robert	Harvard-Smithsonian Center for Astrophysics (USA)
Kozma, Cecilia	Stockholm Observatory (Sweden)
Kumagai, Shiomi	U. Tokyo (Japan)
Landecker, Thomas	DRAO, Penticton (Canada)
Leibundgut, Bruno	U. California Berkeley (USA)

Li, Aigen	Beijing Observatory (China)
Li, Weidong	Beijing Normal U. (China)
Li, Xiangdong	Nanjing U. (China)
Li, Zongwei	Beijing Normal U. (China)
Lin, Xianbin	Shanghai Jiaotong U. (China)
Liu, Ning	Nanjing U. (China)
Livne, Eli	U. Arizona (USA)
Long, Knox	Space Telescope Sci. Inst. (USA)
Lu, Jufu	U. Sci. Technology China, Hefei (China)
Lundqvist, Peter	Stockholm Observatory (Sweden)
Ma, Er	Beijing Observatory (China)
Ma, Feng	Beijing Normal U. (China)
Masai, Kuniaki	CEN Saclay Service d'Astrophysique (France)
Matheson, Thomas	U. California Berkeley (USA)
Mazzali, Paolo	Osservatorio Astronomico di Trieste (Italy)
McCray, Richard	JILA, U. Colorado (USA)
Miller, Douglas	U. Oklahoma (USA)
Milne, Douglas	Australia Telescope Nat. Facility (Australia)
Montes, Marcos	Stanford U. (USA)
Murdin, Paul	Royal Observatory Edinburgh (UK)
Nomoto, Ken'ichi	U. Tokyo (Japan)
Nugent, Peter	U. Oklahoma (USA)
Oestgaard, Erlend	U. Trondheim (Norway)
Oliva, Ernesto	Osservatorio Astrofisico di Arcetri (Italy)
Petre, Robert	NASA - Goddard Space Flight Ctr. (USA)
Pollas, Christian	Obs. de la Cote d'Azur, Nice (France)
Pun, Jason	Harvard-Smithsonian Center for Astrophysics (USA)
Qi, Guanrong	Shan Xi Observatory (China)
Qu, Qinyue	Nanjing U. (China)
Ray, Alak	Tata Inst. Fundamental Res., Bombay (India)
Renzini, Alvio	U. Bologna (Italy)
Reynolds, Stephen	North Carolina State U. (USA)
Rho, Jeonghee	NASA - Goddard Space Flight Ctr. (USA)
Ritossa, Claudio	U. Bologna (Italy)
Ruiz-Lapuente, Pilar	Harvard-Smithsonian Center for Astrophysics (USA)
Sauvageot, Jean Luc	CEN Saclay Service d'Astrophysique (France)
Schlegel, Eric	NASA - Goddard Space Flight Ctr. (USA)
Shigeyama, Toshikazu	U. Tokyo (Japan)
Slane, Patrick	Harvard-Smithsonian Center for Astrophysics (USA)
Spyromilio, Jason	Anglo-Australian Observatory (Australia)
Staveley-Smith, Lister	Australia Telescope Nat. Facility (Australia)
Strom, Richard	NFRA, Dwingeloo (Netherlands)
Suntzeff, Nicholas	Cerro Tololo Interamerican Obs. (Chile)
Suzuki, Tomoharu	U. Tokyo (Japan)
Thielemann, Friedrich K.	Harvard-Smithsonian Center for Astrophysics (USA)
Trushkin, Sergey	Special Astrophysical Obs. RAN (Russia)
Tsiopa, Olga	Pulkovo Observatory (Russia)
Tsunemi, Hiroshi	Osaka U. (Japan)
Turatto, Massimo	Osservatoria Astronomico de Padova (Italy)
Turtle, Anthony	U. Sydney (Australia)

Utrobin, Victor	Inst. Theor. Expt. Phys., Moscow (Russia)
Van Den Bergh, Sidney	Dominion Astrophysical Observatory (Canada)
Van Dyk, Schuyler	Naval Research Lab. (USA)
Vaughan, Thomas	U. Oklahoma (USA)
Wallace, Brad	U. of Calgary (Canada)
Wampler, E. Joseph	European Southern Observatory, Munich (Germany)
Wang, Lifan	Beijing Observatory (China)
Wang, Tinggui	U. Sci. Technology China, Hefei (China)
Wang, Weizhong	Inst. Applied Math., Beijing (China)
Wang, Yiren	Inst. Applied Math., Beijing (China)
Wang, Zhenru	Nanjing U. (China)
Wang, Zhong	IPAC, Calif. Inst. Technology (USA)
Weiler, Kurt W.	Naval Research Lab. (USA)
Wells, Lisa Ann	Nat. Optical Astron. Obs. (USA)
Wheeler, Craig	U. Texas (USA)
Woermann, Beate	Rhodes U. (South Africa)
Wooden, Diane	NASA - Ames Res. Center (USA)
Woosley, Stan	U. California Santa Cruz (USA)
Wu, Xinji	Beijing Observatory (China)
Wu, Xuebing	Hua Zhong Normal U., Wuhan (China)
Xie, Zuoheng	Inst. Applied Math., Beijing (China)
Xu, Wen	Beijing Observatory (China)
Xu, Jun	Columbia U. (USA)
Yang, Pibo	Hua Zhong Normal U., Wuhan (China)
Yang, Tingao	Shan Xi Observatory (China)
Young, Timothy	U. Oklahoma (USA)
Yu, Wenfei	Hua Zhong Normal U., Wuhan (China)
Zhang, Bin	Beijing Observatory (China)
Zhang, Chengmin	Hebei Technical Inst. (China)
Zhang, Qing Chun	Nanjing U. (China)
Zhang, Souchun	Inst. Applied Math., Beijing (China)
Zhang, Xiangling	Beijing Normal U. (China)
Zhang, Xizhen	Beijing Observatory (China)
Zheng, Yijia	Beijing Observatory (China)
Zhu, Jian	Beijing Observatory (China)
Zhu, Luo Ding	Inst. Applied Phys. & Comp. Math., Beijing (China)

Preface

Supernova and supernova remnant research are two of the most active fields of modern astronomy. SN 1987A has given us a chance to observe a supernova explosion and its aftermath in unprecedented detail, a process that continues to unfold today. Meanwhile, thanks to major advances in optical, radio, and X-ray astronomy, we have gained unprecedented views of the populations and spectrum evolution of supernovae of all kinds. These results have spurred a renaissance in theoretical studies of supernovae. Likewise, samples of well-observed supernovae are becoming large enough that we are closing fast on the goal of using supernovae to determine the cosmic distance scale.

Studies of supernovae and supernova remnants are inextricably linked and we are learning fast about the connections. We now recognize that mass loss from the supernova progenitor star can determine the structure of the circumstellar medium with which the supernova ejecta interact. An outstanding example is the ring around SN1987A. There are many supernovae in which much of the early optical, radio and X-ray emission are due to interaction of the ejecta with circumstellar matter rather than radioactivity within the supernova itself. Just in time for this colloquium, nature provided a particularly spectacular example of such an interacting supernova with SN1993J in M81, one of the brightest supernovae of this century. Moreover, the X-ray spectra of supernova remnants provide a powerful new tool to measure supernova nucleosynthesis yields.

It is particularly fitting that this colloquium took place in Xian, the ancient capital of China. The ancient records of supernovae comprise one of the great scientific contributions of classical Chinese civilization and remain valuable research tools for astronomers today. We were delighted that most of the world's leading experts on supernovae and supernova remnants came to Xian to report their work and to contribute to this volume, which we hope will provide a useful record of the exciting state of supernova research today.

Richard McCray
Boulder, Colorado
September, 1995

Acknowledgements

Financial and logistical support for this Colloquium were provided by: the International Astronomical Union, the Basic Research Division of the State Science and Technology Commission of China, the Department of Mathematics and Physics of the Chinese Academy of Science, the National Natural Science Foundation of China, the State Education Commission of China, the Chinese Astronomical Society, Nanjing University, the European Southern Observatory, the Max-Planck Foundation of Germany, the US National Aeronautics and Space Administration, the American Astronomical Society, the US National Science Foundation, and the International Science Foundation.

The international scientific organizing committee consisted of: Richard McCray (JILA, University of Colorado), Zhenru Wang (Nanjing University), Roger Chevalier (University of Virginia), Alex Filippenko (University of California at Berkeley), Claes Fransson (Stockholm Observatory), Robert Kirshner (Harvard University), Kenichi Nomoto (University of Tokyo), and Joseph Wampler (European Southern Observatory).

The local organizing committee consisted of: Qu, Qin Yue (President, Nanjing University); Qi, Quan Rong (Director, Shan Xi Observatory); Lu, Ju Fu (Univ. Science & Technology, Hefei, China); Li, Tipei (Institute of High Energy Physics, China); Li, Zongwei (Beijing Normal University); Ma, Er (Beijing Observatory); Huang, Sixing (Nanjing University); and Yang, Tinggao (Shan Xi Observatory).

Mr. Li Zhangan and Ms. Wang Min Zhen were most helpful with travel arrangements.

This Colloquium would not have been possible without the hard work and generous support of all these people and organizations.

Supernova Rates

By SIDNEY VAN DEN BERGH

Dominion Astrophysical Observatory, National Research Council, 5071 West Saanich Road, Victoria, British Columbia, V8X 4M6, Canada

Extragalactic supernova rates are reviewed. The main uncertainties in calculated rates are due to (1) the influence of the (still poorly known) luminosity function of supernova of a given type on "control times", to (2) uncertain corrections for possible inclination - dependent bias in supernova discovery probabilities, and (3) interstellar absorption. The total supernova rate in late-type galaxies is found to be $\sim 2(H_o/75)^2$ supernovae (SNe) per century per 10^{10} $L_B(\odot)$. This is consistent with the rate of 3 SNe per century that is derived from the historical data on Galactic supernovae. It is, however, a source of some concern that none of the three Galactic SNe expected to have occurred during the last century was actually observed!

The expansion velocities of SNe Ia are found to correlate strongly with parent galaxy Hubble type. This relation is in the sense that low expansion velocities are only observed for those SNe Ia that occur in early-type galaxies. This suggests that V(exp) correlates with the ages of SNe Ia progenitors. It is speculated that the progenitors of a few SNe Ia with high V(exp) values in E and S0 galaxies were formed during recent starbursts.

SNe Ia rates appear to be enhanced in post-starburst galaxies. It is suggested that supernova rates might be quite high in the recently discovered population of faint blue galaxies at intermediate redshifts.

---

1. Extragalactic Supernova Rates

The first estimate of extragalactic supernova rates was made by Zwicky (1938), who introduced the idea that "control time" was a critical factor needed to determine the supernova frequency. References to subsequent discussions of this topic are given in the reviews by van den Bergh (1991), van den Bergh & Tammann (1991) and Tammann (1992). The most extensive databases on supernova discoveries, that have been analysed to derive supernova rates, are those based on the visual search program by Evans in Australia (Evans, van den Bergh & McClure 1989) and on the Asiago and Crimean photographic surveys that have been analysed by Cappellaro *et al.* (1993ab). Supernova rates in early- type galaxies remain uncertain because of small-number statistics. In late-type galaxies the intrinsic supernova rates are poorly determined because inclination-dependent absorption corrections to these rates might be large (Tammann 1974, 1982, van den Bergh 1990, van den Bergh & McClure 1990) and are poorly determined. In fact van den Bergh, McClure & Evans (1987) and van den Bergh (1994) find no evidence for any significant inclination effect for the largest and most homogeneous data samples. Furthermore the discovery probabilities for supernovae are affected by galaxy surface brightness and by crowding. Additional uncertainties are introduced by night-to-night variations in the limiting magnitude of any particular search program. An interesting complication is provided by the fact that calculation of the control time for a specific species of supernova requires that the luminosity and lightcurve shape of that particular kind of supernova be known. Adopting a standard luminosity for all SNe Ia would, for example, overestimate the control time for subluminous objects such as SN 1991bg by an order of magnitude. Finally the relative numbers of supernovae of different types discovered in any particular survey will probably depend on the wavelength at which that search program was carried out. It is, for example, possible that the high frequency

Table 1. Supernova Rates in SNu

Galaxy type	Ia	Ib	II	source
E-S0	0.15	...	...	a
	0.09	...	...	b
	0.13	...	...	c
Sab,Sb	0.15	0.3	0.9	a
	0.13	0.06	0.13	b
	0.17	0.13	0.30	c
Sbc-Sd	0.1	0.2	0.65	a
	0.18	0.08	0.43	b
	0.39	0.27	1.48	c

a observed by Evans *et al.* (1989)
b observed by Cappellaro *et al.* (1993b)
c Cappellaro *et al.* corrected for inclination and for surface brightness effects (Shaw 1979)

of SNe Ibc in the survey by Muller *et al.* (1992) is (at least in part) due to the fact that their unfiltered CCD detectors had a high red sensitivity, which favored discovery of strongly reddened supernovae with massive progenitors.

The supernova rates derived from the surveys of Evans *et al.* (1989) and of Cappellaro *et al.* (1993b) are listed in Table 1. The data in this table are for a Hubble parameter of 75 km s^{-1} Mpc^{-1}. For any other H_o value the entries in this table should be multiplied by $(H_o/75)^2$. The supernova rates in Table 1 are expressed in SNu [1 SNu = one supernova per century per 10^{10} $L_B(\odot)$]. The supernova rates quoted by Evans *et al.* (1989) have been multiplied by a factor of 0.9 to convert them from the value $M_B(\odot) = +5.37$ used in that paper to $M_B(\odot) = +5.48$ adopted by Cappellaro *et al.* (1993b). The differences between the rates of Evans *et al.* (1989) and of Cappellaro *et al.* (1993b) are due to (1) small number statistics, (2) absorption, surface brightness, and inclination corrections, and (3) differences in control times. To derive supernova rates from their observations Cappellaro *et al.* (1993b) apply the same surface brightness corrections (Shaw 1979) for all types of supernova. However, van den Bergh (1994) has recently shown that such corrections are small (or absent) for luminous SNe Ia, while they turn out to be quite large for SNe II which are, on average, much less luminous. The rate of SNe II in Sbc - Sd galaxies adopted by van den Bergh & Tammann (1991) is ~50% higher than the fully corrected rate given in Table 1. The reason for this difference is that Cappellaro *et al.* (1993ab) assume SNe II to be significantly brighter than do van den Bergh & Tammann (1991). As a result Cappellaro *et al.* derive longer control times, and hence lower supernova frequencies. There is, however, also another reason why SNe Ibc and SNe II may be more frequent in late-type galaxies than Cappellaro *et al.* (1993b) find. According to current ideas (Branch, Nomoto & Filippenko 1991, Van Dyk 1992) the progenitors of such supernovae are probably young massive stars. Many of such objects are likely to still be deeply embedded in the dusty clouds from which they were formed. [Van den Bergh (1992) finds that half of all nearby (D < 3kpc) WR Stars have A_V > 7 mag]. This suggests that a substantial fraction of all supernovae in dust-rich late-type galaxies probably suffer so much absorption that they will not be discovered in most survey programs. This suspicion is strengthened by the observation (van den Bergh 1989)

Table 2. Recent Galactic Supernovae

Name	Year	Distance (kpc)	Type
RCW 86	185	0.95 ± 0.4	II
Lupus	1006	> 1.9	Ia
Crab	1054	2.0	II
3C58	1181?	2.6 ± 0.2	II:
Tycho	1572	3 - 4	Ia
Kepler	1604	$\geq 4.1 \pm 0.9$	Ia?
Cas A	1670:	2.8	Ibc

that the frequency of supernovae in galaxies increases with increasing equivalent width of Hα + [NII], but then suddenly appears to decrease in the (probably dusty) starburst galaxies with the largest Hα equivalent widths. Clearly it would be very important to check on this possibility by undertaking supernova searches at infrared wavelengths.

In view of all of the sources of error and bias discussed above extragalactic supernova rates are presently probably still uncertain by a factor of about two.

2. The Galactic Supernova Rate

The first modern discussion of the Galactic supernova rate is by Öpik (1953). He derived a rate of about one supernova per 300 years from the then known historical supernova remnants. However, Öpik already realized that the true supernova rate must be considerably higher than this because of interstellar extinction, and because the historical record of Galactic supernovae is incomplete. A bibliography listing recent estimates of the Galactic supernova frequency is given in van den Bergh & Tammann (1991).

A compilation of data on supernovae that are known to have occurred in the Galaxy during the last two millennia is given in Table 2. The fact that this table lists only one object during the first millenium (0 - 1000) and six during the second millenium (1000 - 2000) strongly suggests that the most ancient historical data are also the most incomplete. A few additional ancient supernova suspects are listed by Wang *et al.* (1986).

More detailed information on the individual supernovae that are listed in Table 2 is given below:

• **SN 185** – From x-ray observations of its remnant RCW 86 Kaastra *et al.* (1992) conclude that this object was a SN II that exploded at a distance of 0.95 ± 0.4 kpc. Alternatively (Kaastra 1993) the progenitor might also have been a SN Ib embedded in a strong stellar wind.

• **SN 1006** – The presence of Fe II absorption lines (Hamilton & Fesen 1988) makes it virtually certain that this object was an SN Ia. From the width of the Balmer lines Smith *et al.* (1991) estimate a distance of 1.4 - 2.8 kpc. Recent HST observations by Wu *et al.* (1993) show that the Fe II lines have a width of 8300 km s^{-1}. From this observation these authors conclude that the distance to the Lupus supernova is > 1.9 kpc. A distance greater than 3 kpc would, however, make the luminosity of SN 1006 excessive.

• **SN 1054** – The Crab nebula contains Balmer line emitting filaments. It must therefore, by definition, be a SN II. The low expansion velocity of the Crab also excludes the

possibility that it might have been a SN Ia. The distance to the Crab is estimated to be 2.0 kpc (Woltjer 1958, Trimble 1968). In their review Davidson & Fesen (1985) place the Crab nebula at a distance of between 1.5 and 2.2 kpc.

• **SN 1181** – The probable association of this object with 3C58 is discussed in Stephenson (1971) and Clark & Stephenson (1977), but see Becker, Helfand & Szymodiak (1982) for a contrary opinion. The similarity of the radio remnant of 3C58 (Wilson & Weiler 1976) to that of the Crab makes it highly probable that the progenitor of SN 1181 was also a SN II. Green & Gull (1982) estimate the distance to 3C58 to be 2.6 kpc, with an (optimistic?) error of ± 0.2 kpc.

• **SN 1572** – Distance determinations to the remnant of Tycho's supernova (3C10) have been reviewed by de Vaucouleurs (1985). From 18 rather discordant distance estimates de Vaucouleurs concludes that its distance is D = 3.2 ± 0.3 kpc. More recently Strom (1988) obtained a distance of 2.5 kpc. However, Strom also finds D(Tycho)/D(Lupus) = 1.74. With D(Lupus) > 1.9 kpc (Wu *et al.* 1993) this would yield D(Tycho) > 4.4 kpc. A smaller distance of 1.5 - 3.1 kpc has been estimated from the width of the Balmer lies by Smith *et al.* (1991). A distance of 3-4 kpc will be tentatively adopted. Following Weiler & Sramek (1988) it will be assumed that SN 1572 was a supernova of type Ia.

• **SN 1604** – Braun (1987) finds a distance of 4.1 ± 0.9 kpc for the remnant of Kepler's supernova. Using similar techniques he also finds D = 2.3 kpc for the remnant of Tycho's supernova. This suggests that the true distance to SN 1604 might actually be somewhat larger than 4.1 kpc. The nature of the progenitor of SN 1604 remains in dispute. Bandiera (1987) has suggested that it was a massive runaway star that originated in the Galactic disk. However, it is difficult to obtain the high space velocity of the remnant (278 ± 12 km s^{-1}) found by Bandiera & van den Bergh (1991) by ejection from a young starcluster (Leonard & Duncan 1988) or by disruption of a massive binary system (Leonard & Dewey 1993). This suggests that the progenitor of SN 1604 is more likely to have been a high-velocity halo star of Population II.

• **SN 1670:** – The absence of hydrogen from the bulk of the fast-moving ejecta of Cassiopeia A suggests that the progenitor of this object was a SN Ibc. However, detection of a few high-velocity knots emitting Hα and [NII] in the outermost part of the remnant of Cas A (Fesen, Becker & Blair 1987) indicates that the progenitor might have had a thin outer hydrogen layer (Fesen, Becker & Goodrich 1988). Possibly it was a late WN star. Intercomparison of the radial velocities and proper motions in the remnant of Cas A yield an uncertain distance of 2.8 kpc.

Taken at face value the data in Table 2 suggest that the total supernova rate within 4 kpc of the sun is three per millennium. By the same token the number of SN Ibc and SN II, which have massive progenitors, and that are located within 4 kpc, is 2 per millennium. A slightly higher rate of three core-collapse SNe per millenium would be derived using only those supernovae that are known to have occurred within 4 kpc during the Second Millennium.

From a rate of 3 supernovae per millenium within 4 kpc, and an assumed thickness of the disk of 0.3 kpc, one finds a local supernova rate of 2 x 10^{-4} SNe kpc^{-3} yr^{-1}. For an assumed disk age of 10 Gyr it then follows that the total number of supernovae that have exploded in the solar neighborhood is 2 x 10^6 kpc^{-3}. On average the nearest supernova would therefore have occurred at a distance of ~5 pc. Such a supernova would have had V ~ -20, which is bright enough to cause some evaporation of gas from the surfaces of comets in the Oort cloud, and perhaps destruction of the Earth's ozone layer (Ellis & Schramm 1993).

SNe with massive progenitors are probably distributed in the Galaxy in much the same fashion as are stars of Population I. Following Ratnatunga & van den Bergh (1989) it will

be assumed that these objects exhibit an exponential radial density distribution with a scale-length of 4 kpc that extends from 3 kpc to 15 kpc. With such a distribution ~9% of all Galactic OB stars will be located within 4 kpc of the Sun, which is assumed to have R_o = 8.5 kpc. If 9% of all supernovae with massive progenitors also occur within 4 kpc of the Sun, then the *total* rate of Galactic supernovae with massive progenitors is 2/0.09 = 22 (or 3/0.09 = 33) per millennium. (Including SNe Ia would increase the Galactic supernova rate by 20 - 25%). It is noted in passing that the Galactic core-collapse supernova rate of 2-3 per century, that was derived above, is marginally higher than the rate of $1.0^{+1.5}_{-0.6}$ per century which Ratnatunga & van den Bergh (1989) derived from the Scalo (1986) luminosity function and the assumption that the progenitors of core-collapse supernovae have M > 8M⊙. The constraint on the rate of core-collapse supernovae, that is provided by the Scalo (1986) luminosity function, might be eased somewhat if some SNe Ibc are formed by mass transfer in binaries with individual main sequence components which have masses that are slightly smaller than 8M⊙.

From a review of all Galactic luminosity indicators van den Bergh (1988) concluded that the Milky Way System has $L_B = (2.3 \pm 0.6) \times 10^{10}\ L_B(\odot)$. This value of the Galactic luminosity, when combined with a supernova rate of 3 per century, yields a Galactic rate of 1.3 SNu for supernovae with massive progenitors. This value is in reasonable agreement with the total (SNe Ib + SNe II) rate of 1.75 SNu for late-type galaxies given in Table 1.

In the Galactic model of Ratnatunga & van den Bergh (1989) 0.5% of all star formation taken place within one kpc of the Sun. For a total Galactic SN Ib + SN II rate of 3 per century the a priori probability of observing a supernova with a massive progenitor at D $\leq$ 1.0 kpc during the last 20 centuries is therefore 3 x 20 x 0.005 = 0.3. The occurrence of SN 185 at a distance of only 950 pc (Kaastra *et al.* 1992) is therefore not unreasonable. It is, however, a source of some concern (Poisson statistics give p $\simeq$ 0.05) that none of the three Galactic supernovae expected to have occurred during the past century was actually observed! Virginia Trimble has, however, reminded me of the remote possibility that a heavily reddened faint Galactic supernova might have been cataloged as a common nova.

3. The Expansion Velocities of Supernovae of Type Ia

Elliptical galaxies consist mainly of old stars, whereas spiral galaxies contain stellar populations with a wide range in ages. If the characteristics of SNe Ia depend on the ages of their progenitors then supernovae of type Ia in ellipticals should exhibit systematic differences from those that occur in spirals. Recently van den Bergh & Pazder (1992) found that SNe Ia in spirals were, on average, ~ 1 mag more luminous than those in ellipticals. However, van den Bergh & Pierce (1992) show that this conclusion depends critically on the values for the intrinsic colors that are assumed for SNe Ia. Such uncertainties are avoided in spectroscopic studies of supernovae.

In a recent paper Branch & van den Bergh (1993) have shown that *the expansion velocities of SNe Ia appear to correlate with Hubble type, in the sense that supernovae in early-type galaxies tend to have lower expansion velocities than do those that occur in late-type galaxies.* All seven SNe Ia with expansion velocities at 10 days past maximum V(10) < 9 500 km s^{-1} occurred in early-type (E,S0,Sa) galaxies. On the other hand only two out of 26 (12%) of the SNe Ia with V(10) $\geq$ 9 500 km s^{-1} occurred in E - Sa galaxies. Taken at face value this observation suggests that SNe Ia with low expansion velocities may belong to an older stellar population than do those with high expansion velocities. This conclusion is consistent with the observation that the SNe Ia in elliptical galaxies

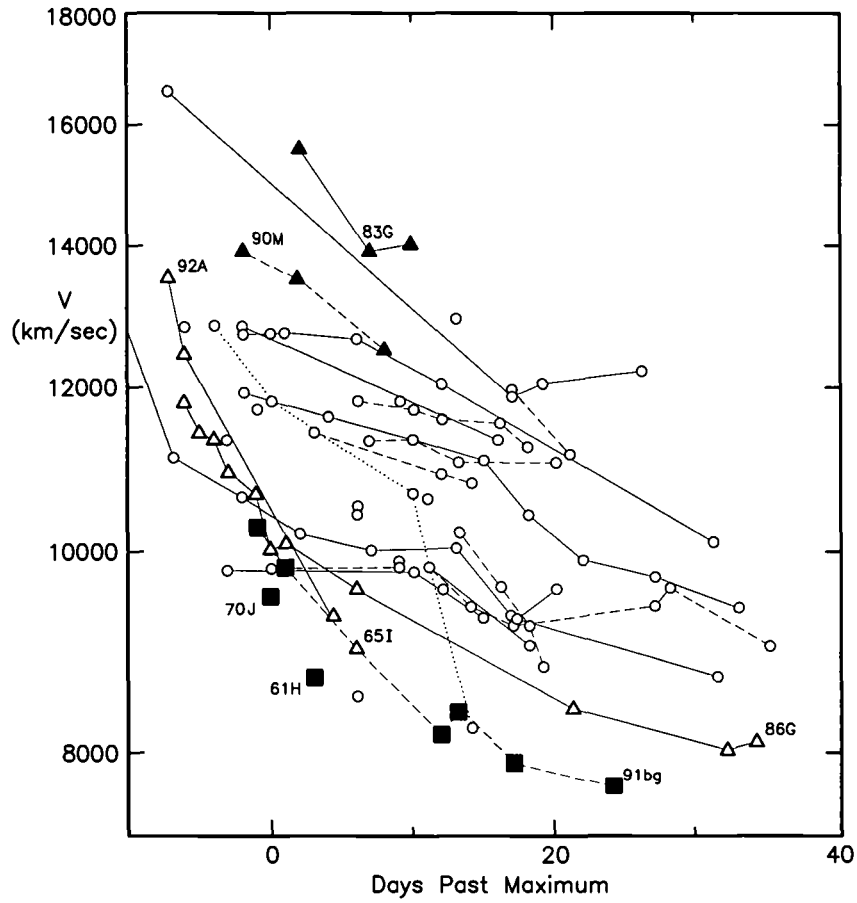

Figure 1. Expansion velocity versus time for supernovae of type Ia. [Adapted from Branch & van den Bergh (1993)]. Points joined by thin lines belong to a single supernova. Note that the SNe Ia in elliptical galaxies (squares) fall below those that occur in other types of galaxies.

all had particularly low velocities of expansion at 10 days past maximum: 8 300 km s^{-1} for SN 1961H in NGC 4564, and 8 500 km s^{-1} for SN 1991bg in NGC 4374, and 8 700 km s^{-1} for SN 1970J in NGC 7619. Fig. 1 shows that the SNe Ia in elliptical galaxies lie along the lower boundary of the observed V(exp) versus expansion age distribution.

The only known exceptions to the rule that SNe Ia in early-type galaxies have low expansion velocities are SN 1983G in NGC 4753 [V(10) = 13 600 km s^{-1}], and SN 1990M in NGC 5493 [V(10) = 12 220 km s^{-1}]. Véron & Véron-Cetty (1985) note that NGC 5493 is one of the three bluest objects in the sample of 69 giant E and S0 galaxies for which they obtained UBV photometry. This result suggests that NGC 5493 contains a sizable young or intermediate-age population with which SN 1990M might have been associated. From the structure of the dust lanes in the very peculiar S0 galaxy NGC 4753 Steiman-Cameron, Kormendy & Durisen (1992) conclude that this galaxy captured a gas- and dust-rich dwarf (0.5 - 1.0) Gyr ago. Possibly the progenitor of the very fast-expanding SN 1983G was a member of the intermediate-age population of this dwarf, or of the star burst population associated with its capture.

It has been noted previously (Oemler & Tinsley 1979, Thompson 1981, van den Bergh & Tammann 1991) that the frequency of SNe Ia appears to be particularly high in

amorphous (Sandage & Brucato 1979) galaxies, which are a subset of the galaxies referred to as I0 by de Vaucouleurs (1959). On deep exposures many of these galaxies show the light distribution that is characteristic of elliptical galaxies (Caldwell 1982). This suggests (Véron & Véron-Cetty 1985) that such objects are E or S0 galaxies in which the true underlying morphology is veiled by dust and overshadowed by the afterglow of a violent burst of star formation that took place in the relatively recent past. Van den Bergh (1980) has, for example, proposed that the amorphous galaxy NGC 5253 experienced a violent burst of star formation after it captured gas from M83 between 0.1 Gyr and 1.0 Gyr ago. In particular he suggested that the occurrence of two SN Ia (1895B and 1972E) in this relatively faint object during the past century was due to the high rate of star formation in this galaxy in the recent past. The fact that the expansion velocity of SN 1972E [V(10) = 10 700 km s^{-1}] was not low is consistent with the hypothesis that only those SNe Ia with low expansion velocities are produced by progenitors that belong to an old stellar population. If the speculations outlined above are correct then a high rate of SNe Ia with large expansion velocities is diagnostic of objects that have experienced a starburst in their recent past (van den Bergh 1993).

4. Supernovae in Distant Blue Galaxies

Recently a number of investigations (Broadhurst, Ellis & Shanks 1988, Colless *et al.* 1990, Lilly, Cowie & Gardner 1991) have found that the number of faint blue galaxies grows more rapidly than expected with increasing lookback time. The number of such objects appears to be 3 to 5 times greater than would be expected from linear extrapolation of the present population of galaxies under the assumption of no evolution (Cowie, Songaila & Hu 1991). At B $\sim$ 23 these blue galaxies are typically observed to have redshift z $\sim$ 0.25 and a median luminosity $M_B \simeq$ -17.5 (H_o = 75 km s^{-1} Mpc^{-1} assumed). A magnitude-selected sample of such faint blue galaxies therefore comprises objects which typically have luminosities comparable to that of the Large Magellanic Cloud (LMC).

There are a number of reasons for suspecting that the blue galaxies at z $\sim$ 0.25 might exhibit a high supernova rate:

(*a*) Many of these objects are probably experiencing starbursts at the present time. They should therefore be producing SNe Ibc and SNe II (which have massive progenitors) at a high rate. Furthermore both theory (Greggio & Renzini 1983) and observations of NGC 5253, which has produced two SNe I during the last century, suggest (van den Bergh 1980) that the SN Ia rate may be greatly enhanced a few hundred million years after a starburst.

(*b*) Supernova in distant blue (dwarf) galaxies will typically have M(max) values that are brighter than, or comparable to, those of their parent galaxies. This should facilitate the discovery of such supernovae.

(*c*) If the blue galaxies at intermediate redshifts are currently undergoing bursts of star formation then their equilibrium (post-starburst) luminosities will be quite low. Such intrinsically faint galaxies are known (van den Bergh & Pierce 1990) to have a low dust content. Their supernovae will therefore not be significantly dimmed by interstellar absorption.

A lower limit to the supernova frequency in faint blue galaxies at B $\sim$ 23 can be obtained by assuming that these objects are similar to nearby galaxies of types Sbc - Sd. Table 1 suggests that such galaxies have supernova rates of 1 to 2 SNu.

Note that time dilation will increase the discovery probability of distant supernova because their lightcurves are stretched by a factor of 1 + z. However, this advantage is nullified by a change in the supernova rates by a factor of $(1 + z)^{-1}$. A search for

supernovae at cosmological distances has recently been started by Couch *et al.* (1992). After maximum light some supernova spectra are observed to contain relatively little energy at $\lambda < 4000$ Å. This suggests that searches for supernovae with $z < 0.5$ are best carried out in the R passband. For nearer galaxies searches for supernovae in the red (Muller *et al.* 1992) will also benefit from lower absorption at longer wavelengths.

Acknowledgements

I thank Drs. Cappellaro, Fesen, Hamilton, Strom, Trimble, Weiler and Wu for helpful comments, preprints and (or) suggestions.

REFERENCES

Bandiera, R. 1987, ApJ, 319, 885

Bandiera, R., & van den Bergh, S. 1991, ApJ, 374, 186

Becker, R.H., Helfand, D.J., & Szymowiak, A.E. 1982, ApJ, 255, 557

Branch, D., Nomoto, K., & Filippenko, A.V. 1991 Comments Astrophys. 15, 221

Branch, D., & van den Bergh, S. 1993, AJ, 105, 2231

Braun, R., 1987 A&A, 171, 233

Broadhurst, T.J., Ellis, R.S., & Shanks, T. 1988, MNRAS, 235, 827

Caldwell, C.N. 1982, unpublished Ph.D. Thesis, Yale University

Cappellaro, E., Turatto, M., Benetti, S., Tsvetkov, D.Yu., Bartunov, O.S., & Makarova, I.N. 1993a, A&A, 268, 472

Cappellaro, E., Turatto, M., Benetti, S., Tsvetkov, D.Yu., Bartunov, O.S., & Markarova, I.N. 1993b, A&A, 273, 383

Clark, D.H. & Stephenson, F.R. 1977, The Historical Supernovae, (Oxford: Pergamon) pp.161-171

Colless, M., Ellis, R.S., Taylor, K., & Hook, R.N. 1990, MNRAS, 244, 408

Couch, W.J., Perlmutter, S., Newburg, H.J.M., Pennypacker, C., Goldhaber, G., Muller, R., & Boyle, B.J. 1992, Proc. Astron. Soc. Australia, 9, 261

Cowie, L.L., Songaila, A., & Hu, E.M. 1991, Nature, 354, 460

Davidson, K., & Fesen, R.A. 1985, ARAA, 23, 119

de Vaucouleurs, G. 1959, Handb. d. Physik, 53, 275

de Vaucouleurs, G. 1985, ApJ, 289, 5

Ellis, J., & Schramm, D.N. 1993, preprint

Evans, R., van den Bergh, S., & McClure, R.D. 1989, ApJ, 345, 752

Fesen, R.A., Becker, R.H. & Blair, W.P. 1987, ApJ, 313, 378

Fesen, R.A., Becker, R.H., & Goodrich, R.W. 1988, ApJ, 329, L89

Green, D.A., & Gull, S.F., 1982, Nature, 299, 606

Greggio, L., & Renzini, A. 1983, A&A, 118, 217

Hamilton, A.J.S., & Fesen, R.A. 1988, ApJ, 327, 178

Kaastra, J.S., 1993, private communication

Kaastra, J.S., Asaoka, I., Koyama, K., & Yamauchi, S. 1992, A&A, 264, 654

Leonard, P.J.T., & Dewey, R.J. 1993, BAAS, 24, 1177

Leonard, P.J.T., & Duncan, M.J. 1988, AJ, 96, 222

Lilly, S.J., Cowie, L.L., & Gardner, J.P. 1991, ApJ, 369, 79

Muller, R.A., Newberg, H.J.M., Pennypacker, C.R., Perlmutter, S., Sasseen, T.P., & Smith, C.K. 1992, ApJ, 384, L9

Oemler, A., & Tinsley, B.M. 1979, AJ, 84, 985

Öpik, E. 1953, Irish A.J., 2, 219

Ratnatunga, K.U., & van den Bergh, S. 1989, ApJ, 343, 713

Sandage, A., & Brucato, R. 1979, AJ, 84, 472

Scalo, J.M. 1986, Fund. Cosmic Phys. 11, 1

Shaw, R.L. 1979, A&A, 76, 188

Smith, C.R., Kirsher, R.P., Blair, W.P., & Winkler, P.F. 1991, ApJ, 375, 650

Steiman-Cameron, T.Y., Kormendy, J., & Durisen, R.H. 1992, AJ, 104, 1339

Stephenson, F.R. 1971, QJRAS, 12, 10

Strom, R.G., 1988, MNRAS, 230, 331

Tammann, G.A. 1974 in Supernovae and Supernova Remnants ed. C.B. Cosmovici (Dordrecht: Reidel) p.155

Tammann, G.A. 1982 in Supernovae: A Survey of Current Research eds. M.J. Rees and R.J. Stonehouse (Dordrecht: Reidel) p.371

Tammann, G.A. 1992, preprint of Les Houches Summer Course Lecture

Thompson, L.A. 1981, PASP, 93, 176

Trimble, V. 1968, AJ, 73, 535

van den Bergh, S. 1971, ApJ, 165, 457

van den Bergh, S. 1980, PASP, 92, 122

van den Bergh, S., 1988, Comments Astrophys., 12, 131

van den Bergh, S., 1989, AJ, 101, 845

van den Bergh, S., 1990, A&A, 231, L27

van den Bergh, S. 1991, Physics Reports, 204, 386

van den Bergh, S. 1992, ApJ, 390, 133

van den Bergh, S. 1993, in preparation

van den Bergh, S. 1994, in preparation

van den Bergh, S., & McClure, R.D. 1990, ApJ, 359, 277

van den Bergh, S., McClure, R.D., & Evans, R. 1987, ApJ, 323, 44

van den Bergh, S., & Pazder, J. 1992, ApJ, 390, 34

van den Bergh, S., & Pierce, M.J. 1990, ApJ, 364, 444

van den Bergh, S., & Pierce, M.J. 1992, PASP, 104, 408

van den Bergh, S., & Tammann, G.A. 1991, ARAA, 29, 363

Van Dyk, S.D. 1992, AJ, 103, 1788

Véron, P., & Véron-Cetty, M.-P. 1985, A&A, 145, 433

Wang, Z.R., Liu, J.Y., Gorenstein, P., & Zombeck, M.V. 1986 in Highlights of Astronomy, ed. J.-P. Swings (Dordrecht: Reidel) p. 583

Weiler, K.W., & Sramek, R.A. 1988, ARAA, 26, 295

Wilson, A.S., & Weiler, K.W. 1976, A&A, 53, 89

Woltjer, L. 1958, Bull. Astr. Inst. Netherlands, 14, 39

Wu, C.C., Crenshaw, D.M., Fesen, R.A., Hamilton, A.J.S., & Sarazin, C.L. 1993, ApJ, 416, 27

Zwicky, F. 1938, ApJ, 88, 529

Light Curves of Supernovae

By BRUNO LIEBUNDGUT†

Department of Astronomy, University of California
Berkeley, CA 94720, USA

Although emerging from a range of progenitor stars and the product of different explosion mechanisms the light curves of the various supernova types are shaped mainly by radioactive power. Core-collapse supernovae have in addition early peaks from shock breakout with a subsequent cooling phase and massive extended stars a recombination (plateau) phase. Variations occur mostly due to differences of the progenitor stars. While there appears to be a fair understanding of the light curves of SNe II, new wrinkles are emerging for SNe Ia. The photometry of SNe Ib and SNe Ic remains unsatisfactory.

1. Introduction

The temporal brightness variation of supernovae (SNe) as measured by photometry contains valuable and unique information on the evolution of the progenitor star and the explosion event. Combined with optical spectroscopy broad-band light curves have been the main tools for supernova investigations in the past (e.g. Minkowski 1964, Woosley & Weaver 1986, Wheeler & Harkness 1990, Kirshner 1990). The light curves are shaped by the size and mass of the progenitor star, various processes within the explosion itself, the radioactive ashes, and, in certain cases, the local environment.

Accurate photometry is mandatory to disentangle the physics driving the emission and the colors provide information on the temperature evolution. Telltale deviations from blackbody emission arise from the effects of the rapidly expanding atmosphere. The decline rates at different epochs and for supernovae of different types are indicative of the power sources, the explosion energy, and the envelope mass. Long after the explosion the light curves probe energy inputs from pulsars, long-lived radioactive isotopes, and shock-interaction with circumstellar material. Finding photometric differences between and within classes of supernovae hinges on the accuracy of the observations, and has hampered such investigations. Finally, photometry is needed for the use of supernovae as distance indicators. The expanding photosphere method (Schmidt *et al.* 1992) rests on reliable color and magnitude information. The hypothesis of SNe Ia as standard candles can be tested with good photometry only.

Obtaining accurate photometric observations of supernovae is not a trivial pursuit. Among the more common problems are unfavorable weather conditions hampering a detailed sampling of the light curve, the disappearance of the object behind the sun for extended periods of time, the complicated brightness structure of the background, combination of different data sets acquired by different observers at different telescopes and with different equipment, and the faintness of most objects. A case in point is SN 1987A, circumpolar for many southern observatories, for which large homogeneous data sets have become available sampling the light curves all year round (e.g., Bouchet *et al.* 1991, Suntzeff *et al.* 1991). The possibility to construct a bolometric light curve for SN 1987A has proven essential to compare the observations with detailed theoretical models (c.f. Arnett *et al.* 1990, McCray 1993 for reviews).

† Present Address: European Southern Observatory, Karl-Schwarzschild-Strasse 2, D–8046 Garching bei München, Germany

Large compilations of broad-band photometric data have been collected and are the basis for comparative studies (Young & Branch 1989, Leibundgut *et al.* 1991c, Patat *et al.* 1993). Such atlases have proven useful while uncovering the limitations of old data at the same time. The addition of new high-quality light curves is highly desirable and is under way at several observatories.

In the following we will first discuss the light curves of type II supernovae (§2), before concentrating on SNe Ia (§3). The state of photometry on SNe Ib/c will briefly be described in section 4. Conclusions are presented in the last section (§5).

2. Type II Supernovae

The light curves of these supernovae have been proposed for a subclassification scheme (Barbon *et al.* 1979, Doggett & Branch 1985, Young & Branch 1989). Some events exhibit a constant brightness for several weeks after maximum light, while others decline at a more or less constant rate. This separation into plateau (II–P) and linear (II–L) light curve types has been applied to many objects (Patat *et al.* 1993), but in the light of the physical models it might be more appropriate to drop such a distinction and assess the length of the plateau phase which depends on the envelope mass and the explosion energy. In the following we will discuss the physical processes dominating the emission of a "generic" light curve of a type II supernova, and point out the most prominent deviations observed to date. Much of the details have been learned from SN 1987A and the reader is referred to the relevant literature.

The optical display of a type II supernova starts with the shock breaking out at the surface of the progenitor star a few hours after core collapse. Up to this moment the star looks like any evolved supergiant, since the envelope does not have enough time to adjust to the rapid changes in the core at advanced burning stages. With the initial X-ray and UV burst the light curve peaks within hours before the cooling of the atmosphere decreases the flux very rapidly. The only observations of this phase we have to date are from SN 1987A (Kirshner *et al.* 1987, Arnett *et al.* 1989) and SN 1993J (c.f. contributions at this conference). For stars with expanded envelopes (red supergiants) this phase lasts longer than for more compact progenitors (Falk & Arnett 1977, Klein & Chevalier 1978). The steep drop following the peak is only stopped once the photosphere is balanced by the expansion of the ejecta. This results in the plateau phase which lasts as long as the photosphere does not run into the diffusion wave formed by decay of radioactive material in the core. The length of the plateau is mainly a function of the explosion energy, and thus the expansion velocity of the ejecta, and the depth of the envelope, i.e. its mass (Chugai 1991, Hsu *et al.* 1993). During this phase the colors of the supernova tend to remain constant implying a constant temperature (Schmidt *et al.* 1992). Once the photosphere has receded deep enough to encounter the additional heating from the decay of ^{56}Ni and ^{56}Co the plateau is extended for a short time (Woosley & Weaver 1986, Hsu *et al.* 1993), before the light curve starts declining at a constant rate. The transition between the plateau and the decline is determined by the decreasing optical depth to optical photons. For stars with massive envelopes all the energy released by the ^{56}Ni – ^{56}Co – ^{56}Fe decay chain is converted into optical emission and the bolometric light curve approaches a decline rate corresponding the life-time of ^{56}Co (Suntzeff & Bouchet 1990, Turatto *et al.* 1990, Schmidt *et al.* 1993). The deviations of SN 1987A and SN 1993J from this general picture point to different progenitor stars. SN 1987A was the explosion of a compact blue supergiant and much of the explosion energy went into overcoming the large potential energy. Thus, the photosphere receded very rapidly and no plateau was formed. The second broad maximum in the light curve was produced

by the heating from the ^{56}Ni and ^{56}Co decays. The large envelope mass resulted in the extended peak for this supernova. In the case of SN 1993J a rather small envelope mass prevented the formation of an extended recombination period and the second maximum was again formed by the diffusion wave from the radioactive decays. The reduced length of this peak also indicates a small envelope.

The decline rate at late times might be changed by dust formation (Lucy *et al.* 1991, Meikle *et al.* 1993) and the ionization freeze-out (Fransson & Kosma 1993) as observed in SN 1987A. The former shifts the flux from optical wavelengths into the infrared by heating of newly formed dust grains, while the second effect arises from the fact that the time of de-excitation becomes comparable to the expansion time of the supernova and this additionally "stored" energy becomes visible. Although probably not uncommon in other supernovae, these processes have been observed only in SN 1987A where they occurred ~6 and ~12 magnitudes below peak brightness.

Eventually, energy sources other than the γ-rays from ^{56}Co become important and shape the light curve. Prime candidates are long-lived radio-isotopes like ^{57}Co, ^{22}Na, and ^{44}Ti (Woosley *et al.* 1989), a buried pulsar loosing angular momentum and ionizing a plerion (Chevalier & Fransson 1992), light echos (Chevalier 1986, Chugai 1992), and shock-interaction with circumstellar matter (Chevalier 1990, Chugai 1992, Chevalier & Fransson 1994). Such changes have been observed in a few supernovae several years past explosion, most prominently in SN 1980K (Fesen & Becker 1990, Leibundgut *et al.* 1991b, Uomoto 1991) where the emission has remained steady at V~23 mag for the last three years. Other supernovae with similar light curves might be SN 1979C (Fesen & Matonick 1993) and SN 1970G (Fesen 1993). The most likely energy source in these cases is the shock heating the circumstellar material lost by the progenitor star as a stellar wind.

A group of SNe II displays remarkable deviations from the above scenario. The peaks of their light curves have never been observed and their decline rates are much smaller than what is expected from ^{56}Co decays. The best observed examples to date are SN 1986J (Rupen *et al.* 1987, Leibundgut *et al.* 1991b), SN 1987F (Filippenko 1989), and SN 1988Z (Stathakis & Sadler 1991, Filippenko 1991, Turatto *et al.* 1993). Although only SN 1988Z has a well-observed light curve (Turatto *et al.* 1993), the slow decline rates are also reflected in the evolution of line fluxes (Filippenko 1989, Leibundgut *et al.* 1991b, Turatto *et al.* 1993). The nature of the emission and its power source are not resolved, but interaction with a very dense material close to the supernova is most likely (Filippenko 1991, Chugai and Danziger 1994). All known objects of this class are evolving very slowly. It appears as if the interactions with the pre-supernova wind dominates the light curve from the start, thus obliterating other processes.

3. Type Ia Supernovae

The apparent homogeneity of SNe Ia has rendered most photometric subclassification useless. The proposed schemes were either too detailed for the available data (Pskovskii 1977, 1984) or not very meaningful (Barbon *et al.* 1973). The adoption of template light curves (Doggett & Branch 1985, Leibundgut 1988) has proven helpful for the comparison of individual events, while not being a satisfactory description for some. Recently the CTIO group has pointed out some severe deviations in the light curve shapes among well-observed SNe Ia (Phillips 1993, Suntzeff, this volume). They consist in different decline rates after maximum, variations in the time of maximum in different filters, and different shapes altogether - especially for the near-infrared light curves (Frogel *et al.* 1987, Suntzeff, this volume).

The physics of SNe Ia light curves has been discussed in several recent publications

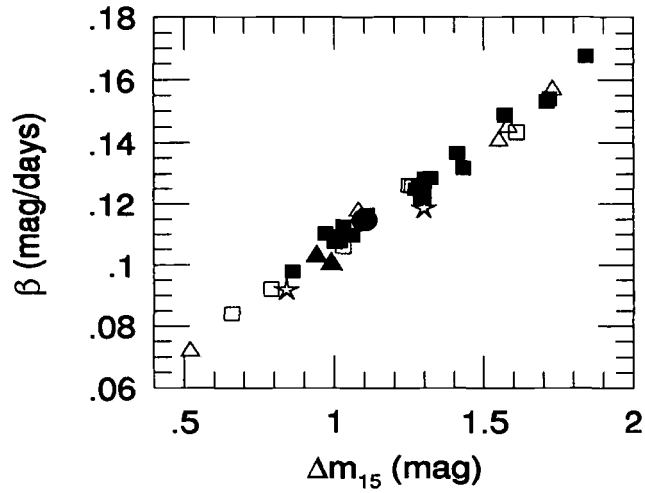

FIGURE 1. Decline rates vs. decline for the first 15 days past maximum. Filled symbols are for B data, while open symbols designate pg data. The squares are SNe Ia and the triangles SNe I. The filled dot is for the template light curve. Two SNe Ib/c are displayed as stars.

(Höflich *et al.* 1993, Khokhlov *et al.* 1993, Leibundgut & Pinto 1992). Although a completely different explosion mechanism is at work, the light curves are shaped not unlike certain phases of SNe II. Two main periods, determined by the optical depth for optical photons in the ejecta, can easily be distinguished: the peak phase, where the energy is diffusing out of the explosion, and the rapid decline after ~40 days past maximum, when the optically thin nebula is cooled by line emission. While this simple description has been valid for the U, B, and V light curves a distinctive "second peak" is observed in the J, H, and K light curves (Elias *et al.* 1981, 1985), and is also obvious in well-sampled R and I light curves (Suntzeff, this volume). The apparent flux redistribution remains unexplained to date.

Severe photometric disparities among SNe Ia have been observed recently. A large range in decline rates after maximum was found by Phillips (1993). To step beyond the template approach a fitting procedure was adopted by Vacca & Leibundgut (1994) that describes the UBV light curves as a gaussian atop a line to match the peak and late decline periods, respectively. This scheme allows to fit individual light curves to the available photometry of SNe Ia in an objective manner. The decline rates, as measured halfway down the initial decline of the light curves, are found to range from ~0.07 mag/day to ~0.17 mag/day and to correlate extremely well with the decline during the first 15 days past maximum as defined by Phillips (1993). Figure 1 displays this correlation for 32 SNe Ia and 8 SNe I (for which no subclassification was available). This vindicates the notion that there is an appreciable range of light curve shapes among SNe Ia.

The fitting procedure determines a number of additional parameters, such as, the peak magnitude, the time of maximum, the slope of the late-time decline, the magnitude drop until the inflection, and the time between maximum date and the inflection. The inflection is a well-defined parameter as it can be chosen to be some fraction of the contribution of the gaussian to the total flux (10% was adopted). Note that these parameters are defined by a mathematical model of the brightness evolution with a least squares procedure and are defined differently than the ones proposed by Pskovskii (1977, 1984). The fixed-shape template curves of Leibundgut (1988) agrees in general with the mean

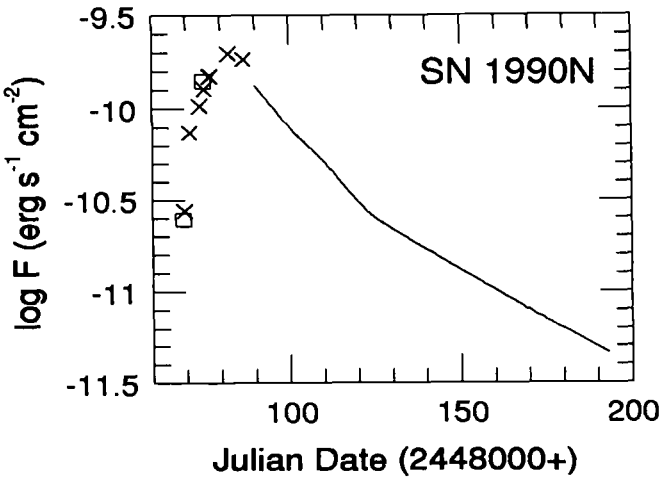

FIGURE 2. The bolometric light curve of SN 1990N. The crosses are UV observations added to the optical fluxes. The squares are direct integrations of UV and optical spectra. The solid line delineates the bolometric light curve derived from the templates

of the distributions of the parameters, but does not account for the observed range in the parameters.

Bolometric light curves for SNe Ia have been rare to date. Leibundgut & Pinto (1992) published a luminosity evolution based on the UBVJHK templates for SNe Ia. The biggest deficiency is the lack of R and I filter photometry and hence the large interpolation in the integration over the wavelengths. This is remedied by the superb data now becoming available (Suntzeff, this volume). Sufficient UV data is needed to determine the peak and are provided by the series of IUE spectra of SN 1990N (Leibundgut *et al.* 1991a) and IUE and HST spectra of SN 1992A (Kirshner *et al.* 1993). The UV contribution is ~10% of the total at the UV peak, but has an important effect on the date of maximum. The lack of infrared data during the maximum phase is unimportant since the fraction of the infrared flux is <5% at 5 days past B maximum and increases only later, while the contribution of the UV decreases after peak as the supernova becomes cooler. In Figure 2 we present the composite bolometric light curve of SN 1990N which includes the maximum. The bolometric light curve peaks approximately 2 to 3 days before B and, with the limits presented in Leibundgut *et al.* (1991a), we find a rise time of the bolometric light curve between 14 and 18 days. Only the slowest deflagration and delayed-detonation models straddle the lower end of this range (Khokhlov *et al.* 1993).

4. Supernovae Type Ib/c

The photometry of SNe Ib and SNe Ic has been buried among the data of SNe Ia for a long time. Very few light curves of these objects are available (c.f. Porter & Filippenko 1987, Swartz & Wheeler 1991, Kirshner 1990). Most of these are sampled poorly so that direct comparisons are difficult. For example, Vacca & Leibundgut (1994) find only two SNe Ib/c with sufficient B/pg photometry to fit their model curves. A difference in the decline rates at late epochs between SNe Ib and SNe Ic has been suggested (Swartz & Wheeler 1991), but has yet to be confirmed with accurate photometry.

The physics of SNe Ib/c light curves is very similar to that of SNe II, since they are presumably also core collapse objects. The peak from the breakout is reduced due to the compact nature of the progenitor and the absence of a substantial envelope (Ensman

& Woosley 1988, Nomoto *et al.* 1990) which also suppresses an extended recombination phase in the light curves. A broad peak is formed much like in SN 1987A and SNe Ia by the diffusion wave. An important diagnostic for the envelope masses will be the decline rates at late times. The light curve of SN 1993J is probably much like a type Ib/c light curve (Wheeler & Filippenko, this volume).

5. Conclusions

The last few years have seen appreciable progress in integrating observations and models. Bright supernovae with an abundance of data have allowed to improve models and develop some of their details. Light curves have been a mainstay for this advance. Bolometric light curves represent the most direct comparison between models and observations. Their construction for SNe II has been eased by improved hydrodynamic calculations that provide "bolometric corrections." The individuality of these supernovae will further increase the range of different characteristics of these explosions and their progenitor stars.

The photometric homogeneity of SNe Ia is put to test with the improved R and I light curves now obtained regularly. Eventually the dominance of B and V data will be replaced by a panchromatic view, and much needed bolometric light curves for individual objects will become available. Whether there exists a large fraction of SNe Ia with very similar behavior, or whether the class stretches evenly across the observed range, will only be answered with good light curves.

SNe Ib/c are photometrically still indistinguishable from SNe Ia in the optical, although they are physically probably more related to SNe II. More data is needed for support of modeling efforts and SN 1993J is a promising candidate for a study of such events.

No attention has been given to external effects which can change the shape of light curves. Background contamination can be a severe problem (Boisseau & Wheeler 1991), which, however, can be tackled with modern photometry programs. Absorption and reddening plague the discussion of homogeneity and the determination of absolute luminosities. They also can change the shape of the light curve due to the strong color evolution of supernovae (Leibundgut 1988). Differences in filter passbands can cause confusion (Menzies 1989, Hamuy *et al.* 1990). Finally, cosmological redshifts affect the light curves of very distant SNe (Hamuy *et al.* 1993).

The combination of photometry and spectroscopy remains a very powerful tool for the analysis of supernovae. With both at hand the progress in our understanding of these fireworks in the universe will be ensured.

Acknowledgements

I am indebted to J. Hsu, P. Pinto, and W. Vacca for many helpful discussions of supernova light curves. Financial support from the Swiss National Science Foundation and NSF grant AST-9115174 are acknowledged.

REFERENCES

Arnett, W. D., Bahcall, J. N., Kirshner, R. P., & Woosley, S. E. 1989, ARA& A 27, 629

Barbon, R., Ciatti, F., & Rosino, L. 1973, A& A 25, 65

Barbon, R., Ciatti, F., & Rosino, L. 1979, A& A 72, 287

Boisseau, J. R. & Wheeler, J. C. 1991, AJ 101, 1281.

Bouchet, P., Danziger, I. J., & Lucy, L. B. 1991, AJ, 102, 1135

Chevalier, R. A. 1986, ApJ 308, 225

Chevalier, R. A. 1990, Supernovae, ed. A. G. Petschek (Springer-Verlag, New York), p. 91

Chevalier, R. A. & Fransson, C. 1992, ApJ 395, 540.

Chevalier, R. A. & Fransson, C. 1994, ApJ, 420, 268

Chugai, N. N. 1991, Sov. Ast. Lett. 17, 210

Chugai, N. N. 1992, Sov. Ast. 36, 63

Chugai, N. N. & Danziger, I. J. 1994, MNRAS, 268, 173.

Doggett, J. B. & Branch, D. 1985, AJ 90, 2303

Elias, J. H., Frogel, J. A., Hackwell, J. A., & Persson, S. E. 1981, ApJ, 251, L 13

Elias, J. H., Matthews, K., Neugebauer, G., & Persson, S. E. 1985, ApJ, 196, 379.

Ensman, L. M. & Woosley, S. E. 1988, ApJ, 333, 754.

Falk, S. W. & Arnett, W. D. 1977, ApJS, 33, 515.

Fesen, R. A. 1993, ApJ, 413, L109

Fesen, R. A. & Becker, R. H. 1990, ApJ, 351, 437

Fesen, R. A. & Matonick, D. M. 1993, ApJ, 407, 110

Filippenko, A. V. 1989, AJ, 97, 726

Filippenko, A. V. 1991, SN1987A and Other Supernovae, eds. I. J. Danziger & K. Kjär (ESO, Garching), p. 343

Fransson, C. & Kosma, C. 1993, ApJ, 408, L25

Frogel, J. A., Gregory, B., Kawara, K., Laney, D., Phillips, M. M., Terndrup, D., Vrba, F., & Whitford, A. E. 1987, ApJ, 315, L129

Hamuy, M., Suntzeff, N. B., Bravo, J., & Phillips, M. M. 1990, PASP, 102, 888

Hamuy, M., Phillips, M. M., Wells, L. A., & Maza, J. 1993, PASP, 105, 787

Höflich, P., Khokhlov, A., & Müller, E. 1993, A& A, 268, 570

Hsu, J. J. L., Joss, P. C., Ross, R. R., & Podsiadlowski, P. 1994, Nature 364, 509

Khokhlov, A., Müller, E., & Höflich, P. 1993, A& A, 270, 223

Kirshner, R. P. 1990, Supernovae, ed. A. G. Petschek (Springer-Verlag, New York), p. 59

Kirshner, R. P., *et al.* 1993, ApJ, 415, 589

Kirshner, R. P., Sonneborn, G., Crenshaw, D. M., & Nassiopoulos, G. E. 1987, ApJ, 320, 602

Klein, R. I. & Chevalier, R. A. 1978, ApJ 223, L109

Leibundgut, B. 1988, Ph.D. Thesis, University of Basel

Leibundgut, B., Kirshner, R. P., Filippenko, A. V., Shields, J. C., Foltz, C. B., Phillips, M. M., & Sonneborn, G. 1991a, ApJ, 371, L23

Leibundgut, B., Kirshner, R. P., Pinto, P. A., Rupen, M. P., Smith, R. C., Gunn, J. E., & Schneider, D. P. 1991b, ApJ, 372, 531

Leibundgut, B. & Pinto, P. A. 1992, ApJ, 401, 49

Leibundgut, B., Tammann, G. A., Cadonau, R., & Cerrito, D. 1991c, A& AS, 89, 537

Lucy, L. B., Danziger, I. J., Gouiffes, C., & Bouchet, P. 1991, Supernovae, ed. S. E. Woosley (Springer-Verlag, New York), p. 82

McCray, R. 1993, ARA& A, 31, 175

Meikle, W. P. S., Spyromilio, J., Allen, D. A., Varani, G.-F., & Cumming, R. J. 1993, MNRAS, 261, 535

Menzies, J. W. 1989, MNRAS, 237, 21p

Minkowski, R. (1 964, ARA & A, 2, 247

Nomoto, K., Filippenko, A. V., & Shigeyama, T. 1990, A& A, 240, Ll

Patat, F., Barbon, R., Cappellaro, R., & Turatto, M. 1993, A& AS, 98, 443

Phillips, M. M. 1993, ApJ, 413, L105

Porter, A. C. & Filippenko, A. V. 1987, AJ, 93, 1372

Pskovskii, Y. P. 1977, Soviet Ast., 21, 675

Pskovskii, Y. P. 1984, Soviet Ast., 28, 658

Rupen, M. P., van Gorkom, J. H., Knapp, G. R., Gunn, J. E., & Schneider, D. P. 1987, AJ, 94, 61

Schmidt, B. P., Kirshner, R. P., & Eastman, R. G. 1992, ApJ, 395, 366

Schmidt, B. P., *et al.* 1993, AJ, 105, 2236

Stathakis, R. A. & Sadler, E. M. 1991, MNRAS, 250, 786

Suntzeff, N. B. & Bouchet, P. 1990, AJ, 99, 650

Suntzeff, N. B., Phillips, M. M., Depoy, D. L., Elias, J. H., & Walker, A. R. 1991, AJ, 102, 1118

Swartz, D. A. & Wheeler, J. C. 1991, ApJ, 379, L13

Turatto, M., Cappellaro, E., Barbon, R., Della Valle, M., Ortolani, S., & Rosino, L. 1990, AJ, 100, 771

Turatto, M., Cappellaro, E., Danziger, I. J., Benetti, S., Gouiffes, C., & Della Valle, M. 1993, MNRAS, 262, 128

Uomoto, A. 1991, AJ, 101, 1275

Vacca, W. D. & Leibundgut, B. 1994, ApJ, in preparation.

Wheeler, J. C. & Harkness, R. P. 1990, Rep. Prog. Phys., 53, 1467

Woosley, S. E., Pinto, P. A., & Ensman, L. M. 1988, ApJ, 324, 466

Woosley, S. E., Pinto, P. A., & Hartmann, D. 1989, ApJ, 346, 395

Woosley, S. E. & Weaver, T. A. 1986, ARA& A, 24, 205

Young, T.R. & Branch, D. 1989, ApJ, 342, L79

Supernovae and the Cosmic Distance Scale

By ROBERT P. KIRSHNER

Harvard-Smithsonian Center for Astrophysics
60 Garden St., Cambridge, MA 02138, USA

Knowledge of the size and age of the Universe depends on understanding supernovae. The direct geometric measurement of the circumstellar ring of SN 1987A using IUE spectra and HST images provides an independent test of the Cepheid distance scale to the Large Magellanic Cloud. Understanding the details of the mass distribution in the circumstellar matter is important to improving the precision of this distance. Type Ia supernovae have a narrow distribution in absolute magnitude, and new Cepheid distances to IC 4182 (the site of SN 1937C) and to NGC 5253 (the site of SN 1972E) obtained with HST by Sandage and his collaborators allow that absolute magnitude to be calibrated. Comparison with more distant SN Ia gives $H_0 = 56 \pm 8$ km s^{-1} Mpc^{-1}. Recent work in supernova spectroscopy and photometry shows that the apparent homogeneity of SN Ia is not quite what it seems, and a deeper understanding of these variations is needed to use the SN Ia to best advantage. The Expanding Photosphere Method (EPM) allows direct measurement to each Type II supernova that has adequate photometry and spectroscopy. There are now 18 such objects. The sample of EPM distances from 4.5 Mpc to 180 Mpc indicates $H_0 = 73 \pm 6$(statistical)± 7(systematic) km s^{-1} Mpc^{-1}. Better understanding of supernova atmospheres can reduce the systematic error in this approach, which is completely independent of all other astronomical distances.

1. Introduction

Measuring the Hubble Constant is one of the goals of observational cosmology. Supernova observations provide powerful and diverse ways to approach this problem. In recent years, work done on Planetary Nebula Luminosity Functions, Surface Brightness Fluctuations, and the Line-Width Luminosity Relation has reached an apparent consensus on the value of the Hubble constant, $H_0 = 80 \pm 10$ km s^{-1} Mpc^{-1} (Jacoby *et al.* 1992). Yet, good arguments for a "long" distance scale have been advanced by Sandage *et al.* (1992, 1994) using SNe Ia as standard candles. If H_0 really is 80 km s^{-1} Mpc^{-1}, and $\Omega_0 = 1$ as preferred by many, then the 8 billion year expansion age of the Universe implied by H_0 is substantially shorter than the lifetime of the oldest stars (Renzini 1991). Since there is disagreement among reliable workers, and our overall picture for cosmic evolution is at stake, it is useful to evaluate the distance scale using different approaches. Supernova 1987A helps to check the Cepheid scale, SN Ia form the basis for the standard candle approach, and the Expanding Photosphere Method applied to SN II provides independent distances that are now sufficiently numerous and accurate to be compared with other estimates of extragalactic distances.

2. The Ring Around SN 1987A and the Distance to the LMC

Supernova 1987A was assiduously studied with the IUE satellite (Pun *et al.* 1984), and one of the most interesting results was the detection of narrow emission lines in the UV, where emission from the supernova debris was very faint. These lines appeared after about 80 days, and grew in strength for about 400 days. Fransson *et al.* (1989) developed an interpretation of this emission, attributing it to fluorescence from a shell of material excited by the initial pulse of UV emission produced by the arrival of the shock

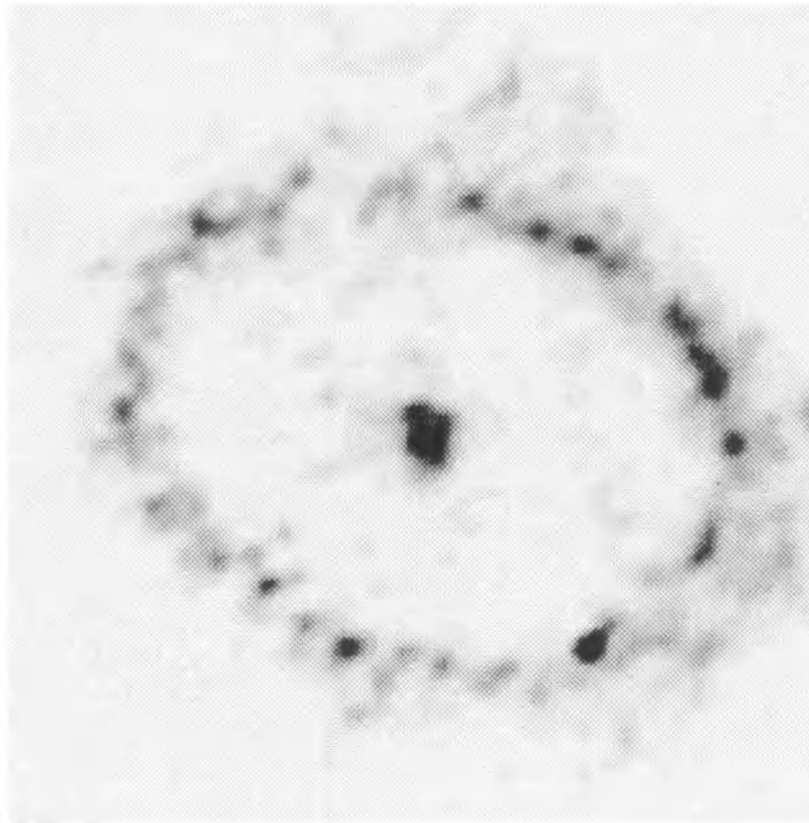

FIGURE 1. An image of the circumstellar ring around SN 1987A taken in the light of [O III] with the Faint Object Camera aboard the Hubble Space Telescope in May 1993.

wave at the surface of the B3 III star. The shell was inferred to lie at a distance of about 200 light days, half the time it took for the exciting pulse to reach the shell and then to reach the observer. In this picture, the emitting gas was a dense shell at the interface between the blue supergiant's wind and the earlier mass loss from the star when it was a red supergiant.

Ground-based observations, and observations with the Faint Object Camera on the Hubble Space Telescope showed that this picture was generally correct, but the details were even more interesting, as shown in Figure 1. Fransson *et al.* were parsimonious with their hypotheses: given a radius, they inferred a sphere. However, nature was more creative, and the surface brightness distribution of the emission indicates that the fluorescent material is more like a torus (Jakobsen *et al.* 1991). The elliptical appearance is most likely the projection of a circular ring, seen inclined at an angle of about 43 degrees.

Since the physical size of the ring can be inferred from the time delay as $1.27 \pm 0.07\ 10^{18}$ cm and the angular size of the major axis is 1.66 ± 0.03" , this gives the distance directly as 51.2 ± 3.1 kpc. This is consistent with the distance to the LMC based on Cepheids (Walker, 1987). Felten (in this conference) has considered a number of systematic effects that might alter the distance and its error estimate, and has drawn attention to the difference between the predicted and the observed time history of the fluorescent emission.

Gould (1993) has also examined this distance estimate and McCall (1993) has emphasized the location of SN 1987A in the LMC.

A complete understanding of the observed narrow-line emission and its time history is not yet in hand, but the HST data we have obtained from 1990 through 1993 will help. An analysis by Plait *et al.* (1994) of these FOC images helps determine the geometry of the ring and the inhomogeneity of the gas distribution.

A second geometric distance to the LMC will result from future HST measurements. We know the expansion velocity of the supernova debris and we are just beginning to measure the angular expansion from our FOC images. If the supernova debris is not too asymmetric, this should yield another direct determination of the distance to SN 1987A.

3. HST Calibration of SN Ia: How Standard the Candles?

Type Ia supernovae form a more-or-less homogeneous class of objects which shows a moderately narrow distribution in absolute magnitude (Branch and Miller 1993). This observational fact is plausible because theory suggests that SN Ia arise from the sudden thermonuclear burning of a carbon-oxygen white dwarf at the Chandrasekhar limit. In that case, the Type Ia event has a well-defined mass and composition and the resulting luminosity would be similar from one event to the next. If the luminosity of a single SN Ia could be determined from a measured distance and apparent magnitude, then the observed Hubble diagram for SN Ia could be used to determine the Hubble Constant.

A novel approach to this problem has been explored by Kirshner *et al.* (1987) and by Smith *et al.* (1991) who have used observations of the remnants of galactic supernovae to determine their distances by comparing observed proper motions with the shock velocity determined from a theory of non-radiative shocks. While this produces distances to SN 1006 and to Tycho's supernova of 1572, the photometry ("dazzling in brightness") is not sufficiently precise to serve as the fiducial point for cosmic distances.

A more conventional approach has been adopted by Sandage and his collaborators (1992, 1994) using the Hubble Space Telescope. They have used HST to search for Cepheid variables in galaxies which have had well-observed SN Ia. In particular, they have surveyed IC 4182, the site of SN 1937C, and NGC 5253, the site of SN 1972E and of SN 1895. The advantages of HST, even with spherical aberration, are that faint stars in crowded fields can be resolved and that the observing schedule is not subject to the same constraints that affect attempts to detect periodic sources from terrestrial sites. In IC 4182, the observations produced 27 Cepheids with periods ranging from 2 days to over 50 days, and in NGC 5253, there are 12 Cepheids with periods on the range from 4 to 16 days. By comparing the apparent magnitudes of these Cepheids with the local period-luminosity relation, Sandage *et al.* infer the distance to the galaxies and the absolute magnitude of SN Ia to be M_V = - 19.5. Using this value of the absolute magnitude to calibrate the Hubble diagram for SN Ia (Sandage and Tammann 1993), yields a value of the Hubble constant: $H_0 = 56 \pm 8$ km s^{-1} Mpc^{-1}.

This interesting result should be subjected to careful examination. Details of the Cepheid photometry and assumptions about reddening seem reasonable, but should be examined by people who are knowledgeable in those areas. The assumptions about supernovae point to interesting areas for future work. There is good evidence for the photometric and spectroscopic variation of SN Ia as reported by Phillips (1993) and by Suntzeff (this volume). In particular, SN 1991bg (Leibundgut *et al.* 1993) and SN 1991T (Phillips *et al.* 1992) appear to be examples SN Ia which are far from typical. This raises the question of whether there are intermediate types of slightly brighter and slightly fainter SN Ia which are lumped together in the usual Hubble diagram for SN Ia. Specif-

ically, it will be interesting to see whether SN 1937C or SN 1972E shares, to a lesser degree, the features of these not-quite-typical supernovae. In any case, it is essential to pursue the observation and analysis of SN Ia with modern detectors since good light curves and spectra will be essential to sorting out the connection between observable distance-independent supernova properties and supernova luminosities.

A correlation between, for example, the rate of decline after maximum light and the luminosity of a supernova is not all bad. If we have good data in hand and we develop an understanding of photometric and spectroscopic clues to the intrinsic luminosity of the event, we can use that information to reduce the scatter in the Hubble diagram and to improve the estimate of H_0 based on SN Ia. While a certain amount of skepticism toward any particular value of H_0 and an understanding that the errors may be larger than quoted is healthy, the deeper lesson may be that the mechanism of SN Ia events is not as thoroughly understood as we might like. In the case of SN 1991bg, Ruiz-Lapuente *et al.* (1993) have shown that the explosion of a star well below the Chandrasekhar limit may be the best explanation for the observations. If that is really correct, then theoretical homogeneity is too simple and should be replaced with an exploration of the theoretical possibilities as carried out by Höflich *et al.* (this volume).

4. The Expanding Photosphere Method: Custom Yardstick for the Cosmos

Kirshner & Kwan (1974) exploited a suggestion by Leonard Searle to use SNe II to measure extragalactic distances in a way that is completely independent of every other step in the cosmic distance ladder. This technique, the Expanding Photosphere Method (EPM), was applied to two nearby SNe II and produced distances consistent with $H_0 = 60$ km s^{-1} Mpc^{-1}. This work, which assumed SNe II emit like perfect blackbodies, was extended by Wagoner (1977), who demonstrated EPM could, in principle, be applied to SNe II at large redshifts to measure q_0. Branch *et al.* (1983) and Kirshner (1985) applied EPM to additional SNe II, but the limitations of these primitive results of EPM were highlighted by Wagoner (1981), who noted that SNe II have scattering-dominated atmospheres, and therefore radiate with a smaller surface flux than a blackbody with the same color temperature. EPM was lifted to solid theoretical and empirical ground after several groups produced sophisticated NLTE atmospheric models of SN 1987A (Eastman & Kirshner 1989; Höflich 1988; Schmutz *et al.* 1990; Chilkuri and Wagoner 1988) that gave distances to the LMC which agreed with those derived using Cepheid variable stars (Walker 1987) and with the geometric measurement described above. Schmidt, Kirshner & Eastman (1992) [SKE92] exploited the tools developed for SN 1987A to measure the distances to ten SNe II, and found these distances consistent with $H_0 = 60 \pm 10$ km s^{-1} Mpc^{-1}. Eastman, Schmidt & Kirshner (1994) [ESK94], have improved these distances using a large grid of models which are not specific to SN 1987A and its compact progenitor. The relation between color temperature and flux inferred from these models generally produces distances 10% smaller than those based on the cruder formulation by SKE92. The distance measurements reported here use these improved models. Recently, Schmidt *et al.* (1994a) demonstrated the range over which EPM could be applied by developing the technique for applying EPM on SNe II at large redshifts, and measuring the distance to SN 1992am at a redshift of $cz = 14\,600$ km s^{-1}. Additional EPM distances to five SNe II observed at Cerro Tololo Inter-American Observatory (CTIO) as part of the Calan/Tololo SN search and monitoring program being carried out as a collaborative effort between the University of Chile and CTIO (Hamuy *et al.* 1993) have been determined by Schmidt *et al.* (1994b). When combined with

previous studies, the new data brings the number of EPM distances to 18. These distances now extend from the LMC (D = 49 kpc) to SN 1992am (D = 180 Mpc) — an unparalleled range of distances for an extragalactic distance indicator. The host galaxies of these SNe II are typically spirals which, if not too distant or face-on, have distances which can be measured using the Line-Width Luminosity Relation (Tully and Fisher 1977). We compare EPM and Tully-Fisher distances to 11 galaxies which have distances measured both ways.

EPM has been discussed in detail by SKE92. They show that the photospheric angular size of a SNe II is given, for $z << 1$, by

$$\theta = \frac{R}{D} = \sqrt{\frac{f_\lambda}{\zeta_\lambda^2 \pi B_\lambda(T)}}, \tag{1}$$

where T is the SN's observed color temperature, f_λ is the observed flux density, $B_\lambda(T)$ is the Planck function evaluated at T, and ζ_λ is a distance correction factor derived from model atmospheres to account for the dilution effects of scattering atmospheres. SNe II expand freely at velocity, v (measured from the absorption minima of optically thin lines such as Fe II 5169), so that a supernova's photospheric radius, R, at any time, t, is

$$R = v(t - t_0) + R_0. \tag{2}$$

The initial radius,R_0, is negligible at all but the earliest epochs, and combining equations (1) and (2) yields

$$t = D\left(\frac{\theta}{v}\right) + t_0. \tag{3}$$

Given at least two measurements of t, θ, and v, determined from a calendar, photometry, and spectra, it is possible to solve for both the distance to the SN, D, and the time of explosion, t_0, simultaneously. It is also possible to test the performance of the method through equation (3) if several measurements of t, v, and θ are available; despite large changes in T, v, R, and θ, the distance D should remain constant.

SKE92 demonstrated that the distance correction factors, ζ_λ, as derived empirically, varied only as a function of color temperature, and not from supernova to supernova. ESK94 have investigated the effects of metallicity, progenitor mass, luminosity, density, and physical structure on the distance correction factor with a grid of 88 models, and found that $\zeta_\lambda(T)$ is not sensitive to details of the progenitor star. However, the new distance correction factors of ESK94 give 10% smaller distances on average than those determined from the models of SKE92.

SKE92 relied on the distance correction factors derived from SN 1987A's VI photometry in their formulation of $\zeta_\lambda(T)$. These distance correction factors were applied to objects for which only BV photometry was available. Although the values of $\zeta_\lambda(T)$ determined from BV and VI are similar, they are not identical, and this small difference is responsible for most of the systematic difference in the distances derived. In addition, SN 1987A , which resulted from the explosion of a compact progenitor, had a slightly different behavior of $\zeta_\lambda(T)$ than typical SNe II with larger initial radii. The custom-crafted models created for SN 1987A (Eastman & Kirshner 1989) are not quite in the center of the distribution of models, which cover a wide range of plausible initial conditions, computed by ESK94. The distance correction factors determined from models by ESK94 are superior to those of SKE92, and we adopt their formulation of $\zeta_\lambda(T)$.

SNe II occur in galaxies with recent star formation, and the effects of extinction cannot be ignored. SKE92 demonstrated that many SNe II have uniform color evolution during their photospheric phases ($\sim$ 100 days following explosion), and it is possible to estimate

the color excess, $E(B-V)$, with a scatter of 0.1 mag. Furthermore, the distances derived using EPM are affected by both attenuation and reddening of the light which cancel to a large extent. The uncertainty that extinction produces in a distance is usually less than 10%. In a worst case example, the distance to SN 1973R, which had more than 2.5 magnitudes of visual extinction, has a distance uncertainty due to extinction of about 20% (SKE92). EPM distances are not uniformly increased or decreased by extinction, but instead depend on the evolution of the SN and the spacing of the observations. Errors in the reddening are unlikely to bias the average result even when they add noise to individual distances.

We have employed both Monte Carlo and bootstrapping techniques to derive realistic errors for our distance measurements. These account very well for the measuring errors, but some of the uncertainty in EPM arises from systematic differences between the derived and actual values of parameters such as v_τ and ζ_λ. Except in pathological cases, these errors will cause θ/v vs. t to deviate from a straight line — if EPM is suffering severe systematic problems, they will be apparent. However, small systematic shifts, which are not time dependent, will not be so obvious, and require a more thoughtful analysis. Several groups have estimated the distance to SN 1987A using different models. The spread in distances suggests that EPM has systematic errors less than $\pm 10\%$. Aside from the measuring accuracy of the photometry and spectra, the precision of EPM depends on the age of the SN at the time of the first observations and the spacing of subsequent observations. Observations which begin within three weeks of the explosion date, and which continue on a regular basis (once per week) afterwards constrain the time of explosion and reduce the uncertainty in a derived distance. When we have a set of 5 or more observations, spaced a week apart, and of good quality (e.g. 5% photometry, absorption features clearly visible), the statistical error is smaller than the systematic uncertainties in EPM. In these cases, increasing the precision of the photometry and quality of the spectra, or increasing the observing frequency, will not improve the accuracy of the derived distances. Some of our recent observations have sufficiently good data that the estimated error in the distance approaches our uncertainty in the systematics of the method.

Some of the host galaxies for these SNe II are close enough that EPM can be compared to distances measured using conventional techniques such as Cepheids, while others are at twice the distance to Coma, so that perturbations in the Hubble flow should be small. In between, we can make a galaxy-by-galaxy comparison with Tully-Fisher distances. Three galaxies have Cepheid and EPM distances in common, the LMC (SN 1987A), M 81 (SN 1993J), and M 101 (SN 1970G). In the case of the LMC and M 101, the distances derived by the Cepheids, 49 ± 4 kpc (Walker 1987) and 7.1 ± 0.3 Mpc (Cook, Aaronson, and Illingworth 1986) respectively, are indistinguishable from those measured with EPM, 49 ± 6 kpc (Eastman & Kirshner 1989) and $7.4^{+1.0}_{-1.5}$ Mpc (ESK94). However, EPM appears to give a distance to M 81, 2.6 ± 0.4 Mpc (Schmidt *et al.* 1993), which is 25% smaller than that derived using Cepheids, 3.6 ± 0.4 Mpc (Freedman *et al.* 1994). It should be noted that SN 1993J has an atypical spectroscopic and photometric evolution which suggests the progenitor lost most of its hydrogen envelope before exploding. These observations, combined with evidence for asymmetry (Januzzi *et al.* 1993), suggest applying EPM to this object demands extreme care and models specific to the event. Baron *et al.* (1993) have specifically modeled SN 1993J, and derive a distance to the SN in perfect agreement with the Cepheid distance. However, the larger distance derived by this group may result from them placing the material which forms the photosphere at a higher velocity than that inferred from the Fe II $\lambda\lambda 5169$, 5018 absorption lines by Schmidt *et al.* (1993). A detailed comparison of the two sets of models is needed to sort out this discrepancy.

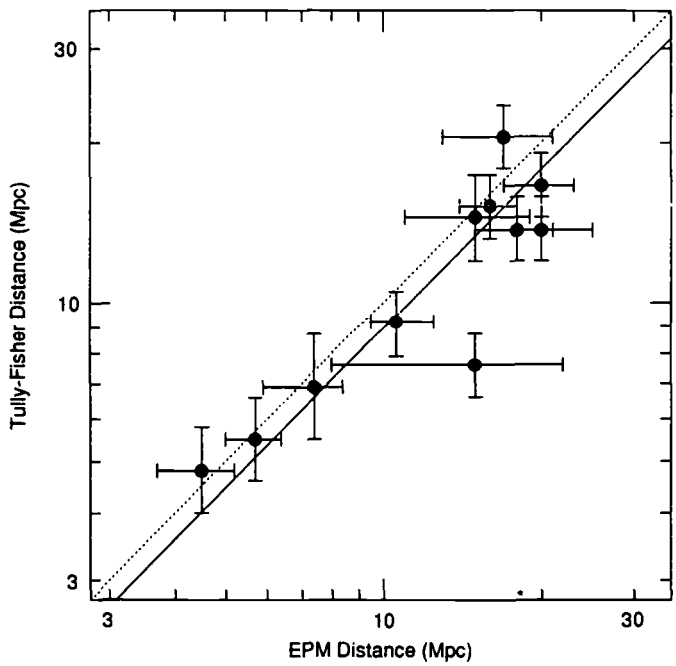

FIGURE 2. Comparison of distances for supernovae with EPM measurements and Tully-Fisher distances to the parent galaxies.

Two other SNe II, SN 1979C and SN 1986L, also have peculiar spectroscopic features (although not to the extent of SN 1993J).

Eleven galaxies have both EPM and Tully-Fisher (TF) distances. Following Pierce (1994), we plot the distances against each other in Figure 2, and find good correlation. However the TF distances average 11% ±7% smaller than those determined using EPM. This difference, which is marginally significant, is not surprising given that both Tully-Fisher or EPM may have systematic errors approaching 10% due to calibration (in the case of TF) and uncertainties in the physics of SNe II (EPM). More interestingly, the slope is unity, within the estimated uncertainties. This means there is no systematic difference between the distances derived by T-F and EPM nearby and far away. Because EPM does not make any standard candle assumption (and is therefore immune to the usual Malmquist Bias problems), the sample of T-F distances here also has no significant distance-dependent error. This conclusion differs from the view presented by Sandage (1994), who attributes the large value of the Hubble Constant obtained through Line-Width Luminosity Relations to Malmquist Bias.

The observed large scale perturbations in the Hubble flow (Aaronson *et al.* 1982; Lynden-Bell *et al.* 1988; Mathewson *et al.* 1992; Lauer and Postman 1993) make measuring H_0 from nearby galaxies a risky proposition. The Virgo cluster significantly affects the local Hubble flow (Aaronson *et al.* 1982), and most of our EPM sample have distances comparable or smaller than the distance to the Virgo Cluster. After correcting the observed heliocentric redshifts for each galaxy for Galactic rotation (220 km s^{-1}), we apply a non-linear infall model (Schechter 1980; SKE92) to the sample using a range of parameters discussed by Huchra (1988). Except for the two SNe which lie in the Virgo Cluster, SN 1979C and SN 1988A, the choice of these parameters does not strongly affect the derived recession velocities. SN 1987A and SN 1993J have redshifts which are

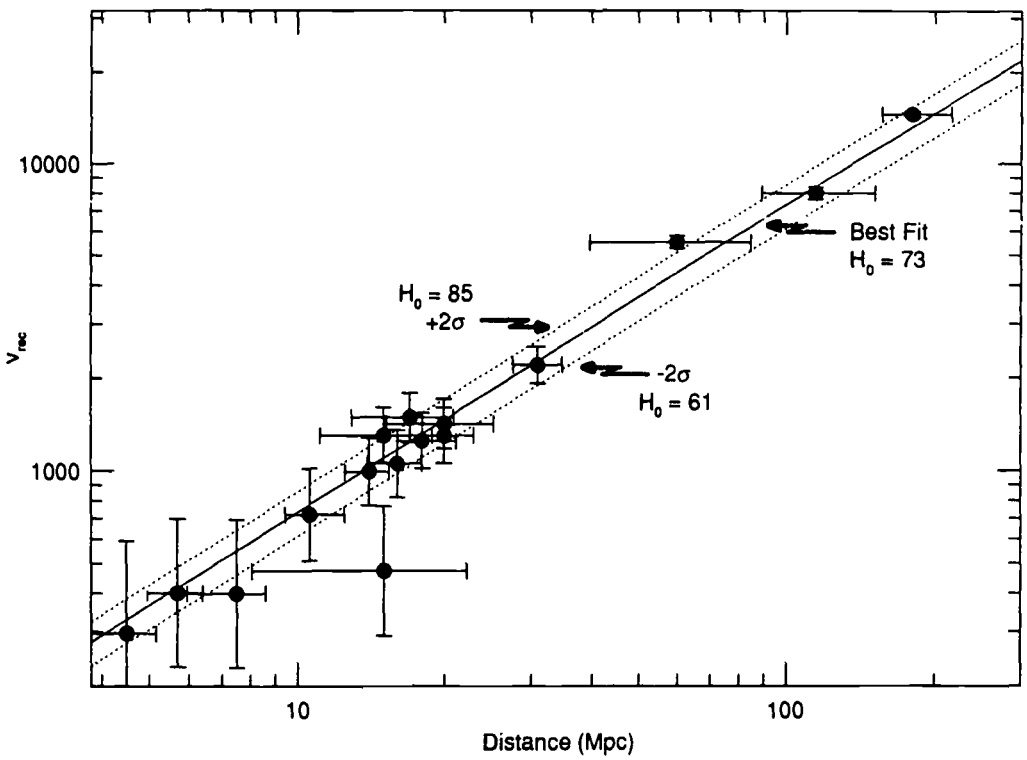

FIGURE 3. Hubble diagram based on EPM distances to SN II.

near zero or negative, and we exclude these objects in our determination of H_0. Using the EPM distances as shown in Figure 3, and assigning 300 km s^{-1} errors (representing uncertainties due to large scale peculiar motions not associated with Virgo infall) to all recession velocities, we derive a value of $H_0 = 73 \pm 6$ (statistical) km s^{-1} Mpc^{-1} , using the least-squares technique for data sets with errors in both directions described by Press *et al.* (1992). The value of H_0 derived from our sample depends somewhat on the velocity errors assigned to each galaxy, ranging from $H_0 = 70 \pm 3$ km s^{-1} Mpc^{-1}, if velocity errors are assumed to be zero, to $H_0 = 75 \pm 7$ km s^{-1} Mpc^{-1} if we assign errors of 600 km s^{-1} to each velocity measurement. The nearby galaxies in our sample give a smaller value of H_0 than those further away, and their weight depends on the error adopted. It is difficult to assign a realistic overall error to our value of H_0 because the statistical uncertainty of the measurement (8%) is of the same order as possible systematic uncertainties in EPM.

The Expanding Photosphere Method is subject to errors due to uncertainties in our understanding of SNe II physics. All of the distances used in this determination of H_0 are based on the atmospheric code developed by Eastman (Eastman & Kirshner 1989; Eastman & Pinto 1993). It may be possible to evaluate the accuracy of EPM by comparing the output of other atmospheric codes which make slightly different physical assumptions in computing model atmospheres. A limited comparison can be made in the case of SN 1987A, a SN which several groups modeled (Eastman & Kirshner 1989; Höflich 1988; Schmutz *et al.* 1990; Chilkuri and Wagoner 1988), where the agreement

is better than ±10%. Assigning an underlying uncertainty of ±10% to EPM, we find $H_0 = 73 \pm 6$(statistical) $\pm$ 7(systematic) km s^{-1} Mpc^{-1}.

The importance of SN searches to this program cannot be overstated. None of the five objects presented here was discovered accidentally: all were found as the result of systematic searches of galaxies for supernovae. As these searches continue, they will enable us to apply EPM to many SNe II at redshifts larger than cz = 5000 km s^{-1}. These objects, which will typically be between $17 < m_v < 20$ mag, combined with those already measured, will allow us to derive a value of H_0 which is robust against large-scale perturbations in the Hubble flow. In addition, there is no technical reason why we cannot apply EPM to SNe II discovered at redshifts beyond $z = 0.1$, giving us the possibility of a direct approach to measuring the deceleration parameter, q_0.

Acknowledgements

Many people do the work: just one gives the talk. I am grateful for the contributions of Brian Schmidt and Ron Eastman to this effort. Supernova research at the Harvard University is supported by NSF grant AST 92-18475 and NASA grants NAG 5-841, NGT-51002, and grant GO-2563.01-87A through the STScI.

REFERENCES

Aaronson, M. *et al.* 1982, ApJS, 50, 241

Baron, E., *et al.* 1993, ApJ, 416, L21

Branch, D., Falk, S. W., McCall, M. L., Rybski, P., Uomoto, A. K., & Wills, B. J. 1983, ApJ, 244, 780.

Branch, D. & Miller,D.L. 1993, ApJ, 405, L5

Chilkuri, M. & Wagoner, R. V. 1988, in Atmospheric Diagnostics of Stellar Evolution, IAU Colloquium 108, ed. K. Nomoto, (Berlin: Springer-Verlag) p295

Cook, K. H., Aaronson, M., & Illingworth, G. 1986, ApJ, 301, L45

Eastman, R. G. & Kirshner, R. P. 1989, ApJ, 347, 771

Eastman, R. G., Schmidt, B. P., & Kirshner, R. P. 1994, ApJ, submitted

Eastman, R. G. & Pinto, P. A. 1993 ApJ, 412, 731

Fransson *et al.* 1989, ApJ, 336, 429

Freedman, W. L. *et al.* 1994, ApJ, 430, 53

Gould, A. 1994, ApJ, 425, 51

Höflich, P. 1988, in Atmospheric Diagnostics of Stellar Evolution, IAU Colloquium 108, ed. K. Nomoto, (Berlin: Springer-Verlag) p288

Hamuy, M. *et al.* 1993, AJ, 106, 2392

Huchra, J. P. 1988, in Proceedings of the A. S. P.: The Extragalactic Distance Scale, ed. S. van den Bergh & C. J. Pritchet, (Provo: Brigham Young University Press) p 257

Jakobsen, P. *et al.* 1991, ApJ, 369, L63

Jacoby, G. H., Branch, D., Ciardullo, R., Harris, W. E., Pierce, M. J., Pritchet, C. J., Tonry, J. L., & Welch, D. L. 1992, PASP, 104, 599

Januzzi, B., Schmidt, G., Elston, R. & Smith, P. 1993, IAU Circular #5776

Kirshner, R. P. 1985, in Lecture Notes in Physics: Supernovae as Distance Indicators, ed. N. Bartel (Berlin: Springer-Verlag), p. 171

Kirshner, R. P. & Kwan, J. 1974, ApJ, 193, 27

Kirshner, R.P., Winkler, P.F., & Chevalier, R.A. 1987, ApJ, 315, L135.

Lauer, T. L. & Postman, M. 1992, ApJ, 400, L47

Lauer, T. R. & Postman, M. 1993, in Texas/PASCOS 92: Relativistic Astrophysics and Particle Cosmology ed. C. W. Akerlof & M. A. Srednicki (Ann. N.Y. Acad. Sci) 688, 531

Leibundgut, B. *et al.* 1993, AJ, 105 310

Lynden-Bell, D., Faber, S. M., Burstein, D., Davies, R. L., Dressler, A., Terlevich, R. J., & Wegner, G. 1988, ApJ, 326, 19

Mathewson, D. S., Ford, V. L., & Buchhorn, M. 1992, ApJ, 389, L5

McCall, M. 1993, ApJ, 417, L75

Phillips, M.M. *et al.* 1992, AJ, 103, 1632

Phillips, M. M. *et al.* 1993, ApJ, 413, L105

Pierce, M. J. 1994, ApJ, 430, 53

Plait, P.C., *et al.* 1994, Ap.J. submitted

Press, W. H., Flannery, B. P., Teukolsky, S. A., & Vettering, W. T. 1992. Numerical Recipes in C, 2nd ed. (Cambridge University Press: Cambridge)

Pun, C.C., Kirshner, R.P., & Sonneborn, G. 1994 in preparation

Renzini, A. 1991. in Observational Tests of Cosmological Inflation, ed. T. Shanks *et al.* (Dordecht: Kluwer), p 313

Ruiz-Lapuente, P. *et al.* 1993, Nature, 365, 728

Sandage, A. 1994, ApJ, submitted

Sandage, A. & Tammann, G. A. 1990 ApJ, 365, 1

Sandage, A. & Tammann, G. A. 1993 ApJ, 415, 1

Sandage, A., Saha, A., Tammann, G. A., Panagia, N., & Machetto, F. D. 1992, ApJ, 401, L7

Sandage, A., Saha, A., Tammann, G. A., Labhardt, L., Schwengeler, H., Panagia, N., & Machetto, F. D. 1994, ApJL, submitted.

Schechter, P. L. 1980, AJ, 85, 801

Schmidt, B. P., Kirshner, R. P., & Eastman, R. G. 1992, ApJ, 395, 366

Schmidt, B. P., Kirshner, R. P., & Eastman, R. G., Grashuis, R., Dell'Antonio, I., Caldwell, N., Foltz, C., Huchra, J., & Milone, A. A. E., 1993, Nature, 364, 600

Schmidt, B. P., Kirshner, R. P., Eastman, R. G., Phillips, M. M., Suntzeff, N. B., Hamuy, M., Aviles, R., Filippenko, A. V., Ho, L., Matheson, T., Grashuis, R., Maza, J., Kirkpatrick, J. D., Kuijken, K., Zucker, D., Bolte, M., & Tyson, N. 1994a, AJ, 107, 1444

Schmidt, B. P. *et al.* 1994b, ApJ, 432, 42

Schmutz, W., Abbot, D. C., Russell, R. S., Hamann, W. R., & Wessolowski, U. 1990, ApJ, 355, 255

Smith, R.C., Kirshner, R.P., Blair, W.P., & Winkler, P.F 1991, ApJ, 375, 652

Tully, R. B. & Fisher J. R. 1977 A&A, 54, 661

Wagoner, R. V. 1977, ApJ, 214, L7

Wagoner, R. V. 1981, ApJ, 250, L65

Walker, A. R. 1987, MNRAS, 225, 627

Individual Light Curve Fits of SN Ia and H_0

By P. HÖFLICH[1], E. MÜLLER[2], AND A. KHOKLOV[3]

[1]Harvard-Smithsonian Center for Astrophysics
60 Garden St., Cambridge, MA 02138, USA

[2]Max Planck Institut für Astrophysik, Karl-Schwarzschild- Str. 1, D-8046 Garching, Germany

[3]Dept. of Astronomy, University of Texas, Austin, TX 78712, USA

1. Models for SN Ia

In order to study the question whether the appearance of SN Ia should be uniform from theoretical point of view, we present light curves (LC) for a broad variety of models using our elaborated LC scheme, including implicit LTE-radiation transport, expansion opacities, MC-γ transport, etc. For more details see Khokhlov (1991), Höflich *et al.* (1992), Höflich *et al.* (1993), Khokhlov *et al.* (1993), and Müller *et al.* (1993).

We consider a set of 19 SN Ia explosion models, which encompass all currently discussed explosion scenarios. The set consists of three deflagration models (DF1, DF1MIX, W7 $\circ$), two detonation models (DET1, DET2 $*$), two delayed detonation models (N21, N32 $\bullet$), detonations in low density white dwarfs (CO095, CO10, CO11 $\star$), six pulsating delayed detonation models (PDD3, PDD5-9 $\triangle$) and three tamped detonation models (DET2ENV2, DET2ENV4, DET2ENV6 $\triangle$). We also included the widely-used deflagration model W7 of Nomoto *et al.* (1984)

Different explosion models can be discriminated well by the slopes of the LCs and changes of spectral features (e.g. line shifts $\Rightarrow$ expansion velocities). The differences can be understood in terms of the expansion rate of the ejecta, the total energy release, the distribution of the radioactive matter, and the total mass and density structure of the envelope.

2. Comparison with Observations and H_0

We found that fast rising LCs (e.g. SN 1972e, SN 1981b, SN 1986g) can be explained by "delayed detonation" models. However, slow rising LCs (e.g. SN 1990n) require models which have formed a compact envelope of typically 0.2 to 0.4 $M_\odot$. Such envelopes can be produced by a pulsation phase during the explosion or by merging white dwarfs. Our interpretation is favored also from the expansion velocities observed in the spectra of the slow rising SN (Müller and Höflich, 1993). LCs from low-mass white dwarfs do not allow for a reasonable reproduction of any LC in our sample. The very peculiar SN 1991bg can be understood by a standard scenario for SN Ia but may be surrounded by a dusty region, or by pulsating delayed detonation models with little Ni (see in a forthcoming paper).

SN Ia should not be used as standard candles but the distances must be determined using the individual LC fits. From our fits, we find a value of 66 ± 10 km (s Mpc)$^{-1}$ for the Hubble constant within a 2σ error.

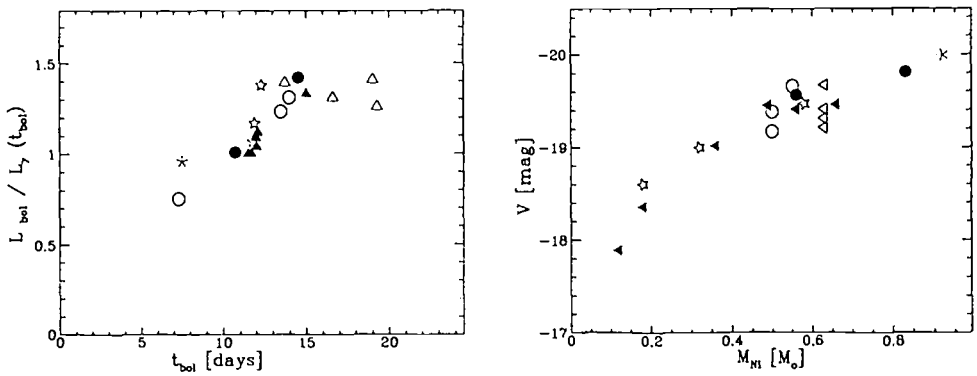

Figure 1. Maximum visual brightness V as a function of the Ni-mass (right) and ratio between bolometric luminosity and the γ-energy input at t_{max} (left). Note the small variation in V for Ni-masses less than $\approx 0.4 M_{\odot}$.

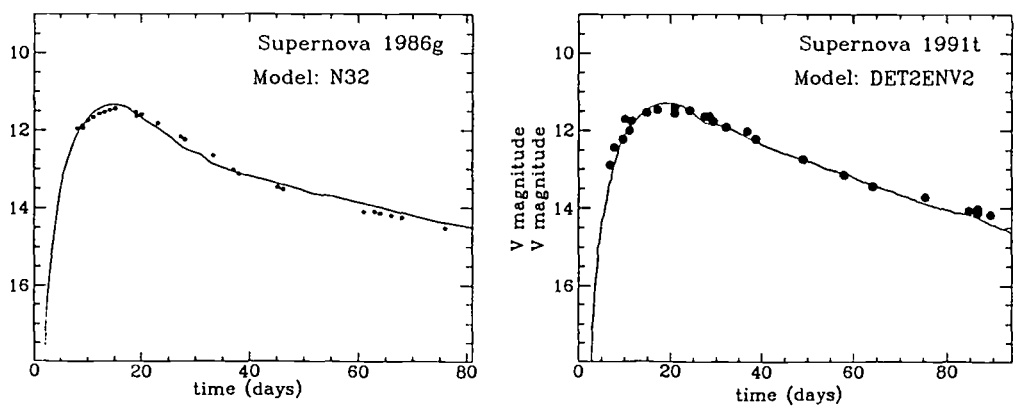

Figure 2. V light curves of SN 1986G (left) and SN 1991T (right) compared with the calculated light curve of the delayed detonation model N32 and the envelope model DET2ENV4, respectively.

REFERENCES

Höflich, P., Müller, E.; Khokhlov, A. 1992, A&A 259, 243

Höflich, P., Müller, E.; Khokhlov, A. 1993, A&A 268, 411

Khokhlov, A. 1991, A&A 246, 383

Khokhlov, A., Müller, E., Höflich, P. 1993, A&A 270, 23

Müller, E.; Höflich, P. A&A in press, MPA 709

Nomoto, K., Thielemann, F.-K., Yokoi, K. 1984, ApJ 286, 644

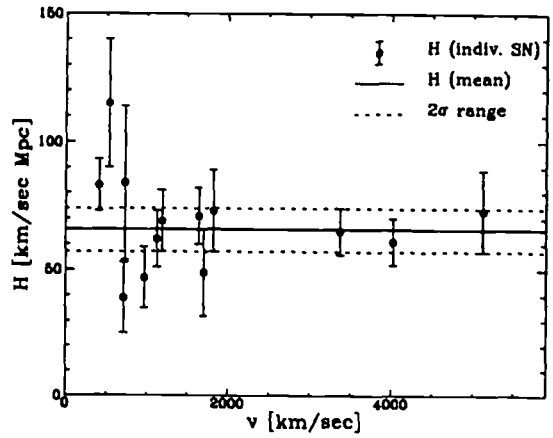

FIGURE 3. Hubble constants inferred by the distances derived for individual SNe. Note that the individual values for H_0 are inconsistent for $v_0 \leq 1000$km s^{-1} because these SN Ia are not yet in the Hubble flow.

TABLE 1. Observed SN Ia for which sufficient monochromatic light curve data are available to allow for a discrimination of theoretical models. Columns 2 to 5 give the parent galaxy, the distance, the color excess according to our models, and the names of the models (see text) which can reproduce the observations within the error bars.

Supernovae	Galaxy	D[*Mpc*]	E_{B-V}	acceptable models
SN 1937C	IC 4182	4.8 ± 1	0.10	N32,W7, DET2
SN 1970J	NGC 7619	66 ± 8	0.01	DET2ENV4/2, (PDD3)
SN 1971G	NGC 4165	35 ± 9	0.0	N32, DET2, W7
SN 1972E	NGC 5253	4.8 ± 0.4	0.03	N21
SN 1972J	NGC 7634	52 ± 8	0.01	N32, W7, DET2, DF1
SN 1973N	NGC 7495	70 ± 20	0.10	N32, W7
SN 1974G	NGC 4414	18.5 ± 5	0.0	N32, W7, DET2
SN 1975N	NGC 7723	25 ± 7	0.32	PDD3/5,DET2ENV2
SN 1981B	NGC 4536	23 ± 4	0.05	N21
SN 1983G	NGC 4753	18 ± 4	0.30	N32, W7
SN 1984A	NGC 4419	17 ± 4	0.24	DET2ENV2, PDD3/5
SN 1986G	NGC 5128	4.6 ± 1.2	0.90	N32, W7
SN 1989B	NGC 3627	8.3 ± 3	0.60	N32, W7
SN 1990N	NGC 4639	21 ± 5	0.01	DET2ENV2/4, PDD3
SN 1991T	NGC 4527	12 ± 2	0.01	PDD3/5, DET2ENV2
SN 1991BG	NGC 4374	23 ± 6	(0.68)[1]	N32, DET2, W7

[1] see text

Towards the Cosmic Distance Scale through Nebular SNe Ia

By P. RUIZ-LAPUENTE[1] AND A. V. FILIPPENKO[2]

[1]Harvard-Smithsonian Center for Astrophysics
60 Garden St., Cambridge, MA 02138, USA

[2]Department of Astronomy, and Center for Particle Astrophysics,
University of California, Berkeley, CA 94720, USA

We give an update of current research on the use of nebular spectra of SNe Ia as distance indicators. Results of the application of the method to a group of SNe Ia are reported. We describe the status of the research including theoretical and observational requirements of the method. Our results point toward a shorter distance scale than methods based on the "standard candle" hypothesis for Type Ia SNe.

1. Introduction

The use of SNe Ia as "standard candles" to determine the extragalactic distance scale has been recurrently debated. The correlation found by Pskovskii (1977, 1984) and by Branch (1981) between the postmaximum decline rate of the light curve and the magnitude at maximum cast doubts concerning this method. The validity of the correlation was questioned by Boisseau & Wheeler (1991), who found that such an effect might reflect contamination from the light of the underlying galaxy. But new evidence on differences in the light curve decline rate (Phillips 1993; Suntzeff, this volume) opens again the question of the correlation of magnitude at maximum and slope of the light curve soon after maximum. The value of the absolute magnitude of SNe Ia as a class loses much of its meaning if the considerable spread in magnitudes found in recent work is confirmed.

Uncertainties in the absolute magnitudes of SNe Ia are amplified by extinction. The discrepant "observationally-inferred" values obtained for SN 1986G (Phillips et al. 1992a; Della Valle & Panagia 1992; Phillips 1993) show that when reddening is high the usual prescriptions to obtain this quantity from the color curves and from the equivalent width of the Na I D interstellar line towards the supernova give different results. These discrepancies occur even if the supernova is not highly affected by extinction, as in the case of SN 1991T (see, for instance, values given in Filippenko et al. 1992, Ruiz-Lapuente et al. 1992, and Phillips et al. 1992a). All the methods using supernovae as distance indicators (Schmidt et al. 1992; Kirshner, this volume; Höflich, this volume) require an accurate estimate of reddening. When spectral modeling is involved, as in the Expanding Photosphere Method for Type II supernovae (Schmidt et al. 1992), a certain degree of cancellation is found in the effects of extinction on the final distance (reddening lowering the level of the flux but making the supernova appear cooler).

Ruiz-Lapuente (1992) and Ruiz-Lapuente & Lucy (1992, hereafter Paper I) investigated the use of the nebular stage of the spectral evolution of SNe Ia to obtain a hint on nucleosynthesis, $E(B-V)$, and distance to particular events. We found that the bulk of the information contained in the optical spectra should make it possible to discriminate between intrinsic variations of the ratio of the luminosities of the lines (due to temperature effects and ionization effects) from extrinsic effects such as extinction. In the analysis of SN 1986G we proved that the correlation coefficients of the involved

physical parameters (^{56}Ni, $E(B-V)$, and distance) were low enough to obtain these quantities separately. This was possible because of the various [Fe II] and [Fe III] lines distributed along the spectra.

In this paper we present further results, and we discuss the possibilities, potential difficulties, and improvements of the method. It is important to link the overall results with the present status of SN Ia research in what concerns the various models and different determinations of the relevant physical quantities.

2. Applicability of the Method

Several observational conditions are desired when using the nebular spectra of Type Ia supernovae for distance determinations. (Hereafter we refer to this approach as the Nebular SN Ia Method.) First, there should be no differential losses in flux between the blue and the red parts of the spectra, since greater losses in the blue result in overestimates of the reddening. These are minimized by aligning the slit along the parallactic angle, and by observing at low airmasses. Second, inaccurate subtraction of the galaxy background should also be avoided, since it typically tends to redden the spectrum and therefore affects the estimate of $E(B-V)$. The method is expected to work best when the supernova is in a region where contamination from the galaxy is low. Third, comparison of the nebular spectra with observed light curves is required to set the absolute fluxes of the spectra. The narrow slit rarely includes all the light, and conditions can vary from night to night or even during the course of a single night. A check of the consistency of the colors obtained from the spectra with those derived from the light curves is also recommended.

3. The Sample of SNe Ia in the Nebular Phase

A number of spectra of SNe Ia are available in the nebular phase: SN 1987L in NGC 2336, SN 1991T in NGC 4527, SN 1989M in NGC 4579, SN 1990N in NGC 4639, SN 1992A in Fornax A, and two SNe Ia in the Centaurus Group (SN 1972E in NGC 5253 and SN 1986G in NGC 5128) are currently the best observed ones. A SN Ia at redshift $z = 0.011$, SN 1991aa in an anonymous galaxy also has adequate spectra for the use of the method. For other SNe Ia, data are available over limited wavelength coverage, or too soon after maximum brightness for the purposes of our study (which is limited to the phase where continuum radiation is negligible). The data now available to us come mainly from observations done at the MMT (CfA archive), Lick Observatory, CTIO, and the WHT (La Palma Observatory). There is work in progress to homogenize the sample of spectra by using light curves; this will allow us to obtain results of higher accuracy.

We review, now, the first steps towards the determination of the cosmic distance scale through SNe Ia in the nebular phase. They are limited to two SNe Ia in the Centaurus Group, a SN Ia in the Virgo Cluster, and a SN Ia beyond the Virgo Cluster. We present here the results obtained by applying our method to the data. These can be seen in Table 1, where comparisons are made with results obtained from other methods.

The application of the method to SN 1991T, for which spectra from different observatories are available, gives a distance towards its host galaxy, NGC 4527, between 12 and 14 Mpc. For these data, the flux level for the different nebular spectra refers to calibration done by spectrophotometry with standard stars. The lack of homogeneity in the calibration of the spectra enters in the quoted error.

These results confirm that SN 1991T is on the near side of the Virgo Cluster, as compared with the distances obtained by applying the Nebular SN Ia Method to other

TABLE 1. Distances to SNe and their host galaxies through the Nebular SN Ia Method

SN	Galaxy	Distance	Other methods
SN 1986G	NGC 5128	3.3 ± 0.3 Mpc [1,2,3]	GC:3 Mpc [4]; PN: 3.6 ± 0.2 [5]; SBF: 3.28 [6]
SN 1972E	NGC 5253	$2.8^{+0.7}_{-0.3}$ Mpc [1,2,3]	PN: 3.-3.9 Mpc [7]; SBF: 2.5 ± 0.1 [7]
SN 1991T	NGC 4527	12-14 Mpc *	TF: 13 Mpc [8,9]
SN 1991AA	Anon.Gal.	37 ± 3 Mpc *	

[1]Ruiz-Lapuente & Lucy 1992
[2]Ruiz-Lapuente 1992
[3]Ruiz-Lapuente, Lucy, & Danziger 1992
[4]Hesser et al. 1984 GC: Globular Clusters
[5]Jacoby et al. 1988 PN: Planetary Nebulae
[6]Tonry & Schechter 1990 SBF: Surface Brightness Fluctuations [7] Phillips et al. 1992b
[8]Tully, Shaya, & Pierce 1992 TF: Tully-Fisher relation
[9]Ruiz-Lapuente et al. 1993a
*This work

SNe Ia such as SN 1990N. The implied distance for NGC 4527 from the use of the nebular spectra of SN 1991T is consistent with the distance determination by Tully, Shaya, & Pierce (1992) using the Tully–Fisher relation. It also agrees with the analysis of the diagram m_B-flux(847 keV) for SN 1991T (Ruiz-Lapuente et al. 1993a). The results of the Nebular SN Ia Method to the most distant SN Ia observed around 250 days after explosion, SN 1991aa ($cz = 3300$ km s^{-1}), suggest that the host galaxy is at a distance of 37 ± 3 Mpc. This galaxy is beyond the Virgo Cluster and does not seem to be associated with any known group. Thus, a tentative corrected Hubble flow velocity around 3100 $\pm$ 200 km s^{-1} would give $H_0 = 84 \pm 10$ km s^{-1}. This value needs to be confirmed by applying the method to other SNe Ia and examining its uncertainties. In Figure 1 we show the calculated spectra compared with the observed spectra around 275 days after explosion for SN 1991T and around 250 days after explosion for SN 1991aa; analysis of the Fe-peak nucleosynthesis in both SNe was published by Ruiz-Lapuente & Filippenko (1993).

Since distance and reddening are important in setting the absolute flux scale of the spectra, we include in Table 2 the reddening obtained for every SN Ia of this set. In Table 3 we present the amount of ^{56}Ni in the Fe-peak region (the former nuclear statistical equilibrium core) derived for every SN Ia. The errors quoted come from the statistical least-squares analysis. For SN 1972E, lack of direct access to the computer-readable data precluded the application of the least-squares analysis. Our inspection of the data as published in Meyerott (1980) gave a distance to NGC 5253 between 2.5 and 3.5 Mpc and a low reddening, from 0 to 0.1 magnitudes (Paper I). A distance to NGC 5128 (SN 1986G) between 3 and 3.6 Mpc is obtained from the least-squares procedure, and the supernova seems to be highly reddened.

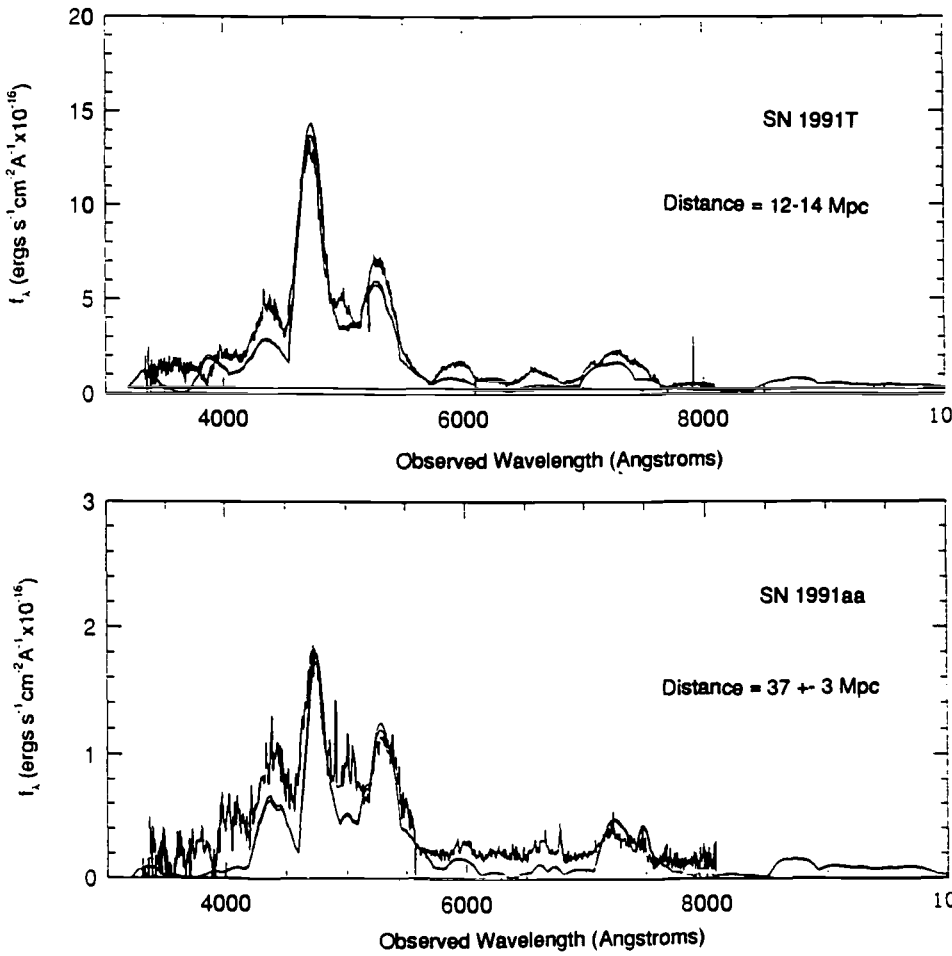

FIGURE 1. Observed and theoretical spectra for SN 1991T (top) and SN 1991aa (bottom) in the nebular phase (see text). The distance inferred by applying the method is 12-14 Mpc for SN 1991T in NGC 4527 and 37 ± 3 Mpc for SN 1991aa in an anonymous galaxy at an observed redshift of $z = 0.011$.

4. Theoretical Issues

Internal errors could arise from our theoretical modeling. However, if we had failed to correctly describe the physical stage of the SN Ia ejecta, we would have been unable to reproduce the overall spectrum: wrong estimates of the electron temperature should manifest themselves in poor fits to the various emission lines in the different bands. Given that the ionization state has been fairly well determined from the spectra, we don't think our model can be grossly in error. To obtain the correct electron temperature from a model, we must know the efficiency in the deposition of the energy in gamma rays and positrons in the envelope. Theoretical modeling done so far seems to give agreement on the electron temperature for a given underlying model (Axelrod 1980; Meyerott 1978, 1980; comparison of our results with those from the code of Eastman & Pinto 1993). The electron temperature is also well determined from the luminosity of the [Fe III] and [Fe II] lines in a model-independent basis, as done in the nebular analysis. The overall modeling suggests that the dominant ion of Fe in the nebular phase is Fe III. Significant amounts

TABLE 2. Reddening E(B-V)

SN	Galaxy	Reddening	Other methods
SN 1986G	NGC 5128	1.09 ± 0.02 [1,2,3]	0.68-1.24 [10,11,12]
SN 1972E	NGC 5253	0.05 ± 0.05 [1,2,3]	0.02 [12]
SN 1991T	NGC 4527	0.1-0.2 *	0.1-0.3 [9,13,14,15]
SN 1991AA	Anon.Gal. (v=3300 km s^{-1})	0.13 ± 0.04 *	

[10]Di Serego Alighieri and Ponz 1987
[11]Phillips et al. 1987
[12]Della Valle and Panagia 1992
[13]Filippenko et al. 1992
[14]Ruiz-Lapuente et al. 1992a
[15]Phillips et al. 1992a
*This work

TABLE 3. ^{56}Ni mass[16]

SN	Galaxy	^{56}Ni mass
SN 1986G	NGC 5128	0.38 ± 0.03 $M_\odot$
SN 1972E	NGC 5253	0.5-0.6 $M_\odot$
SN 1991T	NGC 4527	0.7-0.8 $M_\odot$
SN 1991AA	Anon.Gal. (v=3300 km s^{-1})	0.6 $M_\odot$

[16]Ruiz-Lapuente and Filippenko 1993

of Fe II and Fe IV are also predicted from the ionization balance (taking into account photoionization coming from cascade emission towards the ground term; Paper I). On the other hand, Axelrod (1980) noticed that the lack of [Fe VI] and [Fe VII] lines in the observed optical spectra of SN 1972E (Kirshner & Oke 1975) reflected the inadequacy of some models of SN Ia explosions to reproduce the ionization state of this supernova. The proportion of Fe II should be, according to our investigations, not lower than ~ 10% of the total Fe abundance, in order to reproduce the optical spectra. Eastman reported at this colloquium preliminary results pointing towards a substantial reduction of Fe II in the calculated spectra when taking into account new photoionization cross-sections from excited levels. Such an increase of the ionization towards higher amounts of Fe III and Fe IV, and a much smaller fraction of Fe II, should be further investigated by different methods. At the time of the conference we had not yet evaluated the impact of the new photoionization cross-section in our determinations. However, according to our analyses, a failure to reproduce the observed data would arise if Fe II is drastically reduced, and hardly any model (lowering the amount of ^{56}Ni) would satisfy the different constraints. Fortunately, ionization can be well constrained on an empirical basis through spectra covering a wide wavelength range. Just recently, observations made with *HST* provide

the ultraviolet part of the spectrum of SN 1992A (work in progress of the Supernova INtensive Studies [SINS] group); this will significantly constrain the proportions of all the ions.

Additional issues concern the population of the energy levels and the rate of collisional excitation over spontaneous radiative decays. We use in our calculation the most recent values available for collision strengths of [Fe III] and [Fe II] lines. The first calculations of the [Fe III] values were done by Garstang et al. (1978). More recent calculated collision strengths have been obtained by Berrington et al. (1991). From a comparison of previous and new values, one sees that significant discrepancies are found in the values of the weaker lines (i.e., transitions ^{5}D-^{3}H and ^{3}H-^{3}P), which are not contributing significantly to the spectra). The values for the transitions ^{5}D–^{3}F and ^{5}D–^{3}P, which give rise to the 4600 Å and the 5200 Å emission seen in the spectra, are in much better agreement in both calculations (values by Berrington et al. 1991 and Garstang et al. 1978). The discrepancies between new and old values translate into a final 4% increase in distance (P.R.L. 1993, result presented at the Aspen Winter Conference on the Cosmic Distance Scale). Old distance estimates from this method towards SN 1986G and SN 1972E should change now (with the present values) to 4% larger distances. The collision strengths for [Fe II] by Pradhan & Berrington (1993) seem to show some discrepancies as compared with previous values by Nussbaumer & Storey (1980) and by Nussbaumer et al. (1981). A full analysis of the effect of the reported discrepancies for several transitions, as compared with previous work, is one of our future aims. The bulk of the work being developed by the Opacity Project on atomic data for Fe (Berrington et al. 1987) will help to improve the accuracy of our results.

5. SN Ia Diversity and Distance Scale

Current models of SN Ia are challenged by recent observations (see, for instance, Filippenko in this conference, Suntzeff in this conference, Ruiz-Lapuente et al. 1993b, Wheeler, Swartz, & Harkness 1993). Our first approach has been to investigate the one-zone treatment, which reflects the fact that the Fe-peak region can be well modeled by describing the bulk of emission as arising from the zone where ^{56}Ni is the dominant component. We tested the hypothesis that calculations of the nebular spectra of SNe Ia are well reproduced by the theoretical spectrum of the region where ^{56}Ni is the dominant component of the ejecta for the case of SN 1991bg in NGC 4374. The two different approaches have given similar results in the amount of ^{56}Ni synthesized by the explosion (Ruiz-Lapuente et al. 1993b).

One advantage of this type of method is that it addresses the modeling of SNe Ia on an individual basis, thus showing in every case how well we are able to reproduce the spectra, and not being bound to any particular sample of hydrodynamical models. The set of SNe Ia analyzed thus far points to a shorter distance scale than other methods that use the "standard candle" hypothesis for SNe Ia. Differences in spectroscopic evolution, as well as correlations between the magnitude at maximum and the decline rate of the light curve, suggest that we view the "standard candle" hypothesis with caution. The approach presented in our earlier work (Paper I) has the advantage of being model independent and also not relying on the assumption of "normality" within the class of Type Ia SNe.

Acknowledgements

P.R.L. acknowledges financial assistance through STScI grant GO–2563.01–87A. A.V.F. is supported by NSF grants AST–8957063 and AST–9115174, as well as by the Center for Particle Astrophysics at U.C. Berkeley (NSF Cooperative Agreement AST–8809616).

REFERENCES

Axelrod, T.S. 1980, Ph.D. Thesis, Univ. California at Santa Cruz.

Berrington, K.A., Burke, P.G., Butler, K., Seaton, M.J., Storey, P.J., Taylor, K.T., & Yu Yan. 1987, J.Phys.B, 20, 6379.

Berrington, K.A., Zeippen, C.J., Le Dourneuf, M., Eissner, W., & Burke, P.G. 1991, J.Phys.B, 24, 3467.

Boisseau, J.R., & Wheeler, J.C. 1991, AJ, 101, 1281.

Branch, D. 1981, ApJ, 248, 1076.

Della Valle, M., & Panagia, N. 1992, AJ, 104, 696.

di Serego Alighieri, S., & Ponz, J. D. 1987, in ESO Workshop on the SN 1987A, ed. I. J. Danziger (Garching: ESO), p. 545.

Eastman, R.G. & Pinto, P.A. 1993 ApJ, 412, 731.

Filippenko, A.V., et al. 1992, AJ, 104, 1543.

Garstang, R. H., Robb, W.D., & Rountree, S.P. 1978, ApJ, 222, 384.

Hesser, J.E., Harris, H.C., van den Bergh, S., and Harris, G.L.H. 1984, ApJ, 276, 491.

Jacoby, G.H., Ciardullo, R., & Ford, H.C. 1988, in The Extragalactic Distance Scale, Proceedings of the ASP 100th Anniversary Symposium, ASP Conf. Ser., Vol. 4., ed. S. van den Bergh and C.J. Pritchet (Provo, UT, Astron. Soc. Pacific), p. 42.

Kirshner, R.P., & Oke, J.B. 1975, ApJ, 200, 574.

Meyerott, R.E. 1978, ApJ, 221, 975.

Meyerott, R.E. 1980, ApJ, 259, 257.

Nussbaumer, H., & Storey, P.J. 1980, A&A, 89, 308.

Nussbaumer, H., Pettini, M., & Storey, P.J. 1981, A&A, 102, 351.

Phillips, M.M. 1993, ApJ, 413, L105.

Phillips, M.M., et al. 1987, PASP, 99, 592.

Phillips, M.M., Wells, L.A., Suntzeff, N.B., Hamuy, M., Leibundgut, B., Kirshner, R.P., & Foltz, C.B. 1992a, AJ, 103, 1632.

Phillips, M.M., Jacoby, G.H., Walker, A.R., Tonry, J.L., & Ciardullo, R. 1992b, BAAS, 24, 749.

Pradhan, A.K., & Berrington, K.A. 1993, J.Phys.B, 26, 157.

Pskovskii, Y.P. 1977, Sov. Astron., 21, 675.

Pskovskii, Y.P. 1984, Sov. Astron., 28, 658.

Ruiz-Lapuente, P. 1992, PhD Thesis, University of Barcelona.

Ruiz-Lapuente, P., Cappellaro, E., Turatto, M., Gouiffes, C., Danziger, I.J., Della Valle, M., & Lucy, L.B. 1992a, ApJ, 387, L33.

Ruiz-Lapuente, P., Lucy, L.B., & Danziger, I.J. 1992b, Mem. S.A.It., 63, 233,

Ruiz-Lapuente, P., & Filippenko, A.V. 1993, in Origin and Evolution of the Elements, ed. N. Prantzos, E. Vangioni-Flam, & M. Cassé (Cambridge: Cambridge Univ. Press), p. 318.

Ruiz-Lapuente, P., Lichti, G.G., Lehoucq, R., Canal, R., & Cassé. M. 1993a, ApJ, 417, 547

Ruiz-Lapuente, P., Jeffery, D.J., Challis, P.M., Filippenko, A.V., Kirshner, R.P., Ho, L.C., Schmidt, B.P., Sánchez, F., & Canal, R. 1993b, Nature, 365, 28

Ruiz-Lapuente, P., & Lucy, L.B. 1992, ApJ, 400, 127 (Paper I).

Schmidt, B.P., Kirshner, R.P., & Eastman, R.G. 1992, ApJ, 395, 366.
Tonry, J.L., & Schechter, P.L. 1990, AJ, 100, 1794.
Tully, R.B., Shaya, E.J., & Pierce, M.J. 1992, ApJS, 80, 479.
Wheeler, J.C., Swartz, D.A., & Harkness, R.P. 1993, Phys. Rep., 227, 113.

Observations of Type Ia Supernovae

By NICHOLAS B. SUNTZEFF

Cerro Tololo Inter-American Observatory
Casilla 603, La Serena, Chile

The quality of observational data on Type Ia supernovae has improved remarkably in the last few years, due mainly to monitoring programs with CCD-equipped detectors on small aperture telescopes at observatories across the world, and at the space observatories. I will review the recent observational characteristics of Type Ia supernovae, focusing the discussion on our observations of SN1992A in the S0 galaxy NGC 1380 in the Fornax cluster as a reference to other Type Ia events. We now have strong evidence that Type Ia events are not a homogeneous class, but vary in both color and brightness at maximum light, vary in rise time and decline from maximum, and have spectral characteristics at maximum light that are correlated with these photometric parameters. Insofar as the SBF, PNLF, and infrared Tully-Fisher distance scales are correct, the observed (uvoir) bolometric light curves also indicate that these supernovae are less luminous than expected from the models of the explosion of a C-O white dwarf at the Chandrasekhar mass.

1. Introduction

A stellar explosion is an unlikely physical environment to produce a homogeneous energy flux, given the fantastic brightness of a supernova at maximum light which can reach 10% of the luminosity of the *whole galaxy* for a period of a few weeks. Yet it is the brightness of the event that makes the use of supernovae as "standard candles" so attractive, since they can be readily observed to cosmologically interesting distances. Supernovae with redshifts greater than $z \sim 0.03$ can be used to measure the Hubble constant H_0 almost independent of peculiar velocities and perhaps streaming motions (but with the usual problems of local calibrators). Supernovae with redshifts of $z \sim 0.3$ or greater can be used, in principle, to measure the deceleration parameter q_0.

Almost all of our knowledge of the luminosity evolution of supernovae comes from the heroic work of countless observers who have obtained photographic plates and reduced the photographic images into stellar photometry. The measurement of an accurate magnitude of a stellar image on top of a galaxy of significant surface brightness is made especially difficult by the non-linear sensitivity of the photographic emulsion. A significant improvement in the accuracy of the photometry can be made by using CCD detectors, where the linear nature of the detector allows for much better background subtraction and photometric accuracies.

In this contribution, I will focus on recent results based on CCD photometric and spectroscopic data to explore the homogeneity and inhomogeneity of Type Ia explosions. It is less my goal to discuss the utility of Type Ia supernovae as standard candles, and more to offer a new perspective on the physical evolution of Type Ia explosions as revealed from the new high-quality data. It is my hope that a fresh look based on the new CCD data on these extremely well-studied objects will lead the discussion in this conference to new directions of understanding the underlying physical event.

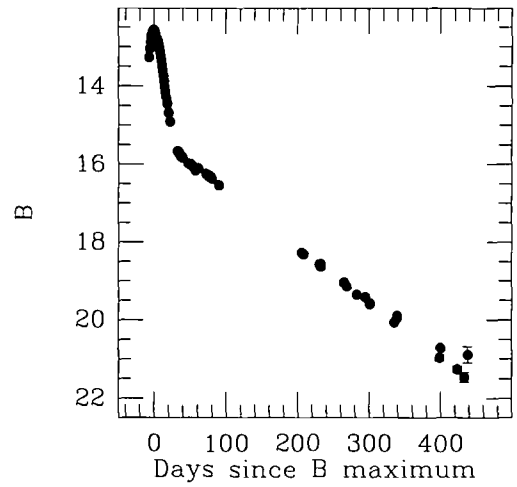

FIGURE 1. B magnitude light curve for the Type Ia SN1992A in NGC 1380

2. A Template Event: SN1992A

SN1992A was a Type Ia supernova discovered by Liller (1992) on 11.2 Jan 1992 (UT) in NGC 1380, an S0 galaxy in the Fornax cluster. Our initial observations showed that this was a typical Type Ia caught well before maximum. Its location in the periphery of the galaxy implied low reddening (an $E(B-V)$ reddening of 0.00 was estimated by Kirshner, *et al.* 1993) and very low galaxy background, making this an easy object to follow to faint magnitudes. Staff astronomers at CTIO immediately began an intensive $UBV(RI)_{KC}$ photometric and spectrophotometric study of the evolution of the object. A parallel effort to monitor the SN with HST and IUE (Kirshner, *et al.* 1993) was made by the HST SINS project group based at CfA.

In Figure 1 I present the B light curve from 92A through day 450 as an example of the quality of the data. No error bars are plotted if the errors are smaller than the symbol size. These data are based on CCD frames taken primarily at the CTIO 0.9m telescope. The data were calibrated relative to field stars in the frame, which were measured on ten photometric nights. Great care was made to measure the color terms of the filter/CCD photometric system to ensure that all the data are on a uniform photometric system. The color terms are averages of typically 5-10 nights of photometric solutions.

The B magnitude evolution in Figure 1 is quite typical for a Type Ia supernova. The SN was caught six days before B maximum which occurred on 19.0 Jan 1992 at B=12.56. The $(B-V)$ color at B maximum was 0.00 ± 0.02. The supernova passed through the photospheric phase and entered the optically thin "exponential tail" phase about 36 ± 2 days past B maximum. The exponential tail has an e-folding time of 76.8 ± 0.5 days and is extremely linear (in magnitudes) from day 36 to 450.

Our perception of the simplicity of the evolution of Type Ia events may be something of a historical accident since almost all light curves have been measured in blue light. The evolution in other colors is not as simple. In Figure 2 I present the $UBV(RI)_{KC}$ evolution of 92A from days -6 to +100. Whereas the UB light curves fall rapidly from maximum until about day 36 and then enter the exponential tail, the $V(RI)_{KC}$ light curves are much more complicated. The I_{KC} light curve reaches a secondary maximum around day 23, and both V and R_{KC} have associated inflection points at the same time. A secondary maximum similar to that seen in the I_{KC} light curve has been seen in the near-infrared by Elias, *et al.* (1985). Since there is evidence of a correlated inflection

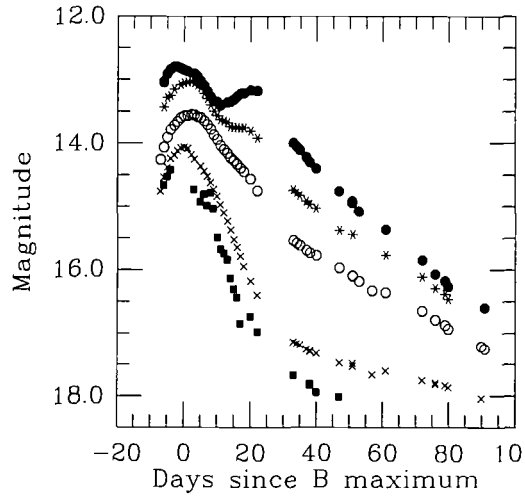

FIGURE 2. $UBV(RI)_{KC}$ evolution of SN1992A. The order of the curves is $IRVBU$ from top to bottom. For presentation, the R curve was shifted by +0.5 mag, the V curve by +1.0 mag, etc.

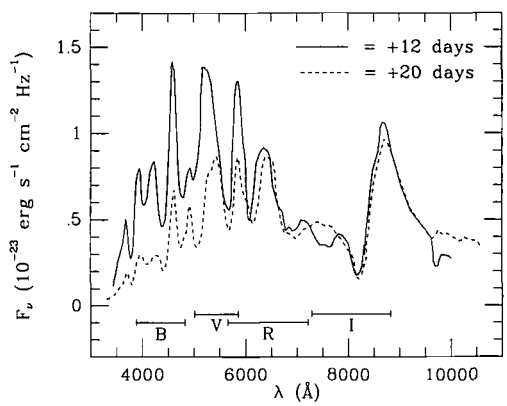

FIGURE 3. Spectrophotometry of SN1972E from Kirshner, *et al.* (1973). The two spectra were observed +12 days (solid line) and +20 days (dashed line) past B maximum.

from V out to K, it would be very difficult to explain this behavior simply as the variation of spectral features: instead, it seems that there is a redistribution of flux from the ultraviolet and blue to redder wavelengths. This redistribution can be best studied with spectrophotometry, but unfortunately, the published spectrophotometric coverage of Type Ia supernovae from days 0 to 30 that extends beyond 7000Å is almost non-existent. The best study to date is still the rather old Kirshner, *et al.* (1973) work on 72E. In Figure 3 I present two spectra from 72E taken on days 12 and 20. There are no obvious large changes in spectral features: rather, the evolution seems to be due to a general decrease in flux in the blue compared to the region redward of 6000Å.

Figure 2 also shows that the time of maximum light is quite different in the different bandpasses. One can see the well-known delay of the time of V maximum with respect to B maximum: in 92A the delay is $\sim 2.2 \pm 0.5$ days. The R_{KC} peaks at the same time as V, but the I_{KC} evolution near maximum is very complicated and apparently peaks at about 2.5 days *before* B maximum. The final peculiarity in the $V(RI)_{KC}$ light curves is that they only begin to fall at the e-folding rate of the B light curve after day ~ 100.

In Figure 4 I compare 92A with some other well-observed supernovae by shifting all the light curves to the same maxima in a given color, but with the time relative to the

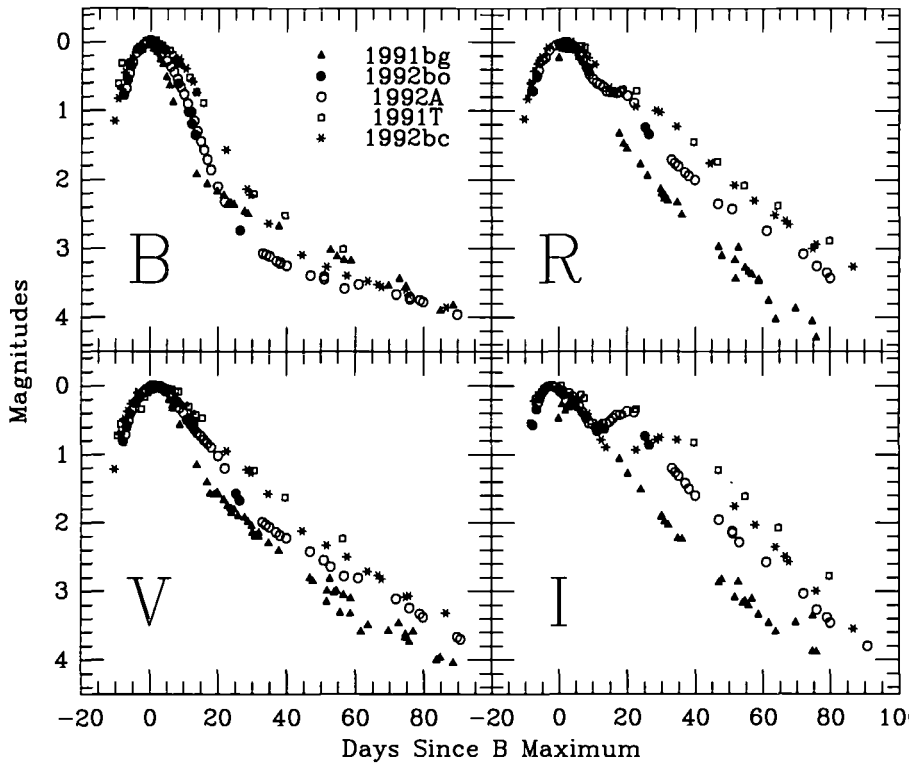

FIGURE 4. BV (left panel) and $(RI)_{KC}$ (right panel) evolution of bright Type Ia

time of B maxima. The comparison in the I_{KC} band is particularly difficult since the I_{KC} evolution near maximum light is quite variable among different supernovae. In the case of 91bg, I have aligned the light curve at day five. This figure reveals spectacular variations in light curve types, especially in the redder colors where most of the flux is produced. One gets the feeling from these diagrams that had the historical data been taken in the I_{KC} band rather than B, questions about the homogeneity of Type Ia events would have been raised much earlier.

The inhomogeneity of Type Ia light curves has been noted by many astronomers but the variations can be seen much more clearly in the CCD photometry. The most obvious variation in the B light curve is the "speed" of evolution away from maximum. A simple parameter β was invented by Pskovskii (1967) to describe this effect: Phillips (1993) has provided a similar but numerically more robust parameter Δm_{15} which is the difference in B magnitude between B maximum and 15 days after maximum. It can be seen in the data plotted in Figure 4 that Type Ia supernovae can differ by more than 1 magnitude in B at 15 days after maximum. Evidently "fast" supernovae such as 91bg both rise to maximum and fall from maximum in B more quickly than "slow" supernovae such as 91T or 92bc. Similar behavior is seen in V in Figure 4, but the differences in the evolutionary speed near maximum light seem to be less than in B.

The evolution from 20 to 100 days (when the B light curve is on the exponential tail) is dramatically variable in Type Ia supernovae, especially in the redder colors. While there is no clear trend in B evolution past day 25 as a function of Δm_{15}, in $V(RI)_{KC}$ the fast supernovae are clearly fainter. The spread in I_{KC} is as large as 2 magnitudes around day 50!

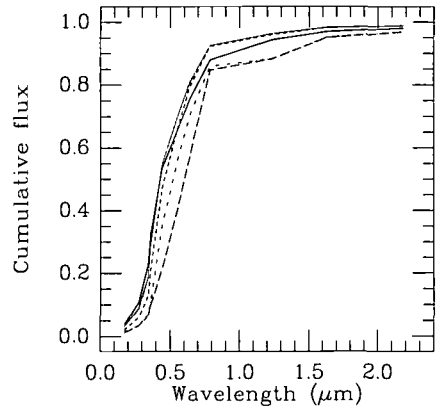

FIGURE 5. Cumulative flux distributions for SN1992A for days −6 to 80. At 3000Å the curves from top to bottom correspond to days −6, 0, 5, 20, and 77.

3. Bolometric light curves for Type Ia supernovae

A common assumption in past papers on the evolution of Type Ia supernovae was that the luminosity evolution of the supernova in some way mimicked the B evolution. From Figure 4 one can see that this is not a valid assumption. Recent careful modeling of the luminosity evolution of these supernovae has produced predicted BV colors based on the convolution of the appropriate filter bandpass and the predicted monochromatic fluxes. Given the uncertain nature of the monochromatic opacities (Harkness 1991), it is important to turn this problem around and try to predict the bolometric luminosity evolution based on the observed colors. The bolometric luminosity, calculated from the observed colors, is often called the "uvoir" bolometric luminosity to emphasize that it represents only the thermalized fraction of the total luminosity, and does not account for the energy escaping directly as gamma rays. Leibundgut & Pinto (1992) give a particularly clear discussion of the energy deposition rates in Type Ia supernovae where they show that by day 25, more than half the energy from the radioactive decay of ^{56}Co is freely escaping the supernova nebula.

To calculate the bolometric luminosity, we not only need $UBV(RI)_{KC}$ photometry, but also estimates of the ultraviolet fluxes below 3000Å and the near-infrared JHK colors. If dust forms at later epochs, mid-infrared colors also would also be needed. While there is no evidence to date which implies that dust forms in Type Ia events, there are so few infrared studies of Type Ia supernovae that one should not rule out the possibility. HST and IUE ultraviolet spectrophotometry for 90N and 92A through day 80 has been published by Kirshner *et al.* (1993), and the ultraviolet evolution, insofar as these SN are typical, is well established. The average JHK evolution based on a number of SN has been published by Elias *et al.* (1985). It is obvious, however, that there is variation among supernovae in the near-infrared, and a much larger survey of the IR evolution of supernovae is long overdue.

In Figure 5 I present the cumulative distribution of flux for 92A from day −6 to day 80. The space ultraviolet fluxes are taken from the Kirshner *et al.* (1993) work, and the infrared photometry is estimated from the average curve given in Elias *et al.* (1985) scaled to a single JHK measurement from ESO on day 4.5. This figure shows that the bolometric light curve is dominated by the optical flux. Even the earliest data at day −6 show that the flux below the optical window is only ∼15% of the total and by day 5 it is well below 10%. Similarly the near-infrared adds at most ∼10% to the total flux at early times and no more than about ∼15% by day 80. The final bolometric light curve for 92A

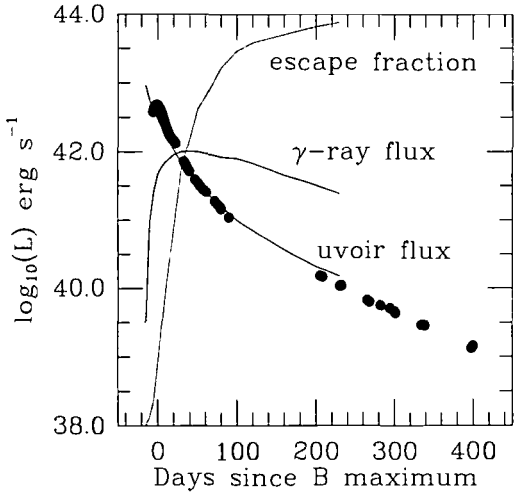

FIGURE 6. "Uvoir" bolometric light curve for SN1992A. The theoretical curves are from Leibundgut & Pinto 1992. The curve "γ" refers to the escaping γ-ray flux. The curve "uvoir flux" refers to the fraction of the γ-ray flux absorbed by the supernova nebula and re-radiated. The escape fraction of γ-rays is plotted with 0 at the bottom and 1 at the top. The theoretical curves have been shifted by $\Delta t = -20$ days, and the model fluxes reduced by 0.7 dex.

is given in Figure 6. For the data through day 100, I have included the HST ultraviolet fluxes in the calculation and the near-infrared fluxes from the scaled Elias *et al.* (1985) curve. For the data past day 100 we only have B to I_{KC} magnitudes. To calculate the late-time bolometric luminosity, I have estimated a "bolometric correction" based on the 92A data from days 75-90 where I have compared the total uvoir flux to that from the B to I_{KC} integration. This correction of 0.24 dex was added to the B to I_{KC} integration.

The bolometric luminosity plotted in Figure 6 has some unusual features. The maximum luminosity is ~42.65 dex, which is significantly less than a "standard model" of an exploding CO white dwarf at the Chandrasekhar mass which predict values closer to 43.3 dex (Arnett, *et al.* 1985). Either the distance scale chosen is grossly in error (the distances are based on the scales by Tonry using the surface brightness fluctuation [SBF] method, or Jacoby and collaborators based on the brightness distribution of planetary nebulae [PNLF]: see Jacoby *et al.* 1992 for a complete discussion of the distance scale problem) or this Type Ia supernova is underluminous with respect to the standard model. The other curious aspect of the bolometric evolution is the inflection in the light curve around day 20. It should not be surprising that the flux integration has not removed the inflection seen in the optical and near-infrared light curves since the inflection is seen in all colors redder than the B band. No model to date has predicted any inflection at this time in the light curve.

I have performed a similar calculation for 91T, 89B, and 91bg for the data through day 120 which is plotted in Figure 7. The 91bg curve is my preliminary estimate: Alain Porter will be publishing a more definitive curve including important new near-infrared photometry that was not available at the time of this article. The distance moduli and reddenings were taken from Phillips (1993). While one may disagree with the scale of the adopted distances, the internal agreement of the SBF and PNLF distance estimates of 5% (Jacoby *et al.* 1992) implies the *relative* distance scales are quite accurate. In Figure 7 one sees that there must be a range in a factor of 10 in the luminosities of Type Ia supernovae. Based on this data and a number of other bright supernovae, Phillips (1993) has shown that the spread in luminosities is well-correlated with the Δm_{15} parameter, in

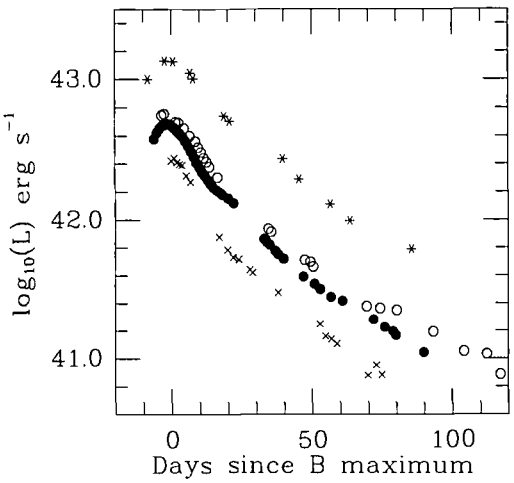

FIGURE 7. "Uvoir" bolometric light curves for (top to bottom) 91T, 89B, 92A, and 91bg

that "slow" supernovae such as 91T are more luminous than "fast" ones like 91bg or 86G. The relative luminosities also correlate well with spectral feature of SiII and TiII seen at maximum light (Phillips, private communication). The strong correlations between the intrinsic luminosities at maximum light and either the photometric or spectrographic characteristics around maximum light mean that is may well be possible that the intrinsic luminosity differences among Type Ia supernovae can be corrected to a "standard" Type Ia event.

The final question perhaps is "Are the majority of Type Ia supernovae homogeneous in luminosity near maximum light, except for a few peculiar ones like 91bg and 86G?" A number of authors, such as Branch & Tammann (1992) and Sandage & Tammann (1993) argue that in a sample of historical supernovae observed with photographic plates, peculiar supernovae are either rare or not important since sub-luminous supernovae will be less likely to be discovered in magnitude limited samples. It is curious however, that only recently have "peculiar" supernovae been accepted as a real phenomenon because of the high quality of the photometric CCD data. Why have almost all the peculiar events been discovered in the last 10 years with CCD photometry? The true incidence of peculiar events, or perhaps more realistically, of a range in luminosities, will only be measured through a systematic analysis of a flux-limited supernova search. A range in luminosity will be seen both as a steepening away from a slope of 5 (due to a Malmquist bias) and a real scatter in the maximum magnitude versus $\log_{10}(z)$ Hubble diagram. To this end, it is interesting to note that the Calán/CTIO survey for supernovae has discovered one supernova (92bo) out of a sample of 7 which appears to be underluminous by 0.8 in B and also has characteristically "fast" photometric behavior (Maza, *et al.* 1994 in preparation).

4. Acknowledgements

I wish to thank Patrice Bouchet, Mario Hamuy, Bruno Leibundgut, José Maza, Mark Phillips, Alain Porter, Lisa Wells, and Stan Woosley for comments on this work and for providing data, both observational and theoretical, that were invaluable in compiling this short review.

REFERENCES

Arnett, W. D., Branch, D., & Wheeler J. C. 1985, Nature, 314, 337

Branch, D., & Tammann, G. A. 1992, ARA&A, 30, 359

Elias, J. E. *et al.* 1985, ApJ, 296, 379

Harkness, R. 1991, In "SN1987A and Other Supernovae", ESO/EIPC Workshop, eds. I.J. Danziger & K. Kjar, 447

Jacoby, G. H., *et al.* 1992, PASP, 104, 599

Kirshner, R. P. *et al.* 1972, ApJ, 185, 303

Kirshner, R. P. *et al.* 1993, ApJ, 415, 589

Leibundgut, B. & Pinto, P. A. 1992, ApJ, 401, 49

Liller, W. 1992, IAU Circ., No. 5428

Phillips, M. M. 1993, ApJ, 413, L105

Pskovskii, Y. P. 1967, Astron. Zhur., 44, 82

Sandage, A., & Tammann, G. A. 1993, ApJ, 415, 1

Type Ia Supernovae: Mechanisms and Nucleosynthesis

By K. NOMOTO,[1] H. YAMAOKA,[2] T. SHIGEYAMA,[1] AND K. IWAMOTO[1]

[1]University of Tokyo, Bunkyo-ku, Tokyo 113, Japan

[2]Kyushu University, Fukuoka 810, Japan

We summarize various explosion models of Type Ia supernovae and their nucleosynthesis features for both Chandrasekhar and sub-Chandrasekhar mass white dwarf models. These models provide different predictions of the photometric and spectroscopic variations among Type Ia supernovae, which are compared with observations. Some attempts to model the peculiar SNe 1991T and 1991bg are shown.

1. Introduction

Type I supernovae (SNe I) are spectroscopically defined by the absence of hydrogen in their optical spectra and further subclassified into Ia, Ib, and Ic (see, e.g., Branch *et al.* 1991). The early-time optical spectra of SNe Ia are characterized by the presence of a deep absorption Si II line near 6150 Å, and their late-time spectra are dominated by strong blends of Fe emission lines (Harkness & Wheeler 1990). Relatively uniform light curves and spectral evolution of SNe Ia have led to the use of SNe Ia as a standard candle to determine cosmological parameters, H_0 and q_0 (Branch & Tammann 1992).

Recent attention has been paid to variations of light curves and spectra among SNe Ia. SNe 1991T and 1991bg have clearly revealed the presence of both spectroscopically and photometrically peculiar SNe Ia. Photometrically, maximum brightness and the decline rate of the light curve show some systematic variations, where SNe 1991T and 1991bg are situated at the two extreme ends of the *brighter–slower* tendency (Phillips 1993; Branch *et al.* 1993). Spectroscopically, the pre-maximum spectra of SNe Ia reveal a significant variation of the composition and expansion velocities of the outermost layers, whereas the post-maximum spectra are relatively uniform except for SN 1991bg.

Theoretically thermonuclear explosions of accreting white dwarfs have been considered to be the most promising models for SNe Ia (e.g., Nomoto 1986, 1994; Woosley & Weaver 1986b). The model that the white dwarf undergoes explosion when its mass becomes close to the Chandrasekhar limit is consistent with the uniformity of SNe Ia. However, the above variations and peculiarities have challenged the Chandrasekhar mass models.

In this review, various types of thermonuclear explosion models and their nucleosynthesis features are summarized. We show some attempts to interpret the variations among SNe Ia including SN 1991T and SN 1991bg and to clarify whether these peculiar SNe Ia belong to a different subclass of SNe I or are only small variant of typical SNe Ia.

2. Evolution of Accreting White Dwarfs

Though the white dwarf models can account for many of the observed features of SNe Ia, the exact binary evolution that leads to SNe Ia has not been identified (e.g., Renzini 1994). The outcome of an accreting white dwarf depends on the accretion rate $\dot{M}$ and the composition (H, He, C+O) of materials transferred from the companion star

as well as the initial mass of the white dwarf (e.g., Nomoto 1982a; Nomoto & Kondo 1991). Chandrasekhar mass white dwarfs could be reached for relatively high accretion rate such as $\dot{M} \approx 10^{-8} - 10^{-6}\ M_\odot\ \mathrm{yr}^{-1}$ thanks to relatively small mass ejection after hydrogen (or helium) shell burning near the surface. Merging of double white dwarfs has been suggested to be an alternative way to form Chandrasekhar mass white dwarfs (Iben & Tutukov 1984; Webbink 1984), though the actual merging process is poorly understood and could lead to different outcome depending on the combination of the white dwarf pair.

The explosion of sub-Chandrasekhar mass white dwarfs is a possible alternative to the above scenario. For $10^{-8}\ M_\odot\ \mathrm{yr}^{-1} \gtrsim \dot{M} \gtrsim 10^{-9}\ M_\odot\ \mathrm{yr}^{-1}$, the ignited helium shell flash is strong enough to initiate an off-center helium detonation (Nomoto 1982b; Woosley *et al.* 1986; Hashimoto *et al.* 1986). This leads to various types of explosions, which includes a central carbon detonation ignited by a helium detonation-induced shock wave (Livne 1990). Also a series of carbon shell flashes during merging of double white dwarfs could produce shock waves that propagate toward the central region to become strong enough to ignite a central carbon detonation because of decreasing area of the converging front (Iben 1988; Wheeler & Harkness 1990; Shigeyama *et al.* 1992).

Among the various models predicted from the possible presupernova evolution, we discuss only the models which would at least satisfy the basic constraints from observations, i.e., the production of a significant amount of ^{56}Ni and intermediate mass elements such as Ca, S, Si, Mg, and O. Thus the carbon detonation in the Chandrasekhar mass white dwarfs (Arnett 1969), the helium detonation in helium white dwarfs (Nomoto & Sugimoto 1977; Woosley *et al.* 1986), and the He/C double detonations (Nomoto 1982b; Woosley *et al.* 1986; Dgani & Livio 1990) are not discussed, since these models produce almost entirely iron peak elements. The good feature of the following models is that the white dwarf has relatively low density layers where the deflagration or detonation synthesizes the intermediate mass elements.

3. Chandrasekhar Mass Models

For the Chandrasekhar mass white dwarf model, carbon burning in the central region leads to thermonuclear runway. At such a high central density as $\sim 3 \times 10^9$ g cm^{-3}, nuclear energy release is only ~ 20 % of the Fermi energy of degenerate electrons. Therefore, the resulting shock wave was found to be not strong enough to directly form a supersonic *detonation* wave (Ivanova *et al.* 1975; Nomoto *et al.* 1976). [Formation of a detonation wave depends on the temperature gradient or preheating in front of the deflagrating region (Blinnikov & Khokhlov 1989; Barkat *et al.* 1990; Woosley 1990), so that studies of convective energy transport during initial thermonuclear runaway are important. Observationally, the nucleosynthesis outcome of carbon detonation, being mostly Fe (Arnett 1969), is not favored, however.]

Afterwards the flame front propagates at a subsonic speed as a *deflagration wave* due to heat transport across the front. Since densities in the burned layers are smaller than the overlying unburned layers, the flame front becomes Rayleigh-Taylor unstable. The resulting mixing of unburned materials into the hot region and the deformation of the burning front enhances the flame speed as simulated in 1D (Nomoto *et al.* 1976, 1984; Woosley & Weaver 1986a,b; Woosley 1990) and 2D (Müller & Arnett 1986; Livne 1993; Arnett 1994) calculations. Since the propagation of the deflagration wave is subsonic, the density it encounters in the outer layer has already decreased due to the expansion of the white dwarf.

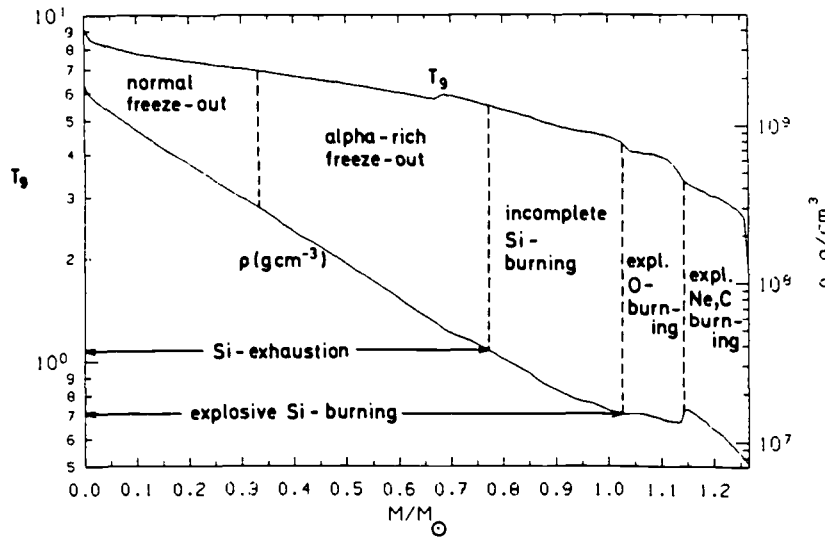

FIGURE 1. Various modes of nuclear burning as a function of peak temperatures and densities attained at the deflagration front of model W7 (Thielemann *et al.* 1986).

3.1. *Fast Carbon Deflagration and Late Detonation*

The carbon deflagration model W7 (Nomoto *et al.* 1984), whose flame speed is on the average about one-fifth of the sound speed, shows a good example of explosive nucleosynthesis as a function of the density at the flame front (Fig. 1: Thielemann *et al.* 1986). In the inner layer ($\rho > 2 \times 10^8$ g cm^{-3}), materials are incinerated into iron-peak elements, mostly ^{56}Ni, while in the outer lower density layers ($\rho \approx 5 - 10 \times 10^7$ g cm^{-3}), the peak temperature is too low to complete silicon burning and thus only Ca, Ar, S, and Si are produced from oxygen burning. In the layers with $\approx 2 - 5 \times 10^7$ g cm^{-3}, explosive burning of carbon and neon synthesizes S, Si, and Mg. In the outermost layers ($\lesssim 1 \times 10^7$ g cm^{-3}), the deflagration wave dies and C+O remain unburned. The composition structure after freeze-out is shown as a function of M_r and the expansion velocity v_{exp} in Figure 2. Synthetic spectra of W7 has been found to be in excellent agreement with the observed optical spectra of SN 1981B (Branch *et al.* 1985) and 1989B (Harkness 1991).

[Since nucleosynthesis in the above model depends on the competition between the propagation of the deflagration wave and the expansion of the white dwarf, the white dwarf model in the hydrodynamical calculation should include a realistic outer layer (or proper outer boundary conditions) owing to the subsonic nature of explosion. The outermost layer of the white dwarf models in Nomoto *et al.* (1976, 1984) is extended to the hydrogen burning shell which processes the accreting matter, thus exerting significantly larger tamping effects on the expansion of the white dwarf than in the zero-pressure boundary models. This might be the source of differences with the deflagration models by Khokhlov *et al.* (1993).]

In the outer layers a relatively fast deflagration induces a formation of a detonation wave. For example, the carbon deflagration model C8, whose propagation velocity v_{def} is slightly higher than W7, has a precursor shock which is strong enough to induce a detonation in the outer layers (Nomoto *et al.* 1984; model F7 in Woosley & Weaver 1986a; delayed detonation models in Khokhlov 1991a). The transition from deflagration to detonation can occur when the flame speed v_{def} is accelerated to the Chapman-Jouguet velocity v_{CJ}. The transition is more likely to occur at lower densities, because the ratio

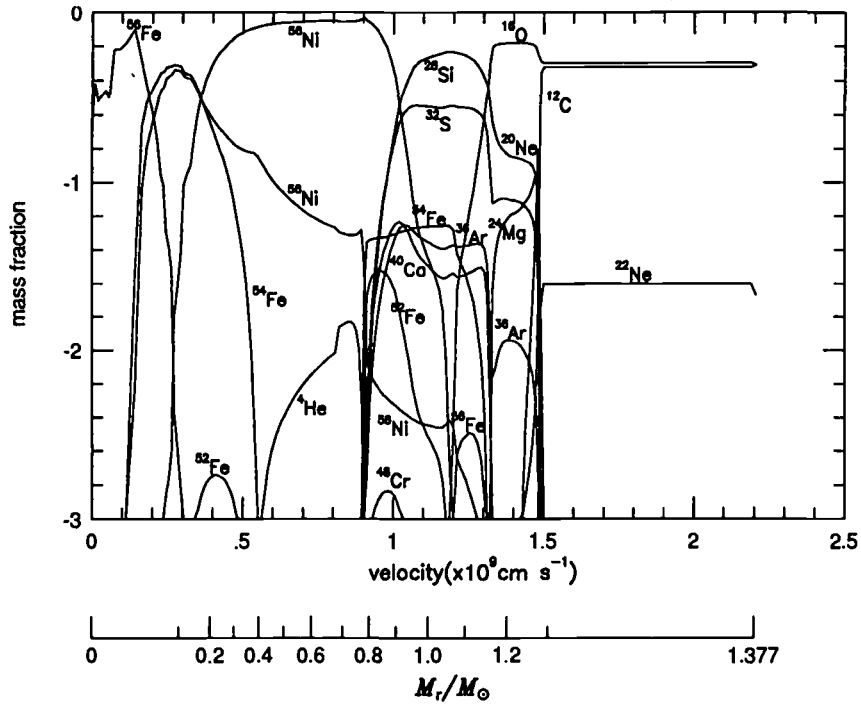

FIGURE 2. Composition of a carbon deflagration model W7 for Type Ia supernovae as a function of interior mass and the expansion velocity (Nomoto *et al.* 1984).

v_{CJ}/v_s (v_s denotes the sound velocity) is smaller due to a larger density jump across the flame front (Khokhlov 1991a), while v_{def}/v_s is larger (Nomoto *et al.* 1984). Since the convective deflagration front may well be quite turbulent and the acceleration of v_{def} may take place in an indeterministic manner, the condition of the transition from deflagration to detonation has not been well understood (e.g., Williams 1985) and it could occur even for $v_{def} < v_{CJ}$ (Khokhlov 1991a; Woosley & Weaver 1994a).

Yamaoka *et al.* (1992) presented several *late detonation* models (W7DN, W7DT, W7DHE, and W8DT) where the fast carbon deflagration like W7 and W8 produces a central Fe/Co/Ni core and an intermediate Si/S/Ca layer and later is transformed into a detonation in the outermost layers. In these models the expansion velocities of Si and S in the outer layers well exceed 20,000 km s^{-1}.

3.2. *Slow Deflagration and Delayed Detonation*

The outcome of carbon deflagration depends on its flame speed, which is highly uncertain. If the flame speed is much lower than in W7, the hydrodynamical behavior is very different. Figure 3 shows the expansion and oscillation of the white dwarf for the propagation speed of 20 times smaller than in W7, i.e., about 1/100 of the sound speed on the average (Nomoto *et al.* 1976). The white dwarf expands to quench nuclear burning at stage 6, where the total energy of the star is still negative. Then the star contracts to burn more material, though the density is too low to produce another ^{56}Ni. This makes the total energy positive ($\sim 5 \times 10^{49}$ erg s^{-1}). Eventually the white dwarf is completely disrupted with the mass of ^{56}Ni $M_{Ni} \sim 0.15\ M_\odot$.

Such a slow flame model with oscillation produces too small a kinetic energy of explosion to account for SN Ia. As mentioned in §3.1, however, the deflagration might induce a detonation at low density layers. In the *delayed detonation* model (Khokhlov 1991a;

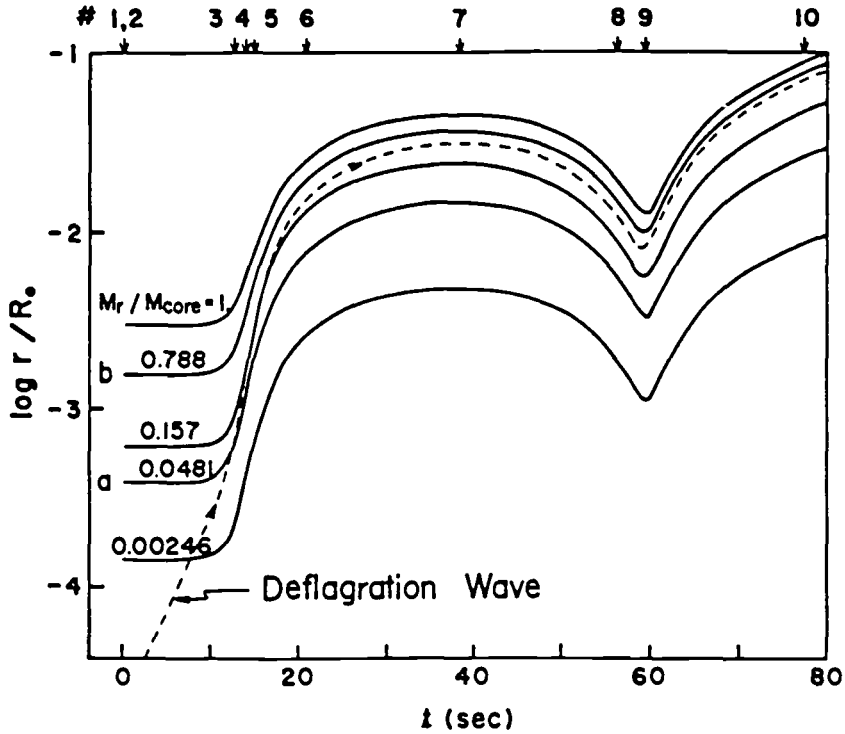

FIGURE 3. Expansion and oscillation of the white dwarf induced by a slow carbon deflagration (Nomoto *et al.* 1976).

Woosley & Weaver 1994a), the deflagration wave is assumed to be transformed into detonation at a certain layer during the first expansion phase; here a quick acceleration of the flame speed to v_{CJ} or quite a turbulent frame is assumed at the transition. In the *pulsating* delayed detonation model (Khokhlov 1991b), the transition to detonation is assumed to occur near the maximum compression due to mixing and compression. In these models, a carbon detonation propagates through the layers with $\rho < 10^8$ g cm^{-3}, which is much lower than in the central carbon detonation model.

Figure 4 shows a composition structure of such a delayed detonation model against the expansion velocity and M_r, which is simulated by assuming that the transition from the deflagration to the detonation occurs when the density at $M_r = 0.6\ M_\odot$ has been decreased to 3×10^7 g cm^{-3} (Nomoto *et al.* 1991, 1994). Because this model includes explosive carbon burning at low densities similar to W7, the composition structure with respect to M_r is not so different from W7 including some unburned C and O, but Si and Ca layers extend to the expansion velocities higher than 15,000 km s^{-1}.

4. Sub-Chandrasekhar Mass Models

As mentioned in §2, a carbon detonation in a sub-Chandrasekhar mass white dwarf may possibly be induced by off-center helium detonation (Livne 1990; Woosley & Weaver 1994b) and by off-center carbon flashes (Shigeyama *et al.* 1992). Because of low central densities, nucleosynthesis in the detonation wave produces a significant amount of intermediate mass elements. This is in contrast to the carbon detonation model where the explosive carbon burning takes place at such high densities as $\gtrsim 10^8$ g cm^{-3} and

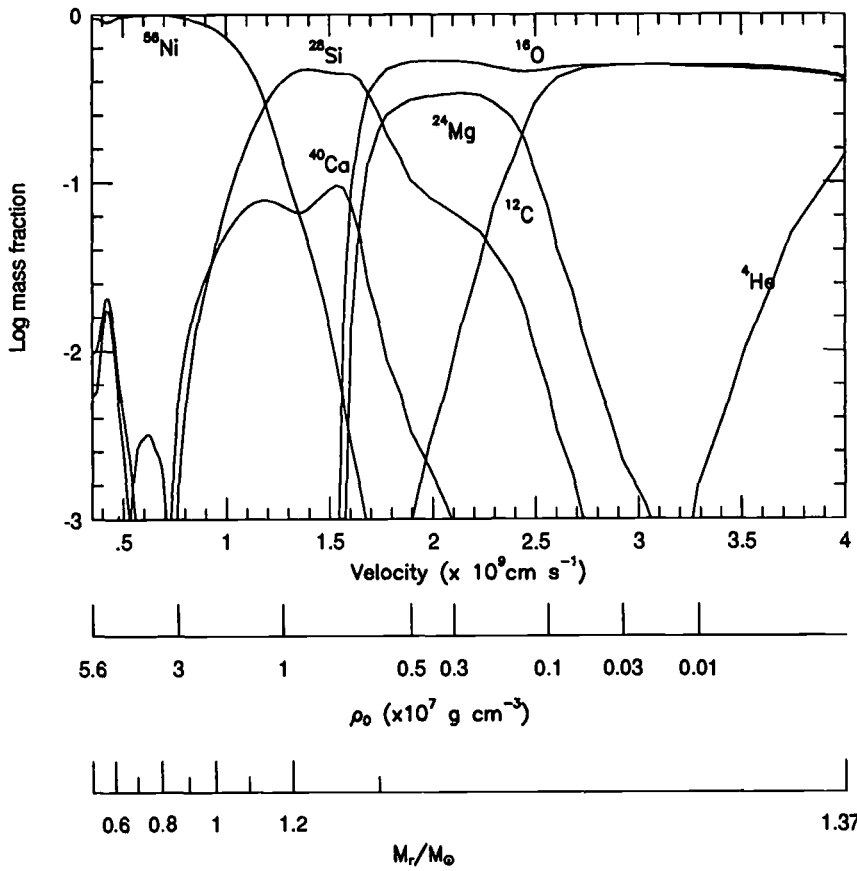

FIGURE 4. Composition of a delayed detonation model as a function of the expansion velocity, M_r, and the initial density (Nomoto *et al.* 1991, 1994).

produces mostly iron-peak elements (Arnett 1969). For the carbon shell flash scenario, hydrodynamical calculations were carried out for the white dwarfs with $M = 1.0 - 1.1$ $M_\odot$ and central densities of $2 - 5 \times 10^7$ g cm^{-3}, where the carbon detonation produces $0.5 - 0.7$ $M_\odot$ ^{56}Ni and the kinetic energy of $1.2 - 1.3 \times 10^{51}$ ergs (Shigeyama *et al.* 1992). Note that the above mass of ^{56}Ni and the explosion energy are not so different from the Chandrasekhar mass models. Figure 5 shows a composition distribution as a function of M_r and the expansion velocity for the carbon detonation in the 1.05 $M_\odot$ white dwarf. The outer layers are Si-rich which is similar to W7, but Si and Ca layers extend to the expansion velocities higher than 15,000 km s^{-1}. Thus the carbon detonation models can account for the basic features of SNe Ia with a restricted range of white dwarf mass ($M \approx 1.0 - 1.2$ $M_\odot$).

In the helium-detonation-induced models, the off-center helium detonation produces ^{56}Ni and He together in the high velocity outermost layers. Because of the presence of radioactive ^{56}Ni near the surface, the spectra would be highly non-LTE. Whether the helium features excited by γ-rays appear or not would be a crucial diagnosis (Lucy 1991; Swartz *et al.* 1993). Examinations of the non-LTE synthetic spectra for these models are necessary. Also, since there is no oxygen in the outermost layers, the velocity of oxygen is much less than 22,000 km s^{-1} (e.g., $\lesssim$ 14,000 km s^{-1} in the W7DHE model; Yamaoka *et al.* 1992) unless some non-spherical effects operate.

If the majority of SNe Ia originate from the sub-Chandrasekhar mass white dwarfs

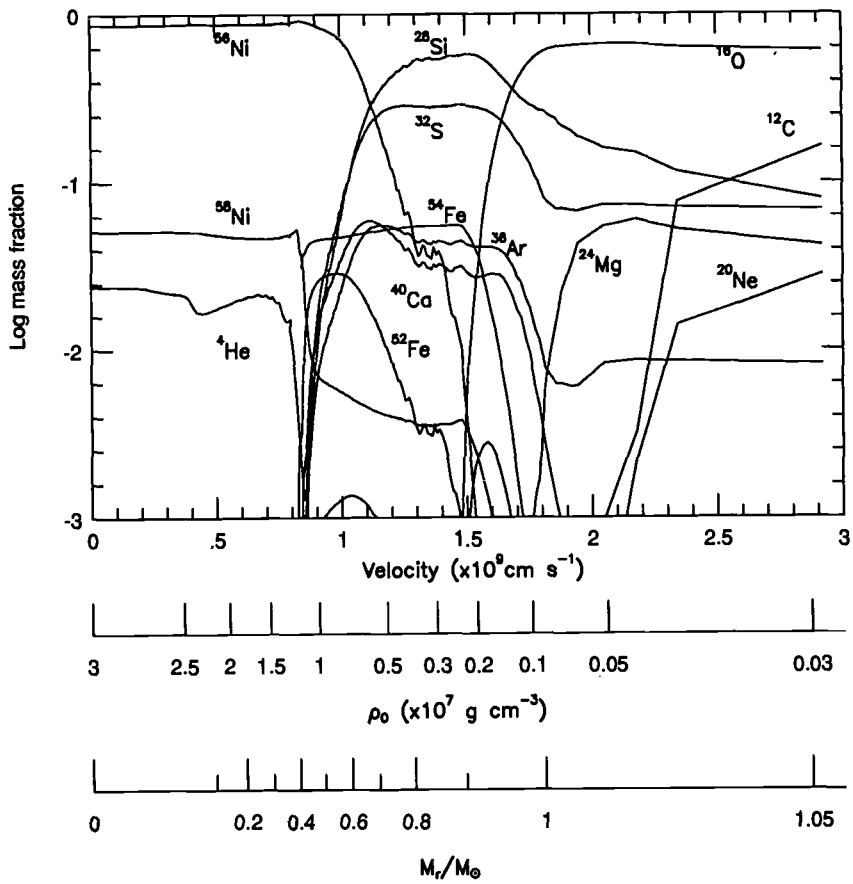

FIGURE 5. Composition of a carbon detonation model of the 1.05 $M_\odot$ white dwarf as functions of the expansion velocity, M_r, and the initial density of the white dwarf (Shigeyama *et al.* 1992).

with possibly a wide range of masses, the question is why SNe Ia are quite uniform. The answer could be as follows: The initial mass of a white dwarf at its formation in a close binary system is likely to be $\sim 1.0\ M_\odot$ rather than $\sim 0.6\ M_\odot$ if it is formed from case BB binary evolution. In case BB, a star with an initial mass of 5 – 8 $M_\odot$ once becomes a helium star of 1.5 – 2 $M_\odot$, which greatly expands to undergo the Roche lobe overflow when its degenerate C+O core grows to $\sim 1\ M_\odot$ (e.g., Sugimoto & Nomoto 1980; Nomoto 1982c). Since the onset stage of the helium envelope expansion depends on the density contrast between the central region and the envelope, the resulting white dwarf mass ($\sim 1\ M_\odot$) is determined strongly by the electron degeneracy in the central region of the core, and thereby depends only weakly on the envelope mass.

5. Peculiar Type Ia Supernovae

5.1. *SN 1991T*

The composition structure of SN 1991T is quite unique (Filippenko *et al.* 1992a; Ruiz-Lapuente *et al.* 1992; Phillips *et al.* 1992; Mazzali *et al.* 1993) consisting of (I) the outermost layer composed of Ni and Fe, (II) the intermediate layer rich in Si/Ca, and (III) the central layer dominated by Fe. In other words, the Si/S/Ca-rich layer (II)

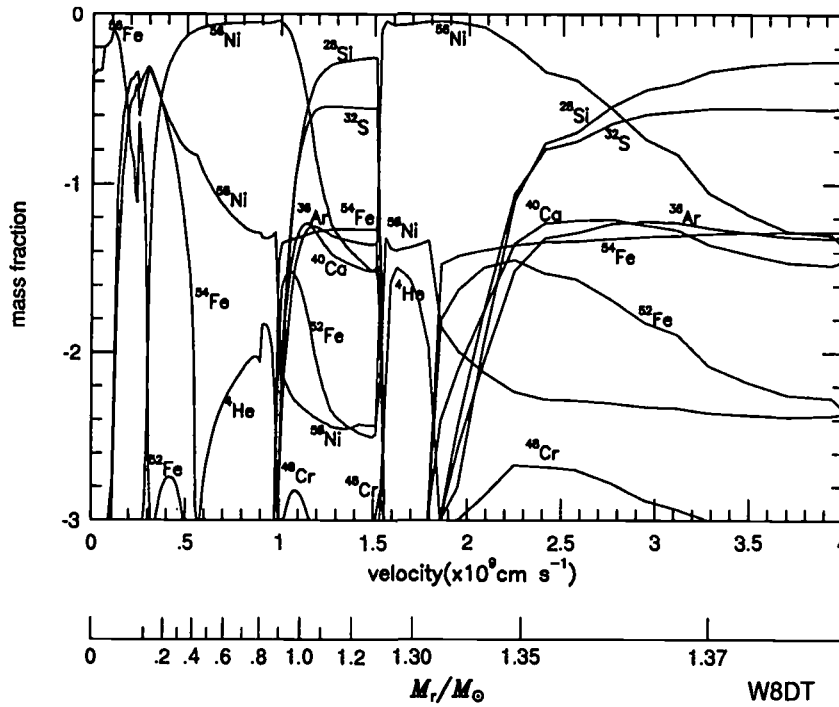

FIGURE 6. Composition of the late detonation model W8DT as a function of the expansion velocity and M_r, where the transition from deflagration to detonation takes place at $M_r = 1.25$ $M_\odot$ where the density ahead of the flame front is 3.5×10^7 g cm^{-3} (Nomoto 1993).

is sandwiched by the two Fe layers (I and III). Such a composition *inversion* with Fe above Si is very different from that inferred from typical SNe Ia. On the other hand, the composition of the inner layers (II and III) is similar to those of typical SNe Ia (Filippenko *et al.* 1992a; Jeffery *et al.* 1992), though the Fe mass seems to be somewhat larger than typical SNe Ia (Mazzali 1992).

The off-center helium detonation model (Filippenko *et al.* 1992a) and the late detonation model (Yamaoka *et al.* 1992) have been suggested to account for the presence of the layer (I). The off-center helium detonation model predicts the presence of a significant amount of He together with ^{56}Ni in the layer (I), thus having the same problem of unseen He lines as discussed in §4.

Yamaoka *et al.* (1992) applied the *late detonation* model to account for not only the high velocity Si features in some SNe Ia but also the above features of SN 1991T in a unified manner. Nucleosynthesis in the detonated matter depends sensitively on the density at the transition from deflagration to detonation; for higher density, more Fe relative to Si is produced as seen from the composition structures of the late detonation models W7DN, W7DT, and W8DT (Fig. 6). In W8DT, the deflagration W8 whose flame speed is 1.2 times faster than W7 is transformed into detonation. Models W7DT and W8DT may account for the basic features of SN 1991T as seen from the good agreement between the calculated light curve for W7DT and observations in Figure 7.

5.2. *SN 1991bg*

SN 1991bg is definitely dimmer than typical SNe Ia; its maximum brightness is about one fourth of SN 1957B which appeared in the same host galaxy NGC 4374 (M84). Also the decline of the light curve after maximum is significantly faster (Filippenko *et al.* 1992b; Leibundgut *et al.* 1993). These features imply that the produced ^{56}Ni is as

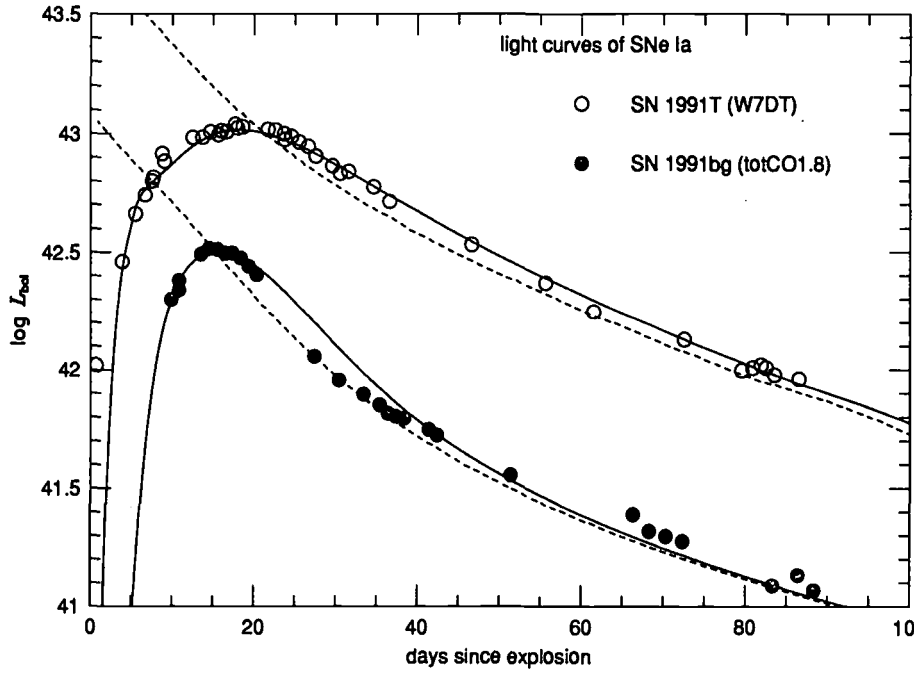

FIGURE 7. The observed visual light curves of the two peculiar SNe Ia, 1991T and 1991bg, are compared with the calculated bolometric light curves for the late detonation model W7DT and the 0.6 $M_\odot$ C+O envelope model, respectively. For both models constant optical opacity κ = 0.3 cm^2 g^{-1} is assumed (Yamaoka *et al.* 1994b).

small as $\sim$ 0.15 $M_\odot$ (Phillips 1993) and the ejected mass is also much smaller than the Chandrasekhar mass.

These features lead to the suggestion that SN 1991bg is the explosion of a white dwarf of $M \sim 0.7\ M_\odot$, which undergoes a carbon detonation induced by an off-center helium detonation (Ruiz-Lapuente *et al.* 1993b; Canal & Ruiz-Lapuente 1994). A problem with such a small mass white dwarf is that more than $\sim 0.2 - 0.3\ M_\odot$ He layer should have been accreted to make the density sufficiently high ($\gtrsim 2 - 3 \times 10^6$ g cm^{-3}) at the base of the accreted layer to initiate an off-center helium detonation. A total white dwarf mass of 0.8 $M_\odot$ of which $\sim$ 0.2 $M_\odot$ is He would be necessary to initiate an off-center He detonation (Nomoto *et al.* 1994). Then the produced ^{56}Ni mass would exceed 0.3 $M_\odot$, and so the supernova would be much brighter than SN 1991bg.

Yamaoka *et al.* (1994b) have constructed a different scenario by invoking a collapse of a white dwarf in the merging of a pair of an O+Ne+Mg white dwarf and a C+O white dwarf. When the smaller mass C+O white dwarf fills its Roche lobe, the resultant rapid mass transfer from the C+O white dwarf would form a thick disk around the more massive O+Ne+Mg white dwarf (Hachisu *et al.* 1986; Benz *et al.* 1990; Mochkovitch & Livio 1990). After the cooling of the outer disk, the O+Ne+Mg white dwarf would collapse due to electron capture (Miyaji *et al.* 1980; Nomoto & Kondo 1991). [A recent update of electron capture rates (Takahara *et al.* 1989) does not alter the above result of collapse (Hashimoto *et al.* 1993).] The collapsing white dwarf is surrounded by the circumstellar envelope composed of original C+O white dwarf matter. If the envelope has become sufficiently cool and as dense as the mantle around the iron core of Type II supernovae (SNe II), the shock wave from the collapsing white dwarf propagates through the envelope to produce some ^{56}Ni and other elements as in SNe II.

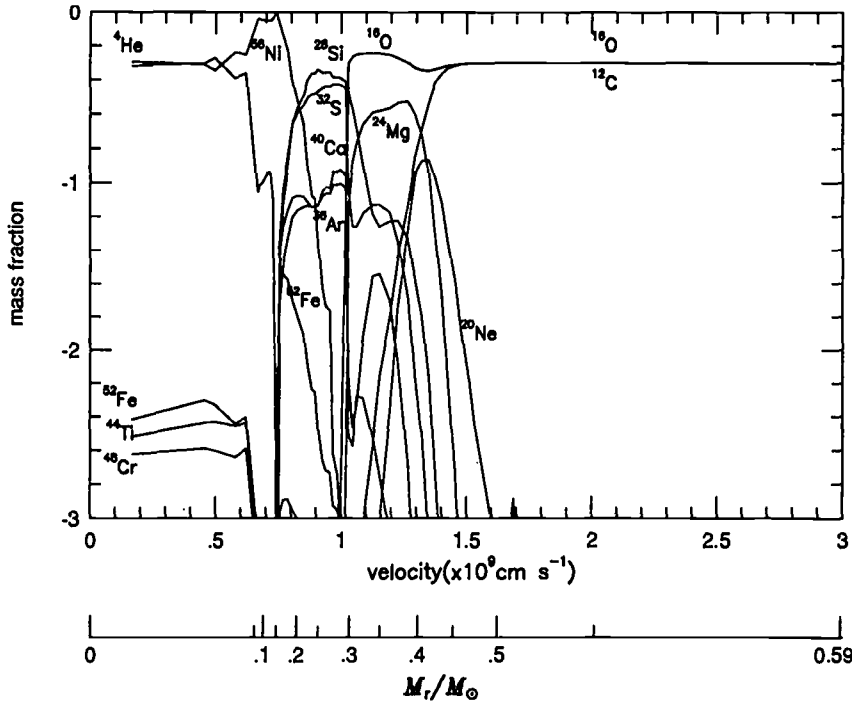

FIGURE 8. Composition of the 0.6 $M_\odot$ ejecta as a function of the expansion velocity and M_r as a model for SN 1991bg. The materials are processed by the shock wave generated at the collapse of a white dwarf (Yamaoka *et al.* 1994b).

Figures 7 and 8 show the composition structure and the optical light curve for the exploding 0.6 $M_\odot$ C+O envelope around the collapsing white dwarf. The initial density structure of the envelope is taken from the presupernova mantle of the 3.3 $M_\odot$ helium star (Nomoto & Hashimoto 1988). Here the explosion energy is assumed to be 1×10^{51} ergs s^{-1} which leads to the synthesis of 0.15 $M_\odot$ ^{56}Ni behind the shock wave. The calculated light curve, powered by the decays of ^{56}Ni and ^{56}Co, reaches much dimmer maximum than typical SNe Ia and declines much faster because of the smaller ejected mass. The good agreement between the calculated light curve and SN 1991bg suggests that the ejecta mass and the kinetic energy of explosion may at least be similar to this model irrespective of the explosion mechanism. Spectroscopic diagnostics would provide a crucial test of this hypothesis.

A Chandrasekhar mass model for SN 1991bg may also be possible. Müller & Höflich (1994) pointed out that opacities must be low in SN 1991bg because of low temperatures due to less ^{56}Ni heating, which could explain the fast light curve of SN 1991bg. This model predicts a very short rise time to maximum. The mass of the ejecta can be better constrained from the light curve decline at later phase, since the decline rate is determined by γ-ray transparency, i.e., the mass and expansion velocities of the ejecta (Leibundgut & Pinto 1992).

Ruiz-Lapuente *et al.* (1993b) noted that the late time spectrum of SN 1991bg shows evidence of emission from low velocity hydrogen gas. If this is confirmed, the companion star might be a hydrogen-rich star, which would be crucial to identify the companion and the explosion mechanism of at least sub-luminous SNe Ia.

6. Variations

6.1. *Light Curves and ^{56}Ni Mass*

In the thermonuclear explosion of white dwarfs, a large amount of ^{56}Ni is synthesized. In these models, the light curves are powered by the radioactive decays $^{56}\mathrm{Ni} \rightarrow {}^{56}\mathrm{Co} \rightarrow {}^{56}\mathrm{Fe}$. Müller & Höflich (1994) presented the currently most sophisticated light curve models. Figure 9 shows simpler approach to the bolometric light curves of W7 and the carbon detonation model of $M = 1.03\ M_\odot$ (CDT3), respectively, where constant optical opacity, $\kappa = 0.1, 0.2, 0.3\ \mathrm{cm^2\ g^{-1}}$, is chosen to reproduce the date of maximum brightness in view of uncertainties of the expansion opacity (Nomoto *et al.* 1994).

The reported variation of the maximum brightness of SNe Ia (Phillips 1993) may be due to the combined variations of the ^{56}Ni mass and the date of maximum. The amount of ^{56}Ni depends on (i) the flame speed in the fast deflagration models, (ii) the location of the transformation into a detonation in the delayed/late detonation models, and (iii) the white dwarf mass in the sub-Chandrasekhar mass models. Because of variations of these parameters, a large variation of the ^{56}Ni mass may be possible.

However, the amount of ^{56}Ni is closely related to the explosion energy E, and therefore is constrained from the abundances and expansion velocities of various elements estimated from the spectra. For the Chandrasekhar mass models, the abundance distribution in the velocity space should be similar to W7 ($M_{\mathrm{Ni}} = 0.58\ M_\odot$ and $E = 1.3 \times 10^{51}$ erg), so that the ^{56}Ni mass is constrained as $0.6 \pm 0.1\ M_\odot$ as is also the case for other favored models DD4 (Woosley & Weaver 1994a) and N32 and PDD3 (Khokhlov 1991b). Sub-Chandrasekhar mass models for $M \approx 1.0 - 1.1\ M_\odot$ produce similar amounts of ^{56}Ni and show an abundance structure in the velocity space similar to W7 (Fig. 5).

For the light curve, the above variations of the ^{56}Ni mass predict a different relation between the maximum brightness and the post-maximum decline rate. The light curve shape depends mainly on the effective diffusion time $\tau_m \propto (\kappa M/v_{\mathrm{exp}}c)^{1/2}$ with $v_{\mathrm{exp}} \propto (M_{\mathrm{Ni}}/M)^{1/2}$ (Arnett 1982). For longer τ_m, the decline of the light curve is slower. First let us assume constant optical opacity κ. Then the model predictions are as follows:
1) For the Chandrasekhar mass models, $M = M_{\mathrm{Ch}}$ is the same but M_{Ni} varies. For larger M_{Ni}, v_{exp} is higher due to larger nuclear energy release and thus τ_m is shorter. This predicts that *brighter* SNe Ia declines *faster*.
2) For the sub-Chandrasekhar mass models, on the contrary, M_{Ni} varies approximately in proportion to M. Then for larger M, M_{Ni} is larger and τ_m is longer; in other words, *brighter* SNe Ia tend to decline more *slowly*.

The effect of optical opacities must also be important as mentioned for SN 1991bg (Müller & Höflich 1994; Höflich *et al.* 1993). Smaller mass ^{56}Ni means less heating of the surface layer, thus lowering κ and τ_m. This effect might explain the *dimmer-faster* relation. However, smaller κ results in a shorter rise time to maximum and thus brighter maximum (Fig. 9). In other words, smaller ^{56}Ni may not necessarily mean dimmer maximum unless ^{56}Ni mass is exceedingly small such as SN 1991bg.

The light curve shape and maximum brightness may be affected by the deceleration of the ejecta due to circumstellar materials or an outer envelope in the pulsating model (Khokhlov *et al.* 1993), though the non-homologous behavior of the pulsating envelope depends on the treatment of outer boundaries (§3.1). With larger deceleration, maximum brightness is reached later and thus dimmer, while the decline of the light curve is slower. Thus this effect enhances the *brighter–faster* tendency of the Chandrasekhar mass models.

If the *brighter–slower* relation suggested by Phillips (1993) is the case, it might favor the sub-Chandrasekhar mass models as noted in Nomoto (1982b). It should be noted that, if SN 1991T and SN 1991bg are not included, variation among other SNe Ia are

rather small (Branch *et al.* 1993). The decay rate of the light curve is also affected by the location of ^{56}Ni (Canal *et al.* 1988; Nomoto & Shigeyama 1991 for SN 1986G).

The interpretation of the maximum brightness $L_{\max}$ of SNe Ia in terms of radioactive decay models has been used to estimate the Hubble constant H_0 (in units of km s^{-1} Mpc^{-1} hereafter: Arnett *et al.* 1985). From the well-observed SNe Ia, Branch (1992) derived $L_{\max} = 2.06 \pm 0.28 \times 10^{43}\ (H_0/50)^{-2}$ erg s^{-1}. Figure 10 shows the dependence of H_0 on the date of maximum brightness $t_{\max}$ for W7 with constant κ, where $t_{\max} = 19 \pm 2$ d leads to $H_0 = 73 \pm 10$ (Shigeyama *et al.* 1992; Yamaoka *et al.* 1994a). From the comparisons with individual SNe Ia, Müller & Höflich (1994) obtained $H_0 = 66 \pm 10$ for the delayed detonation models. If we adopt the above range of H_0 and the Cepheid distance to IC 4182 determined with the HST observation (Sandage et *al.* 1992), SN 1937C would be somewhat brighter than typical SNe Ia, though it depends on the extrapolation to maximum. However, Branch *et al.* (1993) noted that SN 1937C belongs to typical SNe Ia in its spectra and speed class. Further careful study of SN 1937C is needed.

6.2. *Spectra and Mixing*

Supernova spectra are discussed in detail elsewhere in this volume, so that only a few points are discussed here. Important information from the spectra are the expansion velocities of several elements, which can be compared with the theoretical abundance distribution in the velocity space to diagnose the models. Some SNe Ia, 1990N and 1992A, show high velocity Si ($v_{\rm exp} > 20{,}000$ km s^{-1}; see, however, Wheeler *et al.* 1993) and Fe/Co/Ni ($> 15{,}000$ km s^{-1}) as well as O in the wide velocity range from $\approx$ 10,000 to 20,000 km s^{-1} (Leibundgut *et al.* 1991a; Jeffery *et al.* 1992; Mazzali *et al.* 1993; Kirshner *et al.* 1993). SN 1991T has also Fe/Co/Ni at $> 15{,}000$ km s^{-1} and O in the range $\approx$ 10,000 to 20,000 km s^{-1} (Jeffery *et al.* 1992).

The presence of high velocity Si and Fe could be due to (i) mixing of Si and Fe to the outer layers for W7 (Branch *et al.* 1985), (ii) late/delayed detonation, or (iii) carbon detonation in the sub-Chandrasekhar mass white dwarfs (Shigeyama *et al.* 1992).

The presence of low velocity O may provide interesting constraints. Since the production of Fe/Co/Ni implies that the temperature at the burning front becomes high enough ($\gtrsim 4 \times 10^9$ K) to deplete all oxygen (Fig. 1; e.g., Thielemann *et al.* 1994), the local coexistence of O and Fe is difficult to realize. Thus the presence of low velocity O together with higher velocity Fe implies mixing of O and Fe in the velocity space unless Fe is primordial. Such a mixing could occur by convection during the propagation of the deflagration wave (Livne 1993).

Non-spherical explosions induced by late/delayed detonations (see the next section) could also produce non-spherical abundance distribution, i.e., elemental mixing in the velocity space. From the synthetic spectra compared with the observations, mixing is favored by Branch *et al.* (1985) but not by Harkness (1991). Asymmetries of the explosion might also be responsible for the significant variations in the time evolution of the expansion velocity of Si (Branch *et al.* 1988; Barbon *et al.* 1990). However, Filippenko (1989) and Branch and van den Bergh (1993) noted the presence of correlation between the expansion velocity of Si and the type of host galaxies, which may not be accounted for with asymmetries. SNe Ia in E and S0 galaxies show significantly faster decrease in the expansion velocity with time; it would be due to the steeper density gradient in the outer layer, which may reflect the difference in the mass and circumstellar matter of the progenitors. (See also van den Bergh and Pazder 1992 for brightness – host galaxy type relation.)

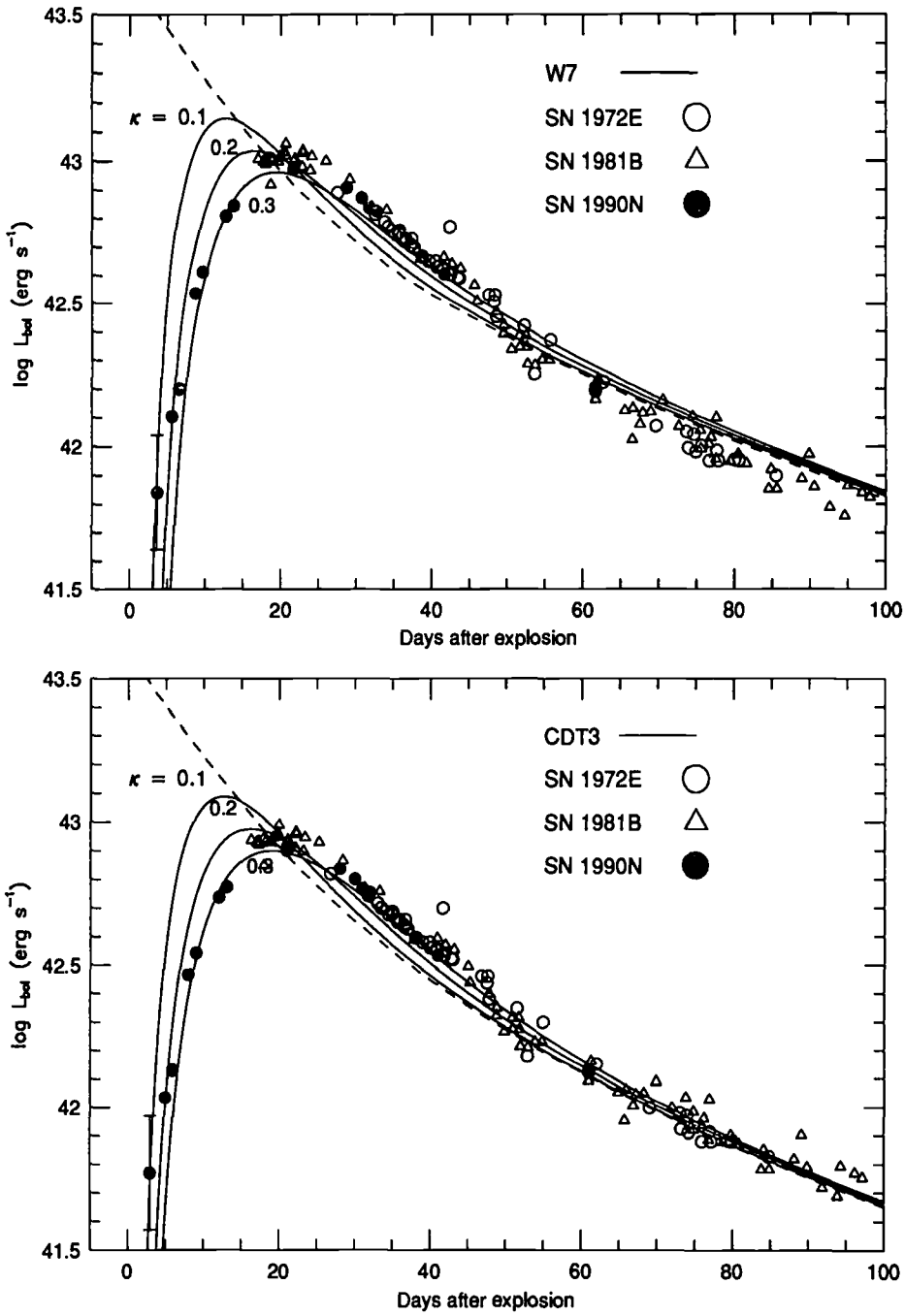

FIGURE 9. The calculated bolometric light curve for the carbon deflagration model W7 (a) and the carbon detonation model CDT3 (b) for κ = 0.1, 0.2, and 0.3 cm^2 g^{-1} as compared with the observed visual light curves of SN 1972E, 1981B, and 1990N (Leibundgut *et al.* 1991a,b) (Nomoto 1993).

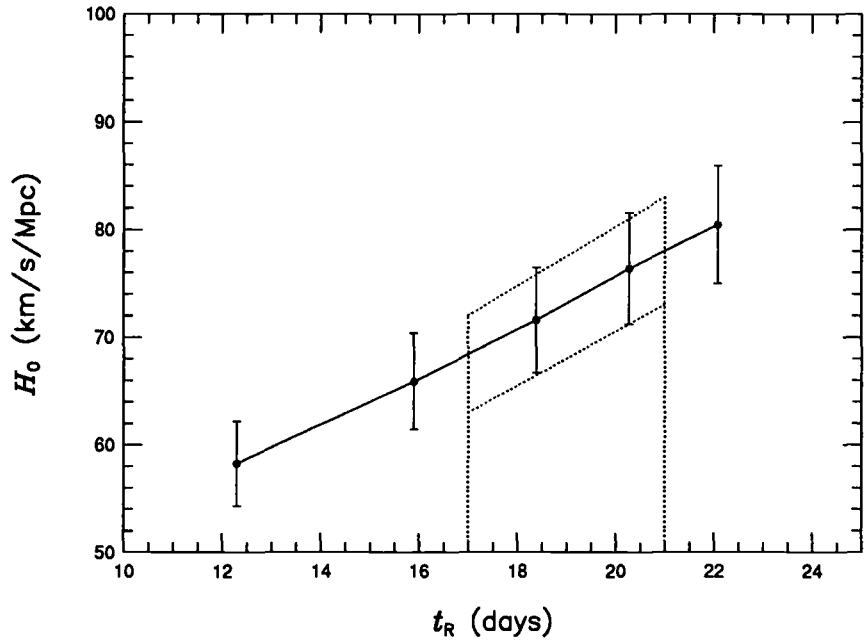

FIGURE 10. Dependence of the Hubble constant H_0 on the date of maximum brightness t_{max} for W7, where t_{max} is obtained as a function of κ (Yamaoka *et al.* 1994a).

6.3. *Aspherical Explosions and Polarization*

Some theoretical models of SNe Ia predict rather large deviation from spherical explosions. 2D simulations of the deflagration wave have shown the formation of a largely deformed burning front (Livne 1993; Arnett 1994). If the delayed/late detonation are induced by such quite a deformed deflagration, the resultant off-center carbon detonation is likely to start from a *point* rather than a spherical shell. Such an explosion is likely to form non-spherical ejecta (e.g., Steinmetz *et al.* 1992). Asymmetries must be a common feature of all the off-center detonation type models, including the He detonation, He/C double detonations, and delayed/late detonation. If large asymmetries do exist as predicted by the above models, they should be seen in polarization (Shapiro & Sutherland 1982; Jeffery 1991). However, spectropolarimetric observations of SN 1992A 2 weeks and 7 weeks after maximum have shown no significant polarization (Fig. 11; Spyromilio & Bailey 1993), which is an important constraint on the theoretical models.

7. Isotopic Abundances and Metallicity

The isotopic ratios of iron peak elements relative to the solar ratios provide important constraints on the models. For the Chandrasekhar mass models, the isotopic ratios are sensitive to the central density at the carbon ignition and metallicity. Overproduction of the sum of ^{54}Fe and ^{58}Ni relative to ^{56}Fe in the deflagration model has been pointed out (Nomoto *et al.* 1984; Woosley & Weaver 1986b). These two isotopes originate from mass zones with intermediate neutron excess, which can be caused either by electron capture in the central layer or initial metallicity of the white dwarf in the outer layers where CNO nuclei were transformed to ^{22}Ne after H and He burning.

As most SNe Ia occur in spiral galaxies on scale heights larger than 300 pc (Della Valle & Panagia 1992) where [Fe/H] values are 0.0 to −0.5, one has *average* metallicities of

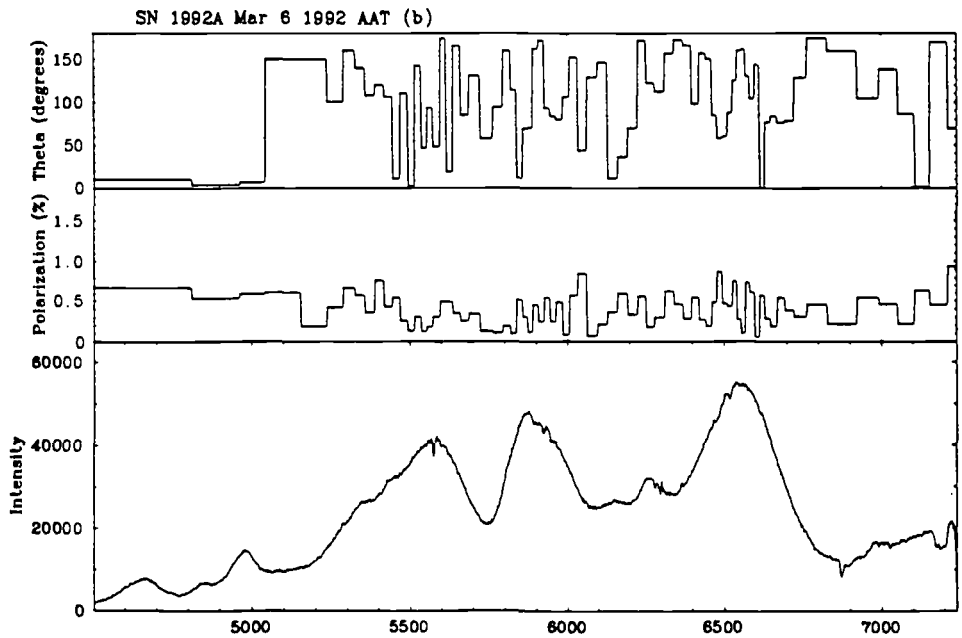

FIGURE 11. Spectropolarimetric observations of SN 1992A 7 weeks after maximum (Spyromilio & Bailey 1993).

0.5–0.6 times solar. This makes the $^{54}Fe/^{56}Fe$ and $^{58}Ni/^{56}Fe$ ratios within a factor of 2 and 3 of the solar ratios, respectively (Thielemann *et al.* 1993), which lie within the present uncertainty range of thermonuclear reaction rates. The chemical separation of ^{22}Ne during the solidification of white dwarfs has the same effects (Isern *et al.* 1991; Ogata *et al.* 1993).

The central region of the delayed detonation model undergoes electron capture behind the slower deflagration for a longer time than in W7, thereby having a rather strong constraint on the initial central density of the white dwarf ($\lesssim 2 \times 10^9$ g cm^{-3}) to avoid overproduction of ^{54}Cr (Khokhlov 1991b). If the carbon ignition density is higher than the threshold for the convective Urca neutrino process due to the Urca pair of ^{23}Na–^{23}Ne (1.8×10^9 g cm^{-3}) and ^{25}Mg–^{25}Ne (1.3×10^9 g cm^{-3}), initiation of the carbon deflagration is delayed to such high density as $\rho_c \gtrsim 4 \times 10^9$ g cm^{-3} (e.g., Iben 1982; Barkat & Wheeler 1990). Then the overproduction of ^{54}Cr is inevitable in the slow deflagration/delayed detonation models.

The carbon ignition density is higher for larger neutrino cooling during accretion phase. To avoid the *convective* Urca phase, neutrino emission due to the *local* Urca shell process of, e.g., ^{21}Ne–^{21}F pair (Paczyński 1973) should be suppressed, i.e., the metallicity of accreting white dwarfs should be low enough. For sufficiently low metallicity, the ignition density could be close to the threshold for the *convective* Urca neutrino process (e.g., Nomoto & Iben 1985), thus requiring further careful study.

For the sub-Chandrasekhar mass carbon detonation models, since central densities are too low for electron capture to operate, neutron excess in the central region is due only to metallicity (i.e., ^{22}Ne), thus being much smaller than in the Chandrasekhar mass models. The isotopic ratios of integrated abundances of ejecta after decay of unstable nuclei with respect to solar abundances is shown in Figure 12 for $M = 1.05\ M_\odot$ (Nomoto *et al.*

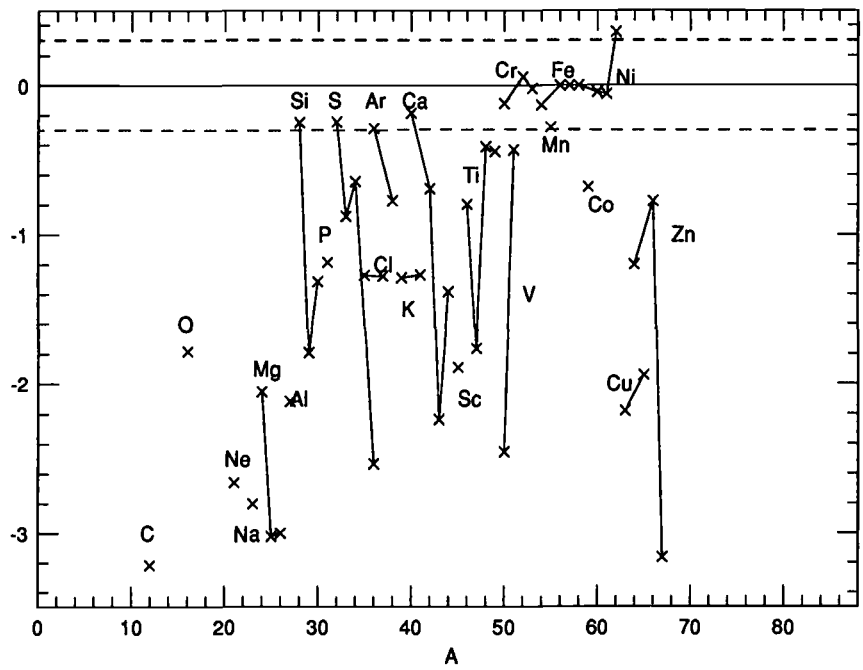

FIGURE 12. The ratios of integrated abundances of the carbon detonation model with $M = 1.05$ $M_\odot$ after decay of unstable nuclei, normalized to ^{56}Fe, relative to solar abundances (Nomoto *et al.* 1994).

1994). Overproductions of ^{54}Fe, ^{58}Ni, and ^{54}Cr are not observed and the isotopic ratios of iron peak elements are within a factor of 2 relative to the solar ratios.

To discuss the degree of overproduction of neutron-rich Fe peak elements, we should taken into account the fact that the observed estimate of SNe Ia frequency is as low as 10 % of the total supernova occurrence so that Fe from SNe Ia is about 50 % of total Fe (van den Bergh & Tammann 1991; Tsujimoto *et al.* 1993; Bravo *et al.* 1993).

8. Discussion

Observations have shown significant variations in the light curves and spectra of SNe Ia with the two extreme ends of SN 1991T and 1991bg, which have challenged the theoretical models. Possible theoretical explanations of these variations and some critical observations to discriminate the models are as follows. For the Chandrasekhar mass models, there exist some variations in the ignition conditions, such as the central density and temperature of the white dwarf, due to variations of age and metallicity of the white dwarf and the mass accretion rate. This would cause some differences in the flame speed $v_{\rm def}$, which in turn would yield a significantly different outcome if the transition from deflagration to detonation occurs.

In the late detonation models, if the difference in $v_{\rm def}/v_{\rm s}$ is small, differences in the composition in the inner regions and thus the expansion velocity at the outer edge of the inner Fe core are small. However, a large variation of the composition in the outermost layer would result due to late detonation, where nucleosynthesis depends sensitively on the density at this transition. The extremely Fe-rich case would correspond to SN 1991T. Si-rich cases would be more common, since the transition to detonation may occur more easily at lower densities. Some variations in the expansion velocities of Si may be

due to the variation of the transition density including the case of no transition (i.e., pure deflagration). For the delayed detonation models including the pulsation cases, the observed variation would also be resulted from the variation of the transition point.

For the sub-Chandrasekhar mass models, variation of the white dwarf mass at the initiation of the carbon detonation may lead to the observed variations. For example, the explosion of a larger white dwarf mass produces larger amount of ^{56}Ni because of the higher densities.

For the light curves, the Chandrasekhar mass models and the sub-Chandrasekhar models predict opposite relationships between the maximum brightness and the decay rate of the bolometric light curve. Therefore, the confirmation of the suggested *brighter – slower* relation in the observed bolometric light curves is crucial (Phillips 1993). With more samples, it should be clarified whether SN 1991T and 1991bg are rather exceptional cases (Branch *et al.* 1993). If opacity effects are significant, variation of the rise time to maximum brightness $t_{\max}$ is expected to be large. Variation of the late decline rate would be more useful, since the late light curve is determined by γ-ray transparencies. Early line γ-ray observations are particularly important to constrain the mass and distribution of ^{56}Ni in SNe Ia (e.g., Burrows *et al.* 1991; Lichti *et al.* 1993; Shigeyama *et al.* 1993; Ruiz-Lapuente *et al.* 1993a).

Spectra suggest a certain non-spherical abundance distribution, i.e., mixing in the velocity space from low velocity O and high velocity Fe in SN 1990N and 1992A; UV observations at early phase are necessary to confirm high velocity Fe and Co (Wheeler & Harkness 1990; Wheeler *et al.* 1993). Theoretically the mechanism of mixing in velocity space should be explored, which would require multi-dimensional high resolution calculations of the propagation of the deflagration/detonation.

Sub-Chandrasekhar mass models that invoke the off-center He detonation predict the presence of He together with ^{56}Ni in the outermost layers. Non-LTE spectral calculations are necessary to see whether He features can be hidden. This is important also to understand the nature of SNe Ic and SNe Ib, i.e., to provide constraint on the amount of He in SNe Ic (Nomoto *et al.* 1990; Swartz *et al.* 1993).

Asymmetries in the explosions are expected to be significant for the off-center detonation type models such as the He/C detonations in the sub-Chandrasekhar mass models and the delayed/late carbon detonations. Asymmetric expansions might cause the spectral variations in the early phase. Therefore, confirmation of the negligible asymmetry by the polarization observations is crucial (Jeffery 1991; Spyromilio & Bailey 1993).

Acknowledgements

We would like to thank M. Hashimoto and F.-K. Thielemann for collaborative work on the subjects discussed in this paper. This work has been supported in part by the grant-in-Aid for Scientific Research (05242102, 05242103, 06233101, 06740181, 4227) of the Ministry of Education, Science, and Culture in Japan.

REFERENCES

Arnett, W.D. 1969, Ap&A 5, 180

Arnett, W.D. 1982, ApJ 253, 785

Arnett, W.D. 1994, in this volume

Arnett, W.D., Branch, D., & Wheeler, J.C. 1985, Nature 314, 337

Barbon, R., Benetti, S., Cappellaro, E., Rosino, L., & Turatto, M. 1990, A&A 237, 79

Barkat, Z., Livne, E., Swartz, D.A., & Wheeler, J.C. 1990, in Supernovae, ed. J.C. Wheeler *et al.* (World Scientific), p. 133

Barkat, Z., & Wheeler, J.C. 1990, ApJ 355, 602

Benz, W., Bowers, R.L., Cameron, A.G.W., & Press, W. 1990, ApJ 348, 647

Blinnikov, S.I., & Kohkhlov, A.M. 1986, Sov. Astron. Let., 12, 131

Branch, D., Doggett, J.B., Nomoto, K., & Thielemann, F.-K. 1985, ApJ 294, 619

Branch, D., Drucker, W., & Jeffery, D.J. 1988, ApJ 330, L117

Branch, D., Fisher, A., & Nugent, P. 1993, AJ 106, 2383

Branch, D., Nomoto, K., & Filippenko, A.V. 1991, Comments on Astrophysics XV, 221

Branch, D., & Tammann, G. 1992, ARA&A 30, 359

Branch, D., & van den Bergh, S. 1993, AJ 105, 2231

Bravo, E., Isern, J., & Canal, R. 1993, A&A 269, 187

Burrows, A., Shankar, A., & Van Riper, K.A. 1991, ApJ 379, L7

Canal, R., Isern, I., & López, R. 1988, ApJ 330, L113

Canal, R., & Ruiz-Lapuente, P. 1994, in this volume

Della Valle, M., & Panagia, N. 1992, AJ 104, 696

Dgani, R., & Livio, M. 1990, ApJ 361, 540

Filippenko, A.V. 1989, PASP 101, 588

Filippenko, A.V., *et al.* 1992a, ApJ 384, L15

Filippenko, A.V., *et al.* 1992b, AJ 104, 1543

Hachisu, I., Eriguchi, Y., & Nomoto, K. 1986, ApJ 308, 161

Harkness, R.P. 1991, in SN 1987A and Other Supernovae, eds. I.J., Danziger & K. Kjär (European Southern Observatory, Garching), p.447

Harkness, R.P., & Wheeler, J.C. 1990, in Supernovae, ed. A. Petschek (Springer, Berlin), p. 1.

Hashimoto, M., Iwamoto, K., & Nomoto, K. 1993, ApJ 414, L105

Hashimoto, M., Nomoto, K., Arai, K., & Kaminisi, K. 1986, ApJ 307, 687

Höflich, P., Müller, E., & Khokhlov, A.M. 1993, A&A 268, 570

Iben, I.Jr. 1982, ApJ 253, 248

Iben, I.Jr. 1988, ApJ 324, 355

Iben, I.Jr., & Tutukov, A. 1984, ApJ Suppl. 55, 335

Isern, J., Canal, R., & Labay, J. 1991, ApJ 372, L83

Ivanova, L.N., Imshennik, V.S., & Chechetkin, V.M. 1975, Ap&SS 31, 497

Jeffery, D. 1991, ApJ 375, 264

Jeffery, D., Leibundgut, B., Kirshner, R.P., Benetti, S., Branch, D., & Sonneborn, G. 1992, ApJ 397, 304

Khokhlov, A.M. 1991a, A&A 245, 114

Khokhlov, A.M. 1991b, A&A 245, L25

Khokhlov, A.M., Müller, E., & Höflich, P. 1993, A&A 270, 23

Kirshner, R.P. *et al.* 1993, ApJ 415, 589

Leibundgut, B., Kirshner R.P., Filippenko, A.V., Shields, J.C., Foltz, C.B., Phillips, M.M., & Sonneborn, G. 1991a, ApJ 371, L23

Leibundgut, B., & Pinto, P.A. 1992, ApJ 401, 49

Leibundgut, B., Tammann, G.A., Cadonau, R., & Cerrito, D. 1991b, A&AS 89, 537

Leibundgut, B., *et al.* 1993, AJ 105, 301

Lichti, G.G. *et al.* A&AS 97, 215

Livne, E. 1990, ApJ 354, L53

Livne, E. 1993, ApJ 406, L17

Lucy, L.B. 1991, ApJ 383, 308

Mazzali, P. 1992, private communication

Mazzali, P., Lucy, L.B., Danziger, I.J., Gouiffes, C., Cappellaro, E.R., & Turatto, M. 1993, A&A 269, 423

Miyaji, S., Nomoto, K., Yokoi, K., & Sugimoto, D. 1980, PASJ 32, 303

Mochkovitch, R., & Livio, M. 1990, A&A 236, 378

Müller, E., & Arnett, W.D. 1986, ApJ 307, 619

Müller, E., & Höflich, P. 1994, A&A 281, 51

Nomoto, K. 1982a, ApJ 253, 798

Nomoto, K. 1982b, ApJ 257, 780

Nomoto, K. 1982c, in Supernovae: A Survey of Current Research, ed. M.J. Rees and R.J. Stoneham (Dordrecht: Reidel), p. 210

Nomoto, K. 1986, Ann. NY Acad. Sci. 470, 294

Nomoto, K. 1993, in The Realm of Interacting Binary Stars, ed. J. Sahade *et al.* (Kluwer, ASSL), p. 247

Nomoto, K., Filippenko, A.V., & Shigeyama, T. 1990, A&A 240, L1

Nomoto, K., & Hashimoto, M. 1988, Phys. Rep. 163, 13

Nomoto, K., & Iben, I.Jr. 1985, ApJ 297, 531

Nomoto, K., & Kondo, Y. 1991, ApJ 367, L19

Nomoto, K., & Shigeyama, T. 1991, in Supernovae, ed. Woosley S.E. (Springer, Berlin), p. 572.

Nomoto, K., & Sugimoto, D. 1977, PASJ 29, 765

Nomoto, K., Sugimoto, D., & Neo, S. 1976, ApSS 39, L37

Nomoto, K., Thielemann, F.-K., & Yokoi, K. 1984, ApJ 286, 644

Nomoto, K., Yamaoka, H., Shigeyama, T., Kumagai, S., & Tsujimoto, T. 1991, in Neutron Stars: Observations and Theory, eds. J. Ventura and D. Pines (Kluwer, NATO ASI) p. 143

Nomoto, K., Yamaoka, H., Shigeyama, T., Kumagai, S., & Tsujimoto, T. 1994, in Supernovae (Les Houches, Session LIV), ed. S. Bludman et al. (Elsevier Sci. Publ.), p. 199

Ogata, S., Iyetomi, H., & Ichimaru, S. 1993, Phys. Rev. E 48, 1344

Paczyński, B. 1973, Acta Astr. 23, 1

Phillips, M.M. 1993, ApJ 413, L105

Phillips, M.M., *et al.* 1992, AJ 103, 1632

Renzini, A. 1994, in this volume

Ruiz-Lapuente, P., Cappellaro, E., Turatto, M., Gouiffes, C., Danziger, I.J., Della Valle, M., & Lucy, L.B. 1992, ApJ 387, L33

Ruiz-Lapuente, P., Jeffery, D.J., Challis, P.M., Filippenko, A.V., Kirshner, R.P., Ho, L.C., Schmidt, B.P., Sanchez, F., & Canal, R. 1993b, Nature 365, 728

Ruiz-Lapuente, P., Lichti, G.G., Lehoucq, R., Canal, R., & Cassé 1993a, ApJ 417, 547

Sandage, A., Saha, A., Tammann, G.A., Panagia, N., & Macchetto, D. 1992, ApJ 401, L7

Shapiro, P.R., & Sutherland, P.G. 1982, ApJ 263, 902

Shigeyama, T., Kumagai, S., Yamaoka, H., Nomoto, K., & Thielemann, F.-K. 1993, A&AS 97, 223

Shigeyama, T., Nomoto, K., Yamaoka, H., & Thielemann, F.-K. 1992, ApJ 386, L13

Spyromilio, J. & Bailey, J.A. 1993, Proc. Astr. Soc. Australia 10, 263

Steinmetz, M., Müller, E., & Hillebrandt, W. 1992, A&A 254, 177

Sugimoto, D., & Nomoto, K. 1980, Space Sci. Rev. 25, 155

Swartz, D.A., Filippenko, A.V., Nomoto, K., & Wheeler, J.C. 1993, ApJ 411, 313

Takahara, M., Hino, M., Oda, T., Muto, K., Wolters, A.A., Glaudemans, P.W.M., & Sato, K., 1989, Nucl. Phys. A504, 167

Thielemann, F.-K., Hashimoto, M., & Nomoto, K. 1990, ApJ 349, 222

Thielemann, F.-K., Nomoto, K., & Hashimoto, M. 1993, in The Origin and Evolution of the Elements, ed. N. Prantzos (Cambridge University Press), p. 297

Thielemann, F.-K., Nomoto, K., & Hashimoto, M. 1994, in Supernovae (Les Houches, Session LIV), ed. S. Bludman et al. (Elsevier Sci. Publ.), p. 629

Thielemann, F.-K., Nomoto, K., & Yokoi, K. 1986, A&A 158, 17

Tsujimoto, T., Iwamoto, K., Hashimoto, M., Nomoto, K., & Thielemann, F.-K., 1993, in Origin and Evolution of the Elements, ed. K. Kubono & T. Kajino (World Scientific), p. 50

van den Bergh, S., & Pazder, J. 1992, ApJ 390, 34

van den Bergh, S., & Tammann, G. 1991, ARA&A 29, 363

Webbink, R. 1984, ApJ 277, 355

Wheeler, J.C., & Harkness, R. 1990, Rep. Prog. Phys. 53, 1467

Wheeler, J.C., Swartz, D., & Harkness, R. 1993, Phys. Rep. 227, 113

Williams, F.A. 1985, Combustion Theory (Menlo Park: Benjamin/Cummings), p. 217

Woosley, S.E. 1990, in Supernovae, ed. A. Petschek (Springer), p. 182

Woosley, S.E., Taam, R.E., & Weaver, T.A. 1986, ApJ 301, 601

Woosley, S.E., & Weaver, T.A. 1986a, Lecture Notes in Physics, 255, 91

Woosley, S.E., & Weaver, T.A. 1986b, ARA&A 24, 205

Woosley, S.E., & Weaver, T.A. 1994a, in Supernovae (Les Houches, Session LIV), ed. S. Bludman et al. (Elsevier Sci. Publ.), p. 63

Woosley, S.E., & Weaver, T.A. 1994b, ApJ, 423, 371

Yamaoka, H., Nomoto, K., Shigeyama, T., & Hashimoto, M. 1994b, in preparation

Yamaoka, H., Shigeyama, T., & Nomoto, K. 1994a, in Evolution of the Universe and its Observational Quest, ed. K. Sato (Universal Academy Press, Tokyo), p. 565

Yamaoka, H., Shigeyama, T., Nomoto, K., & Thielemann, F.-K. 1992, ApJ 393, L55

SN Ia Diversity: Theory and Diagnostics

By R. CANAL[1] AND P. RUIZ-LAPUENTE[2]

[1]Departament d'Astronomia i Meteorologia, Universitat de Barcelona, Barcelona, Spain

[2]Harvard-Smithsonian Center for Astrophysics
60 Garden St., Cambridge, MA 02138, USA

Existing evidence of photometric and spectroscopic diversity among Type Ia supernovae is compared with the predictions from physical modeling of the explosions. Concerning light curves, changes in the central ignition density of massive ($M \simeq M_{Ch}$) C+O white dwarfs alone do not give appreciable variation. Spectroscopic diversity has been found in the nebular phase, the underluminous SN 1991bg providing an extreme case. A range of 0.4–0.8 $M_\odot$ of ^{56}Ni synthesized in the explosions is derived from the nebular spectra of a sample of SNe Ia. For SN 1991bg, however, a ^{56}Ni mass of ~ 0.1 $M_\odot$ only is obtained. That leads us to explore models based on the detonation of low-mass WDs for this SN. Additionally, a nebular spectrum of SN 1991bg shows narrow Hα emission at the position of the SN. If this emission is confirmed against background contamination from the galaxy, it would be first evidence of a nondegenerate, H-rich companion in a SNIa.

1. Introduction

Type Ia supernovae (SNIa) are attributed to the thermonuclear explosion of C+O white dwarfs. Explosive ignition would be the outcome of accretion of matter from a close companion in a binary system and it would completely burn the star, leaving no bound remnant. In most models, explosive C burning starts at the center of the WD as a result of the increase in density and temperature induced by quasistatic mass growth. Explosive ignition densities (determined by the thermonuclear reaction rates in the strong-screening/pycnonuclear regime) always are $\rho_{ign} \gtrsim 2 \times 10^9 g\ cm^{-3}$, which means that the WD mass is $M \gtrsim 1.37 M_\odot$, thus very close to the Chandrasekhar mass for a ^{12}C+^{16}O mixture ($\simeq 1.45$ $M_\odot$). The exact ignition density depends on the mass-accretion rate and also on the mass and temperature of the WD at the start of the accretion process (Hernanz *et al.* 1988), but the range of masses allowed by those models is very small ($\Delta M \lesssim 0.1 M_\odot$). This provides the main theoretical basis to the claim that SNIa explosions are very homogeneous and can thus be used as standard candles for extragalactic distance determinations.

In the "standard" model outlined above, one big unknown is the mechanism that propagates the burning from the center to most of the mass of the WD. Burning might propagate supersonically all the way from the center to the surface, as a *detonation* (Arnett 1969). It might also start subsonically and remain so until being quenched by the expansion of the star (driven by the pressure waves that run ahead of the burning front), as a *deflagration* (Nomoto, Thielemann & Yokoi 1984; Sutherland & Wheeler 1984; Woosley, Axelrod & Weaver 1984). Or, finally, it might start subsonically, as a deflagration, and at some point turn supersonic (*delayed detonation*: Khokhlov 1991; Woosley 1992). Complete detonation of massive ($M \simeq M_{Ch}$) C+O WDs would incinerate the whole star to Fe-peak elements (due to the overall high densities) and thus appears incompatible with the presence of lines of intermediate-mass elements (O through Ca) in the spectra obtained around maximum light (Woosley & Weaver 1986). Deflagrations can produce more admissible explosions, but since the propagation of burning depends

on the development of hydrodynamic instabilities (in full 3–dimensions) there is currently no way to predict the velocities of the flame front (see, however, Arnett and Livne, this volume, for recent progress). Delayed detonations can also produce acceptable explosions (even with some advantage over pure deflagrations as to the nucleosynthesis of neutron–rich Fe–peak nuclides), but they add to the uncertainties of the initial, subsonic stage, that of the point where the burning becomes supersonic (delayed detonations induced by pulsation do not escape this, since the occurrence and characteristics of the pulsation depend on the velocities of the subsonic flame along the previous stage and the start of the detonation is hypothetical).

In the massive C+O WD model, the material accreted from the companion can, in principle, have any chemical composition but it has to be effectively incorporated into the degenerate core to make its central density grow. Lighter material (H, He) has thus to burn (nonexplosively) into C+O in the outer layers. One popular scheme avoids this restriction by having another, less massive C+O WD as the companion of the mass–accreting one (Iben & Tutukov 1984). The actual dearth of suitable systems in the Galaxy now casts strong doubts on this scheme (see Renzini, this volume) and it has renewed interest on the ones where the companion is nondegenerate and has a H–rich envelope (*symbiotic stars*, for instance).

Statistical arguments (Kenyon *et al.* 1993) seem to preclude massive WDs in symbiotics as the progenitors of most SNIa. Lower–mass WDs should thus also be considered. C+O WDs with masses significantly below M_{Ch} cannot be made to explode by quasistatic accretion, but they can do it if they are *dynamically* compressed. That can be achieved by shock waves originated by explosive burning of the outer layers. *He detonation* (either of the He accumulated from burning H or of that accreted from a He–rich companion) has been pointed out as a likely mechanism (Livne 1990; Livne & Glasner 1991; Woosley & Weaver 1993; see also Livne, this volume). It induces C detonation near the center of the low–mass C+O WDs. The difficulty encountered in the detonation of *massive* WDs no longer holds here, since at lower densities detonation leads to partial burning only and thus produces intermediate–mass elements as well as the Fe–peak ones. A much wider range of masses ($M \sim 0.5 - 1.3\ M_\odot$) can work in the detonation model, in contrast with the very narrow range of the "standard", massive WD model.

From the observational point of view, the claimed homogeneity of SNIa is also increasingly challenged. The light curves of different events span a sizeable range and there even seems to be a correlation between peak luminosity and the slope of the light curve after maximum (see Suntzeff, this volume). The recent SN 1991bg has been extremely underluminous (Filippenko *et al.* 1992a; Leibundgut *et al.* 1993; Phillips *et al.* 1993). Spectroscopic diversity is seen in the spectra around maximum (see Filippenko, this volume), and premaximum spectra of the superluminous SN 1991T (Filippenko *et al.* 1992b; Ruiz–Lapuente *et al.* 1992) significantly differ from those of the more "standard" SN 1990N (Leibundgut *et al.* 1991). Differences are also found between nebular spectra of diverse SNIa (Ruiz–Lapuente & Filippenko 1993), SN 1991bg being again an extreme case (Ruiz–Lapuente *et al.* 1993a). In the following we will outline the range of variability allowed by current models and also the diagnostics that can be obtained from modeling of the spectra (especially in the nebular phase) concerning the mass of the progenitors, the explosion mechanism, and also the nature of the companions of the exploding stars.

2. Models and Diagnostics

Let us consider first the range of variation in the observable characteristics of the explosions (peak luminosities, light–curve shapes, spectral evolution) allowed by the "standard", massive C+O WD model. As we have already pointed out, within its very narrow mass interval a sizeable range of explosive ignition densities is possible, depending on the initial mass of the WD, its temperature, and the accretion rate. It is $2 - 3 \times 10^9 g\ cm^{-3} \lesssim \rho_{ign} \lesssim 1.5 \times 10^{10} g\ cm^{-3}$ (Hernanz *et al.* 1988). The upper part of this range ($\rho_{ign} \gtrsim 8 - 8.5 \times 10^9 g\ cm^{-3}$), however, would probably lead to gravitational collapse rather than to thermonuclear explosion (Timmes & Woosley 1992, 1994; García *et al.* 1993). In the remaining density range, the dynamics, nucleosynthesis and light curves of explosions corresponding to different ignition densities and different explosion mechanisms (deflagrations and delayed detonations, with diverse prescriptions and parameters for the propagation of burning) has been systematically explored (Canal *et al.* 1991; Bravo *et al.* 1993). The conclusion is that, for a given mechanism and fixed prescription and parameters, variation in the ignition density alone, within the preceding range, gives almost constant peak luminosity and only minor variations in light curve shape and expansion velocity of the photospheric material.

Larger variations are of course possible if we allow changes in prescriptions and parameters within a given mechanism (in fact, both pure deflagrations and pure detonations are limiting cases of delayed detonations). The problem here is that we have no criterion to determine prescriptions and parameters from the characteristics of a given evolutionary scheme. Models of the light curves and spectra are, in principle, powerful diagnostic tools. Optical luminosities at any stage of SNe Ia depend on the amount of radioactive Ni (^{56}Ni) initially synthesized in the explosion, its distribution within the ejecta, on the total mass of the object, and on the velocity of the ejecta, all these factors entering in the fraction of energy deposited from γ–rays and positrons originated in the decay chain $^{56}\mathrm{Ni} \rightarrow {}^{56}\mathrm{Co} \rightarrow {}^{56}\mathrm{Fe}$. Optical spectra reveal the chemical composition of the material and its distribution in velocity space.

With the possible exception (to be discussed below) of SN 1991bg, no known SNIa light curve cannot be acceptably adjusted within the "standard" model if we allow significant variations of the explosion prescriptions and/or parameters from one explosion to another. Simultaneous measurements of optical magnitudes and γ–ray line fluxes can further restrict the models. In the case of SN 1991T, the lack of detection of the 847 keV line by COMPTEL, together with the measured apparent blue magnitude (m_B) at the same epoch has discarded many variations of the "standard" model (Ruiz–Lapuente *et al.* 1993b, see Höflich *et al.* 1993 for a discussion on the models proposed by these authors).

Photospheric spectra of SNe Ia have been calculated, up to now, mostly for deflagration models (Wheeler, Swartz & Harkness 1993; see Eastman, this volume, and Kirshner *et al.* 1993 for more recent developments). They have chiefly been compared with the spectra of the "standard" SNIa SN 1981B around maximum and the agreement is good. Premaximum spectra of the "normal" SN 1990N and of the "peculiar" SN 1991T have also been calculated from *ad hoc* modifications of the "standard" deflagration model W7 (Nomoto, Thielemann & Yokoi 1984). Jeffery *et al.* (1992), using a LTE procedure, find that SN 1990N might be consistent with the W7 model, except for the outer, higher–velocity material, and that the chemical composition of the outer layers of SN 1991T departs both from that of SN 1990N and from that predicted by the W7 model. From a NLTE analysis, Ruiz–Lapuente *et al.* (1992) conclude that the premaximum spectra of

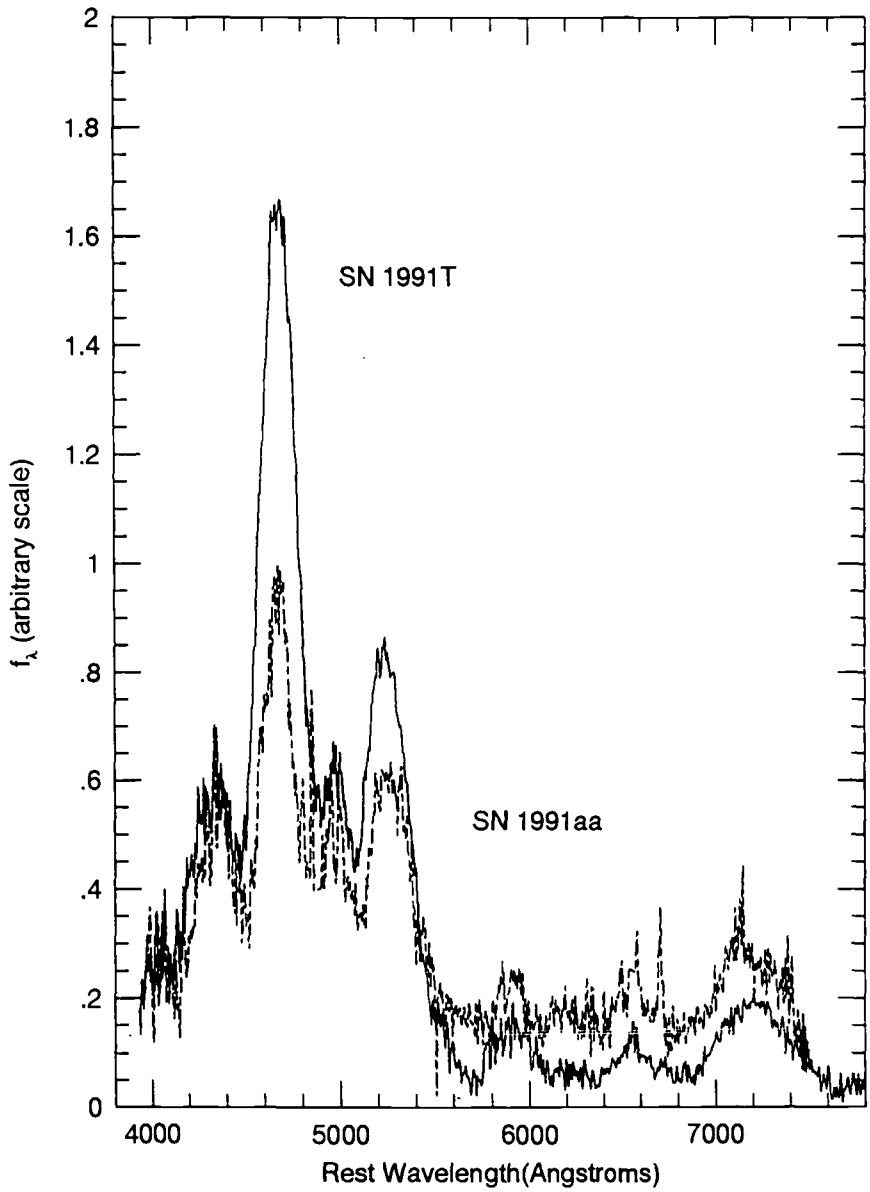

FIGURE 1. Comparison of a nebular spectrum of SN 1991T in NGC 4527 and the nebular spectrum of SN 1991aa in an anonymous galaxy corresponding to a similar phase (around 270 days and 250 days after explosion respectively). The spectra show broader [FeIII], [FeII] and [CoIII] features and a higher emissivity at around 4600 $\AA$ in SN 1991T than in SN 1991aa. We found that the electron temperature in SN 1991T seems to be higher than in SN 1991aa by more than 1000 K (see Ruiz-Lapuente and Filippenko 1993). The spectra have been shifted to agree in the flux scale.

SN 1991T are consistent with a composition made of ^{56}Ni and its decay products ^{56}Co and ^{56}Fe in the outermost layer.

Moreover, Ruiz–Lapuente & Filippenko (1993) find, from the nebular spectra, that the Co+Fe core of SN 1991T extends up to higher velocities than in other SNe Ia observed in their late stages. In Fig. 1 we compare spectra of SN 1991T and SN 1991aa corresponding to a similar phase. Nebular spectra of SNe Ia were first modelled by Axelrod (1980) and Meyerott (1980), based on a Fe+Co composition, and compared with SN 1972E. Among more recent observations of SNe Ia at the nebular phase, differences have been found. Modeling of the spectra (Ruiz–Lapuente & Lucy 1992; Ruiz–Lapuente & Filippenko 1993, Ruiz-Lapuente *et al.* 1993a) points to variable amounts of ^{56}Ni in the Fe-peak core being synthesized in the corresponding explosions: SN 1986G would have produced a low amount (around 0.4 $M_\odot$) and SN 1991T the largest amount of the sample (0.7–0.8 $M_\odot$); SN 1991aa and SN 1972E would have synthesized intermediate amounts (0.5–0.6 $M_\odot$). The lowest tail of the ^{56}Ni production is held so far by SN 1991bg which according to our analysis (Ruiz-Lapuente *et al.* 1993a) would have produced an amount of ^{56}Ni similar to that synthesized in SNe II.

Concerning the nature of the companion of the exploding WD, there are possible diagnostics for the cases in which the companion has a H–rich envelope. In particular, Chugai (1986) predicted that the fraction of the envelope stripped by the explosion would appear as low–velocity material in the nebular spectrum of the SN. This has been confirmed by 2–D hydrodynamical simulations (Livne, Tuchman & Wheeler 1992). The very underluminous SN 1991bg could have provided the first example of it (Ruiz–Lapuente *et al.* 1993a).

SN 1991bg, besides being clearly underluminous at all observed epochs showed by the shape of its light curve and by the early transition to the nebular phase of its spectra signs of having synthesized a small amount of ^{56}Ni, and also of having only a small mass of material on top of the radioactive region (Filippenko *et al.* 1992b; Leibundgut *et al.* 1993). In Fig. 2 we show a nebular spectrum obtained 212 days after explosion. A preliminary analysis (Figure 2a, dotted line) indicated a lower electron temperature and a smaller width of the Fe lines than in "normal" SNIa. That also pointed to a very small initial ^{56}Ni mass ($\lesssim 0.1 - 0.2 M_\odot$). The spectrum cannot be fitted with a pure Fe–peak composition, but requires mixing of intermediate–mass elements with the decay products of ^{56}Ni. All this could be consistent with detonation of a small–mass C+O WD. To check it, we have calculated the spectrum of a detonated C+O WD of 0.65 $M_\odot$. It is also shown in Fig. 2 (Figure 2b, dotted line).

An important point is the feature around 6,570 Å, which would correspond to *Hα emission* at low velocity. This result, if confirmed by a thorough checking against possible galactic Hα emission at the position of the SN, would be the first clear evidence of a nondegenerate, H–rich companion in a SNIa.

3. Discussion

The explosion of massive C+O WDs by variations of the deflagration/delayed detonation mechanisms seems to account rather well for the light curves and spectra of the SNe Ia. However, this agreement may not be unique since models of explosions of less massive C+O WDs have not yet been checked through extensive spectral and light curve calculations. SN 1991bg now poses a new problem to the standard model, since it might be indicating that low–mass C+O WDs can explode as SNIa. Such explosion may occur as C detonation of the core induced by He detonation in the outer layers, with the He resulting from burning of H accreted from a nondegenerate companion (testing the spectral

effects of the He left after the detonation in the outer shell needs further consideration). Contribution from low–mass, H–accreting WDs in symbiotics to the SNIa population might also meet the statistical requirements that seem hard to be fulfilled by massive WDs and/or double degenerates.

Detonation of C+O WDs in the mass range 0.6–1.2 $M_\odot$ would synthesize from extremely low amounts of ^{56}Ni ($\simeq$ 0.01 $M_\odot$) up to $\simeq$ 1.1 $M_\odot$ (Woosley & Weaver 1994; Ruiz–Lapuente *et al.* 1993a; when comparing the yields in the two references, it should be noted that in the second one the mass of the accreted He layer is implicitly included in the total mass of the core). That would largely encompass the range inferred from observed SNIa luminosities, from SN 1991bg up to SN 1991T. There is a gap between SN 1991bg and events such as SN 1986G, but it might perhaps be partially filled by recent estimates of the luminosity of Tycho's SN (van den Bergh 1993).

The singular characteristics of SN 1991bg might also be fitted by other models. Nomoto (this volume) suggests that, in a merging double degenerate system the more massive WD could collapse after accreting 0.2–0.4 $M_\odot$ while the rest of the less massive WD forms an envelope of $\sim$ 0.6 $M_\odot$. A neutron star would result, $\sim$ 0.1 $M_\odot$ of ^{56}Ni would be synthesized at the bottom of the envelope, and the latter would be ejected with a total kinetic energy $\sim 10^{51}$ erg. On the other hand, some pulsating delayed detonation models of massive WDs can equally produce only small amounts of ^{56}Ni (Höflich *et al.*, this volume). Accurate modeling of the light curves and spectra of the different models is thus required. Detection of events similar to SN 1991bg would greatly contribute to clarify the issue.

The possibility that SNIa cover a significant range of peak luminosities does not preclude their use for extragalactic distance determinations. It only means that measurements of distances to individual supernovae, based on adequate models, should be preferred to the classical "standard candle" assumption.

Acknowledgements

We have reviewed here recent work resulting from collaborations with different colleagues and groups: of R.C. with E. Bravo, J. Isern, and J. Labay, on the hydrodynamics and nucleosynthesis of SNIa explosions; of P. R.–L. with P.M. Challis, A.V. Filippenko, L.C. Ho, D.J. Jeffery, R.P.Kirshner, and B.P. Schmidt, on different aspects of the analysis and modeling of optical SNIa spectra. F. Sánchez has collaborated with R.C and P.R.–L in obtaining nebular spectra of SNIa at the WHT during the period in which SN 1991bg and SN 1991aa were observed. The above-mentioned colleagues are coauthors of the work submitted to refereed journals and of the talks given at this Colloquium which we have summarized here.

P.R.L acknowledges support from STScI grant GO-2563.01-87A.

REFERENCES

Arnett, W. D. 1969, A&SS, 5, 180

Axelrod, T. A. 1980, in Type I Supernovae, ed. J. C. Wheeler (Austin: Univ. of Texas Press), 80

Bravo, E. *et al.* 1993, A&A, 269, 187

Canal, R. *et al.* 1991, in SN 1987A and Other Supernovae, ed. I.J. Danziger & K. Kjär (Garching bei München: ESO), 153

Filippenko, A. V. *et al.* 1992a, AJ, 104, 1543

Filippenko, A. V. *et al.* 1992b, ApJ, 384, L15

García, D. *et al.* 1993, in preparation

Hernanz, M., Isern, J., Canal, R., Labay, J., & Mochkovitch, R. 1988, ApJ, 324, 331

Höflich, P., Müller, E. & Khokhlov, A. 1993, ApJS, in press

Iben, I., Jr., & Tutukov, A. V. 1984, ApJS, 54, 335

Jeffery, D. J. *et al.* 1992, ApJ, 397, 304

Kenyon, S. J., Livio, M., Mikolajewska, J., & Tout, C. A 1993, ApJ, 407, L81

Khokhlov, A. M. 1991, A&A, 245, 114

Kirshner, R. P. *et al.* 1993, ApJ, in press

Leibundgut, B. *et al.* 1991, ApJ, 371, L33

Leibundgut, B. *et al.* 1993, AJ, 105, 301

Livne, E. 1990, ApJ, 354, L53

Livne, E. & Glasner, A. S. 1991, ApJ, 370, 272

Livne, E., Tuchman, Y., & Wheeler, J. C. 1992, ApJ, 399, 665

Meyerott, R. E. 1980, ApJ, 259, 257

Nomoto, K., Thielemann, F.-K., & Yokoi, K. 1984, ApJ, 286, 644

Phillips, M. M. 1993, ApJ, 413, L105

Ruiz-Lapuente, P., & Lucy, L. B. 1992, ApJ, 400, 127

Ruiz-Lapuente, P., & Filippenko, A. V. 1993, in Origin and Evolution of the Elements, ed. N. Prantzos, E. Vangioni-Flam, & M. Cassé (Cambridge: Cambridge Univ. Press), p. 318

Ruiz-Lapuente *et al.* 1992, ApJ, 387, L33

Ruiz-Lapuente *et al.* 1993a, ApJ, 365, 728

Ruiz-Lapuente *et al.* 1993b, Nature, 365, 728

Sutherland, P. G., & Wheeler, J. C. 1984, ApJ, 280, 282

Timmes, F. X., & Woosley, S. E. 1992, ApJ, 397, 220

Timmes, F. X., & Woosley, S. E. 1994, ApJ, 420, 348

van den Bergh, S. 1993, ApJ 413, 67

Wheeler, J.C., Swartz, D.A., & Harkness, R.P. 1993, Phys. Rep. 227, 113

Woosley, S.E. 1992, in Gamma-Ray Line Astrophysics, ed. P. Durouchoux & N. Prantzos (New York: AIP), 270

Woosley, S.E., & Weaver, T.A. 1986, ARA&A 24, 205

Woosley, S.E., & Weaver, T.A. 1994, ApJ, 423, 371

Woosley, S.E., Axelrod, T.S., & Weaver, T.A. 1984, in Stellar Nucleosynthesis, ed. C. Chiosi & A. Renzini (Dordrecht: Reidel), p. 263

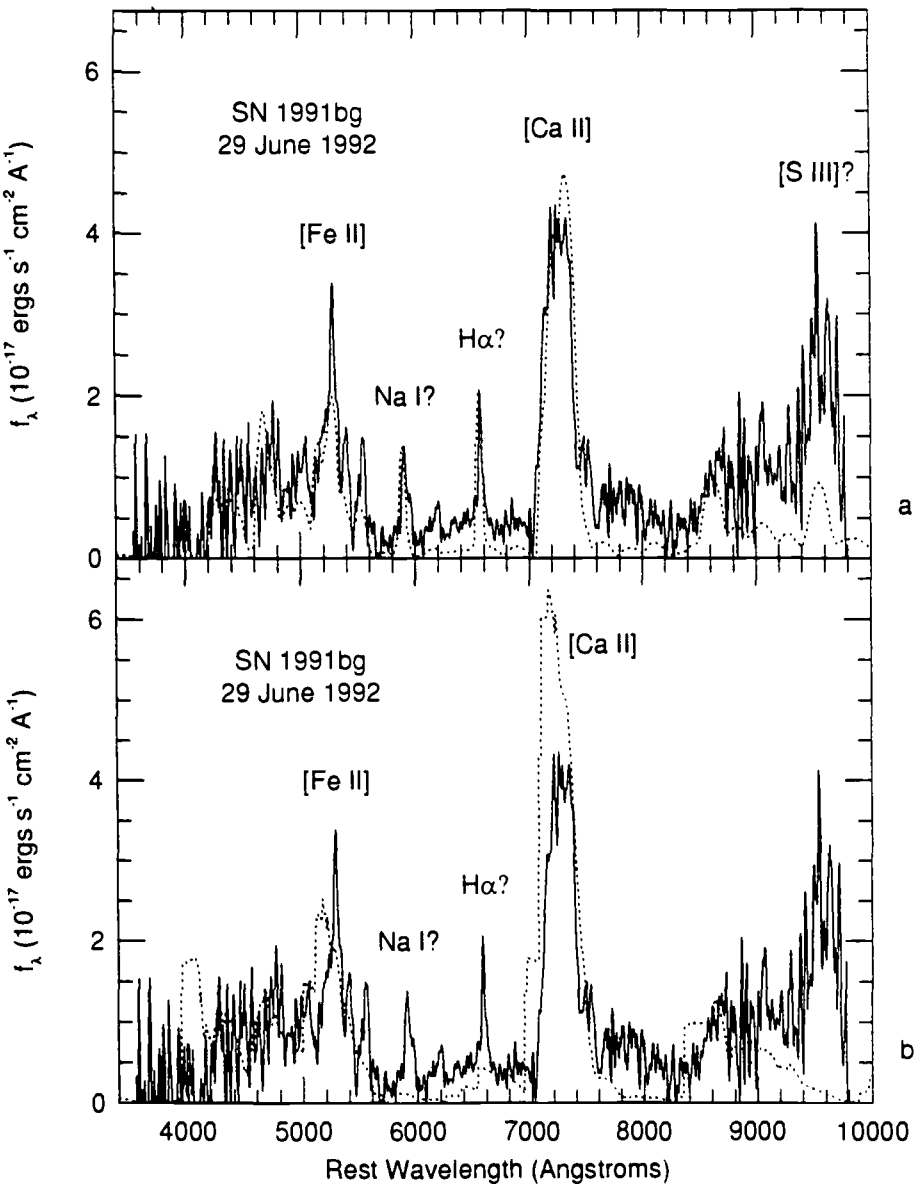

FIGURE 2. (*a*) The nebular spectrum of SN 1991bg 212 days after explosion (solid line), and a synthetic spectrum (dotted line) from a preliminary model (see Ruiz–Lapuente *et al.* 1993a). Slow moving H has been included to test the plausibility of the Hα identification. (*b*) The nebular spectrum of SN 1991bg 212 days after explosion (solid line), and calculated spectrum of a detonation model of a C+O WD of 0.65 $M_\odot$ for the same epoch (dotted line).

Searching for Type Ia Supernova Progenitors

By ALVIO RENZINI

Dipartimento di Astronomia, Università di Bologna,
CP 596, I-40100 Bologna, Italy
and European Southern Observatory

The status for the identification of specific astronomical objects as SNIa progenitors is reviewed. Single or double degenerate progenitors? Chandrasekhar or sub-Chandrasekhar mass exploders? These are the two main questions still to be answered concerning the progenitors of Type Ia supernovae. Although all four combinations may be represented in nature, searches for double degenerates seem to indicate that such systems provide a minor channel for the production of SNIa's. The more promising candidates appear to be symbiotic stars, consisting of a single degenerate star and a sub-Chandrasekhar mass star.

1. Introduction

The nature of the progenitors of Type Ia SNe remains highly conjectural. The fact that SNIa's occur in elliptical galaxies – where star formation ceased a very long time ago – indicates that at least in some cases there is a long delay between the formation of the progenitor and the explosion. Attention has generally concentrated on white dwarfs (WD) in binary systems, in which the explosion of the WD is triggered by accretion from the companion. Various WD explosion mechanisms are discussed by Ken'ichi Nomoto and Eli Livne at this meeting, and I will here deal with the identification of specific astronomical objects as suitable precursor candidates.

The two main questions are schematically represented in Fig. 1. In the SD model (Whelan & Iben 1973) the companion to the WD is a living, evolved star pouring matter onto the WD. In the DD model (Iben & Tutukov 1984; Webbink 1984; Paczyński 1985) the companion is also a WD, and the explosion occurs when the two WDs merge as a result of the angular momentum losses via gravitational wave radiation (GWR). In the SD model only a thermonuclear clock (i.e. the secondary's lifetime) sets the explosion time, while in the DD model also the GWR clock is at work.

In the classical scenario the explosion takes place when the mass of the accreting WD reaches the Chandrasekhar limit ($\sim 1.4\,M_{\odot}$), and carbon is ignited under extremely degenerate conditions. However, reaching the Chandrasekhar limit is not a necessary condition for a WD to explode. Helium detonations and double (He and C) detonations are indeed possible in SD models provided that the accretion rate is in a suitable range (see Nomoto, these proceedings), which may be the case for C/O-WD + He-WD pairs in DD models. Four basic combinations of the two pairs of options are therefore possible, as sketched in Fig. 1. The identification of SNIa progenitors consists primarily in determining the relative weight of the four basic combinations: DD/Ch, SD/Ch, DD/Sub-Ch, and SD/Sub-Ch, all of which might be represented in nature. Such determination would be important for a number of astrophysical problems. In particular, it would help us to figure out how the SNIa rate evolves past a generic burst of star formation, i.e., its rise time to the maximum rate, and the timescale of the subsequent decline. This would be especially relevant for the determination of the rate of iron release in galaxies and clusters of galaxies (see Renzini *et al.* 1993 and references therein), and for the evolution of the SN heating of the interstellar medium, in particular in the case of elliptical galaxies (e.g., Ciotti *et al.* 1991).

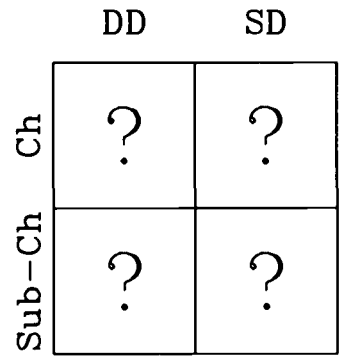

FIGURE 1. The SN Ia Dilemma: Single (SD) or Double Degenerate (DD)? Chandrasekhar (Ch) or Sub-Ch Mass Exploders?

2. The Double Degenerate Scenario and the Search for DD Binaries

2.1. *Binary Evolution Leading to DD Systems*

There is little doubt that DD systems exist, as a large fraction of stars are born as member of a binary, and most stars will leave WD remnants. The question is how *hard* are the DD systems at their formation, when the secondary star also becomes a WD. Once formed, a DD system will merge via GWR losses in a time:

$$t_{\rm GWR}({\rm yr}) = \frac{1.5\times10^8 A_{\rm ff}^4}{M_{\rm 1R}M_{\rm 2R}(M_{\rm 1R}+M_{\rm 2R})} \simeq \frac{8\times10^7 P^{8/3}(M_{\rm 1R}+M_{\rm 2R})^{1/3}}{M_{\rm 1R}M_{\rm 2R}}, \qquad (1)$$

where $A_{\rm ff}$ is the separation in $R_\odot$ units, P its period in hours, and the mass of the two WDs is in $M_\odot$ units. The problem is to determine how the *initial* binary parameters M_1, M_2, and $A_{\rm o}$ map into the corresponding *final* values $M_{\rm 1R}$, $M_{\rm 2R}$, and $A_{\rm ff}$, when the secondary star also becomes a WD. Thus, the merging rate – and the SNIa rate – both depend on (1) the distribution of the initial binary parameters; and (2) how they map into the corresponding final values. The answer to (2) depends on how much mass and angular momentum have been lost during the binary evolution through two common envelope events (CEE), resulting from the Roche lobe filling of the primary and of the secondary component, respectively. As for other hydrodynamical processes in stellar physics (e.g., convection and mass loss) a *reasonable* parameterization is currently unavoidable to describe the outcome of CEEs. In this mood, the so-called α-parameter (Tutukov & Yungelson 1979) has been generally adopted, where α is implicitly defined by:

$$G{M_1}^2/A_{\rm o} = \alpha G M_{\rm 1R}M_2/A_{\rm f}, \qquad (2)$$

where $A_{\rm f}$ is the binary separation after the first CEE. Seemingly:

$$G{M_2}^2/A_f = \alpha G M_{\rm 1R}M_{\rm 2R}/A_{\rm ff}, \qquad (3)$$

for the second CEE. The dimensionless parameter α is thus a measure of the effectiveness of the transformation of the orbital energy into work to eject the CE material from the system. For small α ($\ll 1$) the transformation is *inefficient*, and considerable orbital shrinkage results; for large α ($\gtrsim$1) the orbital shrinkage is very modest, and an energy source other than orbital is required to drive the CE off. According to 2D and 3D hydrodynamical studies (Livio 1989; Taam & Bodenheimer 1989), α could be rather small ($\simeq$ 0.3–0.6), but the current state of the art in these simulations leaves ample room for $\alpha\gtrsim1$.

Unfortunately, $t_{\rm GWR}$ is extremely sensitive to α (actually, $t_{\rm GWR}\propto\alpha^9$, Iben & Webbink

1989). For example, a binary with $\alpha = 1$ would produce a DD that merges in one Hubble time ($\sim$ 15 Gyr), while one with $\alpha = 0.3$ would instead generate a DD merging in only $\sim 3 \times 10^5$ yr. So, a factor of ~ 3 uncertainty in α means a factor $\sim 3^9 \simeq 2 \times 10^4$ uncertainty in the lifetime of the DD systems, which translates into a large uncertainty in their predicted local density. [Such density does not scale precisely as α^9 (or as $\alpha_1^5\alpha_2^4$, if $\alpha_1 \neq \alpha_2$) thanks to a compensating effect, as changing α what changes is the *range* of initial separations that produce DDs with $t_{\rm GWR}$ in a certain range.] Only the case $\alpha = 1$ has been fully explored so far (Iben 1990; Tutukov & Yungelson 1992; Tutukov, Yungelson, & Iben 1992), but the very large dependence of $t_{\rm GWR}$ on this poorly known parameter makes binary evolution theory unable to predict with any degree of confidence the number, period distribution, and merging rate of DD systems. Turning the problem around, one can say that the extreme sensitivity of $t_{\rm GWR}$ to α implies that suitable observations may set tight limits on α. This is the point of view adopted in the next section.

2.2. *Searching for DD Systems*

DD systems that can merge in less than one Hubble time ($t_{\rm GWR} \lesssim$15 Gyr) would have sufficiently large orbital velocity ($v_{\rm ORB} \gtrsim 300$ km s^{-1} (with orbital periods $P \lesssim 10^{\rm h}$) that it should be fairly easy to discover them as spectroscopic binaries. Three systematic surveys of WDs have been undertaken to hunt for DDs, in particular those that could be the precursors of SNIa events. The surveys are all based on looking for radial velocity or line shape variations, though with different sensitivities.

First, Robinson and Shafter (1987, hereafter RS) have completed a survey of 44 WDs (40 DAs and 4 DBs), but with a null result. Their technique allowed only the detection of very short period systems ($P \lesssim 3^{\rm h}$). Second, Foss, Wade, & Green (1991) have surveyed 25 DA WDs. Their survey was also sensitive to somewhat longer periods ($P \lesssim 10^{\rm h}$), but again they found null results. Finally, Bragaglia *et al.* (1990; in prep.) have so far scrutinized 84 WDs (54 DAs and 30 DBs). They found one DD (with $P = 1^{\rm d}.15$) and identified 3 other DD candidates among the DAs and 6 candidates among the DBs. "Candidates" are here defined as those WDs for which at least two spectra give radial velocities differing by more than $\sim$ 100 km s^{-1} (a $\sim 2.5\sigma$ effect). This survey was sensitive up to $P \approx 3^{\rm d}$.

In order to check the DD scenario RS proceeded as follows:
1) They assumed that all DDs in the WD sample, with $P < P_{\rm max}$ $(= 3^{\rm h})$, were detected.
2) They assumed that all DDs form with $P > P_{\rm max}$, and then drift in period via GWR until they merge.
3) They estimated the space density of DDs required to account for the observed SNI rate in the Galaxy, and compared their result with the observed limit.

From their null result RS estimated an upper limit to the observed space density of DDs. Their result, $N_{\rm DD}(P < 3^{\rm h})_{\rm obs} \lesssim 3 \times 10^{-5}\,{\rm pc}^{-3}$, compares to the value $N_{\rm DD}(P < 3^{\rm h})_{\rm req} \simeq 3 \times 10^{-5}\,{\rm pc}^{-3}$ required to account for the SNI rate. RS then conclude that DDs are unlikely to be the precursors of SNIs, unless assumption (2) is wrong, i.e., unless most of DDs form initially with $P < P_{\rm max}$. Indeed, though the two numbers appear to be marginally consistent, one should consider that most DDs will have a combined mass $\lesssim 1.4\,M_\odot$, and are not suitable SN precursors.

To derive the *required* DD space density, RS used a SNI rate 0.02 yr^{-1} (Tammann 1982), a value considerably larger than currently estimated for SNIa's. Indeed, in the old rate all the SNI subtypes were lumped together, while the DD conjecture is supposed to apply only to SNIa's. Thus, with the current Galactic SNIa rate of 0.003 yr^{-1} (van den Bergh & Tammann 1991), the required space density drops to $N_{\rm DD}(P < 3^{\rm h})_{\rm req} \simeq 4 \times 10^{-6}{\rm pc}^{-3}$ and the RS survey alone cannot set a strong constraint on the DD scenario.

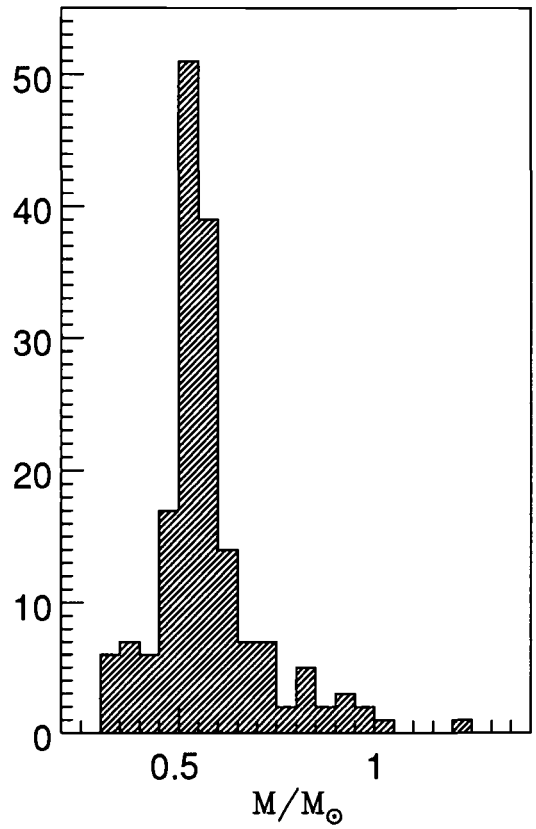

FIGURE 2. The mass distribution for 170 WDs of the DA subtype from the combined samples of Bergeron, Saffer, & Liebert (1992) and Bragaglia *et al.* (1990). The individual masses are estimated from surface gravity via Balmer line fitting (Bragaglia, Renzini, & Bergeron 1993)

Even combining all the three surveys (which gives a total of 118 WDs, none of which is a DD with $P < 3^{\rm h}$) one finds that the upper limit, $N_{\rm DD}(P < 3^{\rm h})_{\rm obs} \lesssim 1 \times 10^{-5}\,{\rm pc}^{-3}$, is still a factor ~ 2.5 above the required value.

However, combining the Bragaglia *et al.* sample of DA WDs with the Foss *et al.* sample one has a total of 89 WDs, none of which is a DD with $P < 10^{\rm h}$. From this I estimate $N_{\rm DD}(P < 10^{\rm h})_{\rm obs} \lesssim 1.5 \times 10^{-5}\,{\rm pc}^{-3}$, which compares to $N_{\rm DD}(P < 10^{\rm h})_{\rm req} \simeq 8.7 \times 10^{-5}\,{\rm pc}^{-3}$. This last estimate implies that about a dozen out of 89 WDs should be DDs with $P < 10^{\rm h}$; but none is found! We must conclude that DDs are NOT the SNIa progenitors, unless RS assumption 2) is violated – i.e., most DDs should form with $P < 10^{\rm h}$, and then $< t_{\rm GWR} > \ll 10^{10}$ yr. One can estimate that most DDs should form with $P \lesssim 5^{\rm h}$, i.e., there must be a lot of orbital shrinkage through the two CEEs for the DD option to be viable for Galactic SNIa. This scenario would require a rather small α (say 0.3–0.4). Still, there might be a problem with the SNIa's in ellipticals, for which a delay of order of one Hubble time is required.

masses are estimated from surface gravity via Balmer line fitting (Bragaglia, Renzini, & Bergeron 1993).

The Bragaglia,*et al.* survey has still more to say – but now for what it did find, rather than for what it did not find. The confirmed and candidate DDs in their sample have all orbital velocities $K \lesssim 100$ km s^{-1}. The same applies to a group of low mass ($\lesssim 0.4 M_\odot$) WDs shown in Fig. 2, which are also likely to be in DD binaries. Indeed, only Roche

lobe overflow could produce such low mass helium WDs. Including the DD studied by Saffer, Liebert, & Olzewski 1988), we have a total of 15 helium WDs which are confirmed or very likely DD members, all with $K \lesssim 100$ km s^{-1}. This result is at variance with the expectation for the $\alpha = 1$ case (Iben 1990), which predicts a nearly equal number of DDs with $K \lesssim 100$ km s^{-1} as with $100 \lesssim K \lesssim 500$ km s^{-1}. Moreover, most WDs in the Bragaglia *et al.* survey are rather bright, hot, most likely young WDs, which should have suffered little GWR orbital decay up to now. Thus, CEEs appear to result in little orbital shrinkage, and a large value of α ($\gtrsim 1$) seems to be needed in order to reconcile the theoretical expectations with the observed distribution of DD orbital velocities (Bragaglia, Greggio, & Renzini 1991).

In summary, the observed DD option for the SNIa precursors requires α to be *small*, while instead the properties of the observed helium WDs in DD systems demand α to be *large*. Since I did not find any clever way of reconciling these two opposite requirements, I am forced for the time being to conclude that the prognosis for the DD scenario does not appear good. It simply appears that binaries evolving in isolation may not lose enough angular momentum to produce hard DDs able to merge in one Hubble time or less. This conclusion does not necessarily imply that DD merging does not take place in nature. In a very high density environment – such as in dense globular clusters and in galactic nuclei – angular momentum removal by encounters with other stars may well lead to very hard DDs, with separation $\lesssim 3 R_\odot$, which are then able to merge in a relatively short time. Perhaps this is the main channel for DD merging, and its outcome – rather than a SNIa – may lead to accretion induced collapse (Nomoto 1988) and the subsequent formation of millisecond pulsars now so copiously found in globular clusters (Grindlay & Baylin 1988).

It is worth emphasizing that the above considerations refer primarily to WDs of the DA variety (those retaining a thin hydrogen envelope). Actually, there are reasons to believe that massive carbon/oxygen WDs in DD systems are likely to have completely lost their hydrogen envelope, thus disguising themselves as non-DA WDs (Bragaglia *et al.* 1991). The above calculations should then be repeated for the sample of 30 DBs so far observed. Of them none is a DD with a period shorter than about one day – which may already say something – but a larger sample would be required before reaching firm conclusions.

The last point concerns the immediate SNIa progenitors. The merging of the two WDs leads to the formation of a thick accretion disk around the more massive WD, leading to an object sometimes depicted as a kind of *flying saucer* (Iben & Tutukov 1984). However, the final fate of the flying saucer, – even if its mass exceeds $1.4\,M_\odot$ – is not necessarily a SNIa. This would happen only if the accretion disk has a long enough lifetime, so as to pour slowly its material onto the WD. Otherwise a neutron star would result, rather than a SNIa explosion (Nomoto & Iben 1985). The accretion process should last $\sim 10^6$ yr for a good explosion to occur. From the Galactic SNIa rate one immediately derives that a few thousand such flying saucers should be wandering around the Galaxy. In order to radiate away the potential energy of the thick disk in $\sim 10^6$ yr, their typical UV luminosity should be 100–1000 $L_\odot$. No such object has been found yet.

3. The Single Degenerate Scenario and SD Candidates

The other way to let WDs to grow is to feed them (H or He) fuel, process it (respectively to He and C+O), until either helium or carbon ignite explosively. This SD scenario comes in two main options, depending on whether companion of the WD is: (1) a main sequence (MS) star; or (2) a red giant (RG) star. Mass transferring WD+MS pairs are usually cataclysmic variables (CV), such as classical novae. The problem with CVs as SNIa

progenitors is that the WD may not grow at all (most of the accreted material should be ejected during nova outbursts), so that too few such systems may eventually manage to explode and produce a SNIa display (Livio & Truran 1992). This leaves WD+RG pairs, objects that are known as symbiotic stars (SS) when mass transfer is active.

SSs possess several attractive properties as SNIa progenitors: (1) the luminosity of the accreting WD is typically in the range $10^2 \lesssim L \lesssim 10^4\ L_\odot$; (2) the accreted H-rich material appears to being burned quasi-statically (no mass ejection such as in nova outburst is taking place); and (3) the observed luminosities – if due to stationary H-burning – imply accretion and burning rates in the range $10^{-9} \lesssim \dot{M}_{\rm acc} \lesssim 10^{-7}\ M_\odot {\rm yr}^{-1}$ or more (see e.g., Mürset *et al.* 1991; Munari & Renzini 1992, hereafter MR). Such values of the accretion rate are indeed very attractive, as they avoid the problem of nova outburst and the associated mass ejection and so allow the WD to grow until explosion (see e.g., Nomoto 1986). The traditional argument against SSs as SNIa progenitors is that there are be too few of them to account for the observed rate (e.g., Wheeler 1991). Supposing that each WD must accrete $0.4\,M_\odot$ before making a SNIa and that $\dot{M}_{\rm acc} \simeq 10^{-8} - 10^{-7}\ M_\odot {\rm yr}^{-1}$, we find that the SS lifetime should be in the range $\tau_{\rm SS} \simeq 0.4/\dot{M}_{\rm acc} \simeq 4 \times 10^6 - 4 \times 10^7$ yr. With a Galactic SNIa rate 0.003 yr^{-1}, the number os SSs in the Galaxy – precursors to SNIa events – should correspondingly be $0.003 \times \tau_{\rm SS} \simeq 10^4 - 10^5$. This compares to an estimate of only 3000 symbiotics in the whole Galaxy by Kenyon (1986), extrapolating from the 150 known SSs.

MR have recently reassessed the SS distance scale, population assignment (bulge/old disk rather than young disk), and discovery probability. The first step suggests an increase by a factor ~ 6 in the number of Galactic SSs, the second, another factor ~ 3, and the third, still another factor ~ 5. From these corrections, MR conclude that the Galactic population of SSs may well amount to ~300,000 objects, some 100 times more than estimated before. If so, SSs could be resurrected as viable SNIa progenitors. With a typical SS lifetime of $\sim 4 \times 10^6$ yr, such a population gives a galactic SS formation rate $\sim 0.07\,{\rm yr}^{-1}$. Is this a reasonable number? Using the luminosity–number relation (Renzini & Buzzoni 1986), we estimate that the rate of red giant formation in the Galactic bulge + old disk (nearly equal to the corresponding stellar death rate) should be $B(t)L_{\rm T} \simeq 2 \times 10^{-11} \times 3 \times 10^{10} \simeq 0.6$ stars yr^{-1}, where $B(t)$ is the specific evolutionary flux and $L_{\rm T}$ is the total luminosity of the bulge + old disk. With a lifetime on the upper red giant branch (RGB) $\sim 10^8$ yr, the galactic population of upper RGB stars should be $\sim 0.6 \times 10^8 = 6 \times 10^7$ RGB stars. Thus, the MR estimate requires that just 1 every 200 RGB stars is a symbiotic, which seems quite reasonable.

Kenyon *et al.* (1993, hereafter KLMT) do not share this optimism. They first adopt a rate of binary formation $r_{\rm bin} \simeq \frac{1}{2} r_{\rm PN} = 0.4\,{\rm yr}^{-1}$, where $r_{\rm PN}$ is the Galactic formation rate of planetary nebulae (almost identical to the Galactic death rate), and then introduce a *Drake-like* equation for the SS formation rate:

$$r_{\rm SS} = r_{\rm bin} f_1 f_2 f_3 = \frac{1}{2} r_{\rm PN} f_1 f_2 f_3, \tag{4}$$

where f_1 is the fraction of binaries with initial period in the range between 1 and 10 yr (with periods out of this range binaries do not go through a SS phase), f_2 is the fraction of binaries that survive the first CEE with still a long period to allow the secondary to become a red giant, and f_3 is the fraction of binaries with a secondary massive enough to evolve to the RGB in less than 15 Gyr. Adopting $f_1 \simeq 0.11$, $f_2 \simeq 0.5$, and $f_3 \simeq 0.3$, KLMT then estimate $r_{\rm SS} \simeq 0.007$, i.e. ~ 10 times less than the MR result. The resulting Galactic population of $\sim 30,000$ symbiotics – 10 times than previously estimated by Kenyon (1986) – is still 10 times less than claimed by MR. Kenyon *et al.* conclude that

for the MR estimate to be correct, a value $f_2 \approx f_3 \approx 1$ is required; they consider such an assumption "unduly optimistic".

I maintain, however, that both factors are – by definition – equal to unity ($f_2 \equiv f_3 \equiv 1$). Indeed, $f_3 \equiv 1$ because eq. (4) relates the SS formation rate to the single star *death rate* (not the birth rate!) and so already accounts for the fact that only a fraction of formed stars are now evolving to death. So KLMT have mistaken death for birth. Concerning f_2, KLMT justify their assumption with the need to allow space for the production of CVs. Yet, CVs are mostly WD+MS pairs, and the dwarf fills its the Roche lobe because of magnetic wind orbital decay rather than by swelling to red giant size (Verbunt & Zwaan 1981). Thus a different clock is at work in the case of CVs, and their production rate cannot be set proportional to the single star death rate, whose clock is exclusively nuclear. With $f_2 = f_3 = 1$ the discrepancy between the two estimates drops from a factor of 10 down to less than a factor of 2, certainly within the reasonable uncertainty in this kind of evaluation. In conclusion, with a Galactic single star death rate ~ 1 star yr^{-1}, a SS formation rate $\sim 0.07\,\mathrm{yr}^{-1}$, and a SNIa rate $\sim 0.003\,\mathrm{yr}^{-1}$ we find that approximately one every 10 stars should become a symbiotic, and one of every 20 SS should eventually become a SNIa. These round numbers sound quite reasonable to me.

On one point made by KLMT I definitely agree: SSs become more likely SNIa progenitors if the accreting WD could explode *before* reaching $1.4\,M_\odot$, as in helium detonation and double detonation models. KLMT make the point that in this case less material need be accreted to produce the explosion. Perhaps more importantly, in this way not only the most massive WDs (with $M_{\rm WD} \gtrsim 1\,M_\odot$) are likely SNIa progenitors (see Fig. 2 how few of them there are!), but objects in the main body of the WD mass distribution immediately become potential progenitors.

Along with arguments supporting the SD scenario, it is worth mentioning at least some of the counterarguments. The absence of hydrogen lines in SNIa spectra has been a traditional point against the SD scenario, though Balmer line emission is not expected to appear before the nebular stage of the supernova. MR mention two known cases with hints of hydrogen lines, and Ruiz-Lapuente *et al.* now report at this meeting a third case (SN1991bg). Systematic observations of SNIa's through the nebular stage would then be very important. The absence of radio emission in SNIa's argues against the existence of a (massive) circumstellar envelope around SNIa precursors, while SSs should be embedded in some circumstellar material. A great difference is expected, however, between the strong winds typical of massive red supergiants (the progenitors of SNII's), which have mass loss rates $10^{-6} - 10^{-5}\,M_\odot\mathrm{yr}^{-1}$, and the weaker winds of SSs, which have ($\dot{M} \lesssim 10^{-8} - 10^{-7}\,M_\odot\mathrm{yr}^{-1}$).

For every scenario, explaining SNIa's in ellipticals is perhaps the most demanding aspect of the problem, and the SD option is no exception. RGB stars in ellipticals have a mass of $\sim 0.85\,M_\odot$, of which $\gtrsim 0.25\,M_\odot$ are locked into the degenerate helium core and are not available for transfer. This leaves a reservoir of only $\sim 0.6\,M_\odot$. Assuming to start with one of the most massive WDs, with $M_{\rm WD} \simeq 1\,M_\odot$, then $\sim 0.4\,M_\odot$ needs to be accreted in order to reach the Chandrasekhar limit, requiring mass transfer with efficiency exceeding $\sim 66\%$. Somewhat less dramatic is the case of Sub-Ch exploders, where the WD needs to accrete $\sim 0.2\,M_\odot$ to lead to a helium detonation (Limongi & Tornambè 1991; Woosley & Weaver 1994). Now the efficiency needs to be *only* $\sim 30\%$, still high, but not high enough to argue in favor of the Sub-Ch option.

It is quite doubtful that accretion from a Roche-lobe filling companion – or from a wind – may reach such high transfer efficiencies. MR suggest a possible way out from this difficulty, noting that the SS red giant member most often does not fill its Roche lobe, while the mass transfer rate appears to exceed the mass loss rate from a single

red giant of the same luminosity and spectral type. MR propose that the soft X-ray and UV radiation from the bright accreting WD may *stimulate* mass extraction from the heated, facing lobe of the red giant, thus leading to a self-regulating mass transfer process. Stimulated mass transfer of this kind has been studied in the context of low mass X-ray binaries, with neutron star + MS and NS + WD pairs. Hydrodynamical simulations show that the velocity of the stimulated wind is generally only a fraction of the escape velocity from the system (Tavani & London 1993). If this situation applies also to WD + RG pairs, then a fraction of the extracted material will be accreted by the WD, a fraction may fall back on the RG (thus remaining available for subsequent transfer), and a fraction may escape from the outer Lagrangian point and be lost. Observations as well as hydrodynamical simulation may test this suggestion, along with the very intriguing possibility that – when the accretor is a compact object – stimulated mass transfer may prevent, and then *suppress* the second CEE. If true, this hypothesis would call for a major revision of our current views on binary evolution. After all, what compelling evidence do we have that binaries experience two – not just one – CEEs?

All in all, of the four options in Fig. 1, the SD/Sub-Ch combination scores somewhat better than the others. Schematically enough, SSs exist while short period DDs are yet to be found. Moreover, the accretion of $\sim 0.2\,M_\odot$ onto a $\sim 0.6-0.8\,M_\odot$ WD must certainly a more frequent event than the accretion of $0.4\,M_\odot$ onto a $\sim 1\,M_\odot$ WD. If reaching the Chandrasekhar limit is really necessary for SNIa's, what other fate can there be for the much more frequent helium detonators?

Acknowledgements

I am deeply indebted with Angela Bragaglia, Laura Greggio, and Ulisse Munari for the joint work on this subject, and I am grateful to Marco Tavani and Amedeo Tornambè for very useful discussions.

REFERENCES

Bergeron, P., Saffer, R. A., and Liebert, J. 1992, ApJ, 394, 228

Bragaglia, A., Greggio, L., Renzini, A., & D'Odorico, S. 1990, ApJ, 365, L13

Bragaglia, A., Greggio, L., Renzini, A., & D'Odorico, S. 1991, in *Supernovae*, ed S.E. Woosley (Berlin: Springer-Verlag), p. 599

Bragaglia, A., Greggio, L., Renzini, A. 1991, in *SN1987A and Other Supernovae*, ed. I.J. Danziger & K. Kjar (Garching: ESO), p. 47

Bragaglia, A., Renzini, A., & Bergeron, P. 1993, in *White Dwarfs*, ed. M. Barstow (Dordrecht: Kluwer), in press

Ciotti, L., D'Ercole, A., Pellegrini, S., & Renzini, A. 1991, ApJ, 376, 380

Foss, D., Wade, R.A., & Green, R. F. 1991, ApJ, 374, 281

Grindlay, J. E., Baylin, C. D. 1988, Nature, 336, 48

Iben, I., Jr. 1990, ApJ, 353, 215

Iben, I., Jr., & Tutukov, A. V. 1984, ApJS, 54, 335

Iben, I., Jr., & Webbink, R. F. 1989, in *White Dwarfs*, ed. G. Wegner (Berlin: Springer–Verlag), p.377

Kenyon, S. J. 1986, The Symbiotic Stars (Cambridge Univ. Press)

Kenyon, S. J., Livio, M., Mikołajewska, J., & Tout, C. A. 1993, ApJ, 407, L81 (KLMT)

Limongi, M., & Tornambè, A. 1991, ApJ, 371, 317

Livio, M. 1989, Space Sci. Rev., 50, 299.

Livio, M., & Truran, J. W. 1992, ApJ, 389, 695

Munari, U., & Renzini, A. 1992, ApJ, 397, L87 (MR)

Mürset, U. Nussbauber, H., Schmidt, H. M., & Vogel, M. 1991, A&A, 248, 458

Nomoto, K. 1986, Progress in Particle and Nuclear Physics, 17, 249

Nomoto, K. 1988, in Origin and Evolution of Neutron Stars, ed. D. Helfand & J. Huang (Dordrecht: Reidel), p. 281

Paczyński, B. 1985, in *Cataclysmic Variables and Low Mass X-ray Binaries*, ed. D. Q. Lamb & J. Patterson (Dordrecht: Reidel), p. 1

Renzini, A., & Buzzoni, A. 1986, in *Spectral Evolution of Galaxies*, ed. C. Chiosi & A. Renzini (Dordrecht: Reidel), p. 135

Renzini, A., Ciotti, L., D'Ercole, A., & Pellegrini, S. 1993, ApJ, 419, 52

Robinson, E. L., & Shafter, A. W. 1987, ApJ, 332, 296 (RS)

Saffer, R.A., Liebert, J., & Olszewski, E.W. 1988, ApJ, 334, 947

Taam, R.E., & Bodenheimer, P. 1989, ApJ, 337, 849

Tavani, M., & London, R. 1993, ApJ, 410, 281

Tutukov, A. A., & Yungelson, L.R. 1979, in *Mass Loss and Evolution of O-Type Stars*, ed. P.S. Conti & C.W.H. De Loore (Dordrecht: Reidel), p. 401.

Tutukov, A. A., & Yungelson, L. R. 1992, Soviet Astr., 36, 266

Tutukov, A. A., Yungelson, L. R., & Iben, I., Jr. 1992, ApJ, 386, 197

Verbunt, F., & Zwaan, C. 1981, A&A, 100, L7

Webbink, R. F. 1984, ApJ, 277, 355

Wheeler, J. C. 1991, in *Evolutionary Processes in Interacting Binary Stars*, ed. Y. Kondo *et al.* (Dordrecht: Kluwer), p. 225

Whelan, J., & Iben, I., Jr. 1973, ApJ, 186, 1007

Woosley, S. E., & Weaver, T. A. 1994, ApJ, 423, 371

2D Simulations of Deflagrations in White Dwarfs

By ELI LIVNE

Steward Observatory, University of Arizona, Tucson, AZ 85721, USA

1. Introduction

The convective deflagration mechanism in white dwarfs became widely used to explain Type Ia Supernovae (SNIa) due the success of a single model, namely model W7 of Nomoto *et al.*(1984). Problems concerning the deflagration model were discussed by Sutherland & Wheeler (1984), Nomoto *et al.*(1984), Woosley & Weaver (1986), Woosley (1990), Khokhlov (1991a) and others. The main question however is still: does the deflagration model have any hydrodynamical basis, or, could the assumed Rayleigh Taylor instability accelerate the flame to the required speed?

Nomoto *et al.*(1984) estimated the turbulent speed from the mixing length arguments to be

$$v_t \approx (gl/2)^{\frac{1}{2}} ,$$

where v_t is the turbulent speed, $g = GM\delta\rho/(r^2\rho)$ is the effective acceleration, and l is the length of the largest unstable modes, usually of the order of the pressure scale height. The relevance of mixing length theory to the deflagration problem is at least questionable. Two different effects may enhance the burning rate, relative to the laminar speed, when the front is unstable. First, mixing of burnt and unburnt matter can widen the front and accelerate its propagation like other dissipation mechanisms (this requires that perturbations, of the size of the front width, be unstable), and secondly, as the front becomes wrinkled, the total burning rate increases in proportion to the surface (Woosley 1990). We now discuss these two effects.

2. Linear Stability of the Deflagration Front

The analysis of the stability of ablation fronts, formed in shells accelerated by laser beams, show that the growth rate can be approximated (Takabe *et al.*1985) by :

$$\omega(k) = \alpha(kg)^{1/2} - \beta k v_f , \qquad (1)$$

where $\alpha = 0.9$, $\beta = 3$ to 4 and v_f is the front speed. Due to the presence of an extra linear term there is a critical wave number, $k_c = \alpha^2 g/(\beta v_f)^2$, above which all modes are stable. Moreover, the growth rates of all other modes are lower than that of the Rayleigh Taylor case, which has a maximum at $k_{max} = 0.25k_c$.

Deflagration fronts have the same structure as ablation fronts, as the only difference being the different source of energy. For the early stages of the burning in a WD, $g \approx 2 \cdot 10^9 \mathrm{cm\ s^{-2}}$ and $v_f \approx 100 \mathrm{km\ s^{-1}}$, so that perturbations with $l < 5$ km are stable while larger scales are unstable. Since the width of the front is less than 1 cm early on, this implies that locally the front propagates with the laminar speed. The most unstable perturbations have scales of 20 km at the early stages of the burning, and their growth rate is about half the Rayleigh Taylor growth rate. The conductive (laminar) flame speed

is approximated (Timmes & Woosley 1992) by:

$$v_c = 92.0 \left(\frac{\rho}{2 \cdot 10^9}\right)^{0.805} \text{ km s}^{-1} \tag{2}$$

for an initial composition of $X(^{12}C) = 0.5$.

3. 2D Numerical Simulations

We performed many 2D simulations of the burning front using several methods. These simulations extend our study into the nonlinear regime and test the importance of the surface effect. The flame propagates in these simulations according $v_f = max(v_c, v_t)$, where the turbulent speed v_t is given by

$$v_t = \left[(\nabla\Phi \cdot D^{\perp})\frac{\delta\rho}{2\rho}\right]^{\frac{1}{2}} . \tag{3}$$

Here Φ is the gravitational potential and $D^{\perp}$ is a vector having the length of the cell face and direction normal to the face.

Coarse grid results were presented in Livne (1993), where we used 90 zones in the radial direction and 41 zones in the angular direction on one quadrant. Subsequent calculations, which used 180×90 and 260×140 zones in the radial and angular direction, respectively, showed similar results. Four snapshots of temperature contours, obtained from the high resolution sequence, are shown in figure 1. The typical pattern of these calculations shows a slow growth of the initial perturbation together with merging of smaller structures to bigger ones. A faster mushroom shape structure along the axis of symmetry is an artifact of the imposed axial symmetry. After roughly one second, expansion becomes dominant and the total burning rate drops slowly. At two seconds there is no more significant burning while the star is still bound. Simulations in which the turbulent flow is set to zero yield less than $0.3 \cdot 10^{51}$ erg, which is roughly twice as much as the energy produced in the spherical case, and is still much less than the binding energy of the WD ($0.51 \cdot 10^{51}$ erg). When the turbulent speed is included in the simulation, the unperturbed case yields $0.3 \cdot 10^{51}$ erg while the perturbed cases produce 2 times more, which was hardly enough to unbind the star but not to generate anything like a SNIa, as it leaves an unacceptable amount of unburnt C-O.

4. Implications on explosion mechanisms

The fate of the explosion is determined by the competition between expansion, which suppresses the burning rates, and the increase of the total burning rate due to the increase of the surface of the front. Our calculations always show that the instability is too slow to enhance the burning rate to the value needed by an acceptable model for SNIa.

The results support the "delayed detonation" mechanism, suggested by Khokhlov (1991a,b) and Woosley (1991). As the deflagration front dies, or at least slows down considerably, Rayleigh Taylor instability is recovered and mixing occurs on all scales. This mixing can be enhanced if the star is bound at this stage, and the positive velocity slope becomes negative. We suggest that this small scales mixing is the trigger for the transition to detonation (after Khokhlov 1991b). The discussion above implies that the transition occurs not by accelerating the front but by slowing it down. Since this occurs at relatively low densities, the condition for obtaining good agreement with observations is automatically fulfilled.

The impact of the detonation wave on the large nonspherical structures formed in

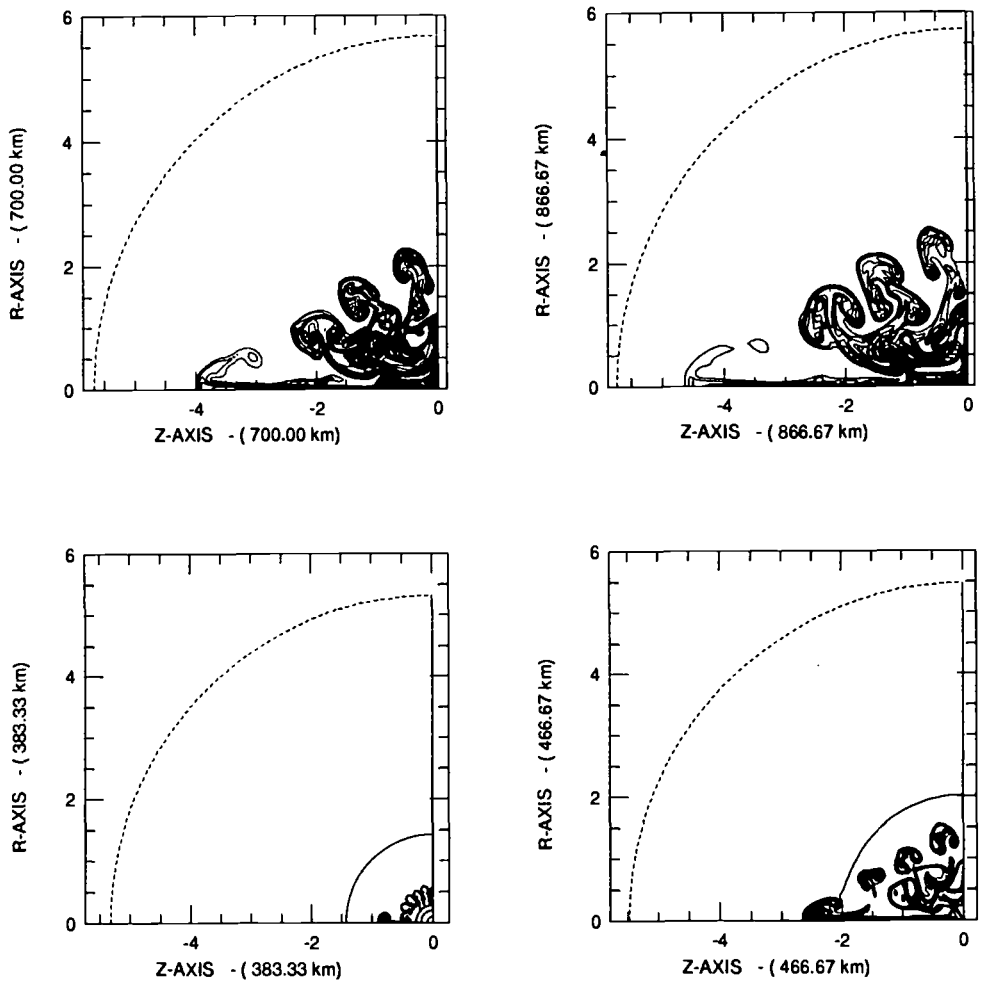

FIGURE 1. Temperature contours at t=0.5 sec (left bottom), t=1 sec (right bottom) , t=1.5 sec (left top) and t=1.9 sec (right top). The dashed line represents the surface of the WD.

the first stage of the burning may lead to a significant mixing and may bring elements of the iron group to the outer layers. More work is needed in order to better understand the transition to detonation. For further implications of the 2D motions upon the nucleosynthesis and the amount of neutronization see a paper by D. Arnett in this volume.

Acknowledgements

I wish to thank Dave Arnett, Alexei Khokhlov, Stan Woosley and Adam Burrows for may useful discussions.

REFERENCES

Khokhlov, A. M. 1991a, A&A, 245, 114.

Khokhlov, A. M. 1991b, A&A, 245, L25.

Livne, E. 1993, ApJL, 406, L20.

Nomoto, K., Thielemann, F. K. & Yokoi, K. 1984, ApJ, 286, 644.

Sutherland, P. G, & Wheeler, J. C. 1984, ApJ, 280, 282.

Takabe, H., Mima, K., Montierth, L., & Morse, R. L. 1985, Phys. Fluids, 28, 3676.

Timmes, F. X. and Woosley, S. E. 1992, ApJ, 396, 649.

Woosley, S. E. 1991, in *'Gamma-Ray Line Astrophysics'* , ed P. Durouchoux & N. Prantzos, New York: American Institute of Physics, 270.

Woosley, S. E. & Weaver., T. A. 1986, in *'Radiation Hydrodynamics in Stars and Compact Objects'* , Springer Verlag, D. Mihalas and K. H. Winkler eds.

2D Simulations of Supernovae

By DAVID ARNETT

Steward Observatory, University of Arizona, Tucson, AZ 85721, USA

1. Introduction

Several multidimensional computations of hydrodynamics related to supernovae have been completed, and are summarized here. More detail may be found in Arnett 1994a,b, Arnett & Livne 1994a,b, and Livne & Arnett 1993. The hydro code PROMETHEUS is based upon an implementation of the piecewise-parabolic method (PPM) of Colella & Woodward 1984, as described in Fryxell et al. 1991. A detailed comparison of PPM with other schemes is given in Woodward & Colella 1984. The method constructs the physics of the flow between grid points by a nonlinear solution of the equations of continuity of mass, momentum and energy (the Riemann problem) rather than the usual mathematical approach of a Taylor expansion about the grid points. This gives it better resolution per grid point, which is highly desirable for multidimensional problems. Although the effort required per grid point is greater, the number of such points is less (often *much* less) for a given level of accuracy. Because the computational load per grid point is greater, more realistic physics (reactions, radiation, gravity, *etc.*) may be added before affecting the runtime significantly. Thus PPM is well suited for multidimensional problems with significant physics beyond the bare hydrodynamics.

The Prometheus project was an effort by the author, Bruce Fryxell and Ewald Müller, to implement a "state of the art" hydrodynamic method with realistic microphysics for stellar problems. After an extensive study of several methods, and direct comparison of the resulting codes (Fryxell, Müller & Arnett 1989), PPM was chosen as the preferred method. The first version of the PROMETHEUS code was written by Fryxell and Müller. It is an extension of basic PPM in that (1) it includes an arbitrary number of separate fluids to keep track of the abundance of different nuclear species, (2) nuclear reactions are included (see below), and (3) modifications were made to allow use of a realistic (not a gamma law) equation of state (Colella & Glaz 1985). Variations of this original code have been used by several other groups (*e.g.,* Blondin, et al. 1991, Cattaneo, et al. 1991, and Burrows, this volume) as well as various collaborations involving Fryxell, Müller and Arnett. PROMETHEUS has a number of added features which are crucial for many scientific problems. It allows the user to choose a coordinate system: 1, 2, and 3 dimensions, with cartesian, cylindrical or spherical coordinates. It has the option of a moving grid, with the grid motion to be defined as needed. This gives enormous improvement in resolution for many stellar problems. Fryxell wrote a superb graphics interface; the slides resulting from it have been widely used by our group and others. PROMETHEUS is a highly structured code, and routinely benchmarks well on vector and modestly parallel computers.

An extensive review (Fryxell, Müller & Arnett 1989) of our first experiences with the coupling of a reaction network (an alpha chain to ^{56}Ni) was widely distributed in preprint form, and was to be published in 1989, but has not appeared (due to no fault of our own). Although the work described below relating to reaction networks is new in this context, it used insights gained in the collaborative effort, and represents an extension

of PROMETHEUS to deal with a new set of problems. Video movies of the following four studies were shown.

2. Supernovae of Type II

2.1. *Static Oxygen Shells*

With new hydrodynamic techniques, the relatively fast evolutionary stages of a star prior to core collapse may be explicitly computed in two spatial dimensions, with a treatment of the microphysics (*e.g.*, nuclear reactions, equation of state, neutrino cooling) which is comparable to typical one-dimensional simulations. The nature of shell oxygen burning in a massive star, prior to core collapse, is used as first example; it is of particular interest because it is (1) the region in which ^{56}Ni will be produced by the supernova shock, (2) the region of the "mass cut", which will separate the collapsed core from the ejected mantle, (3) the site of much of the explosive nucleosynthesis, and (4) a suggested source of symmetry breaking to drive mixing instabilites which were observed in SN1987A. The nature of the shell burning affects the size of the core which will collapse. The method is illustrated on a test case, and the character of the convection is examined. The initial model contained the oxygen burning shell and the overlying convective region, from a star of $20M_{\odot}$ (a model for the progenitor of SN1987A). It is representative of stars of this mass range, as well as helium cores of about $6M_{\odot}$. For efficiency, the computational domain was a wedge of about 30 degrees.

Figure 1 shows contours of the ^{12}C abundance, which is a sensitive (inert) tracer of exposure to the oxygen burning flame zone, after 145 seconds. The spherical symmetry is broken; this time is already about 1% of the evolutionary time for such shell burning.

The first conclusion is that multidimensional hydrodynamics methods have matured to the point that they can provide new insights into difficult theoretical problems in stellar astrophysics. These preliminary computations can be easily surpassed with more powerful technology (by simply switching from a workstation to a supercomputer, or using the next generation workstation), and by more sophisticated use of existing algorithms. In particular, since these simulations were completed, efforts on another topic led to the development of an algorithm for semi-lagrangian grid motion, in which mass flow out of the boundaries is much less than seen here. That will provide a more natural tool for such stellar problems, and should allow evolution to be extended to significantly longer times. *These simulations demonstrate that oxygen burning shells do approach a thermal steady state*, as has been assumed for many years (Arnett 1972a). They show that the profile in abundance of ^{16}O fuel does wander away from the steep form that one dimensional stellar evolutionary codes tend to give, and give a plausible quantitative estimate of this effect. Further, *a new view of the structure of the burning and convective shell appears, in which the density (buoyancy) perturbations and the convective flows interact because of the burning.* This is a consequence of the rapidity of the heating, relative to the milder situation confronted in earlier stages of stellar evolution. However, no light is yet shed on exactly how burning shells move out in mass (Arnett 1972b), which remains a key uncertainty for quantitative estimates of nucleosynthetic yields and massive star structure. On the contrary, these results strengthen the worry that important aspects of the physics of the late evolution of massive stars are still not sufficiently well understood. An understanding of this longer term, "secular" evolution of the oxygen burning shell still eludes us, but with these new tools, it may now be within our capability.

The convective motions simulated here are only two dimensional, have a changing (not static) background state, and are strongly coupled to the energy release by nuclear

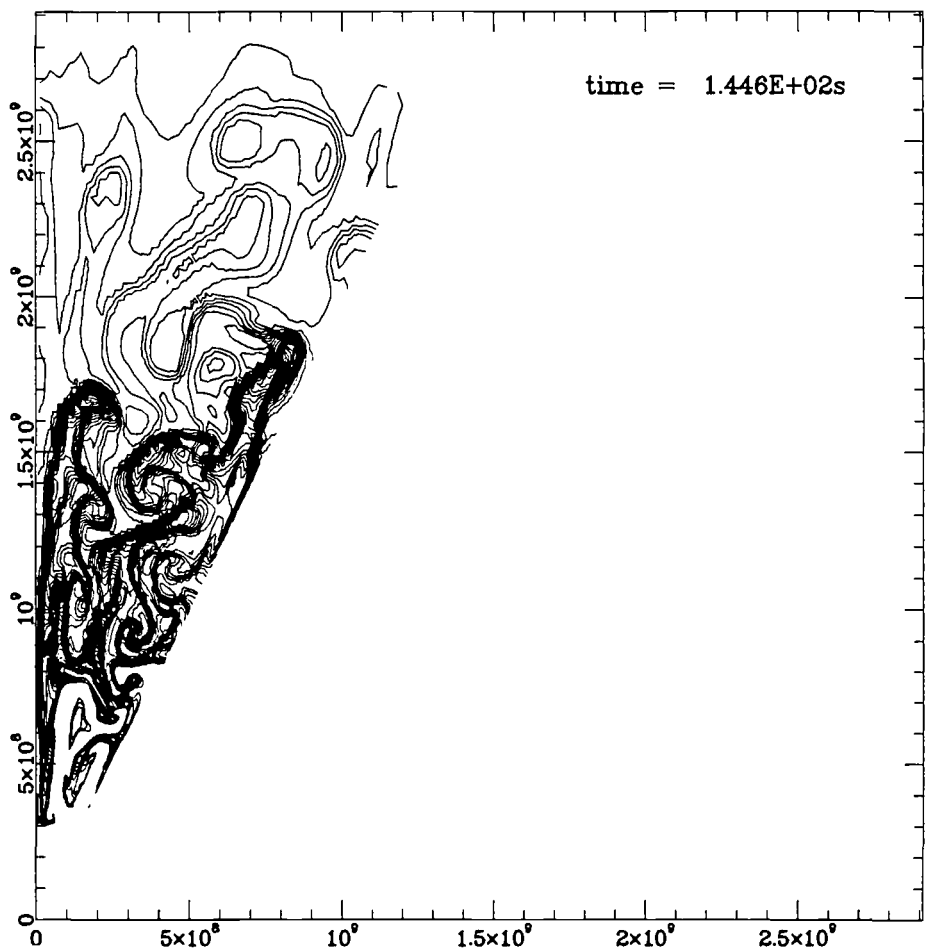

FIGURE 1. Contours of ^{12}C abundance.

burning. Even so, there are similarities to the three dimensional, turbulent convection simulated by Cattaneo, et al. 1991, which was driven only by a simple temperature gradient. For example, the distinction between strong, coherent long lived motions and weaker, disorganized ones is valid here as well; the former dominate the transport of composition, while the latter seem more closely related to net energy flow. Although demanding computationally, an extension of the present efforts into three dimensions and to longer times would provide the basis for a direct comparison.

These simulations give a definite prediction for the amplitude of nonspherical perturbations present in a presupernova. In the oxygen shell, fractional density perturbations of 2.5% and velocity perturbations of about 0.8% of sonic will occur. This sets a *lower* limit, because as the core burns silicon and then contracts toward collapse, the oxygen shell will burn more vigorously (Arnett 1977). Such values are similar to those used in Arnett, Fryxell & Müller 1989, Müller et al. 1991, and Fryxell et al. 1991.

2.2. *Dynamic Oxygen Shells*

The evolution of an oxygen burning shell is simulated from the beginning of core collapse through explosive nucleosynthesis. Again, the hydrodynamic behavior is computed in two

spatial dimensions, with a treatment of the microphysics (*e.g.*, nuclear reactions, equation of state, neutrino cooling) which is comparable to typical one-dimensional simulations. The initial parameters are taken from the previous simulation, in two dimensions, of stationary shell oxygen burning in a massive star prior to core collapse. Previous one dimensional computations are used to define the boundary conditions for the infall and the explosion stages. The simulations produce estimates for (1) the ^{56}Ni produced by the supernova shock, (2) the "mass cut", which separates the collapsed core from the ejected mantle, (3) the explosive nucleosynthesis, and (4) symmetry breaking to drive mixing instabilites which were observed in SN1987A.

After silicon burning increases the mass of the iron core in a massive star, core collapse begins (e.g., Arnett 1977). Initially the contraction is slow, with first the silicon and then the oxygen shells burning vigorously as they move to smaller radii. A second stage follows: as the core contraction accelerates into collapse, an explosion occurs (the details of which are actively debated at present), and a shock propagates outward, heating and ejecting the oxygen burning layer. Here we focus not on the explosion mechanism, but on its implications for the oxygen burning shell.

During the later stages of oxygen burning, electron capture increases the neutron excess so that ^{56}Ni is no longer the end product of nuclear burning. The iron-peak nuclei which are formed (mostly ^{54}Fe and ^{58}Ni) have a much lower cosmic abundance than the ^{56}Fe to which ^{56}Ni decays via the intermediate ^{56}Co. The observed abundances in solar system matter suggest that (usually) this matter does not escape the star. Thus two important questions, the production of ^{56}Ni to power the light curve and the size of the condensed remnant, are related to what happens in this stage of the evolution of the star.

The mass of ^{56}Ni ejected ranged from 0.03 to $0.20 M_\odot$ for explosive energies of 1 to 2 foe. The nucleosynthesis conditions were similar to those needed for production of solar system abundances. The amount of mass which falls back onto the neutron star is sensitive to the inner boundary condition, *i. e.*, to the explosion mechanism. Figure 2 shows a contour plot of the abundance of ^{56}Ni after shock passage. The entropy generated by explosive oxygen burning drives vorticity production and amplifies the nonspherical perturbations left from the previous convective stage (see above).

3. Supernovae of Type Ia

3.1. *Deflagration*

The nature of the "delayed detonation" mechanism (Khokhlov 1991) for the explosion of Type Ia supernovae is investigated by use of two-dimensional numerical hydrodynamics simulations. A new algorithm is used to treat the deflagration front (Arnett & Livne 1994a); it forces the burning rate to be that implied by the speed of the front. Assuming that the front propagates locally at the laminar flame speed (Timmes & Woosley 1992), the deflagration is insufficient to unbind the star. Expansion shuts off the flame; much of this small production of iron group nuclei occurs at lower densities, which reduces the electron-capture problem. The burning front does become wrinkled, but the wavelength of the instability is much larger than the computational grid size, and is resolved (see Livne, this volume); this is consistent with previous analysis (Livne & Arnett 1993).

Because the degenerate star has an adiabatic exponent only slightly above $\frac{4}{3}$, the energy released by deflagration drives a pulsation of large amplitude (see Khokhlov 1991 and also Nomoto, et al. 1976). During the first expansion phase, adiabatic cooling shuts off the burning, and a Rayleigh-Taylor instability then gives mixing of high entropy ashes with low entropy fuel. During the first contraction phase, compressional heating re-ignites

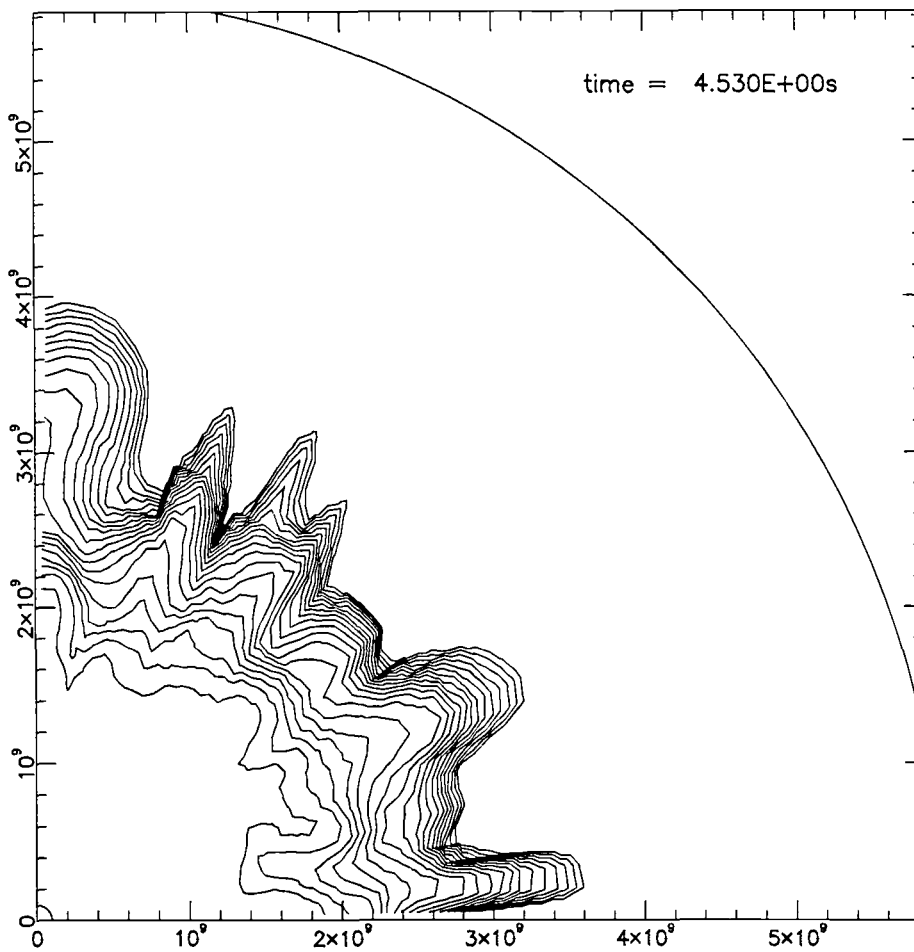

FIGURE 2. Contours of ^{56}Ni abundance.

the material. This section deals with the deflagration phase, from the onset of burning, through expansion and quenching of the flame, to the first contraction.

Figure 3 shows contours of the heating rate from the deflagration front, after 0.21 s. The instability of the front is obvious. As time passes, the smaller "ripples" merge with larger ones, giving fewer but larger perturbations.

The new method for treating stellar deflagrations with complex nucleosynthesis seems successful, and works well with our PPM code. It is computationally efficient, and produces results which are consistent with mathematical analysis of similar systems (e.g., Zeldovich, et al. 1985), and with previous numerical results obtained with very different methods (Livne 1993).

Given the assumption that the propagation velocity is given by that computed for laminar flow, *no explosion results during the deflagration phase.* This is in contradiction to the standard "deflagration model" scenario which is widely used to explain Type Ia supernovae (e.g., Nomoto, et al. 1984, Woosley 1990).

The deflagration front is unstable toward wrinkling, as Figure 3 illustrates, *but the larger wavelengths grow at the expense of the smaller ones.* This is in contradiction with what is generally assumed in the astronomical literature (see Woosley 1990).

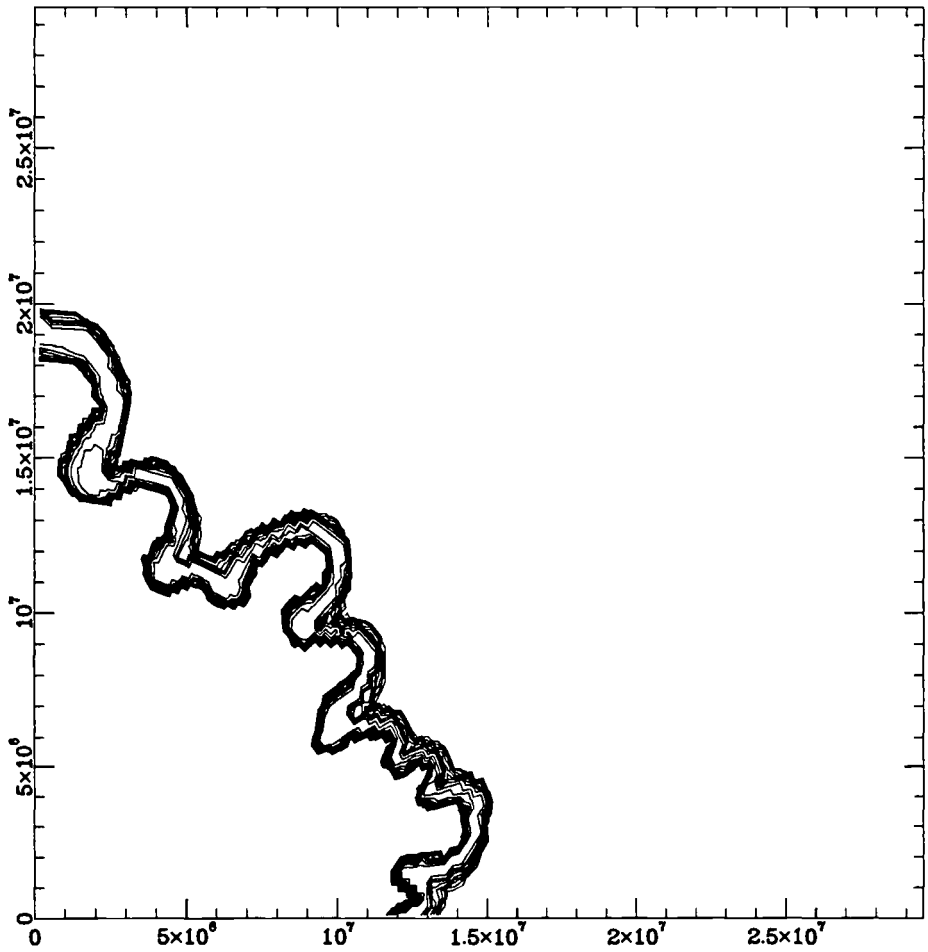

FIGURE 3. Contours of nuclear heating rate in deflagration front.

The amount of neutron enrichment due to electron capture on free protons and on ^{56}Ni is sufficiently small that moderate amounts of ^{56}Ni (about $0.1M_{\odot}$) can dilute the mixture to solar proportions. *The problem of excessive neutronization is eased by a consequence of the two dimensional aspect of the hydrodynamic motion: the newly burned matter rises and expands to lower density, which slows electron capture. Two dimensional computations also give more burning than predicted by spherical calculations; the front wrinkles, and has a larger area, which gives a faster net consuption of fuel.*

The deflagration reduces the gravitational binding of the star to about half its initial value. This drives an overall expansion. Because the adiabatic exponent is close to $\frac{4}{3}$, the amplitude of this expansion is large. This reduces the burning rates to negligible values, and allows a mixing of the hot ashes and cold fuel. Upon contraction, this matter is compressionally heated to temperatures at which burning becomes vigorous again.

3.2. *Detonation*

The investigation, by use of two-dimensional numerical hydrodymanics simulations, of the "delayed detonation" mechanism (Khokhlov 1991) for the explosion of Type Ia supernovae was continued. During the first expansion phase, adiabatic cooling shuts off the

burning, and a Rayleigh-Taylor instability then gives mixing of high entropy ashes with low entropy fuel. During the first contraction phase, compressional heating re-ignites the material. The burning was allowed to develop into a detonation using the nonspherically symmetric models. Although it begins from several "hot spots", the detonation grows toward spherical symmetry at late times. At these densities ($\rho \sim 10^7$ to 10^8 g cm^{-3}), ^{56}Ni and nuclei of the Si-Ca group are the dominant products of the burning. *The bulk yields are sensitive to the density of the star when the transition to detonation occurs.*

These preliminary computations represent a self-consistent treatment from onset of deflagration to after the explosion. Bulk yields and velocity structure for two-dimensional models are now available. The crucial theoretical question which arises is the density at which transition to detonation occurs. The only models which give velocities higher than 8,000 km s^{-1}, as suggested by observations of SNIa spectral lines, do so by burning the underlying matter to ^{56}Ni. This implies, that if these promising models are in fact correct for SNIa's, then the minimum amount of ^{56}Ni produced is $0.7M_{\odot}$. This implies a relatively high intrinsic brightnerss at maximum, and argues against the smaller values of the cosmic distance scale. Crudely speaking, Hubble constants above 80km s^{-1} Mpc^{-1} are unlikely. More to the point, refined use of this effect may give an accurate estimate of the minimum absolute brightness of SNIa's, as well as observational opportunities for internal tests of the procedure.

Acknowledgements

I wish to thank Eli Livne and Alexei Khokhlov for many useful disussions.

REFERENCES

Arnett, D. 1972a, *Ap. J.*, 173, 393

Arnett, D. 1972b, *Ap. J.*, 176, 699

Arnett, D. 1977, *Ap. J.*, 218, 815

Arnett, D. 1994a, *Ap. J.*, 427, 932

Arnett, D. 1994b, in preparation.

Arnett, D., Fryxell, B. A., & Müller, E., 1989, *Ap. J. Lett.*, 341, L63

Arnett, D. & Livne, E., 1994a, *Ap. J.*, 427, 315

Arnett, D. & Livne, E., 1994b, *Ap. J.*, 427, 320

Blondin, J. M., Stevens, I. R., & Kallman, T. R., 1991, *Ap. J.*, 371, 684

Cattaneo, F., Brummel, N. H., Toomre, J., Malagoli, A., & Hurlburt, N. E., 1991, *Ap. J.*, 370, 282

Colella, P. & Glaz, H. M., 1985, J. Comput. Phys., 59, 264

Colella, P. & Woodward, P. R., 1984, J. Comput. Phys., 54, 174

Fryxell, B. A., Müller, E. & Arnett, D., 1989, Numerical Methods in Astrophysics, ed. Paul R. Woodward, to have been published in Computational Techniques by Academic Press; preprint MPA 449, Max-Planck-Institut für Astrophysik, Garching

Fryxell, B. A., Müller, E. & Arnett, D., 1991, *Ap. J.*, 367, 619

Khokhlov, A. 1991, *A. & Ap.*, 245, L25

Livne, E., 1993, *Ap. J. Lett.*, 406, L17

Livne, E. and Arnett, D., 1993, *Ap. J. Lett.*, 415, L107

Müller, E., Fryxell, B. A., and Arnett, W. D., 1991, *A. & Ap.*, 251, 505

Nomoto, K., Sugimoto, D., and Neo, S. 1976, Astrophys. Space Sci., 39, 137

Nomoto, K., Thielemann, F. K., & Yokoi, K. 1984, *Ap. J.*286, 644

Timmes, X. and Woosley, S. E., 1992, *Ap. J.*, 396, 649

Woodward, P. R., & Colella, P. 1984, J. Comput. Phys., 54, 115

Woosley, S. E., 1990, in Supernovae, ed. A. G. Petschek (Dordrecht: Kluwer), 182.

Zeldovich, Ya. B. Barenblat, G. I., Librovich, V. B., & Mikhviladze, G. M., 1985, (New York: Consultants Bureau/Plenum).

Recent Advances in Supernova Theory

By ADAM BURROWS

Steward Observatory, University of Arizona, Tucson, AZ 85721, USA

In this paper, I summarize two new developments in the theory of core-collapse supernovae. The first is the recent establishment of an analytic context for understanding neutrino-driven explosions. Converting the supernova problem into an eigenvalue problem, Burrows & Goshy (1993) have derived a critical condition on neutrino luminosity and mass accretion rate through a stalled bounce shock for instability and explosion. The second development is the recent calculation of Burrows & Fryxell (1993) of the boost in the neutrino luminosities by the Rayleigh-Taylor-like overturn of the shocked mantle of a protoneutron star. This boost may turn duds into explosions and may be the missing ingredient of supernova theory.

1. Introduction

Core-collapse supernova predominate in the supernova bestiary (van den Bergh & Tammann 1991), but have challenged theorists during the entire post-war era of astrophysics. The sparseness of data that directly probe the dynamics of collapse and shock generation has hobbled advances in supernova theory, as has the wider than normal range of physical inputs required from the gravitational, neutrino, hydrodynamic, transport, thermodynamic, and nuclear realms. Extracting the essential elements of the explosion mechanism has not been easy. As a result, supernova theory has been perceived at various times to be confusing, arcane, hopeless, muddled, or vulnerable to the quick fix by a well-meaning Cincinnatus.

However, to those who take the time to understand the science of core-collapse and protoneutron stars, much of supernova theory is mature. In fact, there is a growing feeling that all the pieces of the supernova puzzle are falling into place. In this paper, I summarize two new developments in the theory of supernova explosions. The first development is the establishment by Burrows and Goshy (1993, BG) of an analytic theory of neutrino-driven explosions. These authors have converted the supernova problem into an eigenvalue problem for the shock radius and discovered a critical condition for explosion between the neutrino luminosity and the accretion mass flux ($\dot{M}$). By identifying the early phase of the explosion with a wind and using the results of Duncan, Shapiro, & Wasserman (1986), BG have approximately derived the dependence of the supernova energy on the magnitude of the driving neutrino luminosity and its duration.

The second development is the demonstration by Burrows & Fryxell (1993, BF) that the large neutrino luminosities required to ignite and drive the supernova (BG) can result from the convective overturn of the unstable mantle of the protoneutron star. Within ten milliseconds of shock stagnation, the 2-D hydrodynamic calculations of BF manifest a convective flash that restarts the supernova. By means of this instability, heat and leptons are rapidly advected to the neutrinospheres and radiated at nearly twice the standard rates.

2. A General Theory of Neutrino-Driven Supernovae

Supernova theory has been retarded by the reliance on complicated radiation-hydrodynamic codes that run seldom. The essential elements of the supernova mechanism have been

discovered only piecemeal. What is lacking is a simple and quantitative theory of the mechanism of supernova explosions. Under the assumption that the bounce shock aborts, BG constructed such a theory. They derived a critical condition on the neutrino luminosity and the mass accretion flux such that Wilson's neutrino-mediated mechanism obtains. Their theory attempts to replace partial differential equations (PDE's) with ordinary differential equations (ODE's) and converts the explosion problem into an eigenvalue problem.

A bounce-shock stalls into accretion within 10-20 milliseconds of its creation. The radius that it achieves (R_s) depends predominantly on the mass accretion flux through it ($\dot{M}$) and the core luminosities of the electron (L_{ν_e}) and anti-electron neutrino species, those most strongly coupled to the shocked matter. R_s is analogous to the shock stand-off distance above the white dwarf in an AM Her system (Chevalier and Imamura 1982) and in the steady-state it does not depend on the radius out to which the bounce-shock was originally thrown by the rebounding core. In BG, R_s is derived using the three equations of hydrodynamics, the neutrino transfer equations, with lepton and energy source and sink terms, and suitable boundary conditions at the shock and the neutrinosphere.

Derived from the hydro equations, the basic ODE's are:

$$\frac{dv}{dr} = \frac{\frac{v}{2r}(v_e^2 - 4c^2) + (\gamma_4 - 1)(H - C)}{c^2 - v^2} \tag{2.1}$$

$$\frac{dT}{dr} = \frac{1}{C_V}\left[\frac{(H - C)}{v}\left(1 - \frac{(\gamma_4 - 1)\chi}{c^2 - v^2}\right) + \chi\frac{2(v^2 - 1/4v_e^2)}{r(c^2 - v^2)}\right] \tag{2.2}$$

$$\frac{dP}{dr} = \frac{-\frac{\rho c}{r}(2v^2 - \frac{v_e^2}{2}) + \rho v(\gamma_4 - 1)(H - C)}{c^2 - v^2} \tag{2.3}$$

$$\frac{dY_e}{dr} = (P - M)/v \tag{2.4}$$

$$\dot{M} = -4\pi r^2 \rho v \tag{2.5}$$

$$L_{\nu_e} = \left(\frac{7}{16}\right) 4\pi R_\nu^2 \sigma T_\nu^4 , \tag{2.6}$$

where $\chi = \frac{T}{\rho}\frac{\partial P}{\partial T}\Big|_V$, R_{ν_e} is the ν_e- neutrinosphere radius, C_V is the specific heat at constant volume, $\gamma_4 - 1 = \frac{\partial P}{\partial U}\Big|_V$, c is the speed of sound, $v_e^2 = \frac{2GM}{r}$, H and C are the neutrino heating and cooling rates per mass, respectively, P and M are the electron production and electron-neutrino production rates, respectively, and the other symbols have their standard meanings. H, C, P, and M are obtained using extensions of the same arguments used in Bethe and Wilson (1985).

The luminosity, L_{ν_e}, and T_ν fix the position of the neutrinosphere, R_ν. For a given R_s, equations (2.1)–(2.6) (some are redundant) can be solved between R_ν and R_s. BG's prescription for deriving the eigenvalue, R_s, was to find the R_s at a given L_{ν_e} and $\dot{M}$ at which the ν_e "optical" depth from R_ν to infinity is 2/3.

The crucial discovery of this study is that for a given $\dot{M}$, there is a *critical* L_{ν_e}, above which there is no steady-state solution. BG identify situations with super-critical luminosities with the supernova explosion. Temperature profiles at the critical luminosities for various $\dot{M}$'s are depicted in Figure 1. These profiles are similar to those obtained with a more complete 1-D radiation/hydro code. A critical curve of L_{ν_e} vs. $\dot{M}$ can be derived (Figure 2) that separates success from failure. A power-law fit to the results of

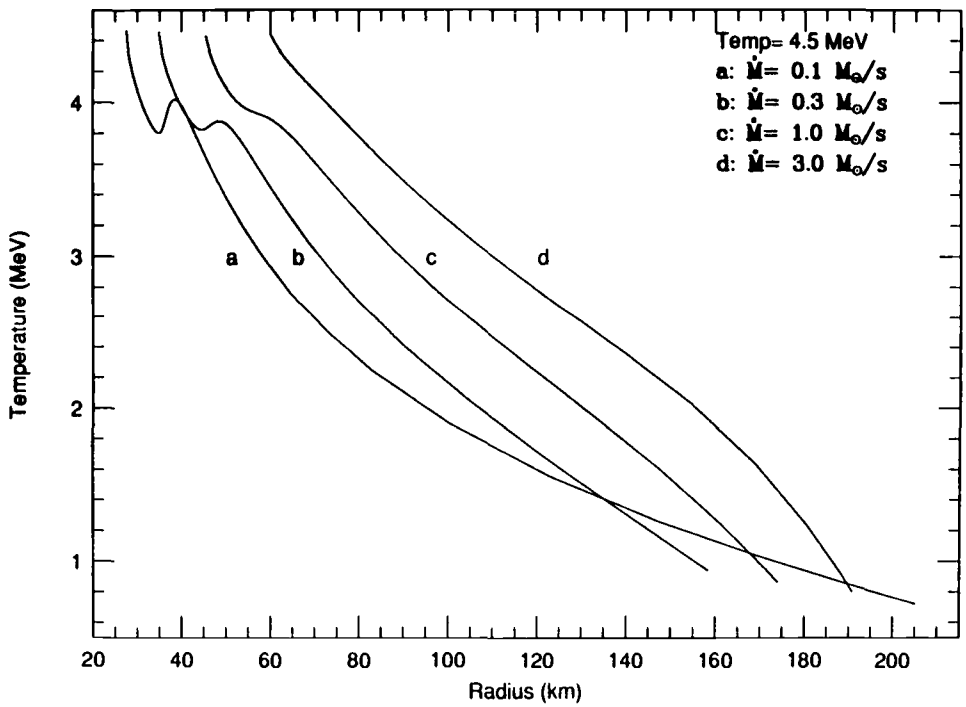

FIGURE 1. The temperature (in MeV) versus the radius (in kilometers) for four values of the accretion mass flux ($\dot{M} = 0.1, 0.2, 1.0, 3.0 M_\odot/\mathrm{s}$). For these curves, L_{ν_e} is at its respective critical value. The neutrinospheric temperature was set equal to 4.5 MeV. The reader should consult Burrows and Goshy (1993) more details.

BG for the critical accretion rate is,

$$\dot{M}_{\mathrm{crit}} \sim 1.1 M_\odot/\mathrm{s} \left(\frac{L_{\nu_e}}{5 \times 10^{52}\,\mathrm{ergs/s}} \right)^{2.3} . \tag{2.7}$$

The high power of 2.3 emphasizes the stiff dependence of explosion on the neutrino luminosity. Improvements in the assumptions and approximations, in particular in the neutrino "transport," and different core masses will change the specific numbers. However, the finiteness of the stable branch and the existence of a critical condition seem to be robust.

Using eq. (2.7), BG concluded that accretion alone does not power a spherical supernova explosion. A core luminosity of whatever provenance (diffusion, convection, etc.) is required, unless the iron core envelopes are much denser than in most current progenitors. This conclusion explains why Wilson and Mayle (1992) have needed to evoke doubly-diffusive core mixing to enhance the driving neutrino luminosities that are otherwise too small.

After the condition in eq. (2.7) is achieved, the explosion should develop into a transient neutrino-driven wind (Burrows 1987). Duncan, Shapiro, and Wasserman (1986) have already performed a preliminary investigation of winds from neutron stars. Scaling up their results to the supernova regime, BG obtain for the mechanical luminosity of the wind,

$$L_w \sim 4.2 \times 10^{51}\,\mathrm{ergs/s} \left(\frac{L_{\nu_e}}{5 \times 10^{52}\mathrm{ergs/s}} \right)^{3.5} \left(\frac{1.3 M_\odot}{M} \right)^2 \left(\frac{30\mathrm{km}}{R_\nu} \right)^{4/3} . \tag{2.8}$$

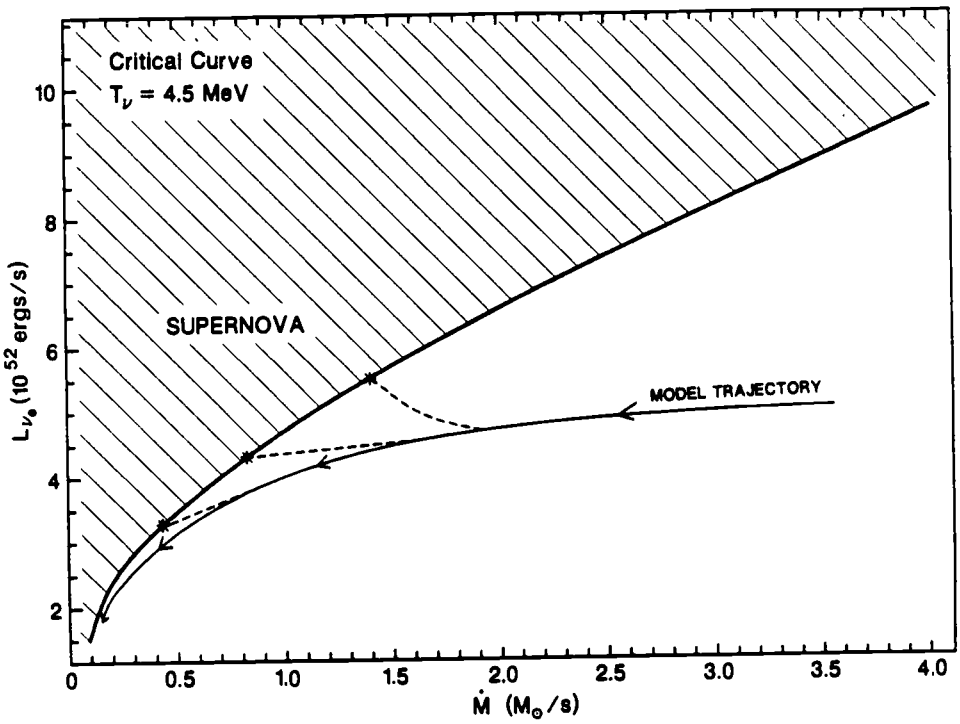

FIGURE 2. The critical curve of L_{ν_e} (in 10^{52} ergs/s) versus accretion mass flux $\dot{M}$ (in $M_\odot$/s). A model in the hatched region should "supernova."

The steep dependence on L_{ν_e} in eq. (2.8) is its most important feature. This high power echoes that in eq. (2.7) and serves to reemphasize the sensitivity of supernova theory to the driving neutrino luminosities. If we integrate L_w over time, we obtain the total mechanical energy pumped into the supernova after the onset of the blast:

$$E_s \sim 4.2 \times 10^{51} \text{ ergs} \left(\frac{\tau}{1s}\right) \left(\frac{L_{\nu_e}}{5 \times 10^{52} \text{ergs/s}}\right)^{3.5} \left(\frac{1.3 M_\odot}{M}\right)^2 \left(\frac{30\text{km}}{R_\nu}\right)^{4/3}, \qquad (2.9)$$

where we have arbitrarily assumed that L_{ν_e} is constant over a time τ. If we constrain E_s to be equal to 10^{51} ergs, we can derive the τ's and E_ν's required at given L_{ν_e}'s. For $L_{\nu_e} = 8.0 \times 10^{52}$ ergs/s, $\tau \sim$45 milliseconds, $E_{\nu_e} \sim 3.6 \times 10^{51}$ ergs, and E_ν(total) $\sim 2 \times 10^{52}$ ergs, all reasonable and within bounds. A slightly higher L_{ν_e} has great leverage in decreasing τ and E_ν, since $\tau \propto E_s / L_{\nu_e}^{3.5}$. Note that the long delays of 100's of milliseconds to seconds seen in the detailed hydro calculations could be artifacts of the missing neutrino flux and that the "long-term" mechanism may be a misnomer.

3. The Convective Trigger

The sputtering shock and electron-capture before and after bounce together create such wildly varying entropy and composition profiles that Rayleigh-Taylor-like instabilities are inevitable (Burrows & Lattimer 1988). The salient discoveries of the earlier work of Burrows & Fryxell (1992) were that the instability does encompass the neutrinospheres, is grossly aspherical, achieves high Mach numbers (~1.0), and starts almost immediately after the shock stalls. Hence, the rapid advection of heat from opaque to transparent regions and the enchancement in the driving neutrino luminosities are naturally achieved.

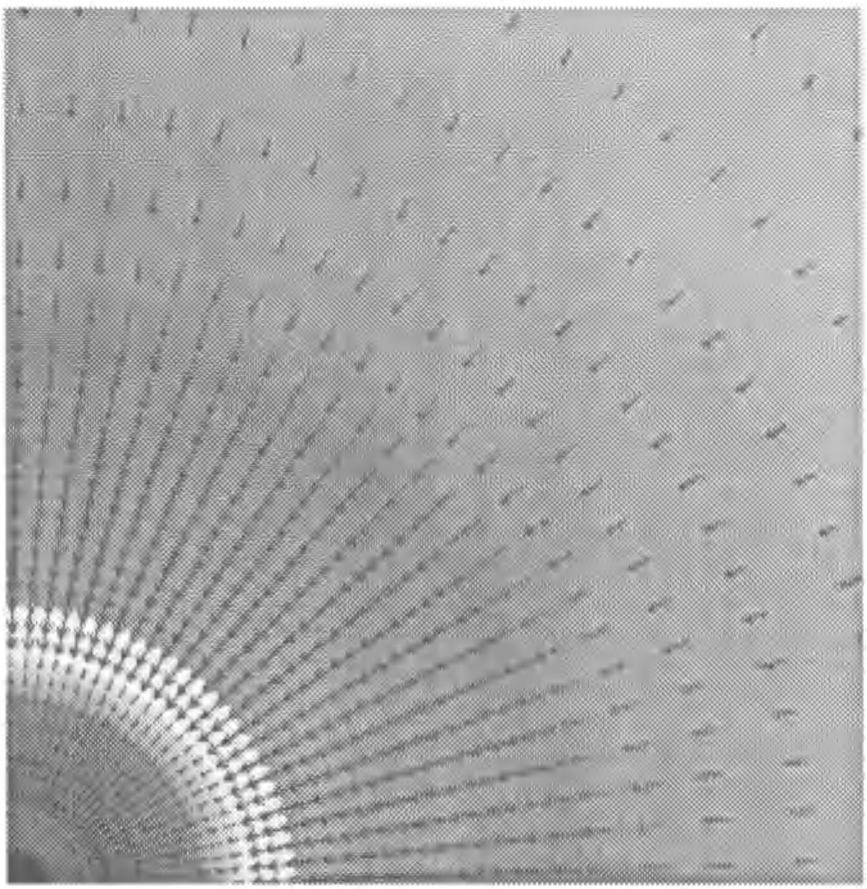

FIGURE 3. The temperature distribution in a protoneutron star just after the bounce shock stalls (2 milliseconds). The inner radius is at 20 kilometers. Refer to Burrows & Fryxell (1993) for details.

With a one-dimensional, transport algorithm coupled to a two-dimensional hydrodynamics code, BF recently showed that when 2-D convection without transport is not adequate, that 2-D hydro with transport with exactly the same initial model and EOS is adequate for explosion. These calculations demonstrated the existence of the convective boost, and showed that it can turn a failure into a success.

The specific algorithms employed by BF will not be discussed here and the reader is referred to that work for details. Figures 3 – 6 depict the temperature distributions during the first 30 milliseconds (at 2, 14, 20, and 30 milliseconds) after the shock stalls, with velocity vectors superposed. As one can see, particularly in Figures 4 and 5, the rapid overturn of the zones from 20 to ~100 kilometers dredges heat outward, creating a grossly asymmetrical luminosity field. In the calculations of BF, the enhanced neutrino luminosities blow a large bubble that is driven into explosion. After only 30 milliseconds, the shock has moved from ~120 kilometers to 360 kilometers. The same structure with the same neutrino-transport algorithm, initial model, and EOS does not explode within this time if constrained to 1-D. L_{ν_e} is enhanced between 10 and 30 milliseconds from $\sim 4 \times 10^{52}$ ergs/s in the 1-D calculations to between 4 and 8.5×10^{52} ergs/s in the 2-D calculations. During the same time, the $\bar{\nu}_e$ luminosity ($L_{\bar{\nu}_e}$) is boosted from 2–4 $\times 10^{52}$

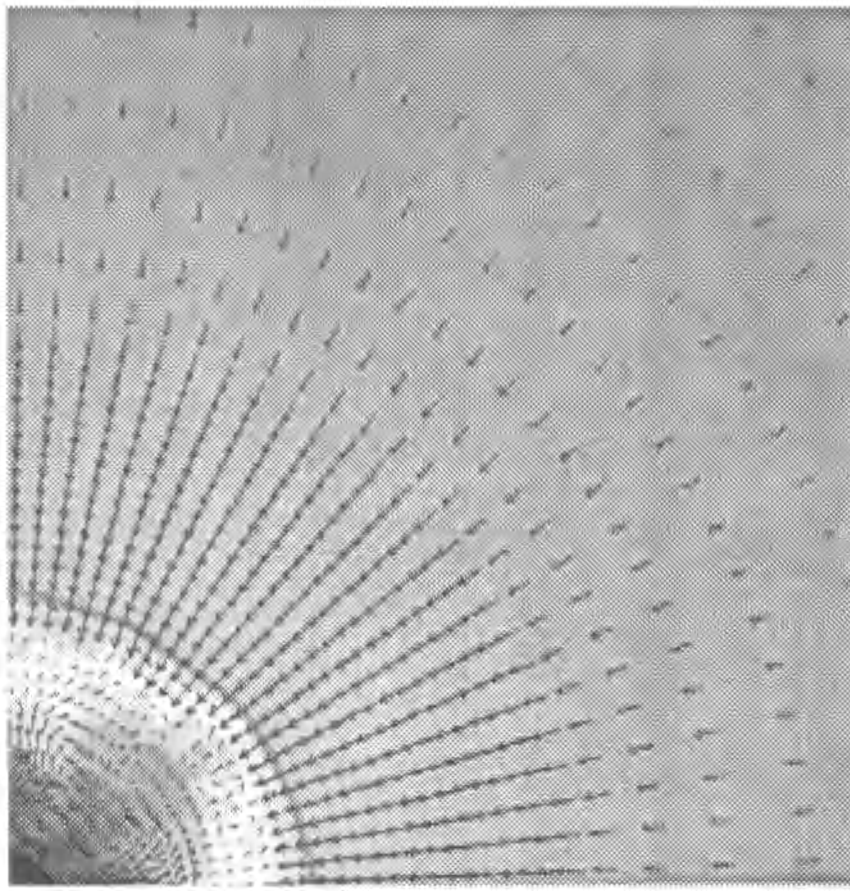

FIGURE 4. Same as Fig. 3, but at $t = 14$ milliseconds. The overturning motions are clearly seen.

ergs/s (1-D) to 2–6 $\times$ 10^{52} ergs/s (2-D). Heat and leptons are rapidly dredged up from the opaque inner zones and radiated from the neutrinospheres (60–80 kilometers) at an accelerated rate. Turning on transport and capture does not suppress the instability. In fact, the more rapid loss of electron and thermal pressure causes the inner zones to sink deeper into the potential well to higher gravities, which increases the overturn speeds and decreases the overturn timescales. The factor-of-two enhancements in L_{ν_e} and $L_{\bar{\nu}_e}$ (the convective "flash") is just what is needed to explode the supernova within only tens of milliseconds of stalling (Burrows & Goshy 1993). This short time suggests that the neutrino-driven mechanism of supernova explosions needn't be as "long-term" (hundreds of milliseconds to seconds) as was originally formulated (Wilson 1985).

If such high luminosities as are quoted above can be maintained for $\sim$ 50 milliseconds, using eq. (2.9) we see than an explosion energy of $\sim 10^{51}$ ergs can easily be achieved. In fact, since for a pre-explosion accretion rate near $3M_\odot$/s the outer mantle may be unbound (BG), and ^{56}Ni production may provide $\sim$10% of the supernova energy, the requirements on the driving luminosity after explosion can be relaxed. Hence, an explosion that starts within tens of milliseconds and is driven for only a quick 50 milliseconds is plausible.

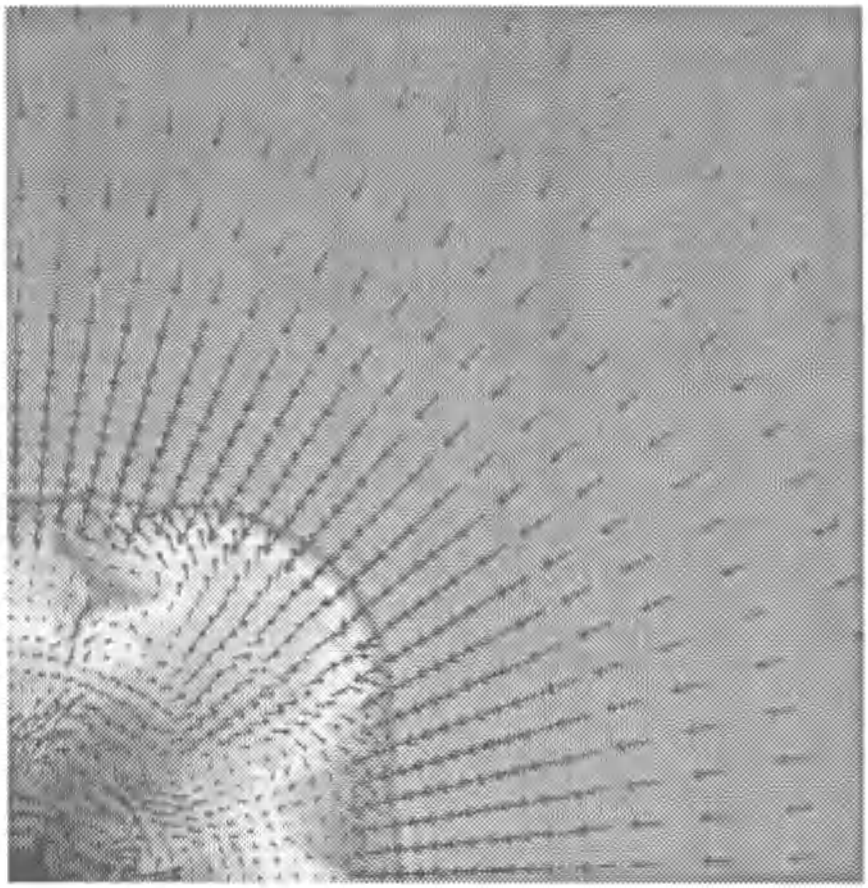

FIGURE 5. Same as Fig. 4, but at $t = 20$ milliseconds.

4. Conclusions

The neutrino signature of the convective flash (its rise time, duration, magnitude, etc.) should be distinctive in the multitude of underground detectors being readied for the next galactic core collapse. Table 1 from Burrows, Klein, & Gandhi (1992) provides some characteristics of these facilities and an estimate of the total integrated event number due to a collapse at 10 kpc.

LVD, MACRO, SNO, and Super Kamiokande (SK) are particularly noteworthy as neutrino telescopes and should all be online (in some capacity) by 1996. SNO and SK should catch at least 50 and 500 events, respectively, at 10 kpc, during the convective flash.

LVD and MACRO may each acquire during this convective flash more events than were garnered in total from SN 1987A by all Earth's detectors.

Clearly, a neutrino light curve from a galactic collapse will speak volumes about the supernova phenomenon. However, the mantle instability that we have highlighted in this paper may also generate sufficient gravitational radiation (GR) to be detected by the second-generation LIGO (Thorne 1987). If the collapsing core is not generally rotating rapidly, the major GR signature of supernova will be due to the overturning convective motions. Frequencies of 50–1000 Hz (peaking near a few hundred Hz?) may predominate and if at least $10^{-10} M_{\odot} c^2$ of this is radiated within 100 milliseconds of bounce, strains

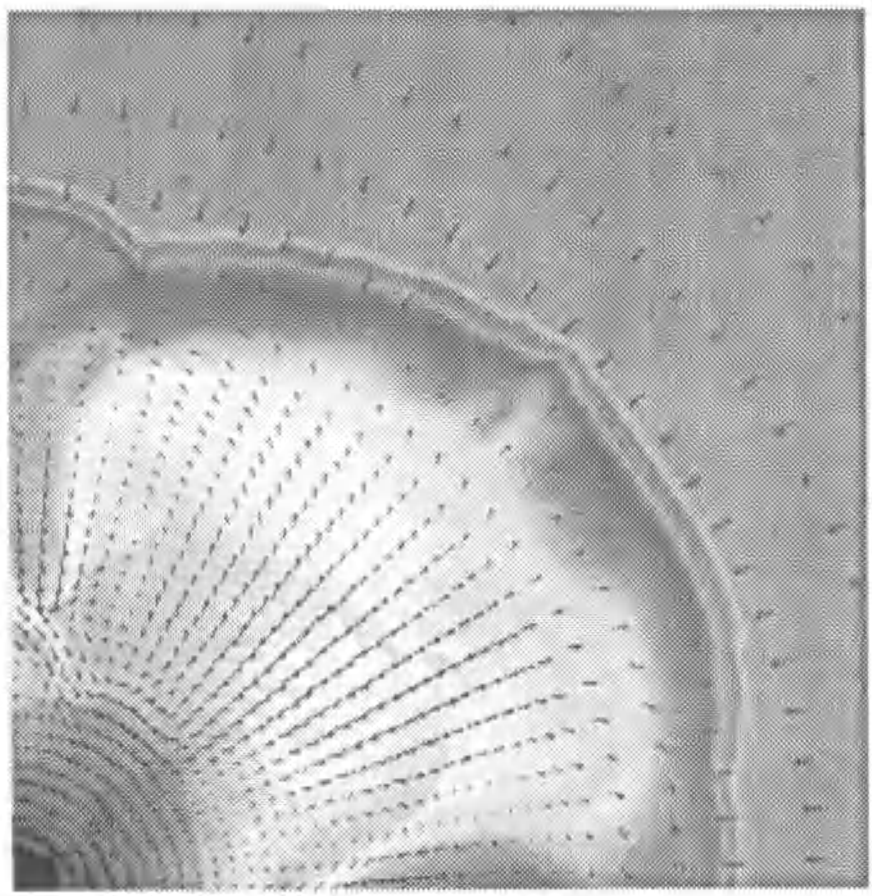

FIGURE 6. Same as Fig. 4, but at $t = 30$ milliseconds. The supernova explosion is well developed.

of $\sim 10^{-21}$ at 10 kpc may be expected. Using the arguments of Thorne (1987), we find a range for supernova detection by the advanced LIGO of 10–30 kpc. This implies that a supernova anywhere in the galaxy may be within reach via gravity waves. Whether we can legitimately conclude this awaits more detailed calculations, but the possibility of probing the multi-dimensional nature of protoneutron stars with GR should not be taken lightly.

The large neutrino luminosity contrasts of BF (as much as a factor of two) lend credence to the possibility that net neutrino emission anisotropies can give the residual neutron star a significant kick. If we assume that 10% of the total neutrino energy radiated is radiated during the convective flash and take the blob sizes and timescales derived in BF, we can derive net anisotropies of $\sim$10%. This yields a neutron star recoil speed of 200–300 km/s, and implies that overturn instabilities may solve more than one problem in the physics of compact objects.

For nucleosynthetic reasons (Thielemann, this volume), it is natural to associate the mass cut with the inner edge of the oxygen-burning shell. It is there that one usually (though not always) finds ledges in $\eta (= 1 - 2Y_e)$ and density. If we assume that this edge falls in at $\frac{1}{\sqrt{2}}$ times the free-fall rates after the collapse rarefaction reaches it, we derive

TABLE 1. Supernova Neutrino Telescope Characteristics

Detector	Total mass (tons) (Fiducial Mass)	Composition	Threshold (MeV) at 10 kpc	# Events
		CERENKOV:		
KIII	3000 (2140)	H_2O	5	370
Super Kamiokande	40,000 (32,000)	H_2O	5	5500
SNO	1600/1000	H_2O/D_2O	5	780
		SCINTILLATION:		
LVD	1800 (1200)	Kerosene	5–7	375
MACRO	1000	"CH_2"	10	240
Baksan	330 (200)	"White Spirits" "CH_2"	10	70
LSND	200	"CH_2"	5	70
Borexino	300	$(BO)_3(OCH_3)_3$	~ 0.2	200
CalTech	1000	–	2.8	290
		DRIFT CHAMBER:		
ICARUS	3600	^{40}Ar	5	120
		RADIOCHEMICAL:		
Homestake ^{37}Cl	610	C_2Cl_4	0.814	4
Homestake ^{127}I	–	NaI	0.664	25
Baksan ^{37}Cl	3000	C_2Cl_4	0.814	22
		EXTRAGALACTIC:		
SNBO	100,000	$CaCO_3$	–	10,000
JULIA	40,000	H_2O	–	10,000

that it takes approximately 100 milliseconds $\left(\frac{R_{ox}}{10^8\mathrm{cm}}\right)^{3/2}\left(\frac{1.4M_\odot}{M_{ox}}\right)^{1/2}$ for the oxygen shell to achieve the inner zones. With realistic values of R_{ox} and M_{ox}, we see that this time may be between 100 and 500 milliseconds. This is long compared to the timescale of the convection-assisted re-ignition, but short compared to the duration of the traditional long-term mechanism. How everything associated with collapse and explosion is timed remains to be seen, but all that is relevant is coming into increasingly sharper view. The basic mechanism of the supernova explosion may soon become clear to all.

Acknowledgements

Thanks are extended to Willy Benz, Eli Livne, John Goshy, Stirling Colgate, and Bruce Fryxell for the many stimulating conversations that have guided the work summarized here. The author thanks the NSF and NASA for support through grants AST89-14346 and AST92-17322, and NAGW-2145.

REFERENCES

Bethe, H. A., & Wilson, J. R. 1985, ApJ, 295, 14

Burrows, A. 1987, ApJ, 318, L57

Burrows, A., & Fryxell, B. 1992, Science, 258, 430

Burrows, A., & Fryxell, B. 1993, ApJ, 418, L33 (BF).

Burrows, A., & Goshy, J. 1993, ApJ, 416, L75 (BG).

Burrows, A., Klein, D., & Gandhi, R. 1992, Phys. Rev. D45, 3361

Burrows, A., & Lattimer, J. 1988, Phys. Repts., 163, 51

Chevalier, R. A., Imamura, J. N. 1982, ApJ, 261, 543

Duncan, R. C., Shapiro, S. L., & Wasserman, I. 1986, ApJ, 309, 141

Thorne, K. 1987, In 300 Years of Gravitation, ed. by S. W. Hawking, & W. Israel (Cambridge Univ. Press), pp. 330–458

van den Bergh, S., & Tammann, G. A. 1991, ARA&A, 29, 363

Wilson, J. R. 1985, in Numerical Astrophysics, ed. J. Centrella, J. M. LeBlanc, R. L. Bowers, p.422. (Boston: Jones & Bartlett).

Wilson, J. R., & Mayle, R. 1992, Report on the Progress of Supernova Research by the Livermore Group

Dynamics of Type-II Supernovae

By H.-Th. JANKA AND E. M. MÜLLER

Max-Planck-Institut für Astrophysik, Karl-Schwarzshild-Strasse 1, D-8046 Garching, Germany

Hydrodynamical simulations of type-II supernovae in one and two dimensions are performed for the revival phase of the delayed shock by neutrino energy deposition. Starting with a post-collapse model of the 1.31 $M_\odot$ iron core of a 15 $M_\odot$ star immediately after the stagnation of the prompt shock about 10 ms after core bounce, the models are followed for several hundred milliseconds with varied neutrino fluxes from the neutrino sphere. The variation of the neutrino luminosities is motivated by the considerable increase of the neutrino emission due to convective processes inside and close to the neutrino sphere (see Janka 1993), which are driven by negative gradients of entropy and electron concentration left behind by the prompt shock (Burrows & Fryxell 1992, Janka & Müller 1992). The size of this luminosity increase remains to be quantitatively analyzed yet and may require multi-dimensional neutrino transport. However, in the presented simulations the region below the neutrino sphere is cut out and replaced by an inner boundary condition, so that the convective zone is only partially included and the neutrino flows are treated as a freely changeable energy source.

For small neutrino luminosities the energy transfer to the matter is insufficient to revive the stalled shock. However, there is a sharp transition to successful explosions, when the neutrino luminosities lie above some 'threshold value'. Once the shock is driven out and the density and temperature of the matter between neutrino sphere and shock start to decrease during the expansion, suitable conditions for further neutrino energy deposition are maintained, and an explosion results. With the neutrino energy deposition the entropy per nucleon in the region between neutrino sphere and shock grows, and convective overturn will set in. Multi-dimensional simulations show that due to the large pressure scale height a large-scale pattern of up-flows and down-flows with velocities close to the local speed of sound develops. Consequently, cold, post-shock material is advected down into the neutrino heating layer close to the neutrino sphere and hot material is transported outwards, thus reducing energy losses by re-emission of neutrinos and increasing the pressure behind the shock. Therefore these convective processes are found to be a very important aid to the delayed supernova explosion. In fact, two-dimensional models explode even in cases where spherically symmetrical computations fail.

1. Type-II Supernova Explosions and Convection

According to the current understanding type-II supernova explosions can be driven by neutrino energy deposition in the layers between the nascent neutron star and the stalled prompt supernova shock (Bethe & Wilson 1985, Wilson *et al.* 1986). The 'delayed' explosion is triggered on the neutrino heating time scale instead of the hydrodynamical time scale, i.e. within (several) 100 milliseconds rather than ten milliseconds after core bounce. Although the neutrinos streaming out of the neutrino decoupling region in the surface of the forming neutron star loose only a small fraction of their energy (at most a few per cent) in the surrounding stellar matter, this energy may be sufficient to 'revive' the core bounce shock, which transformed to a standing accretion shock when energy losses due to dissociation of iron nuclei and emission of neutrinos reduced the pressure in the post shock material. The principle viability of this mechanism seems to be proven. However, there are still crucial questions to be answered. Firstly, it is not well understood, how, and when, the shock revival occurs and what the possibility of a successful explosion is defined by. Controversial results by independent elaborate supernova simulations (Mayle 1985, Wilson *et al.* 1986; Bruenn 1989a,b, 1992) give a

hint that an increase of the neutrino emission by convective processes inside the neutron star may be crucial: While Bruenn (1992) does not regard convection and does not get explosions, Mayle (1985) and Wilson *et al.* (1986) obtain explosions when they include mixing processes by neutron finger instabilities in a parametrical description in their one-dimensional simulations. Secondly, although neutrino heating is able to eject the envelope of the star, the explosion energies in the delayed scenario are too low compared with typical type-II energies as deduced from light curve analyses (see Wilson *et al.* 1986; Janka 1993). This defines a quantitative problem, which still remains to be settled.

Janka (1993) performed long-time hydrodynamical simulations of the post bounce supernova evolution until more than 10 seconds after the revival of the stalled shock. Neutrino heating external to the nascent neutron star was carefully taken into account and the neutrino emission from the neutron star was varied within 'reasonable' limits. The simulations showed that high explosion energies cannot be obtained through energy deposition by the slowly decaying neutrino emission during the Kelvin-Helmholtz cooling of the protoneutron star. Instead, it was found that energetic explosions require the occurrence of an early phase of high neutrino luminosities with efficient heating in the vicinity of the neutron star. This means that the answer to the energy problem has to be searched for in the first few hundred milliseconds after core bounce. In this sense neutrino-driven supernovae are exploded by a *delayed* mechanism, not a *late* one.

When the prompt shock propagates through the outer layers of the collapsed stellar iron core and a luminous outburst radiates away several 10^{56} electron neutrinos within about 10 milliseconds, negative gradients of entropy and lepton number originate, and can give rise to convective instabilities (Burrows 1987; Burrows & Lattimer 1988). Two-dimensional (Burrows & Fryxell 1992, Janka & Müller 1992) and three-dimensional simulations (Müller 1993) indeed show that these instabilities grow on a time scale of about 10 milliseconds and mix a region encompassing the neutrino sphere with maximum velocities close to the local speed of sound. After 10–20 milliseconds a region of about 0.5 $M_\odot$ between 20 and 120 kilometers is involved in the convective overturn and is homogenized within about 20 milliseconds (see Janka & Müller 1992). Neutrino decoupling occurs at densities $\rho \lesssim 10^{11}\,\mathrm{g/cm^3}$, which is inside the convective layer. Therefore a considerable increase of the neutrino emission must be associated with the transport of material with high electron concentration from regions at $\rho \gtrsim 10^{12}\,\mathrm{g/cm^3}$ into the neutrino-transparent regime. This convection takes place *inside* the forming neutron star and is not in direct contact with the exploding layers of the star. Of course, crucially determining the neutrino luminosities during the early post bounce phase, this convection is of immediate importance for the explosion of type-II supernovae in the context of the neutrino-heating mechanism.

Observations of ^{56}Ni mixed into the hydrogen-rich envelope in SN 1987A suggest that convective processes might have occurred also *outside* the protoneutron star at a very early stage during the supernova explosion. This could have brought material originally located close to the new-born neutron star with high velocities into the outer layers of the star. Herant *et al.* (1992) have shown that the energy deposition by neutrinos in the vicinity of the neutron star is able to drive large-scale convective overturn. Together with the turbulence phenomena inside the forming neutron star these instabilities introduce a new level of complexity in our picture of type-II supernova explosions.

The work presented here concentrates on the post-bounce history of the supernova shock. The behaviour of the stalled prompt shock wave under the influence of varied neutrino emission from the protoneutron star is studied by hydrodynamical simulations. One- and two-dimensional simulations are compared to gain evidence about the occur-

rence and importance of turbulence outside the new-born neutron star. In Sect. 2 the model, physical assumptions and some numerical aspects are described, in Sect. 3 the results are discussed, and Sect. 4 ends with a summary and conclusions.

2. Model, Physical Assumptions, and Numerical Aspects

The post bounce evolution of the collapsed 1.31 $M_\odot$ iron core of a 15 $M_\odot$ star is simulated for a period of several hundred milliseconds, starting at a time about 10 milliseconds after core bounce. By that time the prompt shock wave has transformed into a standing accretion shock at a radius of about 115 km, enclosing a mass of 1.25 $M_\odot$. The matter behind the shock has small negative velocities and settles onto the forming neutron star. The initial model was provided by Bruenn (1993, private communication; see also Bruenn 1992), who computed core collapse and core bounce with use of the equation of state developed by Lattimer & Swesty (1991). Following the further history for nearly 700 ms Bruenn did not find an explosion of the star.

As described above, the neutrino luminosities are dependent on convective processes around the neutrino sphere (see Janka 1993, Janka & Müller 1992) and cannot accurately be determined without an elaborate treatment of neutrino transfer in this turbulent region. Possibly even methods to simulate neutrino transport in more than one dimension have to be applied. Therefore, we decided to vary the neutrino luminosities and to study their influence on the destiny of the shock. For this purpose it is adequate to cut out the inner part of the collapsed stellar core, which also helps to save computer time when performing a large number of one-dimensional runs or multi-dimensional simulations. We put the inner boundary to a density of about $10^{12}\,\mathrm{g/cm^3}$, corresponding to an initial radius of 32 km in the considered model. The radius of the inner boundary was either kept fixed, or was allowed to shrink with time to mimic the contraction of the cooling neutron star. Although we located the inner boundary somewhat inside the neutrino sphere, our computational domain did only partially encompass the convective layer in the protoneutron star. Prescriptions for time-dependent fluxes and spectra of the neutrino emission from the inner core were imposed. While the spectra were not changed in different runs, the neutrino luminosities were varied to study their influence.

The simulations (see Sect. 3) were performed by treating the neutrinos in a 'lightball' approximation: The fluxes entering the computational grid at the inner boundary were kept constant with radius (except for Doppler shift and gravitational red shift effects). Although not being correct, this approach is not too bad outside the neutrino sphere and reduces the computational effort, in particular in multi-dimensional simulations. Since we are not interested in the question, how these fluxes are formed, but in their effect on the shock evolution, the neutrino lightball approximation is very likely justified. The validity of this approximation will be tested in forthcoming simulations (Janka & Müller, in preparation). All types of neutrinos (ν_e, $\bar{\nu}_e$, ν_μ, $\bar{\nu}_\mu$, ν_τ, $\bar{\nu}_\tau$) were included, and the processes taken into account were electron neutrino/antineutrino absorption on neutrons/protons, neutrino scattering off neutrons, protons, nuclei, electrons, and positrons, and neutrino pair production and pair annihilation by/into electron-positron pairs. Our simulations were performed with an elaborate, vectorized equation of state, which contains contributions by neutrons, protons, alpha particles and a representative heavy nucleus in nuclear statistical equilibrium. Electrons, treated as an arbitrarily degenerate and relativistic gas, and positrons and photons were taken into account.

We employed two different numerical methods for solving the equations of Newtonian hydrodynamics: An explicit, second order Lagrangian scheme with automatic, conservative rezoning, which handles shocks by use of a tensor artificial viscosity (see Janka *et*

TABLE 1. Model data for one-dimensional (letter 'O' in the model name) and two-dimensional ('T') simulations. The letter 'f' indicates that the radius of the inner boundary was kept fixed, 'c' marks model runs with contracting inner boundary. In case of two-dimensional simulations the numbers in parentheses behind the model name give the numbers of angular zones (of one degree size). $L_{\nu_e}^{52}$ is the electron neutrino luminosity (in 10^{52} erg/s) at the start of the computation, $L_{\nu_x}^{52}$ are the individual luminosities of muon and tauon neutrinos and antineutrinos. The luminosity of electron antineutrinos is constrained by the requirement that the inner part of the neutron star with mass $M_{\rm ic} = 0.85\,M_\odot$ looses an electron fraction of ΔY_e. The total energy loss due to neutrino emission is assumed to equal $\Delta\epsilon \cdot M_\odot c^2$. $t_{\rm exp}$ gives the heating time scale, defined by the moment when the explosion energy $E_{\rm exp}$ (see text) of the model becomes larger than 10^{48} erg. The values in column $E_{\rm exp}$ give the explosion energies at the end of the computation, i.e. at time $t_{\rm end}$ after the start of the simulation.

Model	$L_{\nu_e}^{52}$ [erg/s]	$L_{\nu_x}^{52}$ [erg/s]	$DeltaY_e$	$Delta\epsilon$	$t_{\rm exp}$ [ms]	$t_{\rm end}$ [ms]	$E_{\rm exp}(t_{\rm end})$ [10^{50} erg]
O1f	1.850	1.650	0.05	0.035	∞	462.	0.0
O2f	1.900	1.700	0.05	0.035	270.	796.	7.1
O3f	1.925	1.725	0.05	0.035	211.	735.	8.2
O4f	2.750	2.250	0.25	0.150	48.	635.	48.3
O1c	1.900	1.700	0.05	0.035	∞	341.	0.0
O2c	2.000	1.800	0.05	0.035	∞	365.	0.0
O3c	2.100	1.850	0.06	0.045	∞	372.	0.0
O4c	2.200	1.875	0.06	0.045	162.	697.	4.9
O5c	2.225	1.875	0.06	0.045	122.	927.	9.5
O6c	2.250	1.900	0.07	0.050	97.	485.	13.0
T1f(90)	1.900	1.700	0.05	0.035	93.	720.	8.9
T1c(90)	1.900	1.700	0.05	0.035	88.	214.	0.9
T2c(180)	1.900	1.700	0.05	0.035	85.	199.	1.2

al. 1993). Multi-dimensional simulations were performed with a modified version of the explicit PROMETHEUS code (Fryxell *et al.* 1989), which is a Eulerian implementation of the *Piecewise Parabolic Method* by Colella & Woodward (1984). Comparing results of both codes yields excellent agreement where it required (see also Janka *et al.* 1993).

3. Shock Evolution in One- and Two-Dimensional Simulations

3.1. *Spherically Symmetric Case*

A set of one-dimensional simulations was performed changing the neutrino fluxes from the inner boundary from small values to successively larger ones. The effect on the standing accretion shock was investigated. The results are collected in Table 1. The model sequence 'O#f' was computed with a fixed radius of the inner boundary $R_{\rm ib} = 31.7\,$km, while the inner boundary was contracting in models 'O#c'. The initial electron neutrino luminosity L_{ν_e} and muon and tauon neutrino/antineutrino luminosities L_{ν_x} can also be found in Table 1. The luminosities of all neutrino kinds were assumed to decay exponentially and were constrained by the requirements that a total lepton number $\Delta Y_e \cdot \mathcal{A}\, M_{\rm ic} c^2$ ($M_{\rm ic} = 0.85\,M_\odot$, $\mathcal{A}$ is Avogadro's number) and a total energy $\Delta\epsilon \cdot M_\odot c^2$ is radiated away. Numbers for ΔY_e and $\Delta\epsilon$ are listed in in Table 1.

The models do not explode for low values of the neutrino luminosity. The neutrino emission has to surpass a well defined threshold value to drive a strong expansion of the

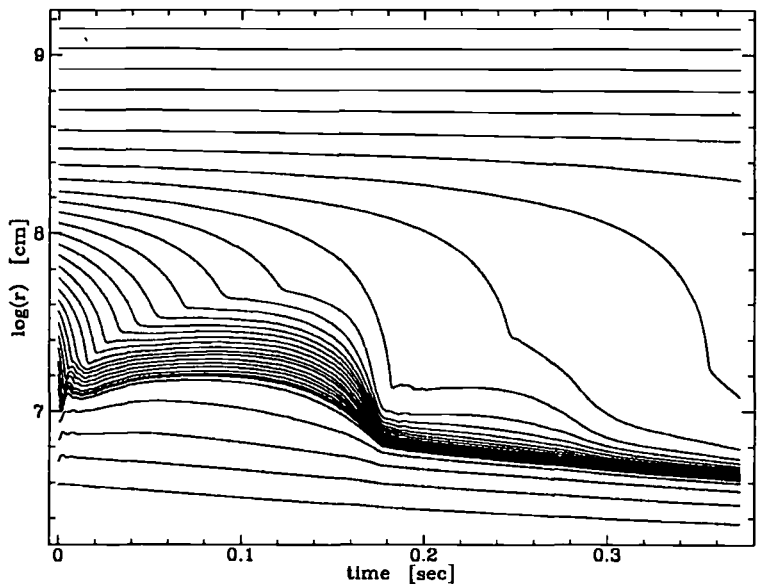

FIGURE 1. Radial positions as functions of time for a sample of mass shells of model O3c (see Table 1). The protoneutron star is sitting at the bottom of the figure, and the position of the supernova shock can be identified at the sharp turns of the curves. The shock exhibits an oscillatory motion and the model does not explode.

layers between neutrino sphere and standing accretion shock against the ram pressure of the material falling into the shock. Only if this expansion is sufficiently fast and strong, a successful explosion is initiated. Examples for both cases, no explosion and explosion, are shown in Figs. 1 and 2. In case of failure the region between neutrino sphere and shock expands and contracts, and the shock position exhibits an oscillatory behaviour (see Fig. 1; model O3c in Table 1). Phases of expansion and net energy gain of the matter alternate with compression and accompanying neutrino energy loss. In contrast, when the neutrino heating is powerful enough, the strong expansion prevents the re-emission of energy deposited by neutrino absorption outside the so called 'gain radius'. This location defines the point in the protoneutron star atmosphere, where neutrino cooling – which dominates at high densities and gas temperatures – is exceeded by neutrino heating (see Bethe & Wilson 1985, Bethe 1990). With the expansion setting in, the temperatures and densities decrease, which maintains favourable conditions for continued neutrino heating. This defines a runaway situation, and finally the shock wave propagates outward to trigger the explosion of the star (Fig. 2; model O4c in Table 1). These results are obtained for the idealized case that the neutrino fluxes originate from an independent central source and are not influenced by the expansion or contraction of the protoneutron star atmosphere. The exact and detailed post bounce history may depend on the coupling between neutrino fluxes and hydrodynamical evolution. Nevertheless, our results show principle features as they were found in the computations by Wilson *et al.* (1986). Comparison with these, however, reveals some fundamental differences, too. In the simulations by Wilson *et al.* (1986) much of the neutrino luminosity was produced by spherical accretion of matter falling through the standing accretion shock onto the new-formed neutron star. When neutrino heating began to drive an expansion, this accretion was turned off and the luminosities dropped. Neutrino cooling took over, and the matter started to contract, again increasing the accretion rate. This resulted in an oscillatory up and down of the

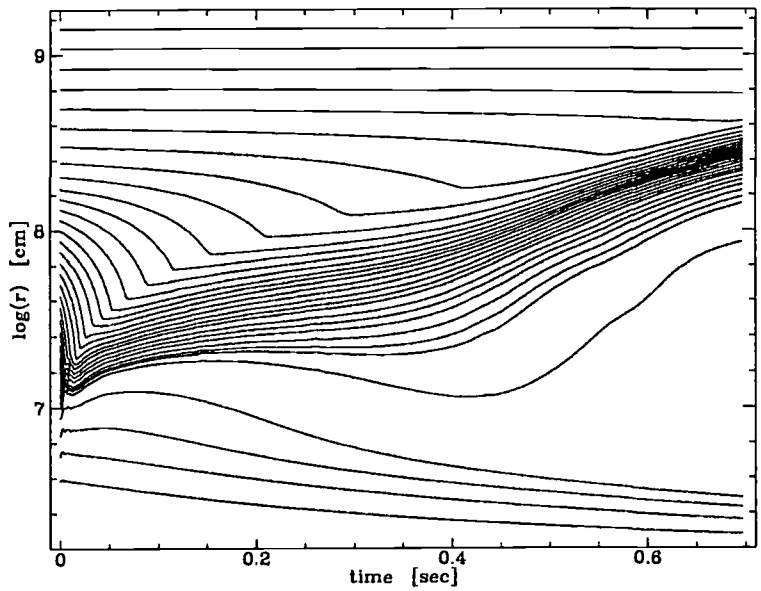

FIGURE 2. Radial positions $r(t)$ for a sample of mass shells of model O4c (see Table 1). After about 400 ms post bounce a strong bifurcation between protoneutron star and stellar mantle develops and the model explodes.

shock front in some of the models of Wilson *et al.* (1986). With our assumption of the neutrino luminosities being produced in the convective mantle region of the protoneutron star we do not have this negative feedback between neutrino emission and matter motion: When a strong neutrino-driven expansion sets in, the matter temperature drops, neutrino re-emission decreases, and neutrino heating by the unchanged neutrino fluxes continues the positive energy transfer to the stellar gas.

This mechanism implies a strong sensitivity to the neutrino luminosities. The explosion energy $E_{\rm exp}$, which is given by the total energy (kinetic plus internal energies minus gravitational binding energy) of all zones with positive values of this energy, increases steeply for higher neutrino fluxes. In Table 1 the corresponding numbers are listed for the final models (column $t_{\rm end}$ gives the time at the end of the simulation runs, measured from the beginning of each computation). The time scale $t_{\rm exp}$ in Table 1 measures the time to start the explosion and is defined as the moment when $E_{\rm exp} = 10^{48}$ erg. This time shrinks for stronger neutrino heating; in any case, however, it was found to be longer than 50 milliseconds. It is remarkable that the threshold value of the neutrino luminosity depends on the treatment of the inner boundary. With fixed radius $R_{\rm ib}$ our one-dimensional models explode for $L_{\nu_e} \gtrsim 1.9 \cdot 10^{52}$ erg/s, whereas the shrinking inner core prevents explosions below $L_{\nu_e} \approx 2.2 \cdot 10^{52}$ erg/s.

3.2. *Two-Dimensional Case*

In a second set of runs we switched to two dimensions (models 'T#f', 'T#c' in Table 1), again treating the two possibilities of fixed inner boundary radius ('T#f') and contraction of the inner boundary ('T#c'). The numbers in parentheses, which follow the model name, indicate the angular size of the grid (90 or 180 degrees); the angular resolution was one degree. As in one dimension, the model did not explode without neutrino heating in two dimensions. When including neutrinos we chose the electron neutrino luminosity to be $L_{\nu_e} = 1.9 \cdot 10^{52}$ erg/s. For this case we found an explosion in the spherically

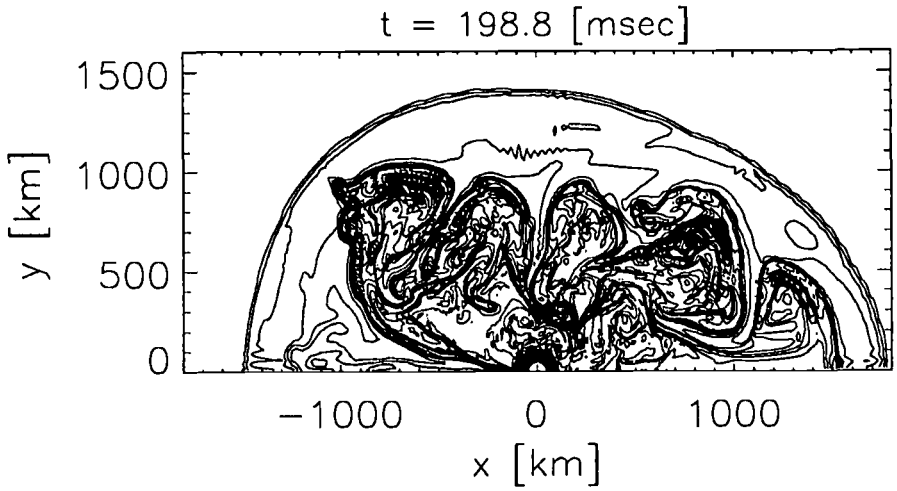

FIGURE 3. Convective overturn between protoneutron star (in the center) and outgoing supernova shock in model T2c(180) (see Table 1) at time $t = 199\,\mathrm{ms}$ after the start of the computation. The contours correspond to 25 equispaced levels of constant entropy between $s_{\min} \approx 5\,k_B$/nucleon and $s_{\max} \approx 17.3\,k_B$/nucleon. Narrow tubes of down-flowing matter and large rising bubbles occur.

symmetric situation, when the radius of the inner boundary was kept constant (model O2f), although it took as long as $t_{\exp} = 270\,\mathrm{ms}$ to start the finally successful expansion. The model with the same neutrino parameters, but with contracting inner boundary, model O1c, did not explode. This appeared to us as an interesting case to be studied in two dimensions.

Neutrino heating produces a region with relatively high entropies per particle outside the gain radius; typical values are around $10\text{–}15\,k_B$ per nucleon, whereas the matter downstream of the standing accretion shock has entropies of about $6\text{–}7\,k_B$/nucleon. Such a situation is convectively unstable. In fact, this is confirmed by our two-dimensional simulations, where convective overturn sets in within a few ten milliseconds. In the beginning, the convective mixing encompasses the whole region between gain radius and standing accretion shock. This moves cold (low entropy) material from behind the shock into the heating region and transports hot matter outwards. The convective velocities are several times $10^8\,\mathrm{cm/s}$ up to about $10^9\,\mathrm{cm/s}$, which is close to the local speed of sound. Without any doubt, this effect aids the explosion; this is clearly visible by comparison of the numbers for $t_{\exp}$ and $E_{\exp}$ for models O2f and T1f: The explosion starts more easily and the explosion energy tends to be higher in the two-dimensional case. Even more dramatic, we found an explosion also in case of a shrinking central core (R_{ib} decreasing with time), i.e. in a situation where the spherically symmetric model O1c failed: Models T1c(90) and T2c(180) show a strengthening of the shock wave and an explosive expansion on a time scale close to that of model T1f.

When the shock starts to move out and a dynamical expansion of the post-shock region begins, the expansion time scale becomes shorter than the typical growth time scale of instabilities. This is the moment when the convective pattern is 'frozen in': The number of structures with upward and downward flows as well as their angular sizes and locations on the sphere essentially do not change during the later evolution. Figure 3 shows the region of convective overturn between central neutron star and outgoing shock for model

T2c(180) at the end of the computation $t_{\rm end} = 199\,{\rm ms}$. We found the structure of the turbulence pattern to be sensitive to the prescribed behaviour of the inner boundary, and dependent on the angular size of the computational grid. Due to the large pressure scale height the structures tend to become quite extended, typical angular diameters being about 30 degrees (compare Fig. 3). With a grid of 90 degrees the structures are artificially confined and cannot fully develop. This reduces the efficiency of the convective transport and explains the difference in the numbers for models T1c(90) and T2c(180).

4. Summary and Conclusions

We have performed one- and two-dimensional hydrodynamical simulations of the revival phase of the stalled prompt supernova shock in a collapsed 1.31 $M_\odot$ stellar iron core.

The results for the spherically symmetric situation demonstrate that the possibility of a successful explosion by the neutrino-driven mechanism depends extremely sensitively on the neutrino luminosities during a phase of 100–300 milliseconds after core bounce. If the luminosities fall below a threshold value, the mechanism fails to explode the star. However, if the luminosities lie above this threshold and initiate a sufficiently strong expansion, then favourable conditions for continuing neutrino heating are established and (energetic) explosions result, provided the neutrino luminosities do not drop when the expansion sets in. This is the case when the neutrino flux is mainly originating from a convective region in the protoneutron star, but it is not the case, if the main contribution to the neutrino emission is generated by spherical accretion of infalling matter onto the protoneutron star (as in one-dimensional simulations). Convection *in* the protoneutron star (Burrows 1987, Burrows & Fryxell 1992, Janka & Müller 1992, Janka 1993) transports energy from deeper layers up to the neutrino decoupling region more efficiently than it is done by neutrino diffusion. Therefore convection around and below the neutrino sphere should be the crucial ingredient to neutrino-driven supernova explosions.

Comparing the one-dimensional simulations with the two-dimensional ones we learn that convection *outside* the protoneutron star clearly and strongly aids the explosion. It transports hot matter from the region of powerful neutrino heating (at the gain radius) into layers farther out behind the shock front. This changes the ν-luminosity threshold for the explosion as well as explosion energies and explosion time scales, and is also crucial to determine the mass of the neutron star remnant. In each of our simulation, one- and two-dimensional, it took at leas. 50 milliseconds for positive explosion energies to develop. This appears to us as the typical neutrino heating time scale required to start the explosion in the considered model. We conclude that high neutrino luminosities from the neutron star have to be maintained for a period which is a multiple of this time scale. Typically, after several hundred milliseconds the expanding material outside the protoneutron star had accumulated an energy comparable with standard type-II supernova energies. For cases of successful explosions the explosion energy is extremely sensitive to the luminosity of the neutrino source. It therefore does not seem likely that neutrino driven type-II supernovae have a uniform value of the explosion energy.

We stress that the effects in two dimensions, quantitatively and qualitatively, depend on the handling of the inner boundary in simulations where the high-density central part of the protoneutron star is cut out. Moreover, they also depend on the angular size of the grid for the simulation. Due to the large pressure scale height in the expanding region between gain radius and shock position the convective overturn proceeds in long tubes of down-flowing material and large rising bubbles. Typical angular diameters of these

structures were found to be about 30 degrees. On an angular grid of 90 degrees (instead of 180 degrees) the convection could not be adequately simulated, but was less violent and less effective in transporting energy into the shock front. We suspect that opening an additional degree of translational freedom by going to three dimensions could have a similar influence on the convection as extending the angular size of the grid. This may be taken as an indication that a satisfactory numerical treatment might actually require three-dimensional simulations.

Acknowledgements

H.-Th. J. would like to thank Prof. K. Nomoto and all the organizers of the IAU Colloquium No. 145 for the great opportunity to visit China.

REFERENCES

Bethe, H. A. 1990, Rev. Mod. Phys., 62, 801

Bethe, H. A., Wilson J.R. 1985, ApJ, 295, 14.

Bruenn, S. W. 1989a, ApJ, 340, 955

Bruenn, S. W. 1989b, ApJ, 341, 385

Bruenn, S. W. 1992, *Numerical Simulations of Core Collapse Supernovae*, in Proc. of 1st Symposium on Nuclear Physics in the Universe, Oak Ridge, Tennessee, Sept. 1992

Burrows, A. 1987, ApJ, 318, L57

Burrows, A., & Lattimer, J. M. 1988, Phys. Rep., 163, 51

Burrows, A., & Fryxell, B. A. 1992, Science, 258, 430

Colella, Ph., & Woodward, P. R. 1984, J. Comp. Phys., 54, 174

Fryxell, B. A., Müller, E.,& Arnett, D. 1989, *Hydrodynamics and Nuclear Burning*, MPA-preprint, 449, Max-Planck-Institut für Astrophysik, Garching.

Herant, M., Benz, W., & Colgate, S. 1992, ApJ, 395, 642.

Janka, H.-Th. 1993, *Neutrinos from Type-II Supernovae and the Neutrino-Driven Supernova Mechanism*, in Frontier Objects in Astrophysics and Particle Physics, Conf. Proc. Vol. 40, Eds. F. Giovannelli & G. Mannocchi, SIF, Bologna, p. 345

Janka, H.-Th., & Müller, E. 1992, *Neutrino-Driven Type-II Supernovae Neutrino Heating and Post Bounce Dynamics*, in Frontiers of Neutrino Astrophysics, Univ. Academy Press, Tokyo, Japan (in press); MPA-preprint, 711

Janka, H.-Th., Zwerger, Th., & Mönchmeyer, R. 1993, A&A, 268, 360

Lattimer, J. M., & Swesty, F. D. 1991, Nucl. Phys., A535, 331

Mayle, R. W. 1985, Ph.D. Thesis, UC Berkeley, UCRL report no. 53713

Müller, E. 1993, *Two- and Three-Dimensional Simulations of Convection in Protoneutron Stars*, in Proc. of 7th Workshop on Nuclear Astrophysics, Ringberg Castle, Tegernsee, March 1993, MPA-report, in press

Wilson, J. R., Mayle, R. W., Woosley, S. E., Weaver, T. 1986, Ann. N.Y. Acad. Sci., 470, 267

Hydrodynamics and Theoretical Light Curves of SNe II

By V. S. IMSHENNIK AND S. I. BLINNIKOV

ITEP, 117259 Moscow, Russia

We discuss a new scenario for the production of SN II explosion and present the results of numerical modelling studies of SNe II light curves which are being done in our group.

1. Exploding Neutron Star

The outburst of SN 1987A has given a powerful impetus for theoretical work on the physical mechanism of supernova explosions. The one-dimensional theory of the SN mechanism has met certain difficulties in explaining the SN II explosion (see, e.g. Imshennik 1992a). Multidimensional effects might be required to resurrect the delayed explosion mechanism (Bethe & Wilson 1985), owing to neutrino heating (see contributions by Burrows 1993 and Janka 1993). Hillebrandt *et al.* (1990) have remarked that we may have to invent complicated scenarios in order to account for the explosions of massive stars, $M = 20M_{\odot}$. We discuss here a bizarre scenario proposed by Imshennik (1992b), where the interested reader can find further details. Here we give only a brief sketch of the main idea and report on the present status of the project.

In the suggested scenario (Imshennik 1992b), the decisive role is played by the rotation of a presupernova core. The idea to connect an SN explosion with the fission instability in a rapidly rotating collapsing star was first put forward by von Weizsäcker (1947). Shklovsky (1970) had also pointed out the possible importance of the rotational instability for type II SNe. Those ideas were expressed in quite general form. The scenario suggested by Imshennik (1992b) specifies the concrete form of the operation of the instability. We note that the magnetic field is not decisive in this scenario, unlike the mechanism of Bisnovatyi-Kogan (1970).

The collapse of the rotating core leads to the formation of a flattened, rapidly rotating protoneutron star. The fission of this configuration results in the formation of a close neutron star binary. Due to the gravitational radiation the binary components approach each other. After the low mass component fills its Roche lobe it is stripped by the high mass one. When its mass drops below the minimum value for a stable neutron star, $\sim 0.1M_{\odot}$, it explodes with the energy release $\sim 10^{51}$ ergs.

To illustrate this scenario we use the numbers from the numerical model of rotating collapsing core computed by Imshennik & Nadyozhin (1992), which is identical to the model used by Imshennik & Nadyozhin (1977). The neutrino transport is treated there as in the work by Nadyozhin (1977) and the effects of rotation are averaged over the polar angle. The initial configuration is approximated by a uniformly rotating polytrope $n = 3$ with mass $M_{\rm t} = 2M_{\odot}$, radius $R_0 = 4.38 \times 10^8$ cm, and angular velocity $\omega_0 = 1.53\ {\rm s}^{-1}$. This choice of parameters gives the initial angular momentum $J_0 = 8.81 \times 10^{49}\ {\rm erg \cdot s}$. If one assumes that this core collapses into one protoneutron star, then one gets the ratio of rotational to gravitational energy, $\eta = E^{\rm rot}/|E^{\rm g}| = 0.42$. It is well known that this value is well above the threshold of the dynamical instability $\eta \simeq 0.27$ (Tassoul 1979), so the outcome of the collapse is most probably the formation of a binary neutron star system. Assuming the conservation of mass and of angular momentum one finds for the

semimajor axis of the system:

$$a = J_0^2/\{GM_t^3[\delta(1-\delta)]^2\}\ , \tag{1.1}$$

where $\delta = M_1/M_t$, if one denotes the mass of components by M_1 and M_2. For the assumed parameters we find from (1.1):

$$a = 18.5[\delta(1-\delta)]^{-2}\ \text{km}\ . \tag{1.2}$$

According to (1.2) the orbit radius a falls in the range 300 – 500 km for the values of δ between 1/4 and 3/4. The bulk of neutrinos observed from SN 1987A is provided by the more massive neutron star just at the moment of fission. The subsequent fate of the binary is determined by its gravitational radiation (cf. the analysis by Blinnikov *et al.* 1984). The timescale for decrease of the semimajor axis a (km) is

$$t_{\rm grav} \simeq 1.71 \times 10^{-7} \left(\frac{M_\odot}{M_t}\right)^3 \frac{a^4}{\delta(1-\delta)}\ \text{sec.} \tag{1.3}$$

Merging of the components may produce the explosion as in some models for γ-ray bursts (e.g., Meszaros & Rees 1992; Narayan, Paczyński & Piran 1992; Woosley 1993a). Here we consider another possibility: the low mass component may be stripped by the high mass one. We follow the scenario discussed by Blinnikov *et al.* (1984) for old neutron star binaries in connection with their possible explosion and production of γ-ray bursts. When a drops by a factor of 10 from its initial value in eq. (1.2) (this factor is virtually independent of the mass ratio δ), the less massive component fills its Roche lobe. This circumstance may lead to an intensive mass transfer from the less massive component to the more massive one (Blinnikov *et al.* 1984). A neutron star with the mass $M < M_{\rm cr} \simeq 0.1M_\odot$ is dynamically unstable. So, when the less massive star loses enough mass, it must explode. The numerical modelling by Blinnikov *et al.* (1990) has demonstrated that the explosion leads to a remarkably constant energy release, $E_{\rm kin} \simeq 8.8 \times 10^{50}$ ergs (~ 4.8 MeV/nucleon).

The gravitational timescale (1.3) is short enough to meet the restrictions posed by the neutrino observations of SN 1987A. Imshennik (1992b) shows that the time between the neutrino burst and the explosion may be less than ~ 1 hour if the parameter δ lies within reasonable limits: $0.3 < \delta < 0.7$. We note that the more massive companion may well collapse into a black hole, so after the less massive component explodes (the event takes place far away from the primary), there is no neutron star left.

Of course, there are many points in the above scenario which deserve confirmation at least by a simplified numerical modelling, and we have started a project intended to do so. The most difficult point is the fragmentation, or fission, of the rotating collapsing core. To simulate this phenomenon, one must perform 3–dimensional computations for gravitating fluid, taking into account the emission of neutrinos and gravitational waves. This is a grandiose task which may be left for future. At present we are testing a 3–dimensional hydrocode which is capable to treat a simplified problem of fission in Newtonian gravity (Aksenov & Imshennik 1993).

The code realizes the Eulerian PPM scheme (Colella & Woodward 1984). Unlike Imshennik & Nadyozhin (1992), who have used the ideal gas approximation, Aksenov & Imshennik (1994) rely on a more realistic equation of state which includes the non-ideal effects in neutron matter (Friedmann & Pandharipande 1981). The real gas approximation implies the necessity to use appropriate solution algorithms for the Riemann problem (Colella & Glas 1985) and to care about the initial model. The hydrocode provides exact conservation of mass and momentum. The energy is conserved exactly only in the absence of gravity. The Poisson equation is solved with the help of expansion in

Legendre polynomials. This procedure is sufficiently efficient: one needs $\propto l_{\max}$ floating point operations per mesh point, where $l_{\max}$ is the highest order of Legendre polynomials used. The same efficiency is reached also in the general 3-dimensional case when one uses the associated Legendre polynomials (Aksenov 1993). The boundary condition for the gravitational potential, $\Phi \to -GM/r$ for $r \to \infty$, is automatically satisfied by this technique.

At present we have detailed calculations only with the 2-dimensional version of the code. The test problem solved is to calculate the hydrodynamical evolution of the rapidly rotating 1-dimensional body (obtained by Imshennik & Nadyozhin 1992) in a more realistic 2-dimensional configuration (this is of course not fully realistic, since 3-dimensional effects can develop already at previous stages of collapse). The numerical solution is found on a 120×64 for $l_{\max} = 28$ grid. The mesh is not uniform over radius r: it is denser for $r < r_{\max}/4$ (this region contains 2/3 of all mesh zones). The difference scheme conserves mass and momentum exactly. The angular momentum is conserved with high accuracy, $\sim 10^{-4}$, and the total energy with accuracy better than 5%.

We present here some results of Aksenov & Imshennik (1994). As usual, we introduce the gravitational energy, $E^{\rm gr} = \frac{1}{2}\int \rho\Phi d\mathbf{r}$, and the kinetic energy, $E^{\rm k} = \frac{1}{2}\int \rho \mathbf{v}^2 d\mathbf{r}$. Let us separate $E^{\rm k}$ into the rotational, $E^{\rm rot}$, and poloidal parts,

$$E^{\rm k0} = \frac{1}{2}\int \rho(v_r^2 + v_\theta^2)d\mathbf{r} = E^{\rm k} - \frac{1}{2}\int \rho v_\varphi^2 d\mathbf{r} = E^{\rm k} - E^{\rm rot}. \qquad (1.4)$$

It is clear that in the case of pure steady rotation $E^{\rm k0} = 0$.

We present in Fig. 1 the relaxation of these integral parameters to a final configuration. The initial configuration is assumed to be spherical, so violent meridional motions begin. Moreover, because the equation of state is different from that used by Imshennik & Nadyozhin (1992), we must modify the initial model slightly; it is not in exact equilibrium. So the meridional energy grows quickly from $E^{\rm k0} = 0$ at $t = 0$ and reaches its maximum value (corresponding to $E^{\rm k0}/|E^{\rm gr}| \simeq 0.08$) at $t \simeq 0.3$ ms. Later, the energy of these motions is quickly dissipated in shock waves. This dissipation leads to the growth of the thermal energy and to the decrease of $E^{\rm k0}$ by more than a factor of ten in a time ~ 6 ms. Due to the overall expansion and conservation of angular momentum, the parameter $\eta = E^{\rm rot}/|E^{\rm gr}|$ also decreases from the initial value $\eta = 0.42$ and stabilizes at the level $\eta = 0.23$.

Fig. 2 demonstrates the shape of the final configuration. The stability of the rotating body thus obtained can be studied either in a linear analysis for this value of η or it can be used as a starting point for 3-dimensional calculations of the fission.

Let us now briefly discuss the outstanding challenges for further research in the project. The problem of fission involves not only the hydrodynamical computations – it is necessary also to analyze the modes of the redistribution of angular momentum and the role of the magnetic fields in this process. The next point is the problem of the mass exchange under the influence of gravitational radiation. Of course, this secular process cannot be studied by a dynamic code, so special techniques and approximations must be developed. Finally, the problem of the explosion of a neutron star below the minimum stable mass deserves special attention. Recently, Colpi, Shapiro & Teukolsky (1993) have found that the energy release by β-decays leads to an explosion with $E^{\rm k} \sim 0.5 \times 10^{50}$ ergs. This is an order of magnitude below than the value found by Blinnikov *et al.* (1990) in the more idealised approximation of the fully catalyzed matter. The numerical approach of Colpi *et al.* (1993) is more accurate than ours; still, improvements in their scheme are still possible. There also remain some interesting questions regarding physical processes: the evolution of a hot newborn neutron star may follow another path than that of an old

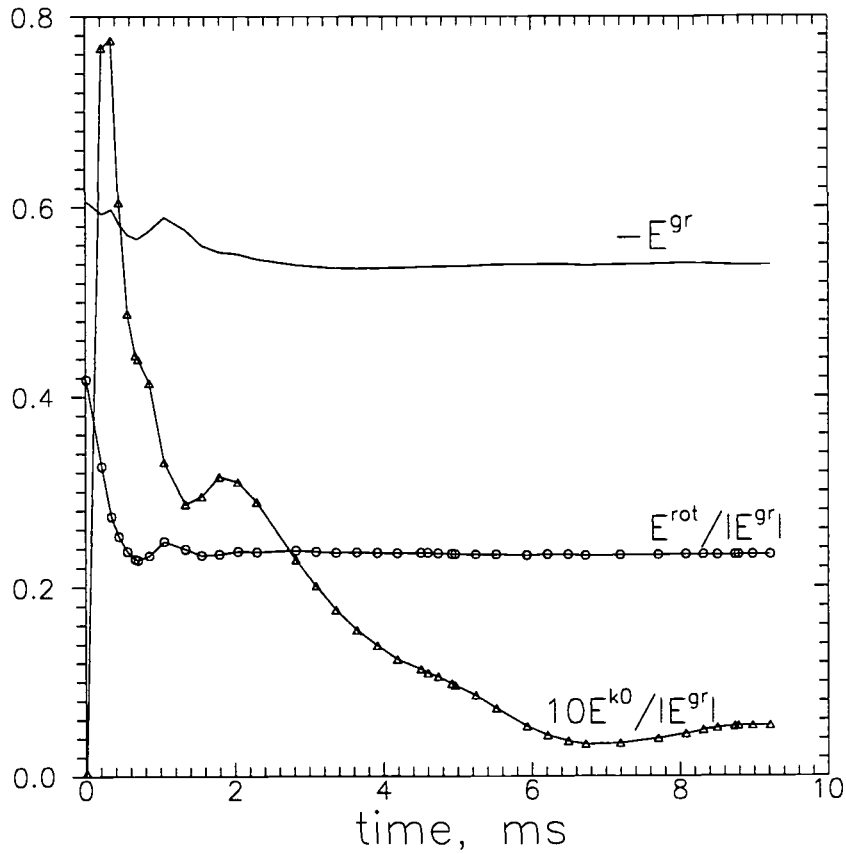

FIGURE 1. Evolution in time of E^{gr}, in units 2×10^{53} erg, and of the fractions $\eta = E^{rot}/|E^{gr}|$, $10E^{k0}/|E^{gr}|$.

cold one, as investigated in the cited papers; the descripton of neutrino transfer may be important, etc. If this "standard bomb" appears to be too weak to account for a normal SN II event, then one can consider a natural combination of this mechanism with the nuclear explosion in the layers overlying the core (Bodenheimer & Woosley 1983). The thermonuclear explosion would be triggered then by the exploding neutron star.

2. Theoretical light curves

The second part of our contribution is devoted to another project which is being developed at ITEP and at Sternberg Astronomical Institute (in close collaboration with MPA, Garching and UC, Santa Cruz). This project involves the modelling of Type II SN light curves. We briefly describe some results of our computations of SN light curves accounting for multi-frequency-group time-dependent radiation transfer. The results are virtually independent of the details of the explosion mechanism, but they are sensitive to the explosion energy, to the structure of the outer layers of the progenitor, and to the amount of the radioactive ^{56}Ni produced. In our computations we use both simplified progenitor models and detailed evolutionary models constructed by Weaver & Woosley (1993) and Woosley, Langer & Weaver (1993). We use our code STELLA which incorporates implicit hydrodynamics coupled to a time-dependent multi-group non-equilibrium

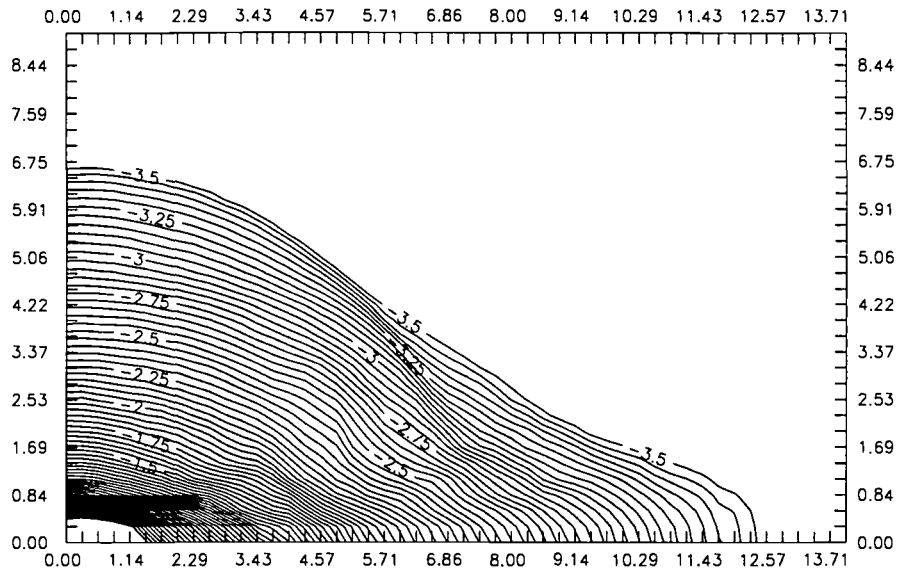

FIGURE 2. The isodensity contours for the final configuration obtained by Aksenov & Imshennik (1994). The lines correspond to the averaged density $\lg(t_{\rm fin}^{-1}\int_0^{t_{\rm fin}}\rho(t)dt)$. The density is in units $10^{14}{\rm g/cm^3}$, and r, z in 10^6 cm.

radiative transfer. For the present runs we use 200 Lagrangean mesh zones and 16 energy groups, spaced geometrically from $\lambda = 10$ Å to $\lambda = 5 \times 10^4$ Å.

The input physics in our code is the same as described in Blinnikov & Bartunov (1993), but for low mass models or for the "tail" phase it is essential to take into account the gamma-ray transfer, which we ignored in our previous work. We have tried various prescriptions for the gamma-ray energy deposition and have chosen the "exact" numerical solution of the time-independent spherically symmetric gamma-ray transport in the one-group approximation, replacing the scattering of gamma-rays by an effective pure absorption with the opacity $\kappa_\gamma = 0.03\ {\rm cm^2/g}$ (Ambwani & Sutherland 1988). We assume that positrons always deposit their energy locally. We take all constants for ^{56}Ni and ^{56}Co decays from the compilation by Nadyozhin (1993).

We present in Fig. 3 examples of computed and observed $B-$light curves for linear type II SNe. Fig. 4 displays our results for a typical type II- P supernova. The models have different values of progenitor mass, M_0, radius, R_0 and hydrogen mass, $M_{\rm H}$, but they have the same assumed values for explosion energy, $E_0 = 2 \times 10^{51}$ erg, and ^{56}Ni mass, $M_{\rm Ni} = 0.078 M_\odot$, approximately the standard parameters for SN 1987A.

Our set of hydrodynamical models shows that the observations of "normal" SNe II-P and II-L are well reproduced by the explosion of a supergiant progenitor with a radius of several hundreds $R_\odot$; but for SNe II-L one must assume a small hydrogen envelope mass $\sim 1-2M_\odot$. The unusual brightness of some events, such as SN 1979C, is naturally explained by re-radiation of ultraviolet photons created at shock breakout in the superwind shell surrounding the exploding star (Blinnikov & Bartunov 1993). Both faint and very bright SN II-P and SN II-L events are explained without requiring large masses of radioactive material. We conclude that all type II supernovae (linear, plateau and 1987A subtypes) are probably produced by an explosion with one and the same energy and that all varieties

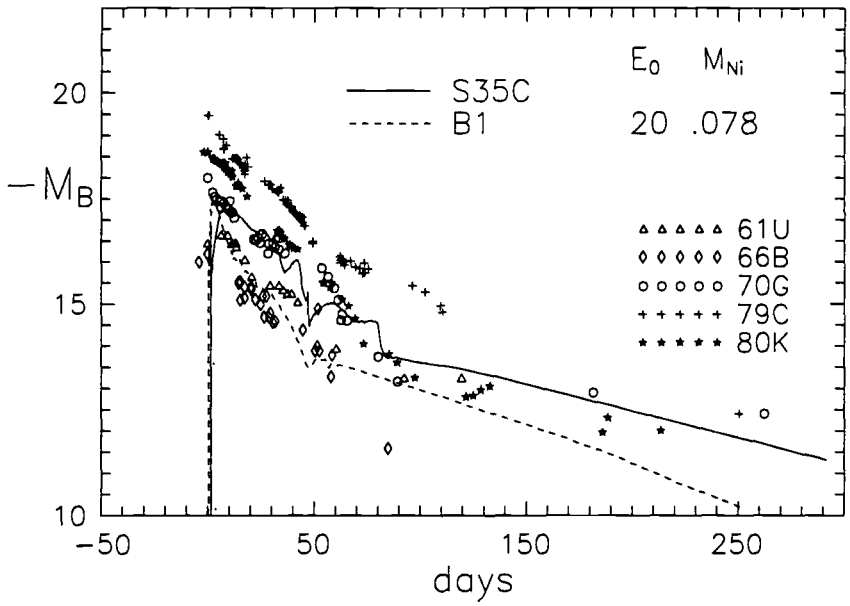

FIGURE 3. Theoretical light curves for SNe II-L. The solid line is for the pre-SN model s35c of Woosley *et al.* (1993) $M_{\rm pSN} = 15.2M_\odot$, $R_0 = 970R_\odot$, $M_{\rm H} = 1.44M_\odot$. The dashed line is the model B1 of Blinnikov & Bartunov (1993) $M_{\rm pSN} = 7.4M_\odot$, $R_0 = 600R_\odot$, $M_{\rm H} = 1.84M_\odot$. The observational data for SNe II-L are compiled and reduced to one system by Bartunov *et al.* (1992).

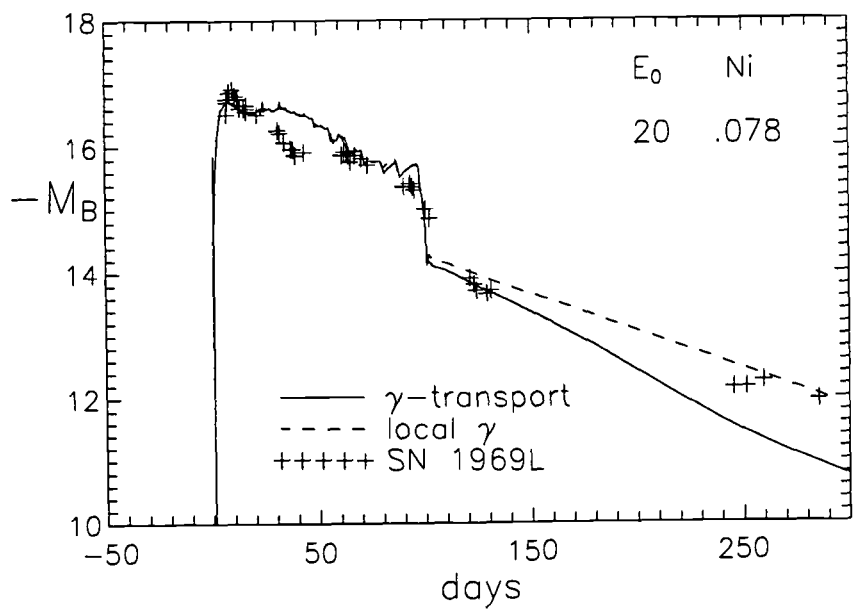

FIGURE 4. The B−light curve for SN 1969L of type II-P. The solid line is our prediction for the pre-SN model s15s7a of Weaver & Woosley (1993) $M_{\rm pSN} = 15.1M_\odot$, $R_0 = 500R_\odot$, $M_{\rm H} = 6.9M_\odot$.

of light curves can be explained by the progenitor radius, by the density of the progenitor wind and by the amount of hydrogen left in the envelope.

It seems that the same is true also for the recent peculiar supernova SN 1993J discovered in NGC 3031 (Garcia 1993). As noted by Woosley (1993b), Nomoto *et al.* (1993) and Shigeyama *et al.* (1993), its light curve is similar to a "Type II-b" (Woosley *et al.* 1987; Woosley 1991). The evolution of the spectrum supports this classification (Filippenko & Matheson 1993).

The type II-b progenitor is a normal type II progenitor which has lost almost all of its hydrogen envelope (Woosley 1991), so it is similar to type II-L (Swartz *et al.* 1991, Blinnikov & Bartunov 1993). After comparison with other models from our set, we assume $R_0 = 200R_\odot$ as initial condition (Bartunov *et al.* 1994). We chose $M = 1.41M_\odot$ for the mass cut of the core. The burst was produced by the release of the thermal energy E_0 in the mass range $1.41 - 1.44M_\odot$ in ten seconds.

Here we present results for the same burst energy, $E_0 = 2\times10^{51}$ ergs, as in other models but with the lower ejecta mass, $M_0 = 3M_\odot$, corresponding to progenitor mass $4.41M_\odot$. The asymptotic kinetic energy is 1.9×10^{51} erg in our model, which of course depends on the position of the mass cut. The mass of hydrogen in our model is $M_{\rm H} = 0.92M_\odot$ and the chemical composition is assumed as in model B1 (Fig.2 in Blinnikov & Bartunov 1993). The parameters of our model are similar to those in independent models by Shigeyama *et al.*(1993), Woosley & Eastman (1993), Ray *et al.*(1993) and Utrobin (1993), although we assume higher $M_{\rm H}$ (especially than the first three papers).

Fig. 5 displays our computed light curve in the B band for first 60 days and the observations of SN 1993J (compilation by Kato 1993). We assume the distance modulus 27.6 for M81 (Freedman 1990). In this plot it is assumed that the Supernova exploded on 1993, March, 26.5. Our results show that the explosion occurred a few hours before the first pre-discovery observation (Neely 1993) recorded on March 28.3, most probably, in the interval March 28.0 – 28.2. (See also the Fig. 6: the shape of the early light curve is more clear there.)

The discovery of X-ray radiation by ROSAT (Zimmermann *et al.* 1993) and ASCA (Tanaka 1993) as well as the detection of radio emission (Weiler *et al.* 1993, Weiler 1993) clearly demonstrate the presence of an extended circumstellar envelope, produced by a progenitor superwind. Panagia *et al.* (1993) estimate the pre-supernova mass loss rate as $\dot{M} \sim 2\times10^{-6}M_\odot$/yr. We have studied the influence of a similar circumstellar envelope on the visible light in the same way as Blinnikov & Bartunov (1993) who followed Grasberg & Nadyozhin (1987). We have assumed the value of $\dot{M}$ a factor of 4 higher than suggested by Panagia *et al.* (1993) and surrounded the model with $R_0 = 100R_\odot$ by a superwind envelope with the density distribution $\rho \propto r^{-2}$. The outer radius of the envelope is fixed at $3\times10^3R_\odot$. For these parameters the photosphere is at $R_{\rm ph} \sim 200$. We compare the results for $M_V(t)$ for the first 3 days of our model $R_0 = 200R_\odot$ without wind with that having the wind in Fig. 6. It is clear that the wind produces more sharp rise and some additional transient features in the light curve.

One of the most interesting conclusions of our modelling is that SNe II of quite different appearance (SN 1969L, SN 1987A, SNe II- L and now SN 1993J) can produced by explosions with the same energy within a factor of 2. In most cases the amount of ^{56}Ni expelled is about the same. This result favors the existence of a universal explosion mechanism for SNe II.

We have no space to discuss here very interesting problems involved in modelling SNe Ib wich are related to SNe II. We just note that we agree with the conclusion of Baron, Young & Branch (1993) that it is difficult to have a very long radioactive "tail"

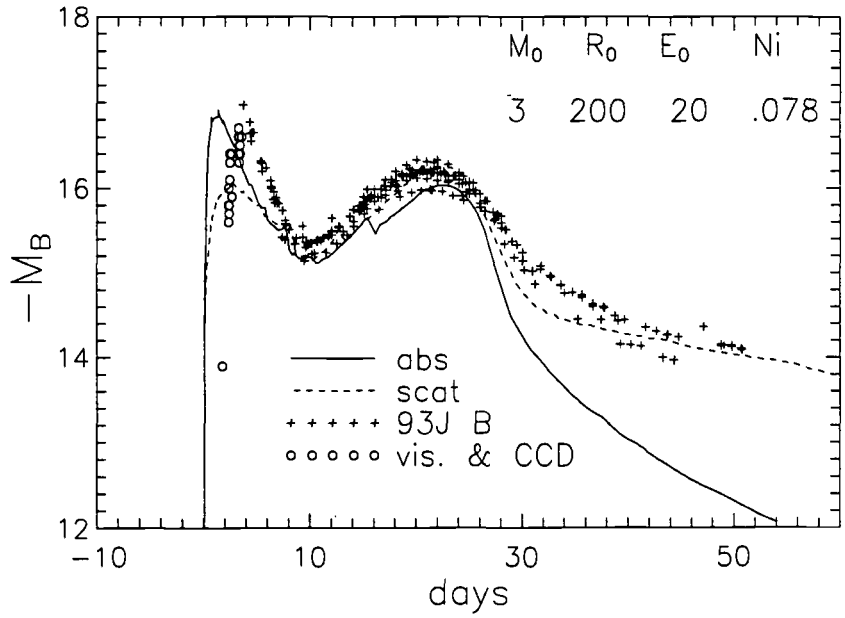

FIGURE 5. The absolute blue magnitude M_B. Pluses show the observed M_B magnitudes of SN 1993J for the distance modulus 27.6 and circles correspond to visual and CCD estimates. The explosion is assumed to occur on March 26.5. The solid line is the theoretical light curve when the absorption is put equal to the total extinction and the dashed line is for the correct treatment of Thomson scattering.

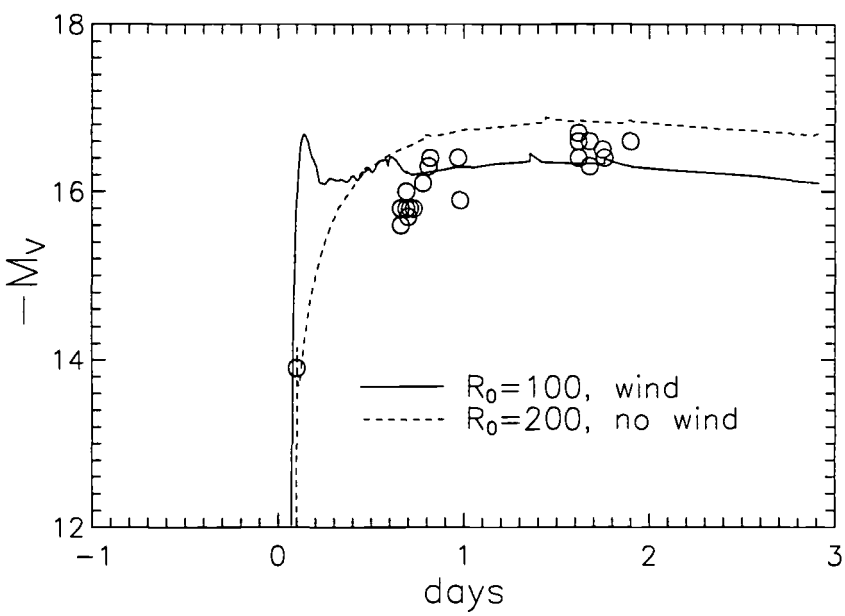

FIGURE 6. Comparison of V−light curves for the first 3 days for a model with the wind (solid), $R_0 = 100R_\odot$, and the standard model $R_0 = 200R_\odot$. Circles show the visual and CCD estimates. Now the explosion is assumed to occur on March 28.2.

together with a narrow "dome" near maximum. We suggest that the discrepancy might be resolved by a shock wave, forming the "tail".

Acknowledgements

The work is partly supported by the Russian Foundation for Fundamental Research grants No 93-02-3637, 93-02-17114. Our visit to the Colloquium No 145 is supported by IAU and ISF. We are especially grateful to R.McCray for his help.

REFERENCES

Aksenov, A. G. 1993, About the Poisson equation solver. Preprint ITEP-45

Aksenov A. G. & Imshennik, V. S. 1994, Pisma Astr. Zh. 20, 32.

Ambwani, K. & Sutherland, P. G. 1988, ApJ, 325, 820

Baron, E., Young, T. R. & Branch, D. 1993, ApJ, 409, 417

Bartunov, O. S., Makarova, I. N. & Tsvetkov, D. Yu. 1992, private communication

Bartunov, O. S., Blinnikov, S. I., Pavlyuk., N. N. & Tsvetkov, D. Yu. 1994, A Model for Supernova 1993J. A&A, 281, L53

Bethe, H. & Wilson, J. 1985, ApJ, 295, 14

Bisnovatyi-Kogan, G. S. 1970, Soviet Ast., 14, 625

Blinnikov, S. I. & Bartunov, O. S. 1993, A&A, 273, 106

Blinnikov, S. I., Novikov, I. D., Perevodchikova, T. V. & Polnarev, A. G. 1984, Soviet Ast. Lett., 10, 177

Blinnikov, S. I., Imshennik, V. S., Nadyozhin, D. K., Novikov, I. D., Perevodchikova, T. V. & Polnarev, A. G. 1990, Soviet Ast. 34, 595

Bodenheimer, P. & Woosley, S. 1983, ApJ, 269, 281.

Burrows, A. 1993, these proceedings.

Colella, P. & Glas, H. M. 1985, J. Comp. Phys., 59, 264

Colella, P. & Woodward, P. R. 1984, J. Comp. Phys., 54, 174

Colpi, M., Shapiro, S. L. & Teukolsky, S. A. 1993, ApJ, 414, 717

Filippenko, A. V. & Matheson, T. 1993, IAU Circ. No 5787

Freedman W. L. 1990, ApJ, 355, L35.

Friedmann, B. & Pandharipande, V. R. 1981, Nucl. Phys. A, 361, 502

Garcia, F. 1993, IAU Circ. No. 5731.

Grasberg, E. K.,& Nadyozhin, D. K. 1987, Soviet Ast., 31, 629

Hillebrandt, W., Müller, E. & Mönchmeyer, R. 1990, in *Nuclear Equation of State*, pp 689–719, Plenum Press, New York.

Imshennik, V. S. 1992a, in Astrophysics on the Threshold of 21st Century, ed. N. S. Kardashev. Gordon & Breach, Philadelphia.

Imshennik, V. S. 1992b, Soviet Ast., 18, 194

Imshennik, V. S. & Nadyozhin, D. K. 1977, Soviet Ast., 3, 33

Imshennik, V. S. & Nadyozhin, D. K. 1992, Soviet Ast. Lett. 18, 79

Janka, H.-Th. 1993, these proceedings.

Kato, T. 1993, SN 1993J photometry update. *E-mail from Kyoto University, May 18th.*

Meszaros, P. & Rees, M. J. 1992, ApJ, 397, 570

Nadyozhin, D. K. 1977, Ap. & Space Sci., 49, 399

Nadyozhin D. K. (1993). *Preprint No. 61*, Astronomical Institute University of Basel

Narayan, R., Paczyński, B. & Piran, T. 1992, ApJ, 395, L83

Neely, A. (1993). *IAU Circ.* No 5740.

Nomoto, K., Suzuki, T., Shigeyama, T., Kumagai, S., Yamaoka, H. & Saio, H. 1993, Nature, 364, 507

Panagia, N., Van Dyk, S. D., & Weiler, K. W. 1993, IAU Circ. No 5762

Ray, A., Singh, K. P. & Sutaria, F. K. 1993, J. Ap. & Astr., 14, 53

Shigeyama, T., Suzuki, T., Kumagai, S., Nomoto, K., Saio, H. & Yamaoka, H. 1994, ApJ, 420, 321

Shklovsky, I. S. 1970, Ap. Lett., 8, 101

Swartz, D. A., Wheeler, J. C. & Harkness, R. P. 1991, ApJ, 374, 266.

Tanaka, Y. 1993, IAU Circ. No 5753.

Tassoul, J.-L. 1979, Theory of Rotating Stars, Princeton Univ. Press

von Weizsäcker, C. F. 1947, Zeitschrift für Astrophys., 24, 181

Utrobin, V. 1993, A&A, 270, 249

Weaver, T. A.,& Woosley, S. E. 1993, Phys. Reports, 227, 65

Weiler, K. W. 1993, Data on radio observation of SN 1993J, *communicated via E-mail.*

Weiler, K. W., Sramek, R. A., Van Dyk, S. D. & Panagia N. 1993, IAU Circ. No 5752.

Woosley S. E. 1991, in Supernovae. Tenth Santa Cruz Workshop in Astr.Astrophys., ed. S. E. Woosley (New York: Springer Verlag), p.202.

Woosley S. E. 1993a, ApJ, 405, 273

Woosley S. E. (1993b). *Private communication via E-mail of May, 9th.*

Woosley, S. E., Langer, N. & Weaver, T. A. 1993, ApJ, 411, 823

Woosley, S. E., Pinto, P. A., Martin, P. G. & Weaver, T. A. 1987, ApJ, 318, 664

Woosley, S. E., Weaver, T. A. & Eastman, R. G. 1993, these proceedings.

Zimmermann, H. U., Lewin, W., Magnier, E., Predehl, P., Hasinger, G., Pietsch, W., Aschenbach, B., Trümper, J., Fabbiano, G., van Paradijs, J., Lubin, L. & Petre, R. 1993, IAU Circ. No 5748

Instabilities and Mixing in Type II-P and II-b Supernovae

By T. SHIGEYAMA,[1] K. IWAMOTO,[1] I. HACHISU,[1] K. NOMOTO,[1] AND H. SAIO[2]

[1]University of Tokyo, Bunkyo-ku, Tokyo 113, Japan

[2]Tohoku University, Sendai 980, Japan

We calculate a nonlinear growth of the Rayleigh-Taylor instability in the exploding red supergiant stars with a two-dimensional hydrodynamical code, and examine how the extent of mixing depends on the progenitor's core mass and the envelope mass. The results are compared with the observations of type II-P supernovae and the recent type II-b supernova 1993J.

1. Introduction

Large scale mixing in supernova ejecta has been indicated in spectroscopic and photometric observations of various types of supernovae. This has stimulated 2D and 3D hydrodynamical calculations of the Rayleigh-Taylor (R-T) instabilities during supernova explosions for SN 1987A (Arnett *et al.* 1989; Hachisu *et al.* 1990, 1992; Fryxell *et al.* 1991; Müller *et al.* 1991; Den *et al.* 1990; Yamada *et al.* 1990; Yamada & Sato 1991; Herant & Benz 1991, 1992), type Ib/Ic supernovae (Hachisu *et al.* 1991, 1994a), type II-P supernovae (Herant & Woosley 1994; Hachisu *et al.* 1994b), and the type II-b supernova 1993J (Iwamoto *et al.* 1994). In particular, Hachisu *et al.* (1991, 1994a) found that development of the R-T instabilities depend sensitively on the presupernova structure, so that the comparison between hydrodynamical simulations and observations can provide a new clue to the understanding of supernova progenitors, their structure, and the explosion mechanism.

In the present paper, we follow a nonlinear growth of the R-T instabilities in the exploding red supergiant stars, i.e., type II-P and II-b supernovae. We find that the extent of mixing depends on the core mass and the envelope mass of red supergiants.

2. Initial Models

We adopt the red-supergiant progenitor models for type II-P and II-b supernovae (Nomoto & Hashimoto 1988; Saio *et al.* 1988). Their main-sequence masses $M_{\rm ms}$, and their presupernova helium core masses $M_{\rm He}$, H-rich envelope masses $M_{\rm H}$, and the radii R at the explosions are summarized in table 1. The assumed neutron star baryonic masses $M_{\rm NS}$ are also given, so that the ejected H-free core masses are given by $M_{\rm He} - M_{\rm NS}$.

For *type II-P models*, no mass loss is assumed. The core of IIP20 progenitor model is the same as adopted for the model of SN 1987A except for the hydrogen-rich envelope (Shigeyama & Nomoto 1990).

For *type II-b models*, large amount of mass loss is assumed so that almost all hydrogen-rich envelopes are lost at presupernova stage (e.g., Nomoto *et al.* 1993; Shigeyama *et al.* 1994).

TABLE 1. Progenitor models of type II-P and II-b supernovae

Model	$M_{\rm ms}/M_\odot$	$M_{\rm H}/M_\odot$	$M_{\rm He}/M_\odot$	$M_{\rm NS}/M_\odot$	$R/R_\odot$
IIP13	13	9.7	3.3	1.2	360
IIP20	20	14	6	1.6	900
IIb3H11	13	0.11	3.3	1.2	450
IIb4H13	15	0.13	4	1.3	580

3. Rayleigh-Taylor Instabilities and Mixing

A shock wave is generated by depositing thermal energy at the mass cut that divides the ejecta and the neutron star. The final kinetic energy of explosion is assumed to be $E = 1 \times 10^{51}$ erg for all the models. The early phase of shock propagation up to the He/C+O interface is calculated with a spherically symmetric Lagrangian code (Shigeyama & Nomoto 1990). When the blast shock arrives at the bottom of the helium layer, the density, velocity, energy etc. are mapped onto our 2-D grids. Just after the mapping, we perturb only the velocity field all over the mesh points; i.e, the velocity field inside the shock front is perturbed but the velocities outside the shock remain zero.

We assume a random perturbation mode as in Hachisu *et al.* (1992). The amplitude of the perturbation is 5% of the expansion velocity. The mode of random perturbation is $n = 128$ (i.e., the azimuthal angle is divided into 128 and the velocity is perturbed randomly at each divided azimuthal angle). The basic part of our code is based on Chakravarthy & Osher's (1985) third-order accurate, TVD (Total Variation Diminishing) method (Hachisu *et al.* 1992).

3.1. *Type II-P Supernovae*

When the shock wave arrives at the composition interface, the expansion of the core is decelerated to generate a reverse shock. Such a deceleration induces the R-T instabilities which lead to mixing of materials. The nonlinear growth of the R-T instabilities for type II-P supernova explosions is shown in the density contours (left), which is linearly spaced by 5% of the maximum density, and the position of marker particles (right) in Figure 1. Marker particles, which are initially placed at each composition interface, follow the deformation of each composition interface, H/He, He/C+O, and O/Si+Ni. The elemental mixing in these type II-P models are plotted in Figure 2. It is found that the mixing of ^{56}Ni depends on the stellar mass, being substantial for the $\sim 13 M_\odot$ star, but much less for the 20 $M_\odot$ star.

Model IIP20: The R-T instability is weak at the He/C+O interface as found in the model for SN 1987A (Hachisu *et al.* 1990, 1992), but it grows at the H/He interface. The development of R-T instabilities in this II-P model is somewhat different from SN 1987A. Because of the lower envelope density and thus the larger density contrast at the H/He interface, the instability grows faster and mix hydrogen well into the core material at the expansion velocity of as low as 1000 km s^{-1} (Figure 2a). The instability is so strong that the hydrogen, helium, and carbon-oxygen are well mixed even for a small amplitude of 1% and 0.2%.

On the other hand, the propagation of the reverse shock is slower than in SN 1987A due to the lower envelope density. When the blast shock breaks out of the surface ($t \sim 3 \times 10^5$

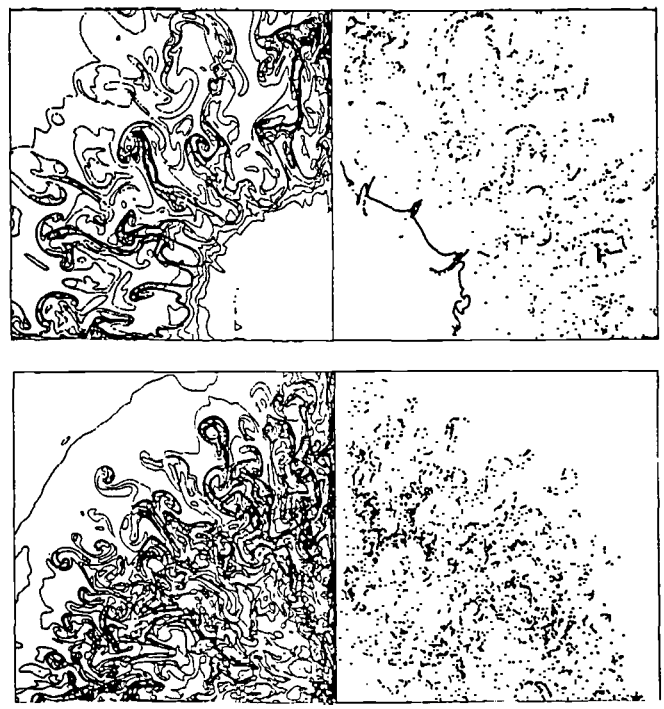

FIGURE 1. Density contour (left) and positions of marker particles (right) on 1025 × 1025 grids for type II-P supernova explosions. (a) *IIP20 (upper)*: Time after the explosion is 8×10^5 s. The size of the computational box is 1.65×10^{14} cm (2400 $R_\odot$). (b) *IIP13 (lower)*: Time after the explosion is 3×10^5 s. The size is 6.8×10^{13} cm (980 $R_\odot$).

s), the reverse shock just arrives at the Si/Ni layer. After the shock breakout, the R-T instability disappears quickly because a rarefaction wave causes the pressure inversion to disappear. Accordingly, the time is too short for the R-T instability to mix the innermost part of the ejecta, i.e., ^{56}Ni is not well mixed as seen from the marker particles at the O/Si+Ni interface (Fig. 1), which is a clear contrast to the model of SN 1987A.

Model IIP13: The R-T instability first grows at the He/C+O interface and then is amplified at the H/He interface. Accordingly ^{56}Ni is well mixed into the middle of the hydrogen-rich envelope. Hydrogen is also well mixed down into the core. The elemental mixing is plotted in Figure 2b. Nickel is mixed up to the layer having the expansion velocity of 2000 km s^{-1} while hydrogen is mixed down to 500 km s^{-1}.

3.2. *SN 1993J*

Figure 3 shows developments of the R-T instabilities as in Figure 1. For both models of 3H11 and 4H13, the R-T instability first grows at the He/C+O interface as in IIP13. For the smaller mass core, the instability is stronger because of larger deceleration due to larger mass ratio between the He-layer and the heavy element layer (Hachisu *et al.* 1991). The instabilities induce mixing of heavy elements (including ^{56}Ni) into the helium layer. The extent of ^{56}Ni mixing is larger for the smaller mass helium core. It also depends on the degree of premixing of ^{56}Ni due to the R-T instability induced by neutrino heating (Herant *et al.* 1992). The R-T instability at the H/He interface also grows because of the large density jump across the core and the low density envelope. The instability is

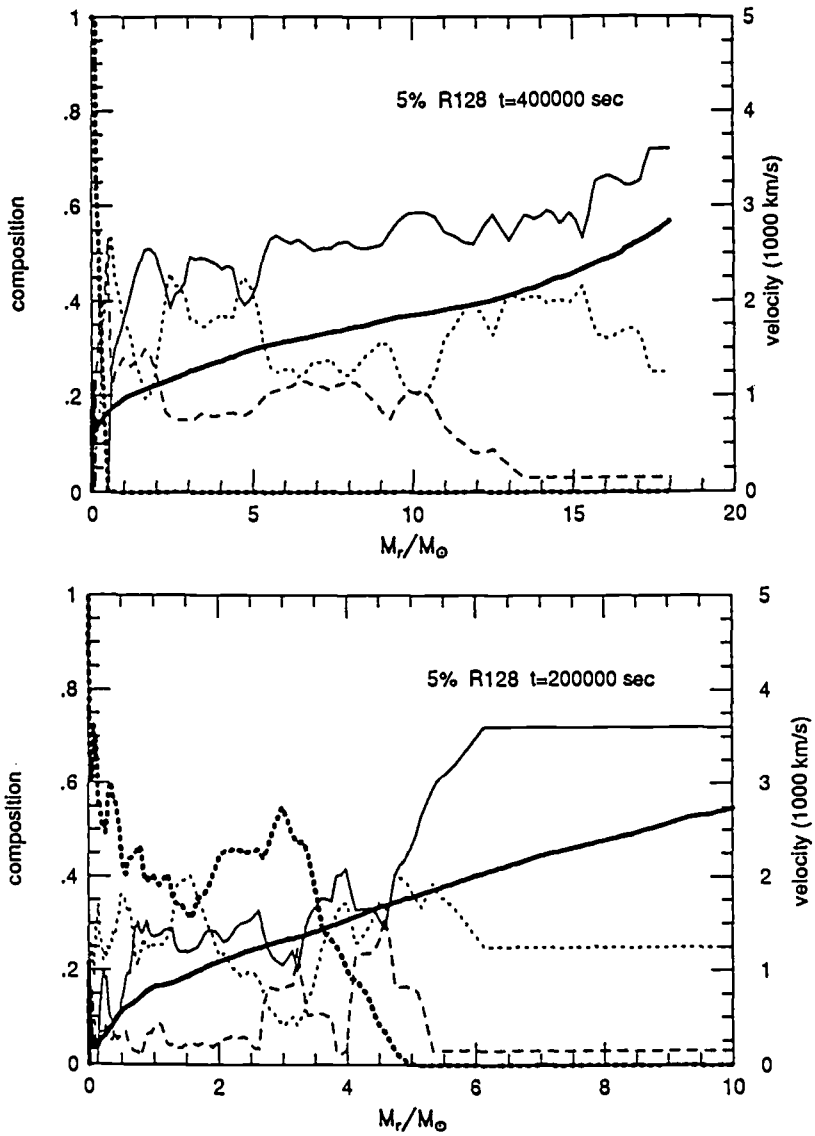

FIGURE 2. Elemental abundances are averaged along the angular direction and plotted against the mass coordinate, M_r, for the models in Figure 1. Shown are H (thin solid), He (short-dashed), C+O (long-dashed), and Si+^{56}Ni (thick-dashed). The averaged expansion velocity (thick solid) is also shown. (a) *IIP20 (upper)*: Ni+Si are localized near the center but hydrogen is well mixed into the core having an expansion velocity of 1000 km s^{-1}. (b) *IIP13 (lower)*: Ni+Si are well mixed into the hydrogen-rich envelope. Conversely hydrogen is mixed down to the layer having an expansion velocity of 500 km s^{-1}.

weaker than in type II-P supernova models and SN 1987A because the deceleration of the core expansion is weaker due to the much smaller envelope mass. However, a certain degree of mixing between the H-rich envelope and the helium layer is found.

Figure 4 shows the abundance distribution of H, He, C+O, and Si+Ni for 3H11 in 2D and 1D calculations (i.e., with and without mixing) against the expansion velocity. Oxygen and ^{56}Ni are mixed up to the expansion velocity of 6000 km s^{-1} and 5300 km s^{-1}, respectively.

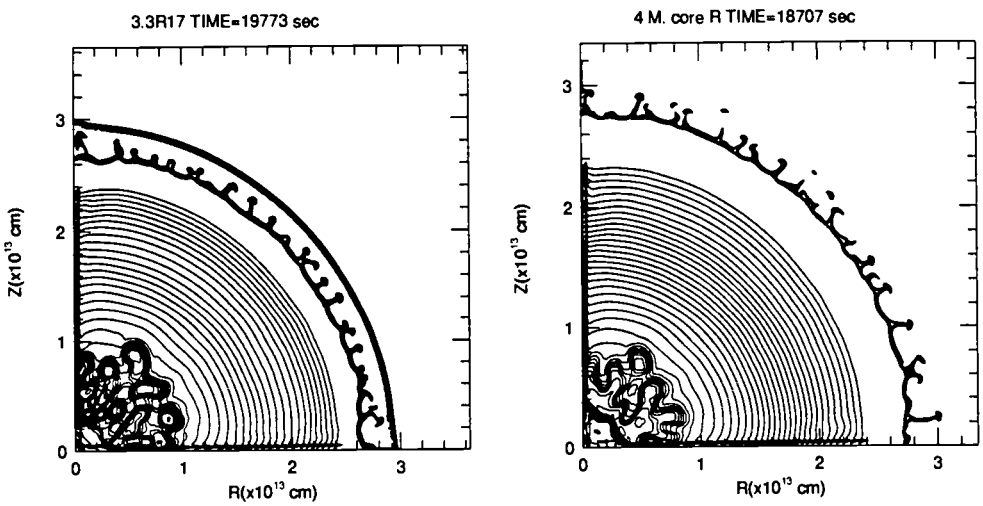

FIGURE 3. Developments of Rayleigh-Taylor instabilities in the models for the type II-b supernova SN 1993J: 4H13 (right) and 3H11 (left). Instabilities at both interfaces of H/He and He/C+O are observed.

4. Comparison with Observations

Light curves of type II-P supernovae are characterized by the plateau which last typically $\sim$ 100 day. The shape of the light curve is determined by the receding hydrogen recombination front in the ejecta (Grasberg *et al.* 1971). The plateau phase is longer as the minimum expansion velocity of hydrogen is lower, i.e., the mass of H-rich envelope is larger and/or the mixing of hydrogen into the low velocity core is deeper (Shigeyama & Nomoto 1990). Therefore, the length of the plateau may provide an indication of mixing as is the case of SN 1987A.

The mixing of ^{56}Ni also affect the light curve due to radioactive heating. Its extent is different between the above two progenitors: ^{56}Ni is mixed up to the middle of the hydrogen-rich envelope in the 13 $M_\odot$, while it is hardly mixed for the 20 $M_\odot$ stars.

The light curve of SN 1993J can be better reproduced with the above models if some ^{56}Ni is mixed into the helium layer. The extent of ^{56}Ni mixing found in these models is consistent with that suggested from the light curve. The small extent of hydrogen mixing is consistent with the relatively high hydrogen velocity in SN 1993J.

More direct indication of mixing in SN 1993J has been provided by the emission line features of oxygen (Wang & Hu 1993; Spyromilio 1993) which indicate the presence of clumps. Since the instabilities at the He/C+O interface grows only for $M_{\rm ms}$ = 13 – 15 $M_\odot$ but not for $M_{\rm ms} \sim 20M_\odot$, such clumps in SN 1993J are consistent with the progenitor mass of $M_{\rm ms}$ = 13 – 15 $M_\odot$ as estimated from the light curve (Nomoto *et al.* 1993; Wheeler & Filippenko 1994).

Acknowledgements

This work has been supported in part by the Grant-in-Aid for Scientific Research (04640265, 05242102, 05242103, 05242207) of the Japanese Ministry of Education, Science, and Culture, KEK, the Space Data Analysis Center of ISAS, and K*i*CFD.

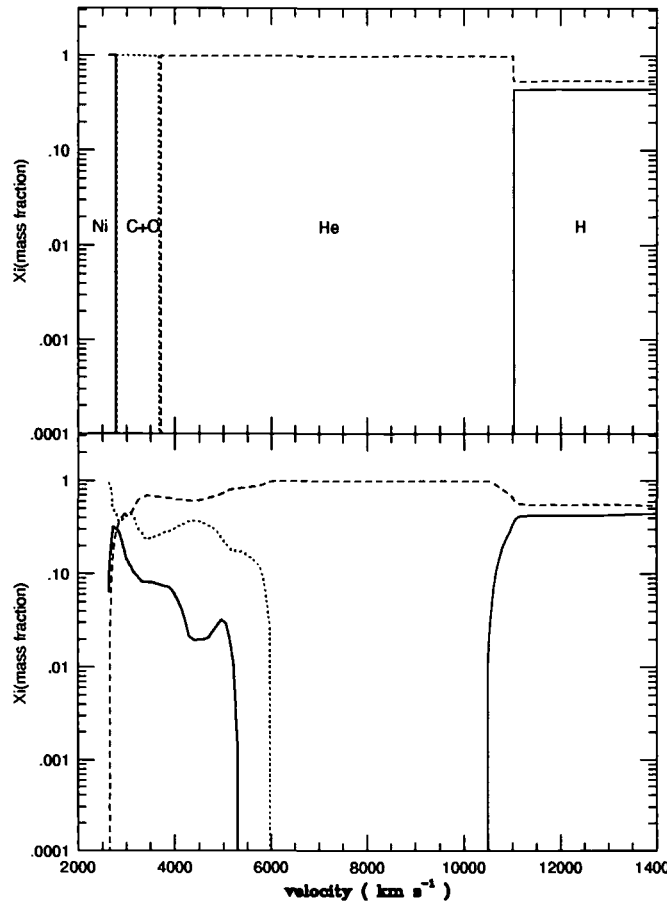

FIGURE 4. The abundance distribution of H, He, C+O, and Si+Ni for 3H11 in 1D and 2D calculations (i.e., with and without the mixing) against the expansion velocity.

REFERENCES

Arnett W.D., Fryxell B.A., & Müller E. 1989, ApJ, 341, L63
Chakravarthy S.R., & Osher S. 1985, AIAA Paper No. 85-0363
Den M., Yoshida T., & Yamada Y. 1990, Progr. Theor. Phys., 83, 723
Fryxell B.A., Müller E., & Arnett W.D. 1991, ApJ, 367, 619
Grasberg E.K., Imshennik, V.S., Nadezhin, D.K. 1971, Ap.Space Sci., 10, 28
Hachisu I., Matsuda T., Nomoto K., & Shigeyama T. 1990, ApJ, 358, L57
Hachisu I., Matsuda T., Nomoto K., & Shigeyama T. 1991, ApJ, 368, L27
Hachisu I., Matsuda T., Nomoto K., & Shigeyama T. 1992, ApJ, 390, 230
Hachisu I., Matsuda T., Nomoto K., & Shigeyama T. 1994a, A&AS, in press
Hachisu, I., Nomoto, K., & Shigeyama, T. 1994b, in ApJ, 390, 230
Herant M., & Benz W. 1991, ApJ, 370, L81
Herant M., & Benz W. 1992, ApJ, 387, 294
Herant M., Benz W. , & Colgate, S. A. 1992, ApJ 395, 642
Herant M., & Woosley, S.E. 1994, ApJ, 425, 814
Iwamoto, K., Hachisu, I., Shigeyama, T., & Nomoto, K. 1994, in preparation
Müller E., Fryxell B., & Arnett W.D. 1991, A&A, 251, 505

Nomoto, K., & Hashimoto, M. 1988, Phys. Rep. 163, 13

Nomoto K., Shigeyama T., Kumagai S., Yamaoka H., & Suzuki T 1993, in: Supernovae (Les Houches, Session LIV), ed. J. Audouze *et al.* , Elsevier Sci. Publ., in press

Nomoto, K., Suzuki, T., Shigeyama, T., Kumagai, S., Yamaoka, H., & Saio, H. 1993, Nature, 364, 507

Saio, H., Nomoto, K., & Kato, M. 1988, Nature ,334, 508

Shigeyama, T., & Nomoto, K. 1990, ApJ, 360, 242

Shigeyama, T., Nomoto, K., Tsujimoto, T & Hashimoto, M. 1990, ApJ, 361, L23

Shigeyama, T., Suzuki, T., Kumagai, S., Nomoto, K., Saio, H., & Yamaoka, H. 1994, ApJ, 420, 341

Wheeler, J.C., & Filippenko, A.V. 1993, in this volume

Yamada Y., Nakamura T., & Oohara K. 1990, Progr. Theor. Phys., 84, 436

Yamada S., & Sato K. 1991, ApJ, 382, 594

Progenitors and Hydrodynamics of Type II and Ib Supernovae

By

S. E. WOOSLEY,[1,2] T. A. WEAVER,[2] AND R. G. EASTMAN[1]

[1]Board of Studies in Astronomy and Astrophysics, UCO/Lick Observatory, UCSC, Santa Cruz CA 95064, USA

[2]General Studies Group, Physics Department, Lawrence Livermore National Laboratory, Livermore, CA 94550, USA

We review critical physics affecting the observational characteristics of those supernovae that occur in massive stars. Particular emphasis is given to 1) how mass loss, either to a binary companion or by a radiatively driven wind, affects the type and light curve of the supernova, and 2) the interaction of the outgoing supernova shock with regions of increasing ρr^3 in the stellar mantle. One conclusion is that Type II-L supernovae may occur in mass exchanging binaries very similar to the one that produced SN 1993J, but with slightly larger initial separations and residual hydrogen envelopes ($\sim$1 $M_\odot$ and radius $\sim$ several AU). The shock interaction, on the other hand, has important implications for the formation of black holes in explosions that are, near peak light, observationally indistinguishable from ordinary Type II-p and Ib supernovae.

1. Some Generalities

There is broad agreement regarding the qualitative evolution of single stars sufficiently massive to ignite carbon burning non-degenerately (e.g., Woosley & Weaver 1986; Weaver & Woosley 1993; Nomoto & Hashimoto 1986, 1988). Given the usual, relevant caveats about the treatment of convective mixing, convective overshoot, and semiconvection, it is agreed that stars of approximately 8 to 12 $M_\odot$($\pm$1 $M_\odot$ depending upon initial helium abundance and convective parameters) will *not* proceed to silicon burning in hydrostatic equilibrium, but will stop prior to central neon ignition and experience a complicated subsequent evolution in which degenerate flashes play an important role. Stars of larger mass, up to perhaps 100 $M_\odot$ on the main sequence, will ignite carbon, neon, oxygen, and silicon burning non-degenerately and develop an iron core of from $\sim$1.25 to 2 $M_\odot$. The collapse of this iron core owing to electron capture and photodisintegration instabilities, will produce either a neutron star or a black hole and, at least frequently, give rise to an outgoing shock which explodes the star (see articles elsewhere in this volume by Janka and by Burrows).

Though of limited mass range, stars of 8 - 12 $M_\odot$ are of considerable interest and uncertain evolution. Stars of 8 to 10 $M_\odot$ (all mass ranges here uncertain to $\pm$1 $M_\odot$) burn carbon to produce degenerate ONeMg cores of about 1.1 $M_\odot$ (Nomoto 1984, 1987; Hashimoto, Iwamoto, & Nomoto 1993). The core grows by accretion through thin hydrogen and helium shells until either a) thin shell flashes lead to the loss of the hydrogen envelope leaving an ONeMg white dwarf (Nomoto 1984; Weaver & Woosley, unpublished), or b) the core grows to 1.38 $M_\odot$ and a central density of $\sim 9.5 \times 10^9$ g cm^{-3} at which point electron capture ignites degenerate oxygen burning. What follows is controversial (Canal, Isern, & Labay 1992; Nomoto & Kondo 1991; Timmes & Woosley 1992) and depends on a careful physical depiction of the propagating burning front. Our own recent calculations (Timmes & Woosley, 1994b) show that central ignition at this density should lead to core collapse. One thus expects a subsequent evolution qualitatively sim-

ilar to that accompanying iron core collapse in larger stars, but with some observational distinctions. First, the density gradient at the edge of the ONeMg core is very steep. Little ^{56}Ni will be produced. Mayle & Wilson (1988) calculate ~0.002 $M_\odot$ of ^{56}Ni for a model of this sort. Also the envelope mass might be smaller than for the higher mass stars (e.g., 15 $M_\odot$) responsible for Type II-p supernovae. Swartz, Wheeler, & Harkness (1991) have suggested that such stars might be the progenitors of Type II-L supernovae, though the ^{56}Ni mass they assume (0.03 $M_\odot$) may be too large for this class of model. More work is needed both on the explosion model and the pre-explosive mass loss to clarify the observational properties of these supernovae.

The range 10 to 12 $M_\odot$ also gives rise to interesting and uncertain evolution. Woosley, Weaver, & Taam (1980) first modelled the evolution of these stars which burn neon and oxygen in a series of degenerate shell flashes while still in stable equilibrium. Similar results have been found by Nomoto & Hashimoto (1988), but much uncertainty remains. Does the series of flashes progress smoothly to the center or are some flashes so violent as to lead to envelope ejection several years before the supernova explodes (as Woosley & Weaver found)? Is an iron core ever produced? A proper study again requires the careful treatment of the burning. This time the burning front propagates *inwards* and is bounded by a convective region. Timmes & Woosley (1994a) have recently determined the physical properties of such flames in the steady state - their temperatures and velocities as a function of composition, radius, and density. It remains to incorporate these analytic results into a stellar evolution code and properly model stars in this mass range. Preliminary indications from this study are, though, that the neon burning flame will propagate smoothly to the center without violent flashes. The flashes observed in earlier studies may have been due to finite zoning. Still the full evolution of these stars, especially beyond neon burning remains very uncertain. Above 11 (or 12) $M_\odot$, the presupernova evolution becomes simpler, less influenced by the effects of degeneracy, and the final configurations better determined. Weaver & Woosley (1993) have calculated a variety of presupernova models for variable masses and rates for $^{12}C(\alpha,\gamma)^{16}O$. A new grid of models which includes more masses and a range of metallicities is in preparation (Weaver & Woosley 1994) and essentially complete. Sample models are available upon request by e-mail. The iron masses for this second set of models, as defined by various criteria, are given in Fig. 1. These models all employed a total rate (E1 + E2) for the $^{12}C(\alpha,\gamma)^{16}O$ rate corresponding to an S-factor at 300 keV of 170 keV barns. This is consistent with recent analyses by Buchmann et al. (1993), who found 57± 13 keV barns for the E1 part, Zhao et al. (1993), who found 95± 44 keV barns for the E1 part, and Barker & Kajino (1992) who estimate that the E2 part is approximately one half of the E1 part. A smaller value, such as the 100 keV barns used by Caughlan & Fowler (1988) and in many stellar evolution studies since, is also consistent with the data.

For the stars considered, the iron core boundary is very nearly the same, whether defined by an abrupt increase in the electron mole number, Y_e, or the inner edge of the silicon shell. For stars in the 11 to 18 $M_\odot$ range this core has a mass near 1.4 $M_\odot$ (because of neutrino losses, the neutron star would be smaller should a mass cut develop here). For stars of 18 $M_\odot$ and above, the star has a substantial silicon shell, the base of the oxygen shell providing an entropy jump that sometimes is relevant in setting the remnant mass in "delayed" explosions. We shall see later that the explosion may have difficulty ejecting all the mass outside of the iron core for stars heavier than 25 $M_\odot$ leading to the possibility of black hole formation. Thus it may be that neutron stars originate from just those stars in the 11 to 25 $M_\odot$ range. Determination of the actual mass cut requires a difficult calculation, but the iron core (baryonic) masses here range from about 1.35 to 1.8 $M_\odot$, a reasonable range for neutron star masses that are observed.

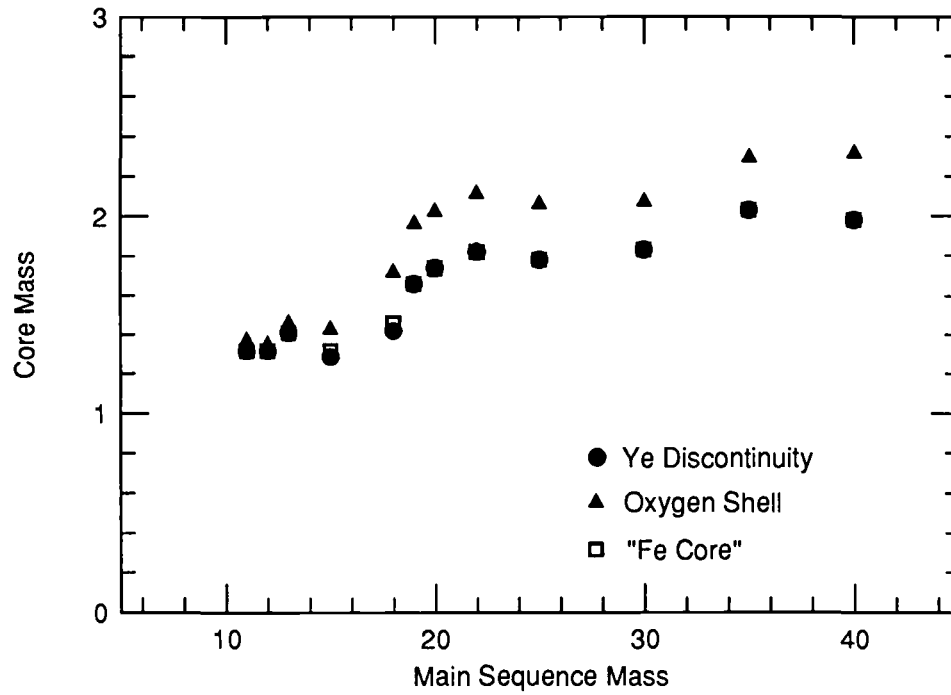

FIGURE 1. Iron core masses as defined by that location where Y_e increases discontinuously to near 0.50 moving outwards in the star and by the condition that the mass fraction of all iron group elements exceed 0.5. Also given is the location of the oxygen burning shell.

Explosion of any of these stars should produce a Type II-p supernova with properties mainly dependent upon how much envelope has been lost (probably a small amount for M less than about 25 $M_\odot$) and the mass of ^{56}Ni produced in the explosion. Eastman et al. (1994) have recently computed the light curve for a typical 15 $M_\odot$ model. The absolute magnitudes are given in Fig. 2.

2. The Effects of Mass Loss

For stars that do not lose their entire envelope, the principal effect of mass loss is to shorten and otherwise alter that stage in the supernova's life when luminosity comes from shock deposited energy released by recombination. For stars that have experienced little mass loss, the envelope has a mass of 10 - 15 $M_\odot$. For stars above 30 $M_\odot$, this mass declines precipitously even for single stars. In a binary, of course, depending upon the initial separation and companion mass, any star may lose all or a portion of its envelope when it becomes a red giant. Consider first those stars that are in binaries. Podsiadlowski, Joss, & Hsu (1992) have surveyed the hydrogen and helium burning evolution of a large number of massive stars and derived statistics for supernova progenitors of Type II-p, Ib (assumed to occur if the star loses its entire envelope), and Type II "stripped" (low mass residual envelope). See their Table 1. Recently, in our attempts to model SN 1993J, we have carried out similar studies but have assumed conservative mass transfer and followed the evolution of the primary to iron core collapse. Some representative models are given in Table 1.

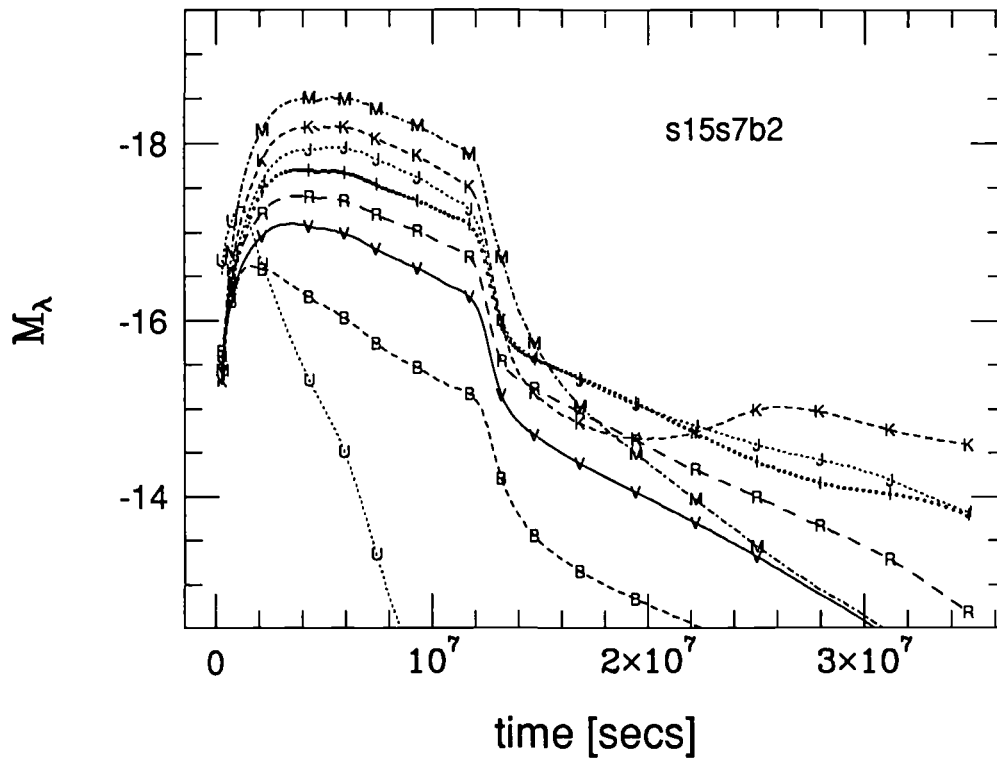

FIGURE 2. Multiband photometry of a 15 $M_\odot$ model supernova (Model s15s7b2 of Weaver & Woosley 1994) which had a final kinetic energy at infinity of 1.23 $\times 10^{51}$ erg and produced and ejected a mass of ^{56}Ni equal to 0.058 $M_\odot$ (Eastman et al. 1994).

TABLE 1. Binary Evolution

Model	Initial a (AU)	Final a (AU)	Companion ($M_\odot$)	Final R_R (AU)	Mass ($M_\odot$)	M_{env} ($M_\odot$)	R_{preSN} (10^{13} cm)	L_{preSN} (10^{38})
11A	2	6.4	8	1.60	3.09	0.20	2.15	1.66
11B	3	8.2	8	2.11	3.43	0.54	2.57	1.67
13A	3	9.1	9	2.29	3.67	0.15	2.86	2.32
13B	4	12.0	9	3.03	3.69	0.18	3.86	2.33
13C	5	14.3	9	3.65	3.80	0.28	4.89	2.32
15A	3	7.8	10	2.03	4.54	0.19	2.80	3.32
15B	4	10.5	10	2.71	4.55	0.19	3.56	3.39
15C	4.5	11.6	10	3.02	4.57	0.21	4.03	3.38
15D	5	9.8	10	2.70	5.51	1.16	3.48	3.31
15E	3	8.1	10	2.08	4.45	0.37	2.76	2.12

Models from Woosley, Eastman, and Weaver (1993); Model name gives mass the star originally had on the main sequence.

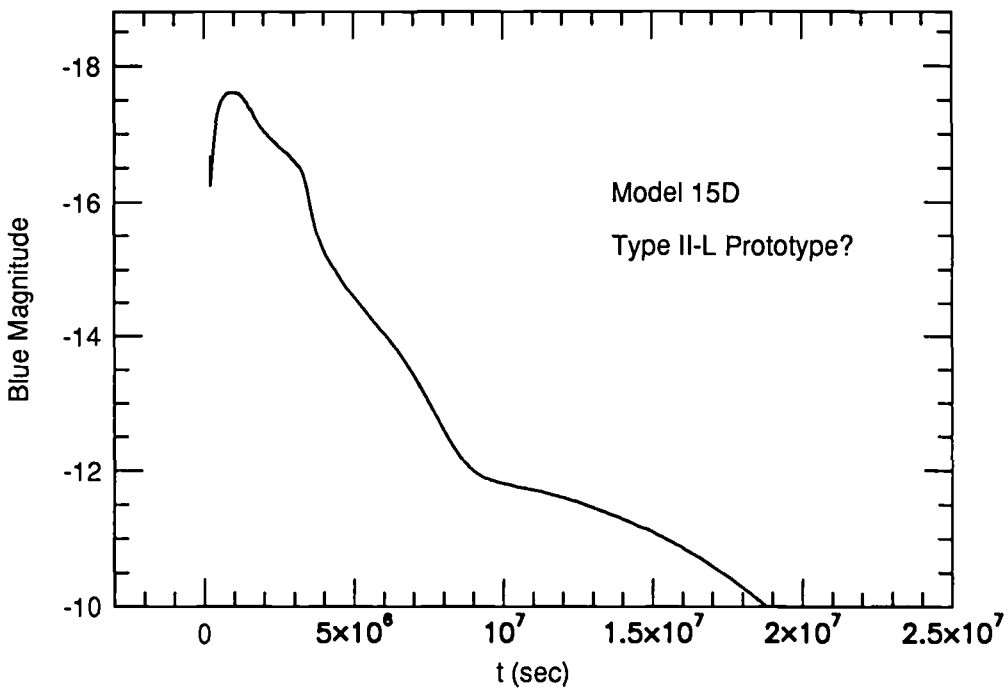

FIGURE 3. The explosion of Model 15D (M_{env} = 1.16 $M_\odot$; ^{56}Ni mass = 0.073 $M_\odot$) produces a blue band light curve very similar to what is seen in Type II-L supernovae (Woosley, Eastman, & Weaver 1994).

The stars in Table 1 all share a quasidynamic phase of mass loss that occurs on approximately a Kelvin-Helmholtz time scale (for the envelope) as the primary first becomes a red supergiant. For stars that employ moderate semiconvective mixing this episode occurs late during helium core burning ($Y_c \sim 0.05$ to 0.15) and removes all but $\sim$ 1 $M_\odot$ of the envelope. A second phase of rapid mass transfer often ensues when the star makes the transition from helium core burning to carbon ignition. During this period, which now occurs on a Kelvin-Helmholtz period for the core (as modified by neutrino losses), the star shifts from a helium core plus hydrogen shell power source to a thick helium shell source. The surface luminosity increases, the radius attempts to increase, and mass loss ensues. We find that all the models in Table 1 are nearly filling their Roche lobes at the time of explosion. The slight difference between the Roche radius (R_R) and the presupernova radius is a consequence of the way we implement the mass loss numerically, $\dot{M} \propto (R/R_R)^n$ with n a large number, here arbitrarily taken to be 50.

Many of these models converge on a final envelope mass less than 0.30 $M_\odot$. Roughly 0.2 $M_\odot$ of (helium-rich) envelope is necessary to sustain a red supergiant photosphere of several AU. Were the mass to drop below this value, owing say to continuing radiative or pulsationally driven mass loss, the radius would shrink rapidly and the explosion would resemble Type Ib. For some choices of orbital separation, however, e.g., Model 15D, the Roche radius of the presupernova star is sufficiently large that the envelope stays at $\sim$ 1 $M_\odot$ at the time of explosion.

As Fig. 3 shows, stars like Model 15D may be promising candidates for producing Type II-L supernovae. There is considerable observational variation in observations of Type II-L, but the blue magnitude of this model is in good qualitative agreement with

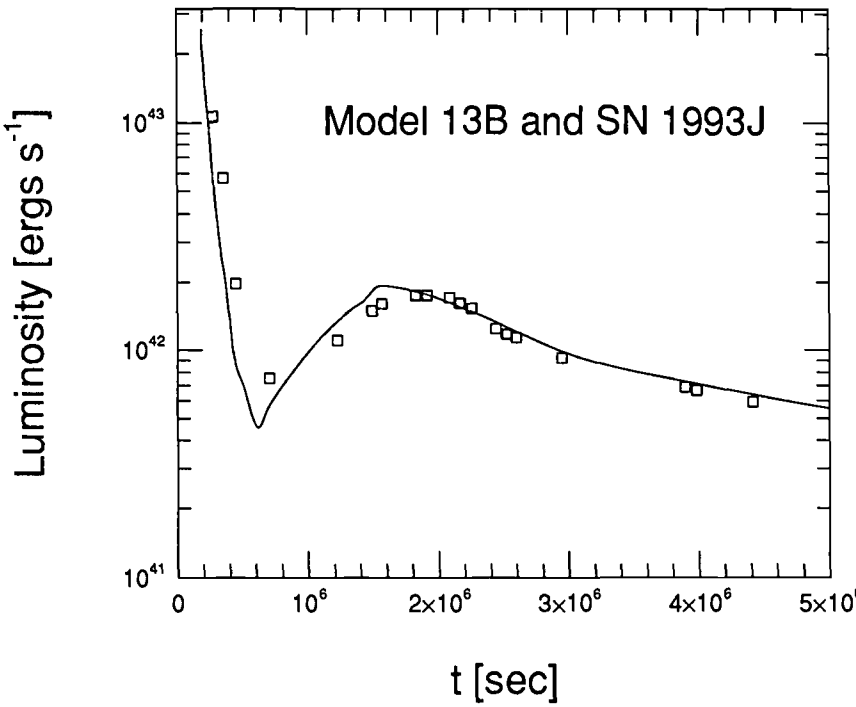

FIGURE 4. The explosion of Model 13B gives a bolometric light curve in good agreement with what was observed in SN 1993J (Woosley, Eastman, & Weaver 1994).

the template defined by Doggett & Branch (1985). Fig. 4 shows the *bolometric* light curve of a model that lost more of its envelope (Model 13B) and now presents a display very similar to what was observed in SN 1993J (Wheeler & Filippenko, this volume; Schmidt et al. 1993). This is typical of many of the models in Table 1.

Should the star lose all, or nearly all, of its remaining envelope, the supernova will be Type Ib. If the mass transfer is in a binary, it is important whether the envelope is removed early in helium burning or late. For the models in Table 1 closer separations or (much) larger mass loss rates while inside the Roche radius would have led to the loss of the entire envelope but little else. In that case the presupernova star would closely resemble a helium core equal to the presupernova mass evolved without mass loss. Such models have been extensively studied in the literature and can give good agreement with observations for helium core masses around 3 or 4 $M_\odot$ (e.g., Ensman & Woosley 1988; Shigeyama et al. 1990). However, there is another way to make Type Ib from a more massive star. Single stars more massive than about 35 $M_\odot$ may lose their envelopes and a substantial part of the helium core mass as well (Woosley, Langer, & Weaver 1993). The same final state may also be characteristic of stars that lose their envelopes to a close binary companion early in their evolution and then have accelerated mass loss as a Wolf-Rayet star (Woosley, Langer, & Weaver 1994). For reasonable assumptions regarding the mass loss rate of Wolf-Rayet stars, there may be a pile up of final masses around 3 to 4 $M_\odot$. Figure 5 shows the composition of a star, initially composed of 10 $M_\odot$ of helium, and evolved assuming a mass dependent mass loss rate. This star is distinguishable from helium cores evolved without mass by the large surface abundances of carbon and oxygen (and correspondingly low abundance of helium). Still more massive progenitors would have similar final masses but less helium at the surface. Perhaps this helium deficiency

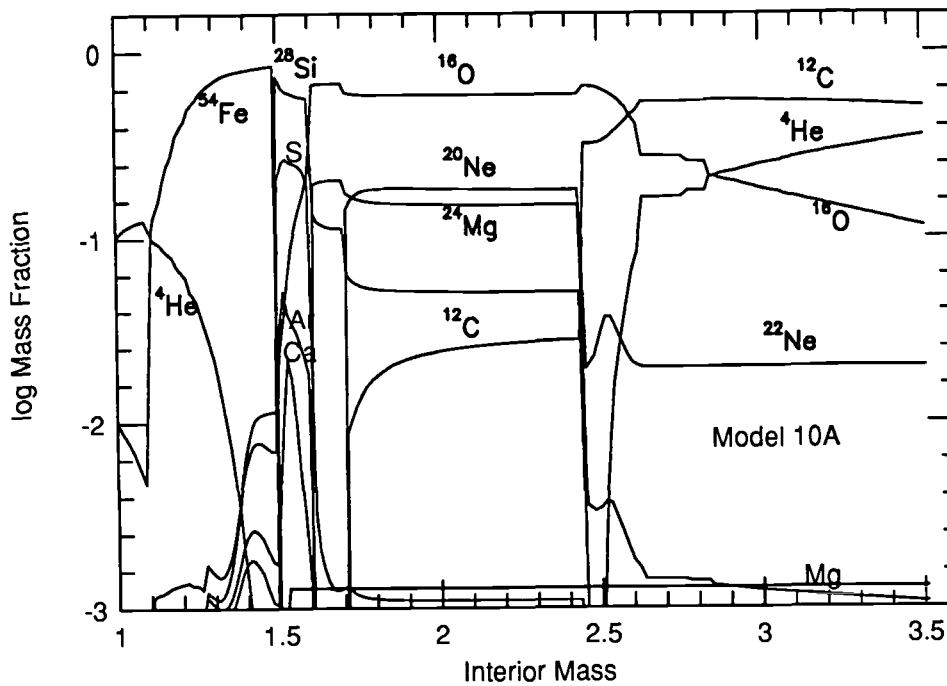

FIGURE 5. Composition of a 10 $M_\odot$ helium core evolved with mass dependent mass loss as a Wolf-Rayet star. The composition is sampled at the time of core collapse (Woosley, Langer, & Weaver 1994).

corresponds to that reported for supernovae of Type "Ic" (Harkness & Wheeler 1990). Chosing a mass cut at the base of the oxygen shell (1.60 $M_\odot$) in this model and simulating an explosion which gives 1.0 $\times 10^{51}$ erg of kinetic energy at infinity produces 0.08 $M_\odot$ of ^{56}Ni and a light curve given in Fig. 6. Unlike the light curves in Figs. 2,3, and 4, this one was calculated using the stellar hydrodynamics code, KEPLER, and is only approximate. Still it is not a bad fit to Type Ib supernovae.

3. Shock Propagation, Mixing, and Fall Back

One of the enduring lessons of SN 1987A has been a better understanding of the Rayleigh-Taylor (RT) instability responsible for mixing in the explosion (Chevalier & Klein 1978; Hachisu et al. 1990; and Fryxell, Müller & Arnett 1991; Herant & Benz 1992). Recently this same sort of mixing has been studied in the explosion of ordinary red supergiants (Herant & Woosley 1994). That paper also discusses the Sedov solution for shock waves propagating in a density gradient ($\rho \propto r^{-n}$) and its relevance for "fall back" in Type II supernovae.

In general, an adiabatic shock passing through a medium with n less than 3, (i.e., increasing ρr^3) must decelerate. One place where ρr^3 increases dramatically is at the interface between the helium core and the hydrogen envelope (Fig. 7), This increase is largely responsible for the formation of the "reverse shock" that gives rise to the RT instability referenced above (Bethe 1990). Because it occurs in a region behind and out of sonic communication with the outgoing shock, the deceleration propagates inwards (in Lagrangian coordinate) as a shock wave.

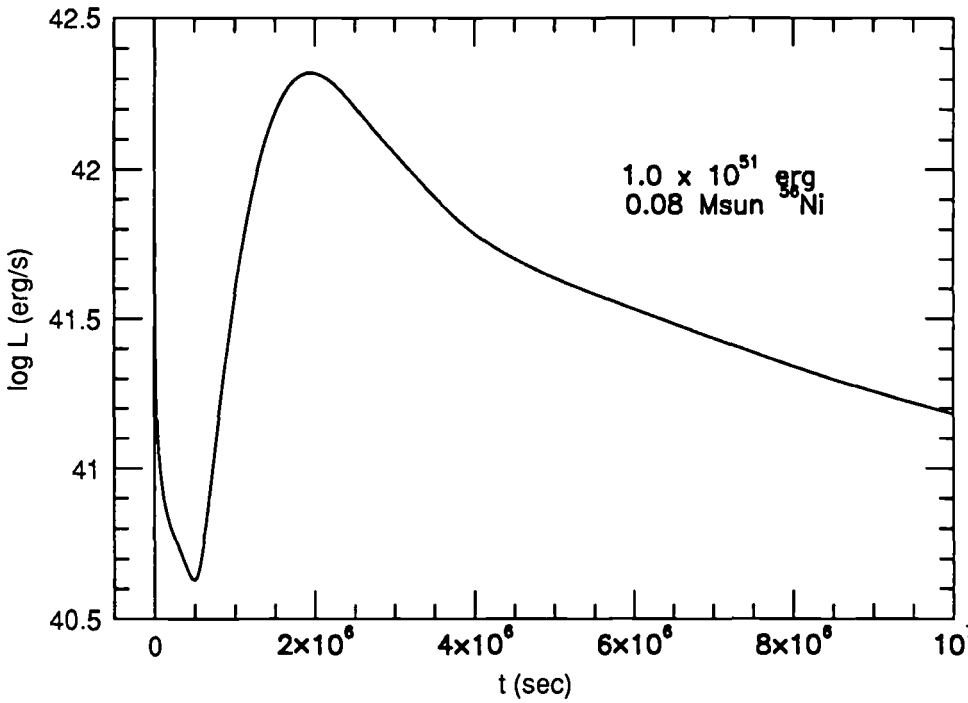

FIGURE 6. Approximate bolometric light curve when the model in Fig.5 is exploded with a piston at 1.60 $M_\odot$.

As Fig. 7 shows, however, there is another important region of increasing ρr^3 especially prominent in the mantles of the more massive stars (e.g., between 3 and 8 $M_\odot$ in the 35 $M_\odot$ model). The outgoing shock also slows in these regions, but because the sound speed is still high, deceleration of the outgoing material occurs smoothly - there is no reverse shock. Nevertheless this deceleration can lead to significant amounts of material falling back into the collapsed remnant. This has some interesting implications for the formation of black holes.

Fig. 8 shows the final mass of the collapsed remnant for a series of simulated explosions in presupernova models of various masses and metallicities (Weaver & Woosley 1994). In each case the piston was located at the Y_e discontinuity (Fig. 1) and given sufficient velocity such that the final kinetic energy at infinity of all ejecta was 1.2×10^{51} erg. *In all cases the entire hydrogen envelope was ejected with high velocity and (for all red supergiants) a normal Type II-p light curve was produced.* However, a variable amount of mass fell back onto the (stationary) piston well after the explosion had been launched. In a 25 $M_\odot$ star with a Y_e jump and piston at 1.78 $M_\odot$ for example, the fall back mass was 0.29 $M_\odot$ which included most, but not all of the 0.39 $M_\odot$ of ^{56}Ni produced in the explosion (0.12 $M_\odot$ of ^{56}Ni was still ejected). In the 30 $M_\odot$ model the piston was at 1.83 $M_\odot$ but the final remnant mass was 4.24 $M_\odot$. All of the ^{56}Ni fell back along with most of the freshly synthesized heavy elements. However, there was still a brilliant Type II-p display which lacked, of course, the radioactive tail. By turning up the explosion energy one can force the ejection of all material external to the piston. For an explosion energy of 2.0×10^{51} erg, the remnant mass in the 30 $M_\odot$ (Pop I) model is decreased to 1.94 $M_\odot$, but this way of counting the energy (KE at infinity) can be misleading. The binding energy of the mantle of the 30 $M_\odot$ presupernova star (beyond 10^9 cm in the

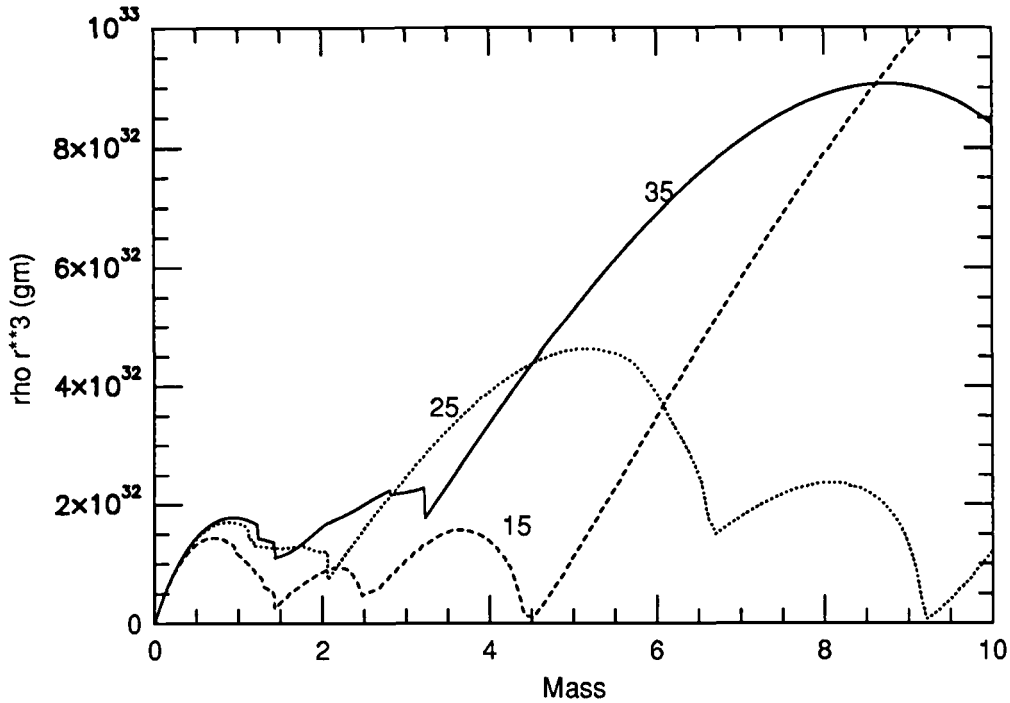

FIGURE 7. The product of density times radius cubed in presupernova stars of several masses. Where ρr^3 decreases a Sedov shock will accelerate; where it increases the shock will slow down. The helium core masses for these stars are 4.2, 9.2, and 14.2 $M_\odot$ for the 15, 25, and 35 $M_\odot$ models respectively.

presupernova model) is also 2.0×10^{51} erg. So the explosion mechanism would actually have to generate 4.0×10^{51} erg, much larger than the inferred explosion energy for SN 1987A. A 35 $M_\odot$ star would have to generate about 4.4×10^{51} erg to leave a remnant of 2.0 $M_\odot$. Whether the explosion energy available from neutrino deposition scales upwards as one moves to stars of larger mass is an interesting question in need of study. Perhaps by providing more ram pressure during the infall stage the inner mantle sets up conditions that extract a larger fraction of the available neutrino energy. Maybe the larger cores provide larger neutrino luminosities. Maybe not.

If not then there should be a mass, perhaps somewhere around 30 $M_\odot$, which separates Type II supernovae that leave neutron stars from those that leave black holes. This would have many important implications for the number of black holes in our galaxy, for galactic chemical evolution, for the late time light curves of some supernovae, and for the formation of accreting x-ray sources in binaries. For now, we want only to leave the reader with this clear message - it is quite possible to produce brilliant optical displays and copious mass ejection (mainly envelope) in supernovae that leave behind as their collapsed remnant black holes of substantial mass.

Acknowledgements

This work has been supported by the National Science Foundation (AST 91-15367), NASA (NAGW-2525), and the Department of Energy (W-7405-ENG-48). The authors appreciate informative conversations with Marc Herant regarding fall back masses and the RT instability in supernova explosions.

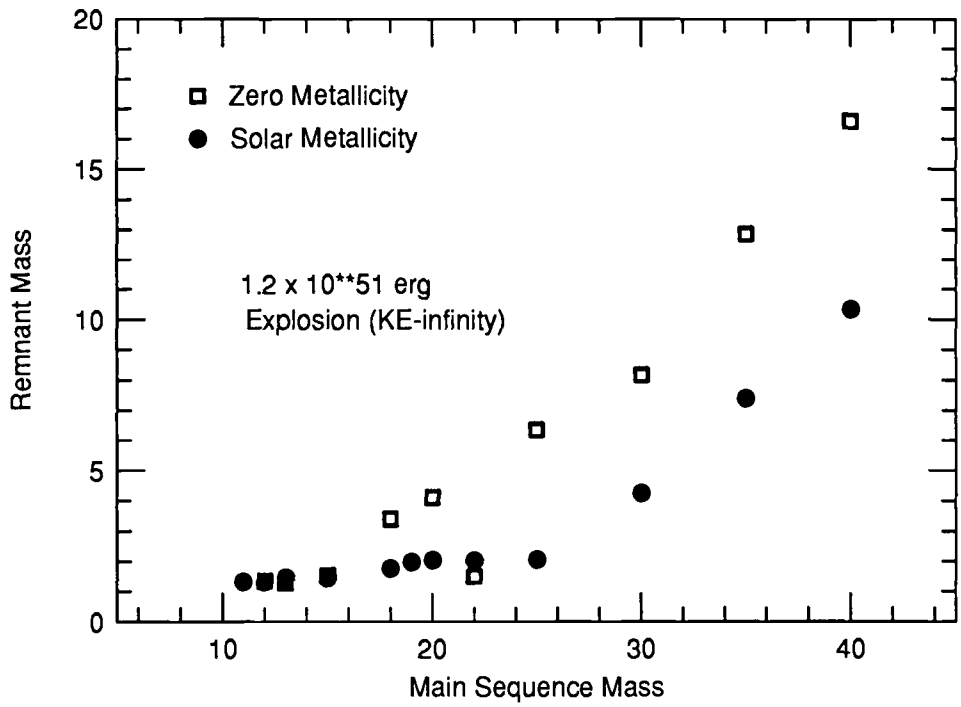

FIGURE 8. Final remnant mass for a series of supernova models that employed pistons at the edge of their iron core which communicated to their ejecta a final kinetic energy at infinity of approximately 1.3 $\times 10^{51}$ erg. All were brilliant Type II-p optical events (Weaver & Woosley 1994).

REFERENCES

Bethe, H. A. 1990, Rev. Mod. Phys, 62, 801

Buchmann, L., Azuma, R. E., Barnes, C. A., D'Auria, J. M., & 11 others 1993, Phys. Rev. Lett., 70, 726

Barker, F. C. & Kajino, T. 1992, in Unstable Nuclei in Astrophysics, eds. S. Kubono & T. Kajino, (Singapore:World Scientific), p. 63

Canal, R., Isern, R., & Labay, J. 1992, ApJ, 398, L49

Caughlan, G. R., & Fowler, W. A. 1988, ADNDT, 40, 238

Chevalier, R. A., & Klein, R. I. 1978, ApJ, 219, 994

Doggett, J. B., & Branch, D. 1985, AJ, 90, 2303.

Eastman, R. G., Woosley, S. E., Weaver. T. A., & Pinto, P. A. 1994, ApJ, 430, 300

Ensman, L. M., & Woosley, S. E. 1988, ApJ, 333, 754

Fryxell, B. A., Arnett, W. D, & Müller, E. 1991, ApJ, 367, 619

Hachisu, I., Matsuda, T., Nomoto, K., & Shigeyama, T. 1992, ApJ, 390, 230

Harkness, R. & Wheeler, J. C. 1990, in Supernovae, ed. A. G. Petschek, (Berlin:Springer Verlag), p. 1.

Herant, M., & Benz, W. 1992, ApJ, 387, 294

Herant, M., & Woosley, S. E., 1994, ApJ, 425, 814

Hashimoto, M., Iwamoto, K. & Nomoto, K. 1993, ApJ, 414, L105

Mayle, R., & Wilson, J. R. 1988, ApJ, 334, 909

Nomoto, K. 1984, ApJ, 277, 791

Nomoto, K. 1987, ApJ, 322, 206

Nomoto, K., & Hashimoto, M. 1986, Prog. Nuc. Part. Phys., 17, 267

Nomoto, K., & Hashimoto, M. 1988, Phys. Reports, 163, 13

Nomoto, K., & Kondo, Y. 1991, ApJ, 367, L19

Podsiadlowski, P., Joss, P. A., & Hsu, J. J. L. (1992), ApJ, 391, 246

Schmidt, B. P., Kirshner, R. P., Eastman, R. G., Grashuis, R., Dell'Antonio, I., Caldwell, N., Foltz, C., Huchra, J. P., & Milone, A. A. E. 1993, Nature, 364, 600

Shigeyama, T., Nomoto, K., Tsujimoto, T., & Hashimoto, M. 1990, ApJ, 36, L23

Swartz, D. A., Wheeler, J. C., & Harkness, R. P. 1991, ApJ, 374, 266

Timmes, F. X., & Woosley, S. E. 1992, ApJ, 396, 649

Timmes, F. X., & Woosley, S. E. 1994a, ApJ, 420, 348

Timmes, F. X., & Woosley, S. E. 1994b, ApJ, in preparation.

Weaver, T. A., & Woosley, S. E. 1993, Phys. Report, 227, 65

Weaver, T. A., & Woosley, S. E. 1994, ApJS, in preparation.

Woosley, S. E., Langer, N., & Weaver, T. A. 1993, ApJ, 411, 823

Woosley, S. E., Langer, N., & Weaver, T. A. 1994, ApJ, in preparation.

Woosley, S. E., Eastman, R. G., & Weaver. T. A. 1994, ApJ, in press

Woosley, S. E., & Weaver, T. A. 1986, ARA&A, 24, 205

Woosley, S. E., Weaver, T. A., & Taam, R. E. 1980, in Type I Supernovae, ed. J. C. Wheeler, (Austin: Univ. Texas Press), p. 96.

Zhao, Z., France, R. H., Lai, K. S., Gai, M., & Wilds, E. L. 1993, Phys. Rev. Lett., 70, 726

Statistical Analysis of Supernovae and the Progenitors of SN Ib and SN Ic

By ZONGWEI LI

Beijing Normal University, Beijing, China, 100875

We review the fundamental classification scheme and statistical analysis of supernovae, emphasizing recently introduced subtypes, SN 1987K, and SN 1993J. Type Ib/Ic and Type II supernovae are of interest for starburst galaxies. We discuss possible progenitors of SN Ib and SN Ic, and the possibility that they may be Wolf-Rayet stars.

1. Introduction

Up to May 1, 1993, 890 supernovae have been discovered, of which 480 have been classified. Today, with data of increasing quantity and precision, we have categorized supernovae into several groups, not just Types I and II, but Types Ia, Ib/Ic, II-L, IIp, 87A, and probably more to come. But, except for SN IIp and SN 1987A, we are still unclear as to the evolution of the progenitor star (or stars). As the rich diversity of supernovae becomes more evident, we are increasingly challenged to ask: what are the stellar progenitors and the explosion mechanisms of the various types and subtypes of supernovae? What makes a SN Ia and what would a progenitor system look like? Are the progenitors of SN Ib/Ic all Wolf-Rayet stars? Here we attempt a brief overview of these questions. For more extensive discussions of issues bearing on supernova progenitors, see recent reviews by Wheeler(1990, 1991) and Branch *et al.* (1990).

We have reached a basic understanding of how the observable properties of SNe depends on the characteristics of the immediate presupernova stars and their explosion parameters. The observed sites (galaxy morphological classes and locations within galaxies) of a supernova type are related to the initial masses of the stellar progenitors. The more massive the progenitors, the more closely the SNe will be associated with regions of recent star formation. Supernova rates are determined by the progenitor initial mass function and by the fraction of such stars that has the requisite binary characteristics. Massive stars are more rare than low mass stars. To predict what kinds of SNe the progenitors will produce, we need to specify the states of the core and the envelope of the presupernova star, the explosion mechanism, and the density of the circumstellar shell. In §II, we discuss the present classification of supernovae. §III is devoted to the statistical analysis of supernovae, §IV is concerned with the progenitors of SN Ib/Ic. The relationship of starburst galaxies Wolf-Rayet stars with supernovae is presented in §V and §VI.

2. Classification of Supernovae

The fundamental classification scheme for supernovae is based on their spectra. As we learn more the scheme becomes more complex; perhaps every supernova is unique in some aspect. Harkness & Wheeler (1990) give an updated summary of supernova spectral classifications.

Almost all of the observed Type II supernovae (SNe II) have been found in spiral galaxies and are associated with both spiral arms and HII regions. A safe generalization is that SNe II come from massive stars.

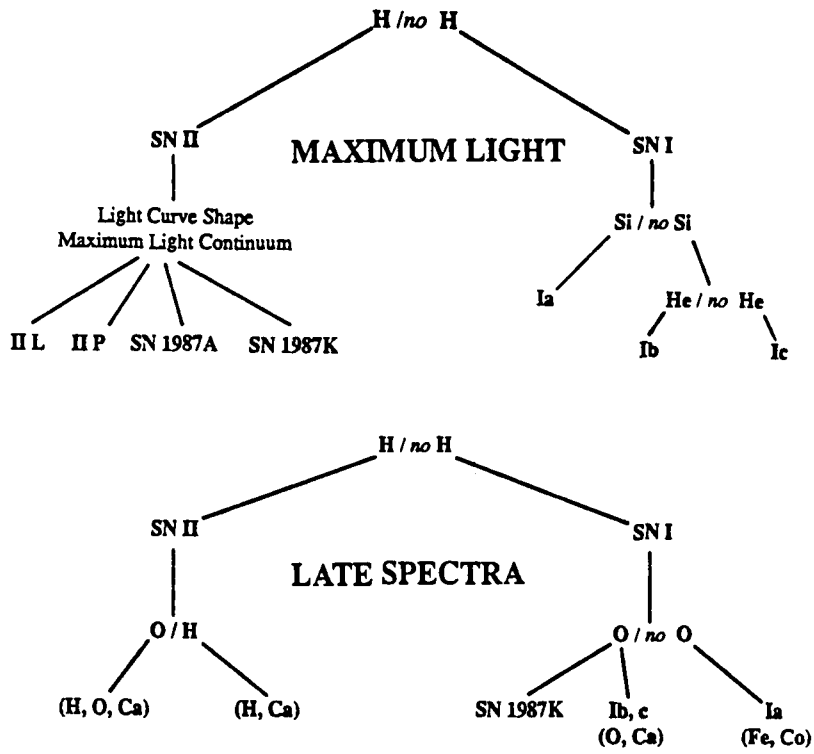

FIGURE 1. Classification scheme for supernovae based on spectral features at maximum light and at late (6 months supernebula) times (Harkness & Wheeler 1990)

2.1. *SNe I and SNe II at Maximum Light*

Figure 1 shows the basic classification scheme. The class of a supernovae has traditionally been determined by its spectrum near maximum light. The basic distinguishing property was whether or not the spectrum showed evidence of hydrogen. If so, the event was classified as Type II; if not, Type I. Among SNe II a further distinction has been proposed based on the shape of the light curve. Those with a pronounced plateau are called Type II plateau (SN II-P), and those that have a nearly linear decline in magnitude after peak light are called Type II linear (SN II-L). With the advent of SN 1987A we now must add a third sub-class. The light curve of SN 1987A was very different, evidently because its progenitor was a compact blue star, although its exponential tail resembles that of SNe II-P. It has been suggested that Type I supernova should be sub-classified according to features of the spectra. One key is the presence or absence of the strong SiIIλ6150 P-Cygni absorption feature. Classical Type Ia events show this feature. Those that do not have come to be known as a separate subclass. The events that show no SiIIλ6150 near maximum light, but do show HeIλ5876, are identified as SN Ib. Wheeler & Harkness (1991) proposed the category SN Ic for these events and then presented atmosphere models suggesting that SN Ib and the candidates for SN Ic might be similar except for the relative concentrations of He in the envelope. These SN Ic events are probably physically closely related to the SN Ib events. We can expect that increasing physical understanding and gradations of properties will ultimately supplant the purely empirical classification schemes.

2.2. *Late-time Nebular Spectra*

In recent years we have seen a great deal of work and new insight into the nature of supernova spectra during the nebular phase. This phase begins roughly six months after maximum, when the photosphere recedes, densities drop, and the spectrum becomes dominated by nebular emission lines. Most nebular spectra preserve the distinction of SN I or SN II as defined by the early-time spectra. Events with H lines near maximum light also show strong Balmer line emission during the nebular phase. Some events show also strong [OI]$\lambda\lambda$6300, 6364 emission as well as hydrogen recombination lines and permitted and forbidden CaII lines. It is not clear whether SN Ic events show identifiable differences from the SN Ib events during the nebular phase.

2.3. *SN 1987K*

It remains an interesting question to determine where SN 1987K fits in the classification and physical scheme of supernovae. Near maximum light, SN 1987K was apparently a Type II from the taxonomical definition that such events show hydrogen in the spectrum. At late times, however, its spectrum was indistinguishable from that of a Type Ib (or Ic) and definitely did not resemble that of a SN II nor a SN Ia. The late-time spectrum suggests that its progenitor was a massive star, given the preponderance of circumstantial evidence that SN Ib events arise in the cores of massive stars. Filippenko (1989) has challenged the standard classification scheme of supernovae with his data on SN 1987K. The most obvious explanation for the SN 1987K phenomenon, that it has a thin outer envelope of hydrogen, does not work. The calculations described above to check the SN Ib model were motivated in part by SN 1987K. Why this event differs from other SN II events is not clear. We need detailed models to understand possible explanations of the differences in spectrum evolution.

2.4. *SN 1993J*

SN 1993J in M81 is providing us with a wealth of new and unique information on the progenitor evolution and explosion mechanism. It was identified as a SN II from hydrogen lines in its early spectrum. But the light curve of SN 1993J is atypical for this class of supernova, with the intensity rising to a second maximum after the initial outburst. The light curve around the second maximum more closely resembles that of the Type Ib SN 1983N. Nomoto *et al.* (1993) suggest that the progenitor lost most of its envelope by mass transfer to a binary companion. A K0 supergiant has been suggested as a possible progenitor of SN 1993J. The detection of X-rays (Tanaka 1993) and radio (Pooley & Green 1993) from SN 1993J are consistent with the idea that the progenitor was a red supergiant with a substantial amount of circumstellar gas. The asymmetry of SN 1993J inferred from the polarization (Trammell *et al.* 1993) and line features (Hu *et al.* 1993) suggest that SN 1993J is a Type IIb supernova that evolved from a binary progenitor. Baron *et al.* (1993) present spectra of SN 1993J, which show strong hydrogen Balmer lines with pronounced P-Cygni profiles. Two groups at Beijing Astronomical Observatory (BAO) have been monitoring SN 1993J continuously from April to July 1993. Zhou *et al* (1993) have conducted UBVRI photometry on the 60 cm Telescope, while Wang *et al.* (1993) have obtained spectroscopic data at the BAO's 2.16 meter telescope. The time evolution of the various absorption and emission lines indicates that the supernovae debris is not spherically symmetric (see Fig.2). The most recent spectra (Wang *et al.* 1993) show that the oxygen lines are blueshifted by about 1775 km/sec .

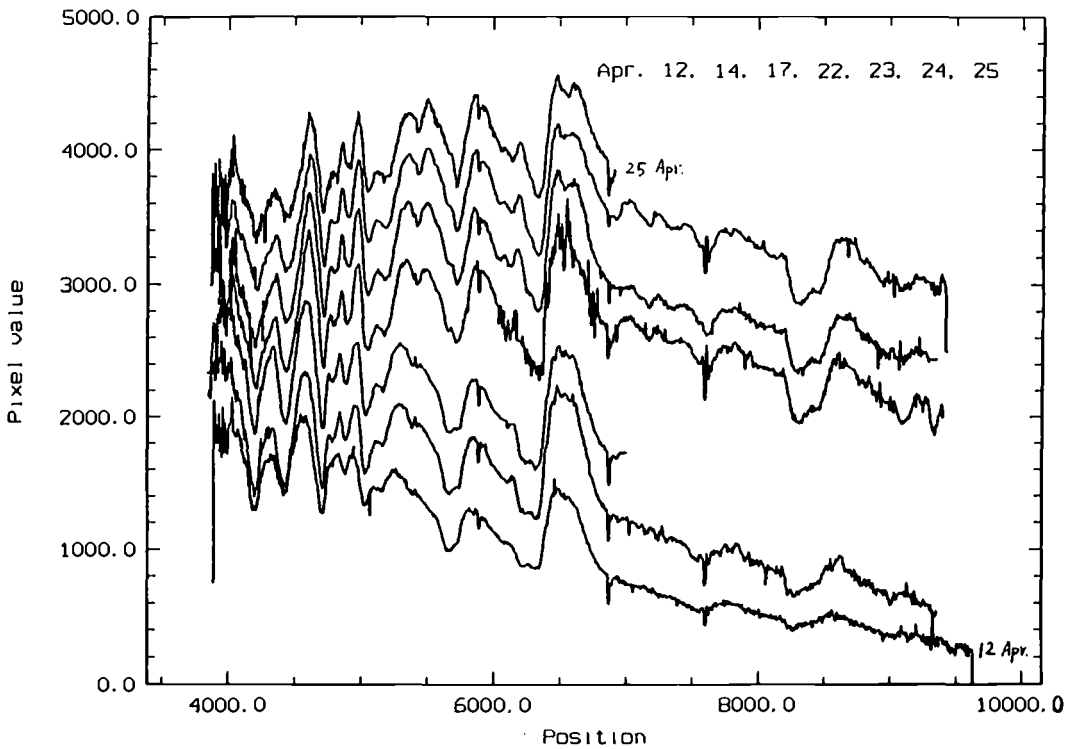

FIGURE 2. The early optical spectrum of SN 1993 J

3. Statistical Analysis of Supernovae

3.1. *Correlation of Supernova Types with Galactic Morphological Types*

The Asiago supernova Catalogue (Turatto 1993) presents data for 890 SNe. We surveyed these data (updated to SN 1993J) and analyzed them statistically. Table 1 shows the frequency distributions of various types of classified supernovae with respect to the different morphological types of their parent galaxies (the label nc means that the objects lack classification).

3.2. *Supernova Rates*

Clues to the origin of supernovae are found in their rates of occurrence in various types of galaxies. SN Ia are associated with old stellar populations; SN II and SN Ib are associated with young populations. For 736 galaxies surveyed, which have produced 51 supernovae, Cappellaro and Turatto (1988) have calculated control times, making allowance for an inclination effect, to estimate the rate of supernovae. Evans & van den Bergh (1989) have surveyed a sample of 855 Shapley-Ames galaxies, in which 24 supernovae occurred during 1980-1988. They calculated control times for SN Ia, SN Ib and SN II in different galaxy-type bins to infer the rate of supernovae frequencies. Van den Bergh & Tammann (1991) give the adopted supernova frequencies.

3.3. *Multiple Supernovae in Spiral Galaxies*

Because supernovae are rare, independent events, the relation of N(SNe) and N(galaxies) should follow a Poisson distribution. However, Guthrie (1990) found that the apparent frequency distributions of multiple supernovae in spiral galaxies is not a Poisson distribution. We (Li & Li 1993) have taken into account the following effects: Hubble types of

TABLE 1. Supernova Types with Galactic Types

	Ia,I	Ib/c	all I	II	Others	nc	total	
E	16	-	16	-	-	29	16	45
SO	19	2	21	-	-	17	21	38
SOa	3	-	3	1	-	1	4	5
Sa	12	1	13	5	1	31	19	50
Sab	4	-	4	6	1	10	11	21
Sb	21	3	24	15	-	63	39	103
Sbc	20	4	24	12	-	31	36	67
Sc	28	14	42	44	6	78	92	170
Scd	7	-	7	17	1	5	25	30
Sd	4	-	4	3	-	2	7	9
Sdm	2	-	2	1	-	2	3	5
Sm	1	1	2	1	-	2	3	5
S	11	-	11	3	-	62	14	76
I0	8	-	8	-	-	1	8	9
Im	-	1	1	1	-	1	2	3
I	-	-	-	1	1	22	2	24
nc	86	4	90	42	-	79	132	211
Total	242	30	272	152	12	445	436	881

galaxies, luminosity, inclination, distance. The sample of 667 galaxies comes from RC2, with some information from the UGC redshift catalogue of galaxies. With a sample of 169 supernovae, updated to Dec 31, 1992, we found that the frequency distribution of multiple SNe in spiral galaxies is still non-Poissonian. Perhaps star formation plays an important role (see §V). We have calculated the radial distributions of supernovae in galaxies that have hosted one, two, three, or four SNe and have used the K-S test to see whether they can belong to the same sample. We found that the radial distributions are not the same. Probably, galaxies with three or more SNe come from a sample of galaxies that are in a starburst phase.

4. Progenitors of Type Ib Supernovae

Recently, there has been a spate of interest in SNe Ib, because of: (1) the independent observations of peculiar infrared light curves among SNe I; and (2) the realization that the optical spectra of SNe Ib differ from those of most SNe I. For a supernova to be classified as a SN Ib, its spectrum must: (1) lack hydrogen emission and absorption lines at all times, as with SNe Ia (Porte & Filippenko 1987); (2) generally resemble the spectra of SNe Ia during the first few months past maximum, except that it must lack the SiIIλ6150 absorption trough 25 days after maximum; (3) exhibit strong [OI]$\lambda\lambda$6300 and [CaII]$\lambda\lambda$7300 emission.

The characteristics of SNe Ib can be summarized as follows (Panagia & Laidler 1991):

- The 6150Å feature is absent from the spectrum;
- The overall spectral distribution is redder and fainter ($\sim$ 1.5 magnitudes) than for SNe Ia;
- The optical light curve is essentially "normal," similar to that of SNe Ia;

- The IR light curve is single peaked, the maximum occurring a few days after the optical maximum;
- They are strong radio emitters with a steep spectrum and a quick temporal decline;
- They are found only in spiral galaxies; and
- They are located in spiral arms, often near an HII region.

Branch (1988) discussed the origin of SNe Ib. Supernovae observed during their photospheric phases display three distinct kinds of spectra: Type II, which by definition show optical hydrogen lines; Type Ia, which have neither hydrogen nor helium lines; and Type Ib, which have helium but not hydrogen lines. However, we should consider four distinct chemical compositions of the outer layers of exploding stars: (1) hydrogen-rich, or, speaking loosely, "solar"; (2) helium-rich, or, loosely, "Wolf-Rayet"; (3) deflagration – initially, a mixture of heavy elements from carbon to radioactive nickel (which decays through cobalt to iron); and (4) detonation – initially a mixture of just helium and radioactive nickel. Three fundamental constraints on the nature of SNe Ib are: (1) the presence of strong optical lines of HeI during the photospheric phase; (2) the presence of strong forbidden lines of oxygen ions during the nebular phase; and (3) the association with regions of recent star formation. These constraints point immediately to the possibility that SNe Ib result from the collapsing cores of massive stars that have lost their hydrogen envelopes, i.e., Wolf-Rayet stars. Alternatively, SNe Ib may result from a thermonuclear explosion in an accreting white dwarf. It is not obvious which (if either) of these two models really produces SNe Ib.

SNe Ic resemble SN Ib spectroscopically, except that HeI lines are weak or absent at early times. Thus SNe Ic are sometimes called "helium-poor" SNe Ib. To clearly identify the progenitors of SNe Ib/Ic, it is necessary to compare the observed bolometric (UV to IR) light curves with theoretical models. Jeffery *et al.* (1991) concluded that a helium star model for SN Ic is adequate and slightly favored for explaining the spectrum of the Type Ic SN M near maximum. Evidence continues to accrue that while SNe Ib/Ic are linked, SNe Ib can be distinguished from SNe Ic. All the well-established light curves of SNe Ic seem to decline rather rapidly, suggesting small ejecta masses, while SN Ib events seem to have rather large ejecta masses (Wheeler *et al.* 1993).

5. Supernovae in Starburst galaxies

A starburst galaxy is one with a region of strong star formation, including massive stars, the deaths of which are expected to result in supernovae. An example is the nuclear region of M82, for which Rieke *et al.* (1980) have estimated a supernova rate of 0.3/yr. SNe II and SNe Ib both show a clear correlation with HII regions and with star formation rates in galaxies. Chevalier (1991) discussed supernovae and supernova remnants in starburst galaxies, and Richmond & Filippenko (1991) presented the results of searches for supernovae in starburst galaxies. SNe Ib and SNe II are of special interest for starburst galaxies because they are thought to have massive progenitors. SNe II generally have red supergiant progenitors (SN 1987A being an exception), while SNe Ib's have more compact progenitors and often show radio emission indicating dense circumstellar matter. We believe that they are massive stars which have lost their hydrogen envelopes prior to the explosion.

Terlevich *et al.* (1991) extended TM85 to include the supernova phase in the evolution of the nuclear starburst. According to the initial mass of the progenitor, two different supernova phases are expected. The first is a SN Ib phase at the end of life-time of the most massive stars ($M > 25M_{\odot}$). These SNe have Wolf-Rayet progenitors; they are

TABLE 2. Type Ib and Ic Supernovae

SN	M_{MAX}	Type	Galaxy	Galaxy Class
1954A	9.8	Ib	NGC4214	Im
1962L	14.0B	Ib	NGC1073	SBc
1964L	13.4	Ib	NGC3938	Sc
1969J	11.4B	Ib	NGC3198	SBc
1975B	15.5	Ib	Anon0316+41	So
1976B	15.2B	Ib	NGC4402	Sc
1982R	14.8B	Ib	NGC1187	SBc
1983I	13.7B	Ib	NGC4051	SBc
1983N	11.6	Ib	NGC5236	SBc
1983V	13.5	Ib	NGC1365	SBb
1984L	14.0B	Ib	NGC991	Sc
1985F	12.1B	Ib	NGC4618	SBm
1986M	16.5	Ib	NGC7499	SAo
1987M	15.0	Ib	NGC2715	Sc
1988L	16.5	Ib	NGC5480	Sc
1989E	18.6B	Ib	MCG+5-32-45	?
1990B	16.0V	Ib	NGC4568	Sbc
1990I	15.6V	Ib	NGC4650A	Sm
1990U:	16.0B	Ic	NGC7479	Sc
1990W:	15.0V	Ic	NGC6221	Sc
1990aa	17.0CCD	Ic	U540	Sc
1990ai	19.0pg	Ibc	0 117+2159	?
1990aj	18.5V	Ib	NGC1640	Sb
1991A	17.0V	Ib	IC2973	Sc
1991K	18.0R	Ib	NGC2851	?
1991L	18.0R	Ibc	MCG+7-34-134	?
1991N	15.0CCD	Ibc	NGC3310	Sbc
1991R	18.0J	Ibc	1552+1907	?
1991ar	17.0J	Ib	IC49	Sc
1992K	16.2V	Ic	ESO269-G57	Sab

predicted to be optically dim and radio loud, and to produce remnants similar to Cas A. During this first phase the starburst should have a spectrum resembling that of a typical Seyfert 2 and should display substantial radio emission. During the second phase, SNe II emission should mark the end of the life-times of intermediate mass ($5M_{\odot} < M < 25M_{\odot}$) stars. These SNe have red supergiant progenitors. The SN ejecta will presumably interact with dense circumstellar/interstellar medium. During this phase the spectrum of the starburst should look like that of a Seyfert 1 or QSO.

6. Wolf-Rayet Stars and Supernovae

In the Milky Way, there are 172 known Wolf-Rayet stars (van der Hucht *et al.* 1991), of which 91 are classified as type WN, 73 are WC, 6 are WN/WC, and 2 are WO. Nomoto (1991) discussed the possible connections between Wolf-Rayet stars and type Ib/Ic/IIb supernovae and concluded that typical SNe Ib/Ic are the explosions of $3 - 5\ M_{\odot}$ helium stars in close binary systems. The low masses are required to successfully model the peak luminosities and rapid decline of the light curves of SNe Ib/Ic. Are Wolf-Rayet

stars the progenitors of type Ib/Ic supernovae? Filippenko (1991) discuss evidence for and against the hypothesis that SNe Ib/Ic are produced by core collapse in a massive evolved progenitor. SNe Ib/Ic probably do represent the explosions (core collapse) of hydrogen-deficient massive stars. However, the question of whether most of these are Wolf-Rayet stars is far from settled.

The author's research on supernovae is supported by National Natural Science Foundation of China. We also gratefully acknowledge the excellent support from the staff of the Beijing Astronomical Observatory.

REFERENCES

Baron, E., Hauschildt, P. H., Branch, D., *et al.* 1993, ApJ, 416, L21

Branch, D. 1988, Lecture Notes in Physics, 305, Ed. K. Nomoto, p281

Branch, D., Nomoto, K., Filippenko, A. V. 1990 Comments Ap, 15, 221

Cappellaro, E., Turatto, M. 1988, A & A, 190, 10

Chevalier, R. 1991, in Massive stars in Starbursts, ed. C. Leitherer, *et al.* Cambridge University Press, p169

Evans, R., van den Bergh, S. 1989, ApJ, 245, 752

Filippenko, A. V., 1989, Proc. Astr. Soc. Australia, 7, 450

Filippenko, A. V. 1991, in Wolf-Rayet Stars and Interactions with Other Massive Stars in Galaxies, ed. K. A. van der Hucht & B. Hidayat (Kluwer) p529

Guthrie, B. N. G. 1990, A& A, 234, 84

Harkness, R., & Wheeler, J. C. 1990, in Supernovae, ed. A. G. Petschek, p1

Hu, J. Y., Li, Z. W., Jian, X. J., & Wang, L. F., 1993, IAU Circular No.5777

Hu, J. Y., Wang, L. F., Jiang, X. J., Li, Z. W. 1993, Acta Astrophys. Sinica, 297

Jeffery, D., Branch, D., Filippenko, A. V. 1991, ApJ, 377, L89

Li, W. D. & Li, Z. W., 1993, in preparation

Nomoto, K. 1991, in Wolf-Rayet Stars and Interactions with Other Massive Stars in Galaxies, p515

Nomoto, K., Suzuki, T., Shigeyama, S. 1993, *et al.* Nature, 364, 507

Panagia, N. & Laidler, V. 1991, in Supernovae, ed. S. Woosley, p559

Pooley, G. C. & Green, D. A., 1993, IAU Circular No. 5751

Porte, A. C. & Filippenko, A. V. 1987, AJ, 93, 1372

Richmond, M., Filippenko, A. V. 1991, in Supernovae, ed. S. Woosley, Springer-Verlag, p731

Rieke, C. H., Lebofsky, M. J., Thompson, R. I., *et al.* 1980, ApJ, 238, 24

Tanaka, Y. 1993, IAU Circular No. 5753

Terlevich, R. 1991, in Starbursts and Galaxy Evolution

Trammell, S. R., Hines, D. C., Wheeler, J. C., 1993, ApJ, 414, L21

Turatto, M., private communication, 1993

van den Bergh, S. & Tammann, G. A. 1991, ARA&A, 29, 363

van der Hucht, K. A. 1991, in Wolf-Rayet Stars and Interactions with Other Massive Stars in Galaxies, p19

Wang, L. F. 1993, IAU Circular No. 5847

Wheeler, J. C. 1991, in Supernovae, eds. J. C. Wheeler *et al.*, World Scientific, p1

Wheeler, J. C., Harkness, R. 1990, Rep. Prog. Phys.,

Wheeler, J. C., Harkness, R. 1991, in Frontiers of Stellar Evolution, ed. D. Lambert, 1991, PASP

Wheeler, J. C., Swartz, D., Harkness, R. 1993, Physics Reports, 227, 113

Zhou, X., Zheng, Z. Y., Wu, H. 1993, Acta Astrophys. Sinica, 295

Supernova Nucleosynthesis in Massive Stars

By M. HASHIMOTO,[1] K. NOMOTO[2] T. TSUJIMOTO, AND F.-K. THIELEMANN[3]

[1]Kyushu University, Fukuoka 810, Japan

[2]University of Tokyo, Bunkyo-ku, Tokyo 113, Japan

[3]Harvard-Smithsonian Center for Astrophysics, 60 Garden St., Cambridge, MA 02138, USA

Presupernova evolution and explosive nucleosynthesis in massive stars for main-sequence masses from 13 $M_\odot$ to 70 $M_\odot$ are calculated. We examine the dependence of the supernova yields on the stellar mass, $^{12}C(\alpha,\gamma)^{16}O$ rate, and explosion energy. The supernova yields integrated over the initial mass function are compared with the solar abundances.

1. Presupernova models and the $^{12}C(\alpha,\gamma)^{16}O$ rate

Presupernova models are obtained for helium stars with masses of M_α = 3.3, 4, 5, 6, 8, 16, and 32 $M_\odot$ as an extension of the studies by Nomoto & Hashimoto (1988), Thielemann *et al.* (1993), and Hashimoto *et al.* (1993). These helium star masses correspond approximately to main-sequence masses of $M_{\rm ms}$ = 13, 15, 18, 20, 25, 40, and 70 $M_\odot$, respectively (Sugimoto & Nomoto 1980). The systematic study for such a dense grid of stellar masses enables us to understand how explosive nucleosynthesis depends on the presupernova stellar structure and to apply the results to the chemical evolution of galaxies. We use the Schwarzschild criterion for convection and neglect overshooting. The initial composition is given by $X(^4\mathrm{He}) = 0.9879$ and $X(^{14}\mathrm{N}) = 0.0121$. These helium stars are evolved from helium burning through the onset of the Fe core collapse.

Nuclear reaction rates are mostly taken from Caughlan & Fowler (1988). For the uncertain rate of $^{12}C(\alpha,\gamma)^{16}O$, we use the rate by Caughlan *et al.* (1985; CFHZ85), which is larger than the rate by Caughlan & Fowler (1988; CF88) by a factor of ~ 2.4. To examine the influence of this difference, we evolve the $M_\alpha = 8\ M_\odot$ helium star, using the $^{12}C(\alpha,\gamma)^{16}O$ rate by CF88 (case 25B). [The 25 $M_\odot$ star model with the $^{12}C(\alpha,\gamma)^{16}O$ rate by CFHZ85 is denoted as case 25A.] At the end of core helium burning, the formation of the carbon-oxygen core and its composition are influenced largely by the $^{12}C(\alpha,\gamma)^{16}O$ rate. The larger rate results in a smaller C/O ratio, which affects the abundances of Ne, Mg, Al relative to O in the more evolved cores.

Comparison of the presupernova density structures for the two cases 25A and 25B shows that case 25B has a more concentrated core at $M_r < 2M_\odot$ (i.e., a steeper density gradient) and more extended outer layers than case 25A. This is due to a larger carbon abundance and thus stronger carbon shell burning in case 25B.

It is found that the size of the iron core is not a monotonic function of the helium core mass as shown by Barkat & Marom (1990) and Woosley (1993). For $M_{\rm ms}$ = 13, 15, 18, 20, 25 (case 25A), 40, and 70 $M_\odot$, the iron core masses are 1.18, 1.28, 1.36, 1.40, 1.42, 1.88, and 1.57 $M_\odot$, respectively. In case 25B, the iron core mass is 1.37 $M_\odot$, which is smaller than in case 25A.

2. Explosive nucleosynthesis

The hydrodynamic phases of supernova explosions for the above eight presupernova models were followed with an extensive nuclear reaction network (Hashimoto *et al.* 1989, 1993; Thielemann *et al.* 1990, 1993).

Since the mechanism of supernova explosions after core collapse is not fully understood yet, the explosion energy and the mass cut (or ^{56}Ni mass) have remaining uncertainties, except for SN 1987A. The final kinetic energy of the explosion is assumed to be $E = 1.0 \times 10^{51}$ erg as inferred from the modeling of SN 1987A and SN 1993J (e.g., Shigeyama & Nomoto 1990; Shigeyama *et al.* 1994).

In the present study, the mass cut is chosen to produce 0.075 $M_\odot$ ^{56}Ni for 13 – 70 $M_\odot$ stars. This is based on the estimates from the light curves of SN 1993J for the 13 – 15 $M_\odot$ stars (e.g., Nomoto *et al.* 1993; Wheeler & Filippenko 1993) and SN 1987A for the 18 – 20 $M_\odot$ stars (e.g., Nomoto *et al.* 1993). For more massive stars, a similar mass of ^{56}Ni is suggested from SN 1990E (Schmidt *et al.* 1993) and also from the absence of very bright type Ib supernovae with slow decline (e.g., Shigeyama *et al.* 1990).

Figures 1 and 2 show the integrated abundances of the ejecta relative to the solar values (Anders & Grevesse 1989) for $M_{\rm ms} = 13$, 15, 18, 20, 40, and 70 $M_\odot$, respectively. Figure 3 shows three cases of $M_{\rm ms} = 25$ $M_\odot$, i.e., cases 25A, 25B, and 25BE (see below).

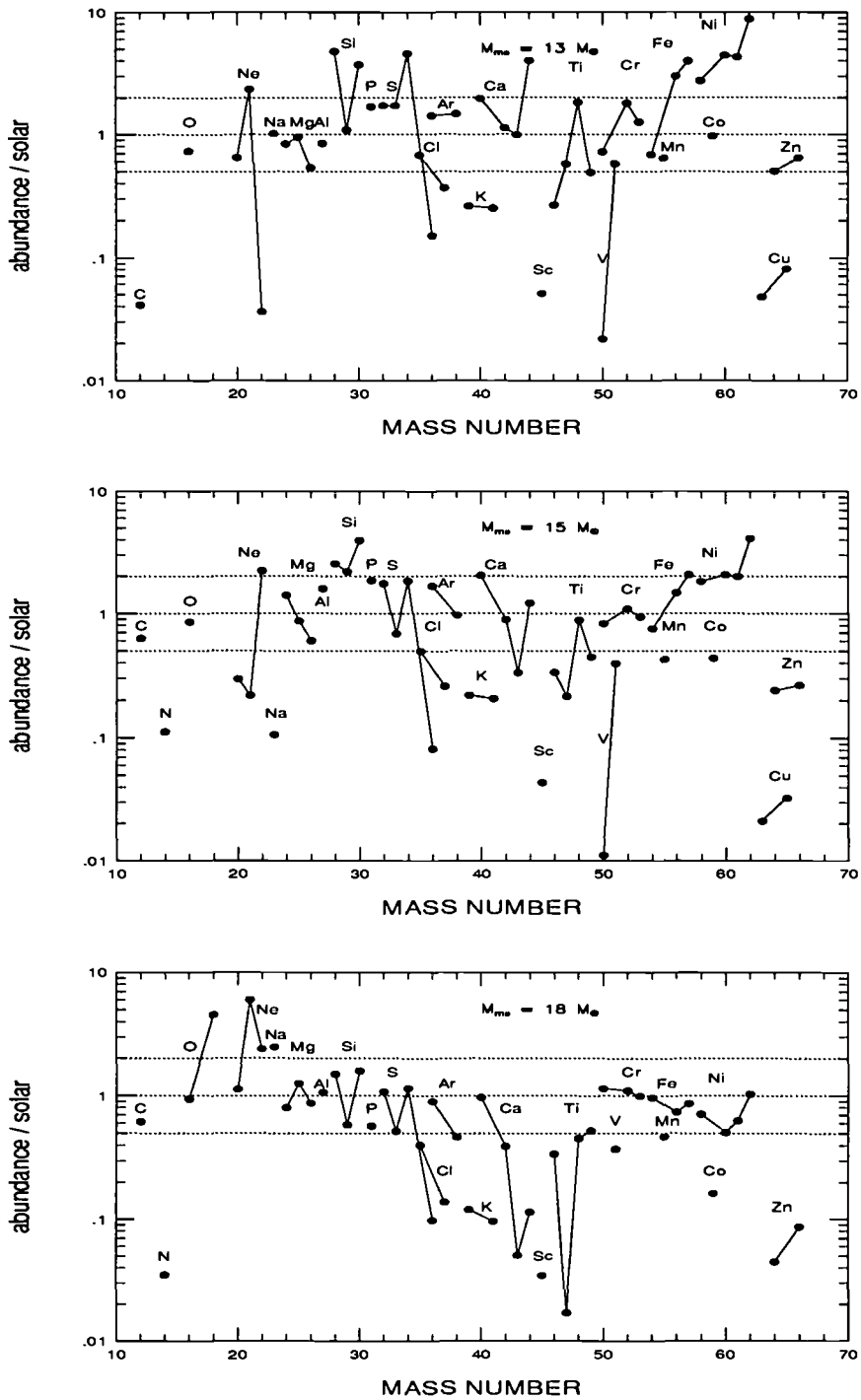

FIGURE 1. Abundances of stable isotopes relative to the solar values for the 13, 15, and 18 $M_\odot$ stars.

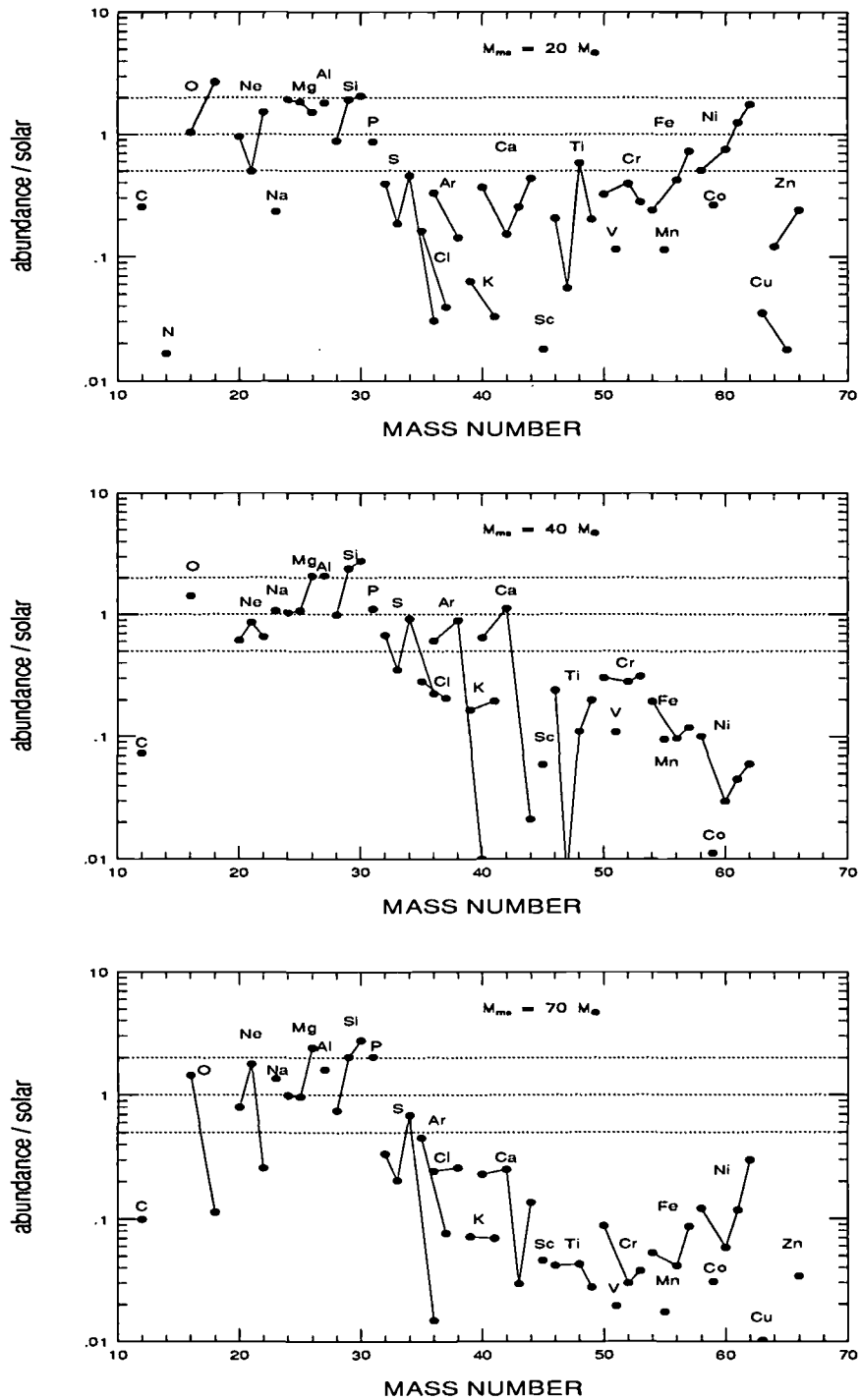

FIGURE 2. Same as Fig. 1 but for the 20, 40, and 70 $M_\odot$ stars.

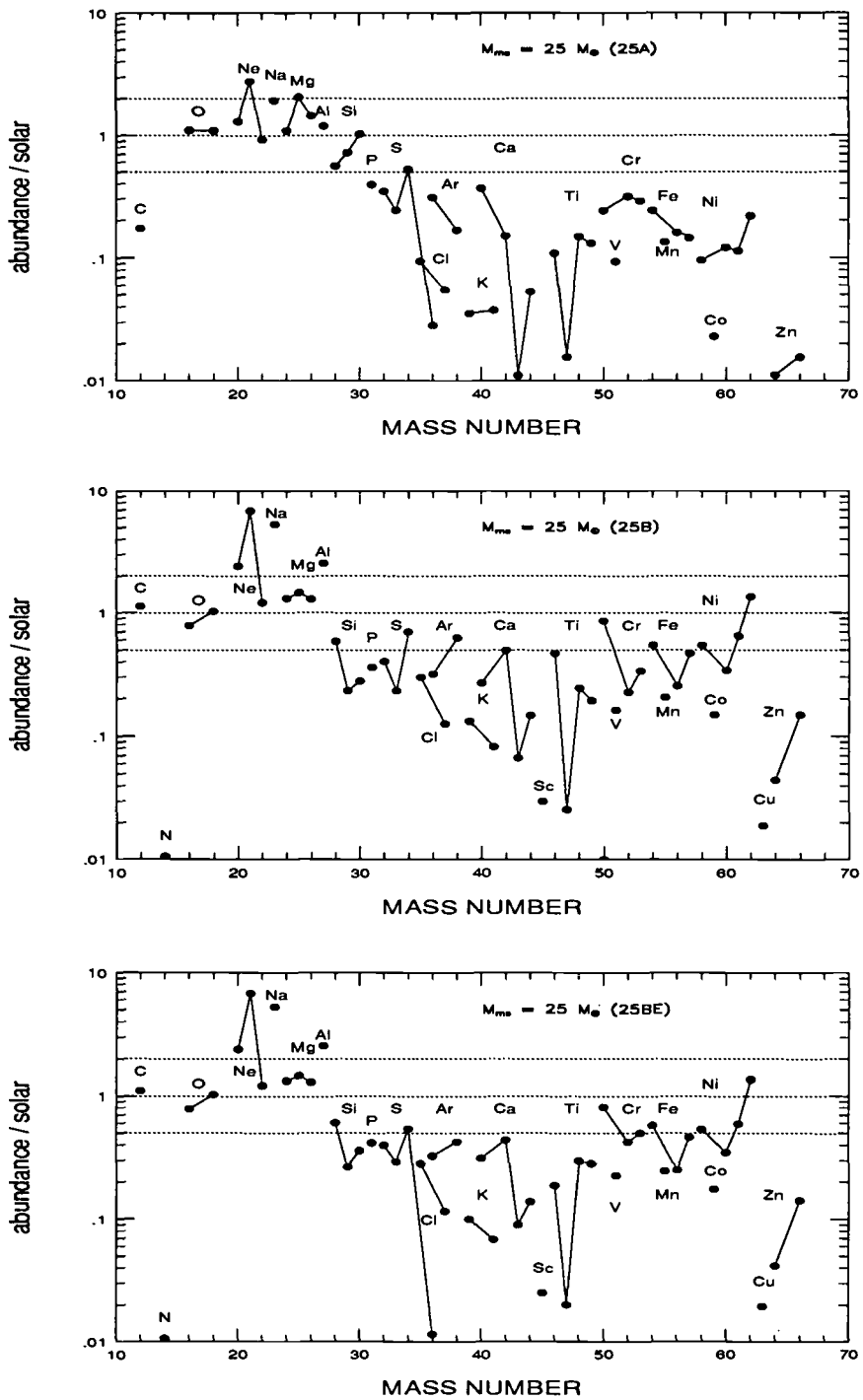

FIGURE 3. Same as in Fig. 1 but for the 25 $M_\odot$ star (case 25A). Case 25B uses the $^{12}C(\alpha,\gamma)^{16}O$ rate by CF88 and case 25BE is the same as 25B but with $E = 1.5 \times 10^{51}$ erg s^{-1}.

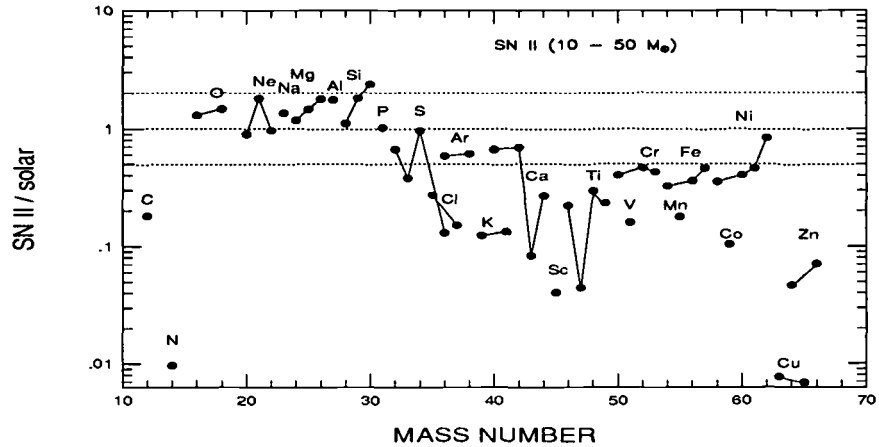

FIGURE 4. Nucleosynthesis products from 10 – 50 $M_\odot$ stars averaged over the IF relative to solar abundances.

TABLE 1. Nucleosynthesis products (in $M_\odot$) from 10 – 50 $M_\odot$ stars averaged over the IMF.

^{12}C	7.93E-02	^{35}Cl	1.01E-04	^{54}Cr	1.83E-08
^{13}C	3.80E-09	^{37}Cl	1.88E-05	^{55}Mn	3.44E-04
^{14}N	1.56E-03	^{36}Ar	6.62E-03	^{54}Fe	3.38E-03
^{15}N	1.66E-08	^{38}Ar	1.37E-03	^{56}Fe	6.10E-02
^{16}O	1.80	^{40}Ar	2.27E-08	^{57}Fe	1.92E-03
^{17}O	9.88E-08	^{39}K	6.23E-05	^{58}Fe	6.43E-09
^{18}O	4.61E-03	^{41}K	5.07E-06	^{59}Co	5.01E-05
^{19}F	1.16E-09	^{40}Ca	5.77E-03	^{58}Ni	2.54E-03
^{20}Ne	2.12E-01	^{42}Ca	4.23E-05	^{60}Ni	1.15E-03
^{21}Ne	1.08E-03	^{43}Ca	1.08E-06	^{61}Ni	5.76E-05
^{22}Ne	1.83E-02	^{44}Ca	5.53E-05	^{62}Ni	3.37E-04
^{23}Na	6.51E-03	^{46}Ca	1.43E-10	^{64}Ni	3.18E-14
^{24}Mg	8.83E-02	^{48}Ca	5.33E-14	^{63}Cu	6.45E-07
^{25}Mg	1.44E-02	^{45}Sc	2.29E-07	^{65}Cu	2.65E-07
^{26}Mg	2.01E-02	^{46}Ti	7.19E-06	^{64}Zn	6.76E-06
^{27}Al	1.48E-02	^{47}Ti	1.34E-06	^{66}Zn	6.06E-06
^{28}Si	1.05E-01	^{48}Ti	9.23E-05	^{67}Zn	1.19E-08
^{29}Si	8.99E-03	^{49}Ti	5.55E-06	^{68}Zn	2.73E-09
^{30}Si	8.05E-03	^{50}Ti	2.95E-10	^{69}Ga	2.60E-12
^{31}P	1.21E-03	^{50}V	6.19E-10	^{71}Ga	1.37E-14
^{32}S	3.84E-02	^{51}V	8.73E-06	^{70}Ge	1.65E-12
^{33}S	1.78E-04	^{50}Cr	4.34E-05	^{72}Ge	1.61E-12
^{34}S	2.62E-03	^{52}Cr	1.01E-03	^{73}Ge	9.25E-17
^{36}S	1.78E-06	^{53}Cr	1.08E-04		

To examine the dependence on the explosion energy, we show the case 25BE, i.e., case 25B with $E = 1.5 \times 10^{51}$ erg. The larger explosion energy leads to the outward shift of the abundance distribution. This leads to minor differences between the abundances for the two explosion energies (Fig. 3).

3. Isotopic abundance ratios

Figure 4 shows the isotopic abundances relative to their solar values (Anders & Grevesse 1989) after averaging over the mass range from 10 to 50 $M_\odot$ with an initial mass function $\propto M^{-1.35}$. Here the upper mass limit 50 $M_\odot$ is chosen from the comparison of [O/Fe] and [Mg/Fe] with those of metal-poor stars (Tsujimoto *et al.* 1994). We also assume no heavy element production below 10 $M_\odot$ and approximate the abundances of 10 – 13 $M_\odot$ stars by a linear interpolation between 10 and 13 $M_\odot$. Table 1 gives the integrated masses ($M_\odot$) of stable species averaged over the initial mass function.

Figure 4 shows that the relative abundance ratios from massive stars are in good agreement with the solar ratios for $A < 27$. [The sum of type Ia and type II products with a ratio of 1 to 9 reproduces well the solar abundances for a wider range of A (Tsujimoto *et al.* 1993).] Note that this agreement is realized for the $^{12}C(\alpha,\gamma)^{16}O$ rate by CFHZ85, i.e., case 25A. For case 25B, Ne, Na, and Al relative to O are overproduced with respect to the solar ratios as seen in Figure 3. This is due to the larger C/O ratio in case 25B after helium burning. Since the products of the 25 $M_\odot$ star dominate type II supernova yields, this result suggests that the $^{12}C(\alpha,\gamma)^{16}O$ rate is higher than that of CF88 and closer to CFHZ85. The presently most reliable experimental investigations give values in between the two rates.

We should note that the isotopic ratios in Figures 1 – 4 depend not only on the $^{12}C(\alpha,\gamma)^{16}O$ rate but also on convective overshooting, mixing fresh He into the core at late high temperature core helium burning stages. The above comparison that favors the CFHZ85 rate is based on the calculations with no convective overshooting. If overshooting during convective core helium burning would reduce the C/O ratio, a smaller $^{12}C(\alpha,\gamma)^{16}O$ rate would be favored (Weaver & Woosley 1993).

Figure 4 also shows that some species, ^{35}Cl, ^{39}K, ^{44}Ca, ^{48}Ti, and ^{59}Co, are underproduced relative to the solar values. If we include the weak component of the s-process nuclei $50 < A < 100$ produced during core helium burning (Prantzos *et al.* 1990), ^{48}Ti and ^{59}Co are enhanced appreciably compared with the seed (solar) abundances. ^{35}Cl, ^{39}K and ^{44}Ca are enhanced only by a factor of ~ 2. Synthesis of s-process elements during carbon shell burning would also be significant (Raiteri *et al.* 1993).

Acknowledgements

This work has been supported in part by the Grant in Aid for Scientific Research (04640265, 05242102, 05242103, 05242207, 05243206, 3883) of the Ministry of Education, Science, and Culture in Japan and NSF-grant AST 89-13799.

REFERENCES

Anders, E., & Grevesse, N. 1989, Geochim. Cosmochim. Acta, 53, 197

Barkat, Z., & Marom, A. 1990, in Supernovae, ed. J.C. Wheeler *et al.* (World Scientific), p. 95

Caughlan, G. R., Fowler, W. A., Harris, M. J., & Zimmerman, B.A. 1985, Atomic Data & Nuclear Data Tables, 32, 197

Caughlan, G. R., & Fowler, W. A. 1988, Atomic Data & Nucl. Data Tables, 40, 283

Hashimoto, M., Nomoto, K., & Shigeyama, T. 1989, A&A 210, L5

Hashimoto, M., Nomoto, K., Tsujimoto, T., & Thielemann, F.-K. 1993, in Nuclei in Cosmos, ed. F. Käppeler & K. Wisshak (Institute Physics Publ.), p. 587

Nomoto, K., & Hashimoto, M. 1988, Phys. Rep., 163, 13

Nomoto, K., Shigeyama, T., Kumagai, S., Yamaoka, H., & Suzuki, T. 1993, in Supernovae (Les Houches, Session LIV), ed. S. Bludman, R. *et al.* (Elsevier Sci. Publ.)

Nomoto, K., Suzuki, T., Shigeyama, T., Kumagai, S., Yamaoka, H., & Saio, H. 1993, Nature, 364, 507

Prantzos, N., Hashimoto, M., & Nomoto, K. 1990, A&A, 234, 211

Raiteri, C. M., Gallino, R., Busso, M., Neuberger, D., & Käppeler F. 1993, ApJ, 419, 207

Schmidt, B. P. *et al.* 1993, AJ, 105, 2236

Shigeyama, T., & Nomoto, K. 1990, ApJ, 360, 242

Shigeyama, T., Nomoto, K., Tsujimoto, T. & Hashimoto, M. 1990, ApJ, 361, L23

Shigeyama, T., Suzuki, T., Kumagai, S., Nomoto, K., Saio, H., & Yamaoka, H. 1994, ApJ, 420, 341

Sugimoto, D., & Nomoto, K. 1980, Space Sci. Rev. 25, 155

Thielemann, F.-K., Hashimoto, M., & Nomoto, K. 1990, ApJ, 349, 222

Thielemann, F.-K., Nomoto, K., & Hashimoto, M. 1993, in Les Houches, Session LIV ed. S. Bludman *et al.* (Elsevier Sci. Publ.)

Tsujimoto, T., Nomoto, K., Hashimoto, M., Yanagida, S., & Thielemann, F.-K. 1993, in Nuclei in Cosmos, ed. F. Käppeler & K. Wisshak (Institute Physics Publ.), p. 581

Tsujimoto, T., Nomoto, K., Hashimoto, M., & Thielemann, F.-K. 1994, ApJ, submitted

Weaver, T., & Woosley, S.E. 1993, Phys. Rep. 227, 65

Wheeler, J.C., & Filippenko, A.V. 1993, in this volume

Woosley, S.E., 1993, in this volume

Nuclear Weak Processes in Presupernova Stars

By A. RAY,[1] T. KAR,[2]
S. SARKAR[2], AND S. CHAKRAVARTI[3]

[1]Tata Institute of Fundamental Research, Bombay 400 005, India

[2]Saha Institute of Nuclear Physics , Calcutta 700 064, India

[3]California State Polytechnic University, Pomona, CA91768, USA

The structure and the size of the core of massive presupernova stars are determined by the electron fraction and entropy of the core during its late stages of evolution; these in turn affect the subsequent evolution during gravitational collapse and supernova explosion phases. Beta decay and electron capture on a number of neutron rich nuclei can contribute substantially towards the reduction of the entropy and possibly the electron fraction in the core. Methods for calculating the weak transition rates for a number of nuclei for which no reliable rates exist (particularly for A > 60) are outlined. The calculations are particularly suited for presupernova matter density ($\rho = 10^7 - 10^9$ g/cc) and temperature (T = $2 - 6 \times 10^9$ °K). We include besides the contributions from the ground state and the known excited states, the Gamow-Teller (GT) resonance states (e.g. for beta decay rates, the GT_+ states) in the mother nucleus which are populated thermally. For the GT strength function for transitions from the ground state (as well as excited states) we use a sum rule calculated by the spectral distribution method where the centroid of the distribution is obtained from experimental data on (p,n) reactions. The contribution of the excited levels and GT_+ resonances turn out to be important at high temperatures which may prevail in presupernova stellar cores.

1. Presupernova Evolution of Massive Stars

Beta decay (β^-) and electron (e^-) capture of neutron rich nuclei play important roles in determining presupernova core structure (Nomoto et al, 1991). The structure of the core is important for later gravitational collapse and supernova explosion phases. These weak interaction rates were compiled by Fuller *et al.* (1982 and references therein) for a series of nuclei up to the mass number (A) of 60. Reliable rates for A > 60 are not available yet. It is important to include contributions of excited states of parent nuclei because presupernova cores are *hot and dense.* In addition there are resonance states in the mother nucleus whose contribution to the overall rates in a hot presupernova core have to be accounted for. For considerations of beta-decay rates for example, the Gamow-Teller$_+$ resonances may be thermally populated and the transitions from these states could in principle be important. The distribution of the GT_+ strengths have been recently obtained experimentally in a few nuclei from (n,p) reactions (e.g. Alford *et al.* 1993) and can be used in calculating the transition strengths from the resonance states.

In the core of the star, the last stage of nuclear fusion involves silicon. When silicon burning is finished the core tends to contract under its own weight. During the contraction phase (the so-called Kelvin-Helmholtz phase) the iron group nuclei capture electrons and emit neutrinos which escape directly from the stellar core without further interaction. This leads not only to a decreased electron fraction, Y_e, but also to lower entropy per nucleon and a cooler core. In addition, the entropy profile has significant effects on presupernova core structure and nucleosynthesis, since the former determines the extent of the convective burning shells. Woosley & Weaver (1988) have emphasized

that electron captures can lead to some neutronization during oxygen burning and in particular after central oxygen depletion. Even though the final distribution of Y_e in the Si core will have little memory of what the conditions during oxygen burning were, a decrease of Y_e *during* oxygen burning might affect the entropy and density structure of the outer core and through this, the location of the oxygen burning shell during the core silicon burning stage. Because of its entropy generation, the location of the oxygen burning shell does ultimately determine the extent of the convective Si burning shell that follows and sets the iron core mass.

So far, out of the weak processes, β^- decays of nuclei are not yet included in the computation of presupernova stellar structure. The electron capture processes are included in the computations (Woosley & Weaver 1988) by using the instantaneous value of the neutron excess (or Y_e) at time t. The abundances of radioactive nuclei (computed from ρ, T, and Y_e) and their decay rates λ_i yield the rate at which Y_e is changing. Obviously in computing the change of Y_e, one must know whether the nuclei with the largest rates are abundant enough under the given conditions of density, temperature and electron fraction. In general, such abundances can be computed only through detailed reaction networks coupled dynamically to stellar evolution. Hence it is necessary to compute capture and decay rates of nuclei under conditions prevailing in the presupernova stage, especially for nuclei in the fp-shell.

For the fp-shell, detailed shell model calculations to obtain rates are formidable computationally. Bloom & Fuller (1985) tried such methods for nuclei with $A < 60$ using a truncated basis space. Among microscopic theories, the best results are from complete shell model diagonalisation for $A > 40$ nuclei (Brown & Wildenthal 1985) and making a Quasiparticle Random Phase Approximation (QRPA) for heavier nuclei (Moller & Randrup, 1990; Klapdor *et al.* 1990). However, extension of the QRPA calculations to non-zero temperatures relevant for presupernova and gravitational collapse phases leading to supernovae are not available yet.

2. Calculation of Rates

Following Kar *et al.* (1991), the we use Gamow-Teller sum rules and employ the average distribution of the quenched sum-rule strength calculated from spectral distribution theory (see French *et al.* 1988; Kota & Kar 1989). A continuous approximation is made for the final states. We calculate the variable phase space factors (as a function of final energy) for the reaction rates using the finite temperature Fermi-Dirac distributions. A filled Fermi-sea of electrons partially blocks the available phase space. We also numerically calculate the electron chemical potential (required in phase space integrals) in the *moderately* degenerate and *mildly* relativistic cases. The *GT* strength distribution is folded in with the variable phase space factor and integrated over the final state energy to yield the rate from a particular mother nucleus state. This procedure is repeated to include the statistically weighted contributions from excited states of the mother nucleus for finite temperature.

The β^- decay rate from the ground state is given by:

$$\lambda_{g.s} = \frac{\ln 2}{(g_V)^2}(6250\ \mathrm{s})^{-1} \sum_j B(E_j) f(Q - E_j) \tag{1}$$

where the summation is over all final states with energy E_j up to the Q-value.

$$B(E_j) = g_V^2 B_F(E_j) + g_A^2 B_{GT}(E_j)\,, \tag{2}$$

[$B_F(E)$ and $B_{GT}(E)$ are the squared Fermi and *GT* matrix elements]. We replace the

actual microscopic strengths by the statistically averaged strength function and approximate the $\sum_j \rightarrow \int dE'$ over $Q_i = Q + E_i$ in the rate equation for λ_{gs}. Therefore the decay rate from the ground state as well as the known excited states taking account of the Boltzmann factors is:

$$\lambda_s = \frac{\ln 2}{(g_V)^2} \frac{(6250\ \mathrm{s})^{-1}}{G} \sum_i (2J_i + 1) \exp(-E_i/kT) \int_0^{Q_i} |M_i(E')|^2 f(Q_i - E') dE' \quad (3)$$

with

$$|M_i(E')|^2 = g_V^2 \rho_i(E') B_i^F(E') + g_A^2 \rho_i(E') B_i^{GT}(E') \,. \quad (4)$$

Here $\rho_i(E')$ is the density of states at final energy E'. The phase-space factor appearing in the equation for the transition rate is:

$$f(T, \mu, E_0) = \int_1^{\epsilon_0} \frac{F(Z, \epsilon) \epsilon (\epsilon^2 - 1)^{1/2} (\epsilon_0 - \epsilon)^2 d\epsilon}{1 + \exp\{(\mu - \epsilon)/kT\}} \quad (5)$$

The factor in the denominator denotes the availability of electron holes in the Fermi sea which the decay electron can enter. $F(Z, \epsilon)$ is the Coulomb correction factor (Schenter & Vogel 1983) and incorporates the effect of relativistic electrons in the presupernova interior and corrects for the finite size of the nucleus. The actual integrals for the phase-space factor and transition rate are obtained by 16 point Gauss-Legendre quadratures. The central temperature at the last nuclear burning stages approach a good fraction of an MeV. Therefore the chemical potential of the electrons are calculated fully numerically at finite temperatures. This includes the effects of the presence of positrons (through electron-positron pair creation).

Apart from the contribution of the ground and the known excited states of the nucleus, the contribution from the GT_+ resonance in the mother nucleus for β^- decay $\lambda_{RE}^{>}$ must be added to get the total rate:

$$\lambda_{tot} = \lambda_s + \lambda_{RE}^{>} \quad (6)$$

3. *GT* Strength Sum and Energy Distribution

For the position of the IAS, the Coulomb displacement energy is: $\Delta_c = 1.44 Z A^{-1/3}$ MeV and the width is $\sigma_c = 0.157 Z A^{-1/3}$ MeV (Morita 1973). For the fp-shell nuclei, as the very narrow Fermi resonance lies far above the energetically allowed region, the Fermi operator makes a negligible contribution to β^- decay rates. However, the collective Gamow-Teller mode can be substantially split among the daughter nuclear levels as compared to the Fermi IAS. See Figure 1. We use the spectral distribution theory for evaluating Gamow-Teller strength sum and the form of the strength distribution. The statistically averaged smoothed form of the Gamow-Teller strength function is a Gaussian in energy E' because according to spectral distribution theory the strength density (i.e. the average strength times the density of states in both the initial and final spaces) has an asymptotic bivariate Gaussian form in the initial and final energies for large spaces (French *et al.* 1988). Experimentally observed total GT strengths from the ground state of the target nucleus through (p, n) reactions show that the rates are consistently smaller than estimates from the shell model or other theoretical models. Movement of a part of the total strength upward in energy beyond the observed giant resonance region due to the tensor interaction as well as due to mixing of $N^{-1}\Delta$ (nucleon-hole Δ particle) with the low-energy N^{-1} N interaction is believed to be the cause of this observed quenching. We take this into account by an including an empirical quenching factor

To specify the Gaussian one needs two quantities – its centroid and its width. We

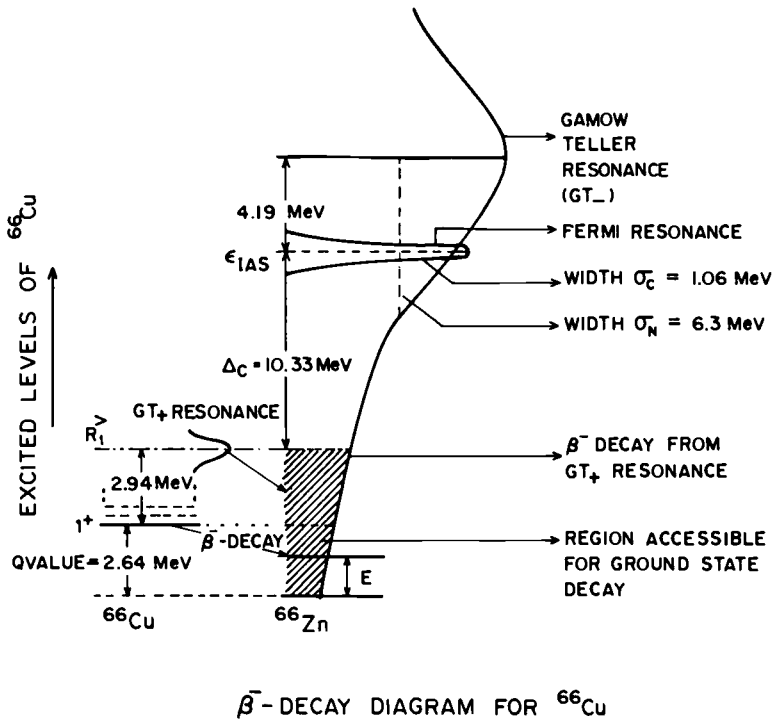

FIGURE 1. β^- decay diagram for ^{66}Cu with Fermi and GT resonances

note here that the physically accessible region through the Q-value of the ground state (the excited states) covers only the tail of the Gaussian. For the GT centroid we use the relation developed by Nakayama *et al.* (1982) which gives a best-fit to the observed centroids from (p,n) reaction data. The expression is

$$\epsilon_{GT} = E_{IAS} + 26A^{-1/3} - 18.5(N-Z)/A \tag{7}$$

where ϵ_{GT} is the GT centroid energy and E_{IAS} is the energy of the IAS. For an excited state, we extend the isobaric analog argument and add the excitation energy of the initial state to fix the centroid energy of its GT distribution. The width of the GT resonance has two parts: $\sigma^2 = \sigma_C^2 + \sigma_N^2$, the first part coming from Coulomb forces and the dominant second part coming from the nuclear interactions. To minimize the deviation of the calculated strength distribution from the actual one, we use the width of the Gaussian as a parameter and fit the experimental half-lives with predictions of the model for a number of nuclei.

4. Transitions from Gamow-Teller Resonances in the Mother Nucleus

For β^- decay, apart from the transitions from individual excited states and the ground state of the mother nucleus, one should also include the resonant states of the mother nucleus (N,Z) which resonates with low-lying states of the daughter nucleus (N-1, Z+1) being connected by the GT_+ operator for β^+ decay (i.e. $\Sigma_i \sigma(i) t_+(i)$) on the daughter states. (For electron capture reactions, one should include the corresponding GT_- states

in the mother nucleus.) Adopting the method of Fuller, Fowler & Newman (FFN II) where one assumes that the centroid energies of the resonances in the mother scale in the same way as the discrete states in the daughter, a simple form for the transition rates ($\lambda^{>}_{RE}$) of β^- decay is given by:

$$\lambda^{>}_{RE} = \lambda^{>}_{re}\left(\frac{G^{<}}{G^{>}}\right)\exp\left(-R^{>}_{1}/kT\right) \tag{8}$$

where $G^{<}$ and $G^{>}$ are partition functions of the daughter and the mother nucleus

$$G(Z,A,T) = \int\int dJdE(2J+1)\rho(E,J)\exp\left(-E/kT\right) \tag{9}$$

where $\rho(E,J)$ is the density of nuclear levels.

For nuclei whose excitation spectra (of both mother and daughter) are known experimentally, the partition functions are calculated up to the same excitation energy in both. For cases in which such spectra are not known, we use the "constant temperature" form of the nuclear level density functions in the partition function integrals (see e.g. von Egidy *et al.* 1988):

$$\rho(E,J) = f(J)\frac{1}{T_n}\exp\left(\frac{E-E_0}{T_n}\right), \tag{10}$$

where $f(J)$ is the spin distribution function. The back-shifting parameter E_0 and the nuclear level density function's parameter T_n (the "constant temperature") have been given by von Egidy *et al.* in parametrized fits depending on the nuclear mass number A and on the pairing energies of the protons and neutrons (Gilbert & Cameron 1965).

In eq. (8), the excitation energy $R^{>}_{1}$ of the first resonance state has three parts:

$$R^{>}_{1} = \Delta E_{s.p} + \Delta E_{p-h} + \Delta E_{pairing} \tag{11}$$

where $\Delta E_{s.p.}$ is due to single particle excitation energy difference between a lower and a higher orbit, ΔE_{p-h} is the effect of the two-body residual interaction on the excitation of the particle and $\Delta E_{pairing}$ is the change in the pairing energy caused by breaking or creation of each pair. For the single particle energies for the neutrons *as well as protons* we use the sequence and the values as given for neutrons by Hillman & Grover (1969). For ^{66}Cu, the centroid of the first resonance GT_+ is at 2.94 MeV above the ground state of the mother. The strength $\lambda^{>}_{re}$ for each single particle transition (from orbit $r \rightarrow s$) is given by

$$\lambda^{>}_{re} = \frac{\ln 2}{(g_V)^2}(6250sec)^{-1}|M^{s.p}_{GT}|^2\frac{n^r_p n^s_h}{(2j_s+1)}f(T,\mu,Q+R^{>}_{1}) \tag{12}$$

where $M^{s.p.}_{GT}$ is the single particle GT matrix element, n^p_p is the number of proton particles in orbit p and n^s_h the number of neutron holes in orbit s (with the total number of particles $(2j_s+1)$ in the daughter nucleus for its β^+ transition). For more than one possible single particle transitions, the strengths have been simply added to get the total $\lambda^{>}_{re}$ to a single state of the daughter nucleus and the energy of that state has been fixed by the scaling argument of FFNII to get the Q-value of the resonance transition. Here, a typical quenching factor of 0.5 is introduced for the GT_+ transition.

5. Rates for Nuclei in the fp-Shell

To test the predictions of the model and to fix the parameter σ_N, we calculate the half-lives of the following nuclei in the fp shell with $A > 60$: ^{69}Cu, ^{68}Cu, ^{67}Ni, ^{66}Cu, ^{65}Ni, ^{65}Co, ^{64}Co, ^{63}Co, ^{63}Fe, ^{62}Co, ^{62}Fe, ^{62}Mn and ^{61}Fe. For the 13 nuclei considered, the best fit to experimental value is obtained with $\sigma_N = 6.3$ MeV. Table 1 compares the

TABLE 1. Comparisons of Calculated and Experimental Half-Lives

Nucleus	Half-life $\tau_{1/2}$(sec) Experiment	This work	Gross theory	QRPA
^{69}Cu	171.	180.1		
^{68}Cu	31.1	25.4		
^{66}Cu	306.	305.0		
^{67}Ni	21.	46.9	94	23.
^{65}Ni	9072.	589.		
^{62}Co	90.	15.1		
^{63}Co	27.4	52.1		
^{64}Co	0.3	3.53		10.0
^{65}Co	1.25	5.64	8	8.59
^{61}Fe	358.8	34.5		
^{62}Fe	68.	197.3		
^{63}Fe	6.1	3.49	10	14.8
^{62}Mn	0.88	0.80	2	0.773

calculated free decay half-lives with the experimental values. It also gives the predictions of microscopic QRPA calculations of Klapdor *et al.* (1990) as well as those of the gross theory (Takahashi *et al.* 1973). For ^{64}Co, an Edgeworth expansion of the GT strength distribution with negative skewness of -0.3 and a $\sigma_N = 7.5$ gives the predicted half life to be 0.907 s (whereas the experimental value is 0.3 sec; note the different calculated value reported in Table 1 which is for standard σ_N and symmetric Gaussian).

The finite temperature and density results for all the nuclei show the general trend that the rates decrease with increasing density of matter in the stellar core. This trend is due to the increasing chemical potential of electrons outside the nuclei impeding the decay process. The phase space factor f is very strongly dependent on the Q value – for free decays $f \propto Q^5$ if the Coulomb correction factor F(Z,E) = 1. For transitions from a given state of the mother nucleus to daughter states of increasing excitation, the Q-value decreases and so does the phase space factor. On the other hand, the GT strength rises because one goes higher up in energy towards the centroid from the tail region. Thus there is a competition between two opposing effects. The inclusion of excited states can increase the rate by a factor as large as 11.4 as seen for ^{69}Cu at the high density of $\log \rho_{10} = -0.5$, $T = 6 \times 10^9$ K and Y_e =0.50.

Table 2 compares the β^- decay rates from the ground state and the known excited states up to 4.85 MeV to the total transition rates from these as well as the GT_+ resonance states. It is clear that the GT_+ resonance state makes an appreciable contribution only at high temperatures. Table 3 gives the electron capture rates of ^{62}Co. (The reported rates do not include the contributions from the corresponding GT_- resonances in the mother.) Rates for all 13 nuclei, cannot be reproduced here due to space restrictions but will be published elsewhere.

It is clear from the previous sections that the strength distribution of GT_- and GT_+ resonances in daughter and mother nuclei are important in calculations of beta decay rates. These have been estimated on theoretical grounds either through shell-model type calculations, QRPA or spectral distribution theory etc. However, charge exchange reactions (e.g. (n,p) or (p,n) reactions on mother and daughter nuclei for beta decay)

TABLE 2. β^- decay rates for ^{66}Cu at $Y_e = 0.42$

log ρ_{10}	T (° K)	$\lambda_{g.s.} + \lambda_{ex}$	λ_{total}	$G^< / G^>$
	3×10^9	2.65×10^{-3}	2.65×10^{-3}	0.076
-2.0	4×10^9	3.58×10^{-3}	3.64×10^{-3}	0.062
	5×10^9	4.74×10^{-3}	5.04×10^{-3}	0.059
	3×10^9	7.16×10^{-5}	7.35×10^{-5}	0.076
-1.0	4×10^9	2.44×10^{-4}	2.71×10^{-4}	0.062
	5×10^9	5.87×10^{-4}	7.32×10^{-4}	0.059

TABLE 3. Electron Capture Rates for ^{62}Co with $Y_e = 0.50$

Temperature (° K)	Capture rates	
	log $\rho_{10} = -2.0$	log $\rho_{10} = -3.0$
3×10^9	9.25×10^{-7}	1.81×10^{-8}
4×10^9	6.17×10^{-6}	3.25×10^{-7}
5×10^9	2.42×10^{-5}	2.31×10^{-6}

can probe these strength distributions [$B(GT_+)$ and $B(GT_-)$] experimentally and can serve as important input data. Approximately a dozen nuclei have been probed via the (n,p) reactions (W. P. Alford, private communication) and a somewhat larger number by the (p,n) reactions. For the case of transitions from a thermally excited GT_+ resonance state, one can use the experimentally probed T_+ distribution to appropriately weight the initial state distribution thermally. Work is in progress to utilize these data and make comparison with the β^--decay or electron capture rates of FFNII and others.

REFERENCES

Bloom, S. D. & Fuller, G. M. 1985, Nucl. Phys. A, 440, 511

Brown, B. A. & Wildenthal, B. H. 1985, Atomic Nucl. Data Tables, 33, 347

French, J. B., Kota, V. K. B., Pandey, A. & Tomsovic, S. 1988, Ann. Phys. (N.Y.), 181, 235

Fuller, G. M., Fowler, W. A. & Newman, M. J. 1982, ApJS, 48, 279

Fuller, G. M., Fowler, W. A. & Newman, M. J. 1982b, ApJ, 252, 715 (FFN II)

Gilbert, A. & Cameron, A. G. W. 1965, Can. J. Phys, 43, 1446

Hillman, M. & Grover, J. 1969, Phys. Rev., 185, 1303

Kar, K., Sarkar, S. & Ray, A. 1991, Phys. Lett. B., 261, 217; 1992, Phys. Lett. B., 277, 528

Klapdor, H. V., Metzinger, J. & Oda, T. 1990, Atomic Nucl. Data Tables, 44, 73

Kota, V. K. B. & Kar, K. 1989, Pramana, 32, 647

Moller, P. & Randrup, J. 1990, Nucl. Phys. A, 514, 1

Morita, M. 1973, Beta decay and muon capture (W.A. Benjamin, Inc).

Nakayama, K., Pio Galeao, A., & Krmpotic, F. 1982, Phys. Lett. B, 114, 217.

Nomoto, K., Shigeyama, T., Kumagai, S. & Yamaoka, H. 1991, in "Supernovae and Stellar Evolution" eds. A. Ray & T. Velusamy (World Scientific) 116.

Schenter, G.K. & Vogel, P. 1983, Nucl. Sci. Engg., 83, 393.

Takahashi, K., Yamada, J. M. & Kondoh, J. T. 1973, Atomic Nucl. Data Tables, 12, 101.

von Egidy, T., Schmidt, H. & Behkami, A. 1988, Nucl. Phys, A481, 189.

Woosley, S. E., & Weaver, T. A. 1988, Phys. Rept., 163, 79.

X-Rays and γ-Rays from SN 1987A

By S. KUMAGAI

University of Tokyo, Bunkyo-ku, Tokyo 113, Japan

Theoretical light curves and spectra of X-rays and γ-rays from SN 1987A are calculated by the Monte Carlo method, based on a model built up from the early observations of neutrinos and optical light. Comparison of the predicted radiation with observational results obtained later confirms the radiation mechanism of supernovae: γ-rays are emitted in the decays of radioactive ^{56}Co and X-rays are generated by the Compton degradation of these γ-rays. It also suggests that large scale mixing occurred and clumpy structure was formed inside the ejecta. These findings lead us to construct the model with a new distribution of elements, which is determined through comparisons of observations of X-rays and γ-rays with numerical simulations based on the assumed distribution. Using this model, the subsequent X-ray and γ-ray emission is predicted: the light curves of X-rays and γ-rays as well as their spectral evolution are in very good agreement with that expected from the radioactive decays of ^{56}Co and ^{57}Co. The mass of newly synthesized ^{44}Ti and the emission from the neutron star will be determined by future satellite and balloon-borne observations.

1. Introduction

SN 1987A has given us an invaluable chance to examine supernova theory, which has predicted the emergence of X-ray and γ-ray radiation from supernovae. Several possible mechanisms for the X-ray and γ-ray emission have been discussed, such as collision of the ejecta with circumstellar matter, nonthermal radiation from a pulsar, and Compton degradation of the line γ-rays emitted by radioactive nuclei. The observed light curve clarified the energy source of the radiation. It started to show the exponential decline $\sim$ 120 days after the explosion with an e-folding time of 111.3 days (Catchpole *et al.* 1987; Hamuy *et al.* 1988). Since this time agrees with the lifetime for ^{56}Co to decay into ^{56}Fe, we infer that the dominant energy source of the optical radiation at this stage must be the decay of ^{56}Co. The ^{56}Co is believed to come from the 8.8d decay of ^{56}Ni, which is produced by the explosive nucleosynthesis and powers the light curve in the earlier stage. The actual mechanism of the X-ray and γ-ray emission from SN 1987A was found to be Compton degradation of line γ-rays emitted at the decays of ^{56}Co. During the first few hundred days after the explosion, the ejecta absorbs most of the energy released by the decay of ^{56}Co and emits it again in ultraviolet, optical and infrared bands (see McCray 1993). However, as the optical depth of the Compton scattering becomes small due to the expansion of the ejecta, (McCray *et al.* 1987) X-rays from SN 1987A were expected to become observable by *Ginga* and Kvant (M. Itoh *et al.* 1987). The line γ-rays were also predicted to be detectable by the satellite *MIR* and *Solar Maximum Mission* (Gehrels *et al.* 1987; Chan and Lingenfelter 1987). These results mandate a more detailed prediction of the light curves of X-rays and γ-rays based on a more realistic model of SN 1987A.

2. Hydrodynamical Model of the Ejecta

To predict the radiation from SN 1987A, a model of SN 1987A proposed by Shigeyama *et al.* (1988) and Nomoto *et al.* (1987a) is employed. The progenitor was a star with $\sim 20M_\odot$ on the main sequence and developed a helium core of $\sim 6M_\odot$ as inferred from the luminosity of SK-69° 202 (Woosley *et al.* 1988b).

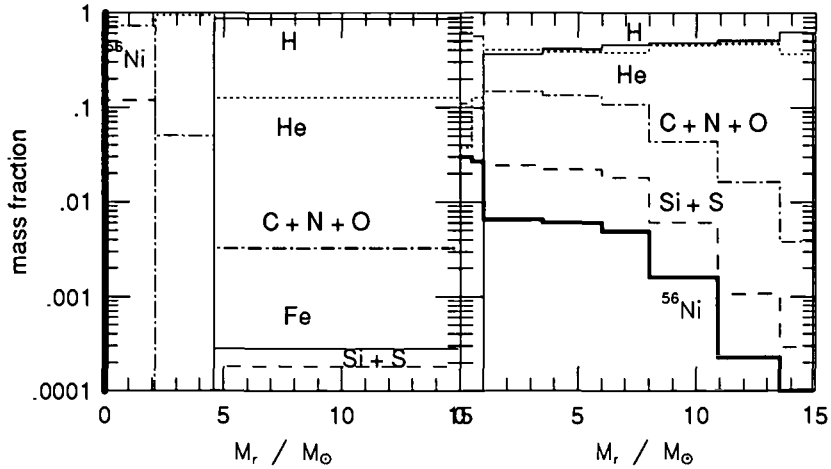

FIGURE 1. The distribution of chemical abundance of model 14E1 before mixing (left; Hashimoto *et al* 1989) and after mixing (right).

A neutron star with mass $1.4M_\odot$ was formed at the explosion, which is inferred from the observed neutrino flux. the chemical composition of the ejecta after the explosive nucleosynthesis is shown in Fig. 1 (left). The ejecta consist of a heavy element core of $2.4M_\odot$ (composed of $0.073M_\odot$ ^{56}Ni, $0.26M_\odot$ Ar-S-Si and $2.07M_\odot$ Mg-Ne-O-C), a $2.2M_\odot$ He-rich layer (4% carbon and 1% oxygen in mass fraction) and a H-rich envelope of mass $10.3M_\odot$ (including heavy elements of 1/4 times the solar abundance). Using the model of the ejecta 14E1 (Nomoto *et al.* 1987a; Shigeyama *et al.* 1988), Monte Carlo simulations are performed to follow the trails of photons inside the ejecta. In evaluating the flux at Earth, we assume the distance to the supernova to be 55 kpc.

3. X-Ray and γ-Ray Light Curves

3.1. *The effects of mixing*

Comparison of the resulting X-ray light curve (dotted curve in Fig. 2) with the early *Ginga* observations (*crosses*; Dotani *et al.* 1987), suggests large scale mixing in the ejecta (M. Itoh *et al.* 1988; Kumagai *et al.* 1988a, 1992; Nomoto *et al.* 1991a, 1991b). Monte Carlo simulations are conducted assuming the region of mixing, and the results show that the model with mixing at $M_r < 13.5M_\odot$ most consistently reproduces the light curve (dashed curve in Fig. 2) with the *Ginga* observation till $300^{\rm d}$ after the explosion. The resulting chemical composition is shown in Fig. 1 (right). After mixing, ^{56}Ni is mixed up to $M_r = 13.5M_\odot$ where the expansion velocity of the material amounts to 4200 km s^{-1}. The column depth to this layer is 2.4 g cm^{-2} at $t = 200^{\rm d}$. At early times, the emergent X-rays originate from ^{56}Co at the outermost layers. Later, the γ-rays and X-rays from ^{56}Co in the deeper layer contribute. Though the mass fraction of original ^{56}Co is much larger in the core than in the envelope, the emergent flux does not increase so steeply because most of the ^{56}Co has already decayed and the absorption by the core material is larger. Thus, the X-ray light curve shows a relatively broad peak. Accordingly, the dashed curve is in good agreement with the *Ginga* observations up to $\sim 300^{\rm d}$.

Fig. 3 shows the calculated line γ-ray light curves based on the above chemical distribution. They are all consistent with *SMM* and balloon borne observations. The early emergence of γ-rays in the model is due to the mixing of ^{56}Co out to $M_r \sim 13.5M_\odot$.

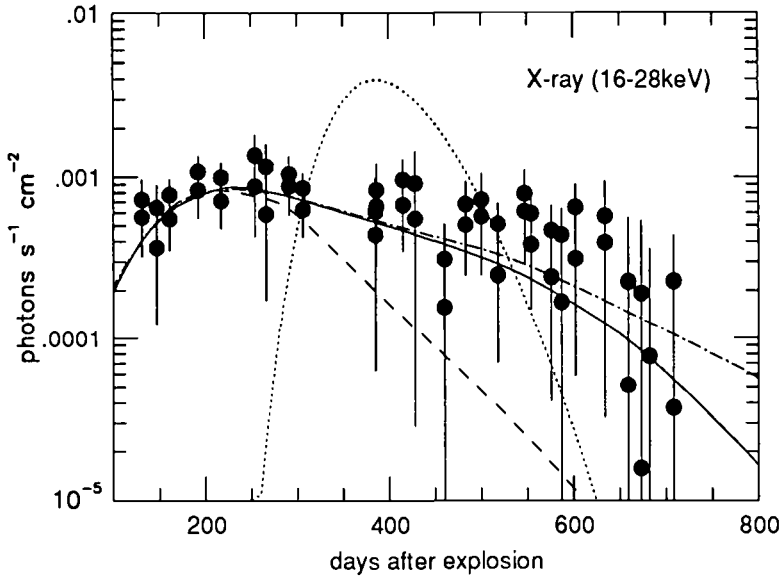

FIGURE 2. X-ray light curves calculated by Monte Carlo simulation based on the model 14E1 (Nomoto *et al.* 1987a: Shigeyama *et al.* 1988) The dotted curve is in the case without mixing and the dashed curve corresponds to spherical mixing at $M_r < 13.5M_\odot$. The solid curve is for the model with the reduction of the photo-electric opacity by a factor 10 at $M_r < 8M_\odot$ in addition to mixing and the dash-dotted curve is obtained by taking account of the effect of ^{57}Co, comparing the *Ginga* observation (Inoue 1991).

The flux ratio between 847 keV and 1238 keV line γ-rays is close to unity at early stages because of the smaller cross section for 1238 keV than for 847 keV. It approaches the experimental value of 0.68 as the column depth decreases.

The predicted light curves of line γ-rays from the decays of ^{57}Co and ^{44}Ti are shown in Fig. 4 (Kumagai *et al.* 1992). Recently, the Compton Gamma Ray Observatory detected the 122 keV line originating from ^{57}Co (Kurfess *et al.* 1992). These observations imply that the isotope ratio of ^{57}Ni and ^{56}Ni synthesized at the explosion 1.5 ± 0.5 times the solar ratio, which is consistent with the velue 1.7 from nucleosynthesis theory. Future observations of these lines should confirm the amount of radioactive nuclei and, hence, the nucleosynthesis theory.

3.2. *The effects of clumps*

At later times, $t > 300^{\rm d}$, the 16 – 28 keV X-ray flux observed by *Ginga* (Inoue 1991) declines very slowly, while the calculated X-ray flux (the dashed curve in Fig. 2) decreases significantly faster than the observation. To be more realistic, we should take account of the effect of clumps on the X-ray absorption in the core, though the above calculation assumes homogeneous and spherically symmetric mixing, which maximizes the absorption.

If the heavy elements are localized in particular clumps, a large fraction of the X-rays could be transported through the hydrogen and helium-rich regions without suffering much photoelectric absorption; this would effectively reduce the opacity. A calculation assuming the photoelectric opacity to be reduced by a factor 10 in $M_r < 8M_\odot$ gives the X-ray light curve most consistent with the *Ginga* observation (solid curve in Fig. 2). The most probable mechanism to mix the supernova ejecta is the Rayleigh-Taylor instability. Numerical simulations of such mixing have been carried out by Arnett *et al.* (1989b), Hachisu *et al.* (1989). For example, Hachisu *et al.* (1989) shows that the materials of Si

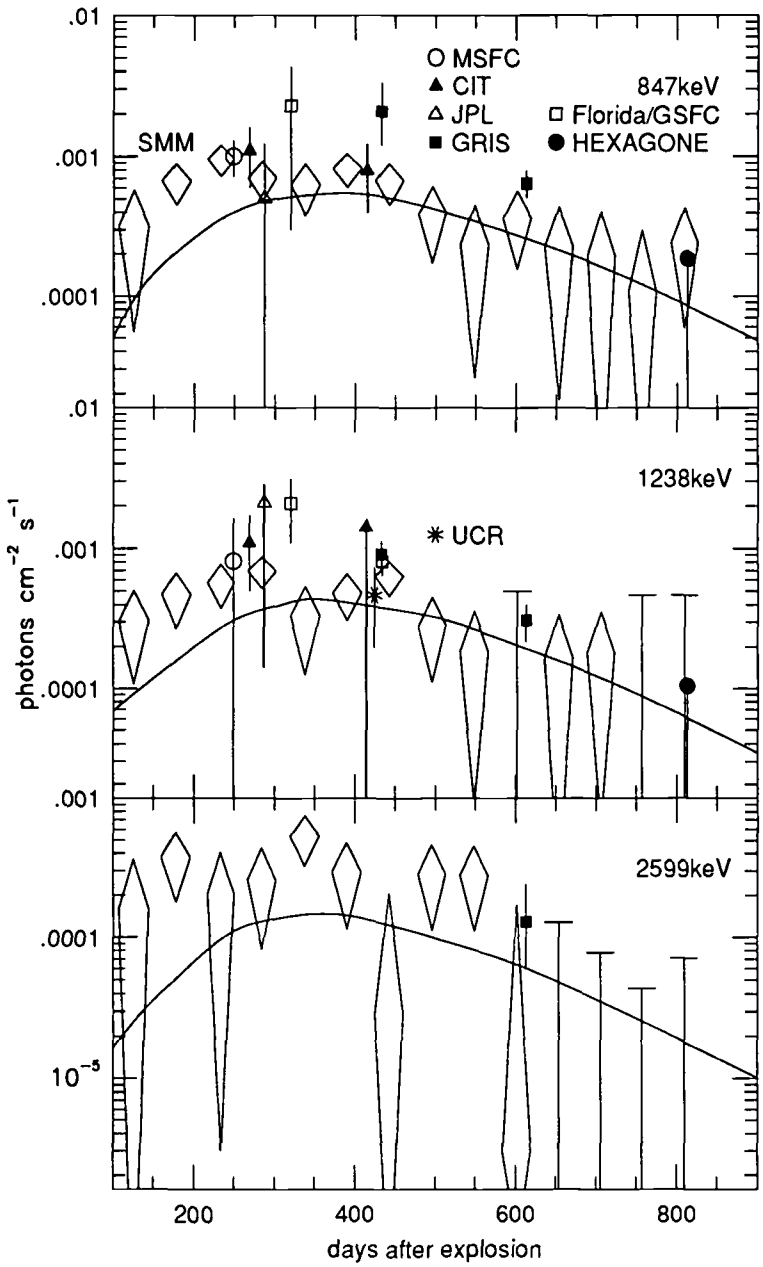

FIGURE 3. The calculated and observed line γ-ray light curves of 847 keV (upper), 1238 keV (middle), and 2599 keV (lower) of model 14E1 comparing with the observation of *SMM* (*diamonds*: Gehrels *et al.* 1987) and balloons (*crosses*: Sandie *et al.* 1988; Cook *et al.* 1988; Mahoney *et al.* 1988; Rester *et al.* 1989).

and O-rich layer are mixed up to $M_r = 8M_\odot$, where the expansion velocity is $\sim$ 2200 km s^{-1}, and that hydrogen is mixed down to $M_r = 1M_\odot$ at the same time. These results can explain the occurrence of mixing in the ejecta, but cannot completely reproduce the extent of ^{56}Co mixing to outer layers presented by the X-ray, γ-ray, and infrared observations.

The dash-dotted curve in Fig. 2 adds a contribution from the decay of ^{57}Co to the

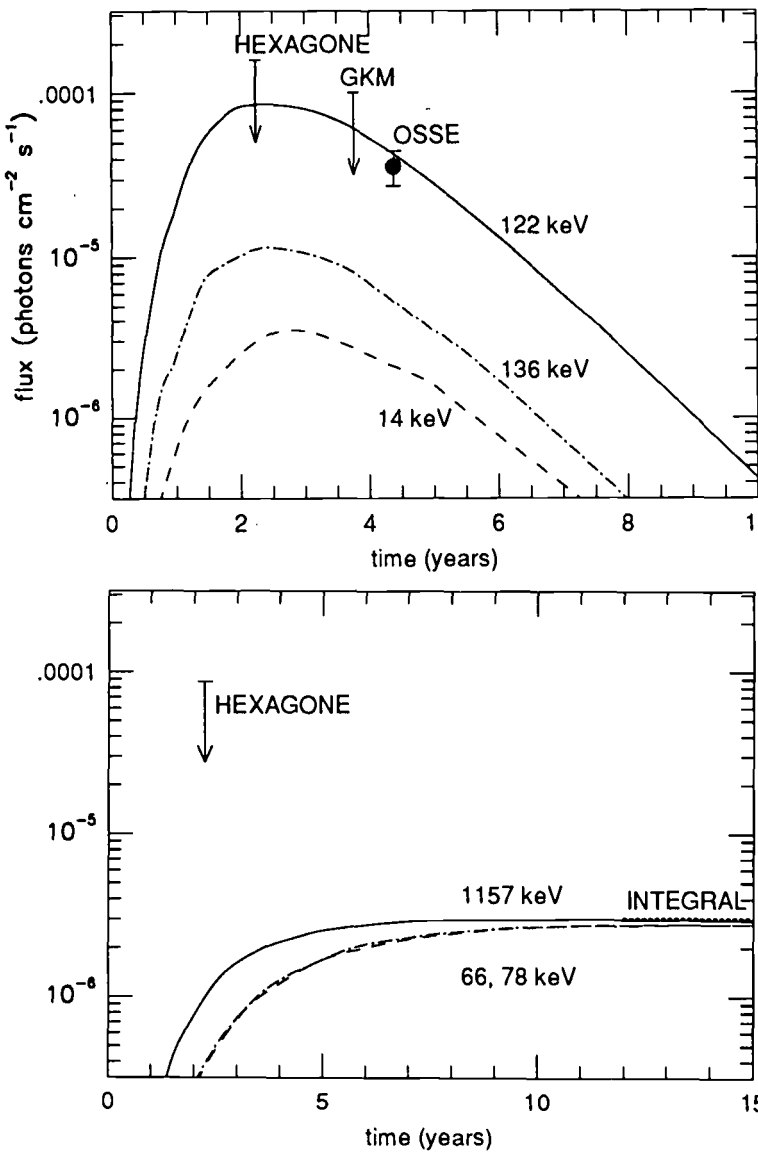

FIGURE 4. (*top*) The calculated line γ-ray light curves of 122 keV (solid curve) from ^{57}Co decay is compared with the upper limits obtained from the balloon experiments (GKM: Gunji *et al.* 1992; HEXAGONE: Chapuis *et al.* 1993) and the flux translated from the OSSE experiments (Kurfess *et al.* 1992). The light curves of 136 keV (dash-dotted curve), and 14 keV (dashed curve) are also shown. (*bottom*) The calculated line γ-ray light curves of 1154 keV (solid curve), 511 keV (dash-dotted curve), 67.9 keV and 78.4 keV (dotted curves) from ^{44}Ti, compared with the upper limit obtained with HEXAGONE (Chapuis *et al.* 1993).

solid curve, which corresponds to ^{56}Co only. This additional X-ray flux exceeds that from the ^{56}Co decay at $t > 600^{d}$ and slows down the decline of the X-ray light curve. However, the effect is not sufficiently large and a reduction of the photo-electric opacity is still necessary to account for the observations for $t > 300^{d}$.

Calculated X-ray light curves of higher energy bands adding the effect of ^{57}Co, based on the mixing model obtained above are shown In Fig. 5. They also agree very well with the *MIR* observations (Sunyaev *et al.* 1988).

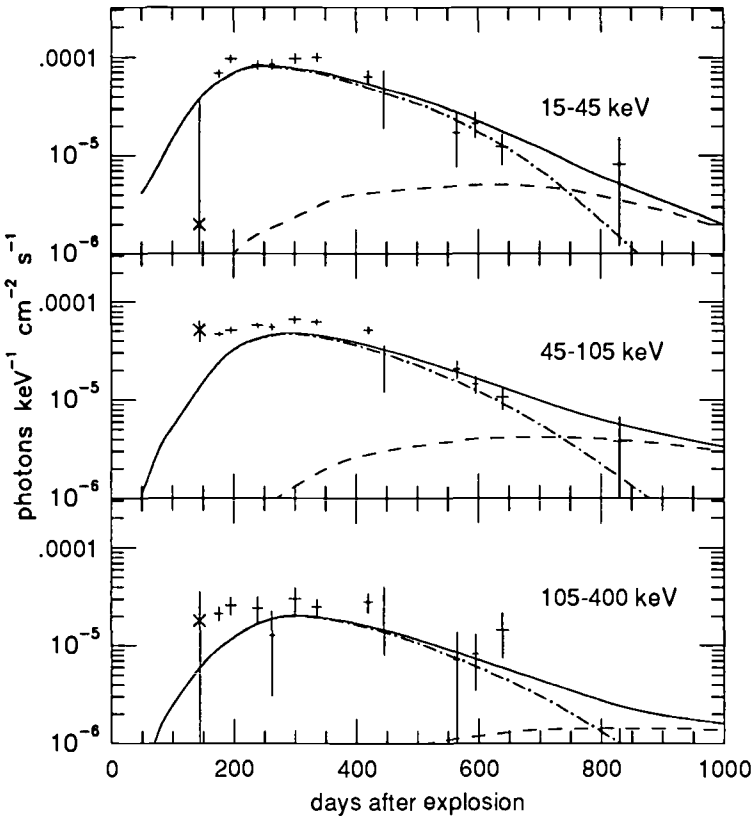

FIGURE 5. Calculated and observed light curves of $15-45$ keV (upper), $45-105$ keV (middle) and $105-400$ keV (lower). Dash-dotted lines and dashed lines are the contributions of ^{56}Co and ^{57}Co, respectively, and the solid lines are their sum. The *MIR* observations are also shown for comparison (Sunyaev *et al.* 1988, 1989).

4. X-Ray and γ-Ray Spectra

It is also important to compare theoretical calculations of the hard X-ray and γ-ray spectra from the decays of ^{56}Co and ^{57}Co with observations. Fig. 6 shows this comparison. The calculated spectra for $E \gtrsim 15$ keV are in good agreement with the observations, which implies that the down-scatterings of γ-rays and hard X-rays in SN 1987A are well modeled by our calculation. The theoretical spectrum does not appreciably change until $t \sim 400^{\rm d}$ and becomes harder as the ejecta expands and the number of Compton scattering decreases.

The dash-dotted curves in Fig. 6 show the emergent spectra due to the degraded line γ-rays from the ^{57}Co decay. Because ^{57}Co has a longer half life ($271^{\rm d}$) than ^{56}Co ($78^{\rm d}$), the X-rays below 122 keV are dominated by the ^{57}Co component for $t > 600^{\rm d}$. This fact is evident in the dash-dotted and solid curves in Fig. 2. It is interesting to compare the predicted hard X-ray spectrum at $t = 600^{\rm d}$ with HEXE observations (Fig. 6; Sunyaev *et al.* 1989). Without a contribution from ^{57}Co decay, the theoretical flux below 100 keV is about a factor of 2 smaller than the observed flux. With the adopted abundance of ^{57}Ni, the contributions from the decays of ^{56}Co and ^{57}Co are comparable at $t \sim 600^{\rm d}$; this choice gives excellent agreement between the predicted and the observed flux, as seen in Fig. 6. This suggests that the abundance ratio of ^{57}Ni/^{56}Ni may be about twice as large as the solar ratio as calculated by Hashimoto *et al.* (1989) (see also Sunyaev *et al.* 1989).

On the other hand, the Compton-degraded γ-rays cannot account for the X-rays below

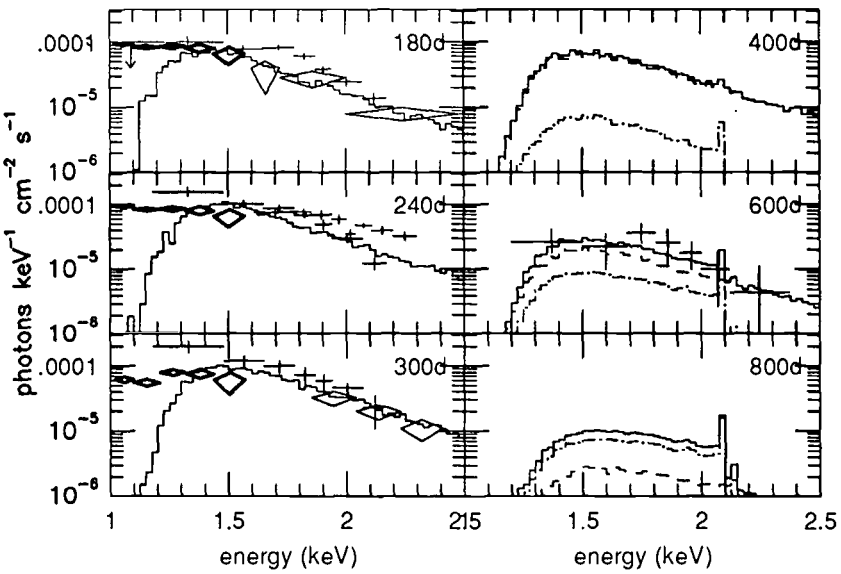

FIGURE 6. Calculated hard X-ray and γ-ray spectra due to the decays of ^{56}Co (solid curve) and ^{57}Co (dash-dotted curve) for model 14E1 with the photoelectric opacity reduced by a factor 10 for $M_r < 8M_\odot$. The thin diamonds show the spectra observed by *Ginga* (Inoue 1991); the thick diamonds and the thick crosses are observations with Pulsar X-1 and HEXE on *Kvant* (Sunyaev *et al.* 1987, 1989); and the thin crosses are balloon-borne observations (Wilson *et al.* 1988). For the figures of $t = 400^d, 600^d$, and 800^d, the ^{56}Co and ^{57}Co components are shown by the dashed and dash-dotted curves, respectively, and the solid curve is their sum.

16 keV observed by *Ginga*, which show the time variations of the intensity and spectrum. Instead, thermal emission from the ejecta heated by collision with preexisting circumstellar matter reproduces them very well (see H. Itoh *et al.* 1987; Masai *et al.* 1987, 1988).

5. Conclusions

Through the comparison of the theoretical light curves and spectra of X-rays and γ-rays from SN 1987A with observational results obtained later, we reach the following conclusions: **(1)** The high energy radiation mechanism of supernovae is confirmed: γ-rays are emitted at the decays of radioactive ^{56}Co and X-rays are generated as Compton degraded γ-rays. **(2)** A new model of supernova ejecta is constructed, in which a large scale mixing occurs and clumpy structure is formed. This model reproduces very well the optical and infrared observation. **(3)** The theoretical UV-IR light curve based on the above model is predicted to decay faster than exponential decline of ^{56}Co at ~ 300 days after the explosion, because a larger fraction of X-rays and γ-rays escape from the ejecta in this stage. This was confirmed later by the observations at SAAO, ESO, and CTIO.

With the new model described above, future X-rays and γ-rays originating from other radioactive nuclei with longer half lives, such as ^{57}Co and ^{44}Ti, and a buried neutron star are predicted. The 122 keV line γ-ray from ^{57}Co has been detected by the Compton Gamma Ray Observatory and its intensity is consistent with the prediction. The intensities of line γ-rays from ^{44}Ti should become almost constant for post-explosion times greater than 5 years and should be observable with future satellites. If a pulsar

with a luminosity of 10^{37} erg s^{-1} exists, the X-ray flux will become intense enough to be observable with *ASCA* in $\sim$ 1995 and with *ASTRO-E* in $\sim$ 2000.

Acknowledgements

It is a great pleasure to thank Professors K. Nomoto, J. Nishimura, Drs. M. Itoh and T. Shigeyama for continuous discussion and valuable comments. I am also deeply grateful to Prof. McCray for offering me an opportunity to attend the meeting.

REFERENCES

Arnett, W. D. 1988, ApJ, 331, 337

Arnett, W. D. & Fu, A. 1989a, ApJ, 340, 396

Arnett, W. D., Fryxel, B. A. & Müller, E. 1989b, ApJ, 341, 163

Bouchet, P., Danziger, I. J. & Lucy, L. 1991a, In SN1987A and other Supernovae, ed. I. J. Danziger (ESO; Garching), p. 281.

Bouchet, P., Danziger, I. J. & Lucy, L. 1991b, AJ, 102, 1135

Burrows, A. & Lattimer, J. M. 1987, ApJ, 318, L63

Burrows, A. & The, L.-S. 1990, AJ, 100, 1575

Catchpole, R. M. *et al.* 1987, MNRAS, 229, 15

Catchpole, R. M. *et al.* 1988, MNRAS, 231, 75

Catchpole, R. M. *et al.* 1989, MNRAS, 237, 55

Chan, K.W. & Lingenfelter, R.E. 1987, ApJ, 318, L51

Chevalier, R. A. & Fransson, C. 1987, Nature, 328, 44

Cook, W. R. *et al.* 1988, ApJ, 334, L87

Danziger, I. J. *et al.* 1989, In Big Bang, Active Galactic Nuclei and Supernovae, ed. S. Hayakawa and K. Sato (Universal Academy Press; Tokyo), p. 249.

Dotani, T. *et al.* 1987, Nature, 330, 230

Ensman, L. & Woosley, S. E. 1988, ApJ, 333, 754

Filippenko, A. V., Porter, A. C. & Sargent, W. L. W. 1990, AJ, 100, 1575

Gehrels, N., MacCallum, C. J. & Leventhal, M. 1987, ApJ, 320, L19

Hamuy, M., Suntzeff, N. B., Gonzalez, R. & Martin, G. 1988, AJ, 95, 63

Hashimoto, M., Nomoto, K. & Shigeyama, T. 1989, A&A, 210, L5

Inoue, H. *et al.* 1991, PASJ, 43, 213.

Itoh, H., Hayakawa, S., Masai, K. & Nomoto, K. 1987, PASJ, 39, 529

Itoh, M. *et al.* 1987, Nature, 330, 233

Itoh, M. *et al.* 1988, In Atmospheric Diagnostics of Stellar Evolution, ed. K. Nomoto (Springer; Berlin), Lecture Notes in Physics, 305, pp. 446

Kirshner, R. *et al.* 1987, ApJ, 320, 602

Kumagai, S. *et al.* 1988a, A&A, 197, L7

Kumagai, S. *et al.* 1988b, In Supernovae 1987A in the Large Magellanic Cloud, ed. M. Kafatos and A. Michalitsianos (Cambridge University Press; Cambridge), p. 414.

Kumagai, S. *et al.* 1989, ApJ, 345, 412

Kumagai, S., Shigeyama, T. & Nomoto, K. 1991a, In SN1987A and other Supernovae, ed. I.J. Danziger, (ESO; Garching), p. 203

Kumagai, S. *et al.* 1991b, A&A, 243, L13

Kumagai, S. & Nomoto, K. 1991c, In Frontiers of X-ray Astronomy, ed. Y. Tanaka (Universal Academy Press; Tokyo), p. 375

Kumagai, S. 1992, Ph.D. thesis, University of Tokyo. In Frontiers of X-ray Astronomy, ed. Y. Tanaka (Universal Academy Press; Tokyo), p. 375

Kurfess, J. D. *et al.* 1992, ApJ, 399, L137.

Leibundgut, B. *et al.* 1991, ApJ, 371, L23

Mahoney, W. A. *et al.* 1988, ApJ, 334, L81

Makino, F. *et al.* 1987, ApJ, 25, 223

Masai, K. *et al.* 1988, Nature, 335, 804

McCray, R., Shull, J. M. & Sutherland, P. 1987, ApJ, 317, L73

McCray, R. 1993, ARA&A, 31, 175

Nagasawa, M. *et al.* 1988, PASJ, 40, 691

Nomoto, K. *et al.* 1987, In SN1987A, ed. I. J. Danziger, (ESO; Garching), p. 325.

Nomoto, K. *et al.* 1991a, in Supernovae, ed. S.E. Woosley (Springer), p. 176

Nomoto, K. *et al.* 1991b, In Supernovae and Stellar Evolution, eds. A. Ray and T. Velusamy (World Scientific; Singapore), p. 116

Rester, A. C. *et al.* 1989, ApJ, 342, L71

Sandie, W. G. *et al.* 1988, ApJ, 334, L91

Shigeyama, T. *et al.* 1987, Nature, 328, 320

Shigeyama, T., Nomoto, K. & Hashimoto, M. 1988, A&A, 196, 141

Suntzeff, N.B. *et al.* 1991, AJ, 102, 1118

Sunyaev, R. A. *et al.* 1987, Nature, 330, 227

Sunyaev, R. A. *et al.* 1988, Soviet Ast. Lett., 14, 247

Sunyaev, R. A. *et al.* 1989, Soviet Ast. Lett., 15, 291

Wheeler, J. C. & Harkness, R. 1990, Rep. Prog. Phys., 53, 1467

Whitelock, P. A. *et al.* 1988) MNRAS, 234, 5

Wilson, R. B. *et al.* 1988, In Nuclear Spectroscopy of Astrophysical Sources, ed. N. Gehrels and G. Share (AIP; New York) p. 6655

Woosley, S. E. & Weaver, T.A. 1986, ARA&A, 24, 205

Woosley, S. E., Pinto, P. A., Martin, P. G. & Weaver, T. A. 1987, ApJ, 318, 664

Woosley, S. E., Pinto, P. & Ensman, L. 1988, ApJ, 324, 466

Woosley, S. E. 1988, ApJ, 330, 218

Xu, Y., Sutherland, P., McCray, R. & Ross, R. R. 1988, ApJ, 327, 197

Spectrophotometry of SN 1987A from the Kuiper Airborne Observatory

By DIANE H. WOODEN

NASA Ames Research Center, MS 245-6, Moffett Field, CA 94035-1000, USA

Explosion calculations of SN 1987A generate pictures of Rayleigh-Taylor fingers of radioactive ^{56}Ni (^{56}Ni $\rightarrow$ ^{56}Co $\rightarrow$ ^{56}Fe) which are boosted to velocities of several thousand km s^{-1}. From the KAO observations of the mid-IR iron lines, a picture of the iron in the ejecta emerges which is consistent with the 'frothy iron fingers' having expanded to fill about 50% of the metal-rich volume of the ejecta ($v_m \leq 2500$ km s^{-1}). The ratio of the nickel line intensities $I([Ni\ I]7.5\mu m)/I([Ni\ II]6.6\mu m)$ yields a high ionization fraction of $x_{Ni} \geq 0.9$ in the volume associated with the iron-group elements at day 415, before dust condenses in the ejecta.

From the KAO observations of the dust's thermal emission (2 μm – 100 μm), it is deduced that when the grains condense their infrared radiation is trapped, their apparent opacity is gray, and they have a surface area filling factor of about 50%. The dust emission from SN 1987A is featureless: no 9.7 μm silicate feature, nor PAH features, nor dust emission features of any kind are seen at any time. The total dust opacity increases with time even though the surface area filling factor and the dust/gas ratio remain constant. This suggests that the dust forms along coherent structures which can maintain their radial line-of-sight opacities, i.e., along fat fingers. The coincidence of the filling factor of the dust and the filling factor of the iron strongly suggests that the dust condenses within the iron, and therefore the dust is iron-rich. It only takes $\sim 10^{-4}$ $M_\odot$ of dust for the ejecta to be optically thick out to $\sim$100 μm; a lower limit of 4×10^{-4} $M_\odot$ of condensed grains exists in the metal-rich volume, but much more dust could be present.

References to KAO observations of SN 1987A include efforts by principal authors Colgan, Dwek, Erickson, Haas, Harvey, Moseley, Rank, Witteborn, & Wooden.

---

1. Iron in SN 1987A

In the first week following the explosion of SN 1987A, the rapid radioactive decay of ^{56}Ni $\rightarrow$ ^{56}Co deposited about 40% of the total ^{56}Ni decay energy into the inner regions of the ejecta forming a hot low density 'nickel bubble' interior to denser overlying layers. This bubble and the denser overlying layers became Rayleigh-Taylor unstable, boosting fingers or bullets of ^{56}Co and iron-group elements to velocities $\sim 3000\ km\ s^{-1}$, penetrating the outer layers of the ejecta. (Without the 'popping of the nickel bubble' the iron group elements are expected to have reached velocities of only about 1000 $km\ s^{-1}$.) Models which include this mixing of ^{56}Co into the outer layers of the ejecta are required to fit the bolometric light curve, to account for the early appearance of x–rays and γ–rays, and to explain the observed γ–ray line ratios. These indirect observations which require models with mixing provoke the following questions regarding the emission lines from the iron-group elements: Do the iron lines provide evidence for the finger structures or high velocity bullets? Does the evolution of the lines indicate how much of the ejecta volume is filled by these fingers? Is there evidence for a large variation in density in the bullets or fingers?

The mid-IR iron forbidden lines are ideal for probing the physical conditions of the iron in the ejecta. They are well separated in wavelength, have upper levels within a few thousand degrees of the ground state, have critical densities of about 10^4 cm^{-3}, and their level populations are well approximated by LTE (Li, McCray, & Sunyaev 1993). The

strongest mid-IR iron lines include the [Fe II] $a^6D_{7/2} - a^6D_{9/2}$ 25.99 μm ground-state transition, and the [Fe II] $a^4F_{7/2} - a^4F_{9/2}$ 17.94 μm and [Fe II] $a^4F_{5/2} - a^4F_{7/2}$ 24.52 μm excited state transitions. With an excitation temperature of only 554 K, the 25.99 μm line intensity is insensitive to electron temperature and most sensitive to local density. The 18 μm line with $E_u/k = 3496$ K and the 24.5 μm line with $E_u/k = 4083$ K depend on electron temperature but have only a fraction of the optical depth as the 26 μm line, as shown in Figure 1a. The near-IR [Fe II] $a^6D_{9/2} - a^4D_{7/2}$ 1.26 μm multiplet member has an excitation temperature greater than 11000K; the 1.26 μm line intensity is very temperature sensitive while its optical depth is negligible.

Figure 1 demonstrates how the electron temperatures derived from the mid-IR line intensity ratios drop substantially when the assumption of optically thin lines (open symbols) is abandoned and the optical depths in the lines are considered (solid symbols and shaded areas). For level populations in LTE, the line intensity is proportional to the product of the upper level population and the escape probability: $I_{ul} \propto N_u(T_e)\ A_{ul}\ P_{esc}(\tau_{lu})$, where the escape probability is given by $P_{esc}(\tau) = (1 - exp(-\tau))/\tau$. The line optical depth is a local phenomenon; in the Sobolev approximation where different velocity components in a line are taken to arise in different physical regions in the ejecta, the optical depth $\tau_{lu}(v)$ in a part of the line depends on the local density in the ejecta at that velocity v (Li *et al.* 1993 Eq. 9):

$$\tau_{lu}(v) = \frac{\lambda_o^3 t}{8\pi} \frac{g_u}{G(T_e)} A_{ul}\, e^{-E_l/kT_e} \left(1 - e^{-(E_u - E_l)/kT_e}\right) N_{Fe^+}(v).$$

If the line is not velocity-resolved, then the optical depth $\bar{\tau}_{lu}$ represents the average of the local conditions in the nebula. The density drops with time as $N \propto t^{-3}$ as the ejecta expands homologously, correspondingly the line optical depth drops as $\tau \propto t^{-2}$; as the line optical depth drops, the line intensity should increase as $I_{ul} \propto t^2$ if the temperature is constant.

As shown in Figure 1b, at 250 days the ratio $I_{18\mu m}/I_{26\mu m}$ yields an electron temperature of $T_e = 6000^{+2000}_{-1000} K$ in the optically thin limit (Moseley *et al.* 1989a). If both ratios $I_{18\mu m}/I_{26\mu m}$ and $I_{24.5\mu m}/I_{26\mu m}$ are considered simultaneously, then a solution is reached with $T_e = 3250 \pm 750$ K and $\bar{\tau}_{26\mu m} = 3 \pm 1$.

At 250 days, only 0.019 $M_\odot$ of Fe^+ are seen in the 26 μm line (Moseley *et al.* 1989a), equal to about 1/3 of the total iron mass existing from the radioactive decay of 0.075 $M_\odot$ of ^{56}Co, and consistent with the optical depth of $\bar{\tau}_{26\mu m} \simeq 3$ derived from the mid-IR line ratios and a high ionization fraction. The non-detection of the mid-IR [Fe I] and [Fe III] forbidden lines also supports a high singly-ionized iron ionization fraction. To produce the optical depth in the 26 μm line, an average local number density of Fe^+ ions of $\bar{N}_{Fe+} = 2.6^{+1.6}_{-1.2} \times 10^6\ cm^{-3}$ is required. This is equal within the uncertainties to the average number density obtained if all the iron is singly-ionized and spread throughout the metal-rich volume (for $x_{Fe} = 1$, $M_{Fe}(250\ days) = 0.067\ M_\odot$, and $v_m(FWHM) = 2500\ km\ s^{-1}$, then $\bar{N}_{Fe+} = 2.2 \times 10^6\ cm^{-3}$). If $x_{Fe} \simeq 0.6$, as deduced from the optically thin near-IR [Fe II] 1.26 μm line at 192 and 225 days (Oliva *et al.* 1987 and Meikle *et al.* 1989, respectively), then the iron ions have a volume filling factor of $f = 0.5^{+0.4}_{-0.2}$. For an ionization fraction of $x_{Fe} = 0.8$ and a higher electron temperature of $T_e \approx 4000$ K, the iron ions have a volume filling factor of $f \geq 0.4$ (as shown by Li *et al.* 1993 in their simultaneous fitting of many cobalt, iron, and nickel lines). Thus the 'frothy iron fingers' must fill about 50% of the metal-rich volume in order to produce the observed optical depth of the 26 μm line: the iron is seen as the leavening in the $\sim$1 $M_\odot$ metal-rich volume.

As shown in Figure 1c, at 415 days the ratio $I_{18\mu m}/I_{26\mu m}$ yields an electron temper-

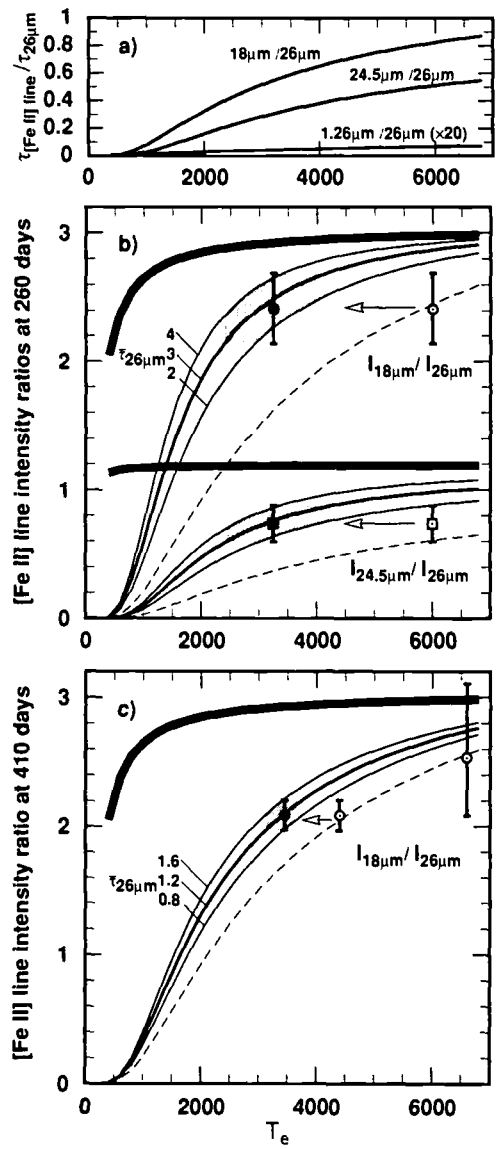

FIGURE 1. a.– τ *vs* T_e; b&c.– [Fe II] line intensity ratios *vs* T_e and $\tau_{26\mu m}$.

ature of $T_e = 6600^{+2800}_{-1700} K$ in the optically thin limit (Haas *et al.* 1990). The 18 μm and the 26 μm lines were measured with a velocity resolution of $\sim$ 400 km s^{-1}, thus providing the velocity-resolved intensity ratio $I_{18\mu m}(\Delta v)/I_{26\mu m}(\Delta v)$ shown in Figure 2a ($(26\mu m/18\mu u)\times$Fig. 3 from Haas *et al.* ; private communication from Colgan). The statistically weighted average over the best signal-to-noise points (solid circles in Figure 2a) yields an average velocity-resolved line intensity ratio of $\langle I_{18\mu m}(\Delta v)/I_{26\mu m}(\Delta v)\rangle = 2.1 \pm 0.1$. This average velocity-resolved line intensity ratio yields an electron temperature of $T_e = 4400 \pm 400 K$ in the optically thin limit as shown in Figure 1c, equal to that derived by Haas *et al.* Between 250 days and 410 days the average optical depth in the 26 μm line is expected to drop a factor of $\sim$ 2.7: $\bar{\tau}_{26}(410\ days) = 3 \pm 1 \rightarrow \bar{\tau}_{26}(410\ days) = 1.2 \pm 0.4$. Taking this range for $\bar{\tau}_{26}(410\ days)$, the electron temperature is $T_e = 3450 \pm 650\ K$, in the same range as the electron temperature derived at 250 days.

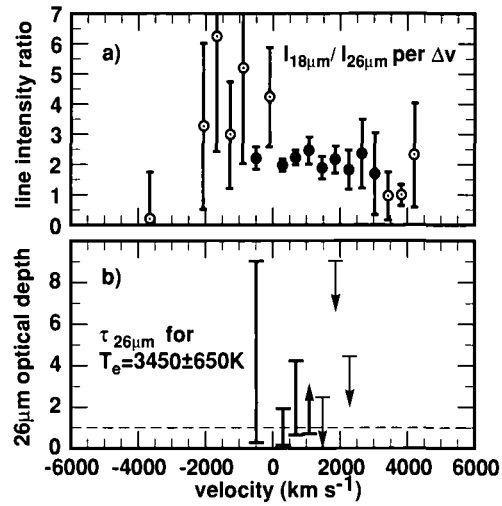

FIGURE 2. (410 days) a.– velocity-resolved line intensity ratio. b.– $\tau_{26\mu m}$.

Figure 2b shows the velocity-resolved optical depth in the 26 μm line for $T_e = 3450 \pm 650\ K$. Different regions of the ejecta corresponding to velocities between 1000 $km\ s^{-1}$ and $-3000\ km\ s^{-1}$ have 26 μm line optical depths ranging from less than one to several, and are thus consistent with an average optical depth of $\bar{\tau}_{26\mu m} \simeq 1$.

Moseley's measurement of the 26 μm line intensity at 395 days yields an Fe^+ mass of 0.033 $M_\odot$ (Dwek 1988), an increase of only 1.7 over the 0.019 $M_\odot$ deduced at 250 days; the iron mass does increases due to an increase in transparency of the 26 μm line, but not by the factor of 2.7 from the expected drop in optical depth. The measurements of the 26 μm line by the Cooled Grating Spectrometer at 250 days (Erickson *et al.* 1988; $\Delta v = 1900\ km\ s^{-1}$) and 410 days (Haas *et al.* 1990; $\Delta v = 400\ km\ s^{-1}$) show, however, no increase in the 26 μm line intensity between these two epochs. Haas *et al.* (1990) argue that the failure of the 26 μm line strengths to increase between 250 days and 410 days implies that the line emission arises from optically thin iron, and the hidden iron is very optically thick. This argues against the line intensity ratios providing a meaningful average optical depth $\bar{\tau}_{26\mu m}$, and argues in favor of regions with $\tau_{26\mu m} < 1$ and other regions with $\tau_{26\mu m} \gg 1$.

If there are regions in the ejecta with $\tau_{26\mu m} \gg 1$, they probably would not be seen in the 18 μm line profile, but could seen in the near-IR 1.26 μm line profile ($\tau_{1.26\mu m} = (0.006 - 0.009) \times \tau_{26\mu m}$ for $T_e = 3000 - 5000$ K). Haas *et al.* (1990)'s Fig. 3 shows the comparison of the 18 μm line profile at 407 days with the 1.26 μm line profile at 377 days. The central portions of the near-IR and the mid-IR line profiles are the same. Furthermore, the detailed shapes of the near-IR forbidden line profiles remain essentially unchanged from 250 days through about 600 days (Spyromilio, Meikle, & Allen 1990); for nearly a year there is no further 'revealing' of highly optically thick iron as the ejecta expands. Thus, there is little evidence from the near-IR forbidden lines for iron in the ejecta with $1 \ll \tau_{26\mu m} < 100$. While the evolution of the 26 μm line intensity provides a challenge, together the temporal constancy of the optically thin near-IR [Fe II] line profiles, the sameness of the near-IR and mid-IR [Fe II] line profiles, and the ratio of the 18 μm to the 26 μm line profiles support the 'frothy iron finger' picture.

The velocity structure of Doppler-broadened profiles can arise through blending, optical depth, electron scattering from an expanding envelope, or asymmetry in the line-

emitting region. Blending and optical depth effects are negligible for the 18μm and 1.26μm lines. Electron scattering shifts the line centroid redward and produces a strong asymmetric red wing (Fransson & Chevalier 1989). Witteborn *et al.* (1989) model the profile of the [Ar II] 6.98 μm line by spherically symmetric electron scattering from the low density 10 $M_\odot$ H envelope with an ionization fraction of 10%, requiring an optical depth of $\tau_e \sim 0.4$ at 415 days. A more recent analysis by Xu *et al.* (1991) indicates that the hydrogen volume emission measure arises from a 1% ionization fraction high-density 1 $M_\odot$ H region near or within the metal-rich volume which produces a negligible electron scattering optical depth. We then are left to consider the asymmetric line profiles as arising from an asymmetric distribution of high-velocity fingers of iron-group elements (Spyromilio *et al.* 1990). The spatially inhomogeneous distribution of iron-group elements arises first by the Rayleigh-Taylor instabilities in the early phases of the explosion, as demonstrated by hydrodynamic simulations by Fryxell, Arnett, & Muller 1991, Herant, Benz, & Colgate 1992, and others. Secondly, the hot ^{56}Co clumps or fingers do work on the surrounding gas, compressing the non-iron group elements and expanding to fill roughly half the metal-rich volume of the ejecta (Li *et al.* 1993).

2. Stable Nickel in the Ejecta

Stable nickel is created along with radioactive nickel in explosive silicon burning and thereby is a trace constituent of the iron-group fingers in the ejecta. All forbidden lines of all ionic species of nickel arising from ground state terms with $E_u/k \leq 5000\ K$ occur in the 2 μm – 14.5 μm wavelength range, including [Ni I], [Ni II], [Ni III], and [Ni IV]. Spectra of the [Ni I] and [Ni II] forbidden lines were obtained from the KAO at 260, 415, 615, 775, and 1140 days (Wooden *et al.* 1993, Colgan *et al.* 1994, Witteborn *et al.* 1990). Forbidden lines of [Ni III] and [Ni IV] were not detected. Owing to the relatively low abundance of nickel compared to iron, the mid-IR forbidden lines of stable nickel suffer less optical depth effects than the mid-IR iron lines. The nickel lines are therefore ideal for studying the degree of ionization in the inner regions of the ejecta.

The only singly-ionized nickel forbidden line with $E_u/k < 10000K$ is the ground state [Ni II] $a^2D_{3/2} - a^2D_{5/2}$ 6.634 μm line with $E_u/k = 2168\ K$; this is the strongest mid-IR forbidden line in the spectrum of SN 1987A through 1140 days. The [Ni II] 6.6 μm line has a critical density of $10^7\ cm^{-3}$ (Nussbaumer & Storey 1988) and must be treated in non-LTE. The strongest mid-IR neutral nickel transition is the ground state [Ni I] $a^3F_3 - a^3F_4$ 7.507 μm line with $E_u/k = 1917\ K$, although there are other [Ni I] forbidden lines at 3.12 μm, 3.95 μm, 5.89 μm, 11.308 μm, and 12.00 μm. The [Ni I] 7.5 μm line has a critical density of $\sim 10^5\ cm^{-3}$, derived using the estimated collision strengths by Hollenbach and McKee (1989) at $T_e \simeq 3000\ K$ (Wooden *et al.* 1993). The [Ni I] 7.5 μm and the [Ni II] 6.6 μm lines originate from upper levels with nearly identical excitation energies. The ratio of these two lines, $I([Ni\ I]7.5\mu m)/I([Ni\ II]6.6\mu m)$, is independent of the electron temperature for $T_e \leq 1000\ K$, weakly dependent on the electron density n_e, and highly sensitive to the ionization fraction x_{Ni}.

Figure 3 shows the predicted line ratio $I([Ni\ I]7.5\mu m)/I([Ni\ II]6.6\mu m)$ as a function of nickel ionization fraction x_{Ni} for LTE ($\sim n_e \geq 10^8\ cm^{-3}$) and for electron densities $n_e = 10^7\ cm^{-3}$, $10^6\ cm^{-3}$, and $10^4\ cm^{-3}$ at $T_e = 3000\ K$. The strongest constraints for both the ionization fraction and the total nickel mass are determined by the measurements at 415 days when both the [Ni II] 6.6 μm and the [Ni I] 7.5 μm lines are optically thin. The statistically weighted averages of the low and medium resolution line strengths are $I(7.5\mu m) = 3.2 \pm 0.9 \times 10^{-18}\ W\ cm^{-2}$ and $I(6.6\mu m) = 60.2 \pm 1.2 \times 10^{-18}\ W\ cm^{-2}$ at 415 days (Wooden *et al.* 1993). For a range of elec-

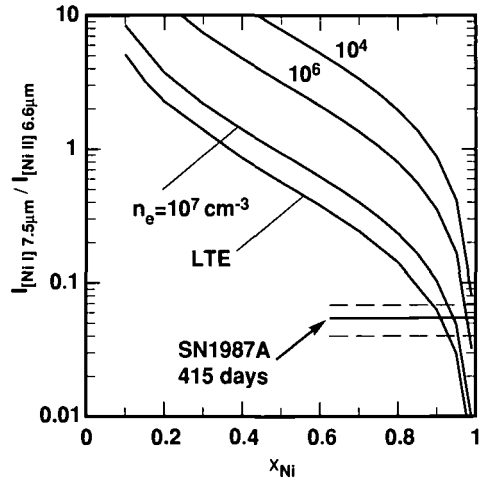

FIGURE 3. nickel ionization fraction

tron temperatures $T_e = 3000 - 4500\ K$ (Haas *et al.* 1990, Li, *et al.* 1993), the line intensity ratio $I([Ni\ I]7.5\mu m)/I([Ni\ II]6.6\mu m) = 0.05 \pm .01$ constrains the ionization fraction to be $x_{Ni} \geq 0.90$. For LTE and $x_{Ni} = 0.90$, a total stable nickel mass of $M_{Ni} = 1.8 - 2.2 \times 10^{-3}\ M_\odot$ is derived for $T_e = 4500 - 3000K$. For a lower electron density of $n_e = 5 \times 10^6\ cm^{-3}$ and $x_{Ni} = 0.95 - 0.97$, a higher mass of $M_{Ni} = 4.5 - 5.0 \times 10^{-3}\ M_\odot$ is derived (Wooden *et al.* 1993). The derived nickel ionization fraction of $x_{Ni}(415\ days) \geq 0.9$ is significantly higher than the $x_{Ni} = 0.6$ predicted by Li *et al.* (1993) for 415 days, but does agree with their predictions for times after 800 days. In Li *et al.* 's models, at about 600 days, the iron ionization fraction drops and the nickel ionization fraction increases to $x_{Ni} \approx 1$ due to charge exchange between iron and nickel, but the charge exchange rates are not enumerated; perhaps these charge exchange effects are operable at 415 days? The derived nickel mass of $M_{Ni} = 4.5 - 5.0 \times 10^{-3}\ M_\odot$ is close to the predicted nickel mass from Woosley, Pinto, & Weaver (1988)'s nucleosynthesis explosion models for an 18 $M_\odot$ and a 20 $M_\odot$ precursor but about 4 times smaller than the nickel mass predicted by Hashimoto, Nomoto, & Shigeyama (1989)'s model for a 20 $M_\odot$ precursor. The similarity of the shapes of the line profiles of the [Ni I]* 3.12 μm, [Fe II] 1.26 μm, [Fe II] 18 μm, and the [Fe II] 26 μm lines (Spyromilio *et al.* 1990, Haas *et al.* 1990) indicates that the stable nickel and the iron occupy the same volume of the ejecta. The nickel has a relatively low abundance by number compared to the iron, so the iron provides the majority of electrons which collide with and excite the forbidden nickel lines.

3. The Thermal Dust Continuum Emission

A dramatic drop in the visual light output of the supernova commenced around 530 days (Whitelock *et al.* 1989): the U to M light curve declined more rapidly than expected for the radioactive decay of ^{56}Co and the ejecta's decreasing opacity to γ–rays. This change in the light curve at 530 days signifies the rapid formation of grains in the ejecta which is supported by the following three observables:

(*a*) At 615 days, the thermalized ^{56}Co γ–ray luminosity $L_{56,\gamma}$ equals the sum of the UV, visual, and IR luminosities. The energy budget is balanced when the drop if the visual light is compensated by the increase in the thermal IR continuum (Suntzeff & Bouchet 1990).

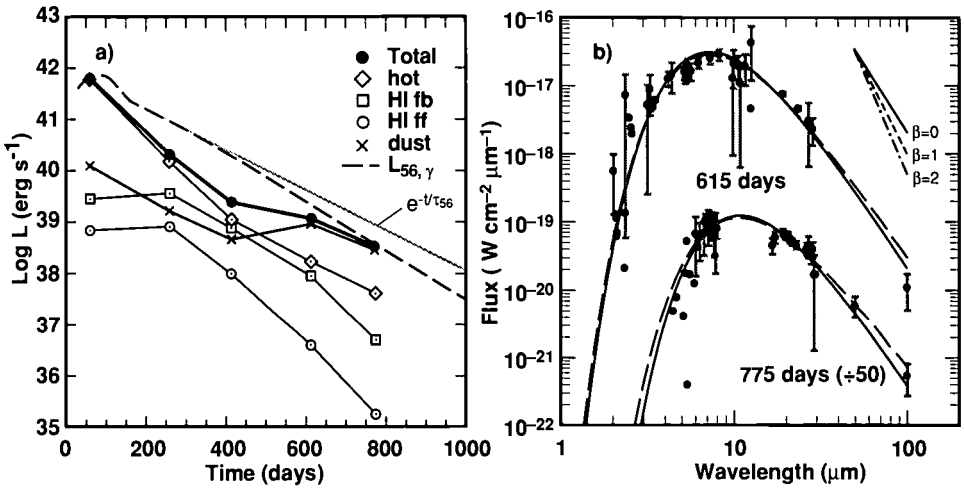

FIGURE 4. a. Temporal evolution of IR continuum luminosities. b. Dust continuum and χ^2-fits.

(*b*) If 100% of the dust luminosity at 415 days is due to an IR echo off the circumstellar ring, then at most 14% of the observed dust luminosity at 615 days can be due to the ring; at 615 days 86% or more of the observed dust luminosity is due to newly condensed dust within the ejecta (Wooden *et al.* 1993).

(*c*) After ~550 days optical line profiles of Mg I] 4571 *Å*, [O I] 6300 *Å*, [C I] 9844 *Å* (Lucy *et al.* 1989a, 1989b), and infrared profiles [Si I], [Fe II], [Ni II] become increasingly blue shifted with time (Spyromilio *et al.* 1990, Colgan *et al.* 1994). As dust condenses interior to a line-emitting volume the emission from the far side of the ejecta suffers greater extinction compared to the near side and the line centroids become blue-shifted.

The thermal dust continuum from SN 1987A comprises one of three IR continuum components, where the HI free-free plus free-bound continuum emission and the Rayleigh-Jeans tail of a hot ~5000 K blackbody continuum emission are the other two components. The best-χ^2-fit IR continuum models yield the luminosity in each of the IR continuum components at 60, 260, 415, 615, and 775 days as shown in Figure 4a (Wooden *et al.* 1993). At early times (60, 260, and 415 days), the dust luminosity is 2% – 3% of the thermalized ^{56}Co γ-ray luminosity ($L_{56,\gamma}$ - Woosley, Pinto, & Hartmann 1988). At 615 days, the dust luminosity increases dramatically to 45% of $L_{56,\gamma}$. At 775 days, the dust luminosity is 83% of $L_{56,\gamma}$. At even later times, the dust luminosity is ~90% of $L_{56+57,\gamma}$ (Bouchet - this volume).

From the KAO observations of the dust's thermal emission spectrum at 615 and 775 days, the grains have a gray emissivity out to 30 μm – 100 μm as shown in Figure 4b. This is unlike other dusty astronomical objects which show grains with emissivities which fall as $\lambda^{-\beta}$ for $\beta = 1, 2$ compared to a blackbody (Hildebrand 1983). Either the grains in the ejecta are very large with radii $a > 6\mu m$ or the optical depth of the IR emission is very high with $\tau_d(30\mu m) > 1$. An optical depth of $\tau_{d,IR}(30\mu m) \approx 1$ requires a dust mass of 3.1×10^{-4} $M_\odot$ at 615 days, and a dust mass of 5.0×10^{-4} $M_\odot$ at 775 days. (The dust masses are derived from the graybody $\beta = 0$ models shown in Fig. 4b with best-fit parameters ($\pm 3\sigma$) from Wooden *et al.* 1993: at 615 days $T_d = 400^{+12}_{-12}$, $F_d(7.8\mu m) = 3.08^{-0.40}_{+0.40} \times 10^{-17}$ $W\ cm^{-2}\ \mu m^{-1}$ and at 775 days $T_d = 266^{+23}_{-23}$, $F_d(7.8\mu m) = 0.46^{-0.15}_{+0.15} \times 10^{-17}$ $W\ cm^{-2}\ \mu m^{-1}$.) The visual light which does escape appears to suffer a λ^{-1} extinction law (Lucy *et al.* 1989a, 1989b). At 775 days, the dust mass required to produce the diffuse selective extinction by small amorphous carbon, graphite, or iron grains is an

order of magnitude smaller than the minimum dust mass derived from the IR thermal continuum (Lucy *et al.* 1989b). A larger mass of small silicate grains comparable to the optically thick dust mass would be required to produce the diffuse selective extinction, but the distinct *absence* of a 9.7 μm silicate emission feature in all mid-IR spectra and narrow band photometry of SN 1987A rules out silicate grains as the dominant grain component.

Taken together the dust's IR thermal continuum and the dust's visual extinction indicate that the grains in the ejecta of SN 1987A are small grains, with the bulk of the grains residing in optically thick regions (Lucy *et al.* 1989b, Wooden *et al.* 1993). In addition, the temporal evolution of the dust temperatures is consistent with the grains being immersed in an optically thick medium with a gas-to-dust ratio that is constant in time (Wooden *et al.* 1993). It is convenient to think of the grains in optically thick 'clumps', although the dust optical depth arises from enhanced grain column depths along the observer's line-of-sight. If the dust is at an expansion velocity of $v_d = 1800\ km\ s^{-1}$ then 400 K dust fills 55% of the surface area at 615 days and 266 K dust fills 56% of the surface area at 775 days. The surface area filling factor stays constant as the volume of the ejecta expands by a factor of 2. At 615 days, 45% of the thermalized ^{56}Co γ–ray luminosity is being reradiated as dust luminosity, requiring that 0.67 $M_\odot$ of gas be participating in converting γ–rays to UV and visible photons which in turn heat the dust. At 775 days, 83% of the thermalized ^{56}Co γ–ray luminosity is being reradiated as dust luminosity, more than doubling the mass of gas to 1.6 $M_\odot$ participating in heating the dust (Wooden *et al.* 1993). The surface area filling factor remains constant while the mass of gas participating in heating the dust more than doubles. Together this suggests that dust forms interior to and along the same radial-lines-of-sight as the first dust formed.

There is evidence for the dust condensation within the iron-rich volume of the ejecta by consideration of the change in the iron-group element emission line profiles after about 575 days. While the He I 1.083 μm, Paschen β 1.282 μm, and Mg I 1.503 μm lines become blue-shifted with the same λ^{-1} dependence as the optical Mg I] and [O I] lines, the iron-group lines ([Fe II] 1.257 μm, [Fe II] 1.553 μm, [Fe II] 1.664 μm, and [Ni I] 3.119 μm) undergo a blueward shift about three times greater (Spyromilio *et al.* 1990). At 615 days and more so at 775 days the [Ni II] 6.634 μm line also becomes blue-shifted (Colgan *et al.* 1994, Wooden *et al.* 1993). The $-440 \pm 270\ km\ s^{-1}$ blue-shift seen in the 615 day high resolution measurements of the [Ni II] 6.634μm line is successfully modeled by placement of optically thick clumps of dust distributed proportional to the gas density interior to $v_d \simeq 1900\ km\ s^{-1}$ (Colgan *et al.* 1994). The line intensities of the near-IR [Fe II] 0.716μm, 0.862μm, and the 1.258μm lines drop significantly between 575 and 735 days: the small mass of emitting iron at 735 days may be due to the iron being hidden in optically thick clumps of dust or the iron condensing into dust (Spyromilio & Graham 1992). The condensation of small iron-rich grains, i.e., Fe/Ni grains or FeS grains, in the ejecta of SN 1987A explains the observed λ^{-1} extinction law, the absence of a 9.7 μm silicate emission feature, and may, in the case of FeS grains (Pollack *et al.* 1994), provide the observed gray emissivity through far-IR wavelengths. The dusty 'clumps' could very well be the 'dusty frothy iron fingers'!

Acknowledgements

We acknowledge NASA's support of the Airborne Astronomy Program and the commitment of the staff and the crew of the Kuiper Airborne Observatory to the acquisition of this unique set of observations of SN 1987A.

REFERENCES

Colgan, S. W. J., Haas, M. R., Erickson, E. F., Lord, S. D., & Hollenbach, D. J. 1994, ApJ, 427, 824

Dwek, E. 1988, Proc. ASA, 7, 468

Dwek, E., Moseley, S. H., Glaccum, W., Graham, J. R., Loewenstein, R. F., Silverberg, R. F., & Smith, R. K. 1992, ApJ, 389, L21

Erickson, E. F., Haas, M. R., Colgan, S. E., Lord, S. D., Burton, M. G., Wolf, J., Hollenbach, D. J., & Werner, M. 1988, ApJ, 330, L39

Fransson, C. & Chevalier, R. A. 1989, ApJ, 343, 323

Fryxell, B., Miller, E., & Arnett, D. 1991, ApJ, 367, 619

Haas, M. R., Colgan, S. W. J., Erickson, E. F., Lord, S. D., Burton, M. G., & Hollenbach, D. J. 1990, ApJ, 360, 257

Harvey, P., Lester, D., Dinerstein, H., Smith, B., & Colome, C. 1989, BAAS, 21, 1215

Hashimoto, M., Nomoto, K., & Shigeyama, T. 1989, A&A, 210, L5

Herant, M., Benz, W., & Colgate, S. 1992, ApJ, 395, 642

Hildebrand, R. H. 1983, QJRAS, 24, 267

Hollenbach, D. & McKee, C. F. 1989, ApJ, 342, 306

Li, H., McCray, R., & Sunyaev, R. A. 1993, ApJ, 419, 824

Lucy, L. B., Danziger, I. J., Gouiffes, C., & Bouchet, P. 1989a, in Proc. IAU. Coll. 120, Structure and Dynamics of the Interstellar Medium, ed. G. Tenorio-Tagle, M. Moles, & J. Melnick (Berlin: Lecture Notes in Physics, Springer-Verlag), 164

Lucy, L. B., Danziger, I. J., Gouiffes, C., & Bouchet, P. 1989b, in Supernovae: The Tenth Santa Cruz Workshop in Astronomy and Astrophysics, ed. S. E. Woosley (New York: Springer-Verlag), 82

Meikle, W. P. S., Allen, D. A., Spyromilio, J., & Varani, G.-F. 1989, MNRAS, 238, 193

Moseley, S. H., Dwek, E., Glaccum, W., Graham, J. R., Loewenstein, R. F., & Silverberg, R. F. 1989a, ApJ, 347, 1119

Moseley, S. H., Dwek, E., Glaccum, W., Graham, J. R., Loewenstein, R. F., & Silverberg, R. F. 1989b, Nature, 340, 697

Nussbaumer, H. & Storey, P. J. 1988, A&A, 200, L25

Oliva, E., Moorwood, A. F. M., & Danziger, I. J. 1987, ESO Messenger, No. 50, 18

Pollack, J. B., Hollenbach, D., Simonelli, D. P., Beckwith, S., Roush, T., & Fong, W. 1994, ApJ, 421, 615

Rank, D., Pinto, P. A., Woosley, S. E., Bregman, J. D., Witteborn, F., Axelrod, T. S., & Cohen, M. 1988b, Nature, 331, 505

Spyromilio, J., Meikle, W. P. S., & Allen, D. A. 1990, MNRAS, 242, 669

Spyromilio, J. & Graham, J. R. 1992, MNRAS, 255, 671

Suntzeff, N. B. & Bouchet, P. 1990, AJ, 99, 650

Whitelock, P. A. *et al.* 1989, MNRAS, 240, 7P

Witteborn, F. C., Bregman, J. D., Wooden, D. H., Pinto, P. A., Rank, D. M., Woosley, S. E., & Cohen, M. 1989, ApJ, 338, L9

Witteborn, F. C. *et al.* 1990, BAAS, 22,1147

Woosley, S. E., Pinto, P. A., & Weaver, T. A. 1988, Proc. ASA, 7, 355

Woosley, S. E., Pinto, P. A., & Hartmann, D. 1989, ApJ, 346, 395

Wooden, D. H., Rank, D. M., Bregman, J. D., Witteborn, F. C., Tielens, A. G. G. M., Cohen, M., Pinto, P. A., Axelrod, T. S. 1993, ApJS, 88, 477

Xu, Y., McCray, R., Oliva, E., & Randich, S. 1991, ApJ, 386, 181

Infrared Spectroscopy of SN 1987A

By JASON SPYROMILIO

Anglo-Australian Observatory, P. O. Box 296, Epping NSW 2121, Australia

Infrared spectra of SN1987A have been obtained at the Anglo-Australian Telescope since the explosion of this supernova. I present highlights from this program which include the analysis of the molecular emission, the determination of the mass of ^{57}Co in the ejecta and the analysis of the emission due to dust in the ejecta. I also show the spectrum of the supernova in the infrared 5 years after explosion.

1. Introduction

Prior to the explosion of supernova 1987A only a few supernovae had been studied spectroscopically in the infrared (see Frogel *et al.* 1987; Graham *et al.* 1986). Although recently a number of very powerful common-user infrared spectrographs have become available to the community most of the observations of supernova 1987A were made using the previous generation of instrumentation. The near-infrared data discussed here were obtained at the Anglo-Australian Telescope using the FIGS and IRIS spectrographs through a collaboration of the author with Peter Meikle (Imperial College London) and David Allen (Anglo-Australian Observatory). Mid-infrared data were also obtained at the AAT using the UCLIR spectrograph by David Aitken (Australian Defence Forces Academy), Pat Roche (University of Oxford) and Craig Smith (ADFA).

Other groups have also been involved in infrared studies of supernova 1987A. The other major southern observatories (CTIO & ESO) have also presented infrared spectra of SN 1987A although these will not be discussed here. In addition the Kuiper Airborne observatory has obtained extremely valuable data in the atmospheric windows not accessible from the ground (see Wooden in these proceedings).

2. Molecular Emission

The most tightly bound molecule is carbon monoxide with a dissociation energy of 11 eV. Emission by CO had been observed in novae (Ferland *et al.* 1979). It was therefore not a major surprise that emission by CO was observed in the infrared spectra of supernova 1987A. Both the fundamental (at 4.6 μm) and the first overtone at 2.3 μm were detected. What was however a surprise was the detection of CO as early as 110 days after explosion. The analysis of Spyromilio *et al.* (1988) showed the CO expanding with a smaller velocity that was observed even for the iron group elements (see Fig. 1). The temperature of the CO was found to be around 2000 – 3000 K while the atomic species in the ejecta at the same time indicated temperatures above 4000 K. This is consistent with the high partition function that molecular species have making them extremely efficient coolants. The expansion velocity of the CO was around 2000 km/s. Manufacturing the CO in the ejecta in the hostile environment present 110 days after explosion could only be achieved if the CO was shielded from the UV recombination radiation. This was the first evidence for density inhomogeneities in the ejecta.

Emission by SiO was also seen in the spectra of SN 1987A (Meikle *et al.* 1989; Roche *et al.* 1992). The parameters derived from the fundamental band at 8.2 μm are in general agreement with those derived for the CO. Miller *et al.* (1992) have shown that features

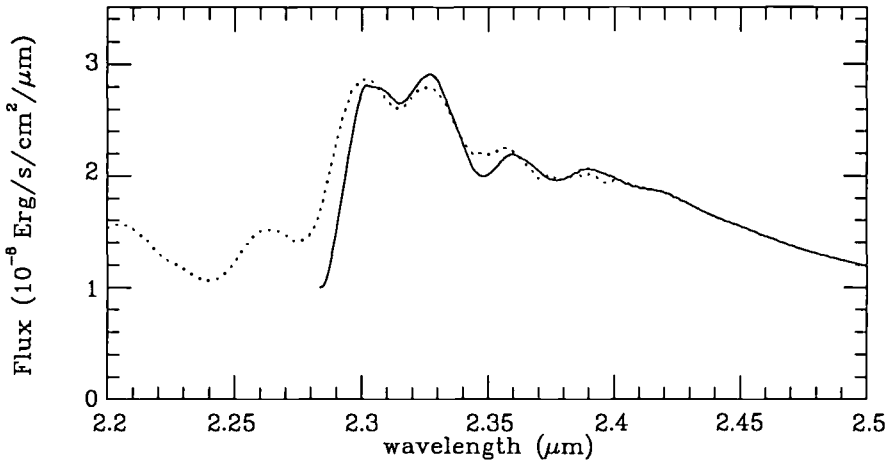

FIGURE 1. Carbon monoxide in supernova 1987A 255 days after explosion. (Spyromilio *et al.* 1988)

in the L window previously unidentified are consistent with emission by H_3^+ although this identification is sensitive to the location of the continuum in that window.

3. Mixing of the Iron Group Elements

Evidence that the radioactive species were mixed out to the fast moving regions of the ejecta came from the study of the infrared line profiles. The transitions emitting in the infrared are ideally suited to study supernovae. They are well separated in wavelength space and therefore even with the high velocities exhibited by supernovae line blending is not a problem. Moreover the temperature and ionization structure in the ejecta of supernovae is such that the low lying transitions of neutral or singly ionized ions are amongst the dominant coolants. These transitions emit strongly in the near infrared. By studying the line profiles of the iron group elements in SN 1987A (see Fig. 2) Spyromilio, Meikle & Allen (1990) showed that the iron group elements were non-uniformly distributed within the ejecta and that some iron was moving at velocities as high as 3000 km/s. Moreover the line profiles were redshifted relative to the nominal velocity of the supernova (as determined by the narrow circumstellar lines). A similar redshift was observed in the γ-ray lines (Tueller 1990) and could be providing evidence for an asymmetric explosion.

4. ^{57}Co

The evolution of the transitions of cobalt in the infrared spectra of SN 1987A was used to show that radioactive ^{57}Co was present in the ejecta. Varani *et al.* (1991) used the ratio of the 1.533 [Fe II], and 1.547μm [Co II] lines which is very insensitive to density and temperature to determine the abundance of ^{57}Co (see Fig. 3). Danziger *et al.* (1991) and Roche *et al.* (1993) used the rate of decay of the mid IR (10.52μm) line to also determine the ^{57}Co abundance. This isotope of cobalt has a much longer lifetime than ^{56}Co and at late times dominates the heating of the ejecta. The determination of its abundance is important for the energetics of the light curve of the supernova. Moreover the determination of the abundance is an important constraint of the nucleosynthesis occurring in supernovae with implications for the enrichment of the interstellar medium. Observations with the GRO satellite have detected ^{57}Co γ-rays (Kurfess *et al.* 1992) in agreement with our results.

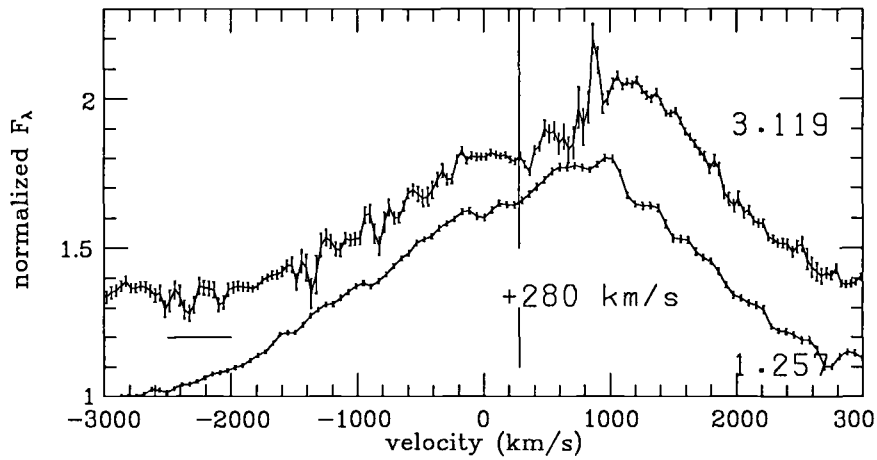

FIGURE 2. SN 1987A IR line profiles of the iron group elements (Spyromilio, Meikle & Allen 1990)

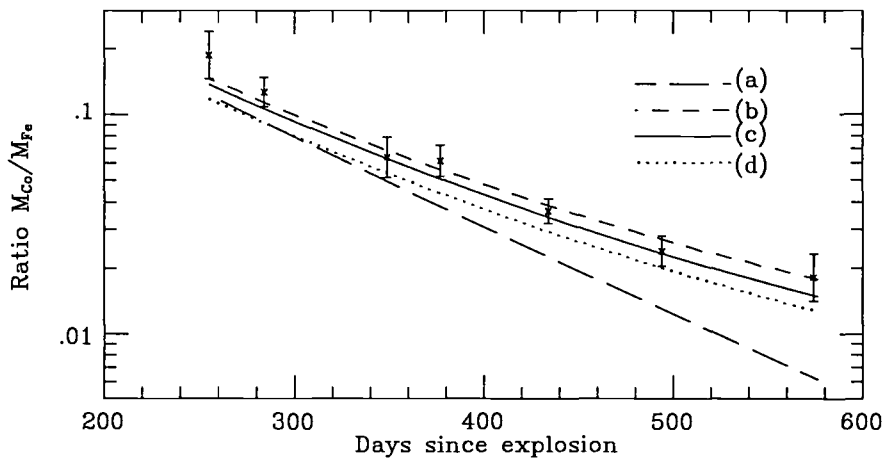

FIGURE 3. evolution of the Fe/Co mass ratio in SN 1987A as derived from near IR observations. Model (a) ^{56}Ni alone; (b)–(d) models described in Varani *et al.* (1990)

5. Dust

Soon after the explosion of supernova 1987A Dwek (1988) suggested that dust would form within the ejecta and totally obscure the supernova at an age of a few hundred days. Dust did indeed form in the ejecta after 500 days but did not totally obscure the ejecta. Like the rest of the ejecta the dust seems to have formed in clumps as well as a diffuse component. Although this effect was discovered from a study of optical transitions (Lucy *et al.* 1991) the bulk of the dust emission appeared, as would be expected, in the mid-infrared (Roche *et al.* 1993; Wooden these proceedings).

The infrared line profiles also moved to the blue as dust obscured the red side of the ejecta. However this shift was of similar extent as the that observed in the optical which is inconsistent with the details of the Lucy *et al.* (1991) model (see Spyromilio *et al.* 1990) but not the spirit of that model. A flat extinction curve can be achieved using more optically thick dust located in clumps. From the mid-infrared data it has been possible to exclude silicates and graphite as the dominant components of the dust since their characteristic spectral features are absent (Wooden these proceedings). The

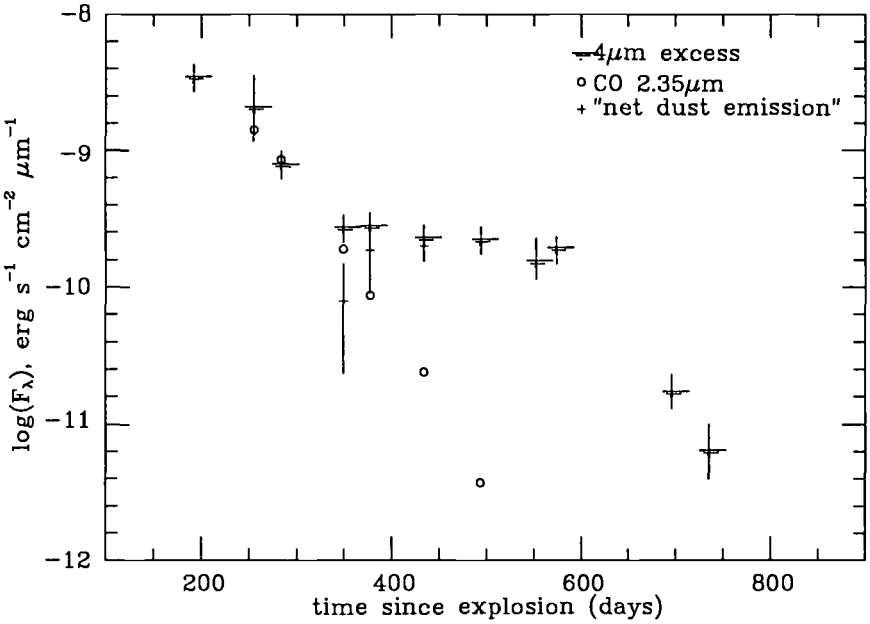

FIGURE 4. The 4μm excess from the AAT data showing no evidence for significant dust contribution prior to day 250. (Meikle *et al.* 1993)

infrared spectra of SN 1987A from the AAT have allowed us to accurately determine that the onset of dust formation occurred 350 days after explosion (Meikle *et al.* 1993; Roche *et al.* 1993).

6. The Infrared Catastrophe

The radioactive decay of ^{56}Co which powers the late-time supernova produces γ-rays and positrons around the MeV range. The γ-rays Compton scatter and produce fast electrons which in turn ionize, excite and heat the gas as they slow down. The division of the energy from the radioactive decay into heating, ionizations and excitations does depend on the composition and the electron fraction of the ejecta but for the purposes of this discussion it can be safely assumed that most of the energy (>80%) goes into heating the thermal electron gas. The ejecta cool through collisionally excited transitions of low ionization species. Excluding molecular species and hydrogen the dominant coolants in the supernova have been forbidden lines of neutral and singly ionized iron, neutral oxygen, singly ionized calcium, neutral carbon and neutral silicon. Apart from calcium and silicon all other species have strong fine structure ground state transitions. These transitions have extremely low excitation temperatures and for most purposes are temperature independent. As the ejecta cool the efficiency of the ionic coolants approaches a plateau where the higher excitation energy levels can no longer be populated but the ground state lines remain saturated. The heating due to the radioactivity declines due to the decrease of the available energy and the increased transparency of the ejecta. The heating and cooling rates around 1000K can no longer be balanced and the ejecta cool rapidly. The result would be that only the mid and far infrared transitions would emit. This effect postulated by Axelrod (1980) is called the 'infrared catastrophe' and has never been directly observed.

Spyromilio & Graham (1992) by modeling (see Fig 5) the combined near-infrared and optical spectrum have shown that the mass of emitting iron plummeted around the epoch

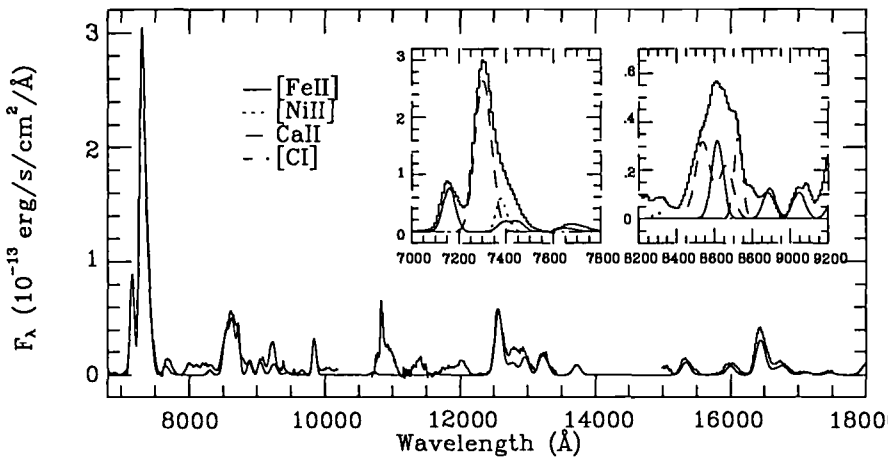

FIGURE 5. Spectra of SN 1987A with model fitting the forbidden emission by FeII (Spyromilio & Graham 1992)

of dust formation. One of the scenarios they proposed to explain this was that the ejecta had cooled catastrophically leaving some material hot which continued to emit. This scenario has been given support by the KAO observations (Dwek *et al.* 1992) and by the recent analysis of the entire iron spectrum by Li *et al.* (1993).

7. The Asymmetric Wind

Around 60 days after explosion, the UV spectrum of SN 1987A began to exhibit narrow lines of highly ionized nitrogen and other species. This emission has been analyzed in great detail by Lundqvist & Fransson (1991) and has been shown to arise from circumstellar gas. The near infrared spectrum around 400 days after explosion exhibited strong narrow emission by the He I 1.083 μm transition. By using the spectral imaging technique Allen, Meikle and Spyromilio (1989) were able to determine the spatial distribution of the helium emission and to show that not only was the emission asymmetric but also that the progenitor had anomalously high helium abundance in the wind preceding the explosion.

8. The spectrum 5 years after explosion

SN 1987A is the only supernova for which continuous high signal to noise data have been obtained for as many as 5 years after explosion in the infrared. Using the new generation of infrared spectrographs based on 2-D IR arrays we have been able to extend the coverage to such an unprecedented epoch. The spectrum has not varied dramatically after the third year and is dominated by the circumstellar emission by He I 1.083 μm. Hydrogen Paschen β and γ are observed as is the He I singlet equivalent of the 1.083 line at 2.058 μm. The emission by the ejecta is of particular interest. Although strong emission is seen in the 1.64 μm blend the weakness of the 1.257 [Fe II] line indicates that the 1.64 μm feature is now again dominated by [Si I] emission. Meikle *et al.* (1993) have shown that the [Si I] contribution to that feature had steadily decreased after day 500 predominantly due the drop of the electron density below the critical value for the excitation of this transition. Its reappearance as the dominant emitter suggests a non-thermal heating mechanism.

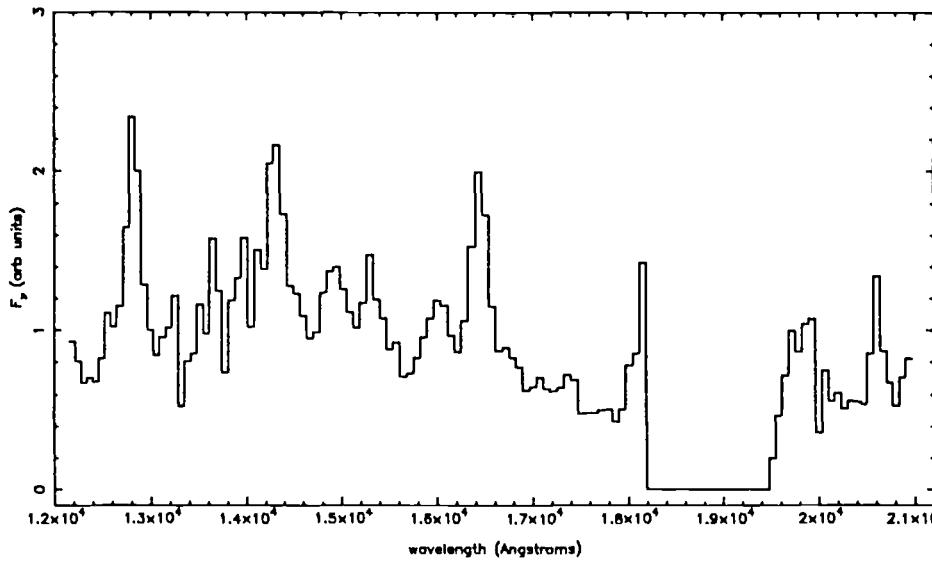

FIGURE 6. SN 1987A 21/2/1992 AAT & IRIS

Acknowledgements

The work presented here is the result of a long collaboration with Peter Meikle, David Allen and Gian Varani. The data could not have been obtained without the excellent support afforded us by the staff at the AAT.

REFERENCES

Allen D. A., Meikle, W. P. S., & Spyromilio, J. 1989, Nature, 342, 403

Axelrod, T. S. 1980, PhD dissertation, University of California

Danziger, I. J., Lucy, L. B., Bouchet P., & Gouiffes C. 1991, in Woosley S.E., ed., Supernovae, Springer-Verlag, New York, p.69

Dwek, E. 1988, ApJ, 329, 814

Dwek, E., *et al.* 1992, ApJ, 389, L21

Ferland, G. J., *et al.* 1979, ApJ, 227, 489

Frogel J. A., *et al.* 1987, ApJ, 315, L129

Graham, J. R., *et al.* 1986, MNRAS, 218, 93

Kurfess, J. D. 1992, ApJ, 399, L137

Li H., McCray R., & Sunyaev R.A. 1993, ApJ, 419, 824

Lucy L. B., Danziger I. J., Gouiffes C., & Bouchet P. 1991, in Woosley S.E., ed., Supernovae, Springer-Verlag, New York, p.82

Lundqvist P., & Fransson, C. 1991, ApJ, 380, 575

Meikle W. P. S., Allen D. A., Spyromilio J., & Varani G.-F. 1989, MNRAS, 238, 193

Meikle W.P.S., Spyromilio J., Allen D. A., Cumming R. J.,& Varani G.-F. 1993, MNRAS, 261, 535

Miller S., Tennyson J., Lepp S., Dalgarno A. 1992, Nature, 355, 420

Roche P. F., Aitken D. K., & Smith C. H. 1992, MNRAS, 252, 39p

Roche P. F., Aitken D. K., & Smith C. H. 1993, MNRAS, 261, 522

Spyromilio J., Meikle W. P. S., Allen D. A., & Learner R. C. M. 1988, Nature, 334, 327.
Spyromilio J., Meikle W. P. S., & Allen D.A. 1990, MNRAS, 242, 669
Spyromilio J., & Graham J. R. 1992, MNRAS, 255, 671
Tueller J. *et al.* 1990, ApJ, 351, L41
Varani G.-F., Meikle W. P. S., Spyromilio J., & Allen D. A. 1990, MNRAS, 245, 570
Wooden D.H., 1993, these proceedings.

SN 1987A: Observations at Later Phases

By P. BOUCHET[1], I. J. DANZIGER[2], C. GOUIFFES[3] M. DELLA VALLE[1] AND A. MONETI[1]

1European Southern Observatory, La Silla (Chile)

[2]European Southern Observatory, Garching (Germany)

3DAPNIA/Sap, C. E. Saclay (France)

The last observations (until April 1993) of SN 1987A made at ESO, La Silla, are presented. Our data show that: (i) the criterion of line shifts proves that dust is still present and is absorbing more strongly than ever; (ii) the I magnitude decreases faster than the other ones after day ~1700; (iii) the 1.3mm flux is constant at about 9mJy, and comes most probably from free-free emission produced by the cooling of the former star envelope still weakly ionized. Previous analyses of the bolometric light curve until day 1444 are briefly reviewed. In spite of the large uncertainties, the flattening of the light curve, observed after day ~900, extends until our latest data points (day 2172). This can be explained by theoretical models including time-dependent effects due to long recombination and cooling times (Fransson and Kozma 1993). However, one cannot rule out the presence of a compact object such as a neutron star, radiating as a pulsar or accreting matter from a disk either continuously or intermittently.

1. The Dust

In order to understand many aspects of the observed behaviour of SN 1987A at later phases, one must appreciate the role of dust in the expanding ejecta of the supernova. Molecules such as CO and SiO were formed at a very early phase (<100 days after outburst) (Bouchet and Danziger 1993). Probably as a result of the presence of molecules, dust formed at approximately day 530 and has since continued to play a dominant role in absorbing much of the harder radiation and thermalizing it. The spectroscopic signature causing an apparent blueward shift of the peak of various broad emission lines ([O I]6300,6363, Mg I]4571 and [C I]9823,9849), together with independent photometric evidence (e.g., the appreciation that the IR excess created after dust formation had to be included in the energy budget to obtain the most plausible bolometric energy), proved beyond doubt that dust had condensated in the envelope and was not originating from an IR echo from surrounding material (Danziger *et al.* 1989, Lucy *et al.* 1989, Suntzeff and Bouchet 1990). Analyses (i) of the shape of the profiles and (ii) of the observed extinction of emission lines revealed that the dust was confined throughout the inner metal rich parts of the envelope, i.e., the ejecta, and that although amorphous silicate dust might be the dominant component, dust also existed in clumps whose optical depths could be very large (Lucy *et al.*, 1989, 1991). These dense thick clumps may still be preventing us from seeing to the centre of the supernova where a compact remnant (neutron star) is predicted to lie.

Our observations show that at day 1806 (February 4, 1992), the peak emission of Mg I]4571 had a blue shift of 810 km/s and that of [O I]6300 of 495 km/s (Fig. 1); at day 2159 (January 22, 1993), the blue shifts were of 780 km/s and 500 km/s for Mg I] and [O I], respectively. This proves that, within the uncertainties, there has been no significant change during this period. These shifts under the model proposed by Lucy *et al.* (1989, 1991) correspond to optical depths of 1.85 and 0.8 at the 2 wavelengths, at least as large as any reported in the past and still indicating a colour effect due to the presence of

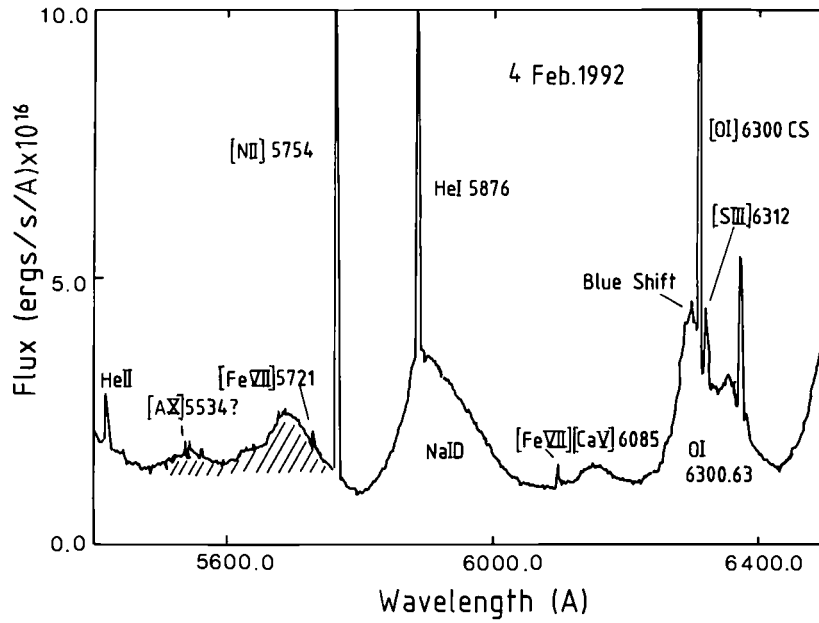

FIGURE 1. A spectrum of SN 1987A taken at day 1806 at ESO, La Silla with the New Technology Telescope (NTT). Narrow lines from the CS gas are identified as are some broad features formed in the expanding envelope. Other broad features with hatching are yet unidentified.

amorphous silicates. While great caution is now required in using this model because the original assumptions may be overstrained, there remains ample evidence of the presence of copious amounts of dust.

2. The ESO data

2.1. *The visible:*

At later phases, the observations of SN 1987A have became very difficult, due to the faintness of the supernova and the contamination of the neighbouring stars. Therefore, even with the ESO New Technology Telescope (NTT) which is well known for providing very good images, observations can only be conducted under very good seing conditions. Moreover, a careful analysis of the data is necessary in order to reduce the contamination from the companions (ROMAFOT has been used for the reduction of our data). Fig. 2 shows the UBVRI lightcurves obtained at ESO and at CTIO (courtesy N.B. Suntzeff; see also Suntzeff *et al.* 1992). It has to be stressed that 70% of the errors in the broad band photometry arise from the uncertainty in the determination of the extinction correction, due to the various volcanoes which have exploded during the past years, and which have spread in the sky a large amount of dust (The Pinatubo in The Philippines being the most prejudicial). These errors are estimated to be $\leq$0.05 magnitude for V, R and I, and $\leq$0.10 magnitude for B. Fig. 2 shows that the I magnitude decreases faster than the other ones after about day 1700. The reason for this behaviour is still unclear, although it is most probably due to the relative absence of emission lines in this band.

2.2. *The infrared:*

The same difficulties as for the visible arise for the near-IR photometry. Moreover, the detectors available for this spectral region are less sensitive. The accuracy in the K band is estimated to be $\leq$0.10 mag. At later phases, the supernova is too faint in L(3.8μm)

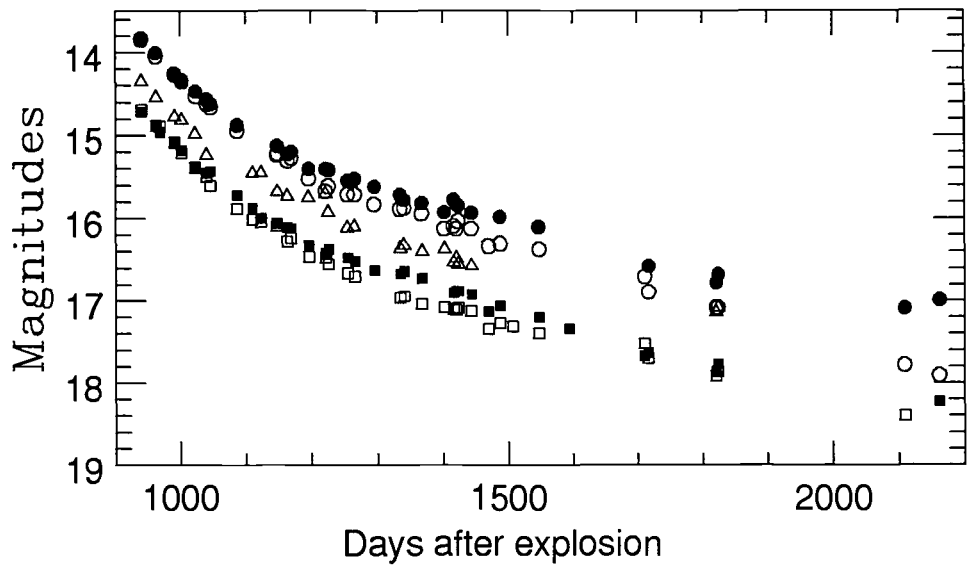

FIGURE 2. The U (open triangles), B (open squares), V (filled squares), R (filled circles) and I (open circles) lightcurves from CTIO and ESO. Note the faster decrease in the I band.

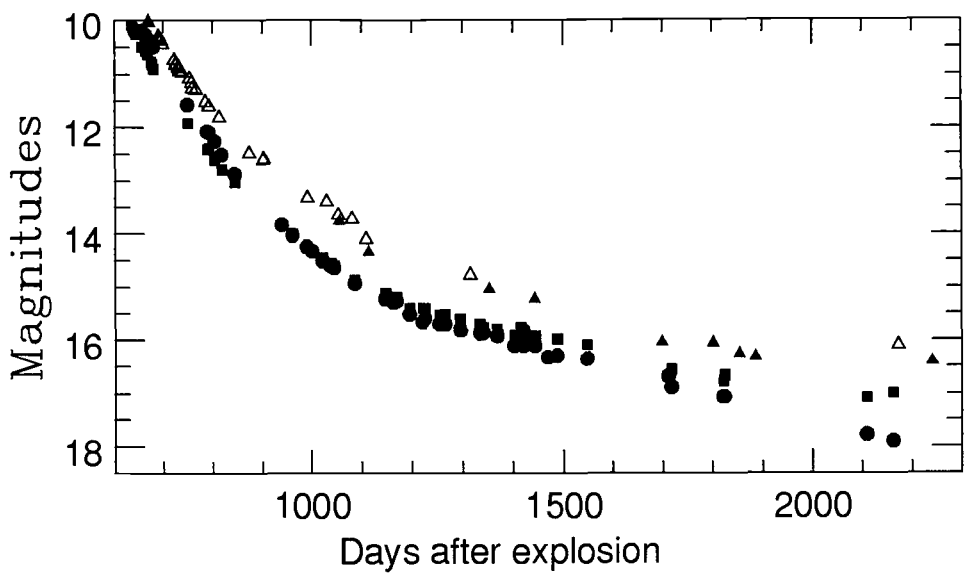

FIGURE 3. The K lightcurves from CTIO (filled triangles) and ESO (open triangles). The R (filled squares) and I (filled circles) lightcurves are also displayed for comparison.

and M (4.6μm) to be measurable. Photometry at 10 and 20μm is also difficult to achieve, and gives high uncertainties. Note that after day ~1500, under very good atmospheric conditions, 5 hours of integration time give about a 3-σ detection only! Fig. 3 and 4 shows the light curves obtained at ESO and CTIO (courtesy N.B. Suntzeff; see also Suntzeff *et al.* 1992). It is well known that discrepancies exist between the results from ESO and

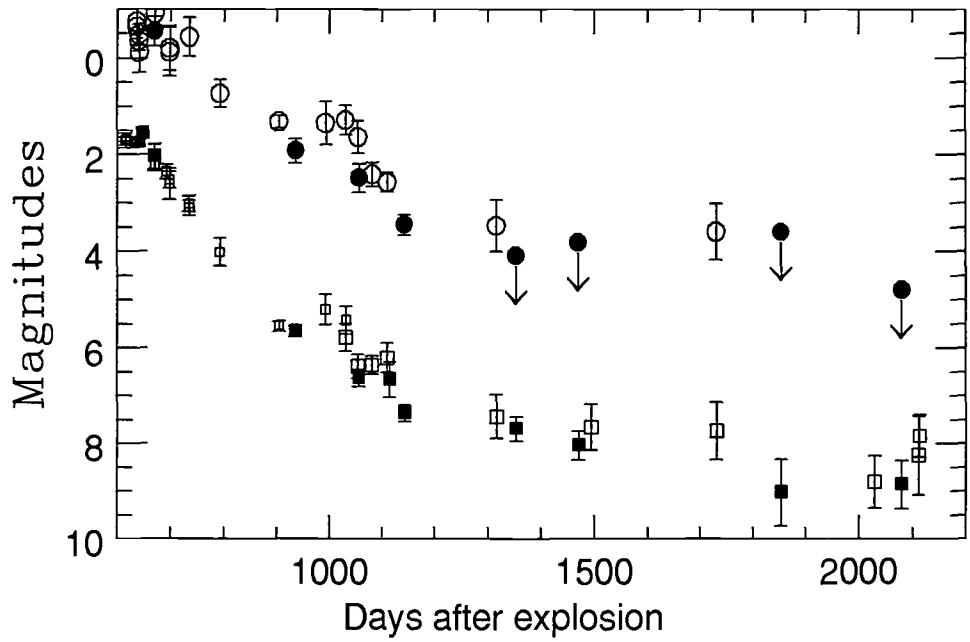

FIGURE 4. The 10 (squares)and 20 μm (circles) lightcurves from CTIO (filled) and ESO (open).

CTIO at 10 and 20μm (Bouchet *et al.* 1991a, Suntzeff *et al.* 1991). The reason for that is still not understood (Bouchet *et al.* 1991b).

The commissioning of the new 10μm camera, TIMMI, at La Silla will undoubtedly increase the accuracy of the measurements. First tests, made in January 1993 under bad atmospheric conditions gave in 2 hours a detection at a 3-σ level of ~15 mJy (N= 8.3), which is very promising.

2.3. *The 1.3mm data:*

Figure 5 shows that after day 800, the flux at 1.3mm (230 GHz) seems to be constant (within unavoidably large errors) at ~8–9 mJy, although a slight increase starting after day 1800 can not be completely ruled out. Further observations will clarify this point. In this figure, data from Biermann *et al.* (1990a,b, 1992) are also shown: the unusually high point at day 1640 may be spuriously high because the next point some days later when the atmospheric conditions were excellent (resulting in a very small uncertainty) is significantly lower and consistent with all subsequent oservations.

The positive detection of the supernova at 1.3mm raises the question of the origin of this flux. Fig. 6 shows the spectral energy distribution of SN 1987A at day 2172. It can be seen from this figure that it is unlikely that dust alone radiating as a black body at ~155K be responsible for the 1.3mm flux. Furthermore, it remains to be demonstrated whether the clumped dust is an efficient emitter at this wavelength. A measurement of the spectral index of this radiation near 1.3mm would help to elucidate this problem. Thus, although clumpiness is undoubtedly a feature of the expanding envelope (Lucy *et al.* 1991), these oservations do not demonstrate this point. A synchrotron radiation

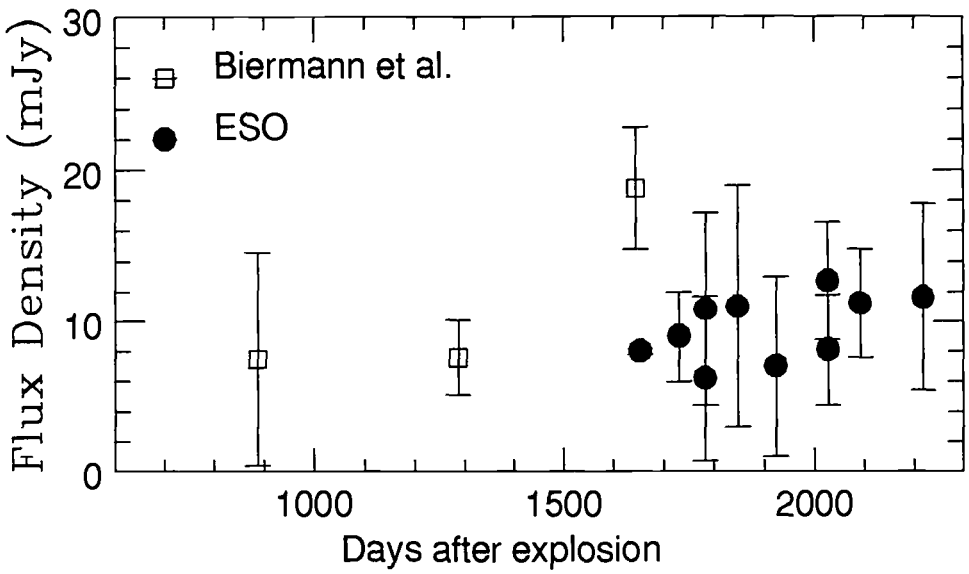

FIGURE 5. The temporal behaviour of the flux at 1.3mm measured with the SEST telescope at La Silla.

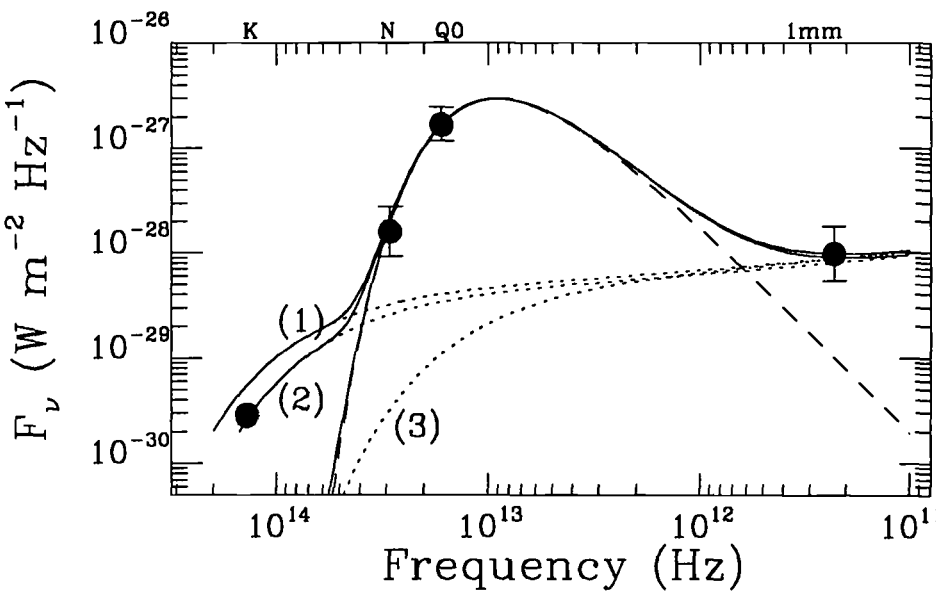

FIGURE 6. The broad band energy distribution of SN 1987A at day 2172. The dotted curves show the free-free radiation at 3000 K (1), 2300 K (2), and 500 K (3); The dashed curve represents the black body at 155 K; The plain curve is the sum of the two contributions.

from a pulsar-powered nebula has also been evoked for the origin of the 1.3mm flux (Bandiera *et al.* 1988; Salvati *et al.* 1989): that seems very doubtful due to the low level of this flux, which implies unrealistic characteristics of the eventual pulsar. The most plausible origin of the 1.3mm radiation seems to be that there is, albeit relatively faint, a component due to free-free emission underlying the black-body emission. This free-

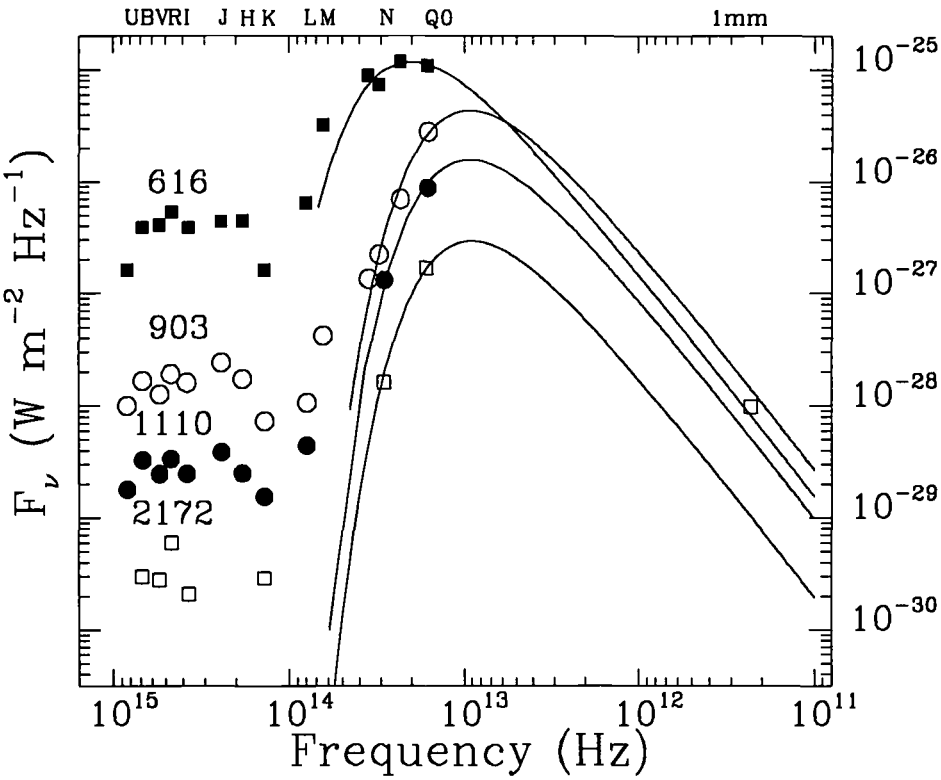

FIGURE 7. The temporal evolution of the broad band energy distribution of SN 1987A, for the indicated dates. The black bodies used for the extrapolation to the far infrared are also shown.

free emission would be produced by the cooling of the former star envelope still weakly ionized (Biermann *et al.* 1990a). The measurements at K and L allows to set a maximum temperature of the free-free emission (see Fig. 6). Our data show that that maximum temperature has decreased from T =3000K at day 1316 to T =2300K at day 2172. At this point, it is worth-while to note that the analysis of the Paschen discontinuity shows that hydrogen is recombining at even lower temperature (500 to 200K) (see Kugai and Wampler, this conference). Much of the hydrogen must be in low temperature regions. Thus, as illustrated by Fig. 6, if all or most of the radiation measured in the K band is not due to the free-free, the temperature infered from the 1.3mm measurement only may be much lower than 2300K.

3. The Bolometric Light Curve

The true bolometric luminosity is the sum of:

(*a*) the "high energy" component (direct or a few times Comptonized energy from radioactive decays of nuclides produced in the supernova event),

(*b*) the UV-Optical-Infrared ("uvoir") spectrum (thermalized radiation from the high energy sources and the emerging shock-wave).

In what follows, we consider only the "uvoir" component. Due to formation of dust (or the accelerated formation of dust), ~85% of the uvoir flux by day 900, and ~97% by day 2172 comes from the infrared. Fig. 7 shows that the bulk of the radiation is inaccessible to observations from the ground (<20μm). Thus an accurate determination

of the bolometric light curve requires not only accurate observations from 5 to 20μm, but also an appropriate extrapolation for longer wavelengths.

Although accurate measurements in N1, N2, N3, and Q0 obtained at earlier stages (when the temperature of the dust was higher) show that they can be nicely fitted with a black body curve, it has to be stressed that the step from broad-band photometry to what is computed as L_{Bol} is a *theoretical* model. Also, since the actual flux is a combination of line emissions and thermal re-radiation from dust, the computed flux from the black body is an upper limit to the thermal radiation.

3.1. *Summary of previous works:*

The bolometric light curve has been computed by several groups:

(*a*) SAAO, using U to M photometry for the period 1–880 days (Whitelock 1991, and references therein),

(*b*) ESO/CTIO, using U to Q0 photometry for the period 1–903 days (Suntzeff and Bouchet 1990),

(*c*) ESO/BOCHUM/CTIO/KAO using spectrophotometry from the visible to the 30μm region, for the period 14–432 days (Bouchet *et al.* 1991c),

(*d*) CTIO, until day 1444 (Suntzeff *et al.* 1991, 1992), and ESO, until day 1316 (Bouchet *et al.* 1991a) using the photometry at late stages.

The main results of these works may be summarized as follows:

(*a*) The sum of the early time uvoir flux and the high-energy flux is consistent with the energy released by 0.055–0.090 $M_\odot$ of ^{56}Co,

(*b*) After day 600, the far infrared component can be fitted with a black body of temperatures decreasing from 400 to 140 K,

(*c*) No more than 30% of the far-IR flux can be due to thermal re-radiation of energy in a cloud behind SN 1987A (the "IR ECHO") without violating the energy budget or requiring a larger fraction of high-energy photons to escape than are predicted by the models. The effective angular radius of the thermal component ($\sim$0.015″ after day 600) is consistent with the velocity of the emitting ejecta,

(*d*) At day $\sim$900 the bolometric light curve exhibits a significant flattening.

3.2. *The bolometric light curve at the later phases:*

At later phases, not only the photometry is inaccurate, but also the extrapolation to the far infrared relies on very few data points (in fact, in some cases, N only!). Therefore, we have to make several assumptions in order to compute the bolometric luminosity:

(*a*) at day 1731, our measurements at 10 and 20μm can be fitted with a black body of temperature $140<T_{eff}<160$K, which is similar to the temperature derived for day 1316 (Bouchet *et al.* 1991a). Then, for the dates at which we don't have 20μm measurements we assume that the temperature of the black body has remained constant at 150K, and we scale it with the 10μm measurement.

(*b*) at day 2172, $L_{IR} = 0.97 \times L_{Total}$, while $L_{IR} = 0.85 \times L_{Total}$ at day 1316. Then, we estimate the L_{IR}/L_{Total} ratio from the colours (V-N) and (V-R).

The uncertainties on the distance modulus (-0.08 to +0.04 dex) and on the reddening (+0.02 dex) are negligible compared to the ones introduced by the extrapolation to the far infrared and the photometric errors. Also, lowering our Q0 by 20% (to match CTIO) gives an increase of the black body temperature of +30 to +15K, which introduces a decrease of the bolometric luminosity of -0.015 dex to -0.090 dex. Table 1 illustrates the small fraction of the actually observed flux regard to the total one, as well as the uncertainties due to the extrapolation to the far infrared and to the photometry (values between brackets have been estimated accordingly to the assumptions (i) and (ii)).

TABLE 1. Uncertainties affecting the bolometric luminosity

Days	Range in T_{eff}	$L_{IR}^{Obs}/L_{IR}^{Tot}$	L_{IR}/L_{Tot}	Infrared extrapolation	Photometric errors
635	350–280	0.72	0.48	±0.01	±0.02
1030	180–150	0.29	0.83	±0.07	±0.03
1316	155–130	0.24	0.85	±0.08	±0.05
1493	(155–130)	0.01	(0.85)	(±0.08)	±0.18
1731	160–150	0.23	(0.90)	±0.06	±0.13
2029	(160–130)	0.01	(0.85)	(±0.08)	±0.22
2113	(160–130)	0.01	(0.95)	(±0.08)	±0.18
2172	(160–130)	0.01	0.97	(±0.08)	±0.25

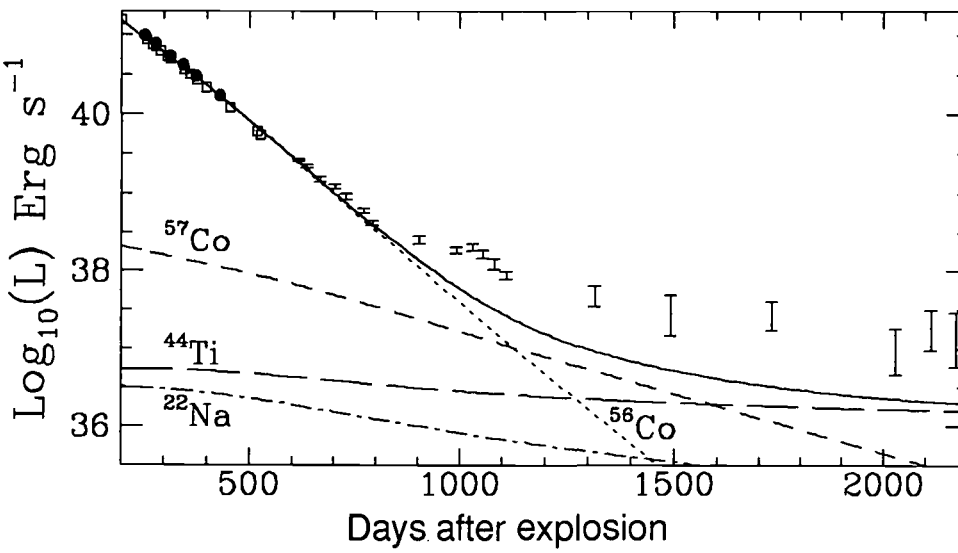

FIGURE 8. The bolometric light curve of SN 1987A; filled dots correspond to the spectrophotometric measurements, open squares to the broad-band photometric measurements. The predicted theoretical curves resulting from Woosley et al.'s model (1989) are shown. The initial ^{56}Co mass has been set to 0.069 $M_\odot$ and the column depth to 9×10^4 g cm^{-2}. The ^{57}Co/^{56}Co ratio is solar; the masses of ^{44}Ti and ^{22}Na are 1.0×10^{-4} $M_\odot$ and 2.0×10^{-6} $M_\odot$, respectively. The plain curve is the sum of all the individual contributions from radioactive decays.

3.3. *Analysis of the bolometric light curve*

In spite of the great uncertainties, the flattening of the bolometric light curve is still observed until day 2172 (see Fig. 8). Although the degree of levelling has been a source of some debate between CTIO and ESO (due to the differences in the photometry), both observatories agree that there is in the bolometric light curve an excess above the line required by radioactive decays alone. Suntzeff *et al.* (1992) and Dwek *et al.* (1992) have argued that an amount of ^{57}Co/^{56}Co~4–6 times the solar ratio of 57/56 stable nuclides would adequately fit the observed light curve. However, the amount of

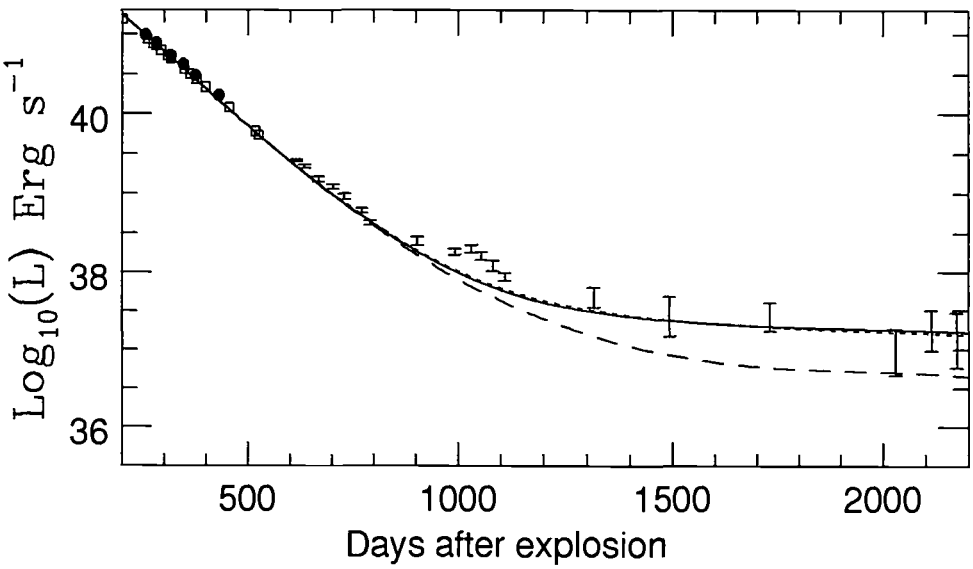

FIGURE 9. The bolometric light curve of SN 1987A as in Fig. 8. Here the $^{57}Co/^{56}Co$ ratio has been taken 2 × solar, and time dependent effects have been considered to compute the energy output from radioactive decays (dashed line) (Fransson and Kozma 1993). A central source has been added to that energy output according to Woosley *et al.* 1989: an accreting x-ray pulsator (plain) of total luminosity 2×10^{37} erg/sec, and a pulsar (dotted) of 5×10^{37} erg/sec.

^{57}Co has to be compatible with observations of the [Fe II] and [Co II] lines (Bouchet and Danziger 1993; Varani *et al.* 1990), with the failed attempts to observe the X-rays resulting from the comptonization of γ-rays from the ^{57}Co decay (Sunyaev *et al.* 1991), and with the OSSE observations of the 122 keV ^{57}Co line (Kurfess *et al.* 1992): these observations give an upper limit of 1.5 times the solar ratio. Also, the amounts of ^{44}Ti and ^{22}Na should be increased by factors 20 and 30 above that predicted by theory (Woosley and Hoffmann 1991), in order to fit the observed light curve. Such amounts of these radioactive species must be considered an unlikely possibility in view of the success of the theoretical work (Woosley 1991, Thielemann *et al.* 1991) in deriving abundances that match the observations (Danziger *et al.* 1991b).

Fransson and Kozma (1993) and Fransson *et al.* (1995) have shown that, after day ~800, time-dependent effects due to long recombination and cooling times lead to a frozen in structure of the ejecta of SN 1987A. The result is a higher bolometric luminosity, compared to models where the emitted luminosity is equal to the instantaneous energy input. Figure 9 displays the resulting theoretical light curve. Clearly, an extra energy output has still to be added in order to fit the observations. This energy could result from a compact object left at the center of the supernova, like a neutron star surrounded by an accretion disk depositing matter either continuously or at varying intervals onto the collapsed object A pulsar either beamed away from our line-of-sight or continually obscured by the dense clumps of dust is, also, still a possibility. The accreting X-rays pulsator and the pulsar models give equally good fits to the data (Fig. 9). However, it has to be stressed that no model has been able yet to reproduce the observed bump around day 1050 (at the time of the flattening). This bump is also seen in the I.U.E. data presented by Pun at this conference.

REFERENCES

Bandiera, R., Pacini, F. & Salvati, M. 1988, Nature, 332, 418

Biermann, P. L., Chini, R., Greybe-Götz, A., Haslam, G., Kreysa, E. & Mezger, P. G. 1990a, A&A, 227, L21

Biermann, P. L., Chini, R., Haslam, G., Kreysa, E. & Lemke, R. 1990b, A&A, 236, L17

Biermann, P. L., Chini, R., Haslam, G., Kreysa, E., Lemke, R. & Sievers, A. 1992, A&A, 255, L5

Bouchet, P. & Danziger, I. J. 1993, A&A, 273, 451

Bouchet, P., Danziger, I. J. & Lucy, L. B. 1991a, A&A, 102, 1135

Bouchet, P., Danziger, I. J. & Lucy, L. B., 1991b, "ESO/EIPC Workshop on SN 1987A and other Supernovae"; I.J.Danziger and K.Kjär (eds.); p.281

Bouchet, P., Phillips, M. M., Suntzeff, N. B., Gouiffes, C., Hanuschik, R. W. & Wooden, D. H. 1991c, A&A, 245, 490

Danziger, I. J., Gouiffes, C., Bouchet, P. & Lucy, L. B. 1989, IAU Circ. No. 4746

Danziger, I. J., Bouchet, P., Gouiffes, C. & Lucy, L. B. 1991a, "ESO/EIPC Workshop on SN 1987A and other Supernovae"; I.J.Danziger and K.Kjär (eds.); p.217

Danziger, I. J., Lucy, L. B., Bouchet, P. & Gouiffes, C. 1991b, "Supernovae"; S.Woosley (ed.) (Springer-Verlag: New York); p.69

Dwek, E., Moseley, S. H., Glaccum, W., Graham, J. R., Loewenstein, R. F., Silverberg, R. F. & Smith, R. K. 1992, ApJ, 389, L21

Fransson, C., & Kozma, C. 1993, ApJ, 408, L25

Fransson, C., Houck, J., & Kozma, C. 1995, these proceedings

Kurfess, J. D. *et al.* 1992, ApJ, 399, L137

Lucy, L. B., Danziger, I. J., Gouiffes, C. & Bouchet, P. 1989, "Structure and dynamics of Interstellar Medium"; G.Tenorio-Tagle, M.Moles, and J.Melnick (eds); Lecture Notes in Physics (Springer, Berlin), 350, 164

Lucy, L. B., Danziger, I. J., Gouiffes, C. & Bouchet, P. 1991, "Supernovae"; S.Woosley (ed.) (Springer-Verlag: New York); p.82

Salvati, M., Pacini, F., Oliva, E. & Bandiera, R. 1989, A&A, 208 L5

Suntzeff, N. B. & Bouchet, P. 1990, AJ 99 650.

Suntzeff, N. B., Phillips, M. M., Depoy, D. L., Elias, J. H. & Walker, A. R. 1991, AJ, 102, 1118

Suntzeff, N. B., Phillips, M. M., Elias, J. H., Depoy, D. L. & Walker, A. R. 1992, ApJ, 384, L33

Sunyaev, R. A. *et al.* 1991, "Supernovae"; S. Woosley (ed.) (Springer-Verlag: New York); p.767

Thielemann, F. -K., Hashimoto, M., Nomoto, K. & Yokoi, K. 1991, "Supernovae"; S.Woosley (ed.) (Springer-Verlag: New York); p.609

Varani, G. -F., Meikle, W. P. S., Spyromilio, J. & Allen, D. A. 1990, MNRAS, 245, 70

Whitelock, P. A. 1991, "ESO/EIPC Workshop on SN 1987A and other Supernovae"; I.J.Danziger and K.Kjär (eds.); p.301.

Woosley, S. E. 1991, "Supernovae"; S.Woosley (ed.) (Springer-Verlag: New York); p.202

Woosley, S. E. & Hoffman, R. 1991, ApJ, 368, L31

Woosley, S. E., Pinto, P.A. & Hartmann, D. 1989, ApJ, 346 395

Freeze out, IR-catastrophes and Non-thermal Emission in SNe

By CLAES FRANSSON, JOHN HOUCK, AND CECILIA KOZMA

Stockholm Observatory, S-133 36 Saltsjöbaden, Sweden

Freeze out effects and the IR-catastrophe are discussed for SN 1987A and for Type Ia SNe. We show that the light curves of the optical lines in SN 1987A provide strong evidence for the IR-catastrophe. We also argue that most optical lines are dominated by non-thermal excitation after $\sim$ 800 days. The level of this emission is set mainly by the total mass of the elements. Models of the [O I]$\lambda\lambda$6300 – 64 light curve show that an oxygen mass of $\sim 1.5 M_\odot$ is needed. Light curve models for Type Ia SNe display a sharp decrease in the optical flux as a result of the IR-catastrophe at $\sim$ 500 days, producing UBV-photometry inconsistent with observations of SN 1972E by Kirshner & Oke (1975).

1. Introduction

Observations of SN 1987A, but also a number of other Type II and Type Ia SNe, at late stages have made it possible to study a number of new features in the evolution of the SN ejecta from explosion to the remnant stage. Here we discuss some recent results in this evolution. A more complete review of the background physics can be found in Fransson (1993).

2. SN 1987A

It is now well established from the bolometric light curve that ~ 0.07 M$_\odot$ of ^{56}Ni was created in SN 1987A, and that this is responsible for most of the observed emission from the SN during the first $\sim$ 800 days. Being based on the bolometric light curve, this is a fairly model independent conclusion. However, to extract any detailed information about abundances or the physical conditions from the spectrum, an understanding of the thermalization process of the γ-rays is necessary. The first step in this process, in which the photons are degraded by Compton scattering, creating a number of non-thermal primary keV-electrons, is fairly straight forward, and can be calculated by e.g. Monte Carlo methods (e.g. Pinto & Woosley 1988). The subsequent slow-down of the electrons and the cascade of secondary electrons is considerably more complicated. Kozma & Fransson (1992, in the following KF92) and Xu & McCray (1991) have modeled this, using the Spencer-Fano formalism. The absorbed γ-ray energy is divided into three channels: H_γ, heating the thermal electrons; $\sum_i \Phi_i$, producing ionizations of the ions i; and $\sum_{i,j} \epsilon_{j,i}$, producing excitations of levels j in the ions i. At low electron fractions these three channels are roughly equal, but above $x_e \sim 0.1$ ionizations and excitations decrease rapidly, and most of the energy goes into heating. To relate the number of ionizations per ion to Φ_i it is convenient to define an effective ionization potential,

$$\chi_{eff,i} = \frac{\chi_i}{\Phi_i X_i}, \tag{2.1}$$

where X_i is the relative abundance of the ion and χ_i the ionization potential.

As the ejecta expand and the γ-input decreases, the number density, n_i of an ion i is

determined by

$$\frac{dn_i}{dt} + \frac{3n_i}{t} = \left\{ 4\pi \frac{J_\gamma \sigma_{\gamma,i}}{\chi_{eff,i}} + 4\pi \int_{\nu_0}^{\infty} \frac{J_\nu \sigma_{\nu,i}}{h\nu} d\nu + \sum_k \zeta_{k+1,i} n_{k+1} \right\} n_i + \left\{ \alpha_{i+1} n_e + \sum_k \zeta_{k,i+1} n_k \right\} n_{i+1} \quad (2.2)$$

The term on the left represents the change due to expansion. The first term on the right is the γ-ray ionization rate, proportional to the mean intensity of the γ-rays, J_γ, and the cross-section for γ-ray scattering, $\sigma_{\gamma,i} = \kappa_\gamma A_i m_p$ with the mass absorption coefficient $\kappa_\gamma = 0.06 Z_i/A_i$ cm^2 g^{-1} (A_i and Z_i are the mass and atomic number of the element). The second term is the rate of photoionization by diffuse emission from line and continuum photons in the remnant. The third term represents ionizations due to charge transfer between the ions i and $k+1$, with rate $\zeta_{k+1,i}$. The next terms are the inverse processes due to recombination and charge transfer involving the higher ionization stage $i+1$. Most of the required effective ionization potentials, $\chi_{eff,i}(x_e)$, can be found in KF92. The charge transfer rates for reactions involving hydrogen and helium are fairly well known. However, for reactions between different metals they are to a large extent unknown, and one has to guess rates based on the positions of the energy levels in the ions involved. This is a major uncertainty in the modeling. If a near-resonance situation is present the rate coefficient is likely to be $\sim 10^{-10}$ cm^3 s^{-1}, or higher. The total rate, $n_{i+1}\zeta_{k,i+1}$, may therefore easily dominate over radiative recombinations, which have rate coefficients proportional to $x_e \alpha_{rec} \approx 10^{-2} \times 10^{-12} = 10^{-14}$ cm^3 s^{-1}.

Neglecting photoionization and charge transfer, and assuming that the atomic time scales are shorter than the expansion time scale and the radioactive decay time scale, we can solve equation (2.2) for the electron fraction, using $n_e \approx n_{i+1}$,

$$x_e \approx \left(\frac{4\pi J_\gamma \sigma_{\gamma,i}}{\chi_{eff,i} \alpha_{i+1} n_{total}} \right)^{1/2}, \quad (2.3)$$

assuming that $x_e << 1$. The γ-ray mean intensity is given by

$$J_\gamma = \frac{D_\gamma L_\gamma}{16\pi^2 r^2} = \frac{D_\gamma L_\gamma}{16\pi^2 (Vt)^2}, \quad (2.4)$$

where D_γ is a geometric factor accounting for the distribution of the radioactive energy source (KF92), and

$$L_\gamma = Ce^{-t/\tau} = 1.3 \times 10^{42} \left(\frac{M(^{56}\mathrm{Ni})}{0.1 \mathrm{M}_\odot} \right) e^{-t/111.3} \text{ ergs} \quad (2.5)$$

if ^{56}Co dominates the energy input. Assuming that the zone has a filling factor f_i and mass M_i, we find

$$x_e \approx C_i f_i^{1/2} D_\gamma^{1/2} \left(\frac{M(^{56}\mathrm{Ni})}{0.1 \mathrm{M}_\odot} \right)^{1/2} \left(\frac{M_i}{\mathrm{M}_\odot} \right)^{-1/2} \times \left(\frac{V_i}{2000 \text{ km s}^{-1}} \right)^{1/2} \left(\frac{t}{1000 \text{ d}} \right)^{1/2} e^{-t/222 \text{ d}} \quad (2.6)$$

where $C_H = 0.15$ for H, $C_{He} = 0.24$ for He, and $C_O = 1.28$ for O. For Type II cores we therefore find that $x_e << 1$. The recombination time, $t_{rec} = 1/(n_e \alpha_{rec})$, increases as $t_{rec} \propto t^{5/2} e^{t/2\tau}$. Eventually, this time scale must become longer than the radioactive decay time scale, τ, or even the expansion time scale, t. This defines the freeze out time (Fransson & Kozma 1993, FK93). The recombination time scale varies quite strongly

from region to region in the core. In the metal rich regions x_e is higher than in the H and He zones, mainly because these regions have fewer atoms per unit mass. Freeze-out effects are therefore strongest in the hydrogen and helium rich regions in the core, and especially in the envelope. For parameters typical of SN 1987A freeze out occurs after 800 – 900 days in these zones. If the density in the ejecta is highly inhomogeneous, as is indicated from mixing calculations, freeze out effects may dominate the evolution in the low density regions, because $t_{rec} \propto n_{total}^{-1/2}$. The effects of the freeze out for the light curve are discussed in FK93. Here we are mainly concerned with the temperature evolution and the emission from the ejecta.

After $\sim$ 800 days radioactive input from ^{57}Co becomes an important energy source if the ^{57}Ni/^{56}Ni ratio is 1.5 – 2 times solar, as is indicated by γ-ray observations (Kurfess *et al.* 1992). After this epoch the recombination and cooling time scales should be compared with the ^{57}Co decay time $\tau = 391$ days. Calculations of the nucleosynthesis indicate that $\sim 10^{-4}$M$_\odot$ of ^{44}Ti is also produced in the explosion, which should dominate after $\sim$ 1500 days. Most of this energy is emitted as positrons, which are likely to be stopped on the spot in the Fe rich gas, resulting in Fe I and Fe II emission. Most of this will be in the far-IR. Even if the γ-ray input is small in the other regions there will still be emission from the Co-poor regions due to the freeze out.

The temperature is determined by

$$\frac{dT_e}{dt} = \frac{2}{3k(1+x_e)}(4\pi H_\gamma J_\gamma \sigma_{\gamma,i} - n_e \Gamma(T_e)) - \frac{2T_e}{t} - \frac{2T_e}{(1+x_e)}\frac{dx_e}{dt} \qquad (2.7)$$

where $\Gamma(T_e)$ is the total cooling rate. The $2\,T_e/t$ term is due to adiabatic expansion, and shows that $T_e \propto t^{-2}$, if the cooling and heating time scales are longer than t. $\Gamma(T_e)$ is the sum of a large number of contributions involving collisional excitation by the thermal electrons in the gas. At temperatures above $\sim$ 2000 K excitations of forbidden, optical and near-IR lines dominate the cooling. Some important examples are [O I]$\lambda\lambda$ 6300 – 64, [Ca II]λ 7300, and [Si I]$\lambda\lambda$ 1.099, 1.645 μ. Hα does not contribute much to the cooling and arises mainly as a result of recombination (see below). Below $\sim$ 2000 K the temperature is too low to excite the optical lines, and far-IR fine structure transitions dominate. Some of the strongest are [Ne II]λ 12.81 μ, [Si II]λ 34.81 μ, [Fe I]$\lambda\lambda$ 24.05, 34.72 μ, [Fe II]$\lambda\lambda$ 25.99, 35.35 μ and [O I]λ 63.00 μ.

The temperature and ionization histories depend strongly on the chemical composition. Microscopic mixing is probably not very efficient (Fryxell, Müller & Arnett 1991), therefore both T_e and x_e are different for each chemical composition zone (Fransson & Chevalier 1989). We have calculated the temperature and ionization structure for a simplified model consisting of an inhomogeneous core with five different chemical zones expanding with a velocity of 1500 km s^{-1}, plus a hydrogen envelope. Each of the core zones have a total mass M_i and a filling factor f_i, while the envelope has a density profile taken from the Shigeyama, Nomoto & Hashimoto (1988) 14E1 model. The core consists of 0.07M$_\odot$ of ^{56}Ni, decaying into Co and Fe, with $f_{Ni} = 0.29$, 0.06M$_\odot$ from the Si-Ca zone, with $f_{Si} = 0.01$, 2.0M$_\odot$ from the O zone, with $f_O = 0.30$, 2.0M$_\odot$ from the He zone, with $f_{He} = 0.20$, and 2M$_\odot$ from mixed H-rich gas, with $f_H = 0.20$. The mass of the H envelope is 10M$_\odot$. Although crude, this mimics the expected macroscopic mixing of the core.

In figure 1 we show the temperature evolution of each of these core zones, and in figure 2 the envelope temperature structure for a few dates. The evolution of the metal rich zones are fairly similar, with a smooth decrease in temperature until $\sim$ 900 days, when a drastic decrease in temperature occurs. This is often referred to as the IR-catastrophe (Axelrod

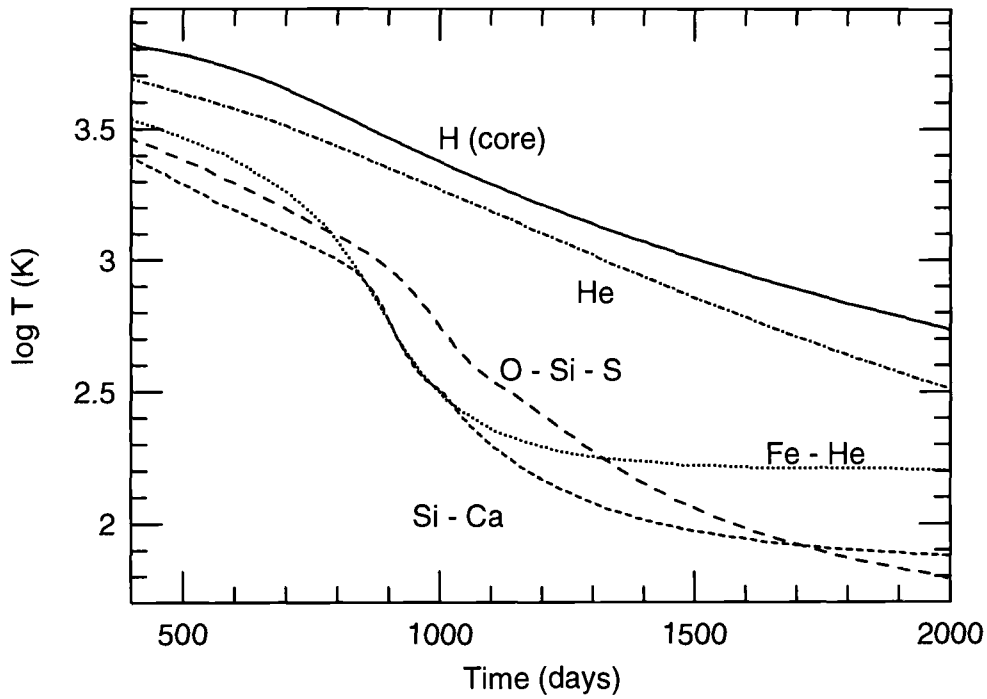

FIGURE 1. Temperature in the different zones as a function of time. In the metal rich zones a thermal instability is obvious at $\sim$ 900 days, while the hydrogen and helium rich zones cool adiabatically

1980; Fransson & Chevalier 1989). A qualitative discussion of the basic physics can be found in Fransson (1993). In the H- and He-rich gas the temperature decreases more smoothly, and has an evolution characteristic of an adiabatic gas, $T_e \propto t^{-2}$. The same is also true for the envelope, where the temperature decreases outward. The temperatures in the hydrogen gas agree well with those reported by Chugai & Danziger (1993) at this conference, based on the width of the Paschen continuum.

Although the IR-catastrophe has long been predicted, observational evidence has been rather scarce. However, clear evidence can be seen in observations of the emission line fluxes at late times. The emitted radiation from an ion i and from a level j can be split schematically into three contributions

$$L_{ij} \propto h\nu_{ij} C_{ij}(T_e) n_e n_i + j_{rec,ij} n_e n_{i+1} + 4\pi\epsilon_{ij} J_\gamma \sigma_{\gamma,i} n_i, \qquad (2.8)$$

where the first term is due to *thermal* collisional excitations, the second to recombinations, and the third to direct *non-thermal* excitations by the fast non-thermal electrons from the γ-ray thermalization. The luminosity due to a collisionally excited line with excitation temperature $T_{ex} = hc/k\lambda$ decreases exponentially with falling temperature, to a first approximation $L_{ij} \propto T_e^{-0.5} e^{-T_{ex}/T_e}$. The recombination emission is less sensitive to temperature, and actually increases slowly, $L_{ij} \propto T_e^{-0.7}$, typically. Finally, the non-thermal excitation rate is independent of T_e. As discussed above, optical and near-IR lines have high excitation temperatures $T_{ex} \gtrsim 1 \times 10^4$ K, and their luminosity decreases rapidly with temperature for $T_e \lesssim 3000$ K. The far-IR lines are much less sensitive

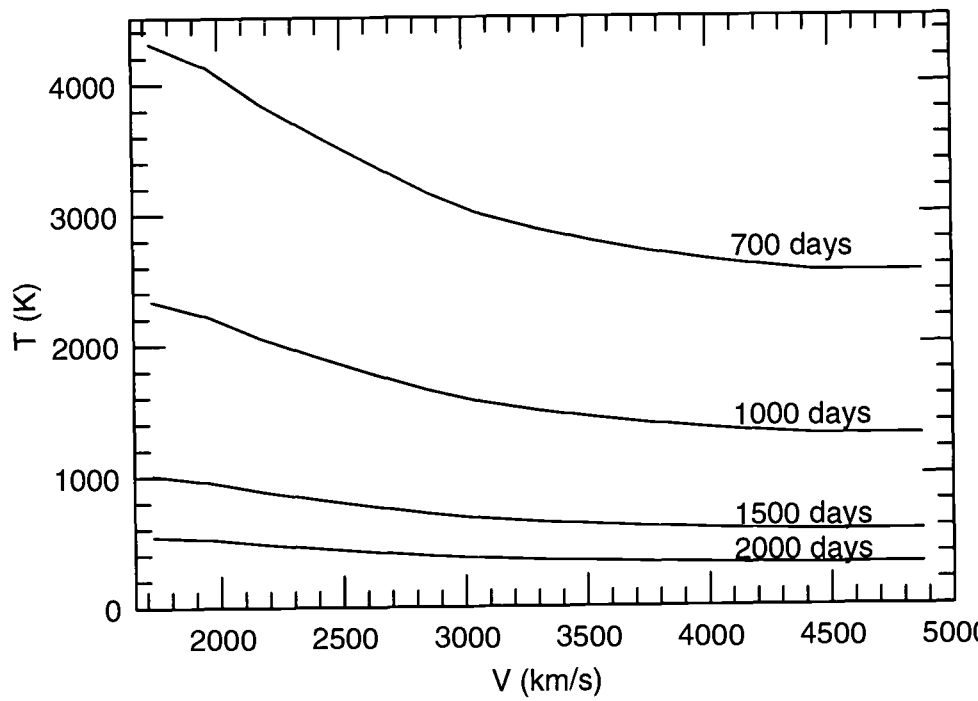

FIGURE 2. Temperature in the hydrogen envelope for different times.

with $T_{ex} \lesssim 1 \times 10^3$ K. Therefore, as the temperature in the core drops with the IR-catastrophe, the collisional excitation contribution of the optical and near-IR lines drops dramatically. Lines which have no recombination contribution, like [O I]$\lambda\lambda$6300 − 64, Mg I]λ4571, [Ca II]λ7300, and [Si I]$\lambda\lambda$1.099, 1.607 − 1.645 μ should display this behavior. This was predicted by the first models for the spectral evolution of SN 1987A (Fransson & Chevalier 1987), and was later basically verified by the observations (e.g. Menzies 1991; Spyromilio *et al.* 1991). The decrease in the [Si I] line has been interpreted as a result of dust formation (Lucy *et al.* 1991), but our calculations show that this need not be the case, and that the amount of dust is therefore not constrained by these observations.

Observations of the emission lines from SN 1987A show a dramatic shift in their evolution at $\sim$ 700 days. This is seen most clearly when the luminosities of the lines relative to the bolometric luminosity, L_j/L_{bol}, are plotted against time (e.g. Menzies 1991). This behavior is exactly what is expected because of the IR-catastrophe. As the temperature drops from $\sim$ 3000 K to a few $\times 10^2$ K because of the instability, the thermal contribution to the collisionally excited optical lines decreases to a negligible level. However, there is still a non-thermal contribution due to excitation by the fast electrons which is *independent of the temperature*, as shown by the third term in equation (2.8). The luminosity of a line j relative to the total bolometric luminosity in this phase is then

$$\frac{L_j}{L_{bol}} = \frac{\int \epsilon_{i,j} J_\gamma \sigma_{\gamma,i} n_i dV}{\int J_\gamma \sigma_\gamma n \, dV} = \epsilon_{i,j} \frac{\tau_{\gamma,i}}{\tau_{\gamma,tot}} \tag{2.9}$$

where $\tau_{\gamma,i}$ is the optical depth of the γ-rays to the ion i and $\tau_{\gamma,tot}$ is the total γ-ray optical depth averaged over the ejecta according to the γ-ray intensity. Since both $\tau_{\gamma,i}$

and $\tau_{\gamma,tot}$ vary with time as t^{-2}, we expect a fairly constant ratio of L_j/L_{bol}. Actually, $\epsilon_{i,j}$ increases slowly with decreasing electron fraction, so a slight deviation from a constant is expected, as is indeed observed. From the bolometric light curve we find that $\tau_{\gamma,tot} \approx 0.5$ on day 1000. The $\epsilon_{i,j}$'s are calculated from the Spencer-Fano equation (KF92) and we can therefore calculate $\tau_{\gamma,i}$ from L_j/L_{bol}. At 1000 days we find from Menzies (1991) and Danziger *et al.* (1991) that for the [O I]$\lambda\lambda$6300 – 64 lines $L_{6300} \approx 3.5 \times 10^{35}$ ergs, or $L_{6300}/L_{bol} \approx 2.9 \times 10^{-3}$ (see figure 3). For a typical value of $x_e = 10^{-2}$ at 1000 days $\epsilon_{6300} \approx 5 \times 10^{-3}$. The optical depth at 1000 days to the γ-rays in the oxygen gas is therefore $\tau_{\gamma,O} \approx 0.25$. The line width is $\sim$ 1500 km s^{-1}. Including γ-ray input from 0.07 M$_\odot$ ^{56}Ni and 2.5$\times 10^{-3}$ M$_\odot$ of ^{57}Ni (1.5 times solar) we estimate the [O I]$\lambda\lambda$ 6300–64 luminosity from

$$L_{6300} = 1.24 \times 10^{38} D_\gamma \left(e^{-t/111.3} + 9.3 \times 10^{-4} e^{-t/391.2}\right) \times \left(\frac{V}{1500 \text{ km s}^{-1}}\right)^{-2} \left(\frac{t}{1000 \text{ d}}\right)^{-2} \left(\frac{M_O}{1 \text{ M}_\odot}\right) \text{ ergs.} \quad (2.10)$$

Unfortunately, the oxygen mass is fairly sensitive to the exact velocity distribution of the oxygen, as well as the nickel distribution, through D_γ (KF92). However, generally $D_\gamma \lesssim 3$, and therefore $M_O \gtrsim 3\ (V/1500 \text{ km s}^{-1})^2$ M$_\odot$. To pin down the distributions of the nickel and oxygen, the line profiles are of great value, since they in principle contain this information. We are currently studying this issue. However, it is encouraging that even this simple type of analysis gives the correct order of the mass. The great advantage of this method of determining the mass is that it is independent of the temperature and ionization, in contrast to the earlier epochs when the mass depends exponentially on the uncertain temperature. It is also insensitive to clumping, since only the column density enters. Similar arguments can be used to determine the mass of the other abundant elements. Since the relative flux is directly proportional to the mass of the element, only fairly abundant elements produce lines with a non-thermal, constant contribution. Other than [O I]$\lambda\lambda$ 6300 – 64, the most interesting are Mg I]λ 4571, [Si I]λ 1.645 μ. All show a nearly constant L_j/L_{bol} after $\sim$ 700 days (Menzies 1991; Meikle *et al.* 1993; Danziger *et al.* 1991; Suntzeff *et al.* 1991).

In figure 3 we show the [O I]$\lambda\lambda$ 6300 – 64 luminosity from a more realistic calculation taking all atomic processes and elements in the oxygen zone into account. After oxygen the most abundant elements are silicon and sulphur. Other zones have not been included in this calculation since they contribute little to the total [O I]$\lambda\lambda$ 6300 – 64 emission. We assume the oxygen blobs are distributed uniformly in the core with a filling factor adjusted to give an oxygen density in agreement with that determined by Spyromilio & Pinto (1991) and Li & McCray (1992). Two sets of calculations are done. In one the total mass of the oxygen zone was 1M$_\odot$ while in the other it was 2M$_\odot$, corresponding to pure oxygen masses of 0.8 M$_\odot$ and 1.6 M$_\odot$, respectively. We have also varied the expansion velocity between 1000 and 2000 km s^{-1}, which probably covers most of the observed range. The corresponding filling factors are in the range 0.05 – 0.78. The temperature evolution is shown for the O-zone in figure 1, with a thermal instability at $\sim$ 900 days. We also show the observed [O I]$\lambda\lambda$ 6300 – 64 luminosity taken from Danziger *et al.* (1991) as filled dots in figure 3. First we note the very good agreement in the shape of the light curves and the observed evolution, with a characteristic break at $\sim$ 750 days. This is a direct consequence of the thermal evolution, and therefore confirms the occurrence of the IR-catastrophe. The level of the emission is sensitive to the expansion velocity and the total oxygen mass, as expected from equation (2.10). We find that for core velocities higher than $\sim$ 1000 km s^{-1}, as are indicated from the line

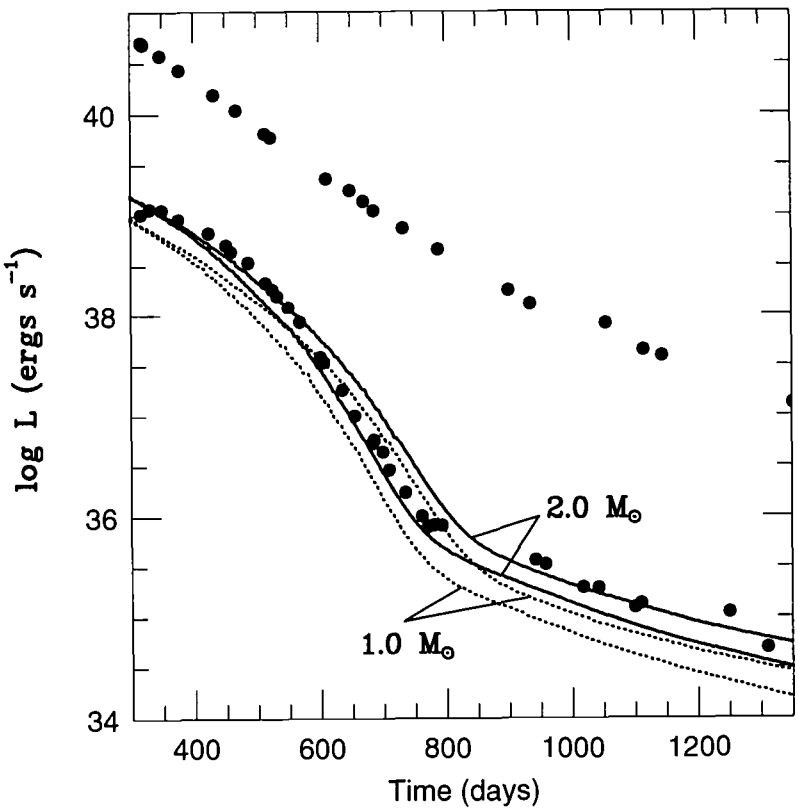

FIGURE 3. Luminosity of [O I]$\lambda\lambda$6300 – 64 as a function of time, together with observations from Danziger *et al.* (1991). The lower curve for each mass corresponds to an expansion velocity of 2000 km s^{-1} and the upper to 1000 km s^{-1}. The bolometric luminosity from Suntzeff *et al.* (1991) is shown as the upper dots. Before 750 days the emission is dominated by thermal excitations, while after this epoch non-thermal excitations dominate. This results in a nearly constant ratio of the line luminosity to the bolometric, as is observed.

profiles (e.g. Phillips & Williams 1991), the oxygen mass must be at least 1.5M$_\odot$. A smaller mass would not absorb enough γ-ray energy because of its small optical depth. Lower masses underestimate both the thermal and non-thermal parts of the light curve. The fact that we can fit both the flat, non-thermal part of the light curve after $\sim$ 750 days and the thermal part before this epoch also means that the calculated temperature evolution is close to the actual temperature evolution.

The strongest line during most of the evolution is Hα. The emission of this line has for SN 1987A been discussed by Xu *et al.* (1992) and in KF92. Hα is formed mainly by recombinations. Xu *et al.* find that during the first $\sim$ 500 days the non-thermal ionizations and excitations from the ground state are not enough to explain the line, but proposed that photoionization from $n = 2$ by the Balmer continuum can account for the extra ionizations needed. This mechanism was discussed earlier by Kirshner & Kwan (1974). KF92 analyzed the diffuse emission from the helium and metal core in order to calculate the UV radiation field and thus the strength of Hα. The emission spectrum from the core is formed by a step-wise degradation of far-UV recombination lines, resulting from γ-ionizations in the metal core, into lines in the optical and Balmer continuum. An example is He I for which $\sim$ 20% of the recombination energy emerges

directly as optical lines. The rest is emitted mainly as two-photon emission between 0 – 20.6 eV. In the He-zone, C is the second most abundant element, making the gas opaque above 11.26 eV. The two-photon emission between 11.26 eV and 20.6 eV therefore results in ionizations of C I, followed by C I recombination emission. Most of this is emitted as UV lines around $\sim$ 1200 Å, which can then be absorbed by the Balmer continuum. In the iron core, where helium has an abundance of $\sim$ 0.56 by number, Fe I plays the same role as C I, but with an ionization threshold of 7.87 eV. This example shows that a fairly complicated transfer of energy takes place from one zone (or element) to another, and that large errors will be introduced if these effects are not taken into account. KF92 find that a fraction $\epsilon_{UV} \approx 30\%$ of the total energy absorbed by the He- and metal core is emitted in the Balmer continuum. In the H-rich gas the recombinations and excitations ending up in the $n = 2$ level of H I will decay by two-photon emission. A fraction ~ 0.88 of this is above 3.4 eV and adds to the Balmer ionization. At $x_e \approx 10^{-2}$, $\chi_{eff} \approx 34$ eV, and a fraction $\chi_i/\chi_{eff} \approx 40\%$ of the γ-ray energy absorbed directly in the hydrogen gas goes into ionizations, and 32% into excitations. The total energy of the two-photon emission above 3.4 eV is then $\sim 0.88 \times (0.75 \times 0.40 + 0.32)\, \tau_H L_\gamma = 0.56\, \tau_H L_\gamma$. Therefore, the ratio of Balmer ionizations to those from the ground state is

$$\frac{\zeta_{Balmer}}{\zeta_{g.s.}} = \frac{(\epsilon_{UV}\tau_{core} + 0.56\tau_H)}{\tau_H} \frac{\chi_{eff}}{\chi_{n=2}} \approx (3.0\frac{\tau_{core}}{\tau_H} + 5.6). \tag{2.11}$$

Below, we find that $\tau_{total}/\tau_H \approx 2.5$, so $\tau_{core}/\tau_H \approx \tau_{total}/\tau_H - 1 \approx 1.5$ and $\zeta_{Balmer}/\zeta_{g.s.} \approx 10$, which is larger than the factor ~ 5 needed by Xu *et al.* (1992).

The fraction of the luminosity emitted as Hα shows a marked decrease at $\sim$ 700 days, after which it remains approximately constant (e.g. Menzies 1991). The decrease is not a temperature effect, but mainly a result of the Balmer continuum becoming optically thin. After $\sim$ 500 days the excitation of the line is dominated by non-thermal ionizations, followed by recombinations, plus direct non-thermal excitations to the $n = 3$ level. The expected decrease is therefore a factor ~ 10 from equation (2.11), in reasonable agreement with the observations. If we neglect freeze out effects for the moment, we find that

$$\begin{aligned} \frac{L_{\rm H\alpha}}{L_{bol}} &= \left(\frac{\chi_i}{\chi_{eff}} \frac{j_{\rm H\alpha}}{\alpha_B \chi_i} + \frac{5}{36} \epsilon_{H,n=3} \right) \frac{\tau_{\gamma,H}}{\tau_{\gamma,tot}} \\ &\approx (0.4 \times 0.070 + 0.14 \times 0.05) \frac{\tau_{\gamma,H}}{\tau_{\gamma,tot}} = 0.035\, \frac{\tau_{\gamma,H}}{\tau_{\gamma,tot}}. \end{aligned} \tag{2.12}$$

If the Balmer lines are optically thick (Case C), the Hα strength may increase by a factor ~ 2 compared to this estimate. Freeze out effects are important after $\sim$ 900 days in the H regions (FK93), and after this epoch the delayed recombination will give an additional contribution to Hα. On day 750 $L_{\rm H\alpha}/L_{bol} \approx 1.4 \times 10^{-2}$ and we find that $\tau_{\gamma,H}/\tau_{\gamma,tot} \approx 0.40$, or translated to 1000 days $\tau_{\gamma,H} \approx 0.20$. This value is somewhat larger than from the Shigeyama *et al.* (1988) 14E1 model, and may indicate an hydrogen mass less than $\sim 10 M_\odot$.

Finally, we note that the evolution of the line luminosities in general offer an interesting possibility to test the radioactive decay time scale, and thus the dominant source of radioactivity or a possible pulsar contribution. Because lines fed by direct excitation decay immediately to the ground state, the luminosity will follow the instantaneous energy input,

$$L_j \propto \epsilon_{i,j}\, \tau_i\, e^{-t/\tau} \propto \epsilon_{i,j}\, t^{-2} e^{-t/\tau} \tag{2.13}$$

if $\tau_\gamma << 1$. This applies to e.g. the [O I] line. If positrons from ^{44}Ti dominate the energy input $L_j \propto \epsilon_{i,j}\, e^{-t/\tau} \approx$ *constant*. A line mainly arising due to recombination will behave

like

$$L_j \propto \int j(T_e)\, n_e n_{i+1}\, dV \propto j(T_e)\, x_e^2 t^{-3} \propto x_e^2 t^{-1.6} \tag{2.14}$$

in the freeze out phase, since for H-like ions $j(T_e) \propto T_e^{-0.7} \propto t^{1.4}$, if adiabatic cooling dominates.

3. Type Ia SNe

While considerable progress has been made on the late emission from Type II SNe, the situation is worse for Type Ia SNe both observationally and theoretically. Few detailed observations exist. In fact, only for SN 1972E does there exist good photometry and spectra beyond a year (Kirshner *et al.* 1973, 1975). Our ability to produce detailed synthetic spectra is also rather limited, in part because of the continuing lack of high quality atomic data for iron ions.

Even neglecting the absence of hydrogen, the physical conditions in Type Ia SNe are quite different from Type II's. In the best studied model, in which a Type Ia supernova is produced by the explosion of a Chandrasekhar mass white dwarf, the total mass $\lesssim 1.4 M_\odot$ is smaller than that of a massive stellar core by a factor ~ 3. The observed expansion velocity of this metal rich material ($\sim 10^4$ km s^{-1}) is considerably greater than the ~ 2000 km s^{-1} typical in the Type II's, so that the total density is smaller by at least a factor ~ 400 in the Type Ia case. Given that the ^{56}Ni mass produced in a Type Ia supernova is also larger by a factor ~ 10 the level of ionization is much higher than in a Type II at a similar epoch (e.g. equation 1.3).

To study the spectral evolution and the photometric light curves, Houck, Fransson & Pinto (1994) calculated the time dependent spectrum for several different explosion models taken from Woosley (1991), Woosley (1992, private communication) and Woosley *et al.* (1986). A time dependent calculation is necessary to treat the freeze out effects properly. Unfortunately, the exact results depend fairly sensitively on the recombination rates of Fe I – Fe V, which are uncertain by embarrassingly large factors. Hopefully, new calculations within the OPACITY project can improve this situation (Le Dourneuf *et al.* 1993). Using rates by Shull & Van Steenberg (1982) we find that the level of ionization at 250 days is much too high to fit the observed optical spectrum of SN 1972E. Because increasing the Fe II and Fe III recombination rates by a factor ~ 3 considerably improves the agreement with the observed spectrum, we calculate the light curves using these enhanced recombination rates instead of the Shull & Van Steenberg rates. This is the primary uncertainty in the model.

Here we describe results for model DD4 from Woosley (1991), corresponding to a "delayed detonation" of a Chandrasekhar mass white dwarf producing $0.62 M_\odot$ of mainly ^{56}Ni. This model produces the best fit to the observed optical spectrum of SN 1972E at 250 days. In figure 4 we show the temperature and ionization evolution for a number of different mass elements from the center to the surface. First, we note that the most abundant ion is Fe II even at very late stages, leading to $x_e \gtrsim 0.5$ as late as ~ 900 days. This confirms the high level of ionization expected. The low ionization zone corresponds to the central region where the ^{56}Ni concentration is quite low. The temperature curves clearly show the onset of the thermal instability at ~ 450 days; over the next 200 days, the temperature rapidly decreases from ~ 3000 K to ~ 300 K. This is the IR-catastrophe originally discussed by Axelrod (1980). After the IR-catastrophe nearly all emission emerges as fine structure lines of [Fe II] (λ 25.99 μ, λ 35.35 μ) and [Fe I] (λ 24.05 μ).

From the calculated spectra we determine the flux in various photometric bands, and

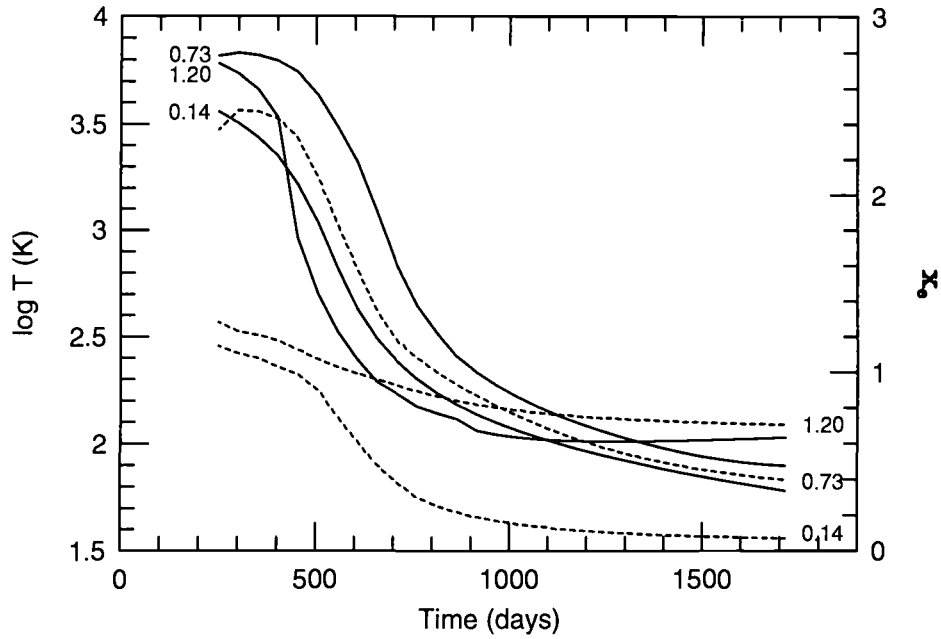

FIGURE 4. Time evolution of the temperature (full lines) and electron fraction (dashed lines) for three different mass shells in the Type Ia SN model DD4 from Woosley (1991). Mass shells with interior mass $M(R_i) = 0.14$, 0.73, and 1.20 $M_\odot$ are shown. Note the thermal instability at 500 - 800 days, and the high degree of ionization even beyond 1000 days.

in figure 5 we show the resulting light curves from the UV to the IR. We have here used a distance of 4 Mpc, appropriate for SN 1972E. For a more common distance of 10 Mpc one should add 2 magnitudes. There is a marked decrease in the fluxes in most of the optical bands between 450 and 600 days, coinciding with the IR-catastrophe. The V magnitude increases from V $\approx$ 18.2 to V $\approx$ 22.8, while the B magnitude increases from B $\approx$ 18.3 to B $\approx$ 23.2. The U band, however increases more smoothly out to 500 days. The J magnitude appears to rise quite slowly with J $\approx$ 16 from 300 until 500 days, when it also increases rapidly J $\approx$ 24.4 at 700 days. The slow decline in J happens at the same time as the rapid decline in B and can be attributed to a shift in emission from the strong [Fe III] blend at $\sim$ 5000Å to the [Fe II] lines at 1.257 μ and 1.644 μ in the near-IR. Despite the rapid cooling during this epoch, we find no brightening in the far-IR photometry because the strongest fine structure lines, e.g. [Fe II]λ 25.99 μ, λ 35.35 μ, [Fe I]λ 24.05 μ are outside the photometric bands, and no strong lines lie in the N and Q bands. Possibly ISO may be sensitive enough to measure the fluxes in the interesting bands (especially the 20 – 36 μ region).

The rapid increase in B magnitude between 450 and 700 days is inconsistent with the B light curve of SN 1972E obtained by Kirshner *et al.* (1975). However, the proper means for avoiding the rapid drop in the computed optical luminosity compared to the near IR is not clear. As in the Type II case, this emission is mainly due to recombinations following non-thermal ionizations which, as was discussed earlier, are relatively insensitive to the temperature. In the Type Ia case, because the electron fraction is $x_e \gtrsim 0.5$ until very late times, $t \sim$ 900 days, most of the non-thermal energy deposited during this epoch goes

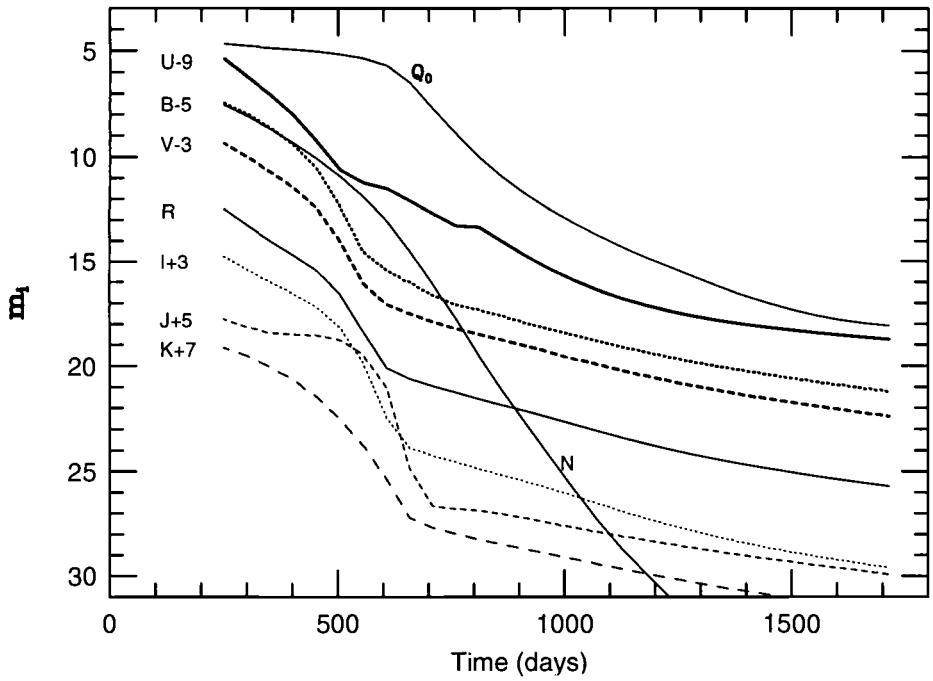

FIGURE 5. Photometric light curves for the same model as in figure 4, for a SN distance of 4 Mpc. The decrease at $\sim$ 600 days is due to the thermal instability.

into heating and ionization and only a negligible fraction goes into direct excitation. Our computed spectrum at 400 days gives a reasonably good fit to the [Fe II]λ 1.257 μ and [Fe II]λ 1.644 μ features observed in SN 1991T by Spyromilio *et al.* (1992), however the optical features in our computed spectrum are too faint by factors $\sim 3-5$. One possible explanation is that our model temperature is too low, perhaps because of clumping in the ejecta. In this case, most of the optical emission might come primarily from the hotter lower density regions between the clumps. Another possibility is that the optical emission, which should come from the recombination cascade, is modeled incorrectly because of the lack of accurate atomic data.

Because of its larger region of higher ^{56}Ni concentration, model DD3 (^{56}Ni mass $0.93M_\odot$) from Woosley (1991) produces a more gradual decrease in the B light curve, with the B magnitude falling to B $\approx$ 23 only after $\sim$ 700 days. The higher ^{56}Ni concentration produces a higher level of ionization and heating so that the IR-catastrophe is postponed. However, even this more extreme model recombines and cools to rapidly to fit the observed light curve of SN 1972E.

At epochs later than $\sim$ 1000 days the light curves stay fairly constant as a result of both the extra energy input from ^{44}Ti and a freeze out. Which of these is the most important is sensitive to the mass of ^{44}Ti, which in turn depends on the particular explosion model. Unfortunately, it will not be easy to distinguish these two effects. Because of recombination to Fe I at very late times $t > 1500$ days, the supernova brightens in the optical so that as much as 50% of the luminosity comes out shortward of 1 μ. However, the details of this result depend on the low temperature ($\sim$ 100 K) Fe I recombination rate and are quite uncertain.

In conclusion, although spectroscopy later than a year is not trivial, photometry should

be fairly easy, and may therefore be the best way to study these phases. Photometry is also likely to be less sensitive to uncertainties in the atomic data. Even in this case, the quality of the atomic data for Fe is the main obstacle in modeling Type Ia spectra.

REFERENCES

Axelrod, T.S., (1980) Ph.D. thesis, Univ. of California, Santa Cruz.

Chevalier, R. A., & Fransson, C., (1992) ApJ, 395, 540

Danziger, I.J., Gouiffes, C., Bouchet, & P. Lucy L.B. , (1991), ESO/EIPC Workshop *Supernova 1987A and Other Supernovae*, eds. I.J. Danziger & K. Kjär, p. 217

Le Dourneuf, M., Nahar, S.N., & Pradhan, A.K., (1993) J. Phys. B, 26, L1

Fransson, C., (1993) in Les Houches, Session LIV, 1990, *Supernovae* eds. J. Audouze, S. Bludman, R. Mochkovitch and J. Zinn-Justin, Elsevier Science Publishers B.V., in press

Fransson, C., & Chevalier, R.A. , (1987) ApJ, 322, L15

Fransson, C., & Chevalier, R. A., (1989) ApJ, 343, 323

Fransson, C., & Kozma, C., (1993) ApJ, 408, L25 (FK93)

Fryxell, B., Müller, E. & Arnett, D., (1991) ApJ, 367, 619

Houck, J., Fransson, C., & Pinto P., (1993) in preparation

Kirshner, R.P., & Kwan, J. , (1975) ApJ, 197, 415

Kirshner, R.P., Oke, J.B., Penston, M.V., & Searle, L., (1973), ApJ, 185, 303

Kirshner, R.P., & Oke, (1975), ApJ, 200, 574

Kozma, C., & Fransson, C., (1992), ApJ, 390, 602 (KF92)

Kurfess, J.D. *et al.* (1992) ApJ, 399, L137

Li, H. & McCray, R., (1992), ApJ 387, 309

Lucy, L.B., Danziger, I.J., Gouiffes, C., & Bouchet P. , (1991) *Supernovae, Proc. of the Tenth Santa Cruz Summer Workshop in Astronomy and Astrophysics*, ed. S.E. Woosley, Springer Verlag, 82

Menzies, J.W. , (1991), ESO/EIPC Workshop *Supernova 1987A and Other Supernovae*, eds. I.J. Danziger & K. Kjär, p. 209

Meikle, W.P.S., Spyromilio, J., Allen, D.A., Varani, G.-F., & Cumming, R.J., (1993) MN 261, 535

Phillips, M.M., & Williams, R.E. (1991) *Supernovae, Proc. of the Tenth Santa Cruz Summer Workshop in Astronomy and Astrophysics*, ed. S.E. Woosley , Springer Verlag, 36

Pinto, P.A. & Woosley, S.E., (1988) Nature, 333, 534

Shigeyama, T., Nomoto, K., & Hashimoto, M., (1988) A&A, 196, 141

Shull, J.M., & Van Steenberg, M., (1982), ApJS., 48, 95

Spyromilio, J. & Pinto, P. A. (1991) , ESO/EIPC Workshop *Supernova 1987A and Other Supernovae*, eds. I.J. Danziger & K. Kjär, p. 423

Spyromilio, J., Stathakis, R.A., Cannon, R.D., Waterman, L. & Couch, W.J., (1991) MN 248, 465

Suntzeff, N.B., Philips, M.M., Depoy, D.L., Elias, J.H., & Walker, A.R., (1991) AJ, 102, 1118

Woosley, S.E., (1991), Gamma-Ray Line Astrophysics, eds. P.Durouchoux & N. Prantzos, (New York: American Institute of Physics), 270.

Woosley, S. E., Pinto, P. A., & Hartmann, D., (1989) ApJ 346, 395

Woosley, S.E., Taam, R.E., & Weaver, T.A., (1986), ApJ 301, 601

Xu, Y., & McCray, R. (1991) ApJ, 375, 190

Xu, Y., McCray, R., Oliva, E., & Randich, S. (1992) ApJ, 386, 181

Understanding the Nebular Spectrum of SN 1987A

By RICHARD McCRAY

JILA, University of Colorado, Boulder, CO 80309-0440, USA

The nebular spectra of supernovae differ from those of better-known emission nebulae in that many of the emission lines are optically thick. Here we sketch the theory for interpreting such spectra, and show how it can be used to interpret prominent emission line systems in the spectrum of SN 1987A. As examples, we describe: (1) a simple method to infer the density of O I from observations of the evolution of the doublet ratio in [O I]$\lambda\lambda$6300; (2) new kind of hydrogen recombination line spectrum; (3) an analysis showing that the Ca II infrared emission lines must come from primordial, not newly-synthesized, calcium; (4) a theory for the Fe/Co/Ni emission lines that shows that the inner envelope of SN 1987A must have a foamy texture, in which low density radioactive bubbles of Fe/Co/Ni reside in a massive substrate of hydrogen, helium, and other elements.

1. Introduction

Conventional wisdom holds that supernova explosions produce most of the heavy elements in the universe, and a major goal of astronomy is to test this hypothesis through observations of supernova spectra. For this purpose, SN 1987A should be a Rosetta Stone. We have observed its spectrum in far greater detail than that of any other supernova: at wavelength bands, such as gamma rays and far infrared, where no other supernova has been observed; with almost daily (nightly!) observations continuing for more than seven years after outburst; and with unprecedented spectral resolution (McCray 1993). What have we learned about the debris of SN 1987A from such observations? About element synthesis? About the physical conditions in the debris? How can we use the knowledge gained from SN 1987A to interpret the spectra of other, more distant supernovae?

We can identify three major components that appear in the spectra of supernovae. The first, called the *photospheric spectrum*, usually dominates during the first few months after outburst (until maximum, and during the plateau phase of the light curve). The photospheric spectrum is characterized by a strong blackbody-like continuum with a characteristic temperature that levels off at ~ 5000 K after a week or two. This continuum is punctuated by strong P-Cygni lines, mainly hydrogen lines in SN II and metal lines in SN I. The second component, called the *nebular spectrum*, dominates after a few months, when the photospheric recedes to the center of the envelope and the continuum fades. In the nebular phase, most of the luminosity appears as emission lines and it is difficult to discern an optical continuum from the many overlapping weak emission lines. When I use the term nebular spectrum, I mean specifically an emission line spectrum that resembles that of SN 1987A after four months. It is characterized by lines from neutral and singly-ionized elements and linewidths with FWHM $\sim 3000-4000$ km s^{-1}; it clearly comes from the glowing radioactive interior of the supernova envelope.

Often, supernova spectra have a third component, which I shall call the *interaction* spectrum. It is also characterized by strong emission lines, but the lines are very different from those seen in the spectrum of SN 1987A. They typically display emission lines of elements ionized twice or more, having broad, often asymmetric, profiles with FWHM $\gtrsim 5000$ km s^{-1}. The interaction spectrum is evidently caused, not by the radioactive

glow of the inner supernova debris, but by the shocks that result from the impact of the debris with circumstellar matter that has been ejected by the progenitor. Up to now, SN 1987A lacks such a spectrum because it is expanding into a bubble of very low density gas created by its blue-giant progenitor. The interaction spectrum of SN 1987A will only appear *ca.* AD 1999 ± 3 when its envelope strikes the circumstellar ring (Suzuki *et al* 1993; Masai & Nomoto 1993; Luo, McCray, & Slavin 1994). But the interaction spectrum is often very prominent, even at relatively early times, in SNe with red giant progenitors, such as SN 1993J (Wheeler & Filippenko, 1995). With SN 1987A we are lucky, because we can be sure that its nebular spectrum comes only from its radioactive interior and is not contaminated by an interaction spectrum.

Here I give a brief summary of the present state of the art of interpreting the nebular spectrum of SN 1987A. Some of the results came as a surprise to us, but are fairly easy to understand in retrospect. As the reader will see, we have learned less than we might have hoped about element synthesis, but more than we might have hoped about the dynamics and thermodynamics of the envelope. Many of the basic principles are universal, and will undoubtedly be very useful in interpreting the nebular spectra of other supernovae.

Two rather different strategies have been used to model the nebular spectrum of SN 1987A. In the first, one calculates a model for the entire spectrum starting with a model for the supernova envelope characterized by a set of parameters representing element composition, etc. One then adjusts the parameters to achieve a best synthesis of the model with observations. This strategy, represented by the pioneering efforts by Fransson & Chevalier (1987), Swartz et al (1987), and Colgan & Hollenbach (1988), had a fair amount of success in predicting and interpreting the evolution of the overall nebular spectrum of SN 1987A; but, as one might expect, did not account for many details.

We have adopted a second strategy, following the pioneering work by Chugai (1987, 1990). Rather than trying to synthesize the whole spectrum at once, we have focused our efforts on developing detailed models for the time development of emission lines from each different element group. We adopted this approach mainly because we suspected (and now we are sure) that the parts of the supernova envelope responsible for emitting the lines of different elements retain their chemical identities – e.g., most of the hydrogen has approximately primordial composition, most of the oxygen is found in zones of relatively pure carbon/oxygen, etc. I.e., hydrodynamic instabilities following the blast caused the supernova envelope to be mixed macroscopically but not microscopically (*stirred, not blended*). We have attempted to model the emission lines from different element groups, one by one, concentrating on those elements responsible for the brightest lines: hydrogen, oxygen, calcium, and the iron group elements.

Our strategy has advantages and disadvantages. The main disadvantage is that it is painstaking and slow. One can reach an overall gestalt of the emitting region more readily through the first, more synthetic, strategy. The main advantage of our strategy is that, by focusing on one element at a time, we can identify more easily the physical processes that control the line emission, and thereby pin down with greater confidence the physical state of the relevant emitting region. Of course, we hope ultimately to combine the results of our detailed studies to produce a synthetic model for the envelope that fairly represents the development of the entire spectrum. As the reader will see, however, we have a few more obstacles to overcome before we reach that goal.

2. Emission Line Formation in Supernova Envelopes

During the nebular phase, most of the luminosity of the supernova envelope emerges as an optical/infrared emission line spectrum. Just as in an H II region or a planetary

nebula, the emission lines from hydrogen are produced mainly by radiative recombination and those from other elements are produced mainly by electron impact excitation. Thus, one can turn to classic texts such as Osterbrock (1989) for details of the physical processes and diagnostic methods. However, supernova envelopes differ from ordinary nebulae in four important ways:

- Supernova envelopes expand hypersonically (Mach number $\mathcal{M} \sim 10^3$), so that resonance scattering of a line photon is confined to a region of fractional thickness $\sim \mathcal{M}^{-1}$.
- Supernova envelopes have atomic densities, $n \sim 10^7 - 10^9$ cm^{-3}, that are much higher than the densities, $n \sim 10^2 - 10^4$ cm^{-3}, in typical nebulae. As a result, many emission lines, even the forbidden lines, have high optical depths.
- Supernova envelopes are ionized by gamma rays, which have low ionization cross-sections and long mean free paths. As a result, the envelope contains no sharp ionization fronts.
- Because the densities are high and the gamma rays have relatively low flux, the envelope is mostly neutral and much colder than ordinary emission line nebulae.

Thus, if we wish to understand what the nebular spectrum of a supernova is telling us about the physical conditions (densities, temperatures, element composition) of the supernova ejecta, we must modify the standard theory of emission nebulae to account for these differences. Let us address them in turn. See McCray (1993) for more details and references; here we merely summarize the main points and illustrate them with a few simple examples.

2.1. *Envelope expansion and line profiles*

Fortunately, the motion of a supernova envelope can be described by the simplest possible dynamics: Hubble's Law! Because acceleration within the envelope ceases within hours or at most days after the explosion, the distance from the center of any parcel of gas is given by $r = vt$, where V is its radial velocity, and t is the time since the explosion. It follows that the *relative* recession velocities, $\Delta v = v_1 - v_2$ of any two mass points is related to their separation $\Delta r = r_1 - r_2$ by the law $\Delta v = H_0 \Delta r$, where the "Hubble constant" $H_0 = t^{-1}$.

Moreover, the emission lines from a supernova envelope have Doppler widths indicative of expansion velocities of the emitting region $v_{exp} \sim 1000 - 3000$ km s^{-1}, much greater than the thermal velocities $v_{th} \sim 1 - 3$ km s^{-1} of the line-emitting atoms or molecules†. Thus, the regions of the supernova envelope responsible for emitting different parts of the line profiles are physically separated. In fact, the region responsible for line emission at a given Doppler shift, $\Delta\lambda = (v_\parallel/c)\lambda_0$, is confined to a thin planar section displaced a distance $\Delta z = ct\Delta\lambda/\lambda_0$ from the midplane of the supernova envelope, as illustrated in Figure 1. The section has thickness $\delta z \sim (v_{th}/v_\parallel)\Delta z$.

It is easy to demonstrate that line emission from a thin spherical shell would have a rectangular line profile. From that fact, one can infer that if the supernova envelope had a laminar, 'onion-like' distribution of element groups (as we believe the progenitor did), the line profiles from different chemical element would have flat tops, with the Doppler widths of the flat tops representing the minimum expansion velocities of the respective elements. But the line profiles in the nebular spectrum of SN 1987A do not have flat tops; indeed, they are all very similar in shape. That fact proves that the different element groups are not radially stratified, but are present in similar proportions throughout the line-emitting part of the envelope.

† Note that the line-emitting region is not the entire envelope, but only the inner, more slowly moving part of the envelope where the gas has greater density and where most of the gamma ray energy is deposited

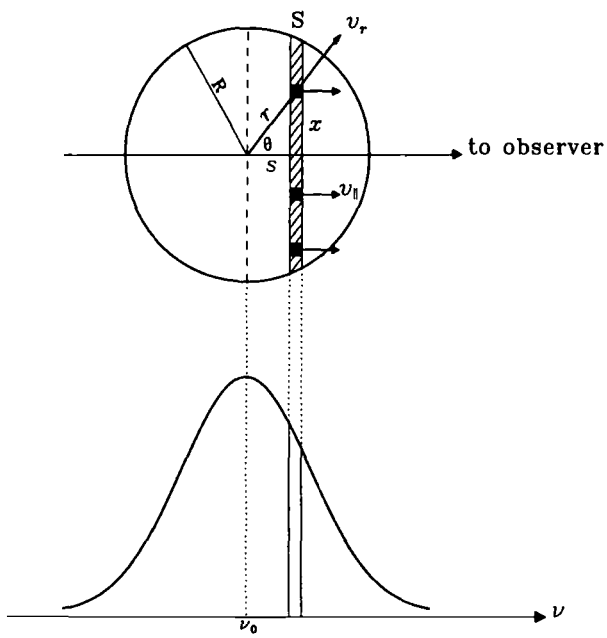

FIGURE 1. Line profile formation in a supernova envelope. The line emission from element A at a given Doppler shift (lower panel) is confined to the intersection of the thin planar section (hatched) with the clumps (solid) containing element A (upper panel).

2.2. *Line Optical Depth and the Sobolev Approximation*

Now we address the issue of line transfer. As we know, this can quickly become a nasty technical problem in a stellar atmosphere. In contrast, line transfer is easy to describe in a supernova envelope because of the hypersonic expansion. Generally, the optical depth is given by an expression of the form $\tau_{lu} = n_a \sigma_{lu}(\nu)\delta z$, where n_l is the atomic density of absorbers in the lower (l) state, $\sigma_{lu}(\nu)$ is the photon resonant scattering cross section, and δz is the path length. Now, let us assume (to keep the algebra simple) that the normalized line profile function is a rectangle, with height $\phi(\delta\nu) = (\delta\nu)^{-1}$ and width $\delta\nu$. Then, a photon will remain in resonance with the line over a path length

$$\delta z = ct\frac{\delta\nu}{\nu_{lu}}. \tag{2.1}$$

But we can write $\sigma_{lu}(\nu) = (\pi e^2/m_e c) f_{lu}\phi(\delta\nu)$, where f_{lu} is the absorption oscillator strength for the transition from the lower to upper (u) level. Putting this all together, we derive an expression for the Sobolev optical depth of an absorption line in an expanding envelope:

$$\tau_{lu} = \frac{\pi e^2}{m_e c} f_{lu}\lambda_{ul} t n_l \left[1 - \frac{g_l n_u}{g_u n_l}\right] = \frac{c^3 t g_u A_{ul} n_l}{8\pi\nu^3 g_l}\left[1 - \frac{g_l n_u}{g_u n_l}\right], \tag{2.2}$$

where we have included the term in square brackets to account for induced emission by a density, n_u, of atoms in the upper state, and the $g's$ are the statistical weights of the respective states. Note that for a freely expanding envelope, $n_l \propto t^{-3}$, so that $\tau_{lu} \propto t^{-2}$.

Now, the "Sobolev escape probability" that a resonance photon emitted by a downward

transition will escape without further scattering is given by

$$P_{esc} = \int_0^1 d\zeta \exp(-\zeta\tau_{lu}) = \tau_{lu}^{-1}[1 - \exp(-\tau_{lu})], \tag{2.3}$$

and the line emissivity per unit volume is given by

$$j_{ul}(\nu) = \frac{1}{4\pi} n_u A_{ul} h\nu_{ul} \phi(\delta\nu) P_{esc}(\nu_{ul}), \tag{2.4}$$

where A_{ul} is the spontaneous decay rate of the upper state. For a freely expanding supernova envelope the equation of transfer has the simple solution

$$I_{ul}(\nu) = j_{ul}(\nu)\delta z = \frac{hct}{4\pi} n_u A_{ul} P_{esc}(\nu_{ul}), \tag{2.5}$$

Note that in the optically thick limit, $\tau_{lu} \gg 1$, $I_{ul}(\nu) \to B_\nu(T)$, as one would expect.

Although we have used the artifice of a rectangular line profile function to derive equations (2.2) and (2.5), the results are valid in general provided that the expansion Mach number is high.

The Sobolev opacity has the curious property that one can see line emission from the entire volume of the envelope even though the emission line may have high optical depth at every velocity. An opaque surface resonant at ν_1 does not obscure the line emission from a surface deeper within the envelope resonant at $\nu_2 < \nu_1 - \delta\nu$.

Consider now the total observed line flux, which is given by

$$F_{ul} = \frac{1}{D^2} \int d\nu A(z) I_{ul}(\nu), \tag{2.6}$$

where D is the distance to the source and $A(z)$ is the cross-sectional area of the line-emitting gas at the plane corresponding to the frequency ν (see Figure 1).

Equation (2.6) has two important limits. In the optically thin limit, $\tau_{lu} \ll 1$, $P_{esc} \to 1$ and we find

$$F_{ul} = \frac{A_{ul} h\nu}{4\pi D^2} \int dz A(z) n_u(z) = \frac{A_{ul} h\nu}{4\pi D^2} N_u, \tag{2.7}$$

where N_u is the total number of excited atoms in the emitting volume. If the atomic level populations are in LTE, we may write

$$N_u = \frac{M_A}{m_A} \frac{g_u}{G(T)} \exp(-E_u/kT), \tag{2.8}$$

where M_A is the total mass of atoms, m_A is their atomic mass, E_u is their excitation energy, and $G(T)$ is the partition function. Note that equation (2.7) gives the result $F_{ul} \propto$ constant for constant T. Therefore, a decreasing line flux implies that the excitation temperature is decreasing.

In the optically thick limit, $\tau_{lu} \gg 1$, $P_{esc} \to \tau_{lu}^{-1}$ and we find

$$F_{ul} = \frac{\nu}{ctD^2} B_\nu(T) \int dz A(z) = \frac{\nu V_A}{ctD^2} B_\nu(T), \tag{2.9}$$

where V_A is the net volume occupied by atoms of element A (the hatched volume in Figure 1). Since $V_A \propto t^3$ for free expansion, we find that $F_{ul} \propto t^2$ for constant T. The fact that the luminosities of several emission lines from SN 1987A actually do increase approximately as t^2 for $t \lesssim 200$ days is evidence that the lines are optically thick and that the temperature is fairly constant.

Note the difference between the optically thin limit (eq. 2.7) and the optically thick limit (eq. 2.9): in the former, the line flux is proportional to the *mass* of the emitting gas times a known function of temperature; whereas in the latter, the line flux is proportional

to the *volume occupied* by the emitting gas times the Planck function. Therefore, if we can observe emission lines from two different excited levels of the same ion, we can infer the gas temperature from the ratio of the line strengths. Then, given the temperature, we can infer from the line fluxes either the net mass of the ion in question if the lines are optically thin or the volume occupied by that ion if the lines are optically thick.

The full width at zero intensity of the line profiles, $\Delta\lambda$, gives a measure of the total volume in which the emitting gas is contained (the volume of the sphere of radius $r_m = v_m t$ in Figure 1),

$$V_E = \frac{4\pi}{3}(v_m t)^3 = \frac{4\pi}{3}\left[\frac{\Delta\lambda}{2\lambda}ct\right]^3 , \tag{2.10}$$

from which we may define the filling factor, $f_A = V_A/V_E$. In deriving equations (2.7), and (2.9), we have assumed that the temperature and density of the emitting gas are spatially uniform. Of course, one may wish to consider more complicated distributions of density and temperature in making detailed models for supernova spectra, in which case one can simply calculate the integral in equation (2.6) directly.

In the following, we will illustrate how the simple formalism described above can be used to infer the physical conditions in the envelope of SN 1987A from a few of the most prominent emission line systems in its nebular spectrum.

3. Optically Thick Forbidden Lines: the [O I]$\lambda\lambda$6300 Doublet

The [O I]$\lambda\lambda$6300 doublet is one of the most prominent emission lines in the nebular spectrum of SN 1987A. The time evolution of the observed line ratio $R = F(6300)/F(6364)$ (actually, peak fluxes) is shown in Figure 2.

These observations provide a lovely example of how one can infer the density of a gas from Sobolev theory (Chugai 1990; Spyromilio & Pinto 1991; Li & McCray 1992). The two transitions, which couple the upper ^{1}D state to the lower ^{3}P state, have spontaneous decay rates related by $A(6300) = 3A(6364)$. Therefore, if the transitions were optically thin, the line ratio should be $R = 3$, according to equation (2.7). But if both transitions were optically thick, then both lines should have identical intensity given by equation (2.9). In fact, we see the line ratio change from $R \approx 1$ at $t \approx 100$ days to $R \approx 2.5$ at $t \approx 500$ days (at which time the doublet is too weak to measure R). Clearly, we are seeing these emission lines make the transition from optically thick to optically thin.

From equations (2.2, 2.3, 2.5, and 2.6), we derive the simple result:

$$R = \frac{1-\exp[-\tau(6300)]}{1-\exp[-\tau(6364)]} = \frac{1-\exp[-3(t_1/t)^2]}{1-\exp[-(t_1/t)^2]} , \tag{3.11}$$

where, in deriving the second expression, we have defined t_1 as the time when $\tau(6364) = 1$ and we have used the facts that $\tau \propto t^{-2}$ and $\tau(6300) = 3\tau(6364)$. The curve in Figure 2 represents a fit of equation (3.11) to the data; it gives $t_1 = 251$ days. Then, we may set $\tau(6364) = 1$ in equation (2.2) to derive $n_l(t_1) = n_{OI}(t_1)/3$. The result is $n_{OI}(t) = 4.0 \times 10^9 (t/t_1)^{-3}$ cm^{-3}.

If the spectrum of SN 1987A displayed other O I emission lines, we would be able to infer the mass, M_O, and temperature evolution, $T_O(t)$, of the O I-emitting gas from the emission line fluxes, as described in § 2. Unfortunately, this is not the case. Therefore, Li & McCray (1992) simply estimated $M_O \approx 1.3 M_\odot$ in accord with supernova nucleosynthesis models (e.g., Nomoto *et al* 1989) in order to infer $T_O(t)$ from the observations. They find that $T_O(t)$ decreases from $T_O(200\,d) \approx 4000$ K to $T_O(500\,d) \approx 3000$ K.

This result raises a very important general point: *thermally excited optical emission*

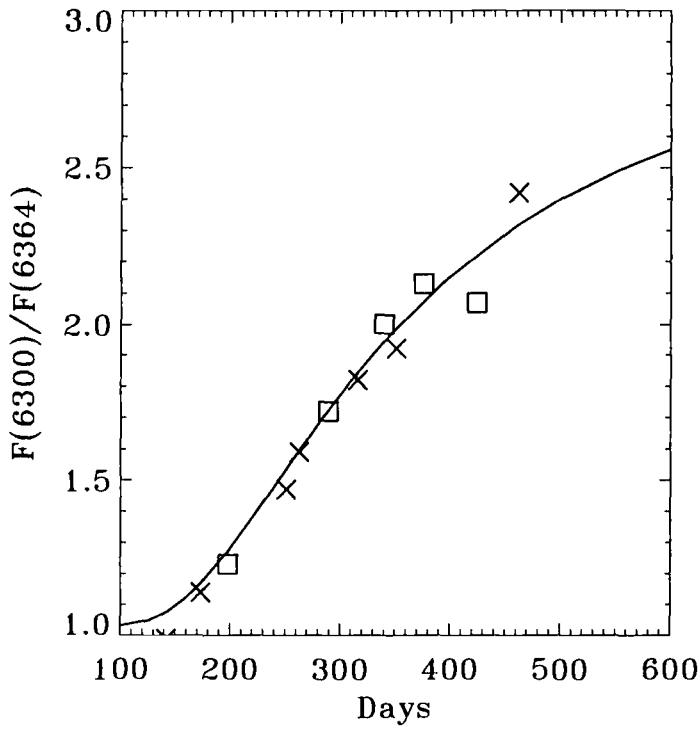

FIGURE 2. Variation with time of the ratio of peak fluxes $R = F(6300)/F(6364)$ of the [O I]$\lambda\lambda$6300 doublet. Data are from Spyromilio & Pinto (1991) *(crosses)* and Phillips & Williams (1991) *(stars)*. The solid curve is a fit to equation (3.11).

lines are poor diagnostics of supernova nucleosynthesis yields. The fluxes of optical emission lines are far more sensitive to temperature than to mass. For example, equations (2.6) and (2.8) give $F(6300) \propto M_O \exp(-22,800/T_O)$. At $T \approx 3000$ K, a 10% increase in $T_O(t)$ will give the same increase in $F(6300)$ as a factor of 2 increase in M_O. By the same token, we can infer gas temperatures fairly accurately from the fluxes of optical emission lines even if our estimate of the emitting mass is very uncertain. But remember: *the observed optical emission line fluxes are strongly biased by the hottest gas, which can easily obscure emission from a greater mass of cooler gas.*

There is a way, however, to infer M_O from the [O I]$\lambda\lambda$6300 emission lines. As Fransson, Houck, & Kozma (1995) point out, the excitation of these lines at late times ($t \gtrsim 750$ days) is dominated by nonthermal electrons produced by gamma ray energy deposition rather than by thermal electrons. Then, the emission line luminosity is proportional to the fraction of the gamma ray luminosity that is absorbed by the O I, which is in turn proportional to $M_O/Menv$, since the gamma rays illuminate the entire envelope fairly uniformly at late times. From such considerations, Fransson *et al* infer $M_O \approx 1.6 M_\odot$, with fairly large uncertainty.

4. Optically Thick Balmer Series: Case C Recombination

The rich spectrum of hydrogen recombination lines from SN 1987A provides a fascinating example of the effects of line transfer (Chugai 1987; Xu *et al* 1992). Emission lines of Hα and several infrared lines of the Paschen, Brackett, Pfund, Humphreys series are prominent (see McCray 1993, Fig. 6). For $t \lesssim 2$ years, however, Hβ and the higher

Balmer lines are absent because the envelope is optically thick in the Balmer series. When a recombination cascade results in the emission of an Hβ, Hγ, or Hδ photon, these photons are resonantly absorbed by a nearby hydrogen atom in the H$^*(n = 2)$ state. This process of emission and resonance absorption repeats a few times until the Balmer line is "split," *i.e.* H$\beta \rightarrow$ Hα + Pα, H$\gamma \rightarrow$ Hα + Pβ, and so forth. Hα, on the other hand, cannot split and so must continue to rattle around until it ultimately escapes. This situation, in which all the higher Balmer lines are split into Hα plus infrared recombination lines, may be called "Case C" recombination by analogy to the standard "Case B," for planetary nebulae and H II regions, in which the Lyman series is optically thick and Ly$\beta \rightarrow$ Lyα + Hα, etc.

It is easy to understand these results using the formalism described in § 2. First, consider the optical depth in Lyα. The density, n_H, of H I atoms is given by

$$n_H = \frac{0.7 M_H}{m_H f_H V_E} \approx 8 \times 10^8 f_H^{-1} \frac{M_H}{M_\odot} t_y^{-3}, \tag{4.12}$$

where we have assumed that the line-emitting hydrogen (with total mass M_H including 30% helium) occupies a filling factor f_H of a sphere expanding with radial velocity 2000 km s^{-1}, and t_y is the time since explosion in years. Then, from eq. (2.2) we derive $\tau(\mathrm{Ly}\alpha) \sim 3 \times 10^9 f_H^{-1} (M_H/M_\odot) t_y^{-2}$. Accordingly, if a hydrogen atom is excited to the $n = 2$ level, the effective rate for decay by Lyα emission is $A_{21}/\tau(\mathrm{Ly}\alpha) \sim 0.14\ \mathrm{s}^{-1} f_H (M_H/M_\odot)^{-1} t_y^2$. Thus, for several years, the $n = 2$ level is effectively metastable and will decay instead by two-photon continuum emission, at a rate $A_{2\gamma} = 2.05\ \mathrm{s}^{-1}$.

We can calculate the optical depths in the Balmer series from equation eq. (2.2) if we know the density, n_2, of H I atoms in the $n = 2$ level. We can estimate n_2 by equating excitations and ionizations of H I (all of which populate the $n = 2$ level) due to gamma ray energy deposition (see Fransson *et al* 1995) to 2-photon decays. Following Xu *et al* (1992), we estimate that the Balmer continuum optical depth is given by

$$\tau_{BC} \approx 8 \times 10^3 t_y^{-2} \exp(-t_y/0.3)[1 - f_\gamma], \tag{4.13}$$

where f_γ is the fraction of the gamma ray luminosity that escapes the line-emitting region (see McCray 1993, Figure 2). According to eq. (4.13), the Balmer continuum should remain optically thick for about two years. If so, the ionization rate of H I by gamma rays is enhanced by a factor 5 – 10 because every ionization of H I from the ground state is accompanied by several photoionizations of metastable H I$(n = 2)$ due to Balmer continuum photons produced by 2-photon decays (Fransson *et al* 1995). This is clearly happening in SN 1987A; in fact, as Xu *et al* (1992) show, one cannot account for the strength of the observed recombination lines without this enhancement. But shortly after two years, the Balmer continuum and Hβ become optically thin, the enhancement vanishes, and the recombination spectrum changes to the more familiar Case B.

5. A Cautionary Tale: the Ca II Infrared Lines

The strongest emission features in the near infrared spectrum of SN 1987A are the [Ca II]$\lambda\lambda$7300 and the Ca II$\lambda\lambda$8600 infrared triplet. Li & McCray (1993) have interpreted these observations, following the pioneering work of Kirshner & Kwan (1975), and their results provide an important lesson about interpreting supernova spectra.

The relevant transitions and energy levels are shown in Figure 3. The [Ca II]$\lambda\lambda$7300 doublet is unresolved. Since the transitions are highly forbidden, the upper $3d^2D$ states are in LTE with the ground state. In contrast, the Ca II$\lambda\lambda$8600 transitions are allowed, and the λ8662 line can be distinguished from the $\lambda\lambda$8498, 8542 blend. Therefore, the

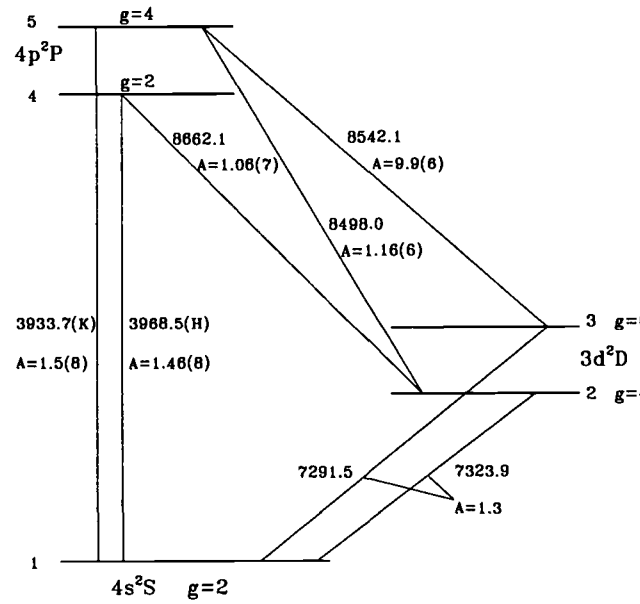

FIGURE 3. Grotrian diagram of Ca II levels. Statistical weights and Einstein A values (s^{-1}) are indicated. The numbers in parentheses are the powers of 10.

upper $4p\,^2P$ states are not in LTE, and in fact their populations are sensitive to temperature, electron density, and the radiation field in the neighborhood of Ca II$\lambda\lambda$3950.

Li & McCray (1993) analyzed these observations with a 5-level atom model that includes all radiative and electron-impact transitions. They fit the data with parameters representing M_{Ca}, the calcium mass, f_{Ca}, the calcium filling factor, $T_{Ca}(t)$ the temperature of the Ca II-emitting gas, $n_e(t)$, the electron density, and a $\zeta_{H,K}$, the rate of pumping of the $4p\,^2P$ levels due to absorption of ultraviolet photons by the Ca II$\lambda\lambda$3950 (H,K) doublet.

Their conclusions are remarkable. First, they could not fit the observations with a typical nucleosynthesis yield of calcium, $M_{Ca} \sim (3-10) \times 10^{-3} M_\odot$ (Woosley 1991; Nomoto 1991) and a relatively small filling factor. In fact, the good fits have a relatively large filling factor, $f_{Ca} \gtrsim 0.1$ and $M_{Ca} \sim (2-5) \times 10^{-4} M_\odot$. Moreover, the Ca II infrared emission lines provide an excellent thermometer of the calcium-emitting gas, and imply temperatures ranging from, $T_{Ca}(200d) \approx 6300$ K to $T_{Ca}(500d) \approx 3800$ K — substantially higher than the temperatures $T_O(t)$ of the [O I]$\lambda\lambda$6300 emitting gas at the same times.

From this analysis, Li & McCray conclude: *the observed Ca II lines are emitted, not by newly-synthesized calcium, but by primordial calcium in the hydrogen- and helium-rich parts of the envelope.*

Does this conclusion preclude the nucleosynthesis yields of calcium predicted by Woosley (1991) and Nomoto (1991)? Not at all! Since the fluxes of the Ca II near-infrared emission lines are very sensitive to temperature, the emission from newly-synthesized calcium would be masked by the emission from a much lower mass of primordial calcium mixed with hydrogen and helium if the newly-synthesized calcium has substantially lower temperature.

Indeed, a simple argument shows that this must be the case. Since the gamma rays have relatively long mean-free paths, the fraction of the gamma ray luminosity that can be absorbed by clumps of newly-synthesized calcium and other $Z \approx 20$ elements must be

proportional to the mass fraction of the emitting region occupied by such material. That fraction must be an upper limit to the fraction of the supernova luminosity that can be emitted by newly-synthesized calcium; but in fact, the net luminosity of the observed Ca II lines exceed that limit. Indeed, the only way to account for this luminosity is to assume that the emitting Ca II is mixed microscopically with a major fraction of the mass of the emitting region. Since the emitting mass must be $\gtrsim 5M_\odot$ in order to absorb the gamma rays (McCray 1993), it can only be hydrogen and helium. A relatively large fraction of the absorbed gamma ray luminosity emerges in the Ca II infrared lines, not because Ca II is particularly abundant, but because it is one of the most effective radiative cooling agents in primordial gas at temperatures characteristic of the envelope.

Li & McCray (1993) noticed one more important point: for $t \gtrsim 350$ days, the emission in the Ca II$\lambda\lambda$8600 lines must be driven by ultraviolet pumping in the Ca II$\lambda\lambda$3950 lines rather than by electron impact excitation.

6. Clues to Explosion Dynamics: the Iron, Cobalt and Nickel Lines

Light curves of more than a dozen emission lines from neutral and once-ionized Fe, Co, and Ni have been observed in the infrared spectrum of SN 1987A. There is no doubt that these lines are emitted by newly-synthesized material. Indeed, one can directly observe the radioactive decays of ^{56}Co $\rightarrow$ ^{56}Fe (mean lifetime $t_{56} = 111.3\,d$) and ^{57}Co $\rightarrow$ ^{57}Fe ($t_{57} = 391\,d$) and infer the initial production ratio of these isotopes from observations of the evolution of the ratio [Co II]$\lambda 1.547\,\mu$m/[Fe II]$\lambda 1.533\,\mu$m (Varani *et al* 1990).

Since we can observe the entire bolometric luminosity of SN 1987A, and we know that it results from the radioactive decays of ^{56}Co and ^{57}Co, we know the masses of the respective isotopes of Fe, Co, and Ni as functions of time. For example, $M(^{56}\mathrm{Co}) = (0.07\,M_\odot)\exp(-t/111.3d)$. Therefore, if we assume that the gas responsible for the Fe/Co/Ni emission line system is distributed throughout the emitting region in clumps, each having the same density and temperature, the development of this system should be characterized fully by the net filling factor of these clumps, f_{Fe}, and the evolution of temperature, $T_{Fe}(t)$, and ionization levels, $x_{Fe} = n(Fe\,II)/n(Fe)$, etc.

Li, McCray, & Sunyaev (1993) have developed a theory to account for the evolution of the Fe/Co/Ni emission line system. Their most important conclusion is that the filling factor, $f_{Fe} \gtrsim 0.25$. This conclusion follows directly from the theory outlined in §2. If we replace $B_\nu(T)$ by the Rayleigh-Jeans limit, we can write equation (2.9) as an upper limit that is valid in general:

$$F_{ul} < f_A \frac{4\pi v_m^3 t^2}{3D^2} \frac{2kT}{\lambda^3}\,. \tag{6.14}$$

Consider, for example, the [Co II]$10.52\,\mu$m emission line, which reaches maximum brightness $F(10.52) \approx 3 \times 10^{-10}$ ergs cm^{-2} s^{-1} at $t \approx 250$ days. With these values, $v_m = 2500$ km s^{-1}, and $D = 50$ kpc, equation (6.14) implies that $f_{Fe}T_3 > 1.0$, where $T_3 = T_{Fe}/(10^3\,\mathrm{K})$. Now, since we can infer from Fe/Co/Ni line ratios that $T_{Fe} \approx 4000$ K, equation (6.14) implies that $f_{Fe} \gtrsim 0.25$. [This result was anticipated by Chugai (1988), Moseley *et al* (1989), and Haas *et al* (1990)].

This result is remarkable because we know that the net mass, $M_{Fe} \approx 0.07M_\odot$, of the Fe/Co/Ni is only about 1% of the total mass, $M_{em} \sim 5 - 10M_\odot$, of the emitting gas, which must be mostly hydrogen and helium. (Such a mass is necessary to absorb the gamma rays.) It follows that *the emitting region has a foamy texture, consisting of low-density bubbles of Fe/Co/Ni gas in a substrate of higher density hydrogen and helium.*

Why should this be so? The answer was anticipated by Woosley (1988), who pointed

out that the decay of ^{56}Ni during the first few weeks might deposit enough thermal energy to cause the Fe/Co/Ni gas to expand relative to its substrate, forming a "nickel bubble." But there is a problem: the net radioactive energy released by the decay of $0.07M_\odot$ of ^{56}Ni, $\approx 4 \times 10^{48}$ ergs, is much less than the kinetic energy, $\approx 2 \times 10^{50}$ ergs, of an expanding uniform sphere of mass $M \approx 5M_\odot$ and surface velocity $v_m = 2500$ km s^{-1}. How can the Fe/Co/Ni clumps push aside such a large fraction of the volume of such a sphere with so little energy? The answer is that there must be many ($N \gtrsim 60$) small clumps originally distributed throughout the substrate (presumably as a result of hydrodynamic instabilities during the explosion). Then, each clump can expand by a factor $\sim 10^2$ without changing the original velocity of the substrate by more than, say, 10%. I.e., many small bubbles dispersed through the substrate can push aside a large fraction of the volume much more efficiently than one large bubble.

Starting with these elementary considerations, Li *et al* (1993) develop a fairly complete theory for the light curves of all the Fe/Co/Ni emission lines from SN 1987A. They calculate $T_{Fe}(t)$ by equating the radioactive luminosity deposited in the Fe/Co/Ni gas to the net luminosity of all the emission lines, and $x_{Fe}(t)$, $x_{Co}(t)$, and $x_{Ni}(t)$ by equating ionization to recombination. From that they can calculate the light curves of all the lines *ab initio*. The theory has essentially no free parameters except the filling factor, f_{Fe}, which is determined by observations. The observed light curves of most of the emission lines agree very well with the theoretical light curves.

There is an important exception, however. The observed fluxes of near infrared lines, such as [Fe II]λ7155, agree fairly well with the theoretical light curves for $t \lesssim 400$ days, but are much greater than the theoretical results thereafter. (The light curves of the longer wavelength lines agree with the theory for all times.) Evidently, some small fraction of the Fe/Co/Ni atoms are hotter than the rest, and dominate the light curves of the shorter wavelength lines at late times. Li *et al* (1993) suggest that these hotter atoms reside on the surfaces of the Fe/Co/Ni bubbles, and are heated by ionizing ultraviolet radiation from the hydrogen/helium substrate. They do not prove this conjecture, however.

7. The Unfinished Agenda

Clearly, we have made substantial progress toward a theory of the spectrum of SN 1987A. We have a fairly complete theory for the Fe/Co/Ni lines. We also have semi-empirical theories for the O I lines, the hydrogen recombination lines, and the Ca II lines; but these models are incomplete because the gas temperature is treated as a parameter of the theory rather than calculated by equating heating with cooling.

To do so, we must identify correctly the main radiative cooling agents of each chemically distinct constituent of the envelope. Here, the Ca II lines teach us an important lesson: trace elements can be important, even dominant, cooling agents. Clearly, we should be guided by observations of the emission line spectrum in order not to overlook important cooling agents. For example, emission bands of CO and SiO are prominent in the infrared spectrum and must play an important role in cooling the oxygen-rich gas.

We have also learned that photoionization and photoexcitation by ultraviolet radiation play important roles in determining the hydrogen recombination line spectrum, the Ca II infrared lines, and the Fe/Co/Ni emission lines at late times. To calculate these processes from first principles, we need a theory to calculate the flux density of ultraviolet radiation within the envelope of SN 1987A. This radiation field is produced by non-thermal excitation resulting from gamma ray illumination and absorbed by resonance scattering by trace elements, dust, and other continuum processes.

Finally, although we have made progress toward modeling the brightest emission lines in the nebular spectrum of SN 1987A, we have not accounted for many of the weaker features. Most significantly, we have no theory to explain the quasi-continuum (color temperature $T_c \sim 5000$ K) that underlies the optical emission line spectrum (Wooden *et al* 1993). Perhaps it is fluorescence following resonance absorption of ultraviolet radiation within the envelope.

REFERENCES

Chugai, N. N. 1987, Soviet Astron. Lett., 13, 282.

Chugai, N. N. 1988, Astron. Tsirk., 1533, 7.

Chugai, N. N. 1990, Soviet Astron. 34, 96.

Colgan, S. W. J., & Hollenbach, D. J. 1988, ApJL, 329, L25.

Fransson, C., & Chevalier, R. A. 1987. ApJL, 322, L15.

Fransson, C. Houck, J. & Kozma, C. 1995, these proceedings.

Haas, M. R., Colgan, S. W. J., Erikson, E. F., Lord, S. D., Burton, M. G., & Hollenbach, D. J. 1990, ApJ, 360, 257.

Kirshner, R., & Kwan, J., 1975, ApJ, 197, 415.

Li, H.-W., & McCray, R. 1992, ApJ, 387, 309.

Li, H.-W., & McCray, R. 1993, ApJ, 405, 730.

Li, H.-W., McCray, R., & Sunyeav, R. A. 1993, ApJ, 419, 824.

Luo, D., McCray, R., & Slavin, J. 1994, ApJ, 430, 264.

Masai, K., & Nomoto, K. 1994, ApJ, 424, 924.

McCray, R. 1993, Ann. Rev. Astr. & Ap., 31, 175.

Moseley, S. H., Dwek, E., Glaccum, W., Graham, J. R., Loewenstein, R. F., & Silverberg, R. F. 1989, ApJ, 347, 119.

Nomoto, K., Shigeyama, T., Kumagai, S., & Yamaoka, H. 1991, in *Supernovae*, ed. S.E. Woosley (New York: Springer-Verlag), p. 176.

Osterbrock, D. E. 1989, *Astrophysics of Gaseous Nebulae and Active Galactic Nuclei* (Mill Valley, CA: University Science Books).

Phillips, M. M., & Williams, R. 1991, in *Supernovae*, ed. S. E. Woosley (New York: Springer-Verlag), p. 36.

Spyromilio, J., & Pinto, P. A. 1991, in *SN1987A and Other Supernovae*, ed. I. J. Danziger, K. Kjär. ESO/EIPC Workshop on Supernovae. Munich: ESO (1991), p. 423.

Suzuki, T., Shigeyama, T., and Nomoto, K. 1993, A&A, 275, 883.

Swartz, D. A., Harkness, R. P., & Wheeler, J. C. 1987, Nature 337, 439

Varani, G.-F., Meikle, W. P. S., Spyromilio, J., & Allen, D. A. 1990, MNRAS, 245, 570.

Wheeler, J. C. & Filippenko, A. V. 1995, these proceedings.

Wooden, D. H., *et al* 1993, ApJS, 88, 477.

Woosley, S. E. 1988, ApJ, 330, 218.

Woosley, S. E. 1991, in Supernovae, ed. S. E. Woosley (New York: Springer-Verlag), p. 202.

Xu, Y., McCray, R., Oliva, E., & Randich, S. 1992, ApJ, 386, 181.

The Oxygen 1.13 μm Fluorescence Line of SN1987A: a Diagnostic for the Ejecta of Hydrogen-Rich Supernovae

By ERNESTO OLIVA

Osservatorio Astrofisico di Arcetri, Largo E. Fermi 5, I-50125 Firenze, Italy

The bright O I λ11287 line observed in SN1987A is produced by the Bowen fluorescence with Lyβ and comes from regions that lie within a Sobolev length ($\delta R \sim 10^{-3} R_{SN}$, the maximum distance over which fluorescence can work) from hydrogen rich gas ionized by the ^{56}Co decay. Its strength relative to hydrogen lines (e.g. Brγ) depends on the O/H relative abundance in the 'fluorescent region' and on the density (i.e. the filling factor) of the gas. The observed evolution of λ11287 can be successfully understood using a relatively simple theory which takes into account the effects of transfer in the O I lines and is the generalization of the classical theory of Bowen fluorescence.

The most important result is that the time evolution of the relative intensities and profiles of O Iλ11287 and Brγ is a powerful diagnostic to determine:
— The filling factor of the hydrogen rich gas;
— The pre-SN O/H relative abundance;
— The amount of small scale mixing between hydrogen and oxygen rich regions and its radial stratification.

In SN1987A the results are the following:
— Inside 2000 km/s the hydrogen rich material is clumped with $f \simeq 0.1$
— Outside 2000 km/s the gas has $f \simeq 1$ and the oxygen relative abundance is quite low: O/H$\simeq 5 \times 10^{-5}$, indicating that only the pre-SN oxygen is fluorescently coupled with hydrogen.
— In the inner regions, on the contrary, the O/H 'fluorescent abundance' is large ($\simeq 10^{-3}$) indicating that the hydrogen and oxygen rich clumps are tightly packed together with $\approx 1\%$ of the freshly synthesized oxygen lying within a Sobolev radius from the hydrogen clumps.

A plausible scenario which could explain these results is the following. Immediately after the explosion, the inner, metal rich regions of SN1987A are fragmented by dynamical instabilities and expelled at velocities $v \leq 2000$ km/s inside the hydrogen rich envelope. In the following days the fragments of nickel are inflated by the fast radioactive decay of ^{56}Ni (Li et al. 1993) and compress the hydrogen rich gas inside 2000 km/s; while outside they overshoot and push forward, but do not compress significantly the pre-existing gas, which therefore remains with $f \simeq 1$ and has no scale mixing between hydrogen and oxygen.

Observations of the O I λ11287 line in other type II supernovae are of interest to verify if such a scenario is typical of these objects. The measurements required are medium–high resolution spectra of λ11287 and Brγ to follow the evolution of their profiles and fluxes from the beginning of the super–nebular phase (when the envelope becomes optically thin in the continuum) till the disappearance of the O I line.

1. Introduction

The large amount of observational data available for SN1987A has demonstrated that its envelope is nothing like the simple minded 'onion' which was often considered as a reasonable representation of a type II supernova. The most direct argument comes from the analysis of the profiles of the lines observed after the beginning of the so called super–nebular phase, i.e. after the envelope continuum becomes optically thin (in SN1987A this

occurs about 150 days after the explosion). In the freely expanding envelope the radial velocity of a given region is strictly proportional to its distance from the center (i.e. the flow is Hubble-like) and the velocity profile of the lines is directly connected to the radial distribution of the emitting gas. An 'onion' with superposed Fe, Si, O, He, H layers should produce narrow [Fe] lines and broader and flat-top [O] and hydrogen lines. The fact that infrared and optical [Fe], [Ni], [O], [Si], H lines have all similar widths is a direct evidence that these elements have similar radial distribution, i.e. are mixed, at least on macroscopic scales.

Several arguments indicate that the mixing is not on microscopic scales. The one I personally prefer is based on the observations of [Fe I] (1.44 μm) and [Ni I] (3.12 μm), from which one derives that, at ≈ 400 days, roughly half of the iron and nickel is neutral but is hot enough to emit these lines. This situation is possible only if the Fe/Ni regions are not in chemical contact with the hydrogen (and proton) rich gas as Fe^o and Ni^o would be quickly ionized by charge exchange with H^+.

The analysis of [O I] and Ca II lines suggests that the oxygen- and hydrogen-rich gas is clumped with filling factor $f \sim 0.1$ while the low opacities of the infrared [Fe], [Co] and [Ni] lines indicate that most of the envelope is occupied by low density, iron rich gas (Li and McCray 1992, 1993, Li et al. 1993). An up-to-date picture of the envelope could be that of a Co-Fe 'foam', which fills most of the volume available, with dense clumps of hydrogen, oxygen and other materials more or less uniformly distributed throughout the envelope (see e.g. McCray 1993). In this scenario the radial stratification originally present in the progenitor is forgotten and one does not expect large differences in the profiles of the various lines.

The O I λ11287 line does not seem to fit in this picture as it is much narrower ($\Delta v \leq$ 2000 km/s) than the other lines from the ejecta. This observation implies that some sort of radial stratification must exist in the envelope. What is the difference between the gas inside and outside 2000 km/s? More generally, does the O I line fit at all in the above scheme and, if so, what can one learn from it?

The answers to the above questions can be found in a long paper recently published in Astronomy & Astrophysics (Oliva 1993). This communication is intended to give a quick overview of the modeling procedure and results, and to emphasize the importance of the O I line as a diagnostic tool for the study of hydrogen rich supernovae.

2. Basic model features

Supernova envelopes are dense, cool and very opaque in emission lines. These unusual conditions are often outside the limits of the 'classical' works dealing with line formation. This is particularly true for the O I line where a blind application of the handy theory developed, among the others, by Grandi (1980) makes one predicting that the ratio I(λ11287)/I(Brγ) should rapidly fade with time following the decrease of Hα opacity ($\approx t^{-4}$) while the observed ratio *increases* by almost a factor of 2 between 200 and 400 days. The discrepancy is resolved by including the effect of transfer in the oxygen lines produced by the Lyβ fluorescence (Fig. 1). Using very reasonable approximations one finds that when λ11287 is opaque (which is the case at early times) the relative intensity of λ11287 does not depend on the O/H relative abundance and is solely determined by the opacities of Hα and Lyα:

$$I(\lambda 11287)/I(\mathrm{Br}\gamma) \propto [\tau(\mathrm{H}\alpha)\,\tau(\mathrm{Ly}\alpha)]^{-1/3} \qquad (2.1)$$

and increases with t_{SN} as the opacities of Hα and Lyα are both decreasing with time.

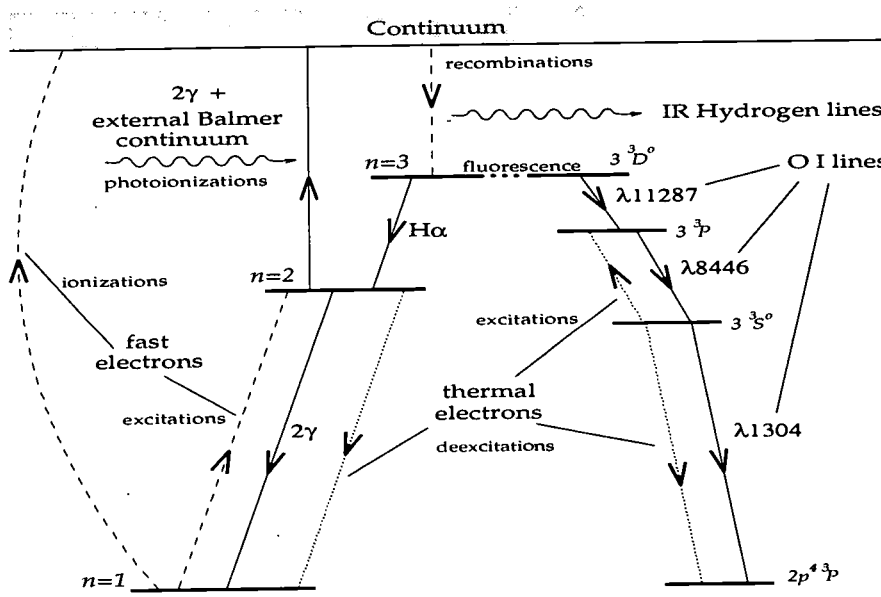

FIGURE 1. Schematic representation of the most important processes involved in the production of λ11287

Once λ11287 becomes transparent its relative intensity is given by the classical relationship:

$$I(\lambda 11287)/I(\mathrm{Br}\gamma) \propto \mathrm{O/H}\,[\tau(\mathrm{H}\alpha)]^{-1} \tag{2.2}$$

and fades with t_{SN} following the decrease of Hα opacity. Therefore, the peak of the λ11287/Brγ 'light curve' marks the time at which the optical depth of λ11287 approaches unity.

The network of processes which must be taken into account for the modeling of λ11287 is sketched in Fig. 1. Basically, one must considered an 'extended' hydrogen atom including the oxygen levels populated by fluorescence. The method for the determination of the hydrogen levels population is that described by Xu et al. (1992) while the oxygen levels are treated in Oliva (1993). The modeling procedure can be outlined as follows.

— The hydrogen recombination rate is given by the observed intensities of IR hydrogen lines

— The above parameter sets the opacities of hydrogen lines once the filling factor f – the first free parameter of the model – is given, the lower the value of f the thicker the lines.

— The second free parameter is the O/H resonant abundance which sets the efficiency of Lyβ fluorescence.

The effect of varying f and O/H can be visualized in Fig. 2 which shows λ11287/Brγ theoretical light curves for several combination of parameters. The two parameters have distinct effects: f determines the time at which the peak occurs (lower f values make the envelope thicker so that λ11287 becomes transparent at later times) while O/H primarily determines the amplitude of the peak. Therefore, one has good chances to independently constrain the values of f and O/H. For simplicity I avoid discussing here the effect of the external Balmer-ionizing field ($\xi_{2,C}$, Xu et al. 1992), which is a 'disturbing' parameter which also influences the amplitude of the peak but has minor effects on the final results.

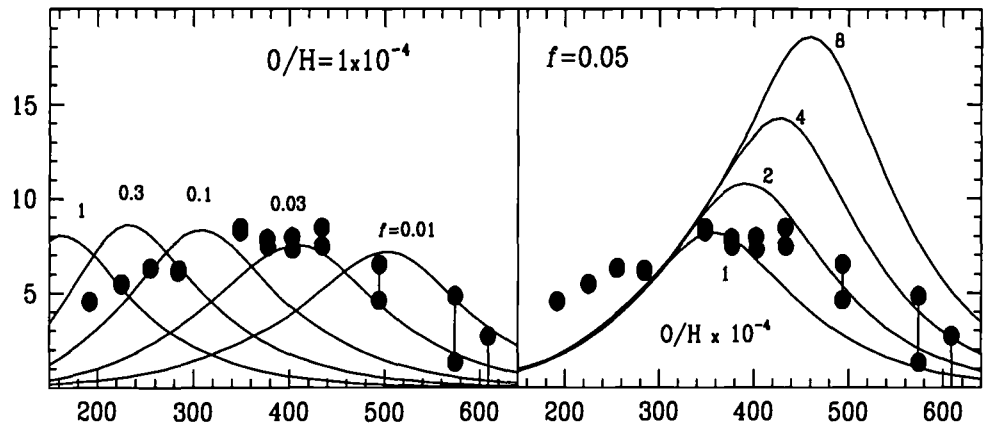

FIGURE 2. Comparison between the observed evolution of O Iλ11287/Brγ (filled circles) and theoretical 'light curves'. The left panel shows the effect of varying the filling factor f while the effect of O/H is displayed in the right hand panel.

3. Results

The only direct result which can be derived by comparing observed and theoretical light curves (Fig. 2) is that the hydrogen-rich gas that pumps the observed O Iλ11287 must be clumped with $f \approx 0.03-0.1$, and this fits well in the current view of the SN1987A envelope. All the other results, namely O/H abundance and radial stratification of the physical conditions, derive from the analysis of the line profile. The observed width of λ11287 is FWHM $\leq$2000 km/s, much narrower than Brγ and any other line, and its profile did not vary significantly from day 200 to beyond day 400 (Fig. 3). This last fact implies that there is no important radial stratification (i.e. variation of physical conditions with radius) of the clumps in the central 2000 km/s. To better understand this, assume for example that the densest hydrogen rich material – i.e. that with the lowest filling factor – is concentrated within a smaller radius (1000 km/s, say). These clumps would dominate the emission at late epochs and the line would narrow with time, in disagreement with the observations.

An analysis of Brγ and λ11287 profiles indicates that roughly half of the hydrogen recombinations occur outside 2000 km/s where the λ11287/Brγ ratio is a factor > 6 lower than inside. What makes the gas outside 2000 km/s a much less efficient O I emitter? There are two possibilities:

— The gas has a lower filling factor, it reaches its O I peak very early and fades before 200 days (time of the first reliable measurements of λ11287).

— The gas has a lower O/H resonant abundance, and never produces significant λ11287.

From Fig. 2 one can easily realize that the first effect is not enough: the least dense component ($f = 1$) peaks just before 200 days and at this epoch the O I line was already narrow (Fig. 3). One therefore requires a variation of O/H which must be large because the amplitude of the λ11287/Brγ peak is a slow function of O/H ($\approx$[O/H]$^{1/3}$). One can easily demonstrate (sect. 3.6 of Oliva 1993) that the gas outside 2000 km/s must have an oxygen abundance at least a factor of 20(!) lower than inside. Is this compatible with our view of SN1987A? At first sight a radial variation of O/H seems unreasonable for the following reasons:

— The value of O/H derived from λ11287 is the oxygen relative abundance averaged over a Sobolev length ($\approx$ a thousandth of the SN size), the maximum distance over which fluorescence can work. Several evidences indicate that the mixing in SN1987A was quite

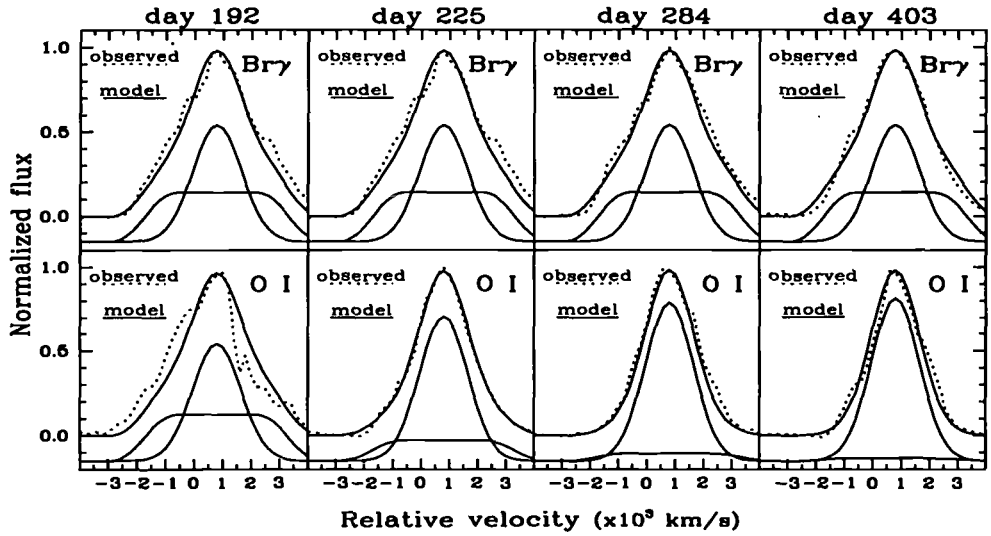

FIGURE 3. The dashed lines are the observed profiles of λ11287 and Brγ at various epochs. The results from a model with a strong radial stratification of O/H (1×10^{-3} inside 2000 km/s and 5×10^{-5} outside) are given as solid lines. The relative contribution of the inner (Gaussian profile) and outer (flat top profile) regions are also shown. See Oliva (1993) for more details.

rough and it is not at all clear if it could work on so small scales.

— From [O I]λ6300 we know that the freshly synthesized oxygen extends to at least 2500 km/s. What is the process which produced small scale mixing inside 2000 km/s but not outside?

A possible explanation is along the line of the 'inflating-Ni-clumps' model of Li et al. (1993, see also McCray 1993). In the first days after the explosion the fragments of the nickel bubble are inflated by the rapid decay of ^{56}Ni and rapidly occupy most of the space available. All the other material in the ejecta is either compressed in between the Co-Fe balloons or pushed aside, the latter occurring in the outermost regions. If the original nickel fragments were mostly concentrated inside 2000 km/s one expects that the Ni 'balloons' overshoot into the outer region without significantly compressing the pre-existing gas, while all the material within the above radius is squeezed by different amounts. Hence, the width of the oxygen line is a direct measurement of the volume originally occupied by the nickel fragments before inflation.

The λ11287 modeling requires O/H$\sim 1 \times 10^{-3}$ hence the mass of 'fluorescently-mixed' oxygen is $M_{mixed}(O) \sim 0.016\, M_{2000}(H)$, $M_{2000}(H)$ being the hydrogen mass in the inner 2000 km/s which can be estimated as follows. To match the observed luminosities of hydrogen recombination lines one requires that $\sim 1\ M_\odot$ of hydrogen is exposed to ^{56}Co decay (Xu et al. 1992). Roughly half of the hydrogen lines are emitted from the central 2000 km/s (Fig. 3), hence $M_{2000}(H) \sim 0.5\ M_\odot$ and $M_{mixed}(O) \sim 0.01$. One therefore requires that roughly 1% of the freshly synthesized oxygen† is mixed with hydrogen on scales smaller than a thousandth of the SN size. Such a fine mixing can be better achieved if the hydrogen and oxygen clumps have a filamentary shape, it would be of interest to verify if the pressure from the inflating Ni 'balloons' is enough to produce filaments so closely packed together.

A last, interesting result concerns the pre-SN oxygen abundance. In the region outside

† The fraction quoted in Oliva (1993, 10%) is wrong as it was computed assuming a too large hydrogen mass ($M_{2000}(H) = 5$), I apologize to the readers for this error.

2000 km/s a very low oxygen abundance is needed to keep the λ11287 emission below the observed upper limit: $O/H \leq 5 \times 10^{-5}$. This indicates that the progenitor of SN1987A had a O/H much smaller than other blue stars in the field. The above value is a factor 1.8 lower than that used to model the spectrum of the ring (Lundqvist & Fransson 1991). It would be of interest to verify if this difference is really significant.

4. Future Observations of Supernovae.

Since the O I λ11287 line is formed by Lyβ fluorescence, it is reasonable to expect that it should be bright in all hydrogen–rich supernovae. The modeling of λ11287 requires a hydrogen recombination line for reference. The best one is probably Brγ, as it is relatively isolated and its emission coefficient is insensitive to the opacity of the gas (Xu et al. 1992). The light curve of λ11287/Brγ, and in particular the position of its peak, can be used to derive the filling factor of the hydrogen rich gas. The most interesting measurement would be that of the O I and Brγ line profiles: finding a narrower O I would be a trace of the 'Ni–inflation'. The main advantage of using λ11287 rather than middle IR lines of [Fe] and [Co] – which can give a more direct check of this theory – is observational: at 1.13 μm one can measure distant objects while observations at $\lambda > 10$ μm are possible only for bright and nearby supernovae. There is a potential limitation for the use of the λ11287 profile: in SN1987A the narrowing of λ11287 is pronounced because the oxygen abundance outside 2000 km/s is quite low, if the supernova progenitor was oxygen rich (or even with cosmic oxygen abundance) it may happen that the mixing in the inner regions does not produce a large increase of O/H. However, even a small O/H contrast should be recognizable by following the time evolution of λ11287 and Brγ profiles, the first should narrow with time.

In conclusion, the oxygen line can give interesting information on the physics of the envelopes of hydrogen rich supernovae. The observations required are medium–high resolution (≤ 300 km/s), high S/N spectra of λ11287 and Brγ from the beginning of the supernebular phase till as late as possible (ideally till the O I line disappears).

REFERENCES

Grandi S.A., 1980, ApJ 238, 10

Li H. W., & McCray, R., 1992, ApJ, 387, 309

Li H. W., & McCray, R., 1993, ApJ, 405, 730

Li H. W., McCray, R., & Sunyaev, R. A., 1993, ApJ, 419, 824

Lundqvist, P., & Fransson, C., 1991, ApJ, 380, 575

McCray, R., 1993, these proceedings

Oliva E., 1993, A&A, 276, 715

Xu Y., McCray R., Oliva E., & Randich S., 1992, ApJ, 386, 181

Review of Contributions to the Workshop on SN1993J

By J. CRAIG WHEELER[1]
AND ALEXEI V. FILIPPENKO[2]

[1]Department of Astronomy, University of Texas, Austin, TX 78712, USA

[2]Department of Astronomy and Center for Particle Astrophysics, University of California, Berkeley, CA 94720, USA

At its peak, SN 1993J was one of the brightest supernovae in this century, and it is being studied more thoroughly than any supernova except SN 1987A. It is proving to be similar to the transition object SN 1987K, which metamorphosed from being a hydrogen-rich Type II near peak to having a hydrogen-deficient nebular phase. SN 1993J has been observed throughout the electromagnetic spectrum and with optical spectropolarimetry. It is interacting with a dense circumstellar nebula and is generating radio and X-ray flux, but it has probably not been detected in gamma rays. The photometric and spectral evolution are consistent with a star of original mass ~ 15 $M_\odot$ that lost appreciable mass to a binary companion leaving an extended, helium-rich hydrogen envelope of $\lesssim 0.5$ $M_\odot$ and a helium core of ~ 4 $M_\odot$. The spectral evolution will put strong constraints on the mixing of ^{56}Ni and other species.

1. Introduction

SN 1993J was discovered on March 28.9 by F. Garcia (Ripero 1993) in the Sab galaxy NGC 3031 = M81. It was the brightest supernova observable from mid-northern latitudes since SN 1972E and has been the subject of intense observation by a large number of major and minor optical observatories, the VLA and other radio telescopes, IUE, the Compton Gamma Ray Observatory, ROSAT, and the newly launched ASCA satellite, as well as by a host of amateur astronomers. In addition, SN 1993J has proven exceptional on a number of grounds and has prompted considerable theoretical modeling. IAU Colloquium 145 provided the first opportunity for a public exchange on the early observational and theoretical results. These were presented in a workshop organized and chaired by one of us (AVF), and in an associated poster session. The organizing committee of the Colloquium determined that a synthesis of the results was preferable to a collection of small individual contributions. This review is the outcome.

2. Prediscovery Observations

Prediscovery observations put useful limits on the progenitor magnitude (Perelmuter 1993; Humphreys *et al.* 1993; Salzer *et al.* 1993; Prugniel 1993). The image is extended slightly in the north/south direction (Blakeslee and Tonry 1993). It is superposed on a ridge of diffuse starlight, about 3″ wide and 20″ long at position angle 40°, that is somewhat stronger in B than in Hα (Tomaney and Crotts 1993) and shows no H II region within 10″ of the supernova (Richmond 1993). There were some early reports of discrepant magnitudes in the IAU Circulars, raising the issue of variability, but no further evidence for such variation has emerged. This may have represented some calibration differences, but a physical variation cannot be ruled out. Filippenko (1993a) pointed out that the colors and magnitudes given by Perelmuter (1993) are consistent with those of a K0 Ia supergiant.

TABLE 1. Progenitor Magnitudes

	U	B	V	R_c	I_c
m^1	21.45	21.73	20.72	19.94	19.43
M^2	−7.0	−6.6	−7.5	−8.2	−8.6

[1] Aldering *et al.* (1993), without Petermuter (1993)
[2] Assuming $E(B-V) = 0.15$ mag and DM = 27.7; de Vaucouleurs (1993).

The image can be separated into two components, with the brighter corresponding to the position of the supernova. Table 1 gives revised colors of this component from Aldering *et al.* (1993). Humphreys *et al.* (1993), Aldering *et al.* (1993), and Podsiadlowski *et al.* (1993) concluded that the colors require the presence of at least two photometric components within the brighter image. One component dominates in the U and B bands; it could be a late B to early A supergiant or an OB association. The other component dominates in the R and I bands in a manner consistent with a late G to early K supergiant. The bolometric magnitudes are in the range −7 to −8 with the best fit about −7.8 for a distance modulus (DM) of 27.7 mag and $A_V = 0.5$ mag (Aldering *et al.* 1993). This marginally excludes an AGB star progenitor with maximum bolometric luminosity of −7.1 mag (but see Blöcker and Schönberner 1991; Hashimoto, Iwamoto, and Nomoto 1993). The corresponding main sequence mass range is $15 - 20$ $M_\odot$ with a best estimate of $\sim$17 $M_\odot$ (Aldering *et al.* 1993).

Care must be taken in interpreting these observations. At the distance of M81 an arc second corresponds to about 17 parsecs, and one could easily be looking at an association or a cluster. There is some temptation to identify the red component of the blended image with the progenitor, but the only sure way to test for the progenitor is to wait until the supernova fades. Podsiadlowski *et al.* (1993) point out that in the binary transfer scenario, the mass gaining companion could be brighter than the progenitor, leaving open the possibility that neither of the two stars arising in the photometric fits represents the progenitor. Nevertheless, some models for the progenitor predict a star with about the right colors and luminosity of the red component of the pre-discovery images, and it is certainly possible that the progenitor was observed.

3. Outburst and Reddening

Wheeler *et al.* (1993) reported that the shock outbreak is estimated to have occurred at JD 2449074.5 ± 0.1 (March 28.0 ± 0.1 UT) and thus is defined to within a few hours. De Vaucouleurs (1993) has revised this to JD 2449074.7 ± 0.1 (March 28.2 ± 0.1). Wheeler *et al.* estimated the color excess to be $E(B-V) \leq 0.3$ mag in order not to violate the limiting value of $B-V$ for high temperatures, and $E(B-V) = 0.15 \pm 0.02$ mag from examinations of residuals to black body fits to spectra on March 31 and April 1 and from UBV colors. Wamsteker *et al.* (1993) estimate $E(B-V) = 0.07$ mag from the weakness of the 2200 Å feature in IUE spectra. Freedman *et al.* (1994) derive a total mean extinction to thirty M81 Cepheids of $E(B-V) = 0.11$ mag. Thus, there is little direct support for the large values of $E(B-V) \approx 0.7$ mag reported by Humphreys *et al.* (1993).

Observations with the Carlsberg Automatic Meridian Circle on La Palma yielded an

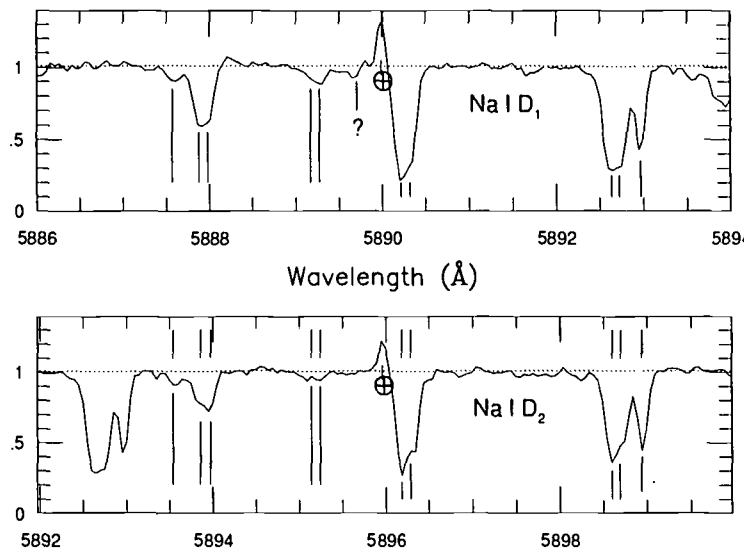

FIGURE 1. High-resolution spectra of the Na I D line. The top panel shows the shorter and the bottom panel the longer wavelength component shifted so that individual velocity components are aligned (Smith and Tomkin 1993).

optical position for the supernova of $\alpha = 09^h55^m24.785^s$, $\delta = +69°01'13.69''$, equinox J2000.0 (Lewis *et al.* 1993). This position supersedes the one given by Morrison, Argyle, and Helmer (1993). A conservative estimate of the accuracy is $0.11''$ in α and δ. This optical position is in excellent agreement with the VLA radio position (accuracy $0.2''$ in α and δ; Van Dyk *et al.* 1993a).

4. Interstellar Lines

Meikle *et al.* (1993) report finding a minimum of 20 velocity components of the intervening interstellar medium in the Na I D, Ca II, and other narrow lines. Wheeler *et al.* (1993) give −140, −125, −120, −61, −55, −6, 0, +117, +122, and +134 km s^{-1} for ten of the strongest components of Na I D. These are illustrated in Figure 1. Wamsteker *et al.* (1993) identify interstellar lines of Si II + O I λ1300, C II λ1335, Si IV λ1400, C IV λ1550, Al II λ1671, Fe II + Mn II λ2600, Mg II λ2800, and Mg I λ2852 Å in IUE spectra. The Mg I line showed components at −117, −63, +12, +129, and +181 km s^{-1}. The largest negative components roughly correspond to the kinematics of interstellar H I features in M81 in the vicinity of the supernova (Rots and Shane 1975); they probably correspond to gas in the local disk. The features at ~ -60 km s^{-1} are near the mean velocity of M81 of about -49 ± 10 km s^{-1} (de Vaucouleurs *et al.* 1991) and so may be gas in the halo of M81, but this component could also represent some local infall into the Galaxy. The very low velocity components are presumably from the local Galactic disk. The components at $\sim +120$ km s^{-1} are especially interesting because they may represent flow within the M81–M82 group and also because they are considerably stronger than the components associated with M81 itself.

Benetti *et al.* (1993) and Wheeler *et al.* (1993) use the Na I column densities to estimate $E(B-V) \lesssim 0.4$ mag, while Richmond *et al.* (1994) find ~ 0.3 mag.

TABLE 2. Revised Early Magnitudes[1]

Observer	Epoch	Magnitude
Merlin	March 27.91=JD 74.41	$V \gtrsim 17$
Neeley	March 28.3=JD 74.8	$V = 13.45 \pm 0.15$
Garcia	March 28.91=JD 75.41	$m_V = 11.8$
Rodriguez	March 28.93=JD 75.43	$m_{CCD} = 11.4$
Garcia	March 28.98=JD 75.48	$m_V = 11.5$
Ulfheden & Hamberg	March 29.02=JD 75.52	$m_{CCD} = 11.2$
Neeley	March 29.15=JD 75.65	$V = 11.05 \pm 0.2$
Neeley	March 30.05=JD 76.55	$V = 10.68 \pm 0.2$

[1]Visual and CCD data still provisional; de Vaucouleurs (1993b).

5. Photometry

UBVRI photometry since March 30 was presented from the automatic imaging telescopes at Leuschner Observatory (Fig. 2; Filippenko *et al.* 1993b; Richmond *et al.* 1994), at the Kapteyn telescope (Lewis *et al.* 1993; Meikle *et al.* 1993), and by Wells *et al.* (1993) primarily from CCD imaging with the Case Western Reserve University Burrell Schmidt telescope at Kitt Peak National Observatory. See also van Driel *et al.* (1993).

Comparisons of star B with other field stars in the V band indicate that it is not variable on short time scales as previously reported, but that one star is a newly discovered W UMa eclipsing binary. Photometry of the field stars has been evaluated by de Vaucouleurs, Corwin, and Skiff (1994). Table 2 gives the best current estimate of the prediscovery data after careful evaluation of filter responses, color corrections, etc. (de Vaucouleurs 1993; but see also Richmond *et al.* 1994). The V light curve first peaked at $V = 10.7$ mag (JD 76.8 = March 30.3), 2.1 days after shock breakout. The color at that first peak was observed to be $B - V \lesssim 0.1$ mag, with the corrected color being even slightly negative. The *UBVRI* light curves all show a post-maximum dip, a second maximum, and a fairly rapid subsequent decline, followed by a more gradual tail. The intermediate minimum was 8.3 days after shock breakout (JD 82.8 = April 5.3). The secondary V maximum was attained on day 21.1 (JD 95.6 = April 18.1; April 15 in U; April 19 in I). On the tail, the slope in V, R, and I is roughly 0.02 mag d^{-1}, but in B it has a substantially smaller slope ($\sim$ 0.01 mag d^{-1}). On May 2, the U band decline leveled off as was seen in SN 1987A at day 125 (Suntzeff *et al.* 1988). Photometry from the week of June 3–10 indicates that U is increasing at a rate of 0.0035 mag d^{-1}. This may be consistent with the buried pulsar model (Ostriker 1987), as was suggested by Wheeler (1993).

The color curves displayed in Figure 3 show a very interesting evolution. The color is very blue at the first peak and reddens rapidly until the first minimum. The color reddens only slowly during the rise to second maximum, but then reddens rapidly once again beginning at the second peak, reaching a nearly constant plateau at the time, probably coincidentally, when the V magnitude returns to the value of the first minimum. One may qualitatively understand the color evolution by interpreting the first reddening as the phase when the photosphere is in the outer, expanding hydrogen-rich layer, the flat portion when the light curve is on the second rise as the phase when the photosphere is in the inner, helium-rich layer, and the rapid post-peak reddening as the phase when the

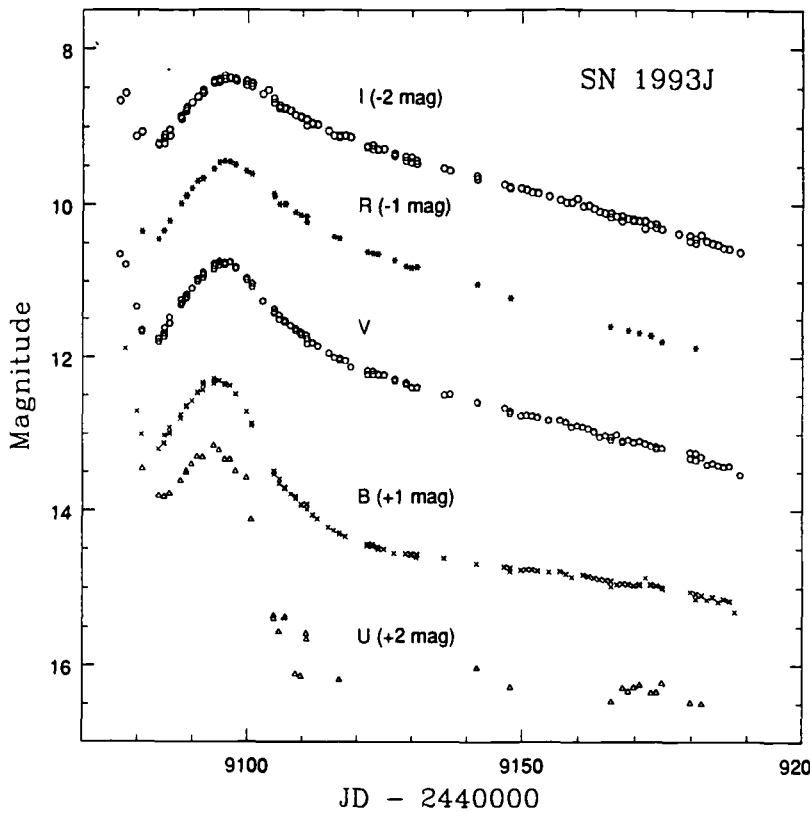

FIGURE 2. *UBVRI* photometry from Richmond *et al.* (1994); 0.76 m automatic imaging telescope at Leuschner Observatory.

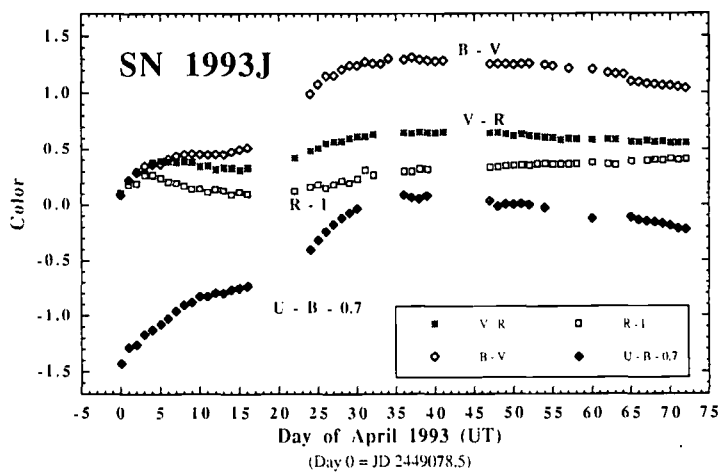

FIGURE 3. Color curves from Wells *et al.* (1993).

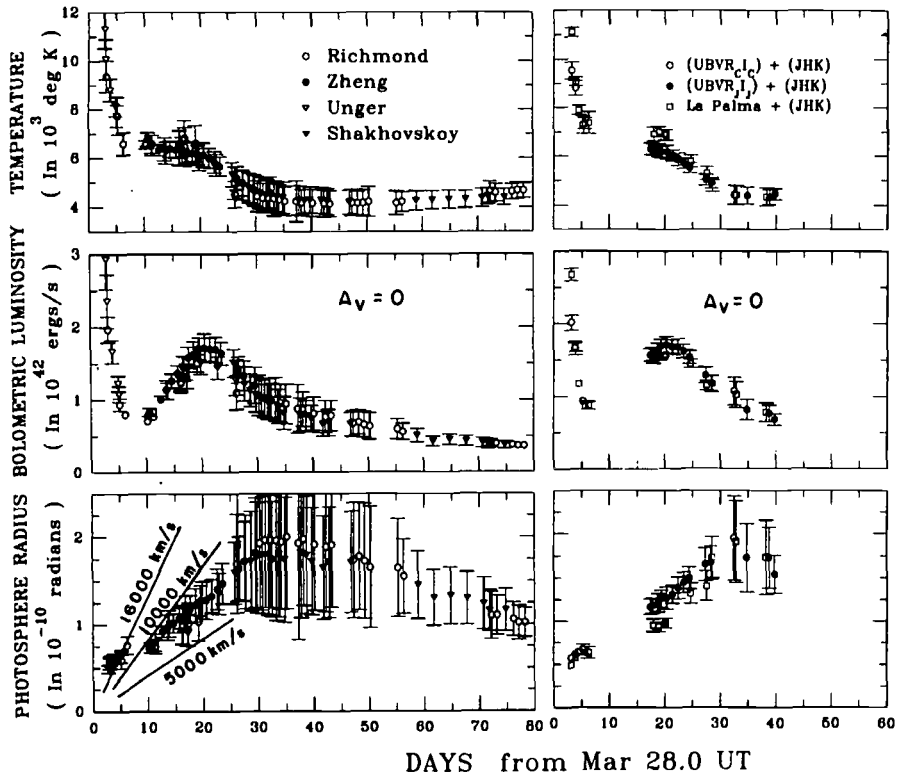

FIGURE 4. Bolometric luminosity, effective temperature, and photospheric radius versus time from Ray *et al.* (1993).

photosphere recedes into the inner, metal-rich core. The latter may yield lower temperatures because iron-peak elements are more efficient coolants than the overlying helium layer (Eastman 1993). If this is the proper interpretation, and that is not completely clear, it has important implications for the structure and composition of the ejecta, since theoretical models dictate different rates of evolution of the photosphere through different layers as a function of the mass of the core and the mixing of envelope hydrogen, freshly synthesized ^{56}Ni , and other elements (§ 12, 13). It is important to understand whether this basic interpretation is also consistent with the observed spectral evolution to be described below.

Ray, Singh, and Sutaria (1993) used *UBVRI* photometric data to determine a bolometric light curve and corresponding effective temperatures and radii of the photosphere, as given in Figure 4. The effective temperature has two plateaus: the first one at $\sim$ 6500 K extends between days 7 and 17. The second is at about 4000 K. The photospheric radius expands with a velocity around 16,000 km s^{-1} in the first few days; thereafter this velocity is between 7500 and 10,000 km s^{-1} (see bottom panels of Fig. 4), and the photosphere starts receding around day 40.

6. UV Spectroscopy

Wamsteker *et al.* (1993) and Sonneborn *et al.* (1993) reported on IUE spectroscopy. The time of maximum UV flux was apparently earlier than March 30.2. The UV continuum flux at 1275, 1735, 2450, and 2900 Å was 126, 115, 75, and 68 in units of 10^{-14} erg

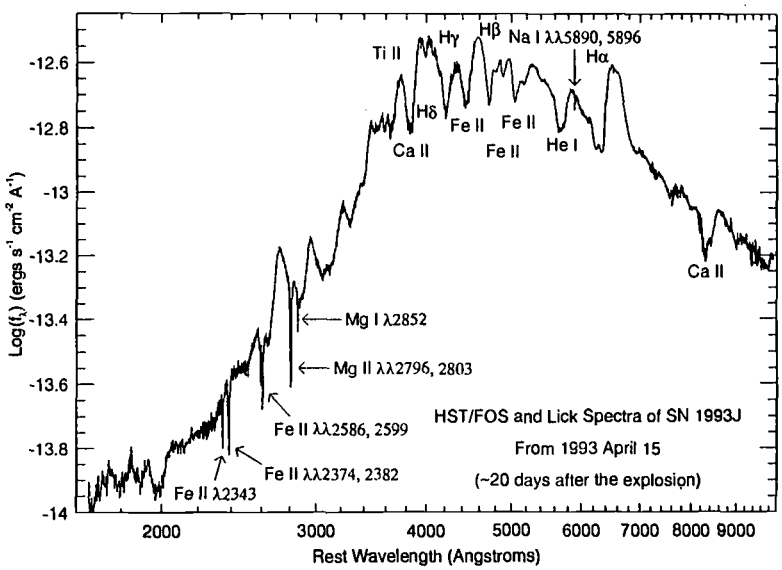

FIGURE 5. HST Faint Object Spectrograph UV spectrum of SN 1993J on April 15 along with a spectrum from Lick Observatory at nearly the same time (Jeffery *et al.* 1994). The spectrum has been corrected for extinction with $E(B-V) = 0.1$ mag.

s^{-1} cm^{-2} $Å^{-1}$ on March 30.2 and decreased by factors of 203, 83, 29, and 11, respectively, between March 30.2 and April 4.6, with the rate of decline slowing after April 2. The spectrum showed few features in the early epochs except for interstellar features and N V λλ1238.8, 1242.8 Å. The 1238.8 Å line had FWHM < 50 km s^{-1} and the 1242.8 Å component a red wing extending > 200 km s^{-1} from line center. The N V integrated line flux was 3.9×10^{-12} erg cm^{-2} s^{-1} on March 30.2 and decreased by a factor of 43 by April 4.6. The narrow width, large flux, prompt appearance, and rapid decay suggest that this emission arises in slowly moving, dense material close to the progenitor, most likely a stellar wind, characteristic of late-type supergiants. The high state of ionization strongly indicates that the wind has been ionized and heated by the UV and X-rays from the shock breakout as well as the radiation resulting from the interaction of the ejecta and circumstellar medium (Lundqvist, Fransson, and Chevalier 1993).

SN 1993J was observed on April 15 with the Hubble Space Telescope. A preliminary reduction of the data is shown in Figure 5 (Jeffery *et al.* 1994) along with a nearly simultaneous optical spectrum obtained by A.V. Filippenko and T. Matheson at Lick Observatory. The spectrum continues to show a definite UV deficit with respect to a Planckian at this epoch.

7. Optical Circumstellar Lines

In addition to the broad features, SN 1993J exhibited several narrow, unresolved (FWHM $\lesssim 5$ Å) emission lines in the earliest spectra that faded rapidly. La Palma spectra from March 29.9 to April 4.9 are shown in Figure 6. Spectra from Lick and La Palma observatories revealed Hα, He II λ4686, [Fe X] λ6374, [Fe XI] λ7892, and [Fe XIV] λ5303 (see also Andrillat 1993; Benetti *et al.* 1993). Benetti *et al.* (1993) give the centroid of the Hα emission at 6561.4 Å, yielding a heliocentric velocity of -82 km s^{-1}. Note that this does not correspond to any of the interstellar velocities. The line is resolved

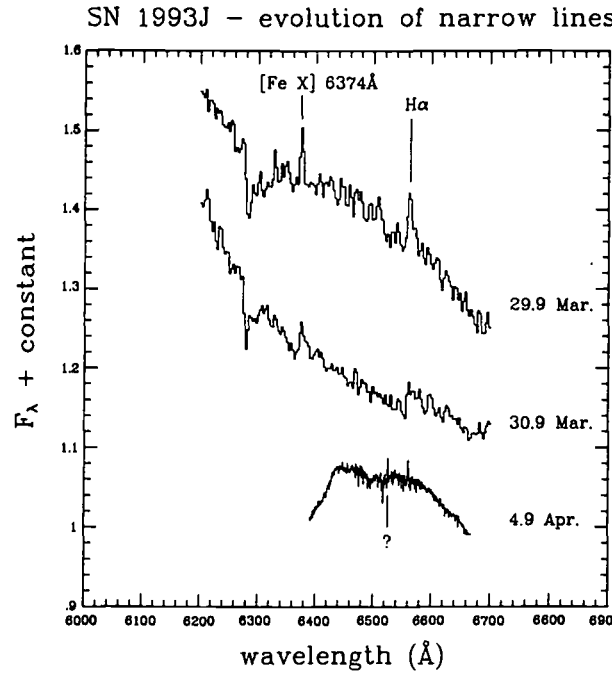

FIGURE 6. Evolution of the narrow circumstellar lines (Lewis *et al.* 1993; Meikle *et al.* 1993).

with a FWHM of 4.5 Å (200 km s^{-1}) and an equivalent width (EW) of 0.34 Å. The March La Palma spectra were taken at a resolution of 6 Å. The Hα line is just resolved, with a FWHM of 8 Å. The iron lines are unresolved. A higher resolution ($R = 0.82$ Å) spectrum on April 4 shows that Hα was still present, though much weaker, and with a FWHM of 2 Å. The measured intensities of these lines are shown in Table 3. The Hα line declined roughly exponentially with an e–folding time of just over 2 days.

The narrow lines indicate the presence of circumstellar material around the progenitor. When the supernova shock wave emerged from the photosphere, the resulting flash of UV and X-rays would have ionized the dense, slow-moving wind of the progenitor which then recombined, producing the narrow lines. The presence of circumstellar material is also supported by the appearance of radio and X-rays, produced when the fast-moving ejecta plowed into the wind (§ 14, 15), and this may have been responsible for the rapid fading of the narrow lines.

8. Low Dispersion Optical Spectra

Early optical spectra have been reported by Garnavich and Ann (1993), Filippenko, Matheson, and Ho (1993a), Liebert (1993), Lewis *et al.* (1993), Schmidt *et al.* (1993), Wheeler *et al.* (1993), Hu *et al.* (1993), and other groups. A series of spectra covering the span from March 29 to May 31 from La Palma is shown in Figure 7. They have *not* been dereddened.

The first spectrum on record seems to be that from La Palma on March 29.9. The early spectra are nearly featureless on large scales, but contain several broad peaks and valleys with relative amplitudes of a few percent (e.g., Filippenko and Matheson 1993a; Taniguchi *et al.* 1993). The exact profiles of these subtle features are affected by telluric lines, and various detector artifacts in some data. A wide slit helps avoid losses due to

TABLE 3. Circumstellar line fluxes and upper limits
(10^{-14} erg s^{-1} cm^{-2})
(Lewis *et al.* 1993; Meikle *et al.* 1993).

line:	Hα	He II	[Fe X]	[Fe XIV]	[Fe XI]
λ_0(Å)	6563	4686	6374	5303	7892
Mar 29.875	6.7	—	3.9	<3.0	0.5
Mar 30.875	4.4	<6.5	2.5	<2.5	<0.4
Apr 01.06	<2	<3	<1	<1	<0.15
Apr 04.87	0.46	—	—	—	—

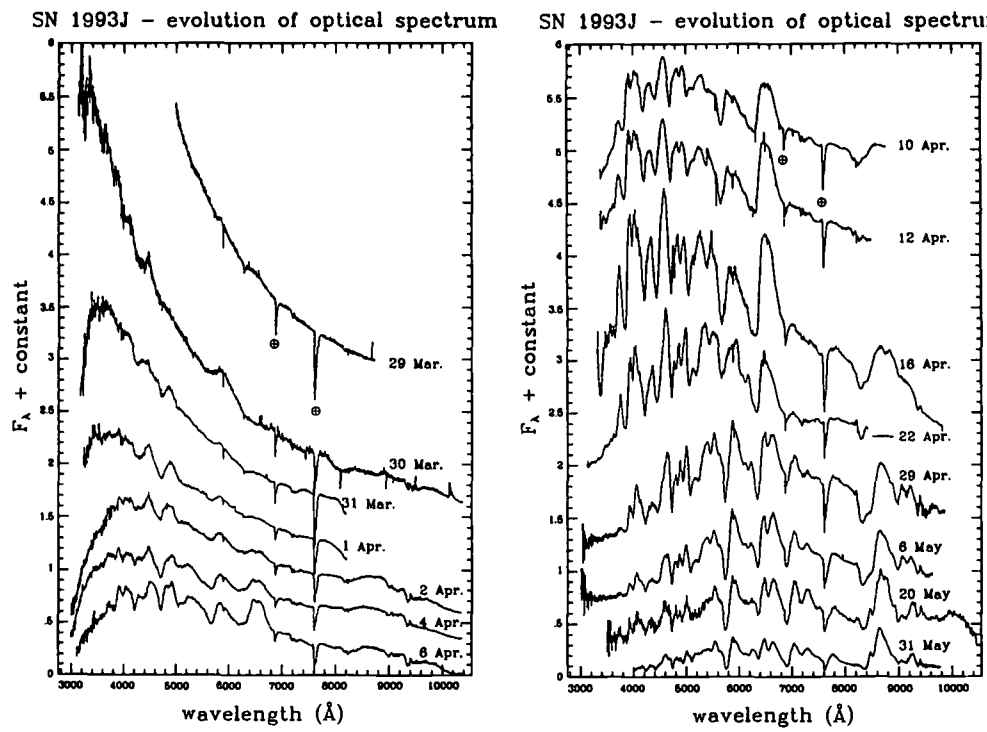

FIGURE 7. Evolution of the optical spectra (Lewis *et al.* 1993; Meikle *et al.* 1993).

atmospheric dispersion. The continuum slopes in the data of Garnavich and Ann (1993) may be affected in this way.

The early continua seem to be well defined black bodies. On March 30, Meikle *et al.* (1993) give a best fit temperature of 16,000 ± 1000 K with an adopted A_V of 0.25 mag. Wheeler *et al.* (1993) give T = 14,900 ± 1000 K on March 31.18 and T = 11,800 ± 700 K on April 1.14, and simultaneously a value of $E(B-V) = 0.15 \pm 0.02$ mag.

The emission feature at 6450 Å has a corresponding absorption trough with a minimum

at 6270 Å. If this is Hα, the expansion velocity derived from the minimum of the trough would be 13,000 km s^{-1}, with an emission peak blueshifted by 5000 km s^{-1} (Filippenko and Matheson 1993a). There is, however, a weak telluric line at 6280 Å that partially obscures the true line profile at this early epoch. The Hα emission is still subtle on April 2, but distinct by April 5 at the first visual minimum. The emission profile is rather unique. Even at this very early stage it is flat-topped with two small emission components or a small absorption dip.

The La Palma spectrum from March 30 (Fig. 7) shows a broad emission peak at about 5900 Å that may be He I λ5876. This peak fades perceptibly the next night and is joined with a broad absorption to the blue on April 1, which is quite definite by April 4. Whether it is He I λ5876, Na I D, or a combination is not clear. By the end of March, Hβ and Hγ P-Cygni lines were clearly present, indicating that SN 1993J was a Type II event. Their profiles show material moving at least as fast as 15,000 km s^{-1}. Wheeler *et al.* (1993) report shallow P-Cygni Hβ with minimum at ~4680 Å corresponding to a velocity of 11,200 km s^{-1} on March 31 – April 1, and P-Cygni He I λ5876 on April 1 with an absorption minimum at ~5593 Å corresponding to a velocity of 14,500 km s^{-1}.

In most data sets, the Hα profile remains basically flat-topped until the strong He I lines intrude around April 25. The La Palma data from April 12, 16, and 22 exhibit a more single-peaked profile with the April 22 data, in particular, showing a central narrow spike that does not seem to appear in other data from nearly the same epoch. A Lick spectrum from April 13 (see Fig. 14 below) shows a similar spike, whereas La Palma spectra on April 12 and 16 show some structure, but not this same spike. This behavior may represent transient emission features as the shock overtakes lumps in the circumstellar matter.

9. The Helium Transition

The character of the optical spectra changed in a dramatic way shortly after April 22, about 25 days after outburst. The most distinct alteration was the "double-peaked" nature of the Hα line (Hu *et al.* 1993). This feature can be recognized (with hindsight) in the April 24 spectrum of Schmidt *et al.* (1993). There was early speculation that this represented some grossly non-spherical flow, but this was clarified by the recognition by Filippenko and Matheson (1993b; see also Filippenko, Matheson, and Ho 1993a) that the spectrum was showing strong lines of He I, and that the second peak in Hα was He I λ6678. With this recognition, there is little, if any, direct evidence for asymmetry in the spectra (but see § 11 for the spectropolarimetry).

There are some earlier hints for this double peaked nature of Hα in the April 6 spectrum of Figure 7, in the April 7 spectrum from the Perkins 1.8 m telescope (Baron *et al.* 1993), and in unpublished spectra from McDonald Observatory on April 5, near the first minimum. Whether this is an early emergence of He I which then fades before its later strong reemergence is a question that needs to be investigated.

Figure 8 illustrates this transition to strong He lines. Note the second peak next to Hα due to He I λ6678, the new absorption corresponding to He I λ7065, and the change in the line profile as He I λ5876 induces a sharp absorption at 5700 Å.

10. IR Spectroscopy

Infrared spectroscopy was conducted at McDonald Observatory on the decline from the first peak. The spectra in the J and K bands on March 31.2 showed only a continuum within the limits of the noise. Spectra on April 1.2 and 2.2 showed definite evidence for

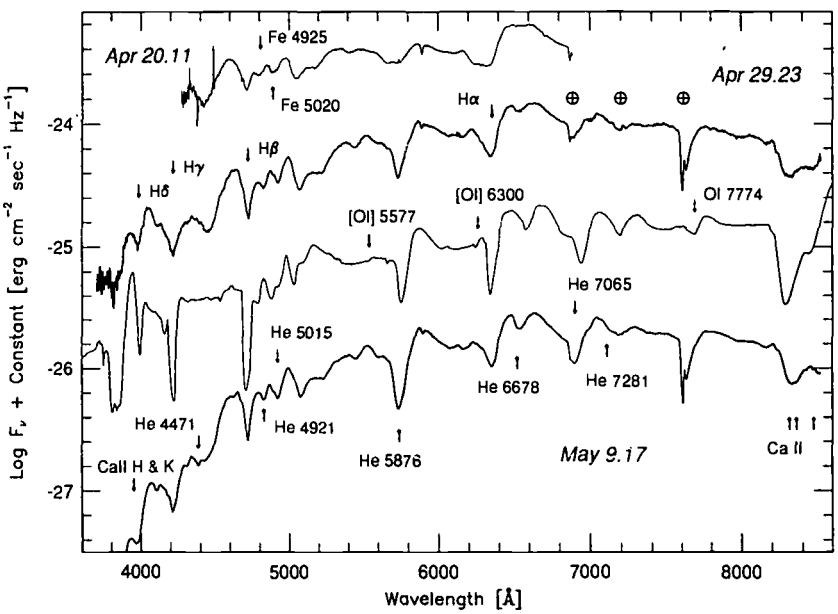

FIGURE 8. Optical spectra from April 20.11, 29.23, and May 9.17 showing the onset of the strong helium lines and a model atmosphere spectrum (Swartz *et al.* 1993b; § 13).

Pa β 1.282 μm as a broad emission bump centered at 1.2874 μm with a total velocity width of $v \approx 11{,}000$ km s^{-1} (Swartz *et al.* 1993b). The IR data of that epoch show no sign of He I or other H lines.

IR spectra from May 3.16, after the onset of the He I lines in the optical, show the 1.083 and 2.058 μm lines of He I, as seen in Figure 9. The former exhibits a P-Cygni profile and the latter an asymmetric absorption with only a broad, low amplitude emission excess to the blue. There was little emission in this line in SN 1987A, but the reasons are unknown. These data also show a P-Cygni profile of Pa β, perhaps flat-topped, and maybe Ca II at 1.195 μm, but this identification is uncertain. Br γ may be present, but is not pronounced. The K-band spectrum is essentially featureless.

11. Spectropolarimetry

Spectropolarimetry was obtained on April 3.2 and 4.2 by Bjorkman and Nordsieck (1993) at the University of Wisconsin Pine Bluff 0.9 m telescope. Weighted over the spectral range 3200–7600 Å, the results were $0.73 \pm 0.13\%$ at a position angle of 179.5° and $0.22 \pm 0.16\%$ at a position angle of 41°, respectively. The spread in these data is probably due to effects caused by the nearly full moon. Formally combining the two data sets gives $0.46 \pm 0.1\%$ at a position angle of $5 \pm 6°$. Measurements made on April 7.22 UT by Smith (1993) yield a V-band polarization of $0.19 \pm 0.11\%$ at a position angle of $178 \pm 17°$. Observations of nearby foreground stars showed less than 0.1% polarization.

Spectropolarimetry was obtained at McDonald Observatory on April 20 (Trammell, Hines, and Wheeler 1993). The total polarization in the continuum was measured to be 0.9% at a position angle of 33°, nearly independent of wavelength. The percent polarization decreased at the location of Hα and the position angle rotated by about 10–15°. On April 26, Jannuzi *et al.* (1993) measured a polarization of 1.04% at PA = 29° with similar structure at Hα. These results are consistent within the errors.

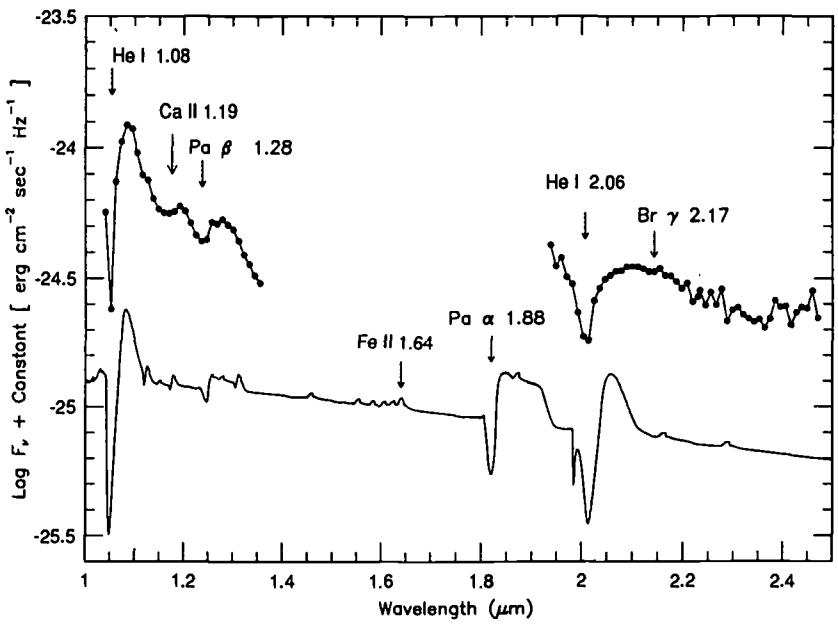

FIGURE 9. Comparison of the May 3.16 infrared spectrum with the spectral model from Fig. 8 (Swartz *et al.* 1993b; § 13).

At Hα the polarized flux consists of the underlying continuum of the supernova and the flux in the emission line, both affected by any polarization induced by the intervening interstellar medium (ISM). After vector subtraction of the continuum polarization, Trammell *et al.* found the polarization of Hα emission alone to be $1.1 \pm 0.1\%$ at a position angle of $150 \pm 4°$, similar to the total in the continuum, but with a significantly different position angle. The orientation of this component is compatible with the position angle of the corresponding spiral arm in M81. Trammell *et al.* assumed this component to be identical to that induced by the ISM in the spiral arm of M81. They then isolated the intrinsic polarization of the supernova by correcting the total polarized flux for the interstellar contribution by means of a Serkowski law. The result for the average continuum polarization of the supernova is then 1.6 ± 0.1% at a position angle of 49 ± 3°. The continuum polarization intrinsic to the supernova is found to be significantly larger than the total continuum polarization. The angle differs from that of the total polarized flux and is independent of wavelength. The latter is further evidence that the ISM has been properly isolated and subtracted and that the source of the polarization is electron scattering. The scattered continuum radiation is then isolated by forming the Stokes flux, which does not suffer from the biased error distribution inherent in the polarized flux. The Stokes flux is formed by first rotating all the polarization into a single, rotated Stokes parameter (Trammell, Dinerstein, and Goodrich 1993). This rotated Stokes parameter is then multiplied by the total flux. The intrinsic polarized flux from the supernova computed in this way shows no peak at the rest wavelength of Hα, by construction. Data taken on April 30 by Tran and Filippenko (1993) at Lick Observatory with excellent signal to noise ratio confirm this basic interpretation of the spectra. Additional Lick observations are also available (Filippenko 1993b; Miller 1993). There are some differences in the data, but it is difficult to know whether these are due to unequal signal to noise ratios or to an evolution of the polarized flux from the supernova.

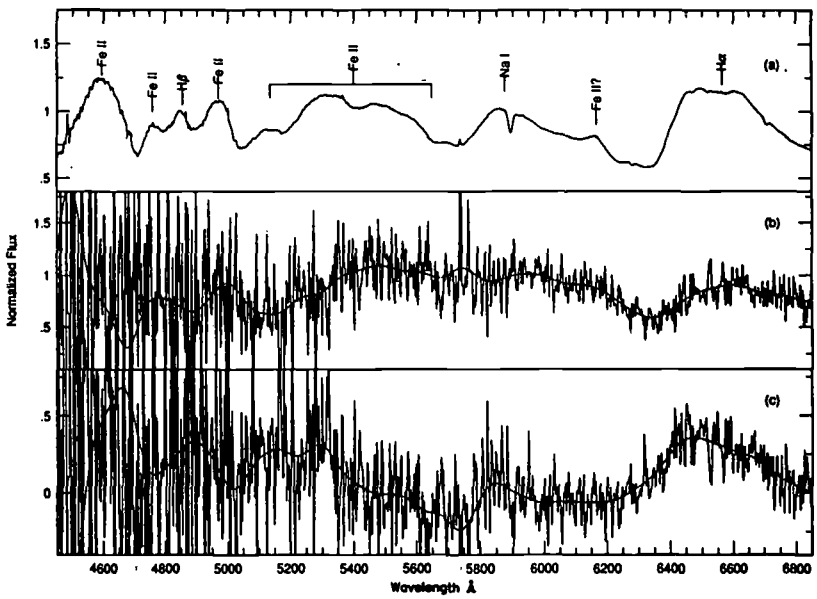

FIGURE 10. The total flux (a), the Stokes (polarized) flux (b), and the unscattered flux spectra (c) on April 20.11 (Trammell *et al.* 1993).

In particular, these data suggest a small amount of polarization at Hα intrinsic to the supernova, but it is not clear that this changes the basic interpretation substantially.

Note that if the ISM component has been correctly isolated by Trammell *et al.* as 1.1% at a position angle of 150°, then the early measurements of Bjorkman and Nordsieck (1993), and especially the "null" result reported for April 7 by Smith (1993), 0.19±0.11% at a position angle of 178±17°, require special attention. The ISM value cannot change with time. Vector subtraction of the ISM polarization deduced by Trammell *et al.* from the total polarization of the combined data of Bjorkman and Nordsieck and the total measured in V by Smith yields a polarization for the supernova on April 3–4 of 1.03±0.1% at a position angle of 48 ± 6° and on April 7 of 1.01 ± 0.15% at position angle 55 ±4° (Trammell and Hines 1993). This implies that the supernova already had an intrinsically polarized component on April 7, just after the first minimum. The close similarity of the position angle (and its significant difference from the position angle of any other component) strongly suggests that the intrinsic polarization from the supernova was roughly constant or perhaps slightly increasing from $\sim$ 1% on April 3–7 to $\sim$ 1.6% on April 20 at essentially constant position angle, $\sim$50°.

The intrinsic polarized flux from the supernova deduced by Trammell *et al.* (1993) shows a broad blueshifted Hα absorption, as shown in Figure 10. This feature has a minimum at $\sim$ 6330 Å corresponding to a velocity of 10,500 km s^{-1} and a FWZI of $\sim$ 395 Å corresponding to a velocity of 18,700 km s^{-1}. This absorption feature demands that the flux is already polarized at a depth such that there is still sufficient Hα column depth to induce the absorption feature by scattering the polarized flux out of the line of sight.

The simplest assumption is that the flux from a scattering layer above the photosphere is already polarized as it impinges on the envelope from below. This flux is then absorbed upon passage through the hydrogen layer. This interpretation has the drawback that if the scattering layer is very near the photosphere, the large intrinsic polarization requires

very large distortions in the core, with axis ratios of order 1.5 to 1 (Shapiro and Sutherland 1982; Trammell *et al.* 1993). This level of polarization is difficult to generate and maintain in polytropes strongly distorted by differential rotation (Steinmetz and Höflich 1992) or by aspherical explosions in core/envelope configurations or with aspherical winds (Khokhlov 1993).

An alternative possibility is that the flux from the core is unpolarized and that a non-spherical configuration in the envelope creates the polarization through scattering. Rather than a distorted core, this could require a distorted envelope. An advantage of this picture is that with a configuration in which an unpolarized, nearly point source (the core) illuminates a distorted scattering envelope, much less distortion is required to produce the same degree of polarization (Brown and McLean 1977; Fox 1991; Trammell *et al.* 1993). A distorted envelope is not out of the question given the evidence in many other contexts for bipolar flow associated with late stages of evolution, especially in binary systems. The challenge to this possibility is that the polarization must be created sufficiently deep in the envelope that there remains enough column depth to induce the observed absorption by Hα in the polarized flux. This may be difficult to accomplish in the small H mass attributed to SN 1993J. We also note that with the understanding that the Hα profile is distorted by He I λ6678, there is no direct evidence in the spectrum at this point for any major asymmetries in the envelope.

Another possible interpretation of the polarization data is that both the core and the envelope are basically spherical, but that the interaction with the circumstellar nebula which gives rise to the early narrow lines, the radio emission, and the X-rays (§ 15) is asymmetric, and that the envelope is thus illuminated by X-rays and ionized asymmetrically (Khokhlov 1993).

Although the understanding of the polarization of SN 1993 is at a very rudimentary level, it is clear that the supernova is intrinsically asymmetric in some regard. Whether the polarization is induced in the core, the envelope, or by some interaction with the circumstellar environment, it should evolve in time and in different ways for different models. The spectropolarimetric data will thus be a critical diagnostic for the models. The data of Jannuzi *et al.* (1993), Tran and Filippenko (1993), and Miller (1993) must be closely examined to check the degree of polarization at Hα. If there is remnant polarization at Hα or if, for some reason, there is a minimum in the intrinsic polarization at the position of the unpolarized Hα, then the interpretation might be changed.

12. Models for the Evolution, Dynamics, and Light Curves

By the time of the meeting a general consensus had emerged about the nature of the progenitor from studies of the light curves. It was accepted that the progenitor had an extended hydrogen envelope of low mass and small hydrogen mass fraction, that the mass of ^{56}Ni ejected was comparable to that of SN 1987A, and that a neutron star remnant was likely. The most common, but not universal, interpretation of the low envelope mass was that it resulted from mass transfer to a binary companion. These models are all variants of the model first presented by Woosley *et al.* (1987; see also Woosley 1991) for a case which they called a "Type IIb," meaning a model with only a thin hydrogen envelope overlying a helium core which would by itself be a model for a Type Ib supernova. SN 1987K in NGC 4651 was the first known example of this phenomenon (Filippenko 1988). As described above, SN 1993J did develop strong helium lines much like a Type Ib. Many people have thus described SN 1993J as a Type IIb supernova.

Within this framework, most theorists had converged to an even more precisely defined configuration with an initial radius of several hundred solar radii, an ejecta mass of 2–

TABLE 4. Light Curve Model Parameters
(masses in $M_\odot$; R in 10^{13} cm; L in 10^{38} erg s^{-1}; KE in 10^{51} ergs)

Ref.	M_{MS}	M_{env}	R_{env}	X_{env}	L	M_{Hecore}	M_{Ni}	M_{ej}	KE	mixing
1.	11-15	.1-.3	2-7	.3-.5	1.5-3.3	2.9-4.5	.06-.08	1.6-4.6	1-1.3	some
2.	12-15	.5-.9	2-3	0.2	2.7	3.3-6	~0.08	–	1-1.2	He
3.	–	<0.2	–	–	–	–	0.05	–	1	–
4.	–	0.75	3	–	–	–	0.055	2.4	1.6	little
5.	–	0.4	3	0.2	–	1.4	0.08	1.8	1	none
6.	15	0.2	–	–	–	–	0.15	–	0.9	none
7.	$\gtrsim$25	3.25	7	0.5	$\gtrsim$4	9.85	0.07	~11	2	He

1. Woosley *et al.* (1994).
2. Shigeyama *et al.* (1994).
3. Ray *et al.* (1993).
4. Utrobin (1993).
5. Wheeler *et al.* (1993).
6. Podsiadlowski *et al.* (1993).
7. Höflich *et al.* (1993b).

3 $M_\odot$, and an outer hydrogen envelope of $\lesssim$ 0.5 $M_\odot$ with a hydrogen mass fraction considerably less than X = 0.5. Allowing for a neutron star remnant of $\sim$ 1.5 $M_\odot$, the original helium core was $\sim$ 4 $M_\odot$, implying an initial main sequence mass of $\sim$ 15 $M_\odot$. An important exception to this interpretation were the models advocated by Höflich, Langer, and Duschinger (1993b) with main sequence mass in excess of 20 $M_\odot$, helium cores of $\gtrsim$ 6 $M_\odot$, ejecta masses of $\gtrsim$ 4 $M_\odot$, and envelopes with more mass and higher hydrogen mass fraction. Various models are summarized in Table 4. The parameters given are the initial main sequence mass, the envelope mass, the progenitor radius, the H mass fraction in the envelope, the progenitor luminosity, the mass of the core of helium and heavier elements, the mass of nickel ejected, the kinetic energy at infinity, and a qualitative indication of the degree of mixing of nickel (through He, etc.). Dashes indicate quantities that were either not pertinent to the model or not readily determined from the paper.

In most models the first peak in the light curve is primarily due to the hot, expanding and cooling "fireball" phase that accompanies shock breakout. In this phase, the inner parts expand adiabatically and the outermost, thin regions radiate by diffusion. This fireball phase attends any supernova model, but is faster for smaller radii (e.g., white dwarfs) and generally unobservable. It was observed in SN 1987A. Chevalier (1992) showed that for power law structures with constant opacity, $L \propto t^{-x}$ with $x \approx 0.5$. The early luminosity of SN 1993J is also very likely to have been affected by interaction with the circumstellar environment (§ 14, 15). Utrobin (1993) proposed that the first maximum is generated entirely by shock heating of an outer shell of matter which might represent the inner layers of a dense wind.

Ray *et al.* (1993) gave analytic estimates of some of the key parameters. Woosley, Shigeyama, and Utrobin each presented "low mass" numerical light curve models with ejecta masses of 2–3 $M_\odot$ and envelope masses of 0.1–0.9 $M_\odot$. Similar light curves are described by Podsiadlowski *et al.* (1993) and Wheeler *et al.* (1993). As the envelope expands and cools to less than 10,000 K, hydrogen can recombine, decreasing the opacity and allowing the photosphere to recede. For a massive hydrogen envelope, this phase

corresponds to the normal SN II "plateau" of constant luminosity. In some of the low mass models for SN 1993J, this phase is completely incorporated in the first decline. In other low mass models the recombination phase is postponed because of heating by radioactive decay. In all models, the light curve turns up because of heating by radioactive decay of ^{56}Ni and ^{56}Co. The evolution of the location of the photosphere and the resulting implications for the predicted photometric and spectral evolution depend on the model. The light curves are affected by the mass and composition of the ejecta, the opacity, and the nickel mass and distribution. In general, as the ejecta turn optically thin, the light curve falls and attains the slope imposed by the decay of radioactive elements. Although the amount of nickel (as well as a number of other parameters) affects the shape and time of maxima, the principal constraint on the nickel mass as given in these calculations (Table 4) is the comparison to the amplitude of the second peak of the bolometric light curve (e.g., Schmidt *et al.* 1993; Ray *et al.* 1993), and hence is proportional to the distance squared.

For models with little or no mixing of the nickel, the photosphere begins to recede shortly after shock breakout and the first minimum is coincident with the photosphere reaching the base of the hydrogen envelope (Woosley *et al.* 1994; Wheeler *et al.* 1993). Without a secondary heat input, the light curve would continue to plummet at that point. With little or no nickel mixing, the diffusion wave from this heating arrives at about the time the photosphere recedes through the outer hydrogen envelope and the light curve rises to the second maximum. With no nickel mixing, the underlying helium layer is already rather cool and the opacity is low, so the photosphere tends to recede rapidly through the helium and into the heavy element core (Wheeler *et al.* 1993). The models of Woosley *et al.* (1994) invoke some nickel mixing into the helium layers, and this tends to heat and ionize the helium and retard the recession of the photosphere through the helium until the second peak. This may be more consistent with the color evolution, and the onset of the strong He I lines after the second peak, but the latter constrains excessive nickel mixing as discussed in § 13. Shigeyama *et al.* (1994) found that if the nickel is mixed through the helium layer, hydrogen recombination is delayed due to heating until near the second peak. Höflich *et al.* (1993b) found similar results for their models, which assumed the nickel to be mixed throughout the helium core. These models also had more massive cores and envelopes, so it is not clear which is the dominant effect. This delayed recession of the hydrogen recombination may not be consistent with the spectral evolution. Most of the low mass models were computed with flux limited diffusion. These models turn optically thin shortly after the second peak. The bolometric luminosity tends to drop too sharply and the colors become completely undetermined. Light curves computed by Podsiadlowski *et al.* (1993) were representative of the general class of "low mass" models, but omitted any core opacity and hence suffered an extreme version of the core-transparency drop. Woosley *et al.* (1994) presented the most sophisticated light curves in various colors based on models with R. G. Eastman's time-dependent LTE atmospheres. The atmosphere models smooth out the sudden decrease in luminosity that plagues some of the low mass models when the photosphere reaches the bottom of the metal core. Shigeyama *et al.* (1994) have managed to avoid the problems associated with the flux-limited diffusion calculations becoming optically thin too precipitously.

Podsiadlowski *et al.* (1993), Woosley *et al.* (1994), and Ray *et al.* (1993) set out the case for a binary companion based on binary evolution computations. They pointed out that binary evolution of moderately massive stars proceeds until the Roche lobe of the mass losing star reaches the inner, helium rich layers left behind by the retreating convective hydrogen-burning core. At this point, the envelope radius drops as further mass is lost, the envelope retreats inside the Roche lobe, and transfer stops. The progenitor

of SN 1987A might have been the recipient of such a transfer (Tuchman and Wheeler 1989; Rathnasree and Ray 1992; Podsiadlowski *et al.* 1992). Podsiadlowski *et al.* (1993) specifically argue that such transfer will leave behind not an M, but a K supergiant of about the right color and luminosity to account for the pre-explosion observations of the site. Thus it is quite plausible that prior photometry is revealing the progenitor, but caution should still be exercised in making this identification.

Woosley *et al.* (1994) argue that the pre-supernova star was filling its Roche lobe at the time of the explosion and thus the hydrogen envelope was highly deformed (about 3:2). This may have implications for the polarization. Woosley *et al.* (1994) note that any companion star would quickly become embedded in the supernova, but should become visible in three years (perhaps earlier in the U band) when the supernova has faded below 10^{38} erg s^{-1}. Podsiadlowski *et al.* (1993) and Woosley *et al.* (1994) point out that if "kicks" have not played an important role, the companion is still bound to the neutron star. For the final separation advocated by Woosley *et al.* (1994) and Ray *et al.* (1993), $\sim$ 10 AU, and characteristic ejecta velocities of $\sim$ 10,000 km s^{-1}, the companion would be engulfed in less than about two days, near the first observed peak. It is unlikely that this resulted in any visible display. The entire kinetic energy of the fraction of the envelope impacting on the solid angle of the companion star in the space of a few days only represents about 10^{39} erg s^{-1}. For the bolometric light curve, Woosley *et al.* (1994) conclude that their lower mass model (11 $M_\odot$ initial mass) does the best job with the atmosphere calculation, but the higher mass model (15 $M_\odot$) performs better with a flux-limited diffusion calculation. The color curves are not quite so successful, especially in the blue. The intermediate mass model (13 $M_\odot$) does the best job with the colors at the second peak, as shown in Figure 11, but this is also the only model in which hydrogen was mixed into the interior, thus increasing the interior opacity and maintaining the photosphere at larger radii and cooler temperatures for a longer time. In this model, the observed V light curve is too bright on the initial decline and through the first minimum by about 1 magnitude, although the second peak is reproduced fairly well. Woosley *et al.* (1994) point out that the progenitor envelope can be radiative or convective depending on circumstances, and that this can affect the light curve. Their envelopes are helium and nitrogen rich and carbon poor.

The bolometric light curves in the models of Woosley *et al.* (1994) never fall on the ^{56}Co radioactive decay line. Their model corresponding to an initial mass of 11 $M_\odot$ with ^{56}Ni unmixed has a long plateau that may be related to the nickel bubble. The light curve then falls more steeply than the ^{56}Co decay line because of γ-ray transparency. A similar model with the ^{56}Ni mixed falls off more steeply than the ^{56}Co decay after the peak as transparency sets in earlier.

Shigeyama presented work on behalf of his group (see also Nomoto *et al.* 1993; Shigeyama *et al.* 1994). They demonstrate that the bolometric light curve of SN 1993J around the second maximum is very similar to that of the Type Ib SN 1983N, and that their helium star models for SN 1983N fit the second bolometric peak of SN 1993J rather well. They conclude that the similarity of SN 1983N and SN 1993J implies that the hydrogen-rich envelope of SN 1993J contains so small a mass that it has relatively little influence on the shape of the second peak. Shigeyama *et al.* (1994) present models for the bolometric light curve based on helium core masses of 4 $M_\odot$ with envelopes of 0.89 and 0.47 $M_\odot$ having Y = 0.80 and 0.79, respectively. We note that SN 1993J actually declined somewhat faster than SN 1983N immediately after the second peak (Richmond *et al.* 1994), although the resemblance is still quite close. Conversely, SN 1983N fell more steeply than SN 1993J on the tail. Nomoto *et al.* (1993) and Shigeyama *et al.* (1994) favor mixing of ^{56}Ni to fit the light curves of both SN 1983N and SN 1993J. In the case of SN 1993J, the helium

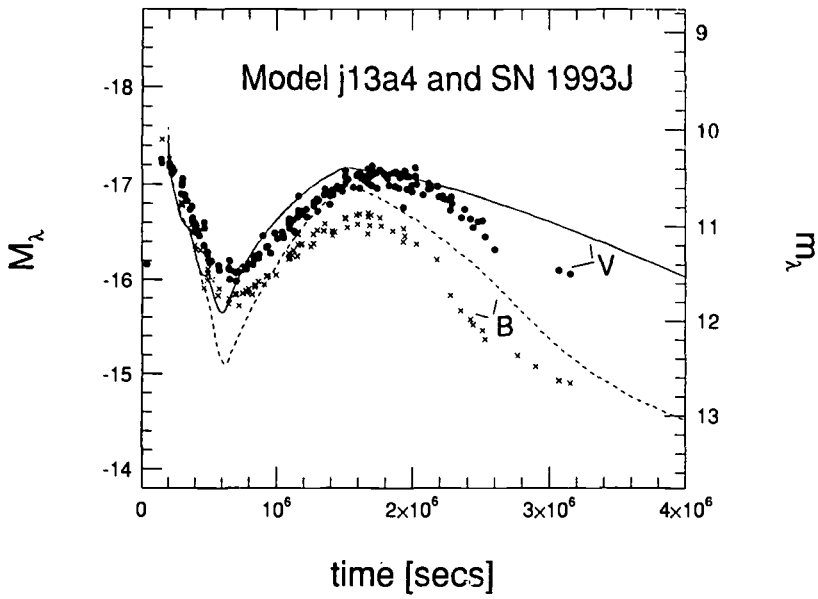

FIGURE 11. Computed B and V color curves compared with the data for SN 1993J (Woosley *et al.* 1994).

core expands more slowly due to interaction with the envelope; this gives rise to greater trapping of γ rays, thereby yielding a less steep decline on the tail. Neglecting the initial peak which requires an extended envelope, the light curve models of Nomoto *et al.* (1993) for SN 1983N based on bare helium cores with no mixing of ^{56}Ni actually fit the second bolometric peak of SN 1993J better than any of the models of Shigeyama *et al.* (1994) specifically designed to do so. In the latter, the rise and decline tend to be too steep, and the amplitude with respect to the minimum too great.

Shigeyama *et al.* (1994) point out that the calculated light curve shape depends on the extent of ^{56}Ni mixing. The time of the light curve minimum is reduced in models with nickel mixing, since it makes heating due to radioactive decays start earlier, as illustrated in Figure 12. They conclude from their models that SN 1993J has actually undergone mixing of ^{56}Ni. They also argue that the fact that their calculated luminosities at the second maximum are higher than SN 1993J can be ascribed to excessive expansion velocities at the bottom of the H-rich envelope in the calculation compared with the actual minimum velocity of hydrogen in SN 1993J. They suggest that this can be improved if hydrogen is mixed down into the core to lower velocities, as suggested from the modeling of SN 1987A. Utrobin (1993) argued that the bulk of the radioactive material that powers the second peak is confined to the innermost layers of ejected envelope expanding with velocities less than $\sim$ 2600 km s^{-1}. He concluded that a shell with a positive gradient of hydrogen and a negative gradient of helium must be present and that the hydrogen should be spread throughout the envelope to reproduce the smooth second peak of the visual light curve. The degree of mixing of nickel, hydrogen, and other elements will be constrained by the photometric and spectral evolution. From their attempt to fit the color evolution as well as the bolometric light curve, Woosley *et al.* (1994) favor a model in which the hydrogen envelope mass is low and the mixing of hydrogen inwards has been small, but in which a small amount of ^{56}Ni has been mixed outwards into the

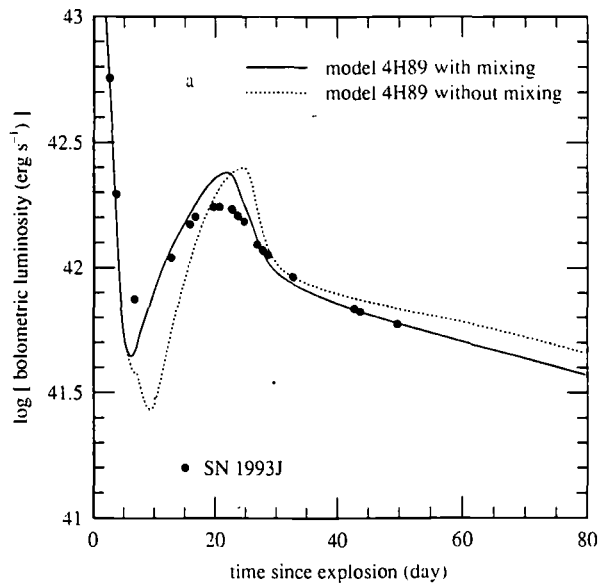

FIGURE 12. The bolometric data of Schmidt *et al.* (1993) are shown with two models by Shigeyama *et al.* (1994), with (solid line) and without (dotted line) mixing of nickel throughout the helium core.

helium core to smooth the light curve near the first minimum. Wheeler *et al.* (1993) present a model based on the 3.3 $M_\odot$ helium core of Shigeyama *et al.* (1990) with the outer 0.4 $M_\odot$ converted to X = 0.2. This model has no extended envelope and cannot reproduce the first visual rise. It produces the best V light curve from day 4 to day 30 of any yet presented, and does an adequate job of the bolometric light curve. Since this model confines H to a distinct layer and includes no ^{56}Ni mixing, it seems premature to come to definite conclusions about the presence of mixing mechanisms. An important additional variable is the opacity. The calculation of Wheeler *et al.* used "expansion opacities" computed by R. P. Harkness from 42 million lines. Despite the excellent fit to V over some epochs, the model of Wheeler *et al.* (1993) is clearly inadequate in other ways. It has the typical limitations of flux limited diffusion calculations when the whole core becomes optically thin. This model also gets too blue very suddenly at the first minimum which can probably be attributed to the total omission of any outward mixing of ^{56}Ni so that when the photosphere reaches the inner edge of the hydrogen layer, it recedes rapidly through the helium to the oxygen layer. In any case, care must be taken to avoid misinterpreting the effects of "missing opacity" with mixing of H or ^{56}Ni, both of which will act to increase the local opacity.

Höflich, Langer, and Duschinger (1993b) favored a similar, but quantitatively different model. They computed the progenitor evolution, explosion, B and V band brightness evolution, spectral features, and γ-ray emission of stellar models in the initial mass range 10 to 30 $M_\odot$ at a metallicity of $Z = 0.02$ from the zero age main sequence through carbon ignition using an implicit hydrodynamic stellar evolution code (Langer 1991) with OPAL opacities (Iglesias *et al.* 1992) and mass loss rates according to Nieuwenhuijzen and de Jager (1990). One model had increased rates for the low mass star. The hydrodynamic simulations of the SN explosions were calculated with an explicit PPM hydro-code coupled to an implicit gray radiation transfer program (Höflich *et al.* 1993a). An extended

region consistent with the mass loss of the progenitor star was added to the pre-SN structure to study the model SN-wind-interaction. The models are Rayleigh-Taylor unstable in the inner region and they assume that all heavy elements including nickel are mixed throughout the helium core.

Höflich *et al.* (1993b) concluded that the failure of the low mass models to reproduce the colors at the second peak, as noted by Woosley *et al.* (1994) and Wheeler *et al.* (1993), was sufficiently serious to abandon the model. They were also concerned that low mass progenitors ($M_{ZAMS} \lesssim 20$ M$_\odot$), which need binary mass transfer in order to get rid of a large fraction of their envelope, may have problems maintaining a sufficiently strong wind ($\gtrsim 10^{-5}$ M$_\odot$ yr^{-1}) during their final evolutionary phase to account for the radio and X-ray observations (§ 14, 15). They thus advocate a model based on a massive, single star progenitor which has lost the major part of its envelope prior to the explosion. There are several systematic changes as the mass increases. Höflich *et al.* (1993b) find that the luminosity at the first peak depends to a certain extent on the interaction with the surrounding nebula. Although the luminosity of the first peak is not dominated by this shock interaction as in the suggestion of Utrobin (1993), it amounts to 30% for their model of initial mass 30 M$_\odot$, 50% for 25 M$_\odot$, and 60% for 20 M$_\odot$. Larger initial mass also gives more massive envelopes with a smaller He enrichment in the envelope, ~ 0.5 versus $\gtrsim 0.8$ in some of the lower mass models. As a consequence, the photosphere reaches the H/He interface not at the first minimum, as in most of the low mass models, but at about the second maximum. For the high mass models, the second rise is mainly due to the recombination energy from the massive C/O core. The result is that the rise to the second maximum is governed by the release of this thermal energy of the helium core as the helium recombination wave proceeds through it. The radioactive decay energy does not become significant until about the second maximum. Since the second peak is affected partially by the rate of recession of the photosphere through the helium in the massive models, the width of the peak is not simply the diffusion time of the radioactive heat from the core. With increasing mass, the overall light curves become brighter because more energy is stored rather than radiated with early recombination. The interaction with a given circumstellar nebula becomes absolutely stronger and the temperatures at the photospheres at the first peak thus increase with mass. To compensate for this effect, a higher reddening is required for a 30 M$_\odot$ than for a 20 or 25 M$_\odot$ model. Figure 13 shows the B and V light curves for the 30 M$_\odot$ model of Höflich *et al.* (1993b) in which they have assumed $E(B-V) = 0.8$ mag. This model reaches the first maximum on day 5, when it achieves approximate homology, and the minimum on day 9. The photospheric temperature is about 55,000 K at the first peak, and declines to 20,000 K on day 14, 12,000 K on day 22, 6000 K on day 35, and 4500 K on day 60.

There are a number of problems with this high mass model which show that it is extreme and that at least a somewhat lower mass is preferred, as concluded by Höflich *et al.* (1993b). The major generic problem is that the assumed reddening to make the model work is much too large. It is not even consistent with the model, since $E(B-V) = 0.8$ mag would imply that the observed color for an infinite temperature black body should be about 0.4 mag, and that value of $B-V$ was not observed until about day 10. The first peak at 5 days is too late. This is a fairly strong constraint, if the time from outbreak to peak of $\sim$2 days (Wheeler *et al.* 1993) is accepted. This suggests both the mass and radius of the model envelope are too large. Höflich *et al.* (1993b) have computed some model spectra and state that they can account for the strong H lines after the photosphere cools to less that 15,000 K. In this model, however, that only occurs after day 14 and the hydrogen lines became strong around day 5, prior to the first minimum,

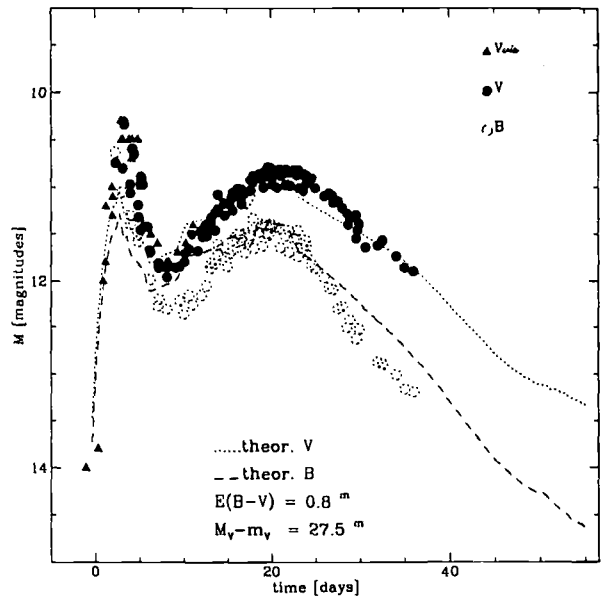

FIGURE 13. Computed B and V color curves compared with the data for SN 1993J (Höflich *et al.* 1993b).

as shown in Figure 7. This massive model thus seems to be in strong contradiction with the observed spectral evolution.

The major advantage of the high mass model is that it generally provides better fits to both the B and V curves than others proposed. The massive models may also give more opportunity for the hydrogen envelope to both polarize and scatter the flux generated in deeper layers, requiring less geometrical distortion to account for the polarization. The disadvantage is that to fit the photometry, the model requires $E(B-V) = 0.8$ mag, and this is simply disallowed by the accumulating evidence that $E(B-V) \approx 0.15$ mag.

13. Spectral Modeling

Although no results were explicitly presented, the evolution of the spectra during the first decline represents a challenge. If the temperature is too low, the hydrogen lines are predicted by atmosphere models to be too strong. This problem has been discussed by Höflich, Baron, Hauschildt, and Harkness (all private communications). Höflich *et al.* (1993b) advocate a hot atmosphere, but the constraints on the reddening, continuum shape, and colors all argue that the continuum was that of a well-defined cooling black body during the decline. It cannot have been substantially hotter and heavily reddened. Another possibility is that the hydrogen abundance is very low. The smallest H abundance considered by Höflich *et al.* was about 40%, as suggested by the more massive evolutionary models. For low mass models, $X \lesssim 0.2$ is plausible. Baron and Hauschildt have considered such models, but without necessarily resolving the problem. The very early spectra with the weak lines need more consideration.

Baron *et al.* (1993) presented atmosphere models of optical spectra obtained on April 7.2 and April 13.2. Their synthetic spectra used an approximate lambda iteration method to solve the fully relativistic radiation transport equation and the NLTE rate equations for H I, He I, Mg II, and Ca II (Hauschildt 1992a,b, 1993; Hauschildt and Baron 1993;

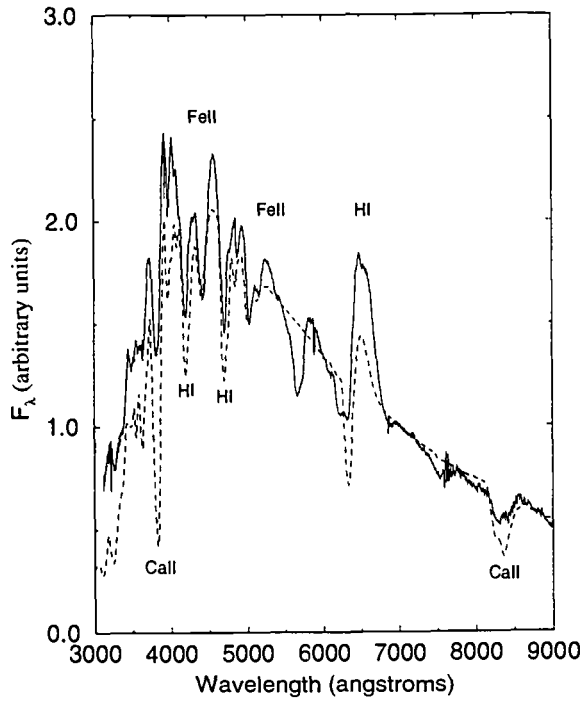

FIGURE 14. A synthetic spectrum (dashed line) is compared to the observed spectrum (solid line) from April 13 (Baron *et al.* 1993).

Rybicki and Hummer 1991). The line list of Kurucz (1991) was used to select the approximately 200,000 strongest lines with the populations assumed to be in LTE. Model atmospheres were constructed assuming that the velocity profile is homologous, $v \propto r$, and that the density profile follows either a power law, $\rho \propto v^{-N}$, or an exponential falloff, $\rho \propto \exp(-v/v_e)$, where N and v_e are parameters to be determined. The radius of the photosphere is given by $R_0 = v_0 t$, where the subscript 0 denotes the photosphere. The explosion date was assumed to be Mar 27–28 and the extinction to be $E(B-V) = 0.1$ mag. They find that the relatively narrow lines are not due to low photospheric velocity, but rather must be formed in an atmosphere of small extension and hence steep density profile.

On April 7, shortly after the first minimum and after the development of strong Hα emission, Baron *et al.* (1993) fit the spectrum with $v_0 = 10,500$ km s^{-1}, $R_0 = 10^{15}$ cm, $T_0 = 7,500$ K, and $v_e = 450$ km s^{-1}. A temperature $T_0 = 8000$ K is allowable, but $T_0 = 7000$ K is too low. Note that Ray *et al.* (1993) derive a temperature of 6500 ± 500 K from the photometry at this time.

Figure 14 displays the April 13 spectrum and a synthetic spectrum with $v_0 = 11,000$ km s^{-1}, $R_0 = 1.6 \times 10^{15}$ cm, $T_0 = 6,500$ K, and $v_e = 450$ km s^{-1}. The photospheric velocity has remained nearly constant in time since April 7. This may be more consistent with the low mass models for which the photosphere is in the core during this time

span than for the high mass models (or those of Shigeyama *et al.* 1994) for which the photosphere is still receding through the H envelope, although the absolute value of the photospheric velocity, $\sim$ 11,000 km s^{-1}, is rather high. The decline in photospheric temperature from 7,500 to 6,500 K is consistent with Ray *et al.* (1993), within the scatter. Raising the temperature to $T_0 = 7,000$ K results in far too much flux below 4000 Å.

The density profiles are extremely steep, with an equivalent power law index $N \gtrsim 20$, especially in comparison with SN 1987A, which had a power law index $N = 4$ at the same epoch (Jeffery and Branch 1990). Baron *et al.* (1993) were not able to produce the strong emission that is seen in Hα. It may be that the nearly pure emission profile of Hα is due to altered level populations produced by radiation from circumstellar interaction or by a flatter density external to the steeply falling profile near the photosphere, as seen in the calculations of Shigeyama *et al.* (1994). They also fail to fit the broad minimum around 5600 Å. Sodium is treated only in LTE in these models, but there is a general feeling that atmospheres at this epoch are too warm for this to be Na I D, so the feature may be He I λ5876 (Baron 1993; Eastman 1993; Schmidt 1993). One must then understand the sharp change in this feature when the strong He I lines appear.

Swartz *et al.* (1993b) have computed atmosphere models at a phase of $\sim$ 40 days after shock breakout that account for the development of the strong He I lines in the optical and IR. In the models, the helium lines become visible after (1) the H/He layer recombines, allowing exposure of the helium mantle, (2) the onset of substantial gamma ray deposition in the helium layer, and (3) the free electron density in the mantle has declined sufficiently due to expansion and cooling to eliminate veiling of the helium lines by electron scattering. The structure models employed are the same as in Swartz *et al.* (1993a), which are helium core models from Shigeyama *et al.* (1990) but with portions of the helium core turned into hydrogen with variable mass fraction. Note that these models, and the analogous ones used by Wheeler *et al.* (1993) for light curves, maintain the same density/velocity structure as the original helium core models. They are thus not consistent in this regard with models that include the outer hydrogen envelope *ab initio* with its associated affect on the dynamics. Likewise, these models could be regarded as the result of some mixing of an outer, more hydrogen-rich layer with part of the helium core. The constraints on hydrogen mixing deduced from these models must be considered in that context.

For a nominal explosion energy of $\sim 10^{51}$ ergs, Swartz *et al.* (1993b) find that an ejecta mass of $\sim$ 4.5 M$_\odot$ is too large and that of $\sim$ 1.8 M$_\odot$ too low to match the expansion velocities implied by the observed spectra. An ejecta mass of $\sim$2.5 M$_\odot$ works well. Of this mass, $\sim$0.4 M$_\odot$ contaminated with about 10% H by mass gives a good spectral fit, as illustrated in Figure 8. The atmosphere models show that the hydrogen must not be homogeneously mixed with all the helium or the helium lines would be excessively veiled and would not appear in the spectrum. The portion of the ejecta forming the P-Cygni He I lines must therefore be substantially more hydrogen deficient than the 10% by mass in the outer layer of the model. The hydrogen to helium ratio in the outer layers is not tightly determined. Changing the ratio in the outer 0.4 M$_\odot$ from 9/1 to 1/9 only changes the He I λ6678 feature from slightly weaker than Hα to slightly stronger. The latter is observed, so a helium-rich atmosphere is suggested and the observations are consistent with the 1 to 9 ratio assumed in the model illustrated in Figures 8 and 9. The atmosphere models constrain the nickel mass to be $\lesssim$0.1 M$_\odot$ so that the hydrogen is not completely ionized at $\sim$40 days past shock breakout. Note that this constraint comes from the spectrum at a single epoch and is distance independent. In a similar fashion the nickel cannot be mixed too far out into the ejecta or hydrogen would again be excessively ionized. Homogeneous mixing of the nickel through the helium core seems

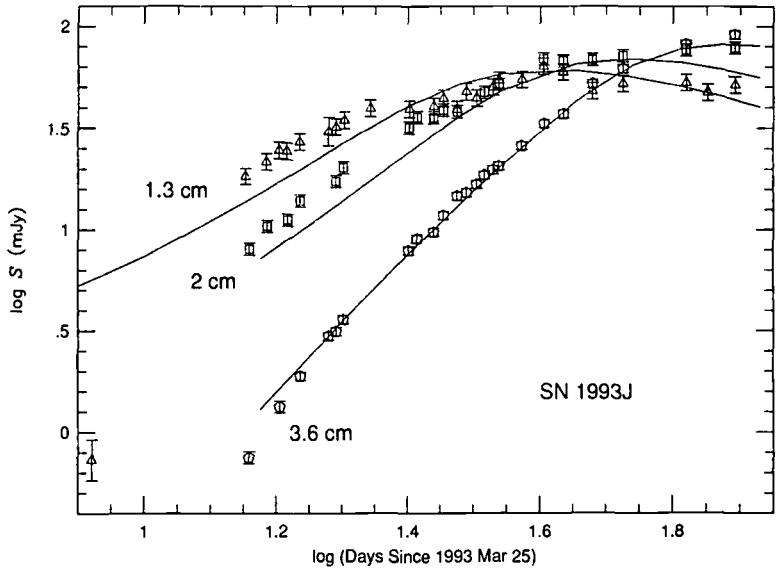

FIGURE 15. VLA radio observations (Van Dyk *et al.* 1993b).

to be excessive by this criterion. The models predict that H and He should be visible for $\sim$ 100 days, but should disappear by $\sim$ 200 days. This gives a quantitative basis for the guess by intuition or comparison to other events (SN 1987K; Filippenko 1988) that SN 1993J will resemble a SN Ib in the nebular phase.

14. Radio

Van Dyk *et al.* (1993b) presented observations of the early radio emission made with the Very Large Array at 1.3, 2, 3.6, 6, and 20 cm, starting on 1993 March 31 UT, less than three days after optical discovery. This radio emission indicates significant interaction of the supernova shock front with circumstellar matter around the progenitor system. The supernova was first detected on April 2 at 0.7 mJy at 1.3 cm. The 1.3 cm radio light curve has flattened and appears to be turning over as shown in Figure 15. Preliminary indications are that the overall radio properties of SN 1993J are similar to those of several previous Type II radio supernovae (SN 1979C, SN 1980K, and SN 1981K), although SN 1993J was detectable earlier than either SN 1980K or SN 1979C.

D. A. Green (Pooley and Green 1993) reported that radio emission was detected at 15.25 GHz, with the Ryle Telescope on Apr 5, only about 8 days after the explosion. As shown in Figure 16, SN 1993J showed an approximately linear increase in flux density from its detection to about 53 mJy at May 3 (day 36) and then a slower rise to a peak of $\sim$ 80 mJy about day 75. The 15.25 GHz emission has since shown a general decline, but with significant variations on the time scale of weeks. The linear increase in flux density seen at this frequency lasted several times the delay in detection of the SN. This is difficult to reconcile with the available "mini-shell" models for radio supernovae (Chevalier 1982). Moreover, upper limits on the radio emission for several days before the detection may also be difficult to reconcile with the gradual increase expected from the "mini-shell" model.

Lundqvist, Fransson, and Chevalier (1993) used model 4H47 of Shigeyama *et al.* (1994) for the evolution of the photosphere to explore the effects of SN 1993J on the circumstellar

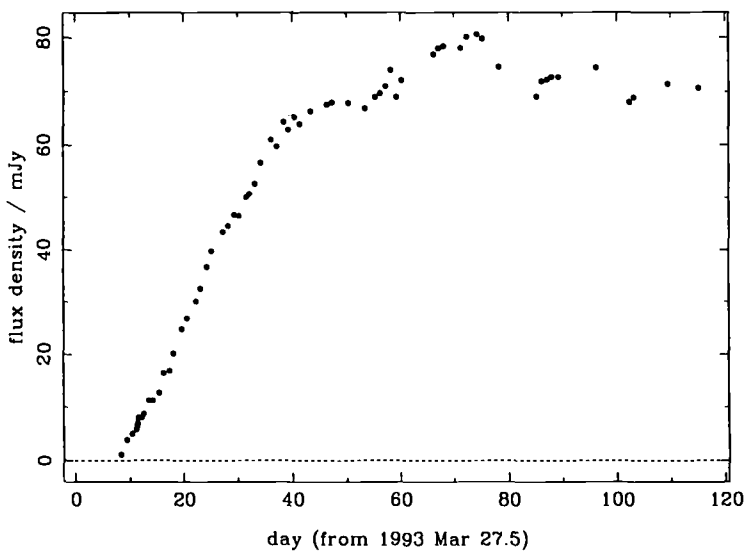

FIGURE 16. 15.25 GHz light curve from Pooley and Green (1993).

medium. The temperature evolution is constrained by IUE observations on March 30.2 and 31.2 when the observed color temperature was $\sim 2 \times 10^4$ K. The peak effective temperature in model 4H47 is $\sim 2.9 \times 10^5$ K. Lundqvist *et al.* found that the wind temperature quickly rises to (1.5–2.3) $\times 10^5$ K, and even beyond that very close to the SN. Carbon, nitrogen, and oxygen attain their He-like stages, and H and He are fully ionized. After ~ 0.5 days, the gas close to the SN starts to recombine. With a mass loss rate of 2×10^{-5} $M_\odot$ yr^{-1} and a wind speed of 10 km s^{-1}, the gas close to the SN cools down to $\sim 2 \times 10^4$ K in $\sim$0.5 days, whereas outside 4×10^{15} cm it is still 2×10^5 K. During the recombination period that follows, the observed Hα and N V λ1240 emission is likely to form. Collisional excitation alone is not sufficient to power the N V line. Photoexcitation is also needed; however, the photospheric continuum flux at 1240 Å in the models of Shigeyama *et al.* drops too fast during the first day, giving an order of magnitude too low a N V λ1240 flux when the line was observed, i.e., after $\sim$2–3 days. It is therefore likely that the N V line was powered by a somewhat harder photospheric flux after $\sim$0.5 days than in model 4H47, and/or by the radiation from the interaction region. The Hα line is due to recombination emission, and indicates a high wind density corresponding to a mass loss rate of at least 5×10^{-5} $(w/10$ km s$^{-1})$ $M_\odot$ yr^{-1}, where w is the wind speed. For a constant speed of $w = 10$ km s^{-1}, Van Dyk *et al.* (1993b) estimated the mass loss rate from the progenitor to be $\dot{M} \approx 4 \times 10^{-6}$ $M_\odot$ yr^{-1} using an assumed unshocked wind temperature $T_w = 10^4$ K and a shock velocity of 10,000 km s^{-1} ($\dot{M} \propto T_w^{0.68} v_{shock}^{1.5}$). Lundqvist *et al.* (1993) noted that the observed slow turn-on is not well modeled by a simple, isothermal, r^{-2} wind, but indicates that $\dot{M}$ is close to 4×10^{-5} $(w/10$ km s$^{-1})$ $(T_w/10^5$ K$)^{3/4}$ $M_\odot$ yr^{-1}. With their estimate that T_w is of order 10^5 K due to the pre-ionization by the shock breakout, they concluded that $\dot{M}/w$ is about an order of magnitude higher than estimated by Van Dyk *et al.*

Lundqvist *et al.* (1993) explored ways of obtaining a slow radio turn-on. A density profile of $\rho \propto r^{-1.5}$, implying a departure from a steady state, agrees with the data. Other ways to produce a slow turn-on are for the wind to be blobby, for the wind temperature close to the shock to decrease with time while the radio optical depth is close to unity,

and for the wind to have an asymmetrical density distribution. Since the slow turn-on is observed at many wavelengths and thus over an extended period of time, it appears as if a decreasing wind temperature is not likely. Van Dyk *et al.* (1993b) argue that the relatively slow radio turn-on may indicate the presence of internal absorption which is generally seen only in supernovae with more massive progenitors. They suggest that such internal absorption may be evidence for the presence of filamentary or "blob" structures or non-spherical distortions in the radio generation region (Weiler *et al.* 1990). Lundqvist *et al.* (1993) noted that asymmetry and blobs may also be helpful in explaining the high wind density needed for the observed high Hα flux. Asymmetry in the radio generation region could be consistent with the binary models presented at the meeting.

15. X Rays

B. Aschenbach reported that on April 3, six days after the optical detection, soft X-ray emission from SN 1993J was detected by the ROSAT observatory during a 2700 sec exposure (Zimmermann *et al.* 1993a). This marks the earliest detection of X-rays after a supernova explosion. A preliminary analysis of the data shows that the mean spectrum in the ROSAT energy range between 0.1 and 2.4 keV can be fit by either a power law with photon index -0.88 ± 0.13 or by thermal models with kT well above 6 keV (Zimmermann *et al.* 1993b). With a distance of 3.5 Mpc to M81 an X-ray luminosity of 1.7×10^{39} erg s^{-1} in the 0.1–2.4 keV band is calculated. The ROSAT position coincides within 5″ to the optical position. H. Tsunemi reported preliminary results for the ASCA team (Tanaka *et al.* 1993). ASCA first detected X-rays from SN 1993J on April 7 in the energy range 0.5–10 keV. Observations were repeated several times until May 18 when they had to be halted due to the solar angle constraint. The maximum luminosity is about 5×10^{39} erg s^{-1}. The X-ray intensity decayed monotonically with an e-folding time about 50–70 days. A linear fit to the SN 1993J flux within the first month shows a decrease of about 30% in 10 days, inconsistent with a constant count rate at a confidence level of more than 4σ (Zimmermann *et al.* 1993c). It is also clear that the supernova flux did not undergo larger changes over the time scale of one month. The hydrogen column density of 5×10^{20} cm^{-2} does not require large amounts of intrinsic absorption above the Galactic value of 4.3×10^{20} cm^{-2} in the direction to M81. This is consistent with the assumption that the strong radiation from the supernova effectively ionized the circumstellar medium in front of the emission region.

Theories for the early X-ray emission must account for the high temperatures in the emission region, a very low intrinsic absorption, the fact that X-rays were detected very early after the explosion when radio emission was just starting to rise, as well as for the relatively constant behavior of the soft X-ray luminosity over a time scale of one month. In many models the early soft X-ray flux is expected to decrease over time scales of a few weeks or months, depending on the density profile of the circumstellar material near to the collapsed object. The present observations do not support these expectations, which were derived using simple assumptions on the mass loss rate and the wind velocities of the red supergiant progenitor.

Lundqvist *et al.* (1993) noted that the observed X-ray spectrum is hard ($kT_X > 10$ keV) and flat, and there is only little material absorbing the X-rays. A lower column density of the gas absorbing the X-rays means that the circumstellar medium should either have a low density or should be nearly fully ionized. In addition, the flux in the observed band decays slowly, roughly as $t^{-0.3}$. The X-rays are likely to be produced behind the reverse shock going into the supernova ejecta. The expected spectrum is very different depending on whether or not the shock is radiative. It is flat if the shock is

adiabatic, but if radiative, the radiation is expected to be blocked out almost entirely by a cool shell next to the contact discontinuity between the shocked ejecta and the shocked circumstellar gas (e.g., Chevalier and Fransson 1994). Because of the low column density of absorbing matter, the shock is therefore most likely adiabatic. Assuming a free-free spectrum, the X-ray luminosity *per energy unit* in the observed band is expected to decay roughly as $t^{-(n-4)/(n-2)}$, where n is a power-law index describing the density structure of the not yet reverse-shocked ejecta, $\rho \propto r^{-n}$. The decay rate may be different if electrons and ions are not in full energy equipartition. From the facts that $kT_X > 10$ keV and that the ratio of the cooling time scale to the dynamical time scale increases with decreasing n, Lundqvist *et al.* find that $n < 10$. Best fits to the luminosity in the ROSAT and ASCA bands indicate $n \approx 7$ and a mass loss rate of $\dot{M} \approx (2\text{–}3)\times 10^{-5}$ $(w/10$ km s$^{-1})$ $M_\odot$ yr^{-1}.

It is not entirely ruled out that the X-rays may come from the forward shock moving into the circumstellar medium, though Lundqvist *et al.* (1993) find it less likely. In early phases, this radiation is dominated by inverse Compton scattering of the photospheric radiation field (e.g., Fransson 1984; Lundqvist and Fransson 1988), and the time when the shock turns adiabatic depends strongly on whether electrons and ions are in full equipartition. For typical parameters one obtains an order of magnitude lower temperature of the electrons (T_e) compared to the ions (T_i) if the electrons are heated only by Coulomb collisions. The Compton scattering creates a high-energy power-law tail to the photospheric spectrum. The power-law index is ~ 1 if $T_e = T_i$, and > 2 if $T_e < T_i$. Because the observed spectrum was flat, the Compton tail is unlikely to have been seen. This may favor a non-equipartition situation.

Suzuki *et al.* (1993) use the hardness ratio $A/R = L_A/L_R$ between the ASCA 1–10 keV luminosity (L_A) and the ROSAT 0.1–2.4 keV luminosity (L_R) to compare models and the observations. Around the dates of the ASCA and ROSAT observations, $L_A \approx 5 \times 10^{39}$ erg s^{-1} and $L_R \approx 1.6 \times 10^{39}$ erg s^{-1}, so that $A/R \approx 3$. Suzuki *et al.* modeled the collisions between the supernova ejecta and the circumstellar matter with a series of models with two parameters, the expansion velocity at the outer edge of the ejecta and the power law index in the density distribution $-n = d\ln\rho/d\ln r$ in the outermost layers. The initial density distribution of the circumstellar matter is assumed to be $n = 1 \times 10^9 (r/1 \times 10^{14}$ cm$)^{-2}$ amu cm^{-3}. This density distribution is required to reproduce the observed X-ray luminosities, hardness, and relatively slow decline rate. It is higher than that of Van Dyk *et al.* (1993b), but consistent with that of Lundqvist *et al.* (1993).

To reproduce the observed hardness of the X-ray emission, the expansion velocity at the outer edge of the ejecta at the beginning of the collision must be as high as $\sim 5 \times 10^4$ km s^{-1}. This can be consistent with models of low envelope mass (Nomoto *et al.* 1993). In addition, the temperature in the shocked ejecta should be as high as $(2 - 3) \times 10^8$ K for a fairly long time. This suggests that the ejecta have a relatively shallow density gradient (n $\approx$ 8). As shown in Figure 17, Suzuki *et al.* (1993) predict the decline of the X-ray luminosity, softening of the spectra, and growing line features which should be fairly broad due to rapid expansion of the shocked ejecta. Shigeyama *et al.* (1994) predict that the hard X-rays from a pulsar can be observed with ASCA in about three years if the pulsar luminosity is as high as that of the Crab Nebula.

16. Gamma Rays

With an optimal model for hard emission, Woosley *et al.* (1994) predict a flux of $\lesssim 2 \times 10^{-5} (2.5$ Mpc$/D)^2$ photons cm^{-2} s^{-1} in the 847 keV line of ^{56}Co at peak during

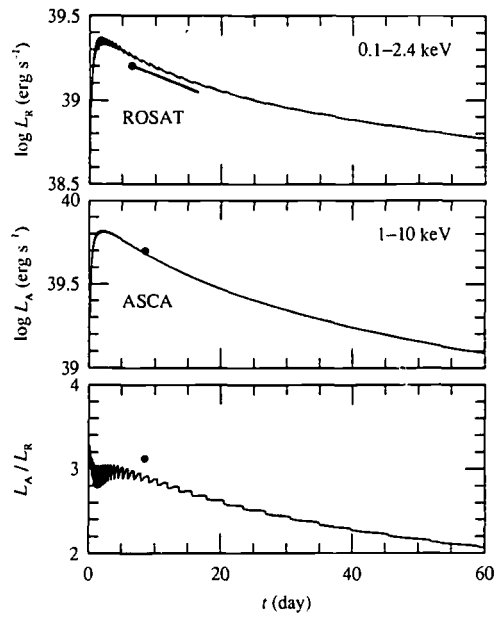

FIGURE 17. ROSAT and ASCA X-ray observations shown in comparison with models of Suzuki *et al.* (1993).

August 1993, and a Comptonized continuum which peaks at a few $\times 10^{-4}$ photons s^{-1} cm^{-2} MeV^{-1} at 40 keV a few months after the explosion. Nomoto *et al.* (1993) and Shigeyama *et al.* (1994) note that if substantial mixing of ^{56}Ni occurred and the mass of ^{56}Ni is as large as ~ 0.15 M$_\odot$, the γ-ray lines (and hard X-rays) from SN 1993J may be marginally observed with CGRO at maximum around day 130. The distance is actually closer to 3.5 Mpc, most models suggest a nickel mass of < 0.1 M$_\odot$, and constraints from the spectral modeling of the helium lines suggest that outward mixing of the nickel is small, so these predictions must be regarded as optimistic.

SN 1993J was observed with OSSE on CGRO during three different intervals, approximately 9–15, 23–36, and 93–121 days after outburst (Chipman 1993). There may be continuum emission below 200 keV in the intervals prior to and near the second optical peak with intensities at 100 keV of $(1.82 \pm 0.39) \times 10^{-3}$ photons cm^{-2} s^{-1} MeV^{-1} and $(0.89 \pm 0.35) \times 10^{-3}$ photons cm^{-2} s^{-1} MeV^{-1}, and photon indices of -2.3 ± 0.5 and -2.2 ± 0.9, respectively. Although this emission cannot be unambiguously attributed to SN 1993J (because of the large OSSE field of view), it is worth noting that OSSE did not observe flux at this level in observations 597 and 443 days prior to SN 1993J. A power law of fixed photon index -1.2 approximately extrapolates from the first OSSE observation to the total luminosity in the range 1–10 keV measured by ASCA one day earlier (Tanaka *et al.* 1993). The flux at 200 keV is probably too bright to be entirely due to Comptonized γ-rays from radioactive ^{56}Ni and ^{56}Co. There was no evidence for line emission in any observation and no evidence for emission of any kind in the longer, more sensitive, third observation when γ-ray lines were most likely to be detectable. Preliminary measured fluxes of the 847 keV and 1238 keV lines are $(1.6 \pm 2.1) \times 10^{-5}$ photons cm^{-2} s^{-1} and $(0.7 \pm 1.9) \times 10^{-5}$ photons cm^{-2} s^{-1}, respectively.

Höflich *et al.* (1993b) noted that the high mass models tended to predict less γ-ray

flux than the lower mass models, but since even very optimistic low mass models did not predict a flux above the 1σ limits reached by CGRO, the mass cannot be constrained by this non-detection.

17. Distance Estimates

A number of recent distance estimates to M81 by different methods including the planetary nebula luminosity function (Jacoby *et al.* 1989) and the surface brightness fluctuations (Tonry 1991) give a distance $D = 3.47 \pm 0.17$ Mpc and distance modulus DM $= 27.7 \pm 0.1$ mag (de Vaucouleurs 1993). A new determination of Cepheid distances with the Hubble Space Telescope gives DM $= 27.8 \pm 0.2$ mag corresponding to $D = 3.63 \pm 0.34$ Mpc (Freedman *et al.* 1994). There are also a variety of ways to use SN 1993J to estimate the distance.

From simultaneous least squares fits to the optical continua, Wheeler *et al.* (1993) determine T = 14,900 ± 1000 K on March 31.18 and T= 11,800 ± 700 K on April 1.14. Adding several other high quality spectra does not seem to change these estimates appreciably. In the black body limit, assuming no significant change in photospheric velocity between March 31 and April 1, Wheeler *et al.* find $D = 4.2 \pm 0.6$ Mpc ($v/10^4$ km s^{-1}), or DM $= 28.1 \pm 0.4$ mag for $v = 10^4$ km s^{-1}. The velocities are not well determined from the weak lines at such an early epoch, but are about that value or perhaps 10% higher. Effects of scattering and geometrical extension may decrease this estimate, although it seems fairly independent of the assumed reddening. The empirical basis for the continuum temperatures appears fairly well established, but the geometry is not well known. If the effective density distribution is very steep because of interaction with the circumstellar matter, then geometrical and scattering effects could be very small.

De Vaucouleurs (1993) has used $U-B$ and $B-V$ colors during the first week after shock breakout to determine the reddening and temperature independently. For $E(B-V) =$ 0.15 mag and $E(U-B) = 0.11$ mag (of which two-thirds is Galactic foreground), he derives T = 14,800 for March 31.2 and 11,400 for April 1.2. Combining the temperature as a function of time, and the radius $R = R_0 + v(t - t_0)$ derived from expansion velocities measured at Lick Observatory and at McDonald Observatory, he obtains a mean distance modulus of 27.7 ± 0.1 mag which is nearly independent of initial conditions. The method begins to fail after day 6 when departures from a Planck curve become significant.

Baron *et al.* (1993) obtain photospheric temperatures, velocities, and radii by adjusting the parameters of their atmosphere models to match the observed continua and lines. They get velocities of about 11,000 km s^{-1} on both April 7 and April 13. By comparing synthetic photometry from these models to observations they estimate the distance modulus to be DM $= 28.0 \pm 0.3$ mag ($D = 4.0 \pm 0.5$ Mpc) and an explosion date of 1993 March 27.5 ± 0.5 UT, assuming $E(B-V) = 0.1$ mag. They caution that their distance estimate is dependent on the assumed extinction, the assumption of spherical symmetry, and whatever changes are required to fit the Hα and 5600 Å features.

Schmidt *et al.* (1993) use the black body corrections as a function of color temperature computed from a grid of Type II models, their own *BVI* photometry for April, and velocities from spectra to estimate distances. They employ the weak metal lines such as Fe II λ5169 and λ5018 to estimate the velocity of the photosphere and find that it dropped from 7900 km s^{-1} on 15.1 April, just before the second peak, to 6600 km s^{-1} on 24.1 April, about a week after the peak, to 5400 km s^{-1} on 17.5 May, about day 50 when the light curve is on the tail. They use these data to determine a distance of 2.6 ± 0.4 Mpc and the time of explosion to be March 26 ± 3. They note that the models adopted

to estimate the black body correction may not apply to events like SN 1993J which have lost a great deal of mass, are colliding with the lost mass, and are asymmetric.

The discrepancy between Baron *et al.* (1993) and Schmidt *et al.* (1993) seems to arise primarily from the different photospheric velocities that they deduce, 11,000 km s^{-1} on April 13 for Baron *et al.* and 7900 km s^{-1} on April 15 for Schmidt *et al.* (Schmidt 1993). Other things being equal, a slower photosphere will give a proportionately smaller distance, and the two distance estimates seem to differ by about the ratio of these velocities. Resolution of this discrepancy should give more insight into the nature of the atmosphere of SN 1993J.

18. Discussion

While its nearby location and relative brightness ensured that it would be very well studied, SN 1993J continues the tradition of SN 1987A by being peculiar and very much worthy of study in its own right.

The light curve and spectral modeling done by the time of the Xian conference point rather strongly to a picture in which a star of initial mass $\sim 15\ M_\odot$ transferred most of its hydrogen envelope to a companion, then exploded by core collapse to form a neutron star. The supernova has only 2–3 $M_\odot$ of ejecta, including a small amount of helium enriched, hydrogen envelope and ~ 0.05–$0.1\ M_\odot$ of ^{56}Ni. This picture is suggested by the following:

- The pre-discovery photometry that is consistent with an early K supergiant progenitor which is, in turn, consistent with extensive mass loss to a binary companion that is shut off when the envelope shrinks in mass to expose helium-rich layers.
- The initial peak about two days after shock outbreak that is reproduced by models with low mass envelopes of low H abundance and initial radii of several hundred solar radii.
- The reproduction of the rise of the bolometric flux from the first minimum to a second maximum in about two weeks and then the subsequent decline onto a tail.
- The radio, UV, and X-ray observations that show the interaction with a dense circumstellar medium that is probably not distributed like a simple steady-state wind.
- Atmosphere models that reproduce the epoch and spectral characteristics of the onset of strong He I lines.

A number of areas need more work to confirm or deny this general model. It is not clear that the progenitor has been properly identified. There are at least two stars within the 17 parsec seeing disk around the supernova, but it is not certain that either is the progenitor. Photometry of the progenitor may not be resolved until the supernova fades. The current photometry can certainly set a color and model dependent upper limit to the mass of the progenitor. A single very massive progenitor ($M \gtrsim 20\ M_\odot$) is unlikely because the measured luminosity of the composite of stars at the position of SN 1993J is too low. The progenitor evolution requires more study. The mass transfer from the red supergiant progenitor is expected to occur on dynamical time scales until the mass ratio is reversed. This causes the companion to expand and leads to a common envelope. There have been no calculations of the response of the mass receiving companion to such a rapid mass accretion. Many of the low mass models that reproduce the initial peak reasonably well have not included any luminosity from the interaction with the circumstellar nebula, nor any effects of the non-homologous expansion that will be induced. None of the light curve models have addressed the effects of ionization from the X-rays produced by the interaction with the circumstellar matter. None of the models have yet been able to reproduce the color evolution properly.

The high mass models presented so far do a better job than most low mass models in

reproducing the color evolution, but require an excessive reddening and do not seem to be in accord with the observed spectral evolution. The high and low mass models can be tested by continued comparison to the light curve and spectral evolution. The high mass models predict a different evolution of the photosphere and so will predict different general properties for the evolution of the helium lines, the onset and nature of the nebular spectrum, and the evolution of the spectropolarimetry. Similar arguments can be made about the degree of mixing of the nickel outward, mixing within the core, and mixing of the core with the envelope. Hydrodynamic models give an *a priori* expectation of mixing, but excessive mixing of nickel outward and hydrogen inward seem discouraged by the spectral constraints, especially the epoch of onset of the strong He I lines. The spectral models can only constrain microscopic mixing of H and He, and so macroscopic mixing of "blobs" may be consistent with the observations. The constraints on the mixing of nickel are more general because of the diffuse effect of the associated gamma rays. It is important to note that the spectrophotometry can constrain the amount and degree of mixing of the nickel even though nickel and its decay products are not observed directly in the spectrum.

Much remains to be done to understand the nature of the circumstellar medium. Given the evidence that the density profile does not simply scale as $\rho \propto r^{-2}$, the surrounding nebula is not simply the product of a spherical steady-state wind. It may thus be very deceptive to speak of an associated "mass loss rate" in the sense that the loss rate is derived by making the steady state assumption. Given the likelihood of binary interaction, we are probably looking at some complex combination of flows and common envelope. While it may be true that stars with initial mass ~ 15 $M_\odot$ are unlikely to drive a wind with the density implied by the radio, UV, and X-ray observations, it is not clear that one must rely on a simple wind to provide the density.

Much more work must be done on the early light curve and spectral modeling to incorporate the effects of the collision with the circumstellar matter. Outward and reverse shocks and the hard radiation from them will affect the density and temperature distribution of the outer ejecta. The evolution near the first peak and even later is unlikely to be homologous. The models with envelopes of $\lesssim 0.2$ $M_\odot$ become homologous in a day or so, but increasing the mass of the envelope or including the circumstellar matter will serve to delay the approach to homologous expansion. The spectra on the first decline are a particular challenge. The features have very small amplitude even though the temperatures are moderately low and simple models predict stronger lines. The expected low H abundance may play a role and the hydrogen may be excessively ionized by the shock-produced X-rays. The X-rays must not, however, heat the photosphere excessively since the observations show $T \lesssim 15{,}000$ K on the first peak.

The H lines and other features begin to get distinct shortly before the first minimum. This will set important constraints on the distribution of the density and composition, including the nickel. The latter affects the location of the photosphere and hence the column depth contributing to the strength of the lines.

SN 1993J has been reasonably well studied in the optical, but it is not clear that coverage in the IR has been adequate. Further IR observations are encouraged to follow the evolution of the H and He lines, to look for evidence of dust and molecule formation, and perhaps even to detect the IR lines of radioactive Co.

The spectropolarimetry has already given exciting clues to the nature of the explosion. Something about the supernova is asymmetric. This will constrain the models, but more spectropolarimetry would be exceedingly valuable. The spectrum should be examined for clues as to whether it is the core or the outer envelope that is distorted.

Clearly the game of searching for and constraining the nature of any compact object

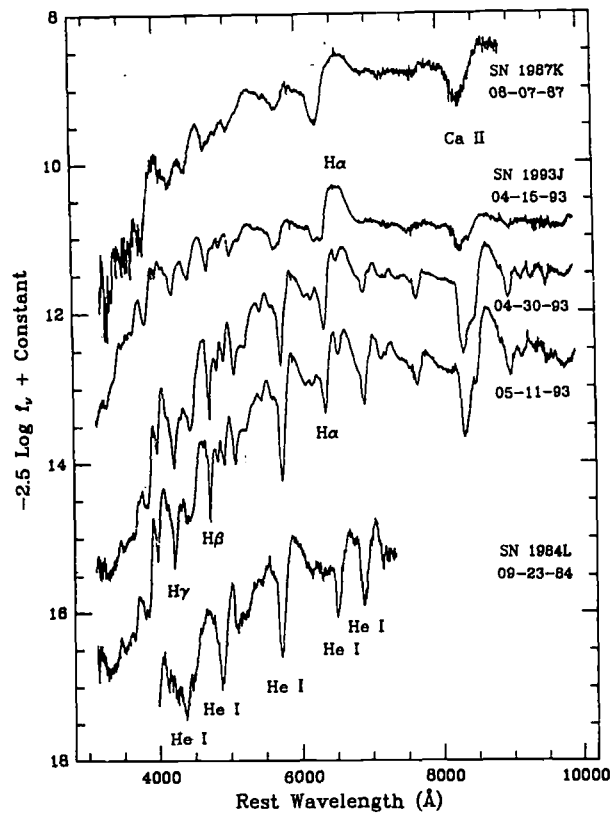

FIGURE 18. Spectra of SN 1993J in comparison with SN 1987K and SN Ib 1984L (Filippenko *et al.* 1993a).

in SN 1993J must be played out. The second peak of SN 1993J is similar in width to that of Type Ia, Ib, and Ic supernovae. SN 1993J is predicted to decline more slowly on the tail than models with comparable mass but no extended envelopes because the core/envelope interaction slows the expansion of the core and traps the γ-rays longer; however, the light curve is flatter on the tail than most of the models predict. Whether this is just the result of dynamics or radiative transfer, or requires an additional source of power, is not clear.

SN 1993J is destined to provide considerably more physical insight into the taxonomy of supernovae. Figure 18 gives a sample of Lick spectra compared to the related events SN 1987K and SN 1984L. SN 1987K made a critical transition from a hydrogen-rich spectrum near maximum to a hydrogen-poor spectrum in the nebular phase. SN 1993J shows that this was not a unique event. There are significant differences in the details of the spectral profiles, but it is clear that SN 1993J and SN 1987K are very closely related. Careful inspection of the spectra of SN 1987K published by Filippenko (1988) reveals, in hindsight, the first hints of the onset of the He I lines that occurred so markedly in SN 1993J. Note in Figure 18 that the He I lines in SN 1993J are very similar to those in the well-studied SN Ib 1984L. Arguments by analogy with other supernovae and based on quantitative spectral modeling predict that the H and He lines should fade in the optical

at about 100 days and that the spectrum should be dominated by strong emission lines of [O I], [Ca II], and Ca II by 200 days.

SN 1993J strengthens the hypothesis that Type Ib and Ic supernovae are triggered by core collapse in massive, evolved stars that have lost their outer envelope of hydrogen (Ib) and perhaps helium as well (Ic), often, but perhaps not always, through mass transfer in close binary systems. These objects are fundamentally related to Type II supernovae. Further study of SN 1993J should provide more insight into the evolutionary processes that lead to the various observed endpoints.

19. Acknowledgments

The contents of this review draw heavily on the plagiarized original contributions and draft submissions of the individuals and groups that presented results at the meeting. We are grateful for their contributions and hope that this summary does their work justice.

We would also like to acknowledge the special contribution made by the astronomers associated with the Isaac Newton group of telescopes that will greatly aid the general accessibility of data on supernovae. The supernova data obtained on La Palma are being reduced at the Royal Greenwich Observatory, and then placed on disk for rapid access by the community over the Internet. Descriptions of how the data have been reduced reside within the same disk areas as the data and, where appropriate, include details of the compromises that have been made. The reduced data are available via Internet using anonymous ftp at the address ftp.ast.cam.ac.uk. Any authors making use of the archive data in a publication should acknowledge the Isaac Newton Group of telescopes. The contact astronomer on La Palma for SN 1993J observations is Nic Walton (e-mail: naw"at"ing.iac.es).

The research of JCW is supported in part by NSF grant AST–9218035, NASA grants NAGW 2905 and GO 2563, and a grant from the R. A. Welch Foundation. AVF is supported by NSF grants AST–8957063 and 9115174, and by NSF Cooperative Agreement AST–8809616 (Center for Particle Astrophysics). We are grateful for the able help of Betty Friedrich in producing the TEX document.

REFERENCES

Aldering, G.S., Humphreys, R.M., Richmond, M.W. (1993). *AJ*, **107**, 662.

Andrillat, Y. (1993). *IAU Circ.* 5736.

Baron, E. (1993). Private communication.

Baron, E., Hauschildt, P.H., Branch, D., Wagner, R.M., Austin, S.J., Filippenko, A.V., Matheson, T. (1993). *ApJ*, **416**, L21.

Benetti, S., Contarini, G., Gratton, R., Turatto, M. (1993). *IAU Circ.* 5751.

Bjorkman, K., Nordsieck, K. (1993). Private communication.

Blakeslee, J., Tonry, J. (1993). *IAU Circ.* 5758.

Blöcker, T., Schönberner, D. (1991). *A&A*, **244**, L43.

Brown, J.C., McLean, I.S. (1977). *A&A*, **57**, 141.

Chevalier, R.A. (1982). *ApJ*, **259**, 302.

Chevalier, R.A. (1992). *ApJ*, **394**, 599.

Chevalier, R.A., Fransson, C. (1994). *ApJ*, **420**, 268.

Chipman, E. (1993). *Compton Obs. Science Report* #132, August 12.

de Vaucouleurs, G. (1993, *The Astronomer*, **29**, 278

de Vaucouleurs, G., Corwin, H.G., Jr., Skiff, B.A. (1994). *PASP*, **106**, 156

de Vaucouleurs, G. de Vaucouleurs, A., Corwin, H.G., Jr., Buta, R.J., Paturel, G., Fouqué, P. (1991). *Third Reference Catalogue of Bright Galaxies* (New York: Springer-Verlag).

Eastman, R.G. (1993). Private communication.

Filippenko, A.V. (1988). *AJ*, **96**, 1941.

Filippenko, A.V. (1993a). *IAU Circ.* 5737.

Filippenko, A.V. (1993b). Private communication.

Filippenko, A.V., Matheson, T. (1993a). *IAU Circ.* 5740.

Filippenko, A.V., Matheson, T. (1993b). *IAU Circ.* 5787.

Filippenko, A.V., Matheson, T., Ho, L.C. (1993a). *ApJ*, **415**, L103.

Filippenko, A.V., Matheson, T., Richmond, M.W., Treffers, R.R., Leibundgut, B., Paik, Y. (1993b). Workshop contribution.

Fox, G. K. (1991). *ApJ*, **379**, 663.

Fransson, C. (1984). *AA*, **133**, 264.

Freedman, W.L., *et al.* (1994). *ApJ*, **427**, 628.

Hashimoto, M., Iwamoto, K., Nomoto, K. (1993). *ApJ*, **414**, L105.

Hauschildt, P.H. (1992a). *JQSRT*, **47**, 433.

Hauschildt, P.H. (1992b). *ApJ*, **398**, 224.

Hauschildt, P.H. (1993). *JQSRT*, **50**, 301.

Hauschildt, P.H., Baron, E. (1993). In preparation.

Höflich, P., Müller, E., Khokhlov, A. (1993a). *A&A*, **268**, 570.

Höflich, P., Langer, N., Duschinger, M. (1993b). *A&A*, **275**, L29.

Hu, J.Y., Li, Z.W., Jiang, X.J., Wang, L.F. (1993). *IAU Circ.* 5777.

Humphreys, R.M., Aldering, G.S., Bryja, C.O., Thurmes, P.M. (1993). *IAU Circ.* 5739.

Iglesias, C.A., Rogers, F.J., Wilson, B.G. (1992). *ApJ*, **397**, 717.

Jacoby, G.H., Ciardullo, R., Ford, H.C., Booth, J. (1989). *ApJ*, **344**, 704.

Jannuzi, B., Schmidt, G., Elston, R., Smith, P. (1993). *IAU Circ.* 5776.

Jeffery, D., Branch, D. (1990). In *Supernovae*, ed. J.C. Wheeler, T. Piran, S. Weinberg (Singapore: World Scientific), p. 149.

Jeffery, D., *et al.* (1994). *ApJ*, **421**, L27.

Khokhlov, A. (1993). Private communication.

Kurucz, R.L. (1991). In *Stellar Atmospheres: Beyond Classical Models*, ed. L. Crivellari, I. Hubeny, D.G. Hummer (Dordrecht: Kluwer), p. 440.

Langer, N. (1991). *A&A*, **252**, 669.

Liebert, J. (1993). Private communication.

Lewis, J., *et al.* (1993). Workshop contribution.

Lundqvist, P., Fransson, C., Chevalier, R.A. (1993). Workshop contribution.

Lundqvist, P., Fransson, C. (1988). *A&A*, **192**, 221.

Meikle, P., *et al.* (1993). *Gemini*, **40**, 1.

Miller, J.S. (1993). Private communication.

Morrison, L.V., Argyle, R.W., Helmer, L. (1993). *IAU Circ.* 5767.

Nieuwenhuijzen H., de Jager, C. (1990). *A&A*, **231**, 134.

Nomoto, K., Susuki, T., Shigeyama, T., Kumagai, S., Yamaoka, H., Saio, H. (1993). *Nature*, **364**, 507.

Ostriker, J.P. (1987). *Nature*, **327**, 287.

Perelmuter, J.M. (1993). *IAU Circ.* 5736.

Podsiadlowski, Ph., Joss, P.C., Hsu, J.J.L. (1992). *ApJ*, **391**, 246.

Podsiadlowski, Ph., Hsu, J.J.L., Joss, P.C., Ross, R.R. (1993). *Nature*, **364**, 509.

Pooley, G.G., Green, D.A. (1993). *MNRAS*, **264**, L17.

Prugniel, P. (1993). *IAU Circ.* 5742.

Rathnasree, N., Ray, A. (1992). *JA&A*, **13**, 3.

Ray, A., Singh, K.P., Sutaria, F.K. (1993). *JA&A*, **14**, 53.

Richmond, M.W. (1993). *IAU Circ.* 5739.

Richmond, M.W., Treffers, R.R., Filippenko, A.V., Paik, Y., Leibundgut, B., Schulman, E., Cox, C.V. (1994). *AJ*, **107**, 1022.

Ripero, J. (1993). *IAU Circ.* 5731.

Rots, A.H., Shane, W.W. (1975). *A&A*, **45**, 25.

Rybicki, G.B., Hummer, D.G. (1991). *A&A*, **245**, 171.

Salzer, J., Herbst, W., Vinton, G. (1993). *IAU Circ.* 5741.

Schmidt, B.P. (1993). Private communication.

Schmidt, B.P., *et al.* (1993). *Nature*, **364**, 600.

Shapiro, P.R., Sutherland, P.G. (1982). *ApJ*, **263**, 902.

Shigeyama, T., Nomoto, K., Tsujimoto, T., Hashimoto, M. (1990). *A&A*, **361**, L23.

Shigeyama, T., Suzuki, T., Kumagai, S., Nomoto, K., Saio, H., Yamaoka, H. (1994). *ApJ*, **420**, 341.

Smith, P. (1993). *IAU Circ.* 5776.

Smith, V.V., Tomkin, J. (1993). Private communication.

Sonneborn, G., Rodriguez, P.M., Wamsteker, W., Fransson, C., Kirshner, R.P. (1993). *IAU Circ.* 5754.

Steinmetz, M., Höflich, P. (1992). *A&A*, **257**, 641.

Suntzeff, N.B., *et al.* (1988). *AJ*, **96**, 1864.

Suzuki, T., Kumagai, S., Shigeyama, T., Nomoto, K., Yamaoka, H., Saio, H. (1994). *ApJ*, **419**, L73.

Swartz, D.A., Filippenko, A.V., Nomoto, K., Wheeler, J.C. (1993a). *ApJ*, **411**, 313.

Swartz, D.A., Clocchiatti, A., Benjamin, R., Lester, D.F., Wheeler, J.C. (1993b,). *Nature*, **365**, 232.

Tanaka, Y., *et al.* (1993). *IAU Circ.* 5753.

Taniguchi, Y., *et al.* (1993). *PASJ Lett.*, **45**, L43.

Tomaney, A., Crotts, A. (1993). *IAU Circ.* 5771.

Tonry, J.L. (1991). *ApJ*, **373**, L1.

Trammell, S.R., Dinerstein, H.L., Goodrich, R.W. (1993). *ApJ*, **402**, 249.

Trammell, S.R., Hines, D.C. (1993). Private communication.

Trammell, S.R., Hines, D.C., Wheeler, J.C. (1993). *ApJ*, **414**, L21.

Tran, H.D., Filippenko, A.V. (1993). Private communication.

Tuchman, Y., Wheeler, J.C. (1989). *ApJ*, **346**, 417.

Utrobin V. (1993). Workshop contribution.

Van Driel, W., *et al.* (1993). *PASJ Lett.*, **45**, L59.

Van Dyk, S.D., Weiler, K.W., Rupen, M.P., Sramek, R.A., Panagia, N. (1993a). *IAU Circ.* 5759.

Van Dyk, S.D., Weiler K.W., Sramek R.A., Rupen, M.P., Panagia, N. (1993b). Workshop contribution.

Wamsteker W., Rodriguez P.M., Gonzalez R., Sonneborn G., Kirshner, R.P. (1993). *IAU Circ.* 5738.

Weiler, K.W., Panagia, N., Sramek, R.A. (1990). *ApJ*, **364**, 611.

Wells, L.A., *et al.* (1993). Submitted, and workshop contribution.

Wheeler, J.C. (1993). SN computer network communication, June 7.

Wheeler, J.C., *et al.* (1993). *ApJ*, **417**, L71 .

Woosley, S.E. 1991, in *Supernovae*, ed. S.E. Woosley (New York: Springer-Verlag), p. 202.

Woosley, S.E., Eastman, R.G., Weaver, T.A., Pinto, P.A. (1994). *ApJ*, **429**, 300.

Woosley, S.E., Pinto, P.A., Martin, P.G., Weaver, T.A. (1987). *ApJ*, **318**, 664.

Zimmermann, H.-U., *et al.* (1993a). *IAU Circ.* 5748; (1993b). *IAU Circ.* 5750; (1993c). *IAU Circ.* 5766.

A Determination of the Properties of the Peculiar SNIa 1991T through Models of its Early-time Spectra

By PAOLO A. MAZZALI[1] AND I. J. DANZIGER[2]

[1]Osservatorio Astronomico di Trieste, Via G. B. Tiepolo, 11, I-34131 Trieste, Italy

[2]European Southern Observatory, Karl-Schwarzschildstr. 2, D-W-8046 Garching, Germany

A series of early-time optical spectra of the peculiar SNIa 1991T, obtained from 2 weeks before to 4 weeks after maximum, have been computed with our Monte Carlo code.

The earlier spectra can be successfully modelled if ^{56}Ni and its decay products, ^{56}Co and ^{56}Fe, dominate the composition of the outer part of the ejecta. This atypical distribution confirms that the explosion mechanism in SN 1991T was different from a simple deflagration wave, the model usually adopted for SNe Ia.

As the photosphere moves further into the ejecta the Ni Co Fe fraction drops, while intermediate mass elements become more abundant. The spectra obtained 3–4 weeks after maximum look very much like those of the standard SN Ia 1990N. A mixed W7 composition produces good fits to these spectra, although Ca and Si are underabundant. Thus, in the inner parts of the progenitor white dwarf the explosion mechanism must have been similar to the standard deflagration model.

The fits were obtained adopting a reddening $E(B-V) = 0.13$. A Tully-Fisher distance modulus $\mu = 30.65$ to NGC 4527 implies that SN 1991T was about 0.5 mag brighter than SN 1990N. At comparable epochs, the photosphere of SN 1991T was thus hotter than that of SN 1990N. The high temperature, together with the anomalous composition stratification, explains the unusual aspect of the earliest spectra of SN 1991T.

The model results allow us to follow the abundances as a function of mass. In particular, spectroscopic evidence is found that about $0.6M_{\odot}$ of ^{56}Ni must have been synthesized in the outermost $1M_{\odot}$ of the exploding white dwarf. This implies that almost twice as much ^{56}Ni was produced in SN 1991T than in normal SNe Ia, and explains the unusual brightness of this SN.

1. Introduction

SN 1991 T in NGC4527 constitutes a peculiar case among recent, well observed SNe Ia. Although it was classified as a SN Ia from the light curve and the presence of the Si II 6135Åline at maximum (Filippenko et al. 1992), SN 1991T was peculiar in many respects. First, it was brighter ($V(Max) = 11.50$ on 30 Apr, $B(Max) = 11.64$ on 28 Apr; Phillips et al. 1992) than the average Virgo SNe Ia. The spectrum before maximum light was also peculiar, since the typical Si II and Ca II lines were not present. Only two major features appeared in the earliest spectra, identified as Fe III lines (Ruiz-Lapuente et al. 1992). Later, the Si II and Ca II lines, and lines of other intermediate mass elements typical of SNe Ia (S II) also appeared, but they were weaker than in normal SNe Ia. The expansion velocities were also unusually high. A possible explanation is that SN 1991T suffered a delayed detonation, which caused burning to NSE in its outer layers (Yamaoka et al. 1992).

We have gathered a complete set of SN 1991T spectra, obtained from ESO, CTIO and Lick Observatory from -2 weeks to +4 weeks of maximum light and modelled the most interesting ones with our Monte Carlo code (Mazzali & Lucy 1993), in an effort to

determine the evolution of L and v_{ph} and the abundances in the envelope as a function of time, and therefore of radius and mass.

2. Basic model features

We used the code described in Mazzali & Lucy (1993), based on the Schuster-Schwarzschild approximation. The SN envelope is assumed to be in homologous expansion. Excitation and ionization are dealt with in the nebular approximation, but corrections are introduced to account for the line and continuum blocking of the radiation field in the UV.

Since the explosion models devised to explain SN 1991T usually yield density structures quite similar to that of the standard W7 model (Nomoto et al. 1984), we retained a W7 density structure and a Chandrasekhar exploding mass. We adopted a Tully-Fisher distance to NGC 4527 of 13.5 Mpc, i.e. $m - M = 30.65$ (Tully 1988), since a TF distance allowed a good fit to SN 1990N (Mazzali et al. 1993). SN 1991T differs from other Virgo SNe Ia in that its light suffered considerable extinction. We adopted the value $E(B-V) = 0.13$ (Phillips et al. 1992), since the even higher value 0.35 suggested by Ruiz-Lapuente et al. (1991) makes it almost impossible to fit the still quite blue color of SN 1991T. We chose a reference time $t_{Max} = 18$ days.

3. Model fitting

We have modelled 8 optical spectra, covering a period of almost 6 weeks, from 16 April ($t = 6$ d, $t_{Max} - 12$d) to 23 May 1991 ($t = 43$ d, $t_{Max} + 25$d), trying to sample that time interval as evenly as possible. All the spectra have been flux-calibrated in B and V. For some of the spectra the original flux calibration could not be recovered, and two different correction factors had to be adopted for the two bands. Space limitation prohibits a thorough description of the fits, which shall be presented elsewhere (Mazzali & Danziger 1993, in preparation), so here we only give a brief account of our results.

Although we tested several abundance combinations, it turned out that two extremes can be defined, which constitute firm upper and lower boundaries. These are on the one hand a composition based on Ni and its subsequent decay into Co (e-folding time 8.8 days) and hence to Fe (113 days), and, on the other hand, a mixed W7 composition, where Ni decay is also considered, but where Ni and its daughter nuclei represent only a small fraction (about 12% by number at early times).

We found that the abundances that give the best fits to the observed spectra are a combination of these two cases, so that the composition is a mixture of IME (C, O, Si, S, Ca, Na, Al, Mg) in a W7 ratio and of Ni, Co, Fe in amounts determined by the initial Ni fraction and the assumed epoch. The IME fraction is smaller than in W7, while the Ni Co Fe fraction is higher, but this difference tends to decrease with time, implying that the peculiar abundances are confined to the outer layers.

In all successful models the luminosity is higher by about 0.5 mag than in the 'standard' SN Ia 1990N (Mazzali et al. 1993). At the earliest epochs the presence of Fe III lines and the absence of both Si II and Ca II lines is due both to the composition, with Ni, Co and Fe dominating in the outermost layers, and to the high temperature, caused by the high luminosity, which reduces the number of Si II and Ca II ions through ionization. In Fig.1 we show our fit to the 16 Apr ($t = 6$d) spectrum. Near maximum light the IME abundance is higher, and the Si II, Ca II and S II lines begin to appear. The lines observed at this epoch are the same as those in SN 1990N at comparable epochs. In fact, SN 1991T has both a higher luminosity and a higher photospheric velocity than

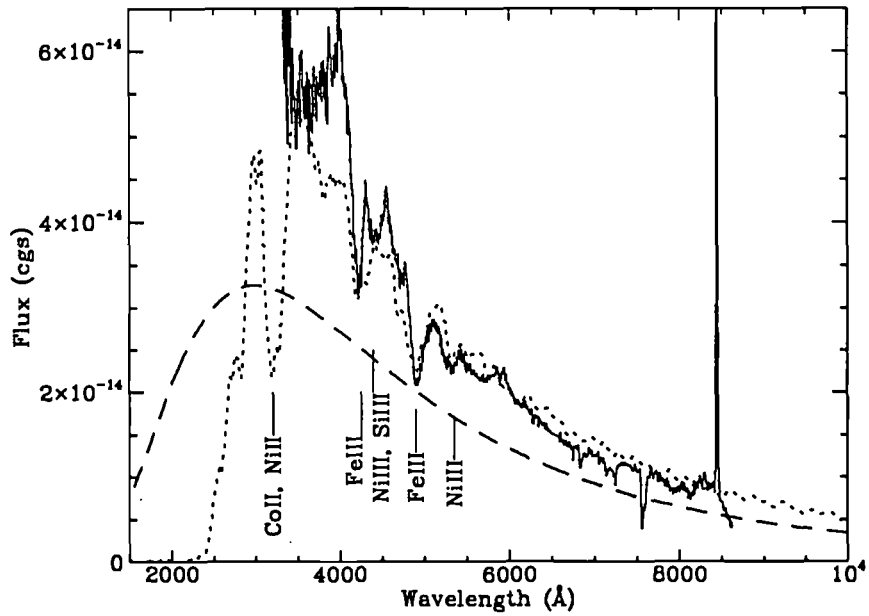

FIGURE 1. The 16 April (t=6 *d*) spectrum (solid line), the best fit (dots) and the photospheric black body (dashed)

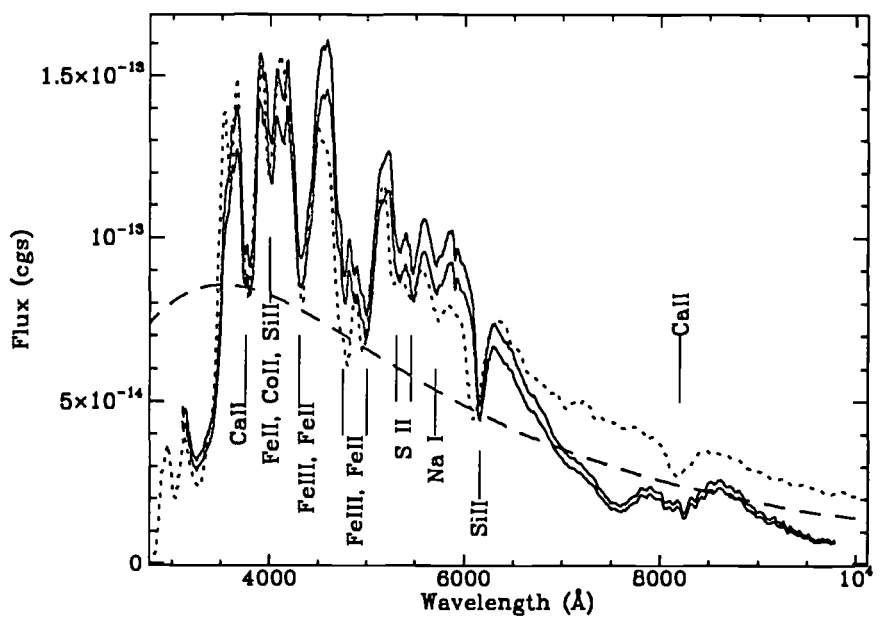

FIGURE 2. The 5 May (t=25 *d*) spectrum: upper solid line – B correction; lower solid line – V correction, the best fit (dots) and the photospheric black body(dashed)

SN 1990N (this is true for all but the very first spectrum we fitted), thus the photospheric temperature is similar in the two SNe, and so are their spectral lines. A higher ejecta velocity in SN 1991T was confirmed also by the nebular lines (Danziger 1993, private communication), and is consistent with the higher explosion energy implied by the higher luminosity and the higher Ni abundance. In Fig. 2 we show the fits for the 5 May (t = 25d) spectrum.

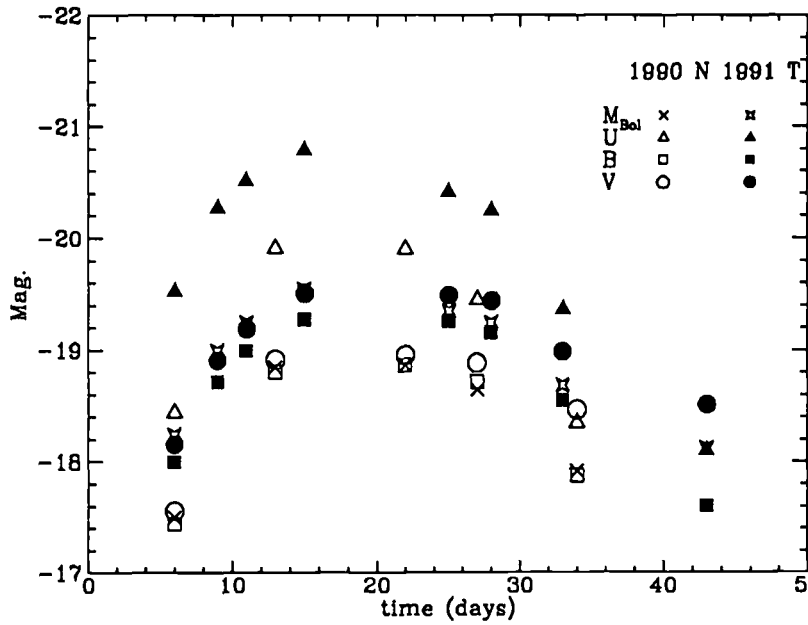

FIGURE 3. Model light curves for SNe 1991T and 1990N

The trend towards an increasing IME abundance continues after maximum, as the photosphere moves deeper into the ejecta. The composition at these epochs is essentially W7, but Si and Ca are underabundant with respect to the other IME, by up to a factor 10 in the innermost shells considered, as already noted by Jeffery et al. (1992). That Si and Ca behave differently from other IME like O and Mg is conceivable, given the nature of the delayed detonation burning. In the post-maximum spectra the Na I D line appears, as it did in SN 1990N, but this is probably a NLTE effect (Mazzali et al. 1993).

4. The global properties of SN 1991T

Fitting a series of spectra of SN 1991T allows us to determine two important properties of this object: the bolometric light curve and the abundance distribution as a function of envelope mass.

The validity of the bolometric light curve obtained from the Monte Carlo model rests on the assumption that our fits are good also in those parts of the spectrum where no data is available, namely the UV and the IR. The value of L_{Bol} obviously also depends on the adopted distance. If this were largely incorrect the model lines would be misplaced in wavelength. An incorrect estimate of the explosion epoch would have a similar effect. In Fig.3 we show the U, B, V and L_{Bol} curves for both SN 1990N and 1991T. The latter is on average 0.5 mag brighter.

The abundance of radioactive Ni in SN 1991T can be determined assuming that the position of the photosphere at each epoch modelled defines a shell in the ejecta, and that the composition adopted to fit the spectrum applies to that shell. The total Ni, Co, Fe abundance in the shell reflects the initial Ni abundance. In this respect modelling a series of spectra is equivalent to analyzing the stratification of the elements synthesized in the explosion. The distribution of Ni in the ejecta as derived from our models is summarized in Table 1. The main conclusion is that in the outermost $1M_{\odot}$ of ejecta about $0.6M_{\odot}$ were ^{56}Ni. We remark that this value was derived from spectroscopy only. If the innermost part of the white dwarf underwent a nuclear deflagration, as suggested

TABLE 1. *Model parameters and radioactive Ni fraction*

t days	v_{ph} km/s	$M_{above}(sh)$ $M_\odot$	$M_{above}(tot)$ $M_\odot$	Ni mass fraction	$M_{Ni}(sh)$ $M_\odot$	$M_{Ni}(tot)$ $M_\odot$
6	17000	0.039	0.039	0.97	0.038	0.038
9	15500	0.090	0.051	0.93	0.047	0.085
11	15000	0.125	0.035	0.89	0.031	0.116
15	13250	0.261	0.136	0.65	0.088	0.204
25	9500	0.558	0.297	0.59	0.175	0.379
28	8500	0.655	0.097	0.57	0.055	0.434
33	6250	0.884	0.229	0.37	0.084	0.518
43	5000	1.034	0.150	0.38	0.057	0.575

by the fact that the composition becomes very similar to W7 there, then most of the innermost $0.4M_\odot$ of the white dwarf must also have been turned into ^{56}Ni (Nomoto et al. 1984).

The total Ni mass produced in the SN 1991T event should thus be close to $1M_\odot$. This agrees with the result obtained by Spyromilio et al. (1992) from fits of the nebular spectrum, and is also in excellent agreement with the high luminosity required to fit the spectra: a Ni mass (and hence L) ratio 1.7 between SN 1991T and SN 1990N implies that the former was brighter by 0.6 mag.

Our models thus confirm that the explosion mechanism at work in SN 1991T was peculiar, making this object brighter than normal SNe Ia. The presence of such deviant events should be considered when using SNe Ia as standard candles. Only a spectroscopic analysis can verify that a SN Ia is 'normal', since an object like SN 1991T differs only marginally from the other SNe Ia as far as the light curve is concerned. The incidence of 'peculiar' SNe Ia may be higher than expected, since several of the recent, well observed SNe Ia (e.g., SN 1986 G, SN 1991bg) are peculiar.

REFERENCES

Filippenko, A. V., Richmond, M. W., Matheson, T., et al., 1992, ApJ, 384, L15
Jeffery, D. J., Leibundgut, B., Kirshner, R. P., et al., 1992, ApJ, 397, 304
Mazzali, P. A. & Lucy, L. B., 1993, A&A, 279, 447
Mazzali, P. A., Lucy, L. B., Danziger, I. J., et al., 1993, A&A, 269, 423
Nomoto, K., Thielemann, F.-K., Yokoi, K., 1984, ApJ, 286, 644
Phillips, M. M., Wells, L. A., Suntzeff, N. B., et al., 1992, AJ, 103, 1632
Ruiz-Lapuente, P., Cappellaro, E., Turatto, M., et al., 1992, ApJ, 387, L33
Spyromilio, J., Meikle, W. P. S., Allen, D. A. & Graham, J. R., 1992, MNRAS, 258, 53P
Tully, R. B., 1988, Nearby Galaxies Catalogue (Cambridge Uni. Press, Cambridge)
Yamaoka, H., Nomoto, K., Shigeyama, T. & Thielemann, F. K., 1992, ApJ, 393, L55

Radio Supernovae

By KURT W. WEILER,[1] SCHUYLER D. VAN DYK,[1] RICHARD A. SRAMEK,[1] AND NINO PANAGIA[1]

[1]Remote Sensing Division, Code 7215, Naval Research Laboratory, Washington, DC 20375-5351, USA

[2]National Radio Astronomy Observatory, P.O. Box O, Soccoro, NM 87801, USA

[3]Space Telescope Science Institute, 3700 San Martin Drive, Baltimore, MD 21218, USA

Radio observations have shown that some supernovae are powerful radio emitters which increase rapidly in brightness to radio luminosities which are hundreds to thousands of times greater than even the brightest known supernova remnant, Cas A. They then fade over a period of weeks, months, or years. This radio emission has been found to provide important information about the nature of the progenitor stars, their mass loss rates, and the circumstellar material surrounding them. RSN observations may also offer the possibility of extragalactic distance measurements and the presence of radio emission appears to be indicator of strong x-ray emission and late time optical emission.

1. Introduction

Detailed studies of radio emission from supernovae have now been carried out for over a decade with SN1979C providing the first example of a radio supernova (RSN) which could be detected and monitored in detail over a lengthy time span. The monitoring of the radio emission from SN1979C is still continuing. Additionally, in the intervening 13 years a number of other SNe have been detected at radio wavelengths and these are listed in Table 1. This list is complete at the present time. However, it is limited to objects which show most or all of the RSN properties which are listed in Section 5, and in practice includes only "young" SNe occurring since the first radio detection of an SN, SN1970G, by Gottesman et al. (1972). This restricts our discussion to a relatively well defined group of objects which can be systematically discussed and classified. The so-called intermediate age RSNe - SN1961V (Branch & Cowan 1985, Cowan, Henry, & Branch 1988), SN1950B (Cowan & Branch 1985), and SN1957D (Cowan & Branch 1985) are discussed separately in Section 4 and the compact radio emitters in M82 (Kronberg & Sramek 1985) are not discussed because of their unusual and poorly understood nature. The two brightest SNe of the past decade, SN1987A and SN1993J, are discussed only in a very limited fashion since SN1987A was a very unusual and atypical SN in all wavelength bands and SN1993J is discussed elsewhere in this volume (Van Dyk et al. 1993). We provide only an overview here; for more detailed information consult the references listed in Table 1. Weiler et al. (1986), Weiler & Sramek (1988), and Sramek & Weiler (1990) also provide an overview of the subject.

2. Type I Radio Supernovae

2.1. *Type Ia Supernovae*

No Type Ia SN has ever been observed to be a RSN, even in cases with quite early observations (SN1981B and SN1980N; Weiler et al. 1986) or a very small distance (SN1972E; (Cowan & Branch 1982, Branch & Cowan 1985, Weiler et al. 1989). This implies that Type Ia are in systems which contain very little circumstellar material at the time of the

TABLE 1. Known RSNe

SN	Optical Type	Refs.
1983N	Ib	1,2
1984L	Ib	2,3
1990B	Ic	4
1970G	II	2
1978K	II	5
1979C	II	2,6,7,8,9
Mkn 297A	II	10,11
1980K	II	2,12
1981K	II	2,13
1986J	II	14
1987A	II	15,16,17
1988Z	II	18
1993J	II	19

explosion. For example, the upper limit to the mass loss rate for SN1981B is less than one third of that measured for Type Ib supernovae SN1983N and SN1984L (see Weiler et al. 1986 and references therein). This represents a major difference between the two Type I SN subclasses and confirms the suggestion that they originate from systems of very different masses.

2.2. *Type Ib/c Supernovae*

2.2.1. *SN1983N*

When the Type Ib supernova SN1983N was discovered in NGC5236 (M83) in the optical, radio observations were started immediately and, due to good fortune in obtaining very early measurements, SN1983N was detected at 6 cm already 11 days before optical maximum. The radio emission evolved extremely rapidly (Sramek, Panagia, & Weiler 1984) and, while the Type II supernovae SN1979C and SN1980K have remained detectable in the radio for many years, in less than one year SN1983N could no longer be detected to the sensitivity limit of the VLA. In addition to the very rapid rise and decline of its radio emission, SN1983N also showed an optically thin spectral index which was significantly steeper ($\alpha \sim -1$) than that found for SN1979C and SN1980K. The radio light curves for SN1983N, which are typical for Type Ib supernovae, are shown in Figure 1.

2.2.2. *SN1984L*

A second Type Ib supernova, SN1984L, has been detected with the VLA and, to the limit of the somewhat sparse data set available, appears to behave in a fashion very similar to SN1983N. The steeper spectral index and rapid rate of decline of the centimeter flux density after maximum are both apparent, again demonstrating that Type Ib SNe are a class which is distinct in its radio properties from either the Type II or the Type Ia supernovae. The results for SN1984L are discussed in more detail in Panagia, Sramek, & Weiler (1986) and Weiler et al. (1986).

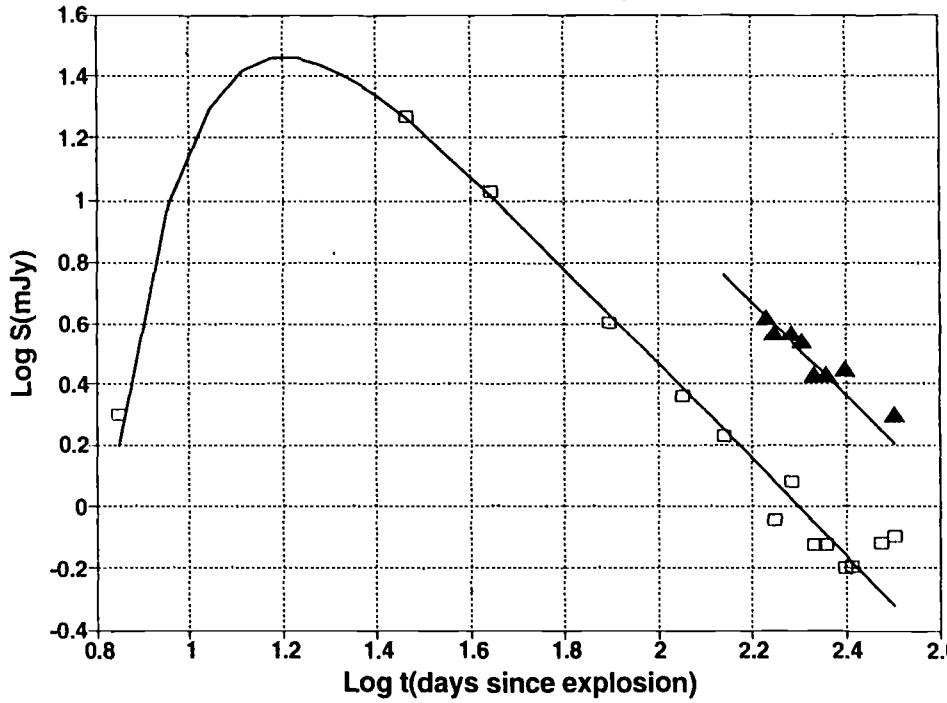

FIGURE 1. Radio light curves at 6 cm (squares) and 20 cm (triangles) wavelength for the Type Ib supernova SN1983N in NGC5236 (M83) (From Weiler et al. 1986).

2.2.3. *SN1990B*

Recently, the Type Ic supernova SN1990B has been detected in the radio. Although weak and distant, its radio light curves and parameters agree well with the values previously found for SN1983N and SN1984L. It is described in detail by Van Dyk et al. (1993a).

3. Type II Radio Supernovae

3.1. *SN1970G*

SN1970G was first detected in the radio by Gottesman et al. (1972) followed by more extended study by Allen et al. (1976). The available early radio data have been discussed by Weiler et al. (1986). More recently, the supernova has been recovered in the radio by Cowan, Goss, & Sramek (1991). Although the data is very poor, the general behavior of the radio emission from SN1970G resembles that from the better studied "normal" Type II RSNe such as SN1979C and SN1980K.

3.2. *SN1978K*

SN1978K has only recently been discovered at radio wavelengths by Ryder et al. (1993). Although the available radio data are still quite sparse, the RSN appears to behave in both its temporal and spectral characteristics like a Type II supernova. In particular, its optical, x-ray, and radio properties all indicate that it is probably an example of a "peculiar" Type II RSN like SN1986J and SN1988Z. Although much of the important turn-on phase of the radio emission has been missed, making it difficult to determine model parameters, future observations will certainly allow rough estimates of the properties of the presupernova stellar system to be made.

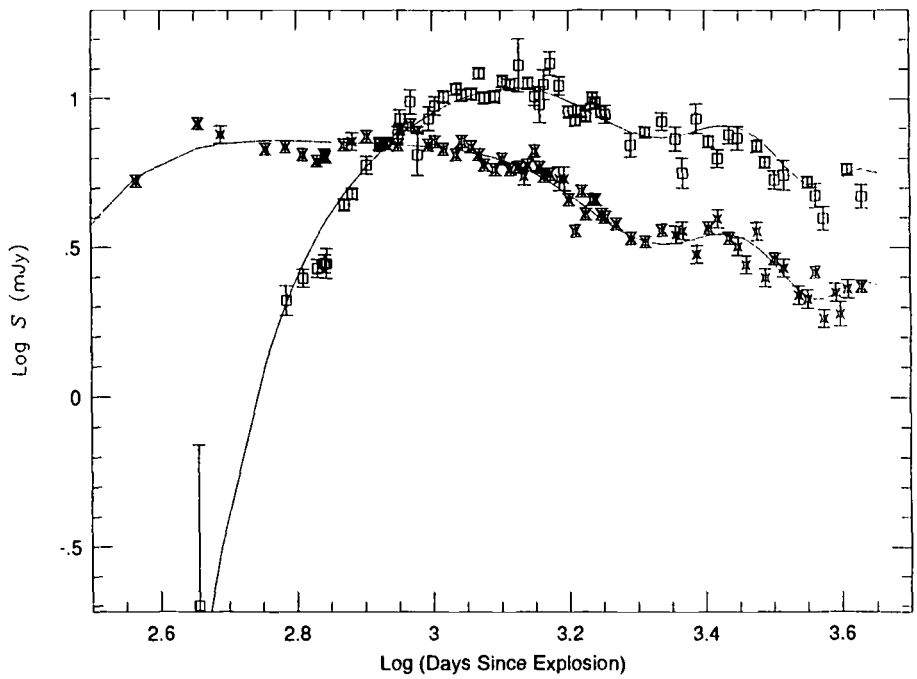

FIGURE 2. Radio light curves at 6 cm (stars) and 20 cm (squares) wavelength for the Type II "normal" supernova SN1979C in NGC4321 (M100) (From Weiler et al. 1992b).

3.3. *SN1979C*

3.3.1. *Radio Light Curves*

In April 1980 observation of the optical position of SN1979C in NGC4321 (M100) showed a bright, unresolved radio source where a year earlier no emission had been detectable. For this supernova the radio data are quite detailed with observations made on an average of once per month from 1980 to 1983 (usually at 20 and 6 cm wavelengths with occasional results at 2 cm) and measurements of $\sim$ 4 times per year since 1984. The radio light curves and spectral index evolution have thus been firmly established and these are shown in Figures 2 and 3. Comparison of Figure 2 with Figure 1 shows that Type II RSNe turn on and off much more slowly in the radio than Type Ib/c's.

SN1979C was identified as a Type II-L supernova and these radio light curves are thought to be typical of the class of "normal" Type II RSNe. The radio emission appears at 6 cm significantly after the optical outburst; there is an initial fast rise of the flux density; the emission brightens first at high frequencies and later at progressively lower frequencies; after the initial sharp rise, the flux density decays slowly over a period of months or years; and after the emitting region becomes optically thin, the radio spectral index is constant and reasonably typical for a non-thermal synchrotron source ($S \propto \nu^{-0.7}$). The early light curves are given by Weiler et al. (1986) and they have been extended by Weiler et al. (1991, 1992b).

3.3.2. *Radio Light Curve Variations*

In the process of analyzing a full decade of radio measurements from SN 1979C, Weiler et al. (1992b) found evidence for a significant, quasi-periodic, variation in the amplitude of the radio emission at 6 cm and 20 cm wavelengths of $\sim$ 15 % with a period of 1575 days or $\sim$ 4.3 years (see Figure 2. They interpreted the variation as due to a minor ($\sim$ 8 %)

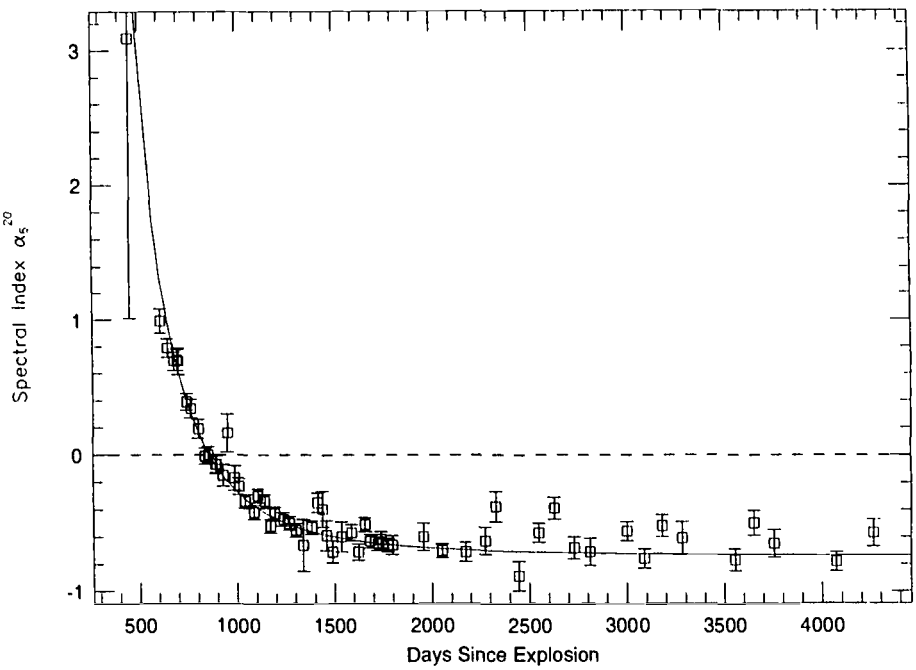

FIGURE 3. Spectral index α ($S \propto \nu^{+\alpha}$) evolution for SN1979C between 20 and 6 cm (from Weiler et al. 1991).

density modulation on the larger, relatively constant presupernova stellar mass loss rate (see model discussions in Section 5) with a period of $\sim$ 4000 years. Since such a long period is inconsistent with most models for stellar pulsations, they concluded that, while thermal pulses and C/He flashes remain a possibility, the modulation may be produced by interaction of a binary companion in an eccentric orbit with the stellar wind from the presupernova RSG.

3.3.3. *VLBI Measurements*

The radio flux density of SN1979C has remained sufficiently high that Very Long Baseline Interferometry (VLBI) measurements have been carried out to establish its structure on the milliarcsecond scale. Bartel et al. (1985) have not only been able to measure the diameter of the radio source but, with successive observations, to show that it is clearly expanding. At 6 cm wavelength the diameter increased from 1.05 milliarcseconds in December 1982 to 1.43 milliarcseconds in December 1983. This rate, combined with the physical expansion velocity inferred from optical line velocity measurements of the SN photosphere, can be used to give an independent estimate of the distance to NGC4321 and of the Hubble Constant H_0 (Bartel et al. 1985). These results have been extended and improved by Bartel (1991a,b). While still not highly accurate, the technique shows promise to provide independent distance and Hubble Constant estimates, particularly for the recent SN1993J where the data is expected to be far superior.

3.4. *Mkn297A*

Radio studies of the galaxy Markarian 297 (NGC6052) by Yin & Heeschen (1991) show a compact radio source which, while not optically identified at the time of its outburst, shows turn-on, turn-off, and radio spectral properties very similar to those observed for RSNe. More recent studies (Yin 1994) appear to confirm this identification and show that

the flux density of the source, designated Mkn297A, has continued to evolve in a manner consistent with an RSN interpretation. The best fit modelling (Yin 1994) implies that Mkn297A exploded on approximately 1979 August 16 and has properties which resemble other RSNe such as SN1979C and SN1986J. Mkn297A appears to be the most luminous RSN ever observed. Unfortunately, Yin (1994) does not allow for the possible presence of mixed, internal, thermal absorbing/non-thermal emitting material (see Section 5) such as found for SN1986J (Weiler et al. 1986) and SN1988Z (Van Dyk et al 1993b) so that a more detailed comparison with possible subtypes cannot be carried out at present.

3.5. *SN1980K*

Only a few months after the radio detection of SN1979C, a new, bright Type II-L supernova, SN1980K, was discovered in NGC6946 in October 1980. Unlike SN1979C which was undetectable at 6 cm for a year, SN1980K could already be detected after a few weeks and the first detection of 0.7 mJy at 6 cm was obtained with the VLA on 4 December 1980. This early detection implies a lower mass loss rate from the progenitor star (see discussion in Section 6. Otherwise, the radio behavior of SN1980K was very similar to that of SN1979C and can be described by the same models. The available data and applicable models are described in detail by Weiler et al. (1986).

3.6. *SN1981K*

At a position where there had been no source detectable in Westerbork Synthesis Radio Telescope (WSRT) maps of NGC4258 made in the late 1970s, a January 1982 VLA map at 20 cm showed a strong point source (van der Hulst et al. 1983). Radio monitoring with the VLA and WSRT showed it to have a non-thermal spectrum and to be decreasing in flux density. A search of optical photographic plates revealed a transient object within 2 arcseconds of the radio position which had to have appeared near the beginning of August 1981. Although the scant optical data does not allow a determination of the type of this supernova, the slow radio decline implies that it was probably a Type II very similar in properties to SN1979C and SN1980K. SN1981K was apparently missed by optical searchers because it was likely quite faint ($\sim 16^m - 17^m$) and was at its optical brightest when NGC4258 was an early evening object. The radio results for SN1981K are discussed in more detail in Van Dyk et al. (1992).

3.7. *SN1986J*

3.7.1. *Radio Light Curves*

In a fashion similar to the discovery of SN1981K, VLA radio maps made of NGC891 at 20 cm in August 1986 showed a new, dominant point source $\sim$ 65 arc-seconds south of the Galactic nucleus where no such object was detectable in earlier WSRT images (Rupen et al. 1987). This object, which received the designation SN1986J, is both one of the brightest (its 6 cm flux density has exceeded 100 mJy) and most radio luminous RSNe known (exceeded only by Mkn297A and SN1988Z).

After radio discovery, an optical counterpart was found for SN1986J in September 1986. Its luminosity in R band (λ6500 Å) at that time was $\sim 19.5^m$ and examination of earlier observations of NGC891 made in January 1984 showed an $\sim$ 18.4 magnitude object, also at R-band. The optical supernova showed a "peculiar" spectrum with narrow lines only $\sim$ 1000 km s^{-1} wide while most SNe show line widths of at least several thousand kilometers per second.

The radio light curves for SN1986J through the end of 1988 are shown in Figure 4. Comparison of Figure 4 with Figure 2 shows that SN1986J was much slower in its turn-on than SN1979C, even though both were Type II RSNe. This is interpreted by

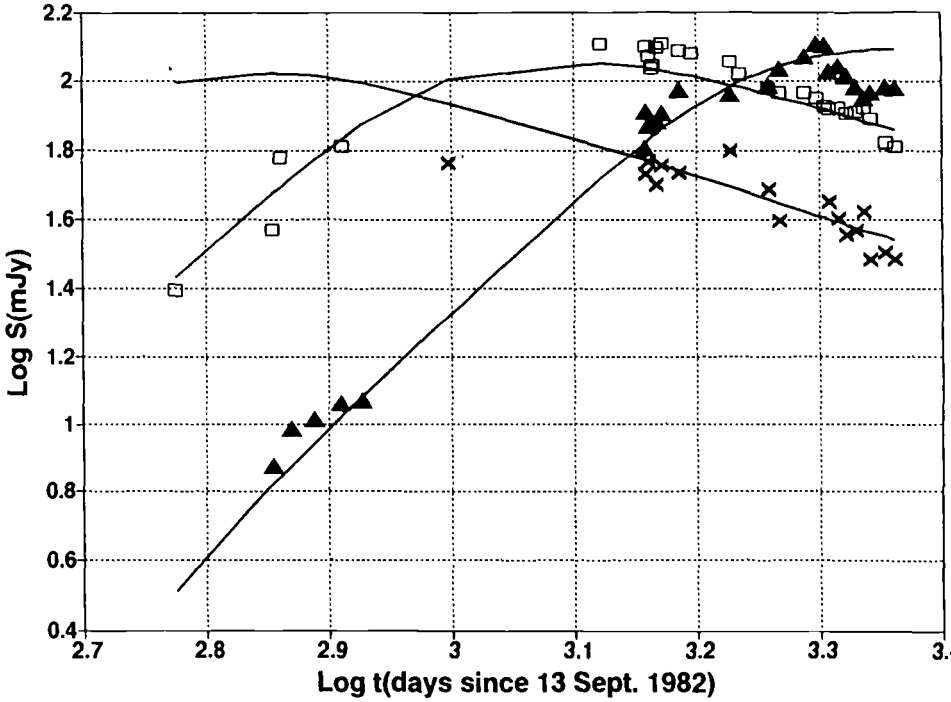

FIGURE 4. Radio light curves at 2 cm (crosses), 6 cm (squares), and 20 cm (triangles) for the Type II "peculiar" supernova SN1986J in NGC891. The age of the supernova is measured in days from the best fit date of explosion on 1982 September 13 (Weiler et al. 1990).

Weiler et al. (1990) as due to a much larger internal, thermal absorbing/non-thermal emitting component in the radio radiation for SN1986J than for SN1979C. Whether the presence of such internal material and its effect on the radio light curves is a fundamental difference between Type II "normal" RSNe such as SN1979C and SN1980K, with less evidence for an internal emitting/absorbing component, and Type II "peculiar" RSNe such as SN1986J and SN1988Z with strong evidence for such an internal component, or just a matter of degree is still not certain at present.

3.7.2. *VLBI Structure*

Because of its high apparent radio brightness, SN1986J is the only other RSN besides SN1979C which could be studied with VLBI before SN1993J. Initial measurements showed a radio diameter for SN1986J of $\sim$ 0.0014 arc-seconds (Bartel et al. 1987, 1989) and, more recently, Bartel (1991b) has been able to obtain an actual VLBI map of SN1986J. It shows a shell-like structure, but is highly irregular with apparent extensions or lobes protruding beyond the shell. Because of this asphericity, SN1986J will not likely provide a very good target for distance or H_0 determinations.

3.8. *SN1987A*

Radio emission was detected from SN1987A already with the first observations made at 0.843 and 1.4 GHz only two days after discovery (Turtle et al. 1987). Observations one day later at 2.3 GHz also detected the supernova but with a flux density which was already declining rapidly. Although the peak radio flux density of SN1987A was >100 mJy, the Magellanic Clouds are so close that this implies an under-luminosity of a factor of more than 3 orders-of-magnitude when compared to, for example, SN1979C. Also, the radio emission from SN1987A declined extraordinarily rapidly and, except at 0.843 GHz,

was undetectably weak within a few days. With such a low radio luminosity and such rapid evolution, SN1987A would almost certainly not have been detected in the radio had it been at a more normal distance for extragalactic SNe such as the Virgo Cluster or even the Local Group during its initial evolution.

In retrospect, the origin of SN1987A in the explosion of a B3 Ia blue supergiant star agrees well with the observed radio properties. Such a star is not expected to have the massive stellar wind and dense circumstellar material produced prior to explosion needed to create a powerful RSN in mini-shell models (Weiler et al. 1986, Storey & Manchester 1987, Chevalier & Fransson 1987).

Recently, Staveley-Smith et al. (1992) have reported that SN1987A has again become detectable as a radio source, presumably due to the shock wave reaching denser material at the blue supergiant wind termination shock. Because of the likely asymmetry of the material (Ball & Kirk 1992) and the fact that the circumstellar material is already completely optically thin to radio emission, the turn-on characteristics and physical interpretation of the returning radio radiation is very different from that for the RSNe we are concerned with here.

3.9. *SN1988Z*

With a redshift of $z = 0.022$, SN1988Z in MCG +03−28−022 is the farthest RSN known with a distance of 89 Mpc ($H_0 = 75$ km s^{-1} Mpc^{-1}). It is also, after Mkn297A, the most luminous RSN known. Radio emission was first detected by Sramek, Weiler, & Panagia (1990) and further study of its radio emission and model fitting to the results by Van Dyk et al. (1993b) indicate that it has properties which are very similar to those of SN1986J. It is thus apparently an example of a Type II "peculiar" RSN like SN1986J which shows the slow radio light curve turn-on which is characteristic of the presence of a significant component of mixed, internal thermal absorbing/non-thermal emitting material in the SN shock interaction region. Unfortunately, because of its great distance it is relatively weak with a maximum flux density at 6 cm of <2 mJy, making it very hard to study with high accuracy. Nevertheless, Van Dyk et al. (1993b) have extensive measurements at four radio frequency bands.

3.10. *SN1993J*

SN1993J was discovered by the Spanish amateur astronomer F. Garcia on 1993 March 26.9 UT in M81 (Ripero 1993) and first detected in the radio at 1.3 cm on 1993 April 2 by Weiler et al. (1993). Since that time extensive monitoring has been carried out by various observers and detections have been obtained at all frequencies from 1.4 GHz to 100 GHz. The behavior of SN1993J in the radio range is apparently rather normal, resembling the evolution of SN1979C and SN1980K. However, the modelling of the preliminary light curves, which is still incomplete, does require a small, but significant internal, thermal absorbing/non-thermal emitting component such as was required for SN1986J. These observations and our preliminary modelling results are discussed further by Van Dyk et al. (1993) in the workshop on SN1993J included as part of this volume.

4. Intermediate Age Radio Supernovae

Monitoring of recent RSNe has shown that centimeter radio emission from Type II SNe can last for several years. Studies of young SNRs such as Cas A (SN 1670) and SNR models (see, e.g., Gull 1973) show that after ~100 years SNRs can become powerful radio sources. However, the question remains as to what the radio properties of SNe and SNR are in the time interval from $10 < t(\text{yrs}) < 300$, the so-called intermediate age SNe.

There is at least a partial answer in the detection of radio emission from SN1957D and, perhaps, SN1950B in M83 (NGC5236) (Cowan & Branch, 1985). The 6 cm luminosity of SN1950B is about 5 times that of Cas A and SN1957D is about 15 times Cas A (Weiler et al. 1986). The optical classifications of these two SNe are unknown, but the radio properties resemble the Type II supernovae SN1979C and SN1980K.

A radio source coincident to better than 0.1 arcseconds with the position of SN1961V was detected with the VLA at 20 cm (Branch & Cowan 1985; Klemola 1986). This source is very weak, 0.19 mJy, which, at the distance of M83, implies an absolute luminosity about equal to that of Cas A. More recent observations of this source at 6 cm (Cowan et al. 1988) show it to have a nonthermal spectrum with index $\alpha \sim -0.4$. Since the supernova is embedded in an HII region some portion of the radio emission may be thermal although the thermal contribution is not thought to be significant (Cowan et al. 1988). SN1961V is particularly interesting because it was considered to be the prototype of the Zwicky Type V supernova, with an optical spectrum like a Type II object but with relatively narrow lines corresponding to an expansion velocity of only ~ 2000 km s^{-1} and a very slowly declining optical light curve. Recently, however, Goodrich, Stringfellow, & Penrod (1989) and Bower et al. (1993) postulate that SN1961V was not a true supernova but an exaggerated η Carinae-type outburst. years.

It is not yet known if the radio sources related to SN1961V, SN1957D, and SN1950B are old RSNe which are slowly declining or young SNR which are brightening as they sweep up interstellar matter. Continued monitoring of the sources should answer this question within the next several years.

5. Models for Radio Supernovae

In their study of a number of RSNe Weiler et al. (1986) established several identifying properties:

(a) non-thermal emission with high brightness temperature;

(b) turn-on first at shorter wavelengths and later at longer wavelengths;

(c) initial rapid increase of flux density with time at each wavelength;

(d) power law decline in flux density at each wavelength after maximum is reached;

(e) initial decrease in spectral index α between any two wavelengths as the longer wavelength goes from optically thick to optically thin, and a final asymptotic approach of the spectral index to an optically thin, non-thermal, constant negative value ($S \propto \nu^{+\alpha}$).

Models for RSNe have to describe the origin and evolution of the relativistic particles and magnetic fields which give rise to these properties. Two classes of models have been developed to describe the radio emission from SNe (see Weiler et al. 1986), the "mini-shell" (Chevalier 1982, 1984) model which utilizes shock acceleration in the region exterior to the supernova ejecta and the "mini-plerion" (Pacini & Salvati 1981) model which utilizes the rotational energy losses of a rapidly spinning, rapidly slowing pulsar left over by the SN explosion. However, all presently available data appear to be best described by the "mini-shell" model.

The mini-shell model utilizes the Rayleigh-Taylor unstable region between the supernova shock, propagating into the preexisting circumstellar shell of dense material which was created by a stellar wind from the presupernova star and the reverse shock propagating back into the supernova envelope to drive turbulence. This results in the magnetic field enhancement and particle acceleration necessary for radio synchrotron radiation (Chevalier 1984). Since the circumstellar shell is ionized and generally optically thick at radio frequencies, emission does not become observable until the shock wave has passed far enough through the shell that the radio optical depth approaches unity. The change

in the remaining optical depth then produces the observed rapid turn on at progressively lower frequencies and the density gradient of the supernova envelope provides a declining radio light curve of the form $S \propto \nu^{\alpha} t^{\beta}$ similar to that observed. Both the intensity and the time scale of the radio emission are dependent on the characteristics of the circumstellar material and are thus an indication of the mass loss rate of the supernova progenitor. Adopting a model with an external thermal, absorbing screen of optical depth τ and an internal, mixed, thermal absorbing/non-thermal emitting medium of optical depth τ', and ruling out such absorbing processes as synchrotron self-absorption and the Razin-Tsytovich effect, the radio "light curves" of the RSNe can be described with the simple mathematical form:

$$S(\mathrm{mJy}) = K_1 \left(\frac{\nu}{5\ \mathrm{GHz}}\right)^{\alpha} \left(\frac{t - t_0}{1\ \mathrm{day}}\right)^{\beta} e^{-\tau}(1 - e^{-\tau})\tau'^{-1}, \tag{5.1}$$

with

$$\tau = K_2 \left(\frac{\nu}{5\ \mathrm{GHz}}\right)^{-2.1} \left(\frac{t - t_0}{1\ \mathrm{day}}\right)^{\delta}, \tag{5.2}$$

and

$$\tau' = K_3 \left(\frac{\nu}{5\ \mathrm{GHz}}\right)^{-2.1} \left(\frac{t - t_0}{1\ \mathrm{day}}\right)^{\delta}, \tag{5.3}$$

This formulation assumes that the flux density S, the external optical depth τ, and the internal optical depth τ' are well described by power-law functions of the supernova age $(t - t_0)$, with powers β, δ, and δ', respectively; that the external absorption τ is purely thermal, free-free absorption in an ionized medium (frequency dependence $\nu^{-2.1}$) with a radial dependence of r^{-2} from a constant speed, red supergiant wind; that the internal absorption τ' is also thermal but mixed, at least statistically, with the non-thermal emitting medium; and that the intrinsic emission is due to the nonthermal synchrotron process with an optically thin spectral index α. The quantities K_1, K_2, and K_3 are three scaling factors for the units of choice of mJy, GHz, and days, and correspond formally to the flux density (K_1), external optical depth (K_2), and internal optical depth (K_3) at 5 GHz 1 day after the SN explosion.

This simple model has proven to be very satisfactory for all known RSNe either of Type II or Type Ib/c. To limit the number of free parameters, we adopt the Chevalier (1981, 1982) model which determines $\delta \equiv \alpha - \beta - 3$. We also adopt a modification of the Chevalier model proposed by Weiler et al. (1990) which fixes $\delta' \equiv 5\delta/3$. It has been noted by Weiler et al. (1990) that the mixing of the thermal absorbing/ non-thermal emitting material is a mixing in a statistical sense, which probably does not involve physical admixture of the two media. The need for such a component is likely evidence for the presence of blobs, filaments, lobes, or other asymmetric structures of thermal material throughout the non-thermal emitting region.

All fits of the data to equations 5.1 – 5.3 are carried out by searching parameter space for a minimum χ^2 and generally yield quite satisfactory descriptions of the RSN radio light curves.

TABLE 2. Parameters for Well Studied RSNe

SN	K_1	α	β	K_2	K_3	m	n	$\dot{M}$
				Type Ib/c SNe				
1983N	4.4×10^3	−1.03	−1.59	5.3×10^2		0.81	7	8.0×10^{-6}
1984L	2.8×10^2	−1.01	−1.48	6.9×10^2		0.84	8	7.3×10^{-6}
1990B	2.0×10^2	−1.12	−1.27	1.5×10^4		0.95	> 20	1.5×10^{-5}
				Type II SNe				
1979C	1.5×10^3	−0.74	−0.78	3.7×10^7		0.99	> 20	5.9×10^{-4}
1980K	7.4×10^1	−0.52	−0.66	3.4×10^5		0.95	> 20	7.2×10^{-5}
1981K	1.9×10^1	−0.74	−0.50	$< 1.5 \times 10^5$		1.08	> 20	1.9×10^{-5}
1986J	6.7×10^5	−0.67	−1.18	3.0×10^5	4.0×10^{12}	0.83	8	1.7×10^{-4}
1988Z	1.5×10^5	−0.80	−1.50	5.8×10^4	1.0×10^{12}	0.77	6	1.2×10^{-4}

6. RSN Model Parameters and Mass Loss Rates

Through the use of the Chevalier model, it is possible to probe the physics of the RSN phenomenon and the presupernova stellar systems. The parameter α is the spectral index of the non-thermal emission and is directly related to the relativistic electron energy distribution index γ ($N(E) \propto E^{-\gamma}$) by $\gamma = -2\alpha + 1$. This electron energy distribution index γ and the index m of the expansion rate of the interaction shell radius R ($R \propto t^m$) are related to the rate of decline of the non-thermal emission β by $\beta = -(\gamma + 5 - 6m)/2$. The index of the expansion rate of the interaction shell m also determines the temporal behavior of the external ($\delta = -3m$) and mixed ($\delta' = 5\delta/3 = -5m$) thermal absorbing material. Under the Chevalier model, the parameter m is also related to the gas density ρ in the outer parts of the supernova ($\rho \propto r^{-n}$ where $m = (n-3)/(n-2)$). Finally, the Chevalier model allows an estimation of the mass loss rate in $M_\odot$ yr^{-1} from the presupernova stellar system. Using the formulation given by Weiler et al. (1986) in their Equation 16 and the assumptions:

(*a*) presupernova RSG wind velocity $w = 10$ km s^{-1},
(*b*) initial supernova ejecta velocity $v_i = 1.5 \times 10^4$ km s^{-1},
(*c*) electron temperature in the RSG wind $T = 10^5$ K

and the other assumptions listed by Weiler et al. (1986), we can estimate presupernova mass loss rates.

For those RSNe where sufficient data exist to obtain satisfactory fits, the best value estimates for the model parameters are listed in Table 2. Note that in many cases the estimated mass loss rates are approximately an order of magnitude larger than previously given values in the literature. While more data and better model fits have altered parameter values slightly for a few of the RSNe, most of the change results from an assumption of a higher electron temperature in the RSG wind ($T \simeq 10^5$ K *vs.* $T \simeq 10^4$ K previously) and a higher estimated ejecta velocity ($v_i \simeq 1.5 \times 10^4$ km s^{-1} *vs.* $v_i \simeq 10^4$ km s^{-1} previously).

7. RSN Results

7.1. *Classifications*

Now that more than a dozen RSNe are known and more than a half dozen are well studied, it is possible to draw a number of conclusions from examining their similarities and differences. For example, Type Ib/c supernovae appear to have steeper spectral indices (α) than Type II supernovae. Examination of Table 2 shows that the spectral index demarcation is at approximately $\alpha = -0.9$ with the Type Ib/c RSNe being steeper and the Type II RSNe being flatter. Additionally, the Type Ib/c RSNe appear to be fairly similar objects in decline rate (β) while the Type II RSNe appear to split into two groups, those like the "normal" RSN SN1979C (SN1979C, SN1980K, SN1981K) and those like the "peculiar" RSN SN1986J (SN1986J, SN1988Z). The former group appears to decline more slowly (β flatter) than the latter group (β steeper) with the SN1986J-like RSNe having decline rates quite similar to Type Ib/c RSNe. The external absorption (K_2) is lower for Type Ib/c RSNe than for Type II's and the internal absorption (K_3) is small to negligible for all RSNe except for the SN1986J-like. Correspondingly, the presupernova mass loss rates ($\dot{M}$ in $M_\odot$ yr^{-1}) for Type Ib/c RSNe are always lower than those for Type II's. The amount of deceleration of the ejecta is more significant (m smaller) for Type Ib/c RSNe than for the SN1979C-like RSNe which indicates a correspondingly much steeper density gradient (n) in the ejecta for the latter. Interestingly enough, the SN1986J-like RSNe have values for m and n which are very similar to those found for Type Ib/c RSNe. The unusually high value of m and n for SN1990B may not be significant, since the SN was very weak in the radio and the data had large errors.

In general, it appears that Type Ib/c RSNe are clearly distinguishable in their radio emission from Type II RSNe. Also, it appears that Type II RSNe split into two distinguishable groupings based on their radio emission, as is also apparent in their optical emission (see the discussion of SN1986J above). Whether this bifurcation of Type II radio properties is an indication of clear physical differences between the two types of SNe or simply a matter of degree, such as mass of the presupernova star, is not clear at present. More examples of Type II RSNe will have to be studied.

7.2. *Luminosity vs. Time delay*

According the Chevalier model, both the radio emission and the initial absorption for a supernova are a function of the mass lost from the presupernova star in a dense stellar wind prior to explosion. As a preliminary investigation of this, we have plotted in Figure 5 the peak observed 6 cm luminosity against the number of days required from explosion to reach that peak. Although the interpretation of this is still preliminary, examination of Figure 5 indicates two possible correlations:

(*a*) Type Ib/c RSNe are quite similar in their maximum 6 cm spectral luminosities and may represent standard radio candles;

(*b*) Type II RSNe, if they do not bifurcate into two groupings as discussed above, may have a direct relation between the maximum 6 cm spectral luminosity and the time after explosion required to reach that maximum.

In particular, the present data are consistent with a relation of the form

$$L_{6\mathrm{cm\ max}} = 1.6 \times 10^{22}(t_{6\mathrm{cm\ max}} - t_0)^{1.90}. \tag{7.4}$$

with L in erg s^{-1} Hz^{-1} and t in days. If such a relation can be strengthened by further observational data, then the Type II RSNe could also be calibrated to yield distance information since direct measurement of the observed turn-on time at 6 cm would indicate the absolute radio spectral luminosity.

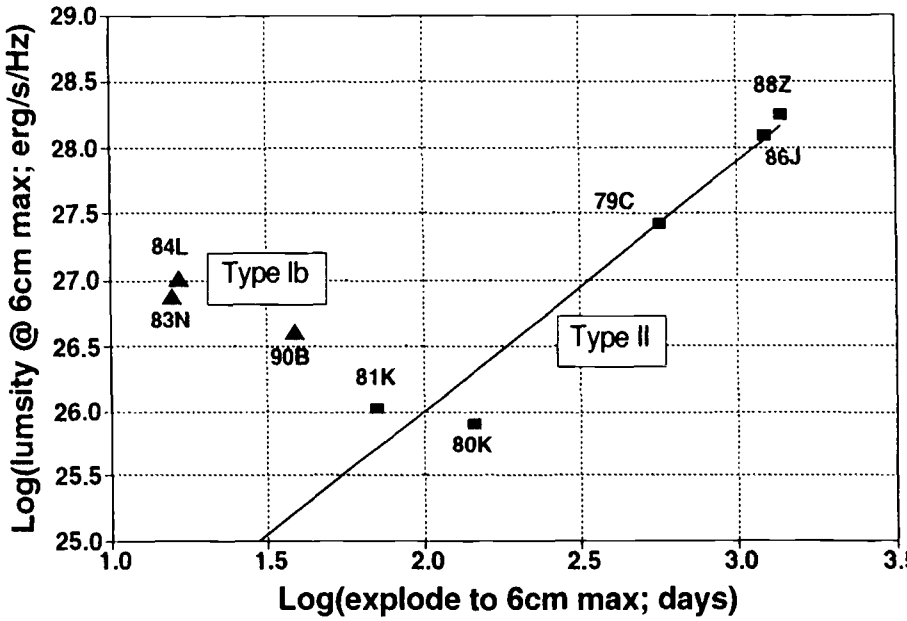

FIGURE 5. Radio peak 6 cm spectral luminosity *vs.* time from explosion to 6 cm maximum flux density.

It must be kept in mind, however, that such relations as proposed here are highly speculative and still must be demonstrated with more certainty.

8. Summary

Although the radio supernova phenomenon is relatively new, having been developed essentially in its entirety since the detection of SN1979C at 6 cm in April 1980, its study has met with considerable success. Detailed multiwavelength radio light curves have been obtained for a number of supernovae; the number of high quality upper limits on other supernovae has been increased significantly; and theoretical interpretation of the phenomenon has developed well. The gross structures of the radio light curves have been determined and can be related to the properties of the supernova's progenitor stellar system, its immediate environment, and its likely state in the last stages of evolution before exploding. As the numbers of well studied examples increases, systematic trends are appearing and the description of presupernova stellar systems based on their radio behavior after explosion is improving rapidly. There is even the speculative possibility that RSNe can serve as independent distance calibrators. Observations are continuing on already known RSNe and new, bright supernovae are being studied with the VLA as they occur. The recent explosion of the close, optical and radio bright SN1993J promises to extend our understanding of these unusual objects even further.

REFERENCES

Allen, R.J., Goss, W.M., Ekers, R.D., & de Bruyn, A.G. 1976, A&A, 48, 253

Ball, L., & Kirk, J.G. 1992, ApJ, 396, L39

Bartel, N. 1991a, in The 10th Santa Cruz Workshop in Astronomy & Astrophysics, ed. S.E. Woosley (Springer Verlag), p. 760

Bartel, N. 1991b, in The 10th Santa Cruz Workshop in Astronomy & Astrophysics, ed. S.E. Woosley (Springer Verlag), p. 503

Bartel, N., Rogers, A.E.E., Shapiro, I.I., Gorenstein, M.V., Gwinn, C.R., Marcaide, J.M., & Weiler, K.W. 1985, Nature, 318, 25

Bartel, N., Rupen, M.P., & Shapiro, I.I. 1987, IAU Circ. No. 4292

Bartel, N., Rupen, M.R., & Shapiro, I.I. 1989, ApJ, 337, L85

Bower, G.C., Filippenko, A.V., Ho., L.C., Stringfellow, G.S., Goodrich, R.W., & Porter, A.C. 1993, BAAS, 25, 819

Branch, D., & Cowan, J.J. 1985, ApJ, 297, L33

Chevalier, R.A. 1981, ApJ, 251, 259

Chevalier, R.A. 1982, ApJ, 259, 302

Chevalier, R.A. 1984, Ann. N. Y. Acad. Sci., 422, 215

Chevalier, R.A., & Fransson, C. 1987, Nature, 328, 44

Cowan, J.J., & Branch, D. 1982, ApJ, 258, 31

Cowan, J.J., & Branch, D. 1985, ApJ, 293, 400

Cowan, J.J., Henry R.B.C., & Branch, D. 1988, ApJ, 329, 116

Cowan, J.J., Goss, W.M., & Sramek, R.A. 1991, ApJ, 379, L49

Goodrich, R.W., Stringfellow, G.S., & Penrod, G.D. 1989, ApJ, 342, 908

Gottesman, S.T., Broderick, J.J., Brown, R.L., Balick, B., & Palmer, P. 1972, ApJ, 174, 383

Gull, S.F. 1973, MNRAS, 161, 47

Klemola, A.R. 1986, PASP, 98, 464

Kronberg, P.P., & Sramek, R.A. 1985, Science, 227, 28

Pacini, F., & Salvati, M. 1981, ApJ, 245, L107

Panagia et al. 1980, MNRAS, 192, 861 (Table 1, Ref. 6)

Panagia, N., Sramek, R.A., & Weiler, K.W. 1986, ApJ, 300, L55 (Table 1, Ref. 3)

Ripero, J. 1993, IAU Circ. No. 5731

Rupen, M.P., van Gorkom, J.H., Knapp, G.R., Gunn, J.E., & Schneider, D.P. 1987, AJ, 94, 61

Ryder, S., Staveley-Smith, L., Dopita, M., Petre, R., Colbert, E., Malin, D., & Schlegel, E. 1993, ApJ, in press (Table 1, Ref. 5)

Sramek, R.A., & Weiler, K.W. 1990, in Supernovae, ed. A.G. Petschek (Springer Verlag), 76

Sramek, R.A., Weiler, K.W., & Panagia, N. 1990 IAU Circ. No. 5112

Sramek, R.A., Panagia, N., & Weiler, K.W. 1984, ApJ, 285, L59 (Table 1, Ref. 1)

Staveley-Smith, L. Manchester, R.N., Kesteven, M.J., Campbell-Wilson, D., Crawford, D.F., Turtle, A.J., Reynolds, J.E., Tzioumis, A.K., Killeen, N.E.B., & Jauncey, D.L. 1992, Nature, 355, 147 (Table 1, Ref. 16)

Storey, M.C., & Manchester, R.N. 1987, Nature, 329, 421 (Table 1, Ref. 17)

Turtle, A.J., Campbell-Wilson, D., Bunton, J.D., Jauncey, D.L., Kesteven, M.J., Manchester, R.N., Norris, R.P., Storey, M.C., & Reynolds, J.E. 1987, Nature, 327, 38 (Table 1, Ref. 15)

van der Hulst, J.M., Hummel, F., Davies, R.D., Pedlar, A., & van Albada, G.D. 1983, Nature, 306, 566

Van Dyk, S.D., Weiler, K.W., Sramek, R.A., & Panagia, N. 1992, ApJ, 396, 195 (Table 1, Ref. 13)

Van Dyk, S.D., Sramek, R.A., Weiler, K.W., & Panagia, N. 1993a, ApJ, 409, 162 (Table 1, Ref. 4)

Van Dyk, S.D., Weiler, K.W., Sramek, R.A., & Panagia, N. 1993b, ApJL, 419, L69 (Table 1, Ref. 18)

Van Dyk, S.D., Weiler, K.W., Sramek, R.A., Rupen, M.P., & Panagia, N. 1993, contribution to the SN1993J Workshop in this volume (Table 1, Ref. 19)

Weiler, K.W., & Sramek, R.A. 1988, Ann. Rev. A&A, 26, 295

Weiler, K.W., van der Hulst, J.M., Sramek, R.A., & Panagia, N. 1981, ApJ, 243, L151 (Table 1, Ref. 7)

Weiler, K.W., Sramek, R.A., Panagia, N., van der Hulst, J.M., & Salvati, M. 1986, ApJ, 301, 790 (Table 1, Ref. 2)

Weiler, K.W., Panagia, N., Sramek, R.A., van der Hulst, J.M., Roberts, M.S., & Nguyen, L. 1989, ApJ, 336, 421

Weiler, K.W., Panagia, N., & Sramek, R.A. 1990, ApJ, 364, 611 (Table 1, Ref. 14)

Weiler, K.W., Van Dyk, S.D., Panagia, N., Sramek, R.A., & Discenna, J.L. 1991, ApJ, 380, 161 (Table 1, Ref. 8)

Weiler, K.W. Van Dyk, S.D., Panagia, N., & Sramek, R.A. 1992a, ApJ, 398, 248 (Table 1, Ref. 12)

Weiler, K.W. Van Dyk, S.D., Pringle, J.E., & Panagia, N. 1992b, ApJ, 399, 195 (Table 1, Ref. 9)

Weiler, K.W. Sramek, R.A., Van Dyk, S.D., & Panagia, N. 1993, IAU Circ. No. 5752

Yin, Q.F. 1994, ApJ, 420, 152 (Table 1, Ref. 11)

Yin, Q.F., & Heeschen, D.S. 1991, Nature, 354, 130 (Table 1, Ref. 10)

The SN1987A Environment

By LIFAN WANG[1] AND E. JOSEPH WAMPLER[2]

[1]Beijing Astronomical Observatory, Beijing 100080, P.R. China

[2]European Southern Observatory, Karl-Schwarzschild-straße 2, Garching bei München, D-85748 Germany

The environment of the SN1987A is quite complex but also very regularly structured. Detailed analyses of direct images taken under good seeing conditions (0.3—0.8 arcsec) from the European Southern Observatory (ESO)'s New Technology Telescope (NTT) show that there are two nebular loops within the 3 arcsec environment of the SN. The inner loop is elliptical in shape. The kinematics of this loop as revealed by spectroscopic data with a spectral resolving power $\lambda/\Delta\lambda \approx 30\,000$ provide further clues for the three dimensional structure of these two loops. The data show that the overall structure of the nebulosity can be understood by an hourglass-shaped shell with significant mass enhancement on its equatorial plane. A diffuse nebulosity called Napoleon's Hat is observed at a distance of about 5 arcsec to the north of the SN. It showed little size evolution since the first observation on Aug. 1989, until it disappeared on Jan, 1992. The Napoleon's Hat nebula appears to be a bow-shock coming from an interaction between the supernova progenitor's stellar wind and the interstellar medium, as the supernova progenitor moved through the interstellar medium with a velocity of around 5 $km\,s^{-1}$. On an even larger scale, there is a huge dark bay of size around 100 arcsec in diameter, we suggested that this bay was also formed by interactions between the supernova progenitor and the interstellar medium.

The narrow emission lines indicate that the electron density and temperature of the emission gas in the loops are steadily decreasing. However, the temperatures inferred from the [OIII] nebular lines remained persistently higher than $2 \times 10^4\,K$. They were around $10^4\,cm^{-3}$ and $2 \times 10^4\,K$ on Aug. 30, 1990. In addition, a global difference in the electron density of the two major axis of the inner loop is observed in the images and spectra taken five years after the supernova explosion. We have also studied the two neighboring stars surrounding the supernova. We find that star 2 is a B star with H_α and H_β emission lines.

The supernova circumstellar nebulosity is remarkably similar to certain types of planetary nebula, *e.g.* NGC2392. Asymmetric wind interaction models for the formation of planetary nebula are applied to produce a model in the form of an hourglass shaped shell. This model invokes both a slow wind while the star was in its red supergiant phase and a fast wind during the later blue supergiant stage before explosion. Although such wind interaction models fit the observed nebular structures satisfactorily, they are so idealized that they tell us little about the origin of the seed asymmetry or the amount of seed asymmetry *needed* to produce the observed real nebula.

1. Introduction

The first evidence of circumstellar gas near SN1987A was the detection, starting on about day 80, of narrow nebular lines in the *IUE* spectra (Wamsteker et al, 1987; Fransson et al. 1989) . Narrow optical lines were first seen on about day 300 (Wampler & Richichi 1989). The UV and optical data gave early information of the size, density, electron temperature of the brightest part of this nebula (Fransson et al 1989; Wampler & Richichi 1989). Later observations began to reveal in more detail the structures of the circumstellar material (Wampler, Richichi & Baade 1989; D'Odorico & Baade 1989; Crotts, Kunkel, & McCarthy 1989, Sparks, Paresce, & Maccheto 1989).

Using observations collected at the European Southern Observatory, we discuss the

structures seen in the SN1987A circum-stellar nebulosity. In section 2, we discuss the structures on different scales, namely, the Nebular loops, the Napoleon's Hat Nebula, and the Dark Bay. At the end of this section, we show that one of the stars near the SN is a B star with emission lines. In Section 3 we briefly review the existing models for the nebular loops and other structures on a larger scale. Finally, we summarize in section 4.

2. Observations of the SN1987A Environment

We base our discussions mainly on observations collected at the European Southern Observatory's New Technology Telescope, and compare these observations with those obtained by other authors. We discuss the geometrical structure of the nebulosity as well as its physical parameters such as electron density and temperature.

2.1. *The Nebular Loops*

The first ESO NTT images of the supernova, taken on Dec. 1989, show that the supernova is surrounded by a regularly structured nebulosity which is remarkably similar to certain planetary nebulae (Wampler et al, 1990, hereafter W90). As shown in Fig. 1, it basically consists of a central oval with two much fainter loops connected to the central oval. This nebulosity is conspicuous in both narrow band filters which emphasize nebular line emissions and in broad–band filters that emphasize continuum emissions. By comparing the size of this nebulosity with previous observations, W90 found little change of the size of these nebula. This behavior is quite different from the outer two rapidly expanding large light echoes (Crotts, et al; Gouiffes et al, 1989). These observations excluded earlier suggestions made by Crotts et al (1990) that the observed structures are due to light echoes of a sheet of background material, and W90 concluded that the observed structure represents the real three-dimensional structure of the nebulosity.

The details of the inner oval described in W90 are shown in an excellent HST image (Jacobson et al, 1991; Panagia et al, 1991). It reveals an elliptical ring whose major and minor axes are $1''.66 \pm 0''.03$ and $1''.21 \pm 0''.03$, respectively. Jakobsen et al (1991) argue that, because there is little emission detected at the center of the ring, the elliptical ring must be the projection of a real circular loop inclined by about 43° to the line of sight. However, the HST image has a very low dynamic range; it fails to show the outer loop which is only about ten–twenty times fainter, so the pure ring geometry for the nebular ring is only an approximation.

If, as W90 argued, the observed structure is due to the projection of a definite physical structure onto the plane of the sky, we can infer a shell geometry that is similar to an hourglass. This model is shown in Fig. 2. In this picture, the inner ellipse is due the waist of the hourglass shell and the outer loop is due to the two lobes of the shell which are limb–brightened when projected to the plane of sky. The distance from the symmetry center of the hourglass shaped shell to its waist is about 1/3 of the distance to the poles (Wang & Wampler, 1992). The density distribution across the shell is not homogeneous; there must be a strong density enhancement on the equatorial plane of the shell to account for the bright inner ring. Slit spectra show that the nebula is expanding at velocities about 10.3 $km\,s^{-1}$ (Crotts & Heathcote, 1991); these kinematics are consistent with the geometry given in Fig. 2.

Both the electron temperature and the electron density of the emission-line region have been found to be decreasing since the detection of the nebula. The highest electron density is estimated from IUE satellite observations (Fransson et al, 1989), and from the optical observations of Wampler & Richichi (1989), and Wampler, Richichi & Baade (1989). The decrease is due apparently to radiative cooling and recombination after

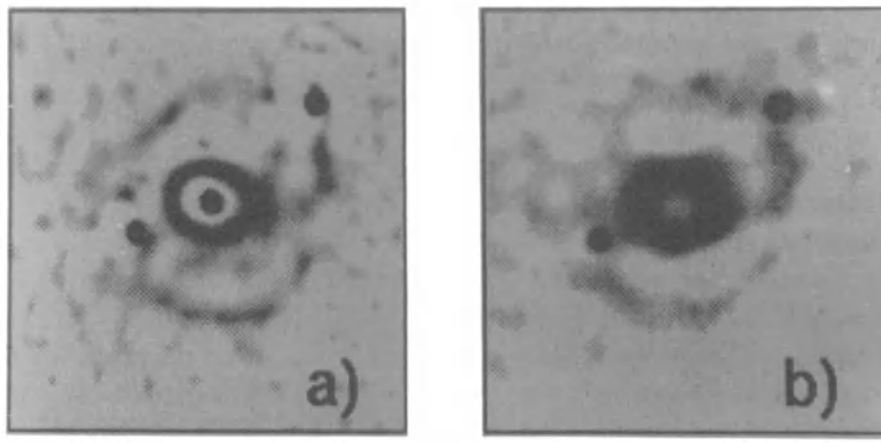

FIGURE 1. [OIII] Images of the nebular loops: (a) Day 1037, and (b) day 1790 after the SN explosion.

the nebulosity was ionized by the initial UV flash from the supernova outburst. Wang (1991) noticed the temperature of the nebulosity is not decreasing as rapidly as predicted by model calculations by Lundqvist & Fransson (1991), and suggested that a mixed structured of different electron density can explain this behavior: at early times we observe mostly the dense part of the nebula which cools faster than the less dense part; but eventually, the dense part has completely recombined and emission from the low density part dominates the emissions. Later models with several density component yields better agreement with observations (Luo, 1991).

Although the inner ellipse is very regular, the distribution of electron densities along the ellipse is probably not homogeneous. Images taken after Jan. 1991 show a clear difference in brightness of the East and West side of the ring. Spectroscopic data taken with slit across the East and West side of the ring show that the density sensitive [SII]671.6,673.1 nm line ratio is not the same on the two sides of the ring, with the electron density of the west side being lower than the east side. A natural explanation is that the west side, having lower electron density than the east side, therefore cools more slowly, and is now brighter than the east side.

2.2. *Napoleon's Hat*

The Napoleon's Hat nebula refers to a diffuse nebulosity to the north of the SN. It was conspicuous in images taken in continuum filters but was only weakly seen in images taken using narrow line filters. Wang & Wampler (1992) compared images taken from Aug., 1989 to Jan. 1992, and found little change in size of the northern extension of this nebulosity, although they detected expansion to the east and west side. It thus seems that the majority of the nebulosity responsible for the Napoleon's Hat nebula was already inside the light travel paraboloid defined by the equal light travel time from the SN to the observer as shown in Fig. 2. It follows that the nebulosity can not be a clump of dusty gas located far from the supernova and along the line of sight to the supernova; its location is strictly constrained to be near the SN (Wang & Wampler, 1992).

Two possibilities were proposed for Napoleon's Hat : 1) a bow-shock model; 2) a tilted disk model (Wang & Wampler, 1992). The bow-shock model gives better fit to the data,

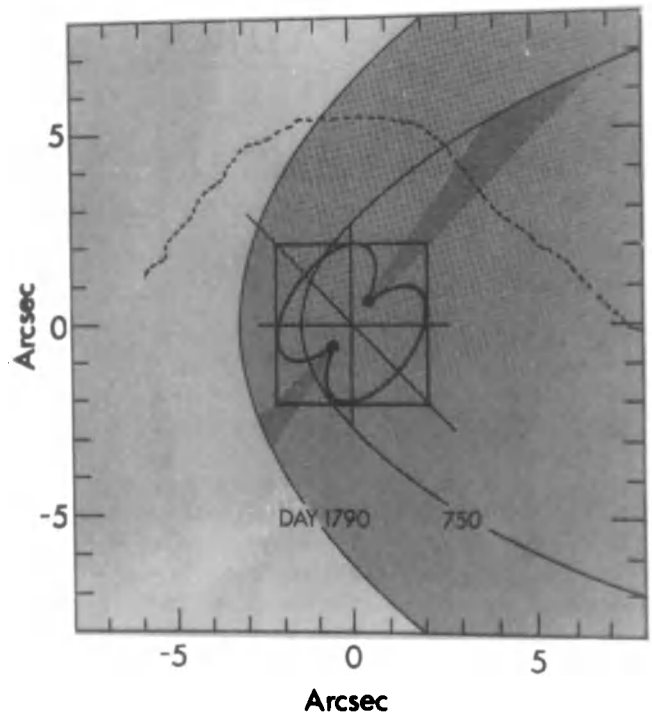

FIGURE 2. Geometry for the Nebular loops and Napoleon's Hat. The light travel paraboloids of the SN light are shown for different dates after the SN explosion. The central box shows the allowed location for the nebulosity responsible for the two nebular loops. Also shown are the observed shape of Napoleon's Hat (Dotted lines) and the hypothesized disk. North is up, right is to the direction of the observer.

while the disk model gave only a rough fit to the size and shape of the light echo when it was first seen. Moreover, it does not at all reproduce the time evolution of Napoleon's Hat, and, in particular, that part that is the top of the Hat. However, a combined structure of a disk and a bow shock may be a possible model for the Napoleon's Hat, especially when considering the details of the brightness distribution across the observed diffuse nebulosity of the Napoleon's Hat. Although we lack firm evidence for a disk, it could provide a natural link between the Napoleon's Hat and hourglass shaped shell.

2.3. *Structures beyond 5 arcsec*

Several larger echoes have been detected near SN1987A. The most spectacular of these are the two echoes discovered by Crotts (1987) and described by Rosa et al (1987). These echoes are rapidly expanding, and it is clear that they are due to reflections of the supernova light by two dusty sheets lying between us and the supernova at distances of 105 *pc* and 316 *pc* from the SN. They show that the SN lies behind two curtains of dusty material, but tell us very little about the supernova progenitor.

A light echo ring of size 10 arcsec was detected on Jan. 1989 (Bond et al, 1990; Sparks et al, 1990; and Crotts & Kunkel, 1991) The echo was interpreted by Chevalier & Emmering (1989) as due to the shock wave arose from the interactions between the supernova progenitor's RSG wind and surrounding interstellar medium. However, this light echo was observed only briefly; it was neither detected in our NTT images taken in 1990 Aug. nor afterwards; this would suggest that the reflecting material is probably

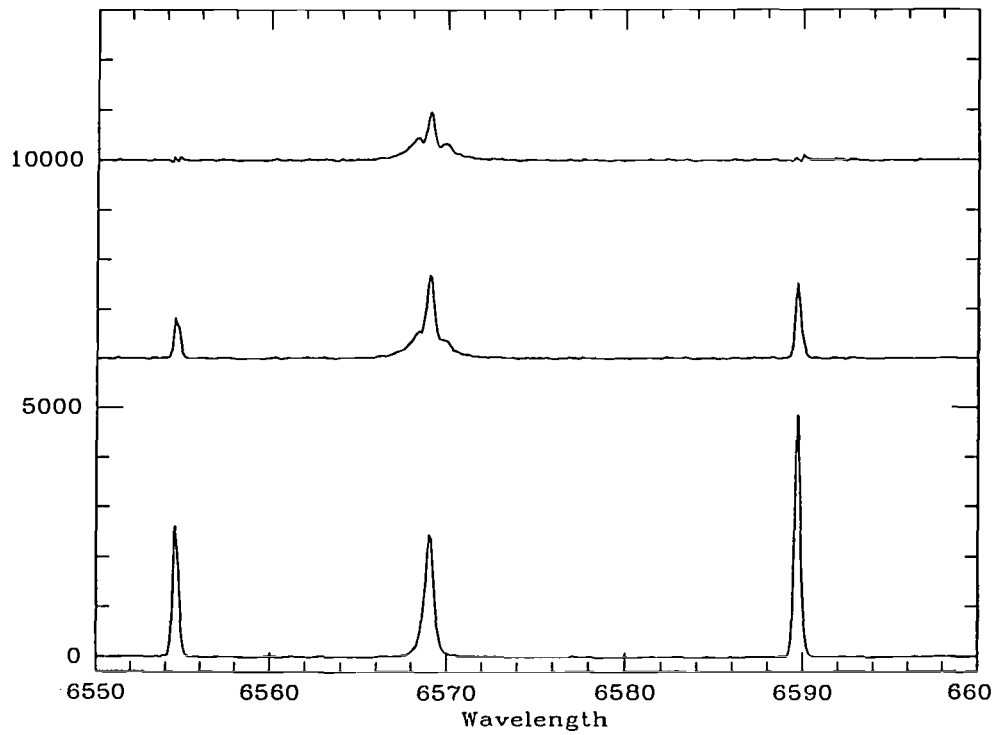

FIGURE 3. The spectrum of star 3 near SN1987A.

not a closed shell of gas centering at the supernova, but is simply a dusty clump in front of the supernova.

2.4. *Star 3*

Since massive stars are usually found in associations, it is interesting to study the stars in the supernova neighborhood. There are two blue stars close to the supernova. We show in Fig. 3 the spectra for star 3, which is located at position angle 110° and 1.5 arcsec away from the supernova. The spectra shown were obtained at the NTT with the ESO Multiple Mode Instrument (EMMI) on Jan. 15, 1993. For the exposure, star 2, the SN and star 3 were simultaneously within the slit. We see a clear broad H_α component close at the position of star 3. This broad component is not seen in the metal lines (Wang et al, 1992). We have compared our NTT direct images taken at seeing conditions of around 0.3 arcsec, and found that the star 3 is brighter than star 2 in the narrow band H_α filter, but is much fainter in other bands.

We have tried to construct spectra of star 2; we subtracted the contamination by the supernova light by removing the neighboring [NII] lines completely. In the subtracting process, we scaled the [NII]658.4 nm line so that in the subtracted spectra this line completely disappears. In doing so we found that the [NII]654.8 nm line also disappeared automatically. The resulting spectra show clearly a broad H_α feature. Combining the above observations with the CTIO photometric data which show star 3 is variable (Elias et al, 1993), we conclude that the emission feature is intrinsic to star 3. The HST images should be able to provide further constraints on the nature of this broad emission feature; this has not been done so far, however.

3. Dynamical Models

3.1. *The Slow-Fast Wind Interaction Model for the Nebular Loops*

Luo & McCray (1990), Wang (1991), Blondin & Lundqvist (1992) proposed that the nebular loops can be modeled in terms of the asymmetric slow and fast wind interaction models used to explain the morphological development of planetary nebulae (Kahn & West, 1985). The model assumes that SK -69 202 was once a RSG before it evolved to a BSG and exploded. In the RSG stage, the star loses mass at a rate of typically $10^{-5} M_{\odot}/year$ and velocity around $10\, km\, s^{-1}$; while in the BSG stage, the mass loss rate decreased by about 10 times to $10^{-6} M_{\odot}/year$, but the wind is much more energetic; the wind velocity is typically about $10^{3}\, km\, s^{-1}$.

An important parameter in this model is the amount of the initial asymmetry in the slow RSG wind. Luo & McCray (1990) used a ratio for the pole to equator mass loss rate of about 1:5, while Wang & Mazzali (1992) used a ratio of only 1:1.2. Wang & Mazzali found that, even with the very small asymmetries they used, a high density cusp forms at the equator of the bubble of the shocked slow wind, and this cusp can account for the observed structure.

The thin-shock approximation allows for a similarity solution (Kahn & West, 1985); this similarity solution, however, breaks down in the region where the cusp develops. In the thin shock approximation, the surface density of the shocked slow wind shell is determined by two effects: 1) the dilution due to radial expansion and 2) the forced non-radial motion due to the pressure in the shocked hot bubble. *A cusp will develop if the compressed motion overtakes the dilution by expansion.* An analytical criteria is given by Wang (1993) for the formation of a high density cusp.

The details of cusp formation must be studied by hydrodynamic simulation. Such calculations were made by Blondin & Lundqvist (1993). Their best fit model has a high concentration of mass loss rate on the equatorial plane of the progenitor star. Their hydrodynamic model fits not only the size of both the inner and outer loops, but also predicts the clumpy structure observed recently by the NTT image for both loops (W90, Wang & Wampler, 1992) and by the HST images for the inner ellipse (Jacobsen et al, 1991; Panagia et al, 1991).

Though it seems that these models successfully reproduce structures observed around the supernova, the uniqueness of the models are not guaranteed. An important problem is that the observed expansion velocity of the inner ellipse is only about $10\, km\, s^{-1}$, a value that is less than typically observed RSG wind velocities. Although the formation of high density cusps can be achieved in thin-shock approximation models they can not be used to estimate the amount of the initial asymmetry in the slow wind. The models fail when the cusps develops; the cusp is a real mathematical *critical point.* This explains why the Luo & McCray (1991) and the Wang & Mazzali (1992) models used different values for the seed asymmetry in the slow wind. Neither author attempted to estimate the exact amount of asymmetries required to produce the supernova nebular shell. More realistic considerations of the wind interactions remain to be explored.

One recent improvement (Wang, 1993) is to assume that the slow wind mass loss rate is not steady; variable mass loss rates are believed to be responsible for the zoo of planetary nebulae morphologies, after the early normal RSG wind stage and before the BSG wind starts there may be a super wind stage. We have run a hydrodynamic code SADIE (Arnold, 1985) kindly provided by E. Müller; the model results are shown in Fig. 4. The model parameters are taken to be similar to those of Wang & Mazzali (1992), but the mass loss rate of the slow wind is assumed to have a sharp jump by a factor of ten.

FIGURE 4. Models with non-steady slow winds

It is readily seen that the final structure deviates more strongly from spherical symmetry in the non-steady slow wind scenario than in the steady slow wind scenario, and thus a reduction in the amount of initial asymmetry required. In the steady slow-wind scenario, the enhancement of materials on the equatorial plane is determined by the nonradial motions onto the equator. On the other hand, in the super wind scenario, the hot bubble and therefore the shocked slow wind shell expands faster in the polar direction than in the equatorial plane. It breaks through the dense superwind first at the two poles, there the ram pressure of the slow wind decreases sharply and the shell is accelerated by the pressure of the hot bubble. On the equatorial plane, this process happens later. By that time, the pressure of the hot bubble is greatly reduced due to expansion in the polar direction. We note that the resolution in our model calculation is rather low; higher resolution calculations should reveal more structural details. The model can possibly resolve the polar caps observed in many planetary nebulae.

One other possibility was proposed recently by Chevalier & Luo (1994), who considered the shaping due to magnetic field; they also found the formation of an equatorial cusp.

3.2. *The Effect of the RSG and the Main Sequence Wind*

It is believed that the progenitor star started as a BSG star on the main sequence and that it later evolved to a RSG star and then to a BSG before exploding (Nomoto et al, 1987; Woosley, 1988). Since massive stars are believed to have stellar winds during their entire life time, these pre-supernova stages can also be effective in forming nebular structures. Wang & Wampler (1992) find that the Napoleon's Hat is the next neighboring structure outside the two nebular loops. The location of the material responsible for the Napoleon's Hat is strictly constrained by the time evolution of the Napoleon's Hat. The Napoleon's Hat is so close to the SN that one can safely say that this nebulosity must be dynamically related to the supernova progenitor. The next structure outside the

Napoleon's Hat nebula is the echo ring at a radius of 10 arcsec. But, if this echo is due to the shell identified with the shock coming from the interaction between the slow wind and the bubble of the reverse shock of the first BSG wind, the echo should be still observable. It is not.

It is difficult to find the boundary of the fast wind lost by the progenitor while it was in its first BSG stage. On such large scales, winds from other associated stars and even supernova explosions that happened earlier may influence the environment into where the wind of the supernova progenitor expanded. A possible identification of this boundary was given by W90 and Wang, Kahn & Dyson (1993), who argue that the dark bay can be the result of the interaction between the main sequence fast wind and the interstellar medium, and the morphology of the dark bay can be easily understood if the star is moving with respect to the interstellar medium at a velocity of about 5 $km\,s^{-1}$. Wang, Dyson & Kahn (1993) have further modeled the structures arising from such interaction, and find that the star itself can move through the shocked interstellar medium by the time the progenitor evolved to a RSG; the RSG wind can interact directly with the interstellar medium, and the resulting structure can be identified with the Napoleon's Hat nebula.

Another possibility for the dark bay was proposed by Felten & Dwek (1991) who argue that the dark bay is due to dust shadowing. However, we think this interpretation is unlikely. Even a very dusty cloud should reflect enough supernova light to produce observable light echoes. The two observed echo rings have already expanded to a larger angular size than the dark bay (Wang & Rosa, 1992) and cannot be reflections from the hypothesized dust cloud. No nebulosity has been found that can be attributed to reflections from the shadowing dust cloud.

4. Summary

We have shown that the environment of the supernova SN1987A is strongly influenced by the wind from the progenitor star. Therefore, the structure of the SN1987A environment provides valuable information about the supernova progenitor. The two nebular loops are identified with the shock arising from the interactions between the progenitor's blue and red supergiant wind. To understand the hourglass morphology, one must assume certain asymmetries in the progenitor's stellar winds. The origin and degree of this asymmetry is not clear: it may be due to a binary star if the degree of asymmetry is large; but a single star model may also be possible if only a small degree of asymmetry is required.

The Napoleon's Hat nebula to the north of the nebular loops can be best fit by a bow-shock. A disk model does not give the right observed morphology at late times. But there are some weak indications of the existence of a disk from the brightness distributions on the surface of Napoleon's Hat in the Dec. 1989 observations. The bow-shock/disc is the next structure outside the nebular loops, and it is affected by the winds from the SN progenitor. A natural explanation is that the progenitor moves through the interstellar medium, and its wind interacts with the surrounding interstellar medium and produces the bow-shock.

The 10 arcsec scale light echo does not seem to be due to a shell enclosing the supernova, but most likely is a dusty clump that happens to be located along the line of sight to the SN. The structure of the Dark bay is much more complex, but may also be influenced by the wind from the supernova progenitor.

Hydrodynamic models for the nebular loops have to reproduce the following three observed properties: (1) the ratio of the radius of the inner and outer loop is about

1:3; (2) the ratio of the emission measure of the inner and outer loop should be larger than 10; and (3) the expansion velocity of the inner ring should be about 10 $km\,s^{-1}$. Models with steady mass loss rate in the BSG an RSG stage have been studied in great detail, but more complicated models seem to be required. A major modification and complication would be to abandon the steady wind assumption. Our low resolution hydrodynamic simulation already shows that this is a promising approach, but higher resolution simulations are needed.

Finally, the supernova ejecta are expanding at velocities up to $30\,000 km\,s^{-1}$. The collision between the ejecta and the circum-stellar material will excite the gas again, and further information can be obtained when this occurs.

We are grateful to R. Chevalier, D. Baade, L. Lucy, P. Lundqvist, D. Luo and K. Nomoto for discussions. L. W. also acknowledges Q. B. Li and J. Y. Hu for supporting this work.

REFERENCES

Blondin, J. & Lundqvist, P. 1993, *ApJ*, 405, 337

Bond, H. E., Gilmozzi, R., Meakes, M. G., & Panagia, N. 1990, *ApJL*, 347, L65.

Chevalier R. A. & Emmering, R. T., 1989, *ApJL*, 342, L75.

Chevalier R. A. & Luo, D., 1994, *ApJ*, 421, 225.

Crotts, A. P. S. 1988. *IAU Circ. 4561*

Crotts, A. P. S., & Heathcote, S. R. 1991, *Nature*, 350, 683.

Crotts, A. P. S., & Kunkel, W. E. 1991, *ApJL* 366, L73.

Crotts, A. P. S., Kunkel, W. E., & McCarthy, P. J. 1989, *ApJL*, 347, L61.

D'Odorico, S., & Baade., D. 1989, *ESO Messenger*, 56, 35.

Elias, J. H., Phillips, M. M., Suntzeff, N. B., Walker, A. R., Gregory, B., & Depoy, D. L. 1993, in *Massive Stars: Their lives in the Interstellar Medium*, Ed. Cassinelli, J. P. & Churchwell, E. B., P408.

Felten, J. E. & Dwek, E., in *SN1987A and Other Supernovae*, ed. Danziger, I. J. & Kjä r, K. P569.

Fransson, C., Cassatella, A., Gilmozzi, R., Kirshner, R. P., Panagia, N., Sonneborn, G., Sauvageot, J. L., & Wamsteker, W., 1989, *ApJ*, 336, 429.

Gouiffes, C., Rosa, M., Melnick, J., Danziger, I. J., Renny, M., Santini, C.,Sauvageot, J. L., Jakobsen, P., & Ruiz, M. T., 1988 *A&A* 198, L9

Jakobsen, P., et al 1991 *ApJL*, L63.

Kahn, F. D., & West, K. A. 1985 *MNRAS*, 212, 837.

Luo, D., 1992, Ph. D. thesis, University of Colorado.

Luo, D., & McCray, R. 1991, *ApJ*, 379, 659.

Lundqvist, P., & Fransson, C. 1991, *ApJ*, 380, 575.

Meikle, W. P. S., Cumming, R. J., Spyromilio, J., Allen, D. A., & Mobasher, B. 1990, in *Proceedings of the ESO/EIPC Workshop on SN 1987A and other Supernovae* ed. I. J. Danziger, p595.

Nomoto, K., Shigeyama, T., Hashimoto, M., in *Proceedings of the ESO/EIPC Workshop on SN 1987A and other Supernovae* ed. I. J. Danziger, p325.

Panagia, N., Gilmozzi, R., Macchetto, F., Adorf, H.-M., Kirshner, R.P. 1991, *ApJL*, 380, L23.

Sonneborn, G., & Wamsteker, W. 1989, *ApJ*, 336, 429.

Sparks, W. B., Paresce, F., & Macchetto, D. 1989, *ApJL*, 347, L65.

Wampler, E. J., & Richichi, A. 1989, *A&A*, 217, L21.

Wampler, E. J., Richichi, A., & Baade, D. 1989, in *IAU Colloquium 120, Structure and Dynamics of the Interstellar Medium*, ed. G. Tenorio-Tagle, M. Moles, & J. Melnick (Berlin-Springer),

P180.

Wampler, E. J, Wang, L., Baade, D., Banse, K., D'Odorico, S., Gouiffes, C., & Tarenghi, M. 1990, *ApJL*, 362, L13 (W90).

Wamsteker, W., Gilmozzi, R., Cassatella, A., & Panagia, N. 1987, IAU Circ, No. 4410.

Wang, L. 1991, *A&A*, 246, L69.

Wang, L., D'Odorico, S., & Wampler, E. J. 1992, *IAU Circ.* 5449.

Wang, L., Dyson, J. E., & Kahn, F. D. 1993, *MNRAS*, 261, 391.

Wang, L., & Mazzali, P. A. 1992, *Nature*, 355, 58.

Wang, L., & Rosa, M. 1992, *ESO Messenger*, 67, 37.

Wang, L. & Wampler, E. J. 1992, *A&A*, 262, L9.

Woosley, S., 1988, *ApJ*, 330, 218.

Radio Emission from SN 1987A

By L. STAVELEY-SMITH[1], R. N. MANCHESTER[1], A. K. TZIOUMIS[1], J. E. REYNOLDS[1], AND D. S. BRIGGS[2]

[1]Australia Telescope National Facility, CSIRO, PO Box 76, Epping, NSW 2121, Australia

[2]National Radio Astronomy Observatory, PO Box 0, Socorro, NM 87801, USA

We review the first six years of radio observations of Supernova 1987A. The evolution can be divided into two phases: the initial radio outburst which lasted a few weeks, and the period from mid-1990 to the present, during which the radio emission has steadily increased. Both phases can be explained by a small fraction (0.1–0.5%) of the post-shock thermal energy being converted to energy in relativistic particles and magnetic fields, which give rise to synchrotron radiation. The optical depths, densities and density profiles for the pre-shocked circumstellar material are somewhat different for the two phases, but consistent with models of the density structure of the material within the circumstellar ring. New high-resolution radio observations show that the SN shock front is already at about three-quarters of the radius of the circumstellar ring, and that there exists a bright equatorial component of emission aligned with this ring which is probably due to a polar density gradient in the 'hourglass' structure.

1. Introduction

Radio studies of supernovae began with the detection of SN 1970G in M101 (Gottesman et al. 1972; Allen et al. 1976), though it wasn't for another decade that detailed radio light curves were available for a statistically useful sample of supernovae. Mainly through the work of Weiler, Sramek and collaborators (this volume) at the Very Large Array, there are now over a dozen well-studied examples of radio supernovae (RSN). These observations have been useful mainly in exploring the distribution of circumstellar material and therefore the progenitor mass-loss history (e.g. Weiler et al. 1989). However, other applications such as the local distance scale from geometric expansion (Bartel et al. 1985) and probing the interstellar medium through spectral line absorption studies (Ryder et al. 1993) are possible. Supernova 1987A has offered us a chance of exploring all of these aspects in detail, and also of following the evolution through the RSN phase and into the much later supernova remnant (SNR) phase, giving us for the first time a direct view of this transition. Additionally, the surprising fact that the progenitor was a blue supergiant, with a much lower density wind, allows us to study an example of a supernova that would not have been detected in the radio outside the Local Group of galaxies.

2. The Prompt Outburst

Radio emission from SN 1987A peaked at 140 mJy at 843 MHz about three days after the explosion (Fig. 1 and Turtle et al. 1987). Emission at higher frequencies peaked slightly earlier, probably as a result of lower thermal absorption. If modelled as the interaction of the shock with an r^{-2} stellar wind, Chevalier and Fransson (1987) estimate a mass-loss rate $\dot{M} = 8.8 \times 10^{-6}(V_w/550\mathrm{km\ s^{-1}})(u/26,000\,\mathrm{km\ s^{-1}})^{3/2}(T/10^5\mathrm{K})^{0.75}$ $\mathrm{M_\odot\ yr^{-1}}$, and a non-thermal energy density $\sim 0.1\%$ of the thermal energy density. Because of clumping and contributory processes such as internal free-free absorption, which can

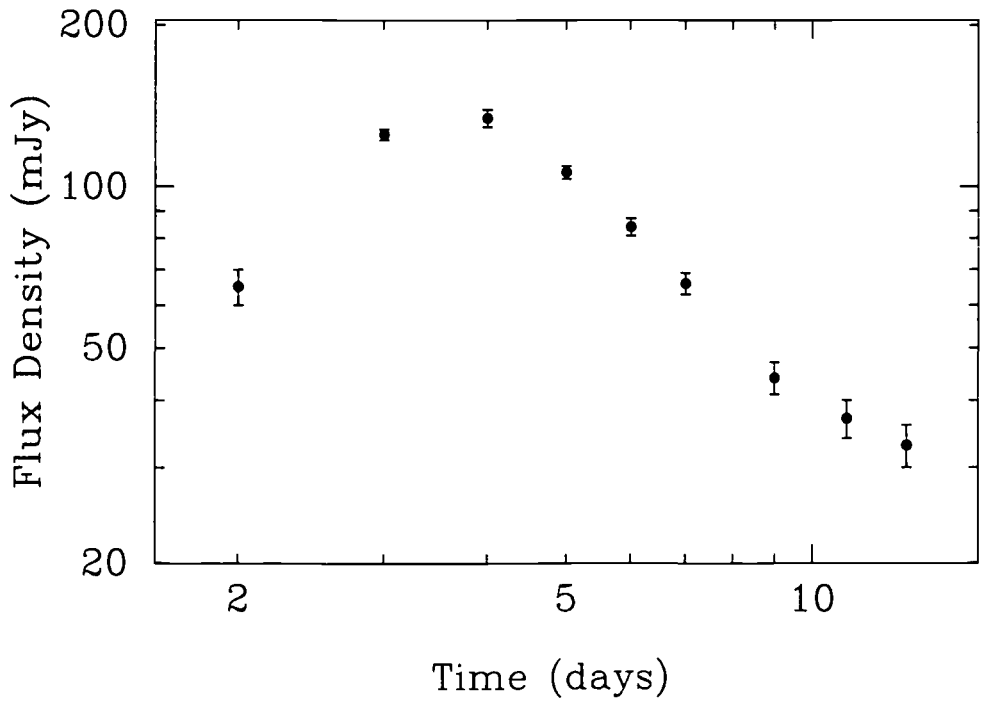

FIGURE 1. 843 MHz radio emission for SN 1987A for two weeks after outburst (from Turtle et al. 1987).

arise from Compton cooling of the ejecta at early times (Chevalier & Fransson 1987) and synchrotron self-absorption (Storey & Manchester 1987; Kirk & Wassmann 1992), this mass-loss rate is an upper-limit. After a few months, no radio emission was detectable.

Very long baseline interferometry observations were attempted very early on, but no emission was detected, implying that the radio photosphere was already resolved out (Jauncey et al. 1988). An initial shock velocity $> 19,000$ km s^{-1} was implied, which is consistent with early optical spectroscopy (Hanuschik & Dachs 1987).

3. Interaction with the Bubble

Radio emission was again detected from SN 1987A in 1990 July by the Molonglo Observatory Synthesis Telescope (MOST) at 843 MHz and the Australia Telescope Compact Array (ATCA) at 1.4 and 5 GHz (Turtle et al. 1990). Flux densities at these frequencies in 1990 mid-August were 4.5, 2.0 and 0.7 mJy, respectively. Since then, the flux density has increased steadily at all frequencies (Staveley-Smith et al. 1992) to its present level of $\sim$ 12 mJy at 5 GHz. ATCA observations at 8.6 GHz show that the radio remnant is $\sim 0''.5$ from the optical position reported for SN 1987A by White and Malin (1987), and others. Although higher than expected, it is not outside the errors present in the Perth 70 catalogue. Resolution of the slight position discrepancy awaits data from the Hipparcos satellite. The spectrum of the radio emission in this phase is non-thermal ($S_\nu \propto \nu^{-1.0}$), with no sign of a free-free turnover, in contrast to the prompt

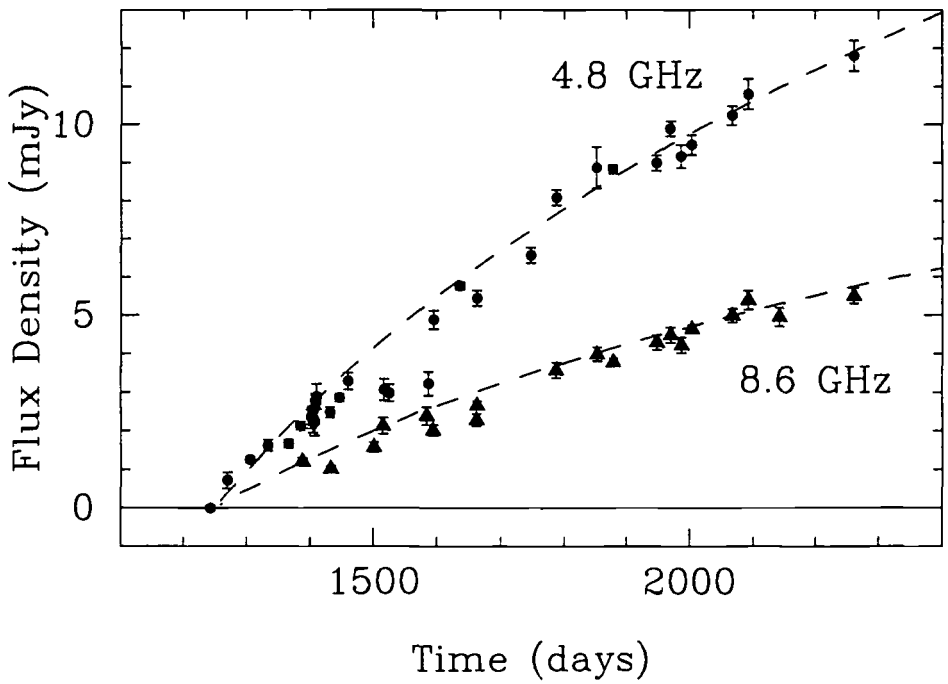

FIGURE 2. Radio emission from SN 1987A between days 1200 and 2300 at 4.8 GHz (circles) and 8.6 GHz (triangles). Observations taken with the Australia Telescope Compact Array. The fits are for the $\gamma = 3$, $s = 0$, $m = 0.65$ circumstellar interaction model described in the text.

outburst and the rising portions of the light curve of all previously observed RSNs. The 10 MHz – 10 GHz radio luminosity of 1.1×10^{33} erg s^{-1} (1993.3) is small compared with other SNRs and RSNs ($\sim 10^{-2}\times$ Cas A and $\sim 10^{-5}\times$ SN 1986J at its peak, Rupen et al. 1987). The minimum energy required in cosmic rays and magnetic fields to produce the synchrotron emission is $1.8 \times 10^{47}\phi^{3/7}$ erg (Pacholczyk 1970), assuming that 1% of the cosmic ray energy is in electrons, and a radiating volume of 0.017ϕ pc^3, where ϕ is the volume filling factor. The magnetic field at minimum energy is $3.4(\phi/0.2)$ mG, and the ratio of the minimum energy to the post-shock thermal energy is $5 \times 10^{-3}(\phi/0.2)^{-4/7}(n_e/6\mathrm{cm}^{-3})^{-1}(u/35,000\mathrm{km\ s}^{-1})^{-2}$, where n_e is the unshocked circumstellar thermal electron density and u is the shock velocity.

Fits to the observed flux density increase have been made by Ball and Kirk (1992). Using a diffusive shock acceleration model with a constant acceleration of relativistic electrons, they were able to produce acceptable fits to the early light curves at 843 MHz and 5 GHz. Chevalier (1992) produced a model in which the radio emission was generated by the interaction of the supernova shock wave with the density jump associated with the termination radius of the blue supergiant progenitor wind. The termination radius was calculated to be $\sim 3 \times 10^{17}$ cm or about half the radius of the circumstellar ring, which fitted with the measured radius of the radio source. However, this acceleration mechanism is limited in its duration by the acceleration timescale and the differential light travel time. Chevalier (1992) estimated a rise time of one year, whereas the light curve has not yet flattened off, even after three years (see Fig. 2).

4. Models

Given the steady increase of the radio emission in the second phase, it is more likely that there is continuous particle acceleration and magnetic field compression. The ultimate source of the energy required for this is the expanding shock wave as it interacts with the surrounding medium. We assume a circumstellar density profile $\rho_c \propto r^{-s}$, and an expansion law for the supernova shock front $r \propto t^m$. At a given radius the post-shock thermal energy density ($\rho_c u^2$) is therefore

$$E_{ps}(r) \propto \rho_o m^2 u_o^2 t^{2m-2-ms}. \tag{4.1}$$

The volume synchrotron emissivity, in the optically thin regime, is

$$j_\nu \propto K B^{\frac{1+\gamma}{2}} \nu^{-(\frac{\gamma 1}{2})}, \tag{4.2}$$

(Ginzburg & Syrovatskii 1965) where B is the magnetic field and γ is the index of the differential electron energy spectrum $N(E)dE \propto KE^{-\gamma}dE$. Following Chevalier (1982a), if we assume that a constant fraction of E_{ps} goes into relativistic electron energy density ($\propto K$) and magnetic field energy density ($\propto B^2$), then the volume synchrotron emissivity becomes

$$j_\nu \propto (\rho_o m^2 u_o^2)^{\frac{5+\gamma}{4}} t^{(2m-2-ms)\frac{5+\gamma}{4}} \nu^{-(\frac{\gamma 1}{2})}. \tag{4.3}$$

The monochromatic synchrotron luminosity L_ν depends on acceleration time scales, loss processes and differential light travel time, but taking the approximation $L_\nu = \frac{4}{3}\pi\phi j_\nu r^3$, we have:

$$L_\nu \propto \phi(\rho_o m^2 u_o^2)^{\frac{5+\gamma}{4}} t^{(22m-10-ms(\gamma+5)+2\gamma(m-1))/4} \nu^{-(\frac{\gamma 1}{2})}. \tag{4.4}$$

For $s = 2$ (the time invariant stellar wind solution), this reduces to a time-dependence $L_\nu \propto t^{-(5+\gamma-6m)/2}$, which is identical to the solution given in Chevalier (1982a). When combined with thermal absorption, this fits the observations of the prompt outburst (as above), and works reasonably successfully for other RSNs (Weiler et al. 1989). For SN 1987A, with a radio spectral index $\alpha = 1.0$ ($L_\nu \propto \nu^{-\alpha}$), and $\alpha = (\gamma - 1)/2$, we require an accelerating shock front ($m > 4/3$) to achieve a radio flux density that increases with time in the optically thin regime. This is unphysical.

However, the $s = 2$ solution is not appropriate at the present shock radius. Models of stellar evolution and observations of the photoionized medium around SN 1987A imply that the blue supergiant phase only lasted for 2×10^4 yr (Crotts & Heathcote 1991). Before this, the star was a red supergiant with a much denser, slower wind. The interaction of fast winds with slow-moving, or stationary, media has been described elsewhere (Dyson & de Vries 1972; Castor et al. 1975; Falle 1975). A number of distinct physical regions are formed (Fig. 3 and Wang & Mazzali 1992). Between the free winds from the blue and red supergiant phases, lies a shocked wind region of approximately constant density. In the case of SN 1987A, this lies between the circumstellar ring and the termination radius mentioned earlier. Can the synchrotron luminosity increase in the region? Take the simplifying case with $s = 0$ and assume that the fast wind termination radius is small enough that the solution remains self-similar. Then we have:

$$L_\nu \propto \phi(\rho_o m^2 u_o^2)^{\frac{5+\gamma}{4}} t^{(22m-10+2\gamma(m-1))/4} \nu^{-(\frac{\gamma 1}{2})}. \tag{4.5}$$

With $\gamma = 3$ (as above), L_ν will increase with time for $m > 4/7$. The expansion index m is related to the density profile of the stellar ejecta $\rho_* \propto r^{-n}$ by $m = (n-3)/(n-s)$ (Chevalier 1982b), which corresponds to $n > 7$. To apply this to SN 1987A, we take the above approximation and assume that the radio emission only turns on at time t_o after

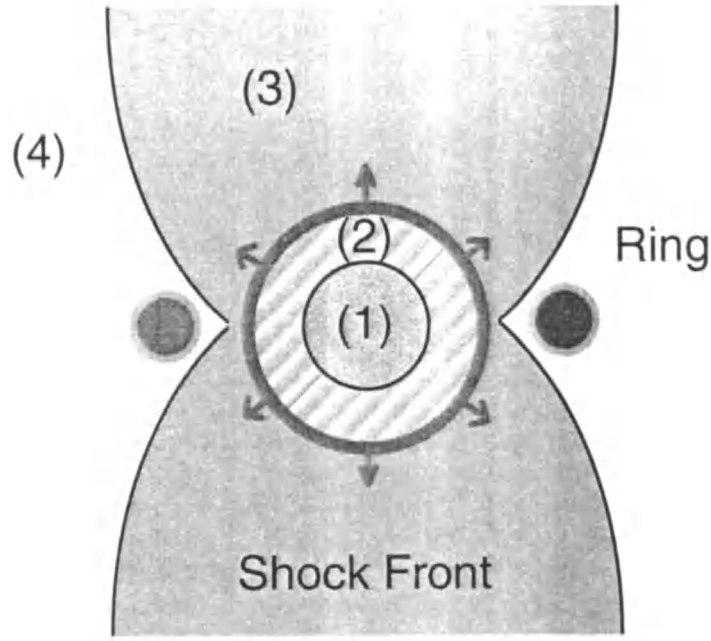

FIGURE 3. The relationship of the SN 1987A shock front to the circumstellar environment. Regions (1) and (2) have been overtaken by the SN shock. Region (1) was occupied by the free wind from the blue supergiant. Region (2) was occupied by the blue supergiant wind, heated up by interaction with the red supergiant wind; region (3) is the same as (2), but has yet to be hit by the SN shock. Region (4) is the free red supergiant wind which the SN shock has yet to reach.

the explosion:

$$\phi(r) = 1 - \left(\frac{t}{t_o}\right)^{-3m}, \qquad t \geq t_o \tag{4.6}$$

and $\phi(r) = 0$ otherwise. For times $t \geq t_o$, we obtain

$$L_\nu \propto \rho_o^2 (m u_o)^4 \left[1 - \left(\frac{t}{t_o}\right)^{-3m}\right] t^{7m-4} \nu^{-(\frac{\gamma-1}{2})}. \tag{4.7}$$

A reasonable fit to the data in Fig. 2 is obtained with $t_o = 1250$ days and $m = 0.65$, corresponding to $n = 8.6$ which is similar to the values obtained by Arnett (1988) from fits to the optical light curve at early stages. Between days 1400 and 1700 the fit in Fig. 2 is not good. The *constant* energy injection model of Ball & Kirk (1992) gives somewhat better fits up to day 1800 by assuming a two-component model and a finite electron acceleration time scale. However, their fit deviates beyond day 1800. Clearly, future work will require a better understanding of electron acceleration and shock deceleration processes, the incorporation of differential light travel time and modifications required by recent high-resolution imaging which imply deviations from spherical symmetry.

5. High-Resolution Imaging

The present size of the remnant (radius $\sim 0''.6$) unfortunately lies between the capabilities of 6 km ATCA (highest diffraction limit $0''.85$ at 9 GHz) and the Australian Long Baseline Array (lowest resolution $\sim 0''.1$ at 1.4 GHz, for an imaging observation). However, the increasing source strength of SN 1987A and recent improvements in ATCA

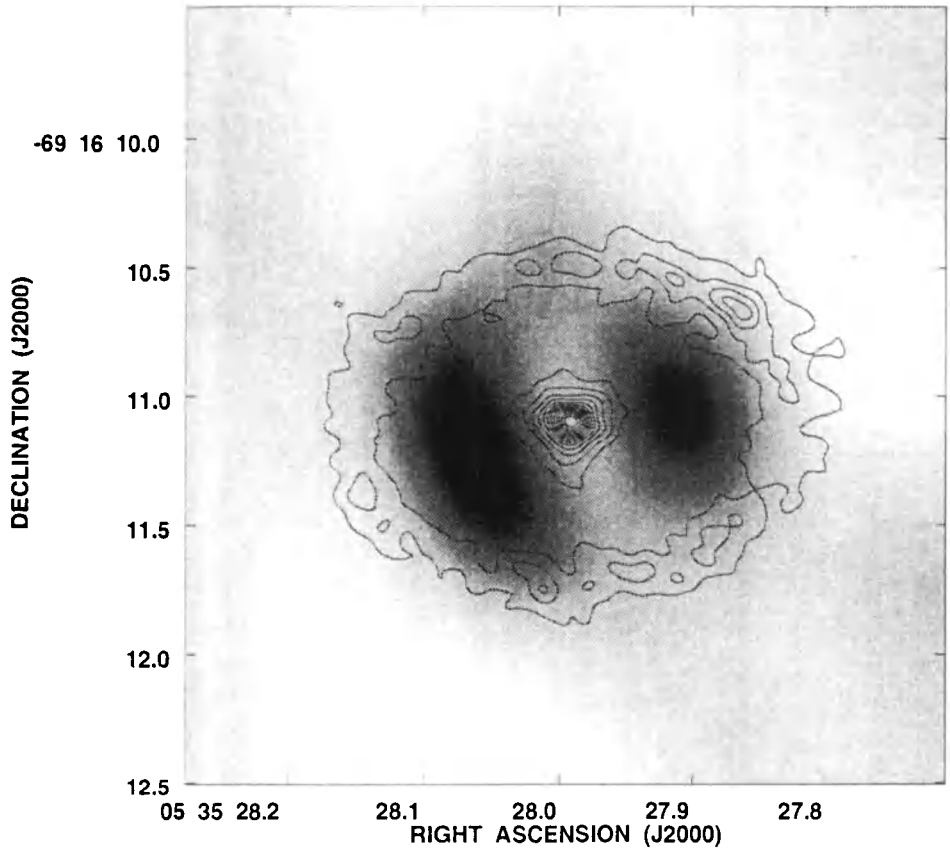

FIGURE 4. Super-resolved observation of SN 1987A at 8.8 GHz (ATCA). Data from 1992 October and 1993 January were used to make the image (Staveley-Smith et al. 1993). The resolution is $\sim 0''.5$. A contour plot of a Hubble Space Telescope [OIII] observation (Jakobsen et al. 1991) has been overlaid (assuming that the SN lies at the centre of the radio remnant).

receiver sensitivity have allowed the use of 'super-resolution' techniques which can improve on the canonical diffraction limit. Using very long integration times (3×12 hr) and high bandwidths (2×128 MHz) at 8.64 and 8.90 GHz during observations between 1992 October and 1993 January, Staveley-Smith et al. (1993) were able to employ maximum entropy deconvolution procedures to achieve an angular resolution of $0''.5$, or 3.6×10^{17} cm, a factor of 1.7 below the diffraction limit. This is sufficient to reveal that the remnant has a limb-brightened structure with two prominent hotspots aligned along the equatorial plane defined by the slightly more distant circumstellar ring (Fig. 4). The mean inferred radius of the remnant is 3.2×10^{17} cm, although model fitting suggests that the true outer radius is probably at $\sim 4.7 \times 10^{17}$ cm, which is 76% of the radius of the circumstellar ring.

The alignment of the radio hotspots with the circumstellar ring suggests that constant density approximation for region (3) needs modifying. The implication is that the shock wave is now passing through a denser medium in the equatorial plane. This may be due to a general polar density gradient, or from the shock wave passing through high density clouds sheared from the interface between regions (3) and (4).

The mean expansion rate (radius/time) inferred from visibility modelling is 34600 ± 1200 km s^{-1} at day 1500, but only 25900 ± 400 km s^{-1} at day 2060. This large apparent deceleration may be due partly to an increase in density towards the circumstellar ring,

which is reflected in the enhanced radio emission in this region. More likely, however, is that the remnant is changing in form and that the visibility modelling procedure has been accordingly biased. For example, it is likely that the volume filling factor ϕ has a time-dependence as discussed above. A true measurement of the deceleration awaits a second-epoch high-resolution observation. Such an observation will be the only direct way to predict the date of onset of the interaction between the shock front and the circumstellar ring.

REFERENCES

Allen, R. J., Goss, W. M., Ekers, R. D. & de Bruyn, A. G. (1976). Astr. Astrophys., **48**, 253–261.

Arnett, W. D. (1988). ApJ, **331**, 377–387.

Ball, L. & Kirk, J. G. (1992). ApJ, **396**, L39–L42.

Bartel, N., Rogers, A. E. E., Shapiro, I. I., Gorenstein, M. V., Gwinn, C. R., Marcaide, J. M. & Weiler, K. W. (1985). Nature, **318**, 25–30.

Castor, J., McCray, R. & Weaver, R. (1975). ApJ, **200**, L107–L110.

Chevalier, R. A. (1982a). ApJ, **259**, 302–310.

Chevalier, R. A. (1982b). ApJ, **258**, 790–797.

Chevalier, R. A. (1992). Nature, **355**, 617–618.

Chevalier, R. A. & Fransson, C. (1987). Nature, **328**, 44–45.

Crotts, A. P. S. & Heathcote, S. R. (1991). Nature, **350**, 683–685.

Dyson, J. E. & de Vries, J. (1972). A&A, **20**, 223–232.

Falle, S. A. E. G. (1975). A&A, **43**, 323–336.

Ginzberg, V. L. & Syrovatskii, S. I. A. (1965). Ann. Rev. Astr. Astrophys., **3**, 297–350.

Gottesman, S. T., Broderick, J. J., Brown, R. L., Balick, B. & Palmer, P. (1972). ApJ, **174**, 383–388.

Hanuschik, R. W. & Dachs, J. (1987). A&A, **182**, L29–L30.

Jakobsen et al. (1991). ApJ, **369**, L63–L66.

Jauncey, et al. (1988). Nature, **334**, 412–415.

Kirk, J. G & Wassmann, M. (1992). A&A, **254**, 167–176.

Pacholczyk, A. G. (1970). Radio Astrophysics, 171. San Francisco: Freeman.

Rupen, M. P., van Gorkom, J. H., Knapp, G. R., Gunn, J. E. & Schneider, D. P. (1987). Astr. J., **94**, 61–70.

Ryder, S., Staveley-Smith, L., Dopita, M., Petre, R., Colbert, E., Malin, D. & Schlegel, E. (1993). ApJ, **416**, 167

Staveley-Smith, L., Manchester, R. N., Kesteven, M. J., Campbell-Wilson, D., Crawford, D. F., Turtle, A. J., Reynolds, J. E., Tzioumis, A. K., Killeen, N. E. B. K. & Jauncey, D. L. (1992). Nature, **355**, 147–149.

Staveley-Smith, L., Briggs, D. S., Rowe, A. C. R., Manchester, R. N., Reynolds, J. E., Tzioumis, A. K. & Kesteven, M. J. (1993). Nature, 366, 166.

Storey, M. C. & Manchester, R. N. (1987). Nature, **329**, 421–423.

Turtle, A. J., Campbell-Wilson, D., Bunton, J. D., Jauncey, D. L., Kesteven, M. J., Manchester, R. N., Norris, R. P., Storey, M. C. & Reynolds, J. E. (1987). Nature, **327**, 38–40.

Turtle, A. J., Campbell-Wilson, D., Manchester, R. N., Staveley-Smith, L. & Kesteven, M. J. (1990). IAU Circular 5086.

Wang, L. & Mazzali, P. A. (1992). Nature, **355**, 58–61.

Weiler, K. W., Panagia, N., Sramek, R. A., van der Hulst, J. M., Roberts, M. S. & Nguyen, L. (1989). ApJ, **336**, 421–428.

White, G. L. & Malin, D. (1987). ESO Workshop on SN 1987A, 11-18. Garching: ESO.

Interaction of supernova ejecta with circumstellar matter and X-ray emission: SN 1987A & SN 1993J

By T. SUZUKI, K. NOMOTO, T. SHIGEYAMA, AND S. KUMAGAI

University of Tokyo, Bunkyo-ku, Tokyo 113, Japan

We perform hydrodynamical calculations of the collision between the supernova ejecta and circumstellar matter for SN 1987A and SN 1993J. For SN 1987A we predict light curves of X-ray emissions from the shocked ring. For SN 1993J, thermal X-rays from the shocked circumstellar matter can consistently account for the observations with ROSAT, ASCA, and OSSE.

1. Introduction

The supernova ejecta collides with the circumstellar matter (CSM) if its progenitor was undergoing significant mass loss. Shock waves arising from this collision compress and heat the ejecta and the CSM. The emission from the shocked material strongly depends on the density distributions of the ejecta and the CSM, thereby providing important information about the nature of the CSM.

2. SN 1987A

The images from the European Southern Observatory (ESO) (Wampler *et al.* 1990) and the Hubble Space Telescope (HST) (Jakobsen *et al.* 1991) revealed the presence of a ring-like structure at $\sim 6 \times 10^{17}$ cm from SN 1987A. The outermost part of the supernova ejecta is expanding at $\sim 10^4\,\mathrm{km\,s^{-1}}$ (Shigeyama & Nomoto 1990), thus being expected to collide with the ring at ~ 10 years after the explosion.

2.1. *Hydrodynamical model*

The progenitor of SN 1987A had once become a red supergiant (RSG) and then contracted to a blue supergiant (BSG) before the explosion (for reviews, see Arnett *et al.* 1989, Hillebrandt & Höflich 1989, Podsiadlowski 1992, and Nomoto *et al.* 1993a). This evolutionary scenario predicts that SN 1987A environment has been formed as follows: The progenitor blew a stellar wind with the velocity $\sim 10\,\mathrm{km\,s^{-1}}$ and the mass loss rate $\sim 10^{-5}\,M_\odot\,\mathrm{yr^{-1}}$ during the RSG stage, and with $\sim 550\,\mathrm{km\,s^{-1}}$ and $\sim 10^{-6}\,M_\odot\,\mathrm{yr^{-1}}$ during the BSG stage (Lundqvist & Fransson 1991). Consequently, the fast BSG wind struck the slow RSG wind, and a shock wave arising from this collision propagates outward through the RSG wind. The dense regions formed behind the shock wave by radiative cooling, which resulted in the high-density nebula. Formation of a ring as observed is due to, for example, the rotation of the progenitor or the magnetic field (Chevalier & Luo 1994; Washimi *et al.* 1994).

Our model consists of four components: the ejecta, the BSG wind, the RSG wind, and the ring (see Suzuki *et al.* 1993a for details). We adopt the model 14E1 by Shigeyama & Nomoto (1990) for the supernova ejecta, in which the density distribution in the outer envelope is power law as $\rho \propto r^{-8.6}$. We assume the density distributions of the BSG and RSG wind as $\rho_{\mathrm{BSG}}(r) = 9\,\mathrm{amu\,cm^{-3}}$ at $3 \times 10^{16}\,\mathrm{cm} < r < 5.7 \times 10^{17}\,\mathrm{cm}$ and

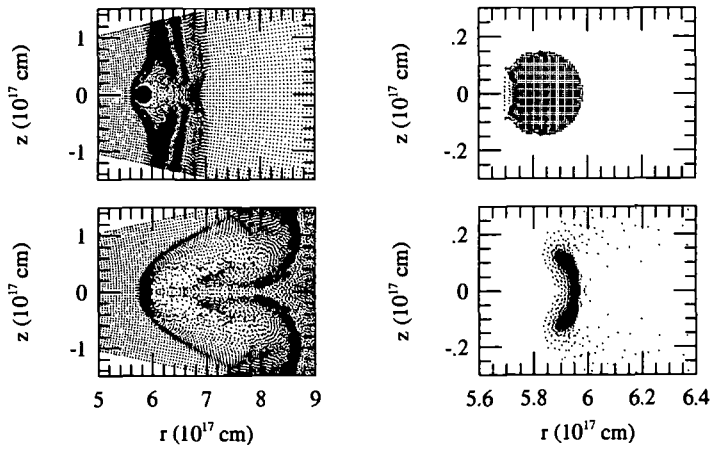

FIGURE 1. [*left*] Hydrodynamical evolution after the second collision. Shown are the configurations of particles at: $t = 16\,\mathrm{yr}$ (*upper*) and $t = 36\,\mathrm{yr}$ (*lower*). [*right*] Same as the *left* figures but the particles constituting the ring are plotted and the scale is magnified.

$\rho_{\mathrm{RSG}}(r) = 3 \times 10^3 (r/10^{17}\,\mathrm{cm})^{-2}\,\mathrm{amu\,cm^{-3}}$ at $r > 5.7 \times 10^{17}\,\mathrm{cm}$, respectively. The ring is sunk in the RSG wind and touched to the contact surface between the spherical RSG and BSG winds. Here we adopt $5.7 \times 10^{17}\,\mathrm{cm}$ for the distance from the supernova to the ring (Jakobsen *et al.* 1991; Panagia *et al.* 1991). We choose $0.05\,M_\odot$ and $2.4 \times 10^4\,\mathrm{amu\,cm^{-3}}$ respectively for the total mass and density of the ring (Lundqvist & Fransson 1991).

The expanding ejecta collides first with the BSG wind (*the first collision*). A shock wave generated by this collision propagates outward through the BSG wind and collides with the ring and the RSG wind (*the second collision*). We thus calculate the shock propagation from the first collision to the second collision with one-dimensional spherical Lagrangian Piecewise Parabolic Method (PPM) (Colella & Woodward 1984), and from the second collision with a two-dimensional cylindrical Smoothed Particle Hydrodynamics (SPH) (e.g., Benz 1990).

After the second collision three shock waves compress the ejecta, the RSG wind, and the ring, respectively (Fig. 1). When the shock wave reaches the edge of the ring at $t \sim 36\,\mathrm{yr}$, the ring material is most strongly compressed and the X-ray emission reaches the maximum as will be described below.

2.2. *X-ray emission*

We calculate the X-ray emission due to thermal bremsstrahlung from the shocked material with assumption that the shocked material is completely ionized. Figure 2 shows the X-ray light curve. X-rays from the ring are dominant because of its high density. The luminosity increases monotonically as the mass of the shocked region increases. At $t \sim 36\,\mathrm{yr}$ when the shock wave reaches the edge of the ring, the ring is compressed most strongly, so that the luminosity attains its maximum of $\sim 10^{37}\,\mathrm{erg\,s^{-1}}$. Afterwards the luminosity decreases because the ring expands adiabatically to cool. The luminosity from the ejecta and the BSG wind also increases monotonically since the second collision. The luminosity from the RSG wind increases for several years, and levels because the shock wave propagates into lower density layers.

Our calculations have shown that the collision between the ejecta and the ring will start at $\sim$ 12–15 years after the supernova explosion (see also Luo *et al.* 1994). The X-ray flux is predicted to reach the observable level with planned X-ray astronomical satellites. Detailed X-ray spectral predictions were made by Masai & Nomoto (1994).

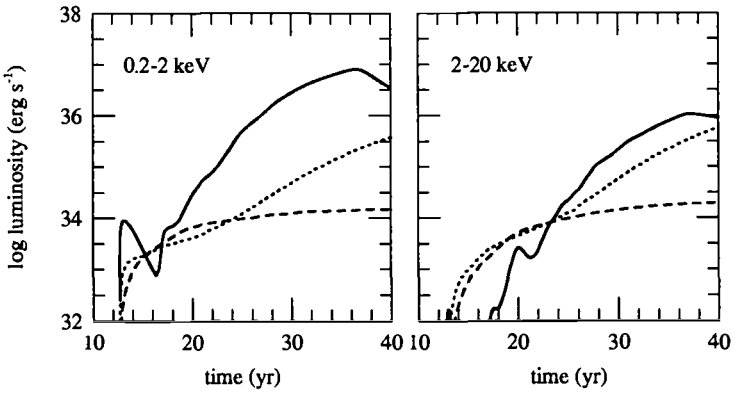

FIGURE 2. Calculated X-ray light curves of $0.2-2$ keV (*left*) and $2-20$ keV (*right*). Three lines indicate the components from the ring (*solid lines*), from the BSG wind and the ejecta (*dotted*), and from the RSG wind (*dashed*), respectively.

Then the future X-ray observations would provide critical information to diagnose the ring formation models (see Luo & McCray 1991, Wang & Mazzali 1992, and Lundqvist 1992).

2.3. *X-rays observed with ROSAT*

Recently, the positive detection of soft X-rays from SN 1987A with ROSAT has been reported (Gorenstein *et al.* 1994; Beuermann *et al.* 1994). The luminosity was $\sim 10^{34}$ erg during 1991–1992. Compared with predictions by our hydrodynamical calculations and others (e.g., Itoh *et al.* 1992; Suzuki *et al.* 1993a; Luo *et al.* 1994; Masai & Nomoto 1994), the observed X-rays must originate from interactions of SN 1987A with the BSG wind matter and the inferred CSM density is 20–30 amu cm^{-3}. This density is higher than that used in our calculations, which implies slightly larger deceleration of the shock wave propagation and thus a slight delay of the onset of the collision with the ring.

Currently only the upper limit has been set by the ASCA observations (M. Itoh, private communication). Since our calculations predict the increase in the X-ray luminosity as the shock wave sweeps more CSM, it is likely that ASCA will observe X-rays from SN 1987A within its lifetime.

3. SN 1993J

X-ray emissions from SN 1993J have been observed from its early stages with ROSAT at 0.1–2.4 keV (Zimmermann *et al.* 1993) and ASCA at 1–10 keV (Tanaka *et al.* 1993). Suzuki *et al.* (1993b) have modeled the X-ray emissions by carrying out hydrodynamical calculations of the collision between the supernova ejecta and the CSM. Suzuki *et al.* (1993b) have found that the observed features of X-rays can be accounted for with thermal bremsstrahlung emission from the reverse-shocked ejecta, if the expansion velocity at the outer edge of the ejecta before the collision is as high as $v_{\rm edge} \sim 5 \times 10^4\,{\rm km\,s^{-1}}$ and if the density gradient of the ejecta is relatively shallow ($\rho \propto r^{-n}$ with $n \sim 8$).

Recently Leising *et al.* (1994) have claimed that the OSSE on board Compton Observatory has detected hard X-rays from SN 1993J around day 10 and 35 after the explosion. The observed luminosity at 50–200 keV is $\sim 5 \times 10^{40}$ erg s^{-1} and the spectrum is approximately fitted to 90 keV thermal bremsstrahlung emission. The Comptonized hard X-rays due to the ^{56}Co decays have been predicted to reach maximum around day 50 but the flux around day 10 is well below the detection limit for the $0.07\,M_\odot$ ^{56}Co (Shigeyama

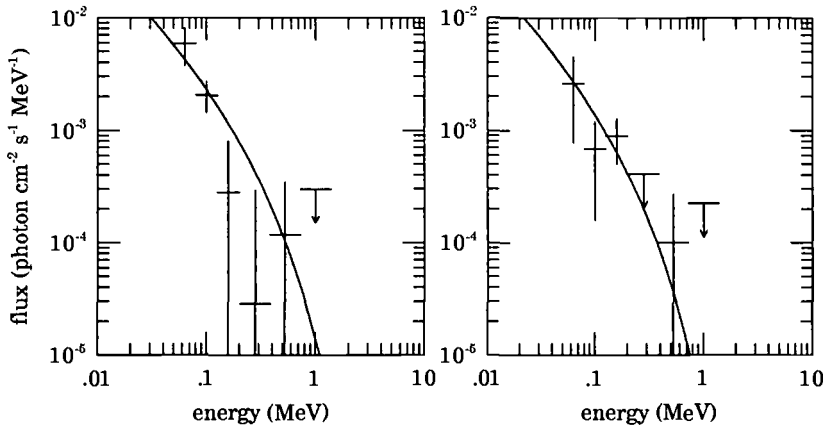

FIGURE 3. Calculated X-ray spectra at 10 (left) and 30 (right) days after the collision. Observations by OSSE during 9.9–15.4 (left) and 23.7–36.9 (right) days are plotted.

et al. 1994; Woosley *et al.* 1994). Compared with the calculated thermal emissions from the shocked ejecta (Suzuki *et al.* 1993b), the observed luminosity is much higher and the spectrum is much harder. These comparisons suggest that the observed hard X-rays are emitted from the shocked CSM rather than the ejecta (Leising *et al.* 1994).

3.1. *Hydrodynamical model*

Here we calculate the collision between the ejecta and the CSM for higher CSM densities than in Suzuki *et al.* (1993b). We also assume that the density distribution of the CSM is $\rho = \rho_0(r/2 \times 10^{14}\,\mathrm{cm})^{-1.8}$ at $r \geq 2 \times 10^{14}\,\mathrm{cm}$ rather than $\propto r^{-2}$, because the slow declines of the X-ray light curves observed with ROSAT (Zimmermann *et al.* 1994) and ASCA (Kohmura 1994) are better reproduced (see below). The outermost layer of ejecta is expanding homologously, so that its velocity distribution is $v = v_{\mathrm{edge}}(r/2 \times 10^{14}\,\mathrm{cm})$ and its density distribution is $\rho = \rho_{\mathrm{edge}}(r/2 \times 10^{14}\,\mathrm{cm})^{-n}$. In this study $\rho_{\mathrm{edge}} = 3\rho_0$ is assumed (see Suzuki *et al.* 1993b).

The collision forms two shock waves: a forward shock propagating into the CSM and a reverse shock back into the ejecta. If the density gradient of the ejecta is as low as $n \sim 8$, the X-ray luminosity is dominated by the shocked ejecta because of higher densities in the ejecta than in the CSM. On the contrary, if the density gradient is as steep as $n > 12$, the shocked outer ejecta form a dense shell due to cooling which absorbs X-rays from the reverse-shocked ejecta. Here we assume $n = 20$ as found in the hydrodynamical models for SN 1993J (Shigeyama *et al.* 1994), so that X-rays from the ejecta are absorbed by the dense shell. We also adopt $v_{\mathrm{edge}} = 5 \times 10^4\,\mathrm{km\,s^{-1}}$ and $\rho_0 = 1 \times 10^{-14}\,\mathrm{g\,cm^{-3}}$ which corresponds to $\dot{M} = 8 \times 10^{-5}\,M_\odot\,\mathrm{yr^{-1}}$ for the wind velocity of $10\,\mathrm{km\,s^{-1}}$. Since Coulomb collisions in the CSM are too slow to establish energy equipartition between electrons and ions, electron temperatures are significantly lower than ion temperatures. Yet, the electron temperatures in the CSM are still as high as $\sim 3 - 6 \times 10^9\,\mathrm{K}$ because of high shock speed.

3.2. *X-ray emission*

Figure 3 shows the calculated X-rays spectra of thermal bremsstrahlung emission from the shocked CSM at day 10 and 30, which are compared with the OSSE observations (Leising *et al.* 1994). Figure 4 shows the light curves of X-rays from the CSM compared with the ROSAT ($L_{0.1-2.4}$) and ASCA (L_{1-10}) observations and their ratio of $L_{0.1-2.4}/L_{1-10}$.

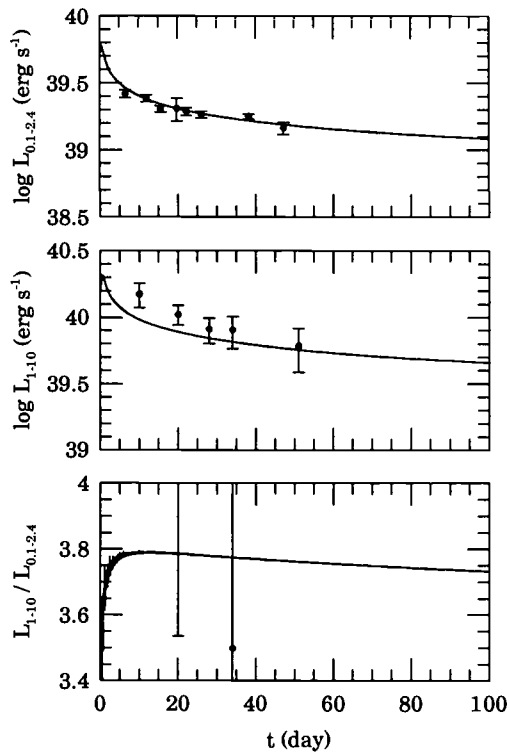

FIGURE 4. Calculated X-ray luminosities at $0.1 - 2.4\,\mathrm{keV}$ $L_{0.1-2.4}$ and $1 - 10\,\mathrm{keV}$ L_{1-10} and their ratio $L_{1-10}/L_{0.1-2.4}$ for the model with $v_{\mathrm{edge}} = 5 \times 10^4\,\mathrm{km\,s^{-1}}$ and $\rho_0 = 1 \times 10^{-14}\,\mathrm{g\,cm^{-3}}$.

These comparisons show that the thermal X-rays from the shocked CSM can indeed account for the hard X-rays observed with OSSE, ASCA, and ROSAT consistently.

To reproduce the observed hardness of the X-ray emission, the expansion velocity at the outer edge of the ejecta before the collision must be fairly high ($v_{\mathrm{edge}} \sim 5 \times 10^4\,\mathrm{km\,s^{-1}}$), which is consistent with a relatively low mass envelope of the progenitor, i.e., the type II-b supernova model. Soft X-rays from the shocked ejecta should be mostly absorbed, which require fairly steep density gradient of the ejecta. To reproduce the slow declines of the ROSAT curve, the CSM with $\rho_{\mathrm{CSM}} \propto r^{-1.8}$ leads to a better agreement, which suggests non-steady and/or asymmetric mass loss.

It should be noted that ASCA has observed iron line features (Kohmura 1994). This implies that the line forming region has a temperature of 2–3 $\times 10^8$ K, thus being the reverse-shocked ejecta. We speculate that a very narrow outermost layer of the ejecta had initially a shallow density gradient, thus undergoing little cooling. Certainly it is important to construct a consistent hydrodynamical model starting from more realistic configuration of the progenitor, i.e., the atmosphere with mass loss which smoothly connected with the CSM. The optical and X-ray light curves and spectra based on such a model would provide more accurate constraints on the still uncertain structures of the progenitor and the CSM. Continuing observations of X-rays with ASCA and ROSAT are highly valuable.

Acknowledgements

This work has been supported in part by the grant-in-Aid for Scientific Research (04640265, 05242102, 05242103, 05242207, 2539, 2780) of the Ministry of Education, Science, and Culture in Japan.

REFERENCES

Arnett, W. D., Bahcall, J. N., Kirshner, R. P. & Woosley, S. E. 1989, ARA&A, **27**, 629.

Benz, W. 1990, In *Numerical Modeling of Nonlinear Stellar Pulsation: Problems and Prospects*, ed. Buchler, J.R., (Dordrecht: Kluwer Academic Publishers), p. 269.

Beuermann, K., Brandt, S. & Pietsch, W. 1994, A& A, **281**, L45.

Chevalier, R. A. & Luo, D. 1994, ApJ, 421, 225.

Colella, P. & Woodward, P. R. 1984, J. Comp. Phys., **54**, 174.

Gorenstein, P., Hughes, J. P. & Tucker, W. H. 1994, ApJ, **420**, L25.

Hillebrandt, W. & Höflich, P. 1989, Rep. Prog. Phys., **52**, 1421.

Itoh, H., Masai, K. & Nomoto, K. 1992, In *Frontiers of X-ray Astronomy*, ed. Tanaka, Y. & Koyama, K., (Tokyo: Universal Academy Press), p. 383.

Jakobsen, P., *et al.* 1991, ApJ, **369**, L63.

Kohmura, Y. 1994, Ph.D. thesis, University of Tokyo.

Leising, M. D., *et al.* 1994, ApJ, 431, L95.

Lundqvist, P. 1992, PASP, **104**, 787.

Lundqvist, P. & Fransson, C. 1991, ApJ, **380**, 575.

Luo, D. & McCray, R. 1991, ApJ, **379**, 659.

Luo, D., McCray, R. & Slavin, J. 1994, ApJ, 430, 264.

Masai, K. & Nomoto, K. 1994, ApJ, 424, 924.

Nomoto, K., Shigeyama, T., Kumagai, S., Yamaoka, H. & Suzuki, T. 1993a, In *Supernovae (Les Houches Summer School, COURSE X, Session LIV)*, ed. Audouze, J. *et al.*, (Amsterdam: Elsevier Science Publishers B.V.), in press.

Nomoto, K., Suzuki, T., Shigeyama, T., Kumagai, S., Yamaoka, H. & Saio, H. 1993b, Nature, **364**, 507.

Panagia, N., Gilmozzi, R., Macchetto, F., Adorf, H.-M. & Kirshner, R. P. 1991, ApJ, **380**, L23.

Podsiadlowski, Ph. 1992, PASP, **104**, 1.

Shigeyama, T. & Nomoto, K. 1990, ApJ, **360**, 242.

Shigeyama, T., Suzuki, T., Kumagai, S., Nomoto, K., Saio, H. & Yamaoka, H. 1994, ApJ, **420**, 341.

Suzuki, T., Shigeyama, T. & Nomoto, K. 1993a, A& A, **274**, 883.

Suzuki, T., Kumagai, S., Shigeyama, T., Nomoto, K., Yamaoka, H. & Saio, H. 1993b, ApJ, **419**, L73.

Tanaka, Y. & the ASCA team. 1993, IAU Circ. No. 5753.

Wampler, E. J., *et al.* 1990, ApJ, **362**, L13.

Wang, L. & Mazzali, P. A. 1992, Nature, **355**, 58.

Washimi, H., Mori, M. & Shibata, S. 1994, Nature, submitted.

Woosley, S. E., Eastman, R. G., Weaver, T. A.,& Pinto, P. A. 1994, ApJ, 429, 300.

Zimmermann, H.-U., *et al.* 1993, IAU Circ. Nos. 5748, 5750, 5766.

Zimmermann, H.-U., *et al.* 1994, Nature, in press.

Historical Supernovae and Supernova Remnants

By ZHENRU WANG

Center of Astronomy and Astrophysics, CCAST World Laboratory
and Department of Astronomy, Nanjing University, Nanjing, China †

The oldest historical supernova (SN), recorded by ancient Chinese in 14th Century B.C. on pieces of tortoise shells or bones, is identified with the aid of modern space γ-ray observations. Hard X-rays with energy up to 20 keV were observed from IC 443 by the X-ray satellite *Ginga*. We infer from these observations the age of IC 443 is $\sim 1000 - 1400$ yrs. The result supports the hypothesis that IC 443 is the remnant of the historical SN 837 that occurred during the Tang Dynasty.

The association between the supernova remnant (SNR) CTB 80 and SN 1408 has been hotly debated for about ten years and is briefly reviewed and discussed here. A new picture is presented to explain this association.

High energy emission from historical SNRs can persist in a multiphase interstellar medium (ISM). As a result, the study of the relationship between SNRs and ancient guest stars has gained new vitality.

1. The First Supernova Observed by Mankind

SN 1987A, the first supernova observed by the naked eye in nearly 400 years, stimulates a high tide in supernova research. It also tempts us to ask: what is the earliest supernova recorded by mankind? Recently, we have discussed this topic in a few articles (Wang 1987 a,b; Xu, Wang & Qu 1992). The earliest supernova recorded by mankind is the great new star that occurred in 14th century B.C. recorded by the ancient Chinese on a piece of Tortoise shell or bone in Yin-Shang Dynasty (Fig. 1). The text of the inscription is shown in Fig. 2.

According to the above inscription, two conclusions can be drawn: (1) The ancient event was described as a great new star instead of a new star. This indicates that it should be very bright – bright enough to be considered as a nearby supernova. (2) Its visual position is near Antares (α Sco).

Searching within one degree of α Sco, we find the γ-ray source 2CG 353+16 detected by the European Satellite COS B (Swanenburg *et al.* 1981). On the basis of the above observed facts, I proposed that 2CG 353+16 might be the compact remnant of the great new star that occurred in the 14th Century B.C. (Wang 1987a, b). The main reason is that neutron stars can be formed in Type II supernova explosions and some well-known young neutron stars, such as Crab and Vela pulsars, have strong and stable γ-ray emission.

As shown by Mayer-Hasselwander (1980), the position of 2GC 353+16 is coincident with that of the ρ Oph cloud. Assuming that it is a supernova with maximum absolute magnitude $M_V = -18^m \pm 2.5$ (Trimble 1982) that exploded in the ρ Oph cloud, at a distance $D = 160$ pc (Encrenaz *et al.* 1975; Whetted 1974) and visual extinction $A_V = 7.1$ (Lose 1986), we estimate that it should have visual magnitude $m_V = M_V + A_V - 5 - 5\log D = -4.9 \pm 2.5$, which could be easily observed by the ancients.

† Project supported by the National Science Foundation of China and the State Education Commission of China

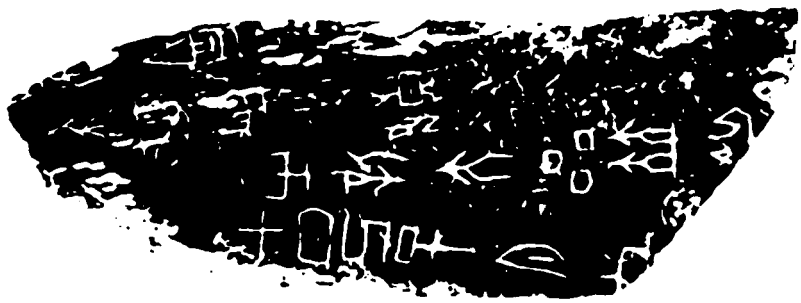

FIGURE 1. An Ancient Chinese Oracle Bone with Inscription about a Great New Star that Occurred in the 14th Century B.C.

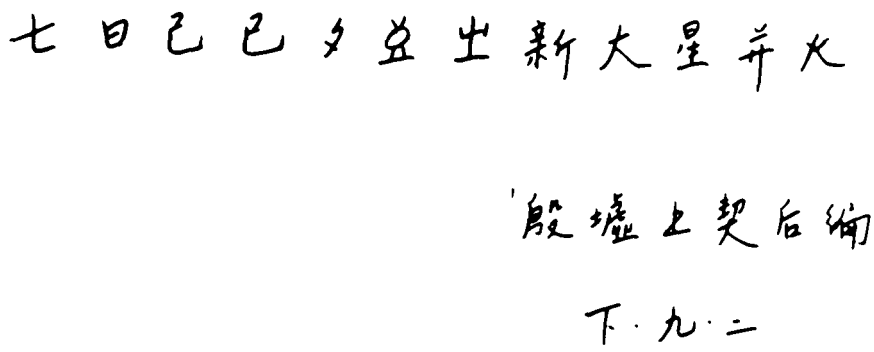

FIGURE 2. Chinese record of the appearance of the great new star observed in the Yin-Shang Dynasty. "On the 7th day of the month, a Ji-Si day, a great new star appears in company with Antares (α Sco)." [From the second part of the ninth chapter of the book *Yin-Xu-Shu-Qi-Hou-Bian*]

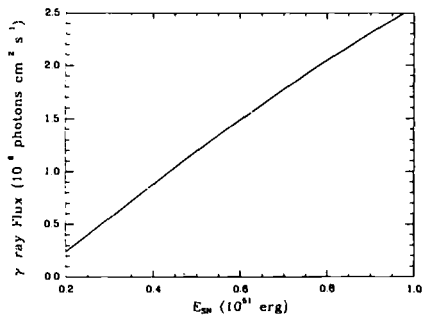

FIGURE 3. The relation between the γ-ray flux and the kinetic energy of the supernova explosion that occurred in the 14th century B.C.

FIGURE 4. Another oracle bone with inscription about a new star

FIGURE 5. Text of the inscriptions on bones or tortoise shells related to Fig. 3

γ-ray emission follows the decay of π_0 mesons produced from the interaction between atomic nuclei in the cloud and high energy protons in cosmic rays. Assuming that the observed γ-ray flux of 2GC 353+16 is due to this mechanism, Black & Fazio (1973) estimated that the mass of the ρ Oph cloud is about five times larger than that implied from its radio observation (Montmerle *et al.* 1983). (Hiller 1984) pointed out the difficulties in accounting for the γ-ray flux of 2GC 353+16 as a result of cosmic ray interactions in the ρ Oph cloud.

Recently we proposed (Xu, Wang, & Qu 1992) that the γ-ray flux of 2GC 353+16 may result from the interaction between protons in the molecular cloud and the high energy protons that originate from a supernova that exploded in a pre-supernova stellar wind cavity within the ρ Oph cloud. The calculated γ-ray photon flux is comparable with the observed one, $(1.1 \pm 0.4)\ 10^{-6}\ \mathrm{cm}^{-2}\ \mathrm{s}^{-1}$ (Fig. 3).

There are some other inscriptions about new stars or great stars on bones or tortoise shells from the Yin-Shang Dynasty. The most certain one among them is shown in Fig. 4 (Guo 1980). The text of its inscription is shown in Fig. 5. Some people considered it to be a record of the same event of Fig. 1. Since no position information is available in Fig. 4 or 5, it is difficult to say any more about it.

2. SNR IC 443 and the guest star AD 837 that occurred during the Tang Dynasty

IC 443 (G189.1+30, 3C157) has been studied extensively in radio, infrared, optical and X-rays. These studies show that there is a radio, optical and soft X-ray enhancement in its NE quadrant and a radio and optical shell with a diameter of about 40' (Petre *et al.* 1988). The NE enhancement is generally believed to be the result of an encounter between the shock and a dense HI cloud (De Noyer 1978). The distance of IC 443 is considered to be about 1.5 kpc (Fesen 1984). Strong infrared emission from IC 443, with luminosity $\sim 10^{37}$ ergs s^{-1}, was observed by IRAS (Mufson *et al.* 1986; Braun & Strom 1986; Dwek *et al.* 1987).

Hard X-rays from IC 443, with energies up to 20 keV, were observed by Ginga (Wang *et al.* 1992a). The X-ray spectrum of IC 443 can be fitted by non-equilibrium model of Masai (1984) with two thermal components, i.e., $kT_s = 0.9$ keV for the soft component and $kT_h = 14.3$ keV for the hard component, as shown in Fig. 6. The IPC map (Petre *et al.* 1988), shows that the soft X-rays come mainly from the NE quadrant. Subtracting this component, we can fit the spectrum of the hard component. The allowed region in the $T_h - T_s$ plane is shown in Fig. 7.

It is natural that the X-rays are brighter from areas with higher number density and lower temperature. This is just the case of the brighter NE quadrant of the IPC map of IC 443. Hence the hard X-ray emission should come from its SW and the W regions, i.e., those areas in the IPC map with lower surface brightness of soft X-rays. This conclusion is consistent with the locations of the error boxes of HED3 (2-60 keV) and MED (2-40 keV) indicated by the HEAO 1 A-2 observation and the IPC hardness ratio map (Petre *et al.* 1988). It is also consistent with the morphology of the multiwavelength map. The curvature radius of the NE area is smaller than the curvature radius of the SW area (Petre *et al.* 1988). This result is consistent with the idea that the SW quadrant has lower density, hence higher shock velocity and a larger curvature radius. We expect that future hard X-ray images from AXAF and ASTRO D will verify the above conclusion.

In a multiphase ISM, supernova explosions will give rise to various morphologies of SNRs. In general, we may expect the velocity of the blast wave to vary substantially in different parts of such a SNR. The morphology of CTB 109 is a wonderful example of the interaction between a supernova explosion and a molecular cloud, which has resulted in a semicircular shell (Wang *et al.* 1992b).

The multi-temperature model of IC 443 indicates an inhomogeneity in density. With a shock velocity corresponding to the hard component as high as $2.5 - 3.5 \times 10^3$ km s^{-1}, we can estimate shock crossing time to be 1000 – 1400 years. If so, the supernova should have occurred in historical times and its outburst may have been recorded by careful observers.

Shklovsky (1954) and Shajn & Gaze (1954a,b) suggested that IC 443 could be the remnant of an ancient guest star recorded in AD 837, because of its positional coincidence. However, Xi (1955) argued against this identification and suggested that the "guest star" was in fact Comet Halley. Moreover, the idea that IC 443 is an old SNR was supported by pre-Ginga observations. Now, however, the hard component observed by Ginga implies that the age of IC 443 is 1000 – 1400 years, which seems consistent with the idea of IC 443 being the remnant of the guest star AD 837. Thus it is imperative to investigate the Chinese records of this event.

Several records of a guest star are found in *Xin-Tang-Shu* (Ouyang and Song 1061) and Weng-Xian-Tong-Kao (Ma 1254). Let us first note the following record for the guest star: "on a Jia-Shen day (April 29) in the 3rd month of the 2nd year of the Tang-Wen-Zong

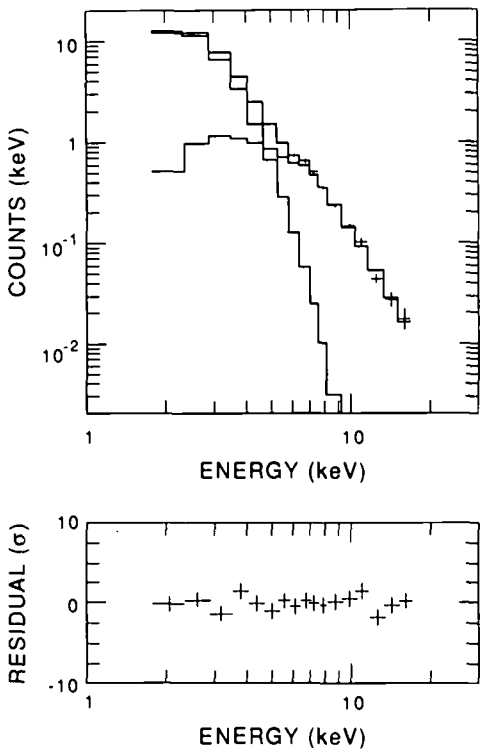

FIGURE 6. The observed spectrum and its best fit with two thermal components $T_h = 14.3$ keV and $T_s = 0.9$ keV

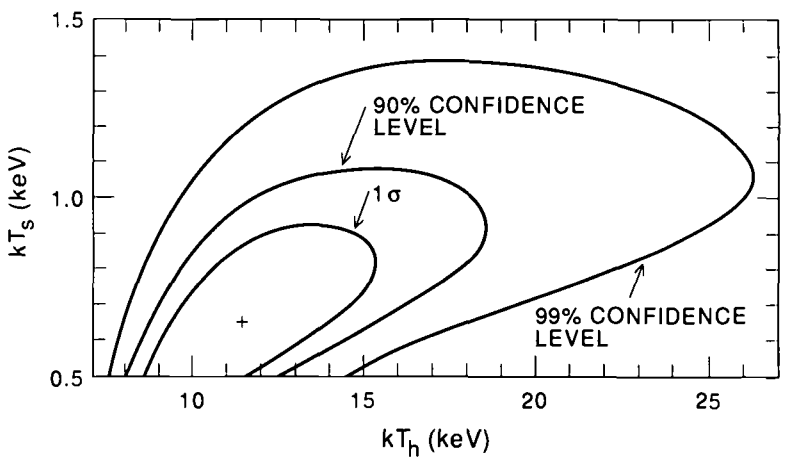

FIGURE 7. The allowed regions of electron of temperature for the two component thermal bremsstrahlung model

Kai-Cheng reign-period AD 837), a guest star appeared below the Dong-Jing (Gem., 22nd lunar mansion). On a Bing-Wu day in the fourth month (May 21), the guest star below the Dong-Jing went out of sight." (Ouyang and Song, 1061; Ma, 1254). See Figs. 8 and 9.

The guest star of AD 837 is included in the supernova catalogues of Biot (1846), Williams (1871), Lundmark (1921), Ho (1962) and Xi & Bo (1965). Some records are

FIGURE 8. A copy of the ancient record in Wen-Xian-Tong-Kao for SN 837

also found for Comet Halley, for example, the following comment in *Xin-Tang-Shu*: "On a Gui-wei day (April 28), it was about 3 ft long. It then disappeared at the right of Xuan Yuan (Leo). It is normal for a comet to point westward in the morning and eastward in the evening." (Ouyang and Song 1061). See Fig. 9.

Clearly, it is not possible for Comet Halley to move from Leo on 28 April to Gemini on 29 April, i.e., a distance of 45° in one day (Xi & Bo 1965), and then to stay at a fixed position in Gemini for 3 weeks. We believe that the records of AD 837 must refer to two separate events, one being a supernova and the other being Comet Halley. Because IC 433 has an age 1000 – 1400 years derived from the hard X-ray observations and a position in agreement with that of the guest star of AD 837, we conclude that it is the remnant of that event, the historical records of which are reproduced in Figures 8 and 9.

3. CTB 80 and the Historical Record of AD 1408

CTB 80 is a very fascinating object. Its nature has been hotly debated for more than ten years. Strom, Angerhofer & Velusamy (1980), Strom, Angerhofer & Dickel (1984),and Wang & Seward (1984) suggested that it is the remnant of SN 1408. However, people have become skeptical about this identification because the pulsar 1951+32 that was discovered within CTB 80 has a characteristic spin-down age $\sim 10^5$ yrs (Kulkarni *et al.* 1988). The detection of the infrared and HI shells around CTB 80 of diameter nearly 1° (Fesen *et al.* 1988, Koo *et al.* 1990) increased the suspicion that the AD 1408 event was a supernova (Stephenson & Yau 1986). Thus, the suggested association between CTB 80 and the AD 1408 has many difficulties. Let us discuss them one by one.

We first consider the historical records of the AD 1408 event. There are many such records. Some of them have been well introduced in recent papers and books (Li 1979, 1987; Wang & Seward 1984; Zhuang *et al.* 1987). Here we just mention a typical one, written in *Ming Taizong Shilu* (essential records of the Ming Dynasty Emperor Taizong) as shown in Fig. 10. The text of Fig. 10 can be translated as follows:

"On Oct. 24, 1408, at night, near the meridian, to the southeast of Niandao (along

FIGURE 9. A copy of the ancient record in Wen-Xian-Tong-Kao. Left – record for SN 837; right – record for Comet Halley

the line from 13, η, θ Lyr to 4, 17 Cyg, Fig. 11), there is a star like a lamp, its color is yellow and its lustre smooth, it shows up and does not move, it is a Zhou-bo, a virtuous star."

Similar texts were recorded during Sept. 10 to Oct. 24, 1408 in China. There are also Japanese records (Imaeda & Kiang 1980; Ho 1962; Xi 1982). The first Japanese record was dated July 14, 1408, 58 days earlier than the first Chinese record.

The most important key word in the records of the AD 1408 event is "Zhou-bo," a very unusual reference to its "nobility" or brightness. This word has been used to describe a guest star on only one other occasion – SN 1006, the brightest recorded supernova in history (see History of Song Dynasty, Astron. Chap. 9, P1226).

Another key phrase is "like a lamp." The only other known use of this phrase in astronomical records was in the historical record of SN 1572 in the Essential Records of the Ming Dynasty Emperor Shenzong. The key phrase indicating the position is the reference to the southwest of Niandao, exactly the location of CTB 80 (Fig. 11).

Summarizing the analyses of the above key words, we have little doubt that the event of AD 1408 was a very bright historical supernova located exactly at the center of CTB 80. This is the most compelling evidence for our conclusion.

Now let us discuss the age of PSR 1951+32. Pulsars are thought to spin down according to the law

$$P^2 - P_o^2 = 2P\dot{P}t\,, \tag{3.1}$$

where P and P_o are the period of a pulsar at the present time and at its birth time respectively. When $P \gg P_o$, we can infer the age from the characteristic spin-down time

$$t = \tau_c = P/2\dot{P} \tag{3.2}$$

where τ_c is the characteristic age of a pulsar. But otherwise, the age of a pulsar is given

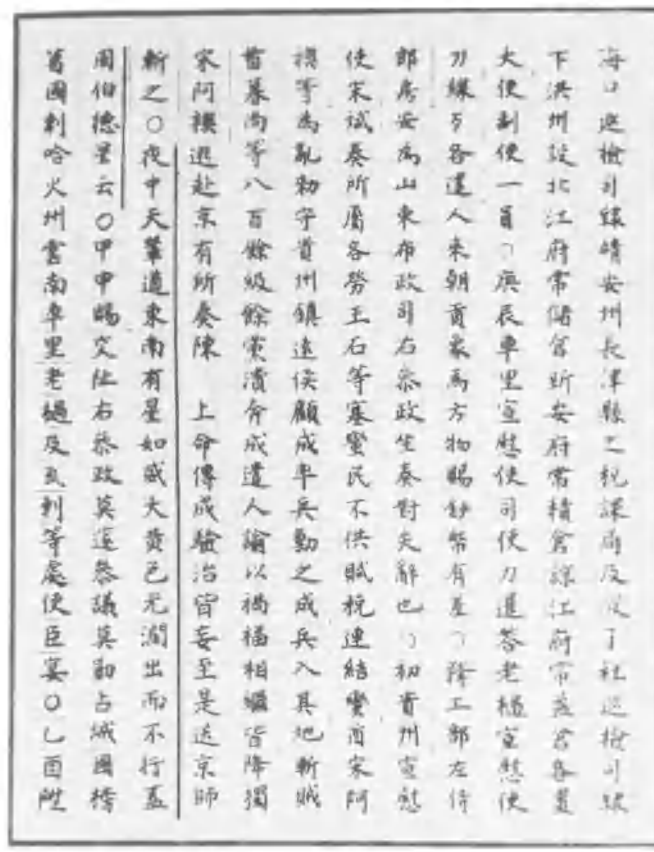

FIGURE 10. A copy of the ancient record for SN 1408.

by

$$t = \frac{P^2 - P_o^2}{2P\dot{P}} \tag{3.3}$$

Equation (3) shows that PSR 1951+32 is not necessarily as old as its spin-down time. It can be a young pulsar with age of 585 yrs if its initial period was $P_0 = 0.0394$ s. If so, there is no difficulty in assuming that PSR 1951+32 was formed in AD 1408.

Since PSR 1951+32 is the central source of CTB 80, the central part of CTB 80 should be the remnant of a Type II supernova explosion. Probably, the IR/HI shell that surrounds CTB 80 was formed some 10^5 yrs earlier by the explosion of another supernova in the same association – perhaps a binary companion of the progenitor of PSR 1951+32. Since then the progenitor of PSR 1951+32 could have moved to the west at a velocity ~ 200 km s^{-1}. The low velocity, high density filaments outside the central core of CTB 80 may be circumstellar matter ejected by the progenitor of PSR 1931+32 itself during its red giant stage. More quantitative work is needed to develop this new picture of the association between CTB 80 and SN 1408.

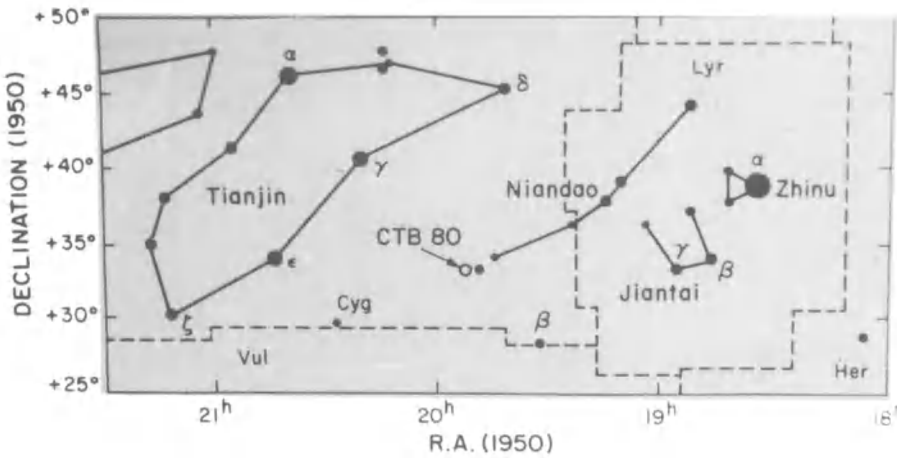

FIGURE 11. The position of CTB 80 related to Niandao

4. Conclusions

The most certain identifications between SNR and historical supernovae are as follows (Clark & Stephenson 1977):

G184.6-5.8(Crab)	SN 1054
G327.6+14.5	SN 1006
G120.1+1.4	SN 1572
G4.5+6.8	SN 1604

Some other probable, possible, and tentative identifications have been proposed by Shklovsky (1954) Shajn & Gaze(1954a,b), Xi & Bo (1955), Clark & Stephenson (1977), Li (1979), Strom *et al.* (1980), Wang *et al.* (1986) and Wang (1987a,b).

Before the 1980's, the identifications between SNRs and historical supernovae were based mainly on positional coincidences and estimates of the age of SNRs deduced from radio and optical observations. Moreover, the model of a uniform ISM was taken for granted. Such identifications easily gained acceptance. Now, we have begun to pay more attention, on the one hand to the X-ray and γ-ray observations, and on the other hand to the possibility that supernova progenitors are embedded in a multiphase medium. The possibilities include a molecular cloud, matter ejected in a stellar wind, the cavity due to a previous supernova, or a wind-driven bubble. As we have discussed, these scenarios give new views to the problem of determining the ages of some SNRs.

We expect that future observations of images of SNRs in hard X-rays and γ-rays will yield some exciting results to the age of SNRs. Theoretical and observational research on the nonuniform ISM and its effect on the evolution of SNRs will provide new paths to determining the ages of some SNRs. The task to identify SNRs with historical supernovae is far from complete, but continues with rosy prospects.

REFERENCES

Biot, M. E. 1846, Connais Temps, Additions, 60

Black, J. H. & Fazio, G. G. 1973, Ap. J., 185, L7

Braun, R. & Strom, R. G. 1986, A. Ap. 164,193

Clark, D. H. & Stephenson, F. R. 1977, The Historical Supernovae (Oxford: Pergamon Press)

DeNoyer, L. K. 1978 , M.N.R.A.S., 183, 18

Dwek, E., Petre, R., Szymkowiak, A., & Rice, W. 1987, Ap. J. 320, L27

Radio Emission from Supernova Remnants

By RICHARD G. STROM

Netherlands Foundation for Research in Astronomy, Radiosterrenwacht, Dwingeloo, The Netherlands

Most of the supernova remnants known in the Galaxy have only been detected at radio frequencies. The reason for this is absorption in the Galactic plane at both optical and X-ray wavelengths. All available evidence suggests that the shock fronts which accompany supernova remnants accelerate enough cosmic rays to GeV energies to produce readily detectable radio emission. This is fortunate, for it enables us to study remnants throughout the Galactic disk, although existing catalogues may be anywhere from 50 to 90 % incomplete. Cosmic rays and the magnetic fields in which they gyrate are the essential ingredients for producing the synchrotron radiation which is observed at radio frequencies. Various methods for estimating magnetic field strengths can be applied to a small number of remnants, and produce values not far from those based upon equipartition between the energy contents of particles and fields. From this, the particle energy content is derived for a number of objects.

1. Introduction

If we could view the heavens with radio eyes, then the majestic sweep of the Galactic disk would dominate the large scale structure we see. This radio version of the Milky Way has greater symmetry about a more dominant Sagittarius than its optical counterpart, as can be seen in the fine 408 MHz map of Haslam *et al* (1982). The main reason for this difference is simply dust, for although both stars and the cosmic rays responsible for decimeter radio emission are similarly distributed in the Galaxy, great clouds of the stuff obscure our optical vision, especially toward the Galactic center.

Returning to the radio view of things, if we sharpen our image of the Galactic plane to bring out more structural detail, improving the 1° resolution of the 408 MHz map by an order of magnitude (linearly), then some of the nonthermal radio emission becomes resolved into extended, by and large shell-like sources (e.g. Reich *et al*, 1990): supernova remnants (SNRs). Like the diffuse emission which dominates low frequency maps, the known SNRs in the Galaxy (e.g. Green, Appendix to these proceedings) lie near the equator, concentrated toward its central region (Fig. 1).

The shock waves produced by a supernova explosion heat the ambient gas to X-ray temperatures and simultaneously accelerate cosmic rays to GeV energies. This last fact is a fortunate turn of fate, for the X-ray emission, like the light from stars (or SNRs for that matter), is heavily absorbed by the interstellar medium. The energetically far less significant cosmic rays, corkscrewing their way through weak ambient magnetic fields, emit synchrotron radiation at radio frequencies which can traverse the entire Galactic disk essentially unattenuated. The existence of the majority of Galactic SNRs is known only from their radio emission.

In the remainder of this brief review, my goal will be to arrive at estimates for the cosmic ray and magnetic contents of typical SNRs, for they constitute the essential building blocks from a radio point of view. Along the way, I will touch upon SNR phenomenology and the morphological diversity to be found. Distances and their determination are also essential to deriving the physical parameters required, and finally methods for estimating magnetic field strengths round off the story.

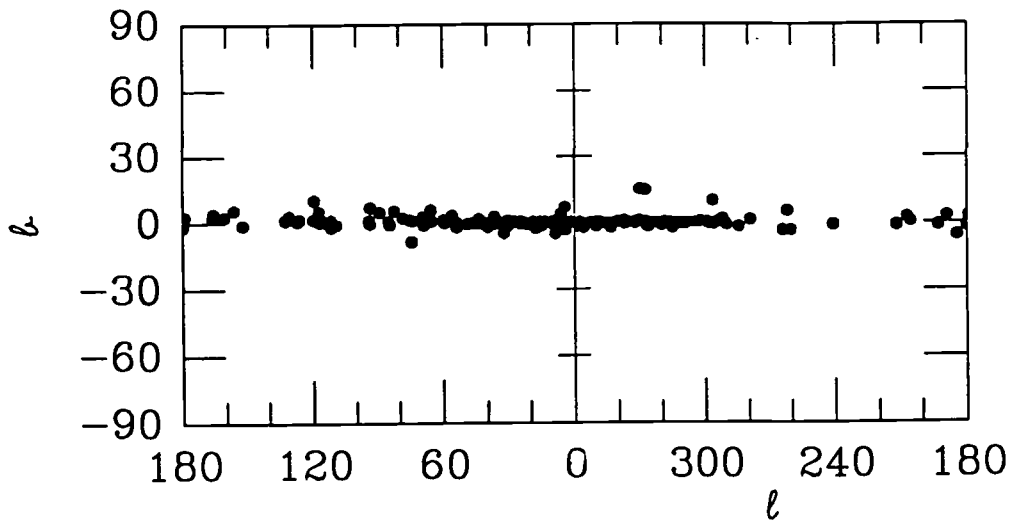

FIGURE 1. The distribution of the 182 known Galactic SNRs shown in Galactic coordinates.

TABLE 1. Statistics of Galactic supernova remnants

SNR or suspected SNR:		182
Morphological type —	Shell:	80 %
	Filled:	10 %
	Combination:	10 %

2. SNR phenomenology

As noted above, both gas heating and cosmic ray acceleration occur in the blast wave which accompanies all known SNRs. The intimate association between these two processes is illustrated by detailed comparison of the (thermal) X-ray emission with the (nonthermal) radio structure in such well-studied remnants as Kepler (e.g. Matsui *et al*, 1984), Tycho (Seward, 1990; Dickel *et al*, 1991) and the Cygnus Loop (Seward, 1990; Green, 1990). In general, morphological details correlate to a striking extent, although the brightness distributions do not necessarily do so.

We can discern two basic kinds of SNR morphology from the radio maps: the rim-brightened shells, and the more amorphous centrally-peaked Crab-Nebula-like remnants; a linear superposition of the two provides a third variant. The existing catalogue shows that, to the extent that they can be morphologically classified (and deviations of various kinds, as well as the quality of existing maps, leave the nature of some SNRs in doubt), the majority of remnants fall into the shell category, while the remainder are split roughly equally between the Crab-like and a combination of the other two. Table 1 summarizes the classification status of the 182 known SNRs (Green, op. cit.). It must be emphasized that such classifications are based upon radio structure alone. Optical emission appears to be much less complete, because of the capriciousness of both the relevant emission mechanisms and interstellar extinction. At X-ray wavelengths (where selective absorption can also play a role), the energy band – and hence gas temperature – may be relevant.

There are a number of radio shells which have centrally-brightened X-ray emission (e.g., W44, 3C 400.2, MSH 11−61A; see Seward, 1990). Of course the majority of Galactic SNRs, having only been detected in the radio, must necessarily be classified on the basis of radio maps.

It is generally accepted that the Crab-type remnants owe their striking characteristics (morphology, synchrotron emission, flat spectrum), just like their renowned namesake, to power released as an energetic neutron star spins down. It is clear from recent discoveries of low-luminosity mini-Crab remnants associated with the pulsars PSR 1951+32 (SNR CTB 80; Strom, 1987), PSR 1757−24 (Milne 56; Frail & Kulkarni, 1991) and others, that such objects cover a wide range of luminosities, although the central pulsar has yet to be seen in a number (like 3C 58 and CTB 87). In any event, the center-filled remnants, constituting a minority of known SNRs, – though an important minority, it must be said, – and being the topic of one of the other discourses (by Chevalier), will not figure prominently in the rest of this review.

Before resuming the thread of my discussion of SNRs in general, however, a word of caution about the statistics reflected in Table 1 is in order. On the face of it, it would seem that only a minority of SNRs comprise neutron-star-driven nebulae, while the majority of supernovae are believed to leave behind neutron stars (see, e.g., Van den Bergh & Tammann, 1991; and Van den Bergh's contribution to these proceedings). While it may be, as has often been conjectured, that the pulsar-nebulosity phase is relatively short-lived compared to shell SNRs, it is not improbable that the former are under-represented in existing catalogues. A thorough understanding of the numerous selection effects to which SNRs have been subjected is required before attempting statistical analyses of data such as contained in Table 1.

One simple inference which can be drawn, although it too should be regarded with a degree of circumspection, has to do with the (radio) SNR content of the Galaxy. If the *average* age attained by SNRs before dissipation is as much as 100 000 yr, and if supernovae occur at the rate of 2 per century (see Van den Bergh & Tammann, 1991; and Van den Bergh, these proceedings), then the Milky Way should contain some 2 000 remnants, about 10 times the number catalogued. If this age is an overestimate, and 20 000 yr is nearer to the mark, then we have discovered nearly half of the Galactic population. The truth probably lies somewhere between these two very approximate estimates.

Besides arming us to slice through the interstellar fog of dust and ionized gas (as well as providing an additional strategem for pinpointing shock fronts), what does the radio emission from SNRs tell us? In the first place, the very existence of (synchrotron) radiation indicates the presence of high energy cosmic rays and magnetic fields to an enhanced degree. The strength of this emission provides information about the (minimum) energy densities present, while its power law spectral index, derived from the energy spectrum of the emitting particles, relates to the acceleration process. Radiation losses will produce a spectral break whose frequency is related to the source age and magnetic field strength. The polarization enables us to probe the magnetic fields within the SNR emission, and radio techniques have provided estimates of the distances to a number of remnants. Let us begin with this last point, as we require distances to calculate many physical parameters.

3. Determining remnant distances

As usual in astronomy, distance determinations are fraught with a variety of uncertainties, and SNRs are no exception. There have been two widely used techniques based

upon radio measurements, one of which can be said to be fairly reliable (though not without its difficulties and limitations), while the other should be regarded as having considerable shortcomings. In addition, there are several other purely radio techniques which can either be applied to only a few objects, or require a number of assumptions.

The most reliable distance determinations by a radio technique are based upon the kinematical distances to clouds which absorb radiation from the object in question. The so-called *HI absorption* technique (other radio lines – OH, H_2CO – can also be used, but are generally weaker) provides a *lower limit* to the remnant's distance, and is obviously only as good as our knowledge of Galactic kinematics. Because of irregular motions and line broadening due to internal dispersion, the technique gives greater fractional accuracy at larger distances; it is essentially useless for objects closer than 1 kpc. In directions where the Galaxy displays large kinematic anomalies, – the SNR Tycho provides an example (Albinson *et al*, 1986), – interpretation of the data is not straightforward. Moreover in the two inner quadrants, where the line of sight crosses the solar circle, the velocities are double-valued, while the technique breaks down toward the Galactic center and anticenter, where circular orbital motion is transverse to the line of sight.

The most dubious, though widely-used, technique is based on the presumed relationship between surface brightness and remnant diameter (or $\Sigma - D$). In its original form, it makes the tacit assumption that all remnants (or at least those of uniform morphological type) will have about the same radio luminosity at a given linear diameter. Despite refinements which attempt to account for distance from the Galactic plane (Caswell & Lerche, 1979), the practical utility of the technique is limited at best (Berkhuijsen, 1986; Green, 1984). Moreover, as Green (1991) has shown, the "relationship", such as it is, arises to a considerable extent from a lack of low surface brightness remnants to which existing SNR surveys are insensitive anyway. What does seem to be a genuine effect, at least to the extent that it is not caused by such instrumental selection, is an upper envelope to the distribution of Σ vs. D: There appears to be a maximum Σ which a SNR of given D can attain. In this limited sense, the $\Sigma - D$ relationship can be used to set an upper limit to a remnant's distance, but it should never be forgotten that the actual distance could be as much as an order of magnitude smaller.

Another radio method for determining SNR distance is applicable to the minority of remnants associated with a pulsar. A pulsar's dispersion measure is related to its distance, which can then be derived. Such distances depend upon models of the electron density in the Milky Way (Taylor & Cordes, 1993), and have an uncertainty of about 50 %. Most of the remaining methods rely upon parameters derived from optical or X-ray observations.

4. Physical parameters

With distances for a significant number of SNRs, we are in a position to calculate their radio-derived properties. The simplest of these is the average diameter, which is based upon the angular diameters found in Green's (1991) latest compilation. Distances are also drawn from Green, although a few have been augmented from the general literature. A histogram showing how Galactic SNRs are distributed according to diameter is shown in Fig. 2 (*upper*), while a similar plot for remnants in the Magellanic Clouds appears in Fig. 2 (*lower*). The deficiency of small-diameter SNRs in the latter is probably due to the limited resolution with which candidate radio sources have been studied in the Clouds. Apart from this difference, the two distributions are roughly similar, suggesting that the Galactic distances used are fairly accurate. From the distances and 1 GHz flux densities, it is also possible to calculate the monochromatic luminosities, and these are shown for the

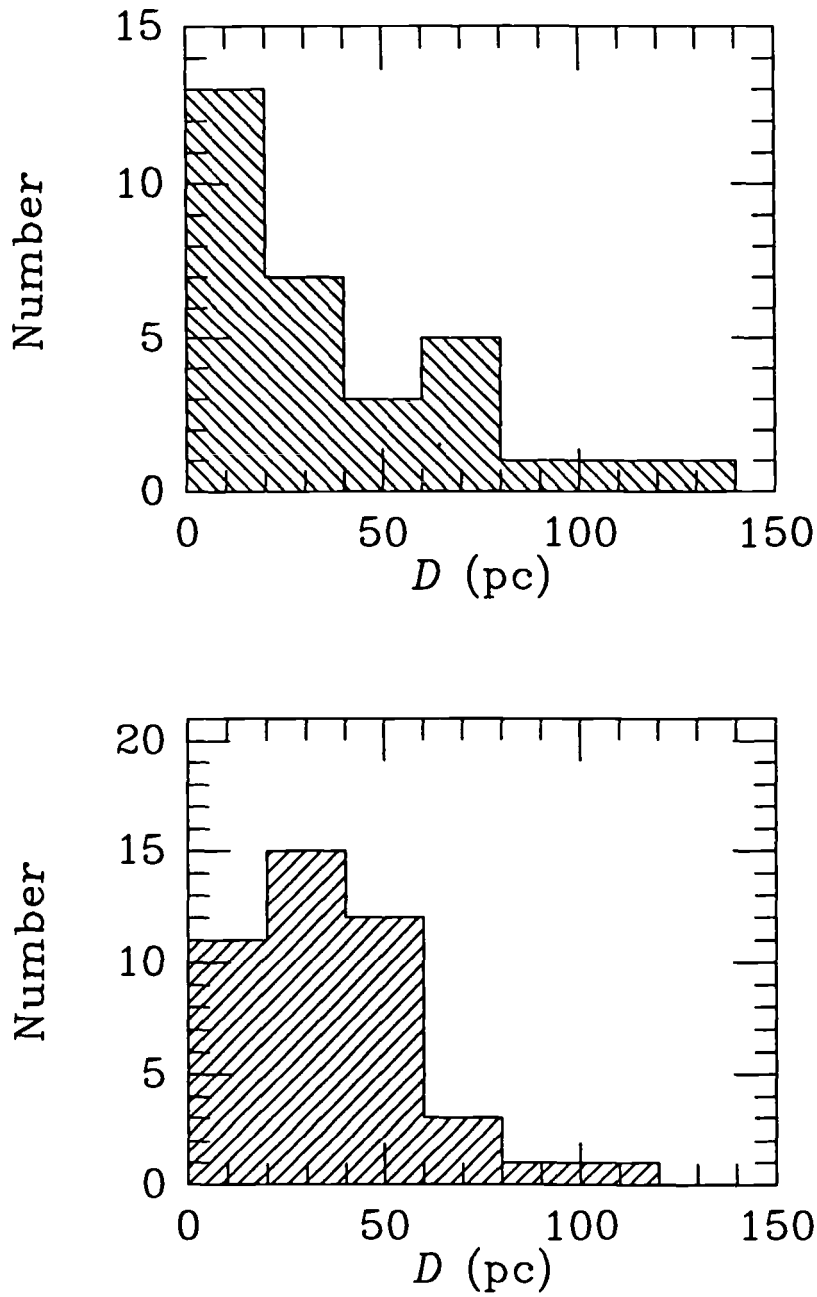

FIGURE 2. (*upper*) The diameters of Galactic SNRs with well-determined distances. (*lower*) The diameters of SNRs in the Large and Small Magellanic Clouds. The ordinates have been scaled to give the two histograms equal areas.

Galactic remnants in Fig. 3, where the median value is $L_{1\mathrm{GHz}} \simeq 4 \times 10^{16}\,\mathrm{W\,Hz^{-1}}$. (The distribution for SNRs in the Magellanic Clouds is similar, except that there are relatively fewer low luminosity remnants, as might be expected from a flux-limited sample.)

The rate at which synchrotron radiation is emitted from a source depends upon both

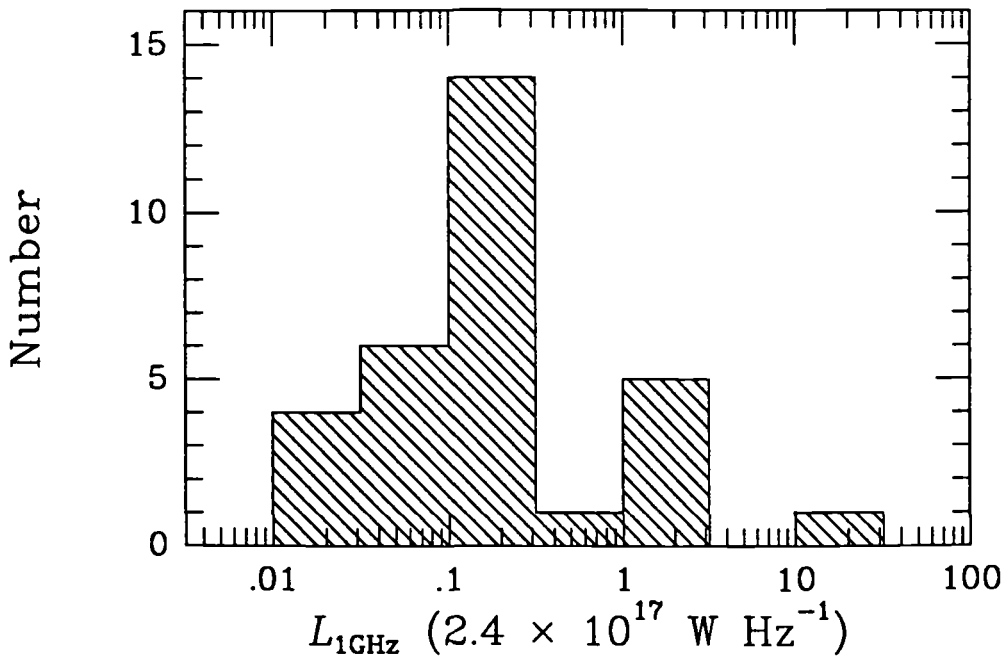

FIGURE 3. The 1 GHz luminosities of Galactic SNRs with well-determined distances.

the particle energy, E, and the magnetic field strength, B:

$$\frac{dE}{dt} \propto E^2 B^2, \tag{4.1}$$

and of course the total power radiated is proportional to the number of emitting particles at a given energy, $N(E)$. Consequently, we need additional information about a source's magnetic field if we are to determine the amount of energy in cosmic rays. Clues about a remnant's magnetic properties are contained in the polarized component of its nonthermal emission.

Synchrotron radiation can be polarized by as much as 70 %, although field irregularities and projection effects usually reduce measured values considerably. The plane of the linearly polarized component at a sufficiently short wavelength can be used to deduce the magnetic field direction projected onto the sky. Low resolution maps of the magnetic field have been constructed in this way for over two-dozen remnants (see Milne, 1987), and they show that the shells tend to have either radially- or tangentially-directed fields. In all young (less than a few thousand years old) shell SNRs, the field is found to run radially. In larger, more mature remnants, the tendency is tangential, although there are objects where it is almost unidirectional, while in others it is complex. The degree of polarization at short wavelengths, which in most remnants is considerably less than the theoretical $\simeq$ 70 %, provides information about how much disorder there is.

Although the linear polarization does not directly depend upon the magnetic field strength, it can provide us with some information via the Faraday effect. The amount of Faraday rotation produced in a source depends upon the rotation measure, $\propto \int n_e \mathbf{B} \cdot \mathbf{dl}$. If the electron density, n_e, can be independently determined (for example, from X-ray observations), and the source depth (**l**) also, then some estimate of the magnetic field strength can be made. This technique has been applied to the young remnant of Kepler's

supernova (Matsui *et al*, 1984), and the resulting field strength was found to be near equipartition.

Another way of determining the magnetic field strength is from the spectral break caused by radiation losses. If the initial maximum energy of particles is arbitrarily high, a simple integration of (4.1) shows that after a time $t_1 \propto E_1^{-1}B^{-2}$, all of the original electrons will have energies $E < E_1$. Even if there is particle reacceleration, the spectrum will steepen above a frequency, $\nu_b = 1.33 \times 10^{16} B_{-5}^{-3} t_4^{-2}$ Hz, where B_{-5} is in units of 10 μG and t_4 in 10^4 yr. For ν_b to fall within the radio regime, old objects with strong magnetic fields are required. The spectral break has been observed in the Crab Nebula, but at infrared wavelengths, where a time-averaged magnetic field strength of 440 μG is inferred (Strom & Greidanus, 1992). Infrared measurements in other SNRs like Cas A, where strong magnetic fields might be expected, are hampered by intense emission from shock-heated dust (e.g., Braun, 1987). A possible effect may have been detected in the flat spectrum remnant 3C 58, although interpretation of the data is not straightforward (Green & Scheuer, 1992). So determination of field strengths through the spectral break, which in any event requires an age estimate, is unlikely to be a realistic possibility in most SNRs.

For a final method of estimating magnetic field strengths, we return to polarization measurements, although now not of linear polarization but the much weaker circular variety. Incoherent synchrotron emission produces small amounts of circular polarization, the magnitude of which depends upon the magnetic field strength and frequency:

$$\frac{V}{I} \simeq 0.1 \left(\frac{B_{-4}}{\nu_{300}} \right)^{\frac{1}{2}} \%, \tag{4.2}$$

where V and I are the Stokes parameters for circular polarization and total intensity, and ν_{300} is the frequency in units of 300 MHz. Even at low frequencies, only sources with fairly substantial magnetic field strengths will produce measurable amounts of circular polarization. Recent 92 cm observations with the Westerbork Telescope suggest that Cas A may have magnetic fields of several hundred μG, although the interpretation is by no means straightforward.

For several of the young, bright SNRs, the magnetic field strengths appear to lie within a small factor of the equipartition value. This is perhaps not too surprising, but since it seems to happen in some of the youngest remnants, there may be some hope that it holds true in the rest. The equipartition magnetic field strengths of several dozen SNRs range from just under 10^{-5} G, to somewhat over 10^{-4} G, with a median value of 3×10^{-5} G. The minimum energies of the same remnants span $10^{48} - 3 \times 10^{50}$ erg (median value of 3×10^{49} erg). The smallest energies are associated with the most compact (youngest) remnants. Since they contain large kinetic energies, while the extended (but old and slowly expanding) SNRs have less kinetic energy, the distribution is consistent with a transfer of energy from gaseous motion to cosmic rays.

Acknowledgements

I am grateful to the IAU for providing me with a travel grant to attend Colloquium 145. The Westerbork Radio Observatory is operated by the Foundation for Research in Astronomy, which receives financial support from the Netherlands Organization for Scientific Research (NWO).

REFERENCES

Albinson, J. S., Tuffs, R. J., Swinbank, E. & Gull, S. F. (1986). MNRAS, 219, 427
Berkhuijsen, E. M. (1986). A&A, 166, 257
Braun, R. (1987). A&A, 171, 233
Caswell, J. L. & Lerche, I. (1979). MNRAS, 187, 201
Dickel, J. R., Van Breugel, W. J. M. & Strom, R. G. (1991). AJ, 101, 2151
Frail, D. A. & Kulkarni, S. R. (1991). Nature, 352, 785
Green, D. A. (1984). MNRAS, 209, 449
Green, D. A. (1990). AJ, 100, 1927
Green, D. A. (1991). PASP, 103, 209
Green, D. A. & Scheuer, P. A. G. (1992). MNRAS, 258, 833
Haslam, C. G. T., Salter, C. J., Stoffel, H. & Wilson, W. E. (1982). A&A, 47, 1
Matsui, Y., Long, K. S., Dickel, J. R. & Greisen, E. W. (1984). ApJ, 287, 295
Milne, D. K. (1987). Aust. J. Phys., 40, 771
Reich, W., Fürst, E., Reich, P. & Reif, K. (1990). AAS, 85, 633
Seward, F. D. (1990). ApJS, 73, 781
Strom, R. G. (1987). ApJ, 319, L103
Strom, R. G. & Greidanus, H. (1992). Nature, 358, 654
Taylor, J. H. & Cordes, J. M. (1993). ApJ, 411, 674
Van den Bergh, S. & Tammann, G. A. (1991). ARA&A, 29, 363

The Distribution of Supernova Remnants in the Galaxy

By D. A. GREEN

Mullard Radio Astronomy Observatory, Cavendish Laboratory, Madingley Road, Cambridge CB3 0HE, UNITED KINGDOM

Observational selection effects and the lack of accurate distances for most Galactic SNRs pose problems for studies of the distribution of SNRs in the Galaxy. However, by comparing the observed Galactic longitude distribution of high surface brightness SNRs with that expected from simple models — which avoids some of the problems with selection effects and the lack of distances — a Gaussian scale length of ≈ 7 kpc in Galactocentric radius is obtained for SNRs.

1. Introduction

The distribution of SNRs in the Galaxy is of interest for many astrophysical studies, particularly in relation to their energy input into the ISM and for comparison with the distributions of possible progenitor populations. Such studies are, however, not straightforward. First, current catalogues of SNRs miss objects due to observational selection effects. Second, there are no reliable distance estimates available for most identified remnants. Here I use a sample of 182 Galactic SNRs from a recently revised catalogue (this proceedings), all but one of which have observed radio flux densities and angular sizes, to derive the distribution of SNRs in the Galaxy by comparing the observed distribution of bright remnants with Galactic longitude with that expected from simple models.

2. The Problems

2.1. *The Selection Effects*

Although, as discussed by Aschenbach (this proceedings), many new SNRs may soon be identified from the ROSAT X-ray survey, the identification of SNRs in *existing* catalogues has, generally, been made at radio wavelengths. Such identifications are, basically, limited by two selection effects: (i) the surface brightness of the remnant must be above the sensitivity limit of the observations and be readily distinguishable from the Galactic background emission, and (ii) the angular size of the remnant must be at least several times the resolution of the observations (these selection effects are discussed in detail in Green 1991). It is thought that current catalogues are nearly complete in the whole Galactic plane down to a surface brightness at 1 GHz, $\Sigma_{1\ \mathrm{GHz}}$, of $\approx 8 \times 10^{-21}$ W m^{-2}Hz^{-1}sr^{-1}. The lower limit for completeness for angular size is ≈ 8 arcmin. This is illustrated in Fig. 1, which shows histograms of the surface brightnesses and angular sizes of catalogued SNRs.

These effects mean that not only are old faint remnants missing from current catalogues, but there is also a deficit of young but distant SNRs. It will be difficult to make catalogues of Galactic remnants complete to much lower surface brightnesses, as some regions of the Galactic plane — such as the Galactic center, and Cygnus — have very complex emission on a wide variety of angular scales. Such "confusion" can, to some extent, be avoided by using multi-frequency or polarization radio observations, or

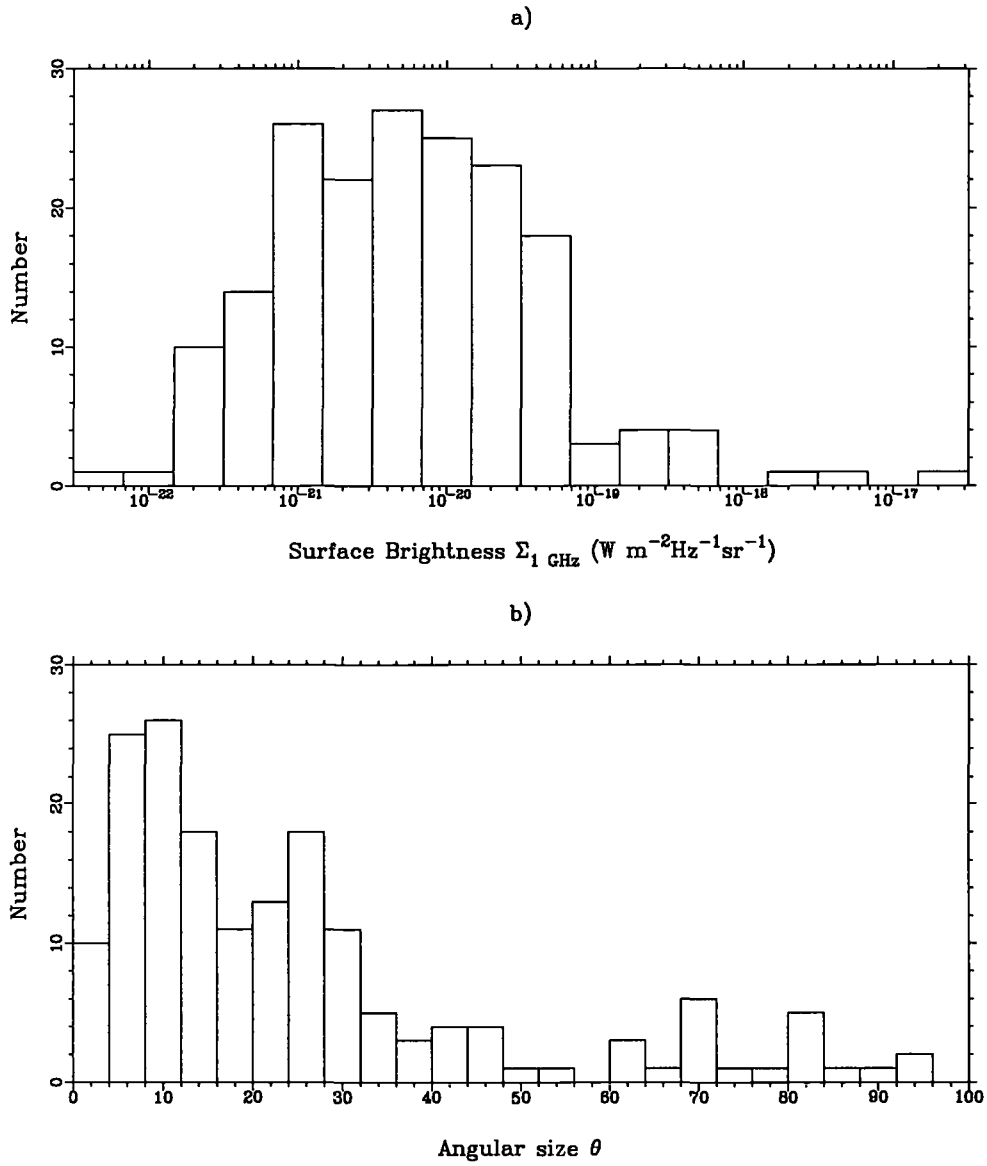

FIGURE 1. Histograms of (a) surface-brightness and (b) angular size, for catalogued SNRs (10 large angular diameter remnants do not fit on this plot). The nominal completeness limits in surface-brightness and angular size are $\approx 8\times10^{-21}$ W $m^{-2}Hz^{-1}sr^{-1}$ and ≈ 8 arcmin respectively.

comparisons with infrared and X-ray surveys, to separate out different components of emission. However, the problem of identifying faint SNRs in the complex regions of the Galactic plane is difficult.

There have been several searches for the missing small SNRs (Green & Gull 1984; Reich et al. 1985; Green 1985, 1989; Helfand et al. 1989; Sramek et al. 1992), but with little success. This is largely due to the large number of compact radio sources in the Galactic plane, most of which are extragalactic. For example, the Effelsberg 2.7-GHz plane survey (of the region $358° < l < 240°$, $|b| < 5°$, with a beam of 4.6 arcmin) contains 6495 small-diameter sources less than 12 arcmin in apparent size (Fürst et al. 1990a), and most of these have *not* been observed in detail. (It is, however, implausible

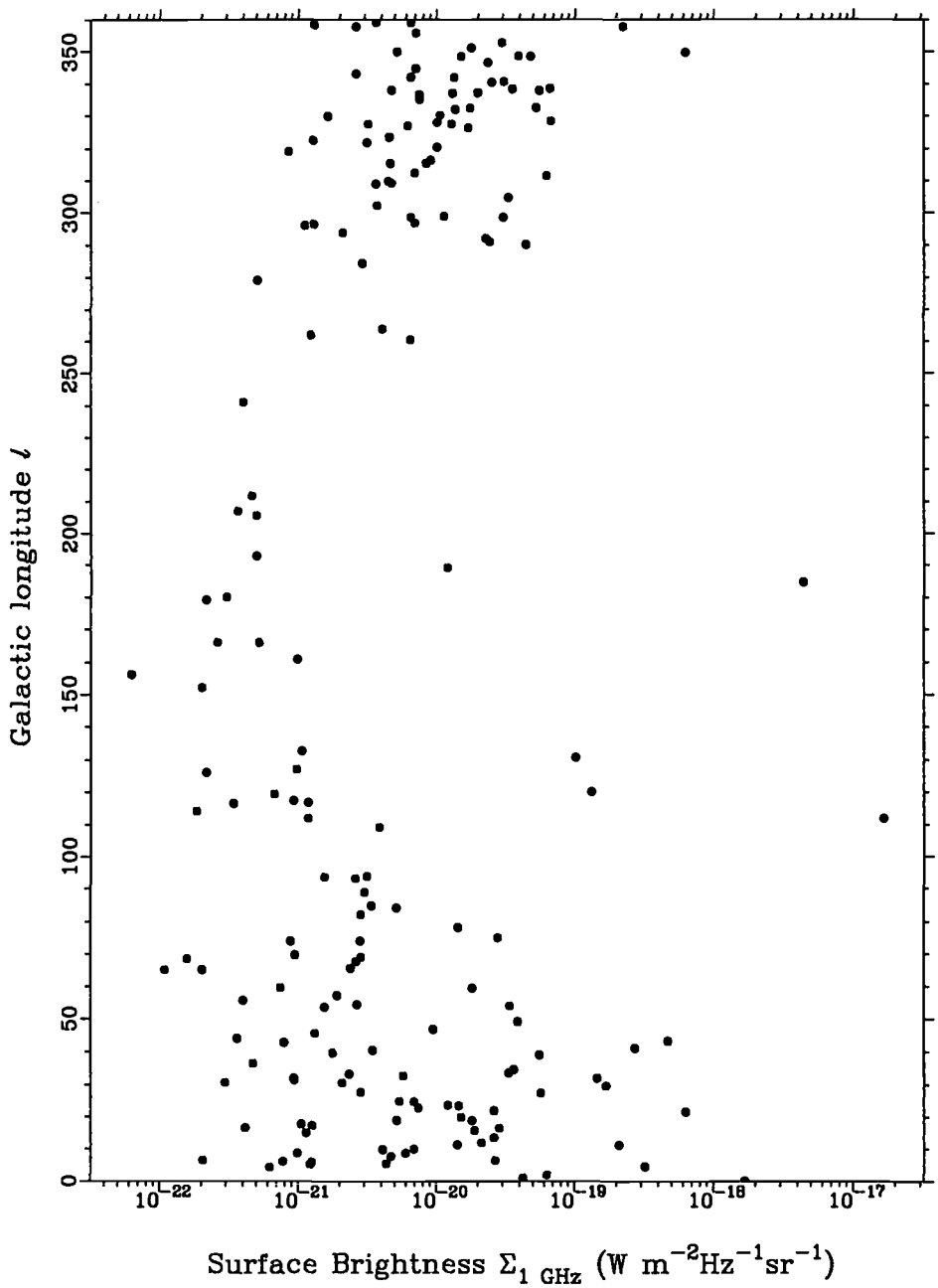

FIGURE 2. Plot of Galactic longitude against surface brightness for catalogued SNRs. Note that there are relatively many more faint remnants in the 2nd and 3rd quadrants — $90° < l < 270°$ — than in the 1st and 4th quadrants.

that any very high surface brightness remnants like Cas A or the Crab nebula have been missed — see Green 1985.)

Although many SNRs have been identified with surface brightnesses less than limit quoted above, these are predominantly in regions of low background Galactic radio emission, such as high Galactic latitudes, or in the 2nd and 3rd Galactic quadrants (the

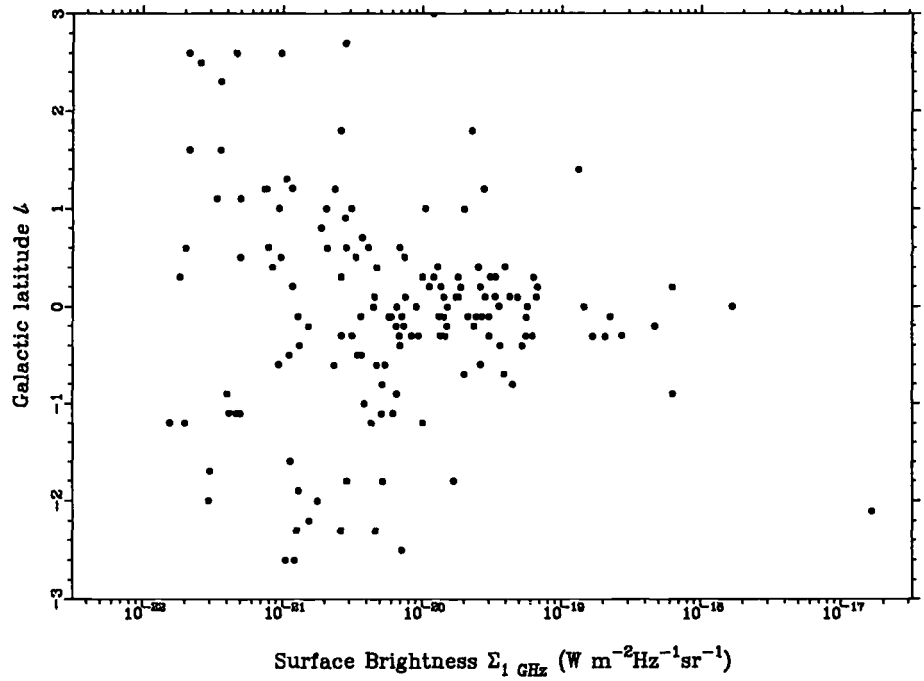

FIGURE 3. Plot of Galactic latitude against surface brightness for catalogued SNRs (25 remnants with $|b| > 3°$ are not included on the plot). Note that there are relatively many more faint remnants away from $b = 0°$.

Galactic "anticenter" region). This is illustrated in Figs 2 and 3, which clearly show that there are relatively more faint remnants in the anticenter region or away from $b = 0°$ where background confusion is less of a problem. (Note also that more fainter SNRs are identified in the 1st quadrant, compared with the 4th, because the Effelsberg 2.7-GHz survey — Reich et al. 1990 and Fürst et al. 1990b — cover these regions). Since all SNRs in the anticenter quadrants are outside the Solar Circle at large Galactocentric radius, it is difficult to disentangle this bias from any intrinsic variation in the properties of SNRs with Galactic coordinates. This selection effect accounts for the very broad distribution of SNRs derived by Li et al. (1990), who included all SNRs in their analyses, and were therefore biased to distributions showing an excess at large Galactocentric radii.

Van den Bergh (1988a,b) discussed the distribution of observed SNRs and noted that high surface brightness remnants (in this case taken to be $\Sigma_{1\ \mathrm{GHz}} > 3 \times 10^{-21}$ W $\mathrm{m^{-2}Hz^{-1}sr^{-1}}$) are concentrated in a thin nuclear disk. As noted by Fürst's comments to van den Bergh 1988b, this conclusion is strengthened by a more realistic surface brightness completeness limit (see Green 1991).

2.2. *The Distances to SNRs*

The fact that there are no high surface brightness SNRs with large diameters has often been expressed in terms of a "$\Sigma - D$" relation (usually of the form $\Sigma \propto D^{-n}$, relating surface brightness, Σ, to linear diameter, D). If such a relation can be calibrated with remnants at known distances, then diameters and hence distances can be derived for any SNR from its *observed* surface brightness. However, the correlation in the $\Sigma - D$ plane is poor (Green 1984; Berkhuijsen 1986), and the full extent of the range of properties of Galactic SNRs in the $\Sigma - D$ plane is not currently known, due to the selection effects described above (see also Green 1991).

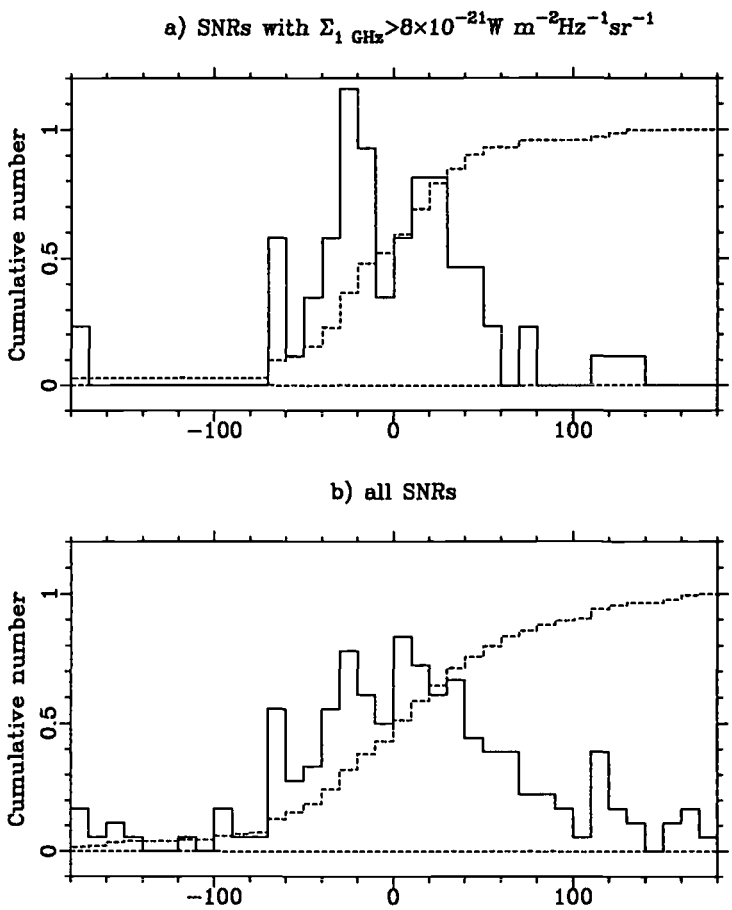

FIGURE 4. Histograms of the distributions of SNRs with Galactic longitude (solid lines) and cumulative distributions (dashed lines) for, (a) high surface brightness remnants (71 with $\Sigma_{1\ GHz} > 8 \times 10^{-21}$ W m^{-2}Hz^{-1}sr^{-1}), and (b) all SNRs.

Consequently only an upper limit to the diameter, and hence to the distance, of an SNR can be deduced with any confidence from a given surface brightness (see Berkhuijsen 1986). This boundary in the $\Sigma - D$ plane is not the result of any observational selection effects, and represents some intrinsic limit to the luminosity of radio emission from SNRs, although it does not necessarily represent the evolutionary path of any individual SNR in the $\Sigma - D$ plane. $\Sigma - D$ studies are only made because Σ is a *distance-independent* observational parameter. Much of the correlation in $\Sigma - D$ is due to an intrinsic "$1/D^2$" bias in this representation compared with the $L-D$ plane (i.e. for a remnant of luminosity L, at a distance d, $L \propto Sd^2$, whereas $\Sigma \propto S/\theta^2$, so $\Sigma \propto L/(\theta d)^2$, or $\Sigma \propto L/D^2$)

3. The Distribution of SNRs in the Galaxy

The problems caused by the Σ-selection effect on statistical studies can be reduced if such studies are restricted to relatively bright remnants, for which current catalogues are thought to be complete (although some high surface brightness remnants with small angular diameters will still be missing). The distribution of remnants perpendicular to the Galactic plane is obviously affected by the surface brightness selection effect, as faint

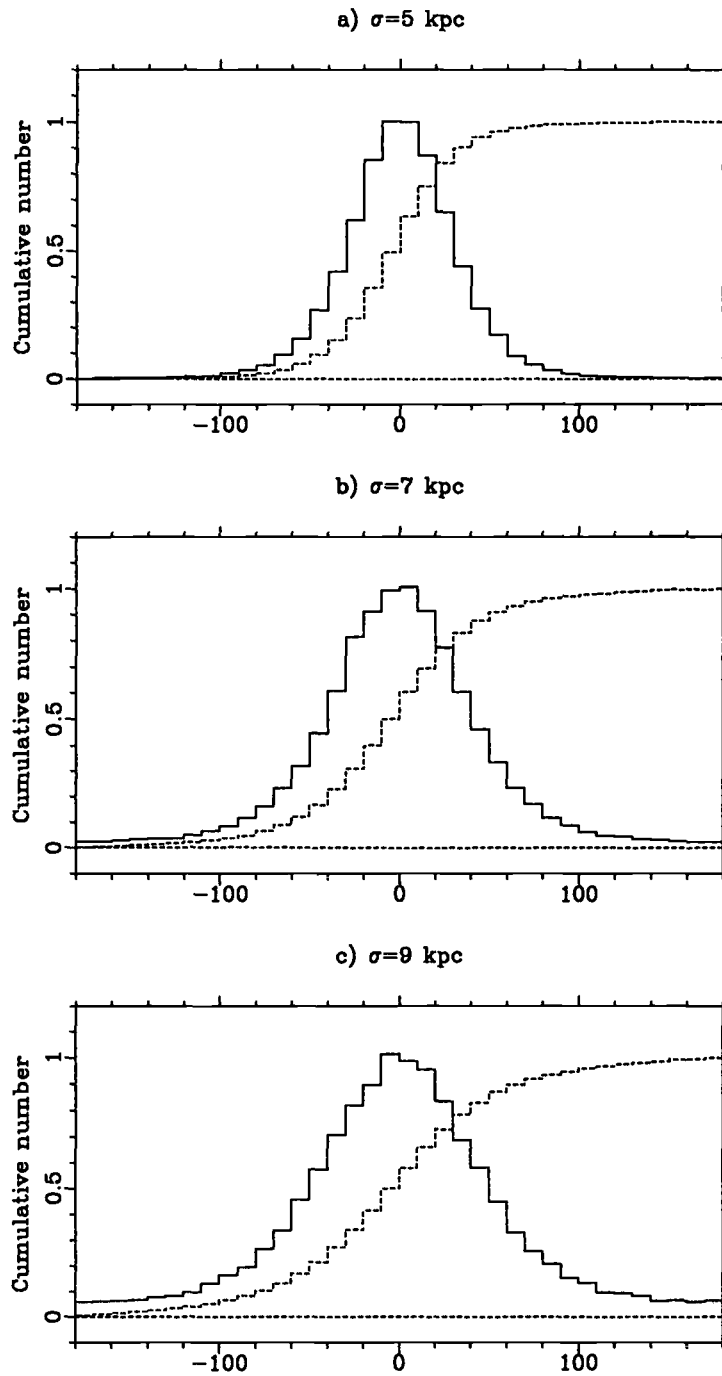

FIGURE 5. Histograms of model distributions of SNRs with Galactic longitude (solid lines) and cumulative distributions (dashed lines) for various Gaussian Galactocentric scale lengths (see text).

remnants are more difficult to identify near $b = 0°$. The distribution perpendicular to the plane is further complicated by the warp of the Galaxy outside the Solar Circle. There are indeed more SNRs identified at large positive values of b in the 1st and 2nd quadrants than elsewhere, as is expected because of the warp of the Galactic plane in these directions. In the subsequent discussion I will not address the question of the distribution of SNRs perpendicular to the plane, but concentrate on constraining the distribution in the disk of the Galaxy. To do this, I use the method of Li et al. — to compare the observed distribution of SNRs with Galactic longitude with that expected from various models. This avoids the problem that we lack accurate distances to individual SNRs.

Fig. 4 shows the observed distribution with Galactic longitude of (a) high surface brightness remnants (71 SNRs in the catalogue with $\Sigma_{1\ \mathrm{GHz}} > 8{\times}10^{-21}$ W m^{-2}Hz^{-1}sr^{-1}), and also (b) for all remnants. This clearly shows that there are relatively many faint remnants in the Galactic anticenter. This also shows evidence for a deficit of SNRs near $l = 0°$. This may be a true deficit, as might be expected for a decrease in the space density of SN progenitors towards the Galactic center. However, it may also be, in part at least, due to the difficulty of finding remnants in this region of the Galactic plane, due to the very complex background emission. Any remaining incompleteness in current catalogues, both for the surface brightness and angular diameter selection effects, are expected to be worse closer to $b = 0°$ (because of the increased confusion in the case of the surface brightness selection effect, and the longer line-of-sight through the Galaxy for missing small, i.e. young but distant remnants). Thus, the true distribution in l is likely to be somewhat *narrower* than is indicated in Fig. 4(a). For comparison with the observed distributions in Galactic longitude I have made simple Monte Carlo models of the distribution of SNRs in the disk of the Galaxy, assuming a simple Gaussian distribution, where the probability distribution varies with Galactocentric radius, R, as

$$\propto \mathrm{e}^{-(R/\sigma)^2},$$

(where σ is the Gaussian Galactocentric scale length, assuming the distance to the Galactic Center of 10 kpc). Fig. 5 shows plots of the expected distribution of SNRs in Galactic longitude of three such models for different scale lengths. Simple comparisons of the observed and model cumulative distributions indicate a scale length of ≈ 7 kpc for the high brightness SNRs. (The much broader distribution in Galactic longitude of *all* catalogued remnants — due to the selection effects — gives a much larger apparent scale length of ≈ 10 kpc, cf. Li et al.). As noted above, the true distribution is likely to be somewhat narrower than that derived from the observations, due to residual selection effects, so that this scale length is an upper limit.

The distribution of SNRs derived above should, however, be interpreted cautiously, especially when making direct comparisons of it with distributions of other Galactic populations. It is far from clear that the observed SNR distribution actually represents the parent supernovae distribution, as the factors that affect the brightness and lifetime of appreciable radio emission from SNRs are not well understood. The distribution of SNRs could simply reflect the distribution of, say density of the ISM, or magnetic field, if they are the crucial factors in determining the brightness and lifetime of radio emission from SNRs.

REFERENCES

Berkhuijsen, E. M., 1986, A&A, 166, 257

Fürst, E., Reich, W., Reich, P., Reif, K., 1990a, A&AS, 85, 805

Fürst, E., Reich, W., Reich, P., Reif, K., 1990b, A&AS, 85, 691

Green D. A., 1984, MNRAS, 209, 449

Green D. A., 1985, MNRAS, 216, 691

Green D. A., 1989, AJ, 98, 1358

Green D. A., 1991, PASP, 103, 209

Green D. A., Gull S. F., 1984, Nature, 312, 527

Helfand, D., Velusamy, T., Becker, R. H., Lockman, F. J., 1989, ApJ, 341, 151

Li, Z.-W., Wheeler, J. C., Bash, F. N., Jefferys, W. H., 1991, ApJ, 378, 93

Sramek, R. A., Cowan, J. J., Roberts, D. A., Goss, W. M., Ekers, R. D., 1992, AJ, 104, 705

Reich, W., Fürst, E., Altenhoff, W. J., Reich, P., Junkes, N., 1985, A&A 151 L10

Reich, W., Fürst, E., Reich, P., Reif, K., 1990, A&AS, 85, 633

van den Bergh, S., 1988a, PASP, 100, 205

van den Bergh, S., 1988b, in Kundt, W., ed., Supernova Shells and Their Birth Events, Springer-Verlag, p. 44

Supernova Remnants in Nearby Spiral Galaxies

By KNOX S. LONG

Space Telescope Science Institute, 3700 San Martin Drive, Baltimore, MD 21218, USA

Large samples of supernova remnants are needed in order to study the global distribution of supernovae in galaxies, for determining how the environment in which a SN explodes affects the appearance of a SNR, for studying abundances and abundance gradients in galaxies, for estimating SN rates, and in order to determine the energetics of SNRs and their expansion. Here we describe techniques which are currently being used to expand SNR samples in nearby spirals.

1. Introduction

The Cygnus Loop is thought to be about 18,000 years old (Ku et al. 1984). Assuming a SN rate of 5 per century (van den Bergh & Tammann 1991), there should be about 900 SNR in the galaxy younger than the Cygnus Loop. However, Green's revised catalog of Galactic SNRs contains 182 SNRs, some of which are clearly more evolved than the Cygnus Loop (Green, these proceedings). As a result, it is clear that the Galactic sample is very incomplete. In the Galaxy, nearly all SNRs have been first recognized as SNRs from radio observations. Since SNRs are found primarily in the Galactic plane and since X-rays and optical light are strongly absorbed by material in the Galactic plane, they are hard to detect in these wavelength bands. In fact, only about 40 Galactic SNRs have been detected at optical wavelengths and only about 50 have been detected at X-ray wavelengths. (However, see Aschenbach [these proceedings] who suggests there may be a population of X-ray bright, radio faint SNRs hidden in the ROSAT survey data.)

Various attempts (e.g. Li et al. [1991]; Green [these proceedings]) have been made to use the Galactic sample of SNRs to determine the radial distribution of SNRs in the Galaxy, the association of SNRs with spiral arms, the progenitor populations of Galactic SNRs, and the SN rate. However, if large samples of extragalactic samples can be assembled, they are likely to be far better samples for answering these kinds of questions (in other galaxies) – because the distances to all the SNRs in a sample will be identical, and because extinction and confusion are less severe in face-on spirals. Extinction along the line of sight to a SNR affects not only basic detectability, but also appearance, which is very important if one hopes to classify the SNRs in a sample. It is also more straightforward to estimate total fluxes from extragalactic SNRs since they have small angular sizes, although this comes at a price, since small size means accurate diameters are difficult to obtain.

The first successful attempt to identify a significant number of SNRs – 12 – in a nearby galaxy – the Large Magellanic Cloud – was made by Mathewson & Clarke (1973). For this survey, they defined a SNR as an emission nebulae which had a [S II] $\lambda\lambda 6717, 6731$:H$\alpha$ ratio large compared to that observed in H II regions and which was associated with a nonthermal radio source.

In the late 1970's and early 1980's, a number of observers, notably D'Odorico et al. (1980), Blair, Kirshner, & Chevalier(1981), Dopita et al. (1984) and Blair & Kirshner (1985), carried out optical interference surveys of nearby galaxies, identifying of order 40 SNRs in Local Group spirals. Radio surveys were also attempted by Dickel & D'Odorico

(1984), Goss et al. (1980), Reynolds & Fix (1987), and others, but only a small number ($\sim$ 20) of SNRs were detected and the ones which were detected were some of the same SNRs previously identified as optical SNRs.

In the same time period, the Einstein Observatory was used to make the first imaging X-ray surveys of the Magellanic Clouds and nearby spirals. Long et al. (1981) identified 25 SNRs in the LMC, including 4 new SNRs with Balmer-dominated optical spectra (Tuohy et al. 1982). Inoue, Koyama & Tanaka (1983) identified 6 SNRs in the SMC, including 1E0102-72, a new oxygen-dominated SNR (Dopita, Tuohy & Mathewson 1981). These surveys were important because they constituted the largest "homogeneous" X-ray samples of SNRs. However, no new SNRs were identified in Local Group spirals, and only a few were detected.

With the advent of new detector technologies – CCDs with linear response functions and high quantum efficiencies, radio telescopes on which multiple frequencies can be observed with the same angular resolution, and X-ray telescopes with higher sensitivity– it has become possible to carry out observations which greatly increase the numbers of SNRs that are likely to be detected. I would like to use the remainder of this review to describe some of these observations.

2. Optical Searches for SNRs

Optically, most SNRs are extended emission line objects. Because the cooling time behind the shock is short compared to age of the SNR, the spectra which are observed show strong lines from a wide range of ionization states. This distinguishes SNRs from H II regions, because in H II regions, photoionization maintains the bulk of the plasma in well-defined ionization states. The most common diagnostic is the [S II] $\lambda\lambda 6717, 6731$: Hα ratio which is typically of order 0.6-1.2 in SNR shocks and of order 0.1 in bright H II regions. (In H II regions, S is mostly double ionized and therefore [S II] $\lambda\lambda 6717, 6731$ is weak.)

The original optical searches for SNRs were made using interference filters with photographic plates as the recording material. Recently, we (W.P Blair [JHU], R. P Kirshner [Harvard College], P.F. Winkler [Middlebury College] and I) have carried out new interference filter surveys using CCDs cameras at Kitt Peak and CTIO and on the 2.5 m at Las Campanas. All of these surveys consist of obtaining images in [S II], Hα , and a nearby continuum band. The analysis of the first of these surveys, which covered the inner 15' of M33, revealed 30 new SNRs (where previously there had been 10) (Long et al. 1990; Smith et al. 1993). In addition to acquiring data which covers a much larger portion of M33, we have now surveyed a number of other galaxies including M83, NGC 247, NGC 300, NGC 6946 and NGC 7793. Our analyses of these data are still underway, but it is quite clear that 10-45 SNRs are identifiable in each galaxy, including the most distant NGC 6946. The results on NGC 300 are illustrative (Long & Blair 1994):

NGC 300 is a nearby Sculptor group spiral; most recent distance estimates lie between 1.5 and 2 Mpc. Following Deharving et al. (1988), we will assume 1.53 Mpc, which means it is about twice as far as M33. Because of its proximity and its low inclination angle (42.3°), it is an excellent galaxy for SNR searches, especially since it lies at high galactic latitude which means Galactic absorption is small. Dopita, D'Odorico & Benvenuti (1980) carried out the only previous search for SNRs in NGC 300; they used Hα and [S II] to identify 7 candidates. Two of these objects – DDB2 and DDB5 – have been confirmed as SNRs based on optical spectroscopy.

We observed 9 fields in NGC 300, each 5.3' on a side with Hα , [S II], and 6100 Å continuum filters using the 2.5 meter at Las Campanas. The dividing line between a SNR

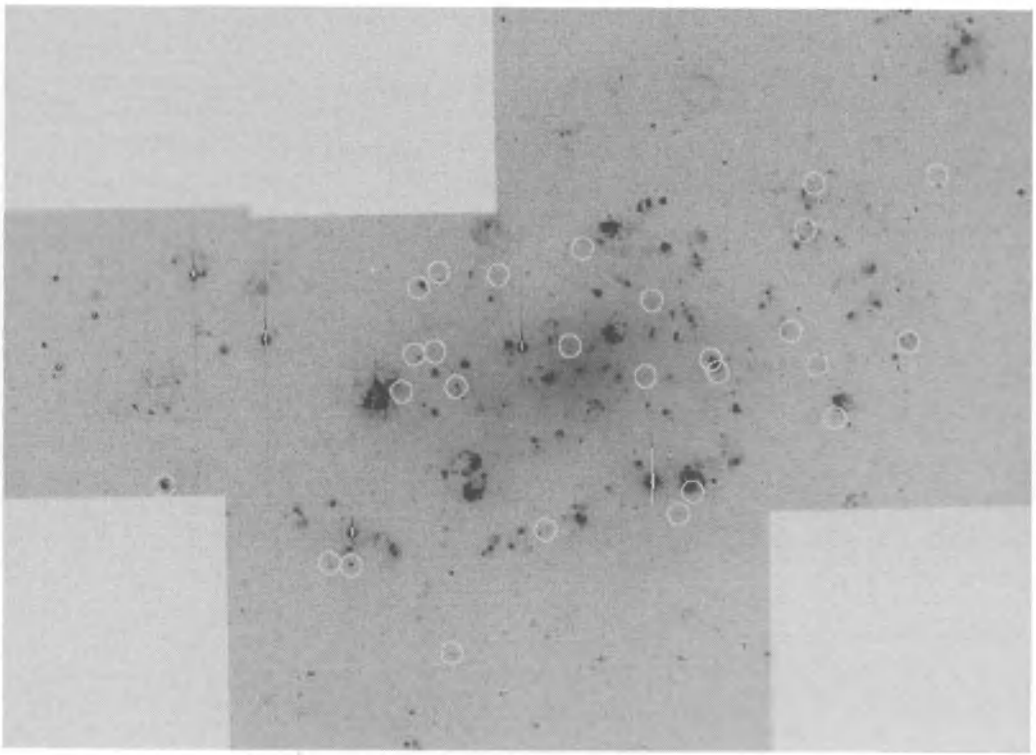

FIGURE 1. A mosaic of the Hα images of NGC 300 with SNRs identified.

and an H II region has usually been taken to be a [S II] : Hα ratio of 0.4 (D'Odorico 1978). Therefore, these data were searched for nebulae with [S II] : Hα ratios exceeding this value with little or no continuum contamination. A total of 27 potential SNRs were identified in this way.

The distribution of the SNRs is shown on the mosaic of the Hα images in Fig. 1. The faintest objects which were identified have Hα surface brightnesses of about 7×10^{-16} ergs cm^{-2} s^{-1} arcsec^{-2}. Five of the 7 objects identified by Dopita, D'Odorico, & Benvenuti as SNRs were within our survey region. Only two of these – DDB2 and DDB5 – were identified as SNR candidates in our survey; the other three – DDB1, DDB4, and DDB7 – are present in our images but are dominated by continuum emission. Dopita, D'Odorico, & Benvenuti did not have continuum images, and therefore it is not surprising that some of the objects in their list are not SNRs. DDB2 and DDB5 have surface brightnesses 30 times that of the faintest objects in our survey.

In order to confirm that the nebulae which we had identified were SNRs, we subsequently obtained spectra of about 2/3 of our sample. All of the candidates we observed did indeed have [S II] : Hα line ratios greater than 0.4, and the higher surface brightness candidates generally showed emission from [O I] $\lambda\lambda$6300, 6363 (which is exceedingly faint in H II regions). Since our confirmation rate was in fact 100%, we are confident that all 27 of the nebulae satisfy the conventional optical definition for a shock heated nebula.

Inspection of Fig. 1 shows that a significant fraction of the SNRs in NGC 300 are associated with the spiral arms of the galaxy. The surface density of SNRs (in our sample) decreases from about 1 kpc^{-2} at a galactocentric radius of 1 kpc to about 0.1 kpc^{-1} at 4 kpc. Except for an overall scale factor, the variation of the surface density resembles that of the H II regions in the catalog compiled by Deharving et al. (1988).

There are 22 SNRs in our sample with a diameter of 50 pc or less. The N(< D) vs. D relationship has a maximum likelihood power law slope of 2.9 ± 0.8 which is close to the value of 2.5 expected from a Sedov expansion law. If we assume our sample is complete to 50 pc and that the ratio of the explosion energy to the ISM density E/n is 10^{51} ergs cm^3, then SNe occur in NGC 300 once every 2300 years. This implies a SN rate of 0.3 SNe (100 yr)$^{-1}$ $(10^{10}L_{\odot})^{-1}$, a factor of 3 lower than derived by Long et al. (1990) for M33.

3. Radio Searches for SNRs

Radio searches for SNRs have been based upon the same criteria as have searches for Galactic SNRs, where the observational definition for a SNR is an extended, typically limb-brightened source with a non-thermal radio spectrum. As at optical wavelengths, H II regions constitute the principle source of confusion (especially for pulsar-dominated SNRs which have flatter spectra). Because the apparent sizes of SNRs are small (5-10" in M33 for example), early surveys were hampered by the fact that beam sizes differed at different wavelengths. Scaled array observations (or more correctly, observations from which multi-frequency maps with the same angular resolution can be constructed) are required in order to obtain accurate spectral indices.

The power of this technique has been best demonstrated by Duric et al. (1993) who studied M33. Duric et al. used the VLA and Westerbork to obtain continuum images of M33 at 6 and 20 cm with a resolution of about 7". The rms noise ratio of the images was about 50 μJy at both frequencies, roughly 1000 times smaller than the expected flux from a SNR like Cas A at the distance of M33. Duric et al. concentrated on 53 optically-identified SNRs in M33, which they took from the survey carried out by Long et al. (1990), supplemented by 10 optically-confirmed SNRs outside the region studied by Long et al. Using a method which involved searching for excess emission at 20 cm (over that observed at 6 cm), Duric et al. detected nonthermal emission from 26 of the 53 optically-identified SNRs. However, the brightest of these SNRs, DDB9, is considerably fainter ($S_{\nu}(30\,\mathrm{cm}) = 5.1$ mJy) than Cas A would be at the distance of M33 (45 mJy). In fact, there are approximately 20 Galactic SNRs which are more luminous than the brightest SNR in M33.

S. Gordon and his collaborators (these proceedings) are continuing to analyze the new radio data on M33 and are comparing it to an expanded sample of 72 optically-identified SNRs in M33. There appear to be approximately 110 nonthermal sources in the field. Thirty-eight of these are spatially coincident with optically-identified SNRs. About 30 of the nonthermal sources in the field are likely to be background galaxies at the flux limit of the radio survey. Therefore, it is possible that there are as many as 80 radio-detected SNRs in the survey.

One of the nonthermal sources in M33 is coincident with the giant H II region NGC 592. Gordon et al. (1993) used the position of the nonthermal source to identify a portion of the nebula with a high [S II]:Hα ratio and subsequently obtained optical spectra which confirm it is a SNR. The new source is also coincident with a soft Einstein (and ROSAT) X-ray source.

4. X-ray Searches for SNRs

X-ray surveys of SNRs in external galaxies are important because most of the energy in shock-dominated SNRs is contained in the hot thermal plasma which produces X-ray emission. SNRs are the only extended sources in galaxies with soft X-ray spectra and

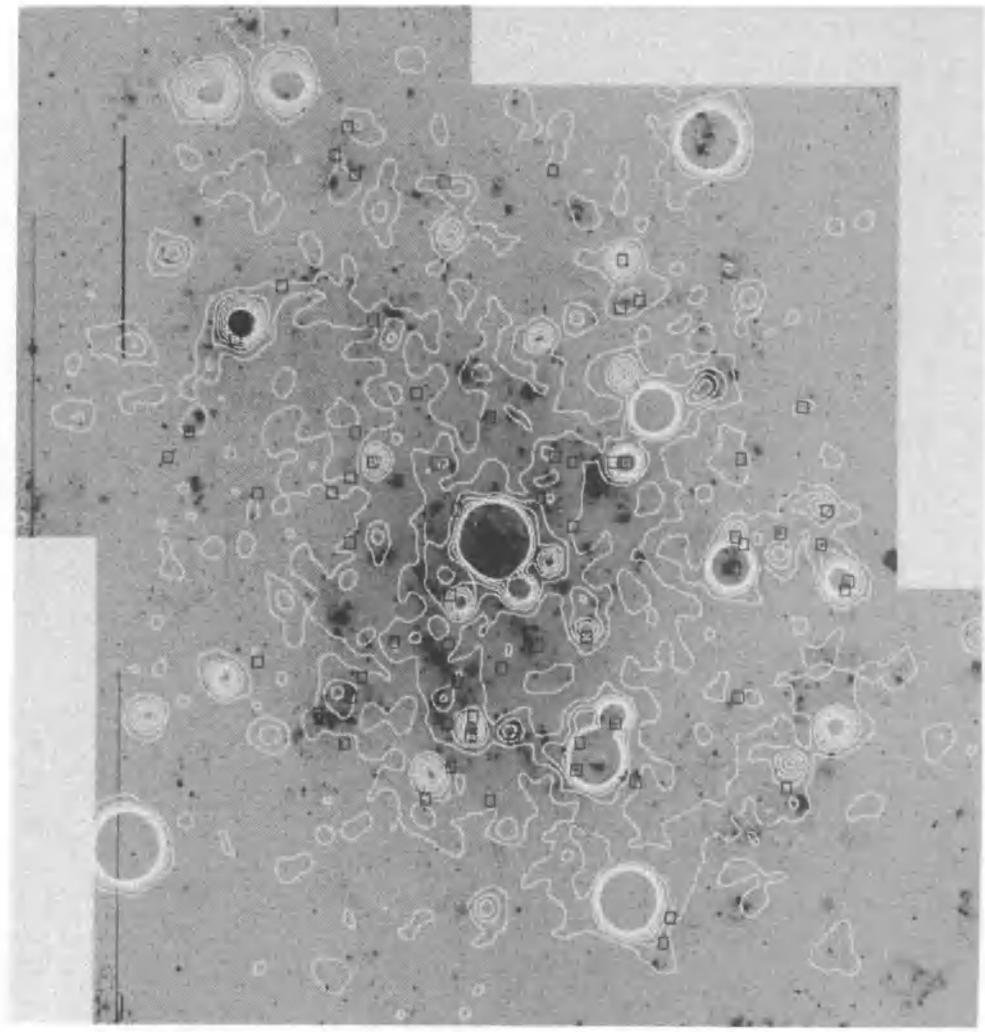

FIGURE 2. An X-ray contour map of M33 superposed on an Hα mosaic. The positions of our current working list of 72 optically-identified SNRs are also indicated.

luminosities in excess of 10^{34} ergs s^{-1}. An advantage of X-ray searches over searches at other wavelengths is that H II regions do not compromise one's ability to identify an object as a SNR. In principle, therefore, X-ray observations provide a powerful way to search for SNRs in nearby galaxies.

The launch of the first imaging X-ray telescope, Einstein made it possible to carry out searches for SNRs in nearby galaxies. As noted above, the searches succeeded but primarily in the Magellanic Clouds. ROSAT, with a larger effective area, lower background rate, and improved imaging performance, is now enabling searches with about an order of magnitude more sensitivity than Einstein. Even so, SNR searches are likely to remain difficult. Except in the Magellanic Clouds, it will be extremely difficult to detect SNRs with the HRI, and therefore it will be hard to determine whether a candidate source is extended. As a result, most SNR searches will rely on a more problematic attempt to identify SNRs as soft X-ray sources. This introduces confusion since some binary X-ray sources have soft spectra. Therefore, firm identification of a source as a SNR will require confirmation using optical or radio tests.

As an example of what is likely to be accomplished, however, let us consider M33. Because of its proximity (840 kpc; Freedman, Wilson & Madore 1991), relatively low inclination angle (57°; Searle 1971), and well-defined open spiral arms, M33 is an ideal galaxy for studying the X-ray properties of spiral galaxies, including their SNR populations. As a result it was observed with the IPC and HRI on Einstein (Long et al. 1981; Markert et al. 1983; Trinchieri, Fabbiano & Peres 1988). These studies revealed a dominant nuclear source, the brightest in the Local Group ($L_x \sim 10^{39}$ ergs s^{-1}) and 14 other sources ($L_x \geq 10^{37}$ ergs s^{-1}) thought to be associated with M33. Of these sources, 3 are positionally coincident with known optical SNRs in M33.

X-ray contours from a 50 ksec exposure with the PSPC on ROSAT are shown in Fig. 2 superposed on an Hα mosaic obtained as part of the expanded optical search for SNRs in M33. There are about 31 individual sources in the image within 15' of the nucleus of M33. All of the bright sources which had been detected with Einstein are visible. Many of the sources are clearly associated with H II regions. Diffuse emission (perhaps simply a superposition of low luminosity sources) can be traced along the northern and southern spiral arms. Also shown on the Figure are the positions of our current working sample of optically-identified SNRs in M33.

In an attempt to determine how many of these sources are SNRs we have examined the positional coincidences between X-ray sources and optically-identified SNRs. Ten of the 31 X-ray sources lie within 30" of known SNRs in M33. If one assumes that both source populations are uniformly distributed over M33, one would expect to find only two chance coincidences, which suggests either that there are a number of SNRs in the X-ray sample or alternatively that both SNRs and X-ray sources have similar parent populations.

ROSAT has a relatively limited spectral range – 0.1-2.4 keV. M33 sources are also affected by galactic absorption of about 6×10^{20}cm^{-2}, which strongly absorbs X-rays below 0.6 keV. Nevertheless, in an attempt to separate the sources according to their X-ray spectra, we have constructed hardness ratios, defined as (H-S)/(H+S) where H is the count rate above 1 keV and S is the count rate below 1 keV, for all the point sources. A histogram of the hardness ratios we obtained is shown in Fig. 3. Eight of the eighteen sources with hardness ratios less than 0.0 lie within 30" of a SNR. This suggests that we have in fact detected X-ray emission from at least 8 SNRs, that it may be possible to identify candidate SNRs on the basis of their X-ray spectra, and (more speculatively) that a substantial fraction of the other soft sources are SNRs. Obviously, detailed spectroscopic studies are required to verify these suggestions.

5. Conclusion

It is now possible to assemble relatively homogeneous large samples of SNRs for galaxies as distant as 10 Mpc. In galaxies, such as M31 and M33, the numbers of SNRs which can be detected (at optical wavelengths) will be comparable to the numbers of SNRs known in the Galaxy. Although the selection effects are clearly not yet fully understood, these samples should allow us to understand a great deal more about the distribution of SNRs and hence SNe in galaxies than is possible with the current Galactic sample.

Acknowledgments

Very few of the programs I have described here would have been possible without the diligence of my collaborators – W. P. Blair, N. Duric, S. Gordon, R. P. Kirshner, R.

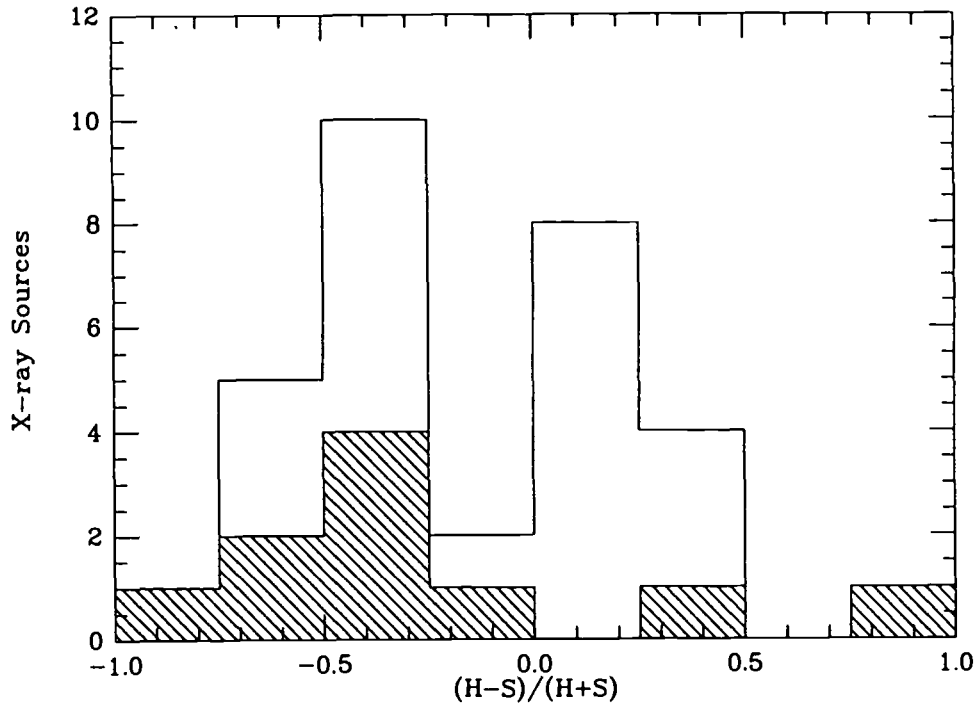

FIGURE 3. Hardness ratios of the 31 point sources within 15' of the nucleus of M33 as observed with the ROSAT. X-ray sources which are positionally coincident with optically-identified SNRs are shaded.

C. Smith, and P. F. Winkler. This work has been supported in part by NASA grant NAG5-1539.

REFERENCES

Blair, W. P., & Kirshner, R. P. 1985, ApJ, 289, 582

Blair, W. P., Kirshner, R. P., & Chevalier, R. A. 1981, ApJ, 247, 879

Deharving, L., Caplan, J., Leqeaux, J., Azzopardi, M., Bresacher, J, Terengi, M., & Westerlund B. 1988, A&AS, 73, 407

Dickel, J. R., and D'Odorico, S. 1984, MNRAS, 206, 351

D'Odorico, S. 1978, Mem. Soc. Astr. Italiana, 49, 563

Dopita, M. A., Binnette, L., D'Odorico, S., and Benvenuti, P. 1984, ApJ, 276, 653

Dopita, M. A., D'Odorico, S., & Benvenuti, P. 1980, ApJ, 236, 628

Dopita, M. A., Tuohy, I. R., & Mathewson, D. S., ApJ, 248, L105

Duric, N., Viallefond, F., Goss, W. M., and van der Hulst, J. M. 1993, A&AS, 99, 217

Freedman, W. L., Wilson, C. D., & Madore, B. F. 1991, ApJ, 372, 455

Gordon, S. M., Kirshner, R. P., Duric, N., & Long, K. S. 1993, ApJ, 418, 743

Goss, W. M., Ekers, R. D., Danziger, I. J., and Israel, F. P. 1980, MNRAS, 193, 901

Inoue, H., Koyama, K., & Tanaka, Y. 1983, in "IAU Symposium No. 101 Supernova Remnants and Their X-ray Emission", ed. by J. Danziger & P. Gorenstein (Dordrecht: Reidel Publ. Co.), pp. 535

Ku, W. H-M, Kahn, S. M., Pisarski, R., & Long, K. S. 1984, ApJ, 278, 615

Li, Z., Wheeler, J. C., Bash, F. N., Jefferys, W. H. 1991, ApJ, 378, 93

Long, K. S., & Blair, W. P. 1994, in preparation.

Long, K. S., Blair, W. P., Kirshner, R. P., & Winkler, ApJS, 72, 61

Long, K. S., D'Odorico, S., Charles, P. A., & Dopita, M. A. 1981, ApJ, 246, L61

Long, K. S., Helfand, D. J, & Grabelsky, D. A., ApJ, 248, 925

Markert, T. H., & Rallis, A. D. 1983, ApJ, 275, 571

Mathewson, D. S., & Clarke, J. N. 1973, ApJ, 180, 725

Reynolds, S. P. & Fix, J. D. 1987, ApJ, 322, 671

Searle, L. 1971, ApJ, 168, 327

Smith, R. C., Kirshner, R. P., Blair, W. P., Long, K. S., & Winkler, P. F. 1993, ApJ, 407, 564

Trinchieri, G., Fabbiano, G., & Peres, G. 1988, ApJ, 325, 531

Tuohy, I. R., Dopita, M. A., Mathewson, D. S., Long, K. S., & Helfand, D. J. 1982, ApJ, 261, 485

van den Bergh, S., & Tammann, G. A. 1991, ARAA, 29, 363

X-Ray Spectroscopy of Supernova Remnants

By R. PETRE

NASA/Goddard Space Flight Center, Code 660, Greenbelt, MD 20771, USA

X-ray spectroscopy can provide vital information about the progenitors and environments of supernova remnants. Plasma diagnostics and spectral modelling can be used to infer the energy of the remnant, the density and composition of the surrounding medium, and the degree of equilibrium in the shock heated gas. A new generation of X-ray spectrometers, the first of which was the Broad-Band X-Ray Telescope (BBXRT), has improved our ability to make precise measurements of X-ray line fluxes and energies. We summarize the results obtained from the BBXRT mission. These include a definitive measurement of the Fe K line centroid in the Tycho remnant, production of the first narrow-band X-ray maps (of Puppis A) and the first measurement of an electron-ion equipartition timescales in evolved remnants.

1. Introduction

Supernova remnants may be grouped into three broad categories, based on their X-ray and radio morphologies. The first of these shows shell-like structure in both bands. The X-rays from these are thermal, arising from the shock heating of ejecta and interstellar material. Prominent examples of this class of remnant are Tycho and the Cygnus Loop. The second category shows centrally peaked emission in both bands; these are the plerions, or Crab-like remnants, after the class archetype. The X-ray emission is a non-thermal power law, dominated by synchrotron processes from the energetic electrons produced by the pulsar. A third category combines elements of the previous two. Some remnants, like Vela, possess both a thermal shell and a non-thermal synchrotron nebula, while others, like W44 and W28, have a shell-like radio structure combined with a center-filled X-ray morphology that nevertheless arises from thermal X-rays. This presentation focuses on remnants dominated by thermal X-ray emission, as we are primarily interested in what the plasma diagnostics can tell us about the supernova progenitor and the surrounding medium.

X-ray observations, particularly spectroscopy, offer the most direct means of determining many fundamental properties of supernova remnants. The production of X-rays is tied directly to the non-radiative shock heating of diffuse ISM material and ejecta by the expanding blast wave or the reverse shock, so measuring the temperature of the X-ray emitting gas offers the most direct measure of the shock velocity and hence the energy of the initial explosion. X-ray spectroscopy facilitates measurement of the abundances of O, Ne, Mg, Si, S, and Fe in shock heated material, and thus allows a determination of how enriched it has become from SN nucleosynthesis products, or, in evolved remnants, the composition of the gaseous ISM. While optical measurements facilitate plasma diagnostics of radiatively cooling filaments, with densities typically 10^4 cm^{-3} and a small filling factor in a typical ISM ($\leq 1\%$), X-ray spectroscopy allows density measurements of the much more prevalent diffuse ISM and low density clouds, typically with densities $0.1 - 10$ cm^{-3}. Most recently, spatially resolved X-ray spectroscopy has allowed us to examine the variation of density and abundances across and around remnants, which can ultimately lead to inferences regarding the symmetry of the explosion and the pre- and post-shock conditions in the ISM.

The X-ray spectra of thermal supernova remnants are dominated by strong line emission from highly ionized nucleosysnthesis products. The X-ray band includes K shell

TABLE 1. Prominent X-ray Lines from Supernova Remnants

Element	He-α transition energy (keV) (average of triplet)	Ly-α transition energy (keV)
Oxygen	**0.570**	**0.653**
Neon	**0.916**	**1.016**
Magnesium	**1.34**	1.476
Silicon	**1.86**	2.006
Sulfur	**2.46**	2.622
Argon	3.14	3.315
Calcium	3.90	4.093
Iron	6.70	6.970
Iron L blend	**0.68-1.15**	

Bold face indicates strongest lines.

emission lines from carbon through nickel; the most prominent lines, as listed in Table 1 are from O, Ne, Mg, Si, S and Fe. In addition, the Fe L band around 1 keV is covered. As these lines originate from a recently shock- heated, low density (~ 1 cm^{-3}) plasma, it is almost certain that ionization equilibrium has not been attained. The non-equilibrium effects can be pronounced. For instance, in a 10^7 K plasma in thermal equilibrium, one would find fully stripped Mg ions, S ions with one remaining electron, and Si ions with two electrons. Yet for most SNR the dominant line from all these elements is the 2-1 transition of the helium-like (two-electron) state. Thus fitting to a coronal plasma model (e.g., Raymond & Smith, 1977) will yield too low a temperature. Additionally, these lines tend to be much stronger than in equilibrium, leading to the incorrect conclusion that the abundances of these metals are substantially enhanced (e.g., Becker *et al.*, 1979, 1980). The only mechanism for ionizing the atoms in the low density plasma is collisions with electrons. These collisions are so infrequent that a substantial amount of time is required for the ionization state of the gas to approach that expected for the temperature of the ions. An upwardly ionizing gas will spend a shorter or longer amount of time in a given ionization state, depending on the ionization potential to the next state. In particular, since the ionization potential of an He-like ion to its H-like state is high, it spends a relatively long time in the He-like state. The net result is that the He-like lines dominate SNR X-ray spectra. The absolute timescale for the upward ionization can be parameterized by either nt, where n is the preshock density and t is the age, or $\eta = n^2 E$, where E is the thermal energy associated with the explosion (typically 10^{51} erg).

In addition to the line emission, there is also a continuum component arising primarily from bremsstrahlung radiation. Its shape is dependent on the degree of thermal equipartition between the ions and electrons. The presence of this continuum underlying the line emission must be taken into account when line strengths are inferred.

It is only in recent years that spectrometers with sufficient spectral resolution, collecting area and bandpass have made it possible to take into account the possibly complicated conditions in SNR in inferring properties. The first instruments to offer sufficient spectral resolution were the *Einstein* SSS and FPCS. While these clearly resolved many lines and allowed the first true plasma diagnostics to be performed, the SSS suffered from insufficient resolution to distinguish, e.g., the He-like line from the H-like line in Si, and the

FPCS was limited by its small collecting area to observing only the very brightest remnants. However, the FPCS and SSS clearly established the ubiquity of non-equilibrium conditions in SNR (Hamilton, Sarazin & Szymkowiak, 1986a; b; Winkler *et al.*, 1982; Hwang *et al.* 1993). The most recent generation of X-ray spectrometers has overcome these shortcomings and offer the added dimension of spatial resolution. These include the Broad-Band X-Ray Telescope (BBXRT) and the spectrometers on the ASCA satellite. As the ASCA results are still in a preliminary state and the first data are presented elsewhere in these proceedings, this paper will focus on the more thoroughly analyzed BBXRT data.

The BBXRT was the first instrument to offer high-throughput, modest resolution X-ray spectroscopy across the 0.3-10 keV band, allowing the first simultaneous spectroscopy of all K lines from O through Ni. It had a spectral resolution of $\sim$ 100 eV at 1 keV and $\sim$ 155 eV at 7 keV. Its focal plane spectrometers had five discrete detection elements, making possible crude spatially resolved spectroscopy. A more complete description can be found in Serlemitsos *et al.* (1993). The BBXRT was flown as part of the 9-day Astro-1 mission on the Space Shuttle *Columbia.* Of the more than 50 targets it observed, eight were supernova remnants (in addition to SN1987a). The main results of these observations are summarized below.

Because of its broad bandpass and moderate spectral resolution, the BBXRT facilitates possible the use of either of the two most often employed spectral analysis techniques: line diagnostics and broad-band model fitting. We make use of both below; in general the results yielded by the two are identical. We compare our data with the grid of non-time-dependent ionization models by Hamilton, Sarazin & Chevalier (1983), which model the development of X-ray lines in a Sedov blast wave. The Sedov solution formally describes self-similar adiabatic expansion of a blast wave from a point explosion in a cold, uniform medium. Work by Itoh (1977) and others have shown that an adiabatically expanding blast wave relaxes toward a Sedov solution when the mass of swept-up ISM exceeds $\sim$ 10 times the mass of the SN ejecta. The Sedov solution can be completely characterized by three parameters corresponding to suitable choices of mass, length and time. A typical combination of such parameters is the age t of the remnant, its energy E and the ambient interstellar hydrogen density n. However, when modelling the X-ray spectrum, using either a coronal equilibrium or a non-equilibrium ionization (NEI) model, the spectral shape is characterized by only two parameters. The parameters used by Hamilton, Sarazin & Chevalier in creating their grid of NEI models are T_s, the temperature of the shock, and $\eta = n^2E$. The parameter grid covered by their models, and the relationship of T_s and η to other parameters, is shown in Fig. 4. One parameter of note is the product nt, where t is the remnant age. The larger the nt product, (towards high η and low T_s), the closer the plasma approaches ionization equilibrium.

No observed supernova remnant is completely described by the Sedov solution: many of the best studied remnants are too young to have swept up sufficient mass, and most if not all remnants have encountered ISM inhomogeneities, both small and large. However, Hamilton & Sarazin (1984) have shown that for SNR expanding into non-uniform media, and for young SNR which have not yet swept up the requisite ISM mass to physically approximate a Sedov solution, the X-ray spectrum can be modeled by using two or more NEI components.

2. Historical SNR - Tycho and Cas A

Tycho, the remnant of a Type Ia supernova, and Cas A, the remnant of a Type II, are the most extensively studied thermal SNR in X-rays. This is because they are bright and

hot, thus accessible by virtually any X-ray observatory, and display strong Fe K lines. As they are both younger than 450 y, their X-ray spectra are dominated by ejecta, and the X-ray spectra therefore allow us to make inferences about the nature of the progenitor star.

For Tycho, the current best model of the X-ray spectrum, incorporating data from a number of instruments to cover the 0.1-20 keV band, invokes two time-dependent ionization components, one representing the propagating blast wave, and the other a reverse shock encountering layered ejecta (Hamilton, Sarazin and Szymkowiak, 1986b). With the BBXRT it was possible for the first time to observe simultaneously the high and low energy components and thus remove any systematic uncertainties associated with instrumental cross calibrations, and to seek detailed spectral differences around the remnant. A BBXRT spectrum is compared with the spectrum from a much longer *Einstein* SSS exposure in Fig. 1. Two BBXRT spectra, of opposite sides of the remnant, yield identical line strengths to $\leq 5\%$ despite the fact that they sample emission from regions separated by a distance of approximately 6 pc. This provides the first X-ray constraint on the azimuthal symmetry of a supernova explosion and suggests that the medium into which Tycho is expanding is also uniform to $\sim 5\%$. Despite the limited number of counts in the BBXRT spectrum, a number of strong lines are visible to the eye, including some that were previously never resolved (for example the "beta" transition of Si XIV at 2.01 keV). Merely measuring the energy centroids and the intensity ratios of the prominent lines provides some new and interesting information. For instance, one source of controversy based on the results of lower resolution spectrometers has been the centroid energy of the Fe K line (Hamilton, Sarazin & Szymkowiak, 1986b). The BBXRT measures the centroid directly, without the need for accounting for the slope of the underlying continuum. The measured value of 6.41 ± 0.02 keV indicates a very low ionization state (Fe XIX or lower).

We have used the diagnostics for non-equilibrium plasmas from Hamilton, Sarazin, & Chevalier (1983) to constrain the parameters characterizing the plasma, T_s and η. The parameter values allowed by these diagnostics using the lighter elements (Mg, Si and S) are disjoint from those allowed by the Fe K line energy. We conclude that the environment in which the Fe is embedded, presumably the innermost shell of ejecta, is hotter and less dense than the other shells. While the possibility of this was suggested by Hamilton, Sarazin & Szymkowiak (1986b), the BBXRT provides a direct measurement almost trivially.

While the Cas A spectrum in Fig. 2 displays the same general properties as that of Tycho, namely strong lines from Mg, Si, S, and Fe, the line shapes and relative strengths are different, as is the strength of the high energy continuum. In particular, the Si line is not as prominent as in Tycho, the Fe K emission is substantially stronger, and all lines are intrinsically broadened. Markert *et al.* (1983) ascribed the shape of the Si line to Doppler broadening from an expanding ring of ejecta observed at a range of velocities. In contrast to the Fe K line in Tycho, the centroid energy in Cas A is around 6.6 keV, more consistent with mostly stripped Fe. Also, the BBXRT reveals for the first time that its shape is inconsistent with a single, narrow line. It can be fit with a single broad line at 6.6 keV of intrinsic width 84 eV, or as two narrow lines with energies 6.46 and 6.65 keV. If we assume a single, broad line, then the centroid is larger than any value on the grid of models for a single Sedov-Taylor blast wave constructed by Hamilton, Sarazin, & Chevalier (1983). This suggests the need to model Cas A as the sum of multiple non-equilibrium models, as was done for Tycho.

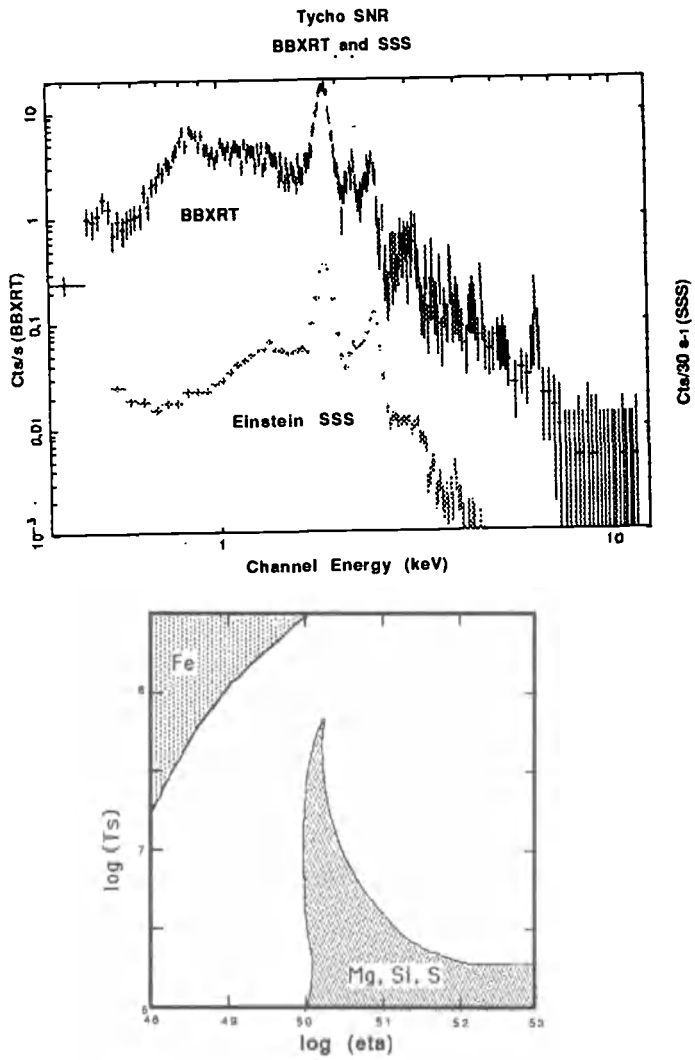

FIGURE 1. (*upper*). BBXRT spectrum of Tycho SNR (top trace), compared with *Einstein* SSS spectrum (bottom trace). (*lower*). Allowed 90 percent confidence regions of T_s and η for Tycho. Allowed regions for Fe K diagnostics and those for lighter elements are completely disjoint.

3. Evolved SNR

For evolved supernova remnants, whose X-ray emission is dominated by swept up ISM material instead of ejecta, X-ray spectroscopy reveals more information about the ISM and shock physics than about the progenitor and the supernova event. The BBXRT observed all or part of five evolved SNR: IC 443, CTB109, Vela, N132D, and Puppis A. Below we briefly discuss our findings on each of these.

The global morphology of the evolved remnant IC 443 has been strongly influenced by the presence of a molecular cloud in the line of sight (Petre *et al.*, 1988). Bright X-ray emission, relatively unobscured by the molecular cloud, arises in a region of enhanced density in the vicinity of (but not associated with) bright optical filamentation in the northern portion of the remnant. In Fig. 3 we show spectra from the edge of the shell and the interior of the bright knot, about 6 pc behind the shell. Spectral differences are

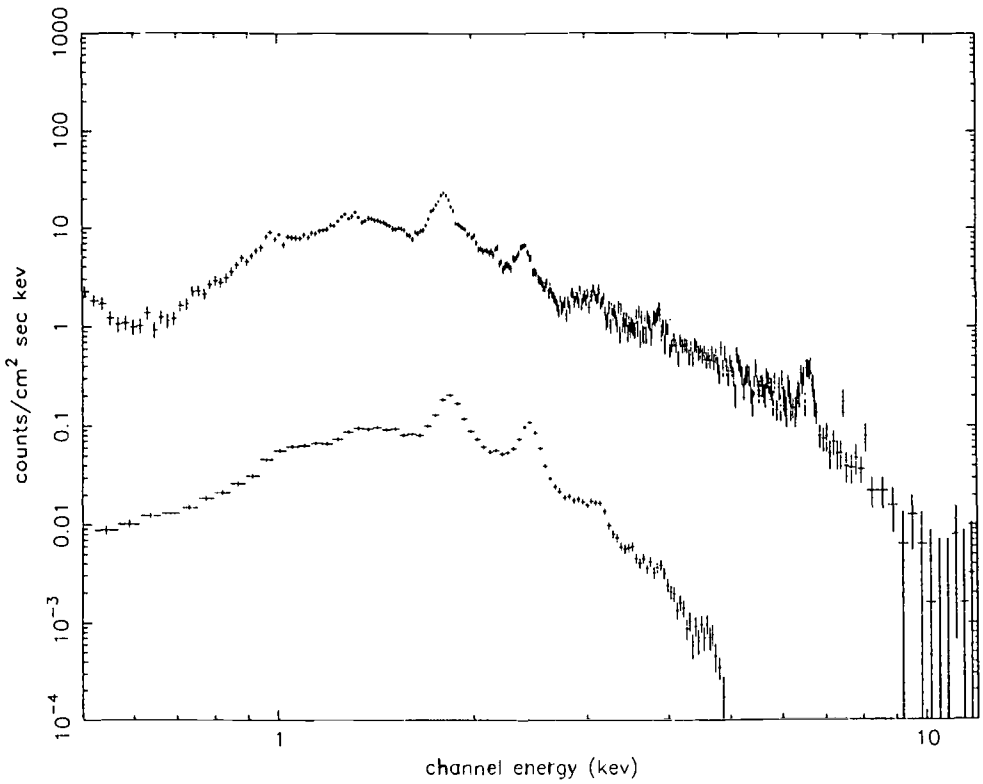

FIGURE 2. (*top*). BBXRT spectrum of Cas A. (top trace), compared with *Einstein* SSS spectrum (bottom trace). (*bottom*) Fe K region of Cas A spectrum. Line is fit using two narrow components, at 6.46 and 6.65 keV.

quite apparent. There is a clear trend with increasing distance behind the shock towards lines of higher ionization state in the band around 1 keV (a band dominated by Ne IX, Ne X, and the Fe L blend), the Mg K region around 1.35 keV and the Si K band around 1.80 keV.

Compared with the spectra of the younger remnants, the lines from IC 443 are not nearly as strong. In fact, model fitting suggests that all the elements from Ne through Fe are underabundant with respect to solar (see Table 2). Despite the relatively weak line emission, the spectral resolution and broad bandpass of the BBXRT facilitate for the first time on this remnant the kind of plasma diagnostics performed previously on only the bright, young remnants. In Fig. 4 we show the location in the η-T_s plane of the best-fit non-equilibrium model. The primary difference between the rim and the interior is that at the rim a model in which electron-ion equipartition has not been reached ($T_i \neq T_e$) is preferred, while in the interior, an equipartition model is preferred. This is the first measurement of an equipartition timescale in a supernova remnant: from Sedov dynamics, we estimate an equipartition time of ~1,000 y. The allowed values of η and

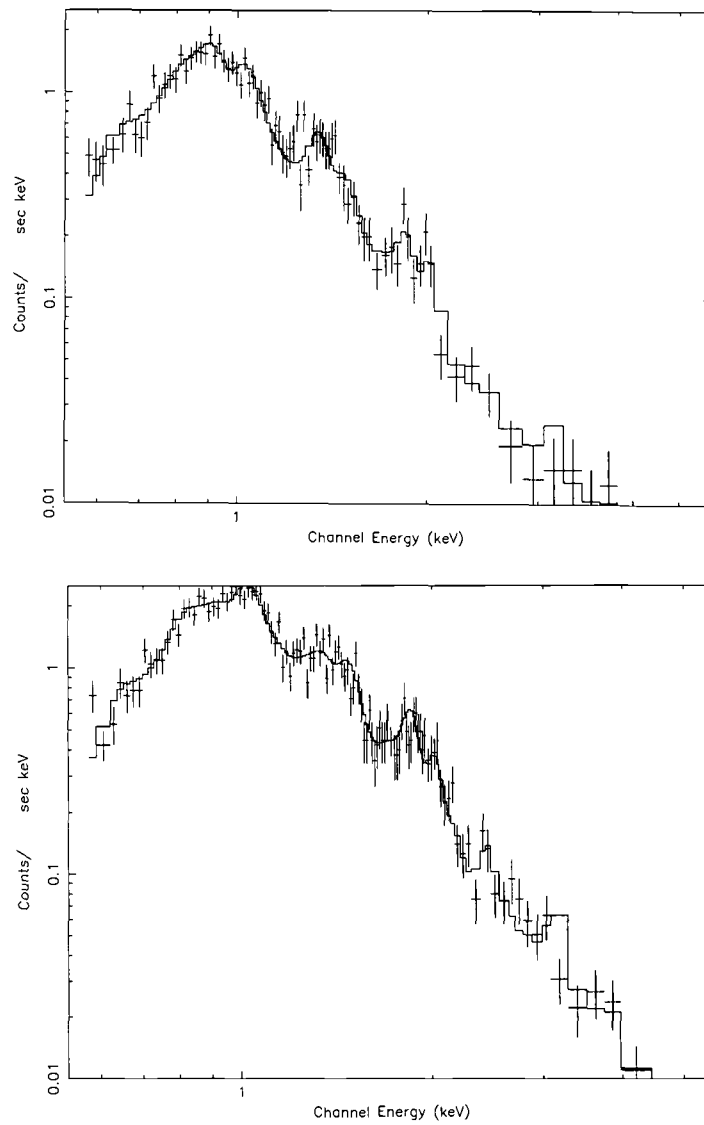

FIGURE 3. Spectra from the rim (top) and interior (bottom) of the X-ray bright knot in IC 443. Changes in the spectrum around 1 keV and 1.85 keV are readily apparent.

T_s are in a region where the differences between non-equilibrium and equilibrium models becomes small, suggesting a rather evolved remnant.

The remnant CTB109 (G109.1−1.0) is unique among galactic supernova remnants: in addition to a well-defined semicircular shell, it contains a centrally situated binary X-ray pulsar, 1E2259+586 (Gregory & Fahlman, 1979; Fahlman & Gregory, 1980). The angular extent is sufficient so that BBXRT could simultaneously obtain spectra of both the diffuse emission and the pulsar in different detector elements. The BBXRT observation represents the first high quality spectrum ever obtained of CTB109. The spectrum displays prominently the He α lines of Ne, Mg, and Si. Fitting it with a single NEI model has turned out to be quite problematic. The Ne IX/Ne X ratio is very large, suggesting

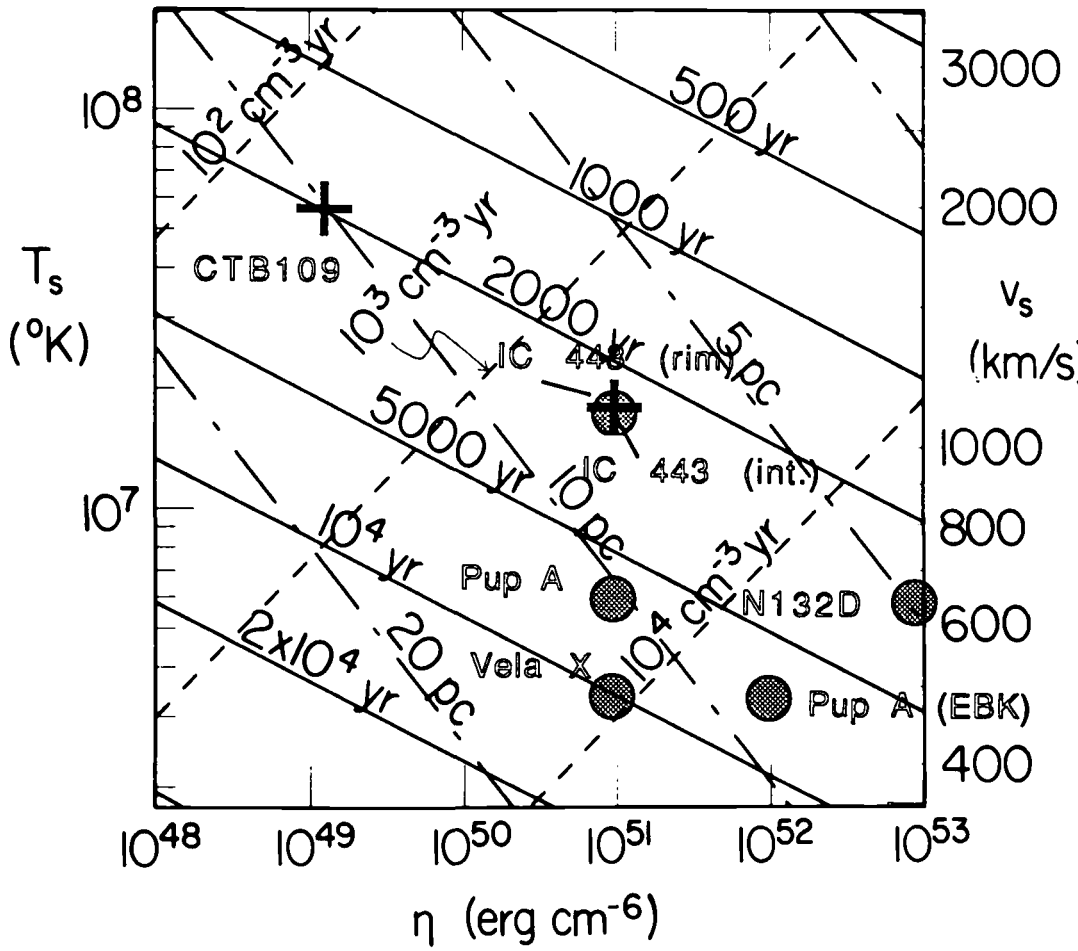

FIGURE 4. Best fit solutions for evolved remnants observed by the BBXRT, displayed in η-T_s plane from Hamilton, Sarazin & Chevalier (1983). Filled circles are for fits where $T_i \neq T_e$, and plus signs represent fits for which $T_i = T_e$

either a low temperature or small nt product. At the same time, the continuum above 2 keV is strong, requiring a high shock temperature. While this might suggest the presence of two NEI components, the BBXRT data are well fit by a single component model, with $T_s = 5\times10^7$ K, $\eta = 10^{49}$ erg cm^{-6}, $nt = 300$ cm^{-3} y, and $T_i = T_e$. The approximate time since the shock passed this region is $\sim 2,000$ y, comparable with the equipartition time estimated for IC 443. Another interesting result is the large abundances of oxygen and neon, and the low abundance of iron, required by the fits (see Table 2). If we are observing ejecta, this offers strong evidence that CTB109 in the remnant of a Type II supernova. It is interesting that the both spectra for which an ion-electron equipartition models is preferred sample remnant interiors. Vela X is a very complex region of the Vela supernova remnant containing the Vela pulsar and its associated synchrotron nebula. Despite the dominance of the hard non-thermal component, it was possible using the BBXRT to measure the temperature of the hot gas in the Vela X region. Our best fit model yields $T_s = 3\times10^6$ K and $\eta = 10^{51}$ erg cm^{-6}. Again, the relatively high nt product, 10^4 cm^{-3} y, suggests that the gas is approaching ionization equilibrium. Even in the interior of this very evolved SNR, we find $T_i \neq T_e$. The relatively small number

TABLE 2. Abundance Measurements of Evolved SNR using BBXRT

Remnant	CNO/Si	Ne/Si	(Fe+Ni)/Si	Si/solar
IC 443 (rim)	0.5	0.3	1.0	0.2
IC 443 (interior)	0.4	0.5	1.8	0.1
CTB109	3.5	1.5	0.0	2.4
Vela X	1.0	1.0	1.0	1.0
N132D	0.7	0.6	0.9	0.1
Puppis A (E. knot)	0.6	0.8	0.6	1.0
Puppis A (composite)	0.7	0.9	0.9	0.6

of counts in the spectrum precludes any statement about abundances, except that they are not substantially different from solar.

N132D, the most X-ray luminous SNR in the Large Magellanic Cloud, is thought to be the remnant of a Type II explosion, based on its oxygen-rich optical spectrum (Lasker, 1978). Despite the very brief BBXRT exposure (475 s), we derive a unique solution from model fitting. The best fit NEI model has $T_s = 5 \times 10^6$ K, $\eta = 10^{52}$ erg cm^{-6}, and $T_i \neq T_e$. The large nt product ($3x10^4$ cm^{-3} y) indicates near-equilibrium conditions. The lack of strong line emission above 1 keV is apparent. This is due to reduced abundances of Mg, Si and Fe. To compare our results with those from the Einstein FPCS (Hwang *et al.*, 1993), we explicitly incorporated into our fitting the strong lines of O VII, and O VIII. The ratio between these lines is only marginally consistent with the FPCS result. There is also a statistically significant detection of a line at 500 eV, consistent with N VII Ly α.

While the BBXRT was unmatched in its combination of spectral resolution, sensitivity and bandpass, its observation of Puppis A offers something truly unique. The BBXRT performed a scanning observation across Puppis A, covering virtually the entire remnant. Attitude reconstruction has been performed on these data, yielding a map of the entire remnant with $\sim$ 6 arc-minute resolution. Taking advantage of BBXRT's spectral resolution, we have created maps containing only those events which appear in the various lines, thus producing the first ever narrow-band X-ray images of a supernova remnant (or any cosmic X-ray source). These maps offer a new technique for studying how the abundances and ionization structures vary across a supernova remnant. Figs. 5 and 6 provide examples of the promise of this technique. In Fig. 5, we show the flux ratio between O VII and O VIII, and in Fig. 6, the flux ratio between Ne IX and Ne X. There is clearly structure in both ratios across the remnant, indicating variations either in temperature or ionization state. More interestingly, there are clear differences between the two ratios, which indicate clear differences in ionization state across the remnant. As there maps are preliminary, we draw no strong inferences from them, but merely point out the potential usefulness of narrow band X-ray images as diagnostics. We have also carried out a more conventional analysis of two spectra from Puppis A, a composite spectrum and a spectrum of the brightest X-ray feature in the remnant, the eastern bright knot (Petre *et al.*, 1982). We find both spectra require $T_i \neq T_e$, and in Fig. 4, the two can be seen to lie along a line of constant age. The primary difference is that due to its higher density the eastern bright knot has a higher nt product than the remnant as a whole.

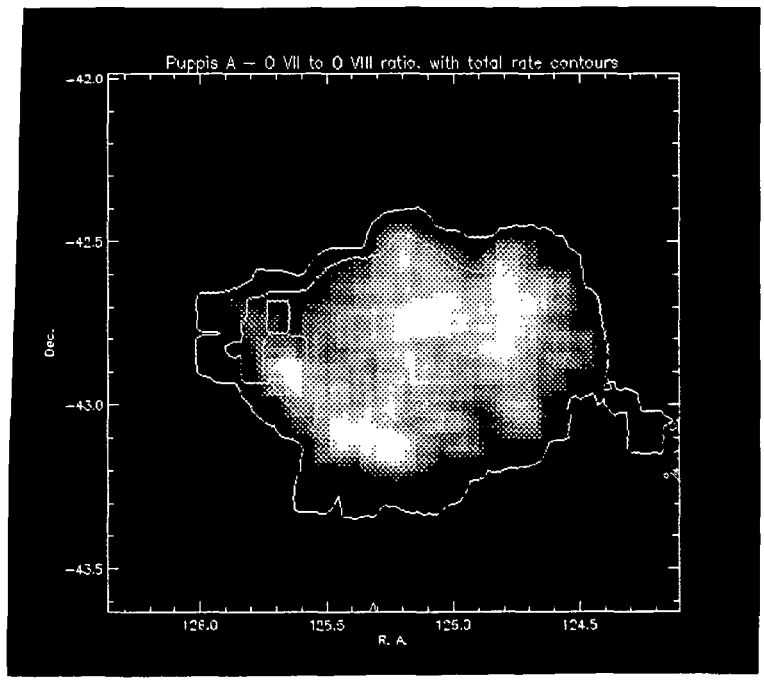

FIGURE 5. O VII to O VIII line ratio in Puppis A, overlaid on surface brightness contours.

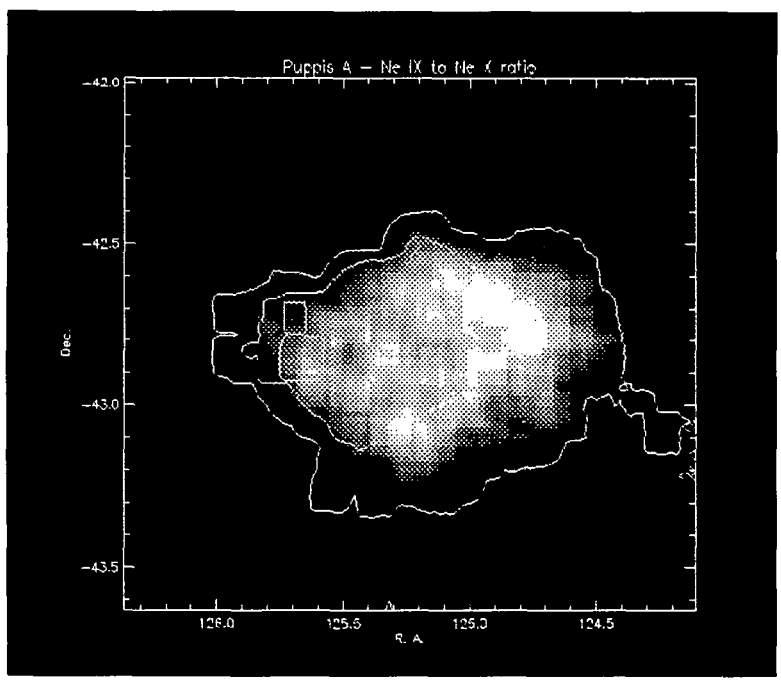

FIGURE 6. Ne IX to Ne X flux in Puppis A, overlaid on surface brightness contours. Comparison with O ratio indicates differences in ionization structure.

4. Summary

With the BBXRT and its successors, X-ray spectroscopy of SNRs has entered a new era. No longer can the starting point of spectral analysis be fitting a one- or two-temperature coronal plasma model to the data. As the spectra of Cas A and Tycho demonstrate, even a single component NEI model is insufficient. Our ability to refine information regarding progenitor properties will become even more dependent on the input models and the degree of certainty of the atomic physics line strength calculations.

For the evolved supernova remnants, the data and our knowledge have not yet reached such a critical juncture; we have much to learn from our first application of NEI models to these data. In Fig. 4 and Table 2, we have summarized the BBXRT fit results for the evolved remnants. Fig. 4 shows the range of physical conditions found in SNR, from extreme nonequilibrium in the interior of CTB109, to near equilibrium in N132D. It also shows that $T_i \neq T_e$ is found in many locations, but not everywhere. In particular, we find electron-ion equipartition only in the interiors of these remnants (though not all interiors show equipartition). In Table 2, we have compiled the best-fit abundance values, scaled to that of Si, plus the absolute value of the Si abundance compared with the cosmic value. The only general conclusion that can be reached is that abundances vary strongly from remnant to remnant. Reaching more general conclusions about whether the abundances within the hot gas also vary strongly across remnants, and whether the suggestion that electron-ion equilibration times can be inferred in many remnants, requires a more comprehensive program of spatially resolved X-ray spectroscopy. That capability is currently available using the newly-launched Japanese/US observatory ASCA.

The author would like to gratefully acknowledge the many individuals whose efforts made possible the BBXRT mission and the results presented here. P. Serlemitsos, the BBXRT Principal Investigator, is the prime mover behind the entire effort. A. Szymkowiak has performed the analysis of the Cas A data, and together with K. Arnaud and J.-H. Rho made the Hamilton NEI models available in XSPEC. A. Smale is responsible for the BBXRT data extraction software and K. Weaver played the key role in development of the BBXRT spectral response matrices. Finally S. Snowden helped the author overcome the needless complexities of TeX.

REFERENCES

Becker, R. H.,*et al.* 1979, ApJL, **246**, L73-6.

Becker, R. H., *et al.* 1980, ApJL, **235**, L5-8.

Fahlman, G. G., & Gregory, P. C. 1981, Nature, **293**, 202-4.

Gregory, P. C., &Fahlman, G. G. 1980, Nature, **287**, 805- 7.

Hamilton, A. J. S., Sarazin, C. L., & Chevalier, R. A., 1983, ApJS, **51**, 115-48.

Hamilton, A. J. S., Sarazin, C. L. 1984, ApJ **284**, 601-11.

Hamilton, A. J. S., Sarazin, C. L., & Szymkowiak, A. E. 1986a, ApJ, **300**, 698-712.

Hamilton, A. J. S., Sarazin, C. L., & Szymkowiak, A. E. 1986b, ApJ, **300**, 713-21.

Hwang, U., Hughes,J. P., Canizares, C. R.,& Markert, T. H. 1993, ApJ, 414, 219.

Itoh, H. 1979, Pub. Astr. Soc. Japan, **29**, 813-27.

Lasker, B. M. 1978, ApJ, **223**, 109-21.

Markert, T. H., Canizares, C. R., Clark, G. W., & Winkler, P. F., 1983, ApJ, **268**, 134-44.

Petre, R., Szymkowiak, A. E., Seward, F. D., & Willingale, R. 1988, ApJ, **335**, 215-38.

Raymond, J. C. & Smith, B. W. 1977, ApJS, **35**, 419-66.

Serlemitsos, P. *et al.*, 1992, *Frontiers of X-Ray Astronomy*, ed. Y. Tanaka and K. Koyama, pp. 221- 231. Tokyo: Universal Academy Press.

Winkler, P. F., Canizares, C. R., Clark, G. W., Markert, T. H., Kalata, K., & Schnopper, H. W. 1982, ApJL, **246**, L27-32.

ASCA Observations of Supernova Remnants

By HIROSHI TSUNEMI AND THE ASCA TEAM

Department of Earth and Space Science, Faculty of Science, Osaka University, Japan

We present here preliminary results of the *ASCA* satellite. *ASCA* is equipped with X-ray telescopes that can observe the energy range up to 12 keV. There are two types of detector systems: GIS and SIS. The energy resolution of the SIS is 130 eV (FWHM at 6 keV) and can resolve emission lines clearly. For the PV phase, we planned to observe about 150 sources. Among them, there are 23 SNR's, some of which are presented here. We will be able to study the evolution of thin hot plasma in the SNRs.

1. Introduction

The fourth Japanese X-ray Astronomy satellite was successfully launched on February 20, 1993, from Kagoshima Space Center. The satellite's pre-launch name, Astro-D, was changed to it ASCA once it achieved orbit. *ASCA* is equipped with four thin foil X-ray mirror telescopes (XRT) that can collect X-rays up to 12 keV. Fig. 1 shows the effective area of the XRT. The XRT has a point spread function (PSF) with a half power diameter (HPD) about 2.7 arcmin. There is a sharp core of about 20 arcsec diameter in the PSF that enables us to separate point sources separated by less than one arcmin.

ASCA has two types of detectors: one is the imaging gas scintillation proportional counter, (IGSPC, Ohashi et al, 1991) and the other is the X-ray CCD camera (Burke, et al., 1993). They are called the gas imaging spectrometers (GIS) and the solid-state imaging spectrometers (SIS), respectively. There are two GIS detectors and two SIS detectors. Each detector is at the focal plane of its own XRT. One SIS detector has 4 CCD chips which can observe a field of view of 22×22 arcmin^2. The basic parameters for the GIS and SIS are summarized in table 1.

The GIS can observe the whole effective field of view of the XRT and has a time resolution down to 61 μsec. Although it cannot observe the energy range below 0.7 keV due to the thickness of its beryllium window, it can observe the energy range up to 12 keV with high detection efficiency (greater than 70 %). The SIS has a smaller field of view, poorer time resolution, but a broader energy range and higher energy resolution. The CCD chip is designed for X-ray studies in orbit: low read-out noise, thick depletion region and radiation-hardness (Burke, et al., 1991). The detection efficiency around 10 keV is inferior to that of the GIS. Taken together, these two detector systems complement each other.

The satellite pointing has a sun angle constraint. The optical axis of the XRT is the Z-axis while the solar paddle is facing the Y-axis. We have to point the satellite such that the sun should be placed within 30 degree from the Y-axis. Given this constraint, we can access any part of the sky in six months.

At the end of March, 1993, all the detector systems were activated for initial checkout. All the instruments functioned properly. In mid-April, performance of verification (PV) phase started. It would last about 6 months. Then, the guest observer (GO) phase would start.

TABLE 1. The basic properties of GIS and SIS.

Item	GIS	SIS
field of view (arcmin)	40ϕ	22×22
energy range (keV)	$0.7 \sim 12$	$0.4 \sim 12$
energy resolution (keV) (FWHM at 6 keV)	0.45	0.13

TABLE 2. The SNRs to be observed during the PV phase

Crab	Cassiopeia-A	PSR0540-69	Kes 75
Puppis A	Kepler	SN1006	Kes73
W49B	W50	RCW 86	RX04591+5147
Vela-X	CTB80	SN1987A	MSH 15-52
E0102-72	G292.0+1.8	Tycho-SNR	N132D
Cygnus Loop	G21.5-0.9	RCW 103	

2. Observation plan during the PV phase

During the PV phase, *ASCA* will observe about 150 targets. There are seven categories: AGNs, Binaries, Clusters, CXB (Cosmic X-ray Background), Galaxies, Stars and SNRs. In the SNR category, there are 23 targets listed in table 2.

3. Observation results

We present here the X-ray images and spectra for various SNR observed during the PV phase. Most of them show interesting spectral features rather than the temporal variation. Therefore, the focus of this paper will be on the results obtained with the SIS. Most of the background generated by the particles can be easily separated from the X-ray events by the difference in charge distribution in the CCD. The X-ray background level of the SIS (several $\times 10^{-4}$ counts $s^{-1}cm^{-2}keV^{-1}$) is so low that we need not subtract the background spectrum, particularly for a point-like source. Therefore, all the spectra shown in this paper have not been background subtracted. Extended sources like the Cygnus Loop are slightly affected by the diffuse X-ray background. Since the in-orbit self calibration for the detectors has not been finished by the writing of this paper, all the data shown here are preliminary.

The energy resolving power of the SIS can clearly separate the K-α emission lines from various ion species. Typical K-α lines resolved with the SIS are listed in table 3. Among others in the energy range between 0.4 keV and 12 keV, there are $Fe - L$ emission line blends distributed from 0.7 keV to 1.2 keV.

3.1. *The Crab Nebula*

We observed the Crab Nebula at various locations in the field of view to study the image quality of the XRT. The XRT functions properly as we expected based on the ground

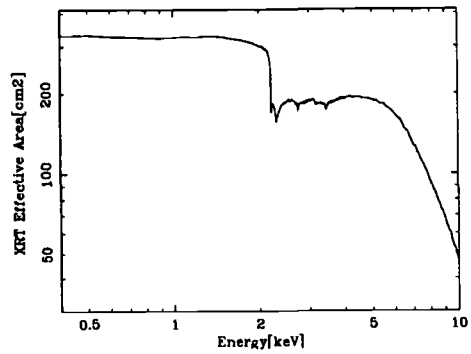

FIGURE 1. The effective area of one XRT.

TABLE 3. K α emission line energies from various ions

ion	keV	ion	keV	ion	keV	ion	keV
O VII	0.57	Mg XI	1.35	S XV	2.46	Ca XIX	3.91
O VIII	0.65	Mg XII	1.47	S XVI	2.62	Ca XX	4.11
Ne IX	0.92	Si XIII	1.86	A XVII	3.14	Fe XXV	6.70
Ne X	1.02	Si XIV	2.01	A XVIII	3.31	Fe XXVI	6.96

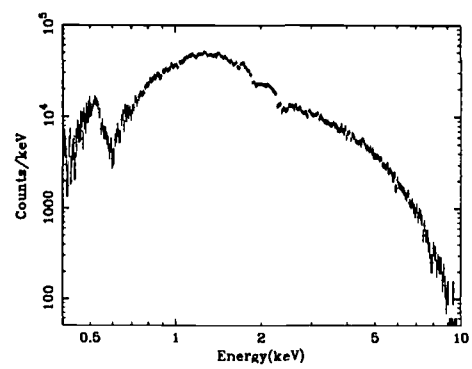

FIGURE 2. The X-ray spectrum of the Crab nebula.

calibration. Fig. 2 shows the X-ray spectrum of the Crab nebula obtained with the SIS. It can be well fitted with a power law spectrum without emission lines. There are several spectral features due to the detector system. The clear features seen here are due to the $Au - M$ edges ($2.2 \sim 3.4$ keV), the $Si - K$ edge (1.8 keV), the $Al - K$ edge (1.5 keV), the $O - K$ edge (0.53 keV). The $Au - M$ edges come from the gold coating on the XRT surface. The $Al - K$ edge comes from the optical block filter placed just above the CCD

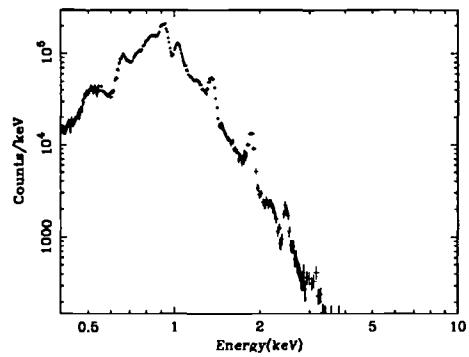

FIGURE 3. The X-ray spectrum of the eastern knot of Puppis-A.

and the XRT thermal shield. The Si and O edges come from the dead layer of the CCD that is made of SiO_2 and Si.

3.2. *Puppis-A*

Puppis-A has an incomplete shell-structure with a radius of about 30 arcmin (Gorenstein et al., 1974, Levine et al., 1979). Its X-ray emission comes from a thin thermal plasma that contains many emission lines (Winkler et al., 1981). There are several bright knots showing the inhomogeneities in the interstellar matter (Petre et al., 1982).

Fig. 3 shows the X-ray spectrum of the eastern bright knot. There are several emission lines clearly resolved. Most of these are K-α emission lines from O, Ne, Mg, Si and S. The complicated structure around $0.7 \sim 0.9$ keV mainly comes from $Fe - L$ emissions. The emission above 5 keV is just below the detection limit of *ASCA*. The continuum spectrum shows the temperature to be about 0.3 keV. During the PV phase, we planned to observe the whole remnant with the SIS.

3.3. *W49B*

W49B has a shell structure in the radio band while it shows a center-filled structure in X-ray (Pye et al., 1984). It is classified as a plerion-type SNR in the X-ray region (Seward, 1990). Smith et al. (1985) reported on the X-ray spectrum up to 10 keV with *EXOSAT* and obtained an $Fe - K$ emission line with an equivalent width of about 4.7(+0.2-0.6) keV. Other line features have not been clearly resolved due to the energy resolution of the *EXOSAT* detector.

Fig. 4 shows the X-ray spectrum obtained with the *SIS*. There are several emission lines easily resolved. Most of them are K-α line emissions from helium-like and hydrogen-like ions of Si, S, Ar, Ca and Fe. The continuum spectrum can be well fitted with a thermal Bremsstrahlung model of about 2 keV. However, the emission line ratios between the helium-like ion and the hydrogen-like ion show that these elements have not reached collisional ionization equilibrium at this temperature. We found that the spectrum could not be reproduced with a simple non-equilibrium ionization (NEI) model which is parameterized with a single electron temperature and a single plasma parameter (the product of the electron density and the elapsed time after the shock heating).

The X-ray spectrum shows a strong cutoff at around 1 keV. We found that the column density is about 3×10^{22} H atom cm^{-2}, which is consistent with that obtained by Smith et al. (1985). W49B is expected to be a typical shell-like SNR taking into account

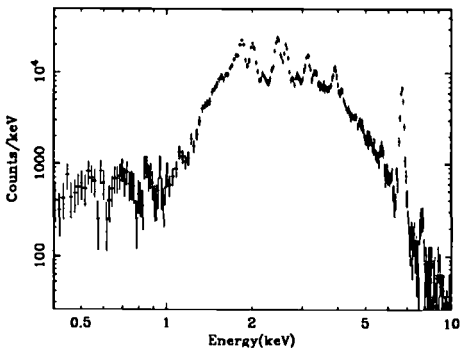

FIGURE 4. The X-ray spectrum of W49B.

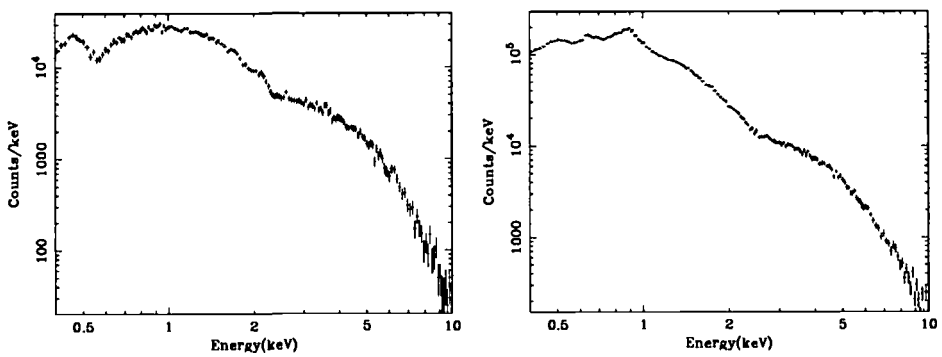

FIGURE 5. The X-ray spectrum of Vela-X (Vela pulsar) (5a, left) and its surrounding nebula (5b, right).

the facts that there is no clear point-like source inside the remnant and that the X-ray emission is thermal in origin. The emission can be roughly divided into two parts: one is from the reverse shock and the other is from the forward shock. The emission from the reverse shock shows a higher temperature than that from the forward shock. We can understand that the low-temperature emission from the forward shock is absorbed while the high-temperature emission from the reverse shock is seen.

W49B is about 2 $\sim$ 3 arcmin in angular diameter. Since the PSF of the XRT is a little smaller than this size, we may be able to study the spectral distribution of the X-ray image. According to preliminary analysis, the extent of each X-ray emission line is slightly different for each ion. The higher Z elements show a smaller size. This result suggests an onion-skin structure in the reverse shock. A detailed analysis will be done elsewhere.

3.4. *Vela-X*

Fig. 5a,b show the X-ray spectra of Vela-X and its surrounding area obtained with the SIS. The spectrum for Vela-X is obtained from a circular area with a radius of 1.5 arcmin

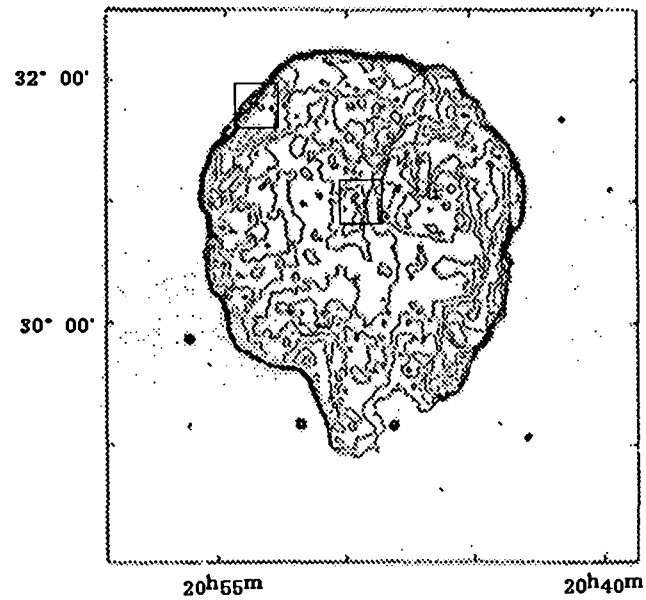

FIGURE 6. The whole image of the Cygnus Loop observed with *Einstein* (Seward, 1990). Rectangles show the NE rim and the central region which were observed with the SIS.

centered on the Vela pulsar. The spectrum of the surrounding area is obtained from the region that is more than 5 arcmin away from the Vela pulsar. The spectrum of Vela pulsar is similar to that of Crab. There are no clear emission lines. Some instrumental spectral features due to the XRT and the SIS are evident. In contrast, the spectrum of the surrounding region shows some emission line features, probably due to the $O-K$ line and $Fe-L$ line blends. We should note that the spectrum of fig. 5b is partly contaminated by the Vela pulsar due to the PSF of the XRT.

3.5. *Cygnus Loop*

The Cygnus Loop is one of the strongest X-ray sources below 1 keV. It exhibits a typical shell-structure about 3 degrees in diameter. Ku et al. (1984) measured the temperature of the shell region to be about $2 \times 10^6 K$ and found a temperature gradient inside the shell. Tsunemi et al. (1988) observed emission lines of Si and S from the whole remnant with *GSPC* on *Tenma*. Hatsukade and Tsunemi (1990) reported on emission above 1.5 keV and found its extent to be smaller than that below 1.5 keV. Therefore, we can expect that the emission from the shell region shows a low temperature with a high emission measure while regions inside the shell show a high temperature with a low emission measure. Vedder et al. (1986) observed a small portion of the northern rim with the *FPCS* on *Einstein*. They showed that the plasma did not reach the collisional ionization condition based on observations of the oxygen lines.

We observed two small regions of the Loop shown in fig. 6. The rectangles in this figure show the field of view of the SIS. One pointing was centered on the north-eastern bright (NE) rim and the other pointing was centered on the central region. The X-ray image for the NE rim is shown in fig. 7.

The X-ray spectra for these two regions are shown in figs. 8a,b. The X-ray spectrum of the central region shows emission lines of S and Si. The broad hump around 0.8 keV mainly comes from $Fe-L$ line blends. The NE rim spectrum is different than the central region spectrum. There is a clear emission line from Mg while there are almost no lines

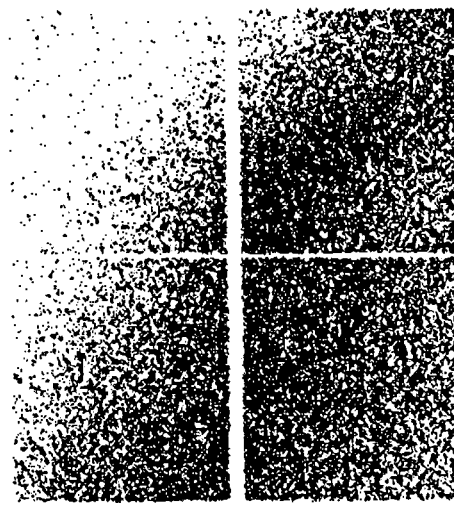

FIGURE 7. The X-ray image of the NE rim of the Cygnus Loop shown in the left figure obtained with the SIS (four CCD chips). The gap between the CCD chips is seen.

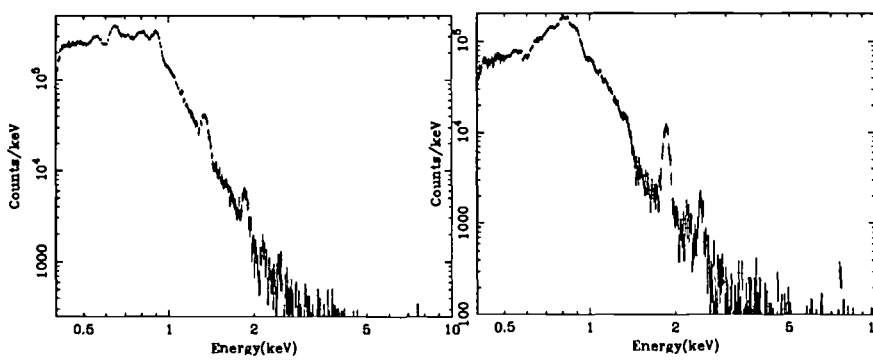

FIGURE 8. X-ray spectra of two parts of the Cygnus Loop (see Fig. 6). Fig. 8a (left) – north east (NE) rim; Fig. 8b (right) – central region.

from S. Furthermore, there are clear emission lines of $OVII$, $OVIII$ and $NeIX$. These differences show that the temperature in the central region is much higher than that in the NE region.

We found that a single temperature collisional ionization equilibrium model does not fit the X-ray spectrum of the NE region. The average plasma parameter in the NE rim is about $10^{11\sim12}$ cm^{-3} s with an electron temperature $0.2 \sim 0.25$ keV. The spatially resolved analyses along the radial direction of the shell will reveal the plasma structure of the shock front.

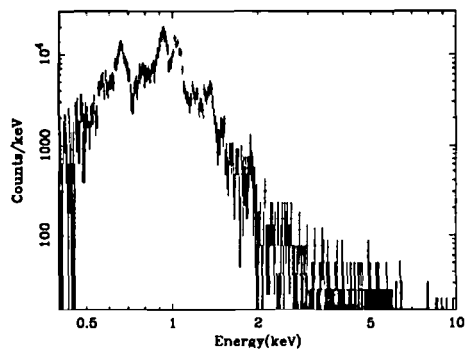

FIGURE 9. The X-ray spectrum of E0102-72

3.6. *E0102-72*

E0102-72 is the second brightest X-ray source in the SMC at X-ray energies. It was discovered in the *Einstein IPC* survey of the SMC (Seward and Mitchell, 1981). The observation with *HRI* on *Einstein* (Inoue et al., 1983) revealed a shell structure with a diameter about 30 arcsec. The optical observation (Dopita et al., 1981) shows that it is a young, oxygen-rich SNR.

Fig. 9 shows the X-ray spectrum obtained with the SIS. We can see the K-α emission lines from $Ne-IX$ and $Ne-X$ as well $O-VIII$. The emission line from $O-VII$ seems to be quite strong since it is seen in the trough due to the oxygen absorption edge in the CCD response. The intensity of $Fe-L$ line blends is quite weak compared to those of Ne and O. These results are consistent with those discussed by Hughes (1987). The spatial extent of this source is small, such that it looks like a point source with *ASCA*. Therefore, we can get only the overall spectrum.

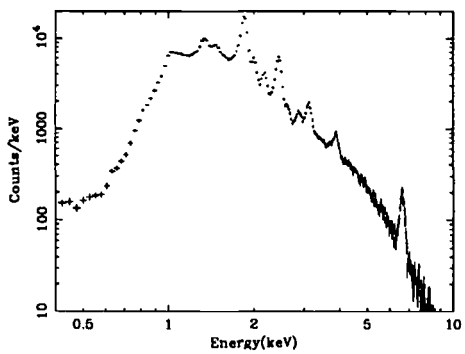

FIGURE 10. The X-ray spectrum of Cassiopeia-A.

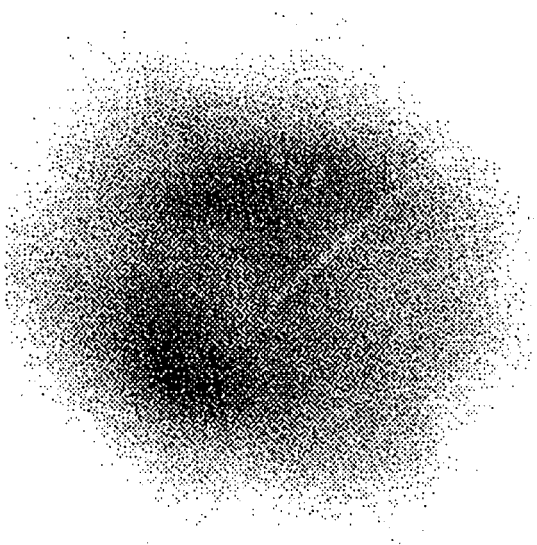

FIGURE 11. The X-ray image of Cassiopeia-A obtained with the SIS (one CCD chip). North is up. A scar from the center to the upper right is due to a bad column in the CCD.

3.7. *Cassiopeia-A*

Cas-A forms a circular structure both in X-rays and in radio with a diameter of $3 \sim 4$ arcmin. Becker et al. (1979) discovered many emission lines with *SSS* on *Einstein*. It is believed to be the result of a type II SN. Tsunemi et al. (1986) observed Cas-A with *GSPC* on *Tenma* and found that the plasma did not reach collisional ionization equilibrium. They obtained the mean energy of the $Fe-K$ line blends to be about 6.6 keV.

Fig. 10 shows the X-ray spectrum obtained with the SIS. There are several emission lines. In particular, the $Fe-K$ line blend seems to be broader than that of the detector response. Markert et al. (1983) obtained the Doppler shift broadening of 5000 km/sec by using the *FPCS* on *Einstein*. The energy resolution of the SIS should be able to see this broadening. Fig. 11 shows the X-ray image with the SIS. The image quality is restricted by the PSF of the XRT. We noticed that there are two bright parts. We will be able to get some spatially resolved spectra.

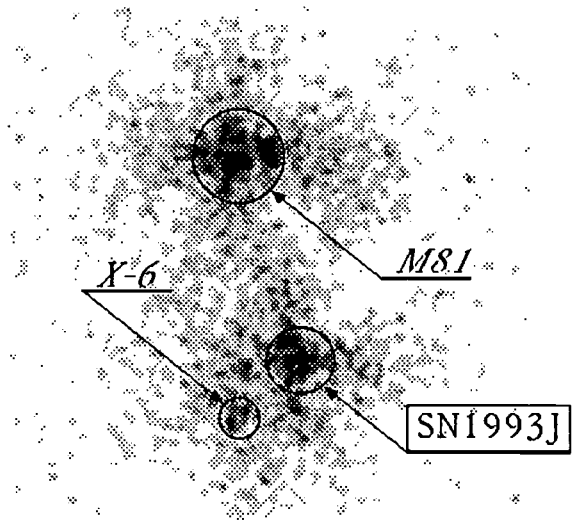

FIGURE 12. The X-ray image around SN1993J observed with the SIS. There are three sources seen here. Three statistically significant sources are seen. North is up. See text.

3.8. *SN1993J*

When a SN appeared in M81 at the end of March, 1993 (Ripero, 1993), we rescheduled the observation plan and observed the M81 region on April 7. We detected X-rays from SN1993J in the energy range of 0.4 to 12 keV (Tanaka et al., 1993). Fig. 12 shows the X-ray image obtained with the SIS. The complicated intensity structure is due to the Poisson statistics as well as the pattern of the PSF of the XRT. There are three peaks in the figure which are shown by circles. The strongest one in the north comes from X-5 of M81 (the core of M81). The second strongest one in the lower east coincides with the location of SN1993J. About 1 arcmin to the west of SN1993J, there is the known X-ray source X-6 in M81. We continued observations until mid-May when we met a solar angle constraint on the satellite. The X-ray intensity monotonically decayed with an e-folding time about 50 $\sim$ 70 days. The maximum luminosity was about 5×10^{39} erg s^{-1}. We plan to observe SN1993J again when the solar angle constraint allows.

4. Conclusion

We report here initial results of SNR observations with *ASCA's* SIS detectors. The energy resolving power of the SIS is much better than the non-dispersive instruments employed in previous satellites. It can easily separate the K-α emission of helium-like ions from that of hydrogen-like ions. We have learned that the most of the thin hot plasma in SNRs observed thus far have not reached the collisional ionization equilibrium condition. *ASCA* will reveal the plasma condition in detail by resolving many emission lines. In addition, the ability to make spatially resolved spectra enables us to study the evolution of hot plasmas.

Acknowledgments

The author expresses his special thanks to all the members of the *ASCA* team. E. Miyata helped me to arrange the Tex format. Dr. K. C. Gendreau read the manuscript carefully.

REFERENCES

Becker, R. H., Boldt, E. A., Holt, S. S., Mushotzky, R. F., Serlemitsos, P. J., Smith, G. W., and White, N. E. (1979), ApJ, **234**, L73.

Burke, B. E., Mountain, R. W., Harrison, D. C., Bautz, M. W., Doty, J. P., Ricker, G. R., and Daniels, R. J., (1991), *IEEE Trans.* **ED-38**, 1069.

Burke, B. E., Mountain, R. W., Daniels, R. J., and Cooper, M. J. (1993), *SPIE*, 2006-31.

Dopita, M. A., Tuohy, I. R., and Mathewson, D. S. (1981), ApJ, **248**, L105.

Gorenstein P., Harnden, F. R. Jr., and Tucker, W. H. (1974), ApJ, **192**, 661.

Hatsukade, I. and Tsunemi, H. (1990), ApJ, **362**, 566

Hughes, J. P., (1987), in IAU Colloq. 101, *Supernova Remnants and the Interstellar Medium*, ed. R. S. Roger and T. L. Landecker (Cambridge University Press), p. 125)

Inoue, H., Koyama, K., and Tanaka, Y. 1983, in IAU Symp. 101, *Supernova Remnants and Their X-ray Emission*, ed. I. J. Danziger and P. Gorenstein (Dordrecht: Reidel), p. 535)

Ku, W. H.-M, Kahn, S. M., Long, L, S., and Pisarski, R. L., (1984), ApJ, **278**, 615.

Markert, T. H., Canizares, S. R., Clark, G. W., and Winkler, P. F., Jr. (1983), ApJ, **268**, 134.

Ohashi, T., Makishima, K., Ishida, M., Tsuru, T., Tashiro, M., Mihara, T., Kohmura, Y., and Inoue, H. (1991), *SPIE*, **9-19**, 1549.

Peter, R., Canizares, C. R., Kriss, G. A., and Winkler, P. F., Jr. (1982), ApJ, **258**, 82.

Pye, J. P., Becker, R. H., Seward, F. D., and Thomas, N. (1984), MNRAS, **207**, 649.

Ripero, J., (1993), *IAUC*, No.5731.

Seward, F. D. and Mitchell, M., (1981), ApJ, **243**, 736.

Seward F. D., (1990), ApJS, **73**, 781.

Smith, A., Jones, L. R., Peacock, A., and Pye, J. P. (1985), ApJ, **296**, 469.

Tanaka, Y., and ASCA team. (1993), *IAUC*, No.5753.

Tsunemi, H., Yamashita, K., Masai, K., Hayakawa, S., and Koyama, K. (1986), ApJ, **306**, 248.

Tsunemi, H., Manabe, M., Yamashita, K., and Koyama, K. (1988), Pub. Astr. Soc. Japan, **40**, 449.

Vedder P. W., Canizares, C. R., and Markert, T. H. (1986), ApJ, **307**, 269.

Winkler P. F., Jr., Canizares, C. R., Clark, G. W., Kalata, K., Markert, T. H., and Schnopper, H. W., (1981), ApJ, **246**, L27.

Optical and UV Observations of Supernova Remnants

By ROBERT A. FESEN

Dartmouth College, Dept. of Physics and Astronomy, Hanover, NH 03755, USA

Recent observations of the galactic supernova remnants the Crab Nebula, SN 1006, Cas A, and the Cygnus Loop are reviewed. New studies of the Crab Nebula suggest its progenitor may have had appreciable mass loss in the form of a circumstellar disk resulting in both a bipolar expansion and formation of the synchrotron 'bays'. Unusually high proper motion knots near to and possibly directed away from the pulsar also have been reported. In the Cas A remnant, a NE jet of ejecta appears to be a plume of mantle material with expansion velocities up to 12000 km s^{-1} or nearly twice that seen in the main ejecta shell. HST observations of the sdOB star located behind SN 1006 indicate symmetrically expanding Fe II ejecta out to 8100 km s^{-1}. Lastly, deep images of the Cygnus Loop reveal emission structures similar to those seen in 2D & 3D shocked cloud simulations.

Optical research on the properties of galactic supernova remnants (SNRs) continues to yield important new results. Though only a small fraction of the radio catalogued 170+ galactic SNRs are optically detectable, optical measurements permit one to investigate such SNR properties as chemical abundances relative to hydrogen, expansion velocities, gas densities and temperatures, and ejecta filament morphologies and distribution. With the advent of the International Ultraviolet Explorer (IUE) in 1978 and now the Hubble Space Telescope (HST), UV observations on the brighter and less reddened optical SNRs are possible, substantially adding to our knowledge. While many of the brighter galactic SNRs, like the Crab Nebula and the Cygnus Loop, have been studied for many decades by dozens of researchers, important and sometimes unexpected results based on optical and UV observations have been recently reported on even these well studied objects. Many of these findings have significance not only for SNR research but for SN studies as well since they often provide insights into the nature of the progenitor star or on the explosion dynamics. Below is brief (and rather biased) survey of a small sample of recent optical and UV research on four galactic SNRs: the Crab Nebula, the remnant of SN 1006, Cas A, and the Cygnus Loop.

1. The Crab Nebula (SN 1054)

Despite the hundreds of research papers devoted to it and its luminous pulsar, the Crab Nebula remains today an active research target for investigating the physical processes which occur in pulsar driven SNRs. Recent optical and UV investigations underscore this assessment by revealing just how incomplete our understanding really has been on this remarkable object. Curiously, the Crab Nebula's filaments, which should be virtually undiluted by interstellar gas, show a definite overabundance of only one element – helium, with little trace of freshly synthesized heavy elements (Henry & MacAlpine 1982; Pequignot & Dennefeld 1983). In 1987, Uomoto & MacAlpine found that the differences of He content among filaments was not random, but showed instead a He concentration along an east-west band which they referred to as the High Helium Band (HHeB). Soon after, MacAlpine et al. (1989) found a filament expansion anisotropy in the form of a north-south bipolar bubble above and below the HHeB. No cause for the HHeB or this velocity 'pinching' was proposed. However, new work may point to a

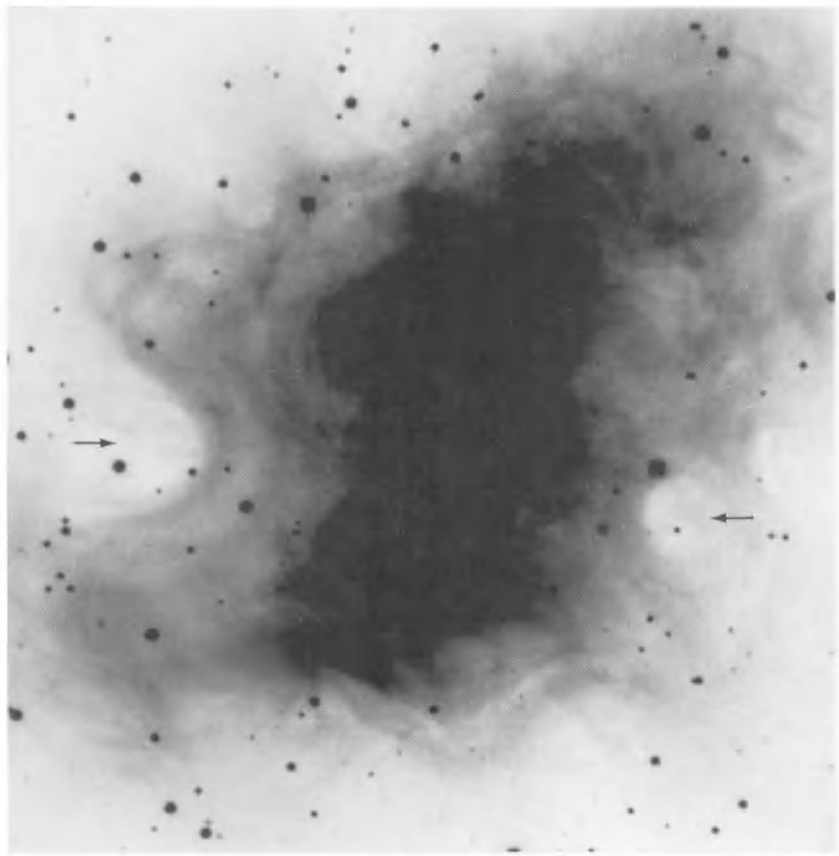

FIGURE 1. A 8100 Å continuum image of the Crab Nebula showing presence of the East and West indentations or 'bays' in the pulsar's synchrotron emission nebula. North is to the top, east to the left.

possible physical connection between the He-rich filament band, the bipolar expansion, and formation of the remnant's synchrotron emission 'bays'.

Among the remnant's most conspicuous large-scale features on optical images taken with interference-filters which avoid the filaments' emission lines are east and west synchrotron nebula indentations or 'bays' (see Fig. 1). Although often ignored in studies of the remnant, observations indicated that these bays are associated with the remnant's magnetic field. For example, to a high degree of coherence, large radial polarization vectors follow the bays' edges indicating large and very orderly magnetic field loops parallel to bay boundaries (see Michel et al. 1991 and references therein). An optical study of the bays by Fesen, Martin, and Shull (1992: hereafter FMS) found the bays to be old, long lasting remnant features which exhibit proper motions not unlike the brighter central filaments. FMS suggested that the bays are manifestations of a magnetic torus encircling the remnant's center of expansion which effectively blocks the pulsar's relativistic particles thus creating the observed synchrotron emission bays. The E-W bays' rough coincidence with the extent of the HHeB led FMS to further propose that the magnetic torus is due to a component of the pulsar's magnetic field anchored to a thermal pre-SN disk, whose remains include the HHeB.

While unclear if the HHeB is composed more of SN ejecta than circumstellar material,

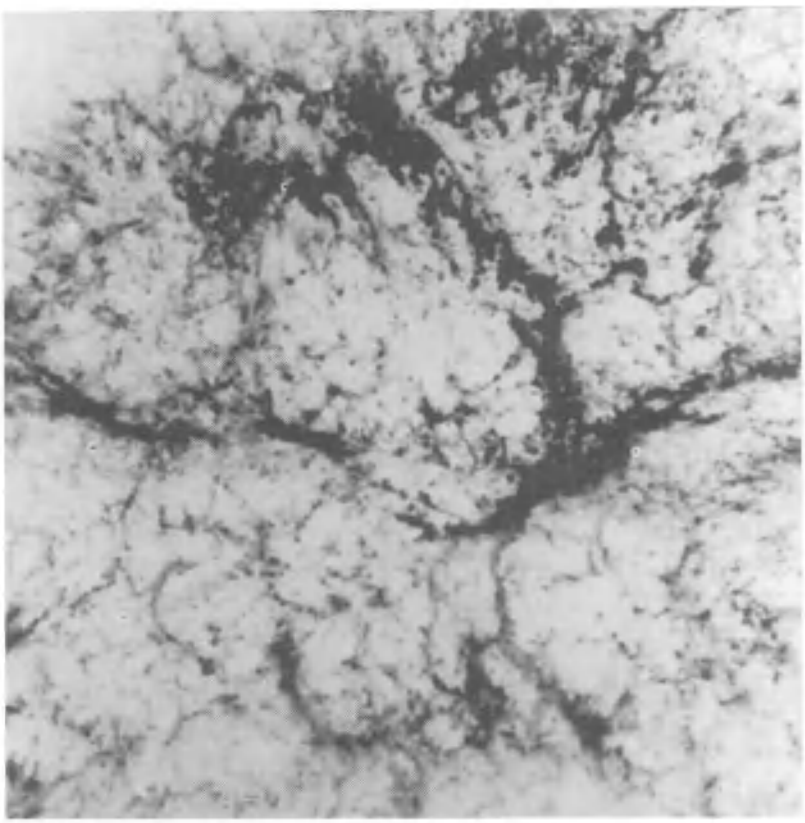

FIGURE 2. Hα image of the middle section of the Crab Nebula illustrating the considerable complexity of the remnant's filamentary structure.

FMS's suggestion of a pre-SN mass loss disk may explain MacAlpine et al.'s (1989) observation of a bipolar expansion. Although optical images such as the Hα image presented in Figure 2 show a highly complex filamentary structure with no apparent symmetry axis, spectroscopic scans do reveal a surprising NS symmetry. A long north-south slit scanned east-west across the central region of the nebula (see Fig. 3) reveals a well defined shell structure with a sharp inner boundary and a strong velocity pinching near the center of the remnant. This orderly expansion structure means that, contrary to expectations, the nebula's highest expansion velocities are not found towards the center. Combining these data with images that show a virtual absence of filamentary emission in the direction of the east bay (FMS), a picture that emerges is that of a circumstellar disk which both partially blocked the SN's free expansion along an east-west plane and helped focus the pulsar's magnetic field into a EW torus leading to development of the east and west bays. If this model is correct, then it may turn out that the Crab Nebula is somewhat related to SN 1987A in the sense that its progenitor also underwent significant mass loss in a disk-like structure.

Recent work on the UV spectra of the Crab filaments has also re-opened the question of significant heavy element abundance variations among filaments. Using the Hopkins Ultraviolet Telescope aboard the ASTRO-1 Space Shuttle mission of December 1990, Blair et al. (1992) examined the nebula's bright concentration of filaments just west of the pulsar. While both blue and redshifted C IV 1550 emission features were detected,

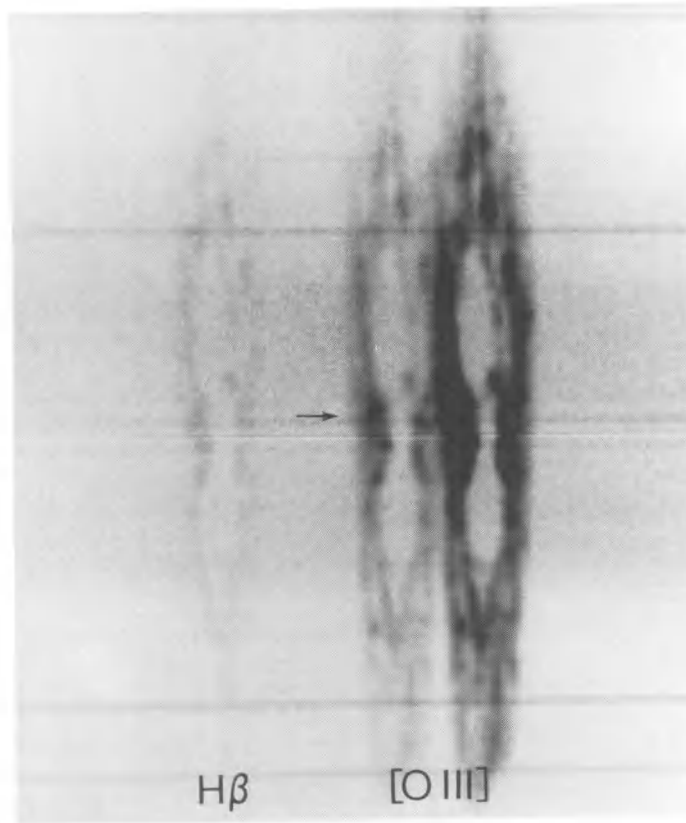

FIGURE 3. Results of a NS slit scan of the Crab's inner section (between the East and West bays) showing the spectral region around Hβ and [O III] 4959, 5007. Note the strong velocity decrease near the remnant's expansion center (arrow). (From Fesen & Shull 1993)

only blueshifted He II 1660 emission was seen. This is the first evidence of substantial UV emission line variations in the Crab and may imply large C/He abundance differences among filaments in and around the HHeB region.

Finally, nearly a dozen semi-stellar emission knots have been reported near the Crab pulsar which seem to exhibit remarkable spectral and kinematic properties (MacAlpine et al. 1993). These knots appear roughly aligned in two arcs, one to the north containing seven knots and four to the south. They appear brightest in [O III] emission and have unusually strong [Ar III] 7135 line emission nearly rivaling Hα. In addition, proper motion measurements over a two year baseline indicate that while most of these knots have $\mu \leq 0.25''$ yr^{-1}, several may have $\mu = 0.5'' - 0.8''$ yr^{-1}. If these high proper motions are confirmed, these knots would then have the highest velocities known in the remnant, approaching 5000 to 8000 km s^{-1}, or more than twice the maximum observed values even in the Crab's northern jet (Fesen & Staker 1993). The motions appear to be directed away from the pulsar and not the remnant's center of expansion. The nature of these knots is unknown, but they may be related to the pulsar's strong relativistic wind and magnetic field. In any case, these data along with the others described above, make it clear that the Crab Nebula still has things to teach us.

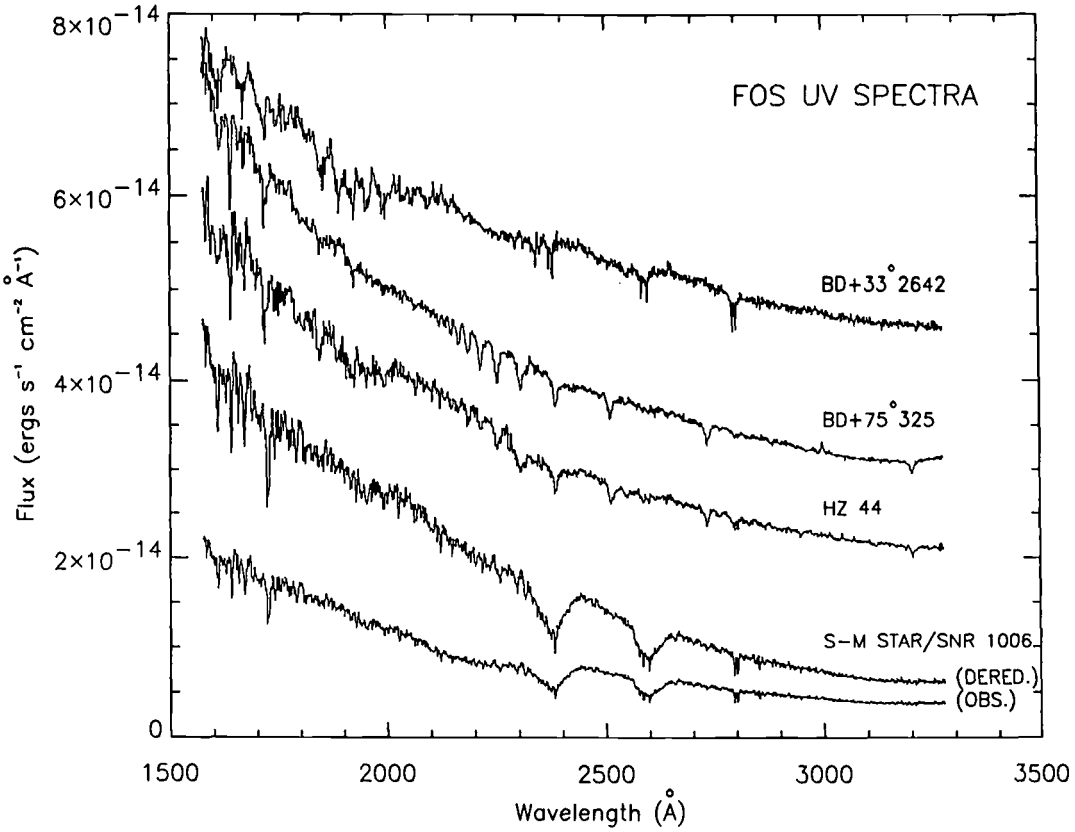

FIGURE 4. HST FOS spectra of the sdOB star behind SN 1006 (bottom two plots) along with FOS spectra of three sdO and early type stars for comparison. (From Wu et al. 1993)

2. SN 1006 AD

The galactic SNR G327.6+14.6 is the probable remnant of the bright historical supernova observed in AD 1006. In radio and X-rays, the remnant appears as a limb brightened 30′ diameter shell. Morphological similarities between this SNR and that of Tycho's SNR (SN 1572), SN 1006's high galactic latitude, SN 1006's reported brilliance ($m \sim -9$), and a lack of a nearby OB association have all pointed to a likely Type Ia classification. Support for this includes IUE observations of a faint sdOB star fortuitously positioned behind the remnant's center. Low dispersion IUE spectra of this star revealed several strong and broad absorption features including the Fe II resonance lines near 2370 and 2600 Å with an expansion velocity of 5000 km s^{-1}, consistent with Type Ia model predictions (Fesen et al. 1988).

Higher resolution and better quality FOS spectra using HST (Fig. 4) greatly clarify SN 1006's induced Fe II absorption features at 2343, 2374, 2382, 2586, and 2599 Å (Wu et al. 1993). After removal of the narrow interstellar absorption lines, the observed line profiles suggest a very symmetric expansion core of Fe II with a FWHM = 8100 km s^{-1} and FWZI = 16600 km s^{-1} (the velocity difference with IUE's measurements is due to significantly better signal-to-noise data in the line wings). This expansion velocity, when combined with the SNR's known age, gives a reverse shock radius $\geq$ 8.4 pc, which in turn with a SNR dia = 30′, implies a distance of $\geq$ 1.9 kpc. Assuming spherical symmetry,

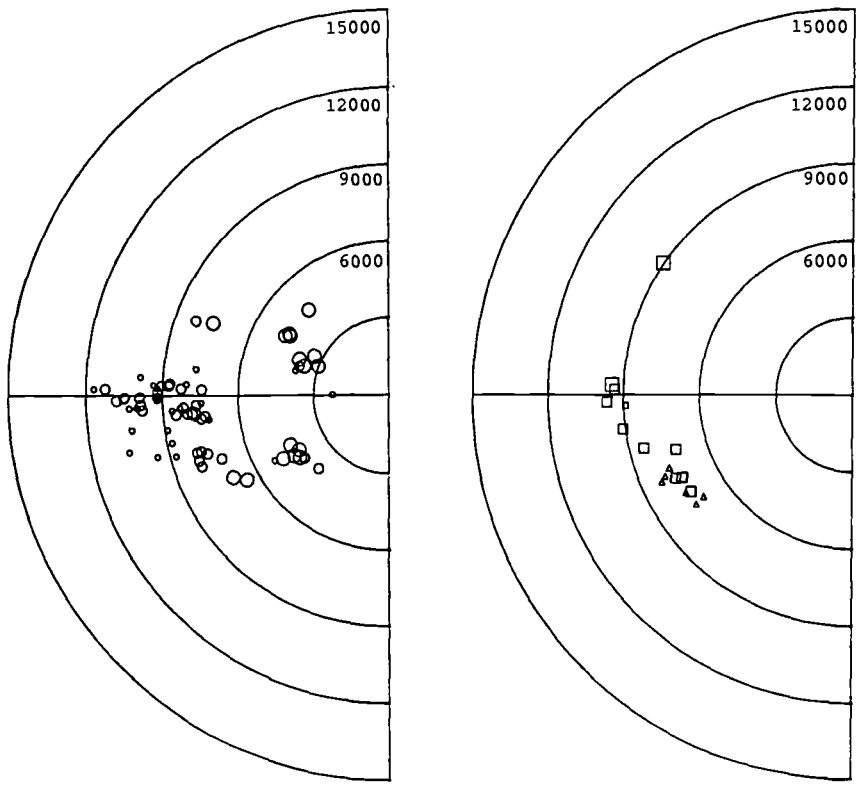

FIGURE 5. Total space velocities (km s^{-1}) for optical emission knots in and nearby the Cas A jet as viewed from above. Circles indicate position of the FMKs, squares the FMFs, and triangles the 'mixed ejecta knots'. Symbol size indicates relative brightness. (From Gunderson & Fesen 1993)

the Fe II line profiles indicate a 0.014 $M_\odot$ or the equivalent of just a few percent of the total expected Fe mass (0.3 – 0.7 $M_\odot$) from model calculations.

3. Cas A (SN $\approx$ 1670)

Whereas SN 1006 appears to be an example of symmetrical SN expansion, the SNR Cassiopeia A (Cas A) may be a case of a massive star SN (Type Ib/Type II) which underwent a partially asymmetric explosion. Optically, Cas A is a faint nebula of knots and short filaments the majority of which exhibit strong emission lines of O, S, Ar, and Ca but no detectable H or He line emissions. The spectral properties of these fast moving knots ('FMKs') are consistent with models for undiluted core ejecta from a massive progenitor star (Chevalier & Kirshner 1979). In addition to the FMKs, a few dozen slow moving N, H, and He emitting emission clumps ('QSFs') are seen which appear to be shocked pre-SN circumstellar mass-loss material.

Several years ago, a dozen or so faint outlying knots were found having both high-velocity and H & N line emission ('FMFs') suggestive of outer N-rich photospheric layer ejecta. A bright knot was later found to have characteristics of both FMKs & FMFs and thus appeared to represent a possible mixing of outer and inner layers of the star (Fesen

& Becker 1991). If true, this chemically mixed knot then also suggests that, at the time of its supernova outburst, the Cas A star still possessed a thin outer layer of H + N. Interestingly, this mixed knot is located along Cas A's northeastern rim where there is a 'jet' of filaments (mostly FMKs) extending a considerable distance beyond the SNR's bright radio and X-ray emission shell. A mixing of mantle and envelope material might have occurred if the jet represents a plume of underlying material ejected at unusually high velocity.

In order to explore the jet's kinematics and chemical composition with distance from the expansion center, long slit spectra yielding radial velocity and relative line emission strengths for 80 knots were recently obtained and analyzed (Gunderson & Fesen 1993). These spectra well sampled the jet's three main 'sprays' of filaments, representing the bulk of the jet's optical emission. The spectra, which offer a detailed look at the Cas A jet, reveal several interesting properties. The jet's structure appears quite extensive with over a hundred [S II] $\lambda\lambda$6716,6731 ejecta knots extending out to 12000 km s^{-1} in expansion velocity – nearly twice that of the remnant's main shell of ejecta. The [S II]/[O I] ratio appears to increase in knots with increasing radial distance, implying a possible S/O abundance gradient along the length of the jet. About a dozen 'mixed ejecta knots' were identified confirming that mixing of the star's original inner and outer layers did occur and is not limited to just one peculiar knot. Both the jet's FMFs and mixed ejecta knots appear within a surprisingly narrow velocity range between 7000 and 9500 km s^{-1}. In summary, a highly asymmetric explosion in this section of the Cas A SNR is suggested which may have relevance in some asymmetrical line emissions observed in extragalactic SNe.

4. The Cygnus Loop SNR

High velocity intercloud shocks present in older supernova remnants (V = 10^2 – 10^3 km s^{-1}) can often be detected optically as faint filamentary Hα emission along the SNR's limb if the shock moves through a partially neutral medium. These intercloud shocks exhibit a hydrogen Balmer dominated spectrum and are often referred to as Balmer-dominated or nonradiative shock filaments. Both radiative and nonradiative filaments mark locations where portions of the shock front are viewed tangentially (the 'wavy sheet' model; Hester 1987). The Cygnus Loop is a relatively nearby (0.75 kpc), bright, low obscuration [E(B-V) = 0.08] SNR making it an excellent subject for detailed spatial studies of SNR shock emissions. Wide-field Schmidt Hα images of portions of the Cygnus Loop (Fesen, Kwitter, & Downes 1992) found many of the 2D and 3D numerical shock cloud simulation predictions of Klein et al. (1991) and Stone & Norman (1992) including cloud deformation, gas stripping, shock reflection and diffraction around clouds. For example, the morphology of an isolated SE cloud suggested formation of Kelvin-Helmholtz and Rayleigh-Taylor instabilities. Unfortunately, however, this SE cloud represents a rather late phase of shock – cloud interaction, involves a fairly dense preshock cloud precluding analysis of internal shock propagation, and has projection ambiguities; e.g. spectra now indicate that an initially suspected 'reverse shock' emission filament just west of the cloud is not that after all.

For testing the detailed hydrodynamical shocked cloud simulations that are now becoming available, ideally one would like to have the following: (a) a relatively isolated cloud with a low enough density to limit internal shock emission structure confusion due to superimposed cloud density variations, (b) an ISM cloud in a fairly early phase of shock interaction so that the complex interaction processes can be investigated right from the start as they first develop, and (c) a clear and simple interaction geometry with no

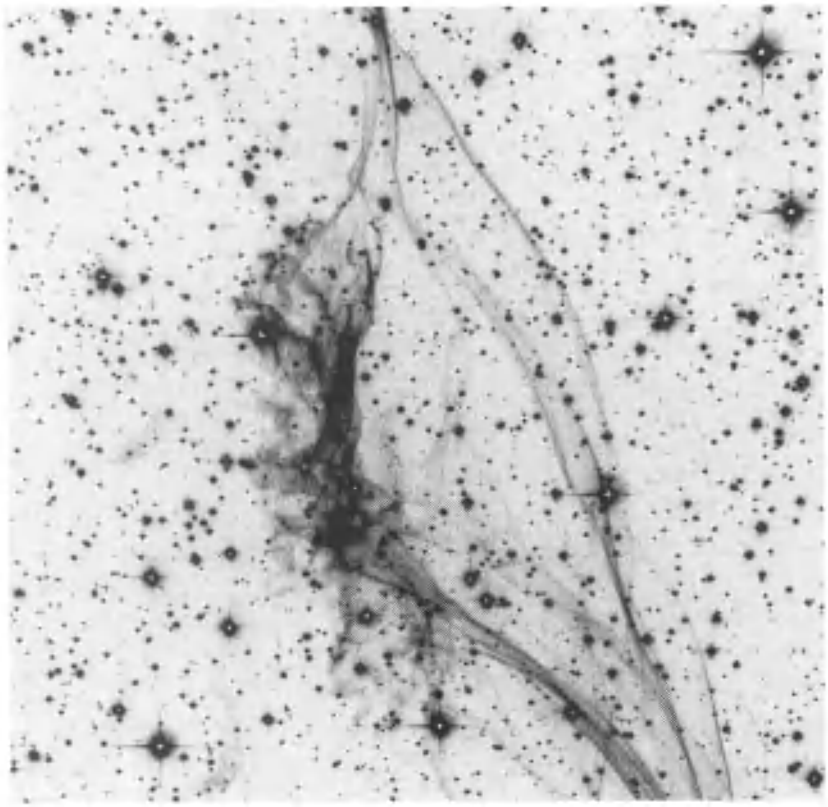

FIGURE 6. Hα image of an isolated shocked emission cloud in the southwestern region of the Cygnus Loop. (From Downes & Fesen 1993)

line-of-sight ambiguity as to location of the shock front or phase of shock-cloud collision. Does such an ideal shocked cloud exist in the Cygnus Loop? The answer appears to be yes.

A wide-field Hα reconnaissance of the entire Cygnus Loop recently uncovered a faint, isolated filamentary complex along the remnant's SW rim which offers an extraordinarily clear view of a single ISM cloud being engulfed by a high Mach shock wave (see Fig. 6). Distinct multiple radiative shock fronts can be seen in the cloud's interior with nonradiative fast shock emissions present along the cloud's sides and the undisturbed expanding shock front surface. Unlike any other filament regions so far studied in the Cygnus Loop, this cloud offers a particularly good view of an isolated cloud caught in the process of being overrun by the SNR's 200 – 400 km s^{-1} shock front. Spatial [O III] vs Hα emission comparisons indicate a $2'' - 5''$ separation between nonradiative and radiative regions in the cloud suggestive of extended cooling and recombination postshock zones due to a low density around 1 cm^{-3}. This also suggests a possible time dependent emission sequencing which is spread-out spatially many times larger than typically seen in SNRs. It is hoped that detailed spectral studies of this region may provide useful insights into the dynamical and line emission properties of shocked interstellar clouds.

REFERENCES

Blair, W. P., Long, K. S., Vancura, O., Bowers, C. W., Conger, S., Davidsen, A. F., Kriss, G. A. & Henry, R. B. C. 1992, *ApJ*, **399**, 611.

Chevalier, R. A. & Kirshner, R. P. 1979, *ApJ*, **233**, 154.

Downes, R. A. & Fesen, R. A. 1993, in preparation.

Fesen, R. A. & Becker, R. H. 1991, *ApJ*, **371**, 621.

Fesen, R. A., Kwitter, K. B., & Downes, R. A. 1992, *AJ*, **104**, 719.

Fesen, R. A., Martin, C. L., & Shull, J. M. 1992, *ApJ*, **399**, 599.

Fesen, R. A. & Staker, B. 1993, *MNRAS*, **263**, 69.

Fesen, R. A., Wu, C.-C., Leventhal, M. & Hamilton, A. J. S. 1988, *ApJ*, **327**, 164.

Gunderson, K., & Fesen, R. A. 1993, in preparation.

Henry, R. B. C. & MacAlpine, G. 1982, *ApJ*, **258**, 11.

Hester, J. J. 1987, *ApJ*, **314**, 187.

Klein, R. I., McKee, C. F. & Colella, P. 1991, In *Supernovae*, ed. S. E. Woosley (Springer: New York) pp. 696.

MacAlpine, G. M., McGaugh, S. S., Mazzarella, J. M. & Uomoto, A. 1989, *ApJ*, **342**, 364.

MacAlpine, G. M., Lawrence, S. S., Uomoto, A., Lowenthal, J. D., Woodgate, B. E., Brown, L. W., & Oliversen, R. J. 1993, *ApJ*, **432**, L131

Michel, F. C., Scowen, P. A., Dufour, R. J. & Hester, J. J. 1991, *ApJ*, **368**, 363.

Pequignot, D. & Dennefeld, M. 1983, *A&A*, **120**, 249.

Stone, J. M. & Norman, M. L. 1992, *ApJ*, **390**, L17.

Uomoto, A & MacAlpine, G. M. 1987, *AJ*, **93** 1511.

Wu, C.-C., Crenshaw, D. M., Fesen, R. A., Hamilton, A. J. S. & Sarazin, C. L. 1993, *ApJ*, **416**, 247.

Far-Ultraviolet Observations of Supernova Remnants

By WILLIAM P. BLAIR

The Johns Hopkins University, Dept. of Physics and Astronomy, Baltimore, MD 21218, USA

New observations of supernova remnants in the far ultraviolet, especially in the sub-Ly α region, are changing the way we look at the interaction between blast waves and the interstellar medium. I briefly review some of the recent FUV observations of supernova remnants from the Hopkins Ultraviolet Telescope, the *Voyager* Ultraviolet Spectrometers, as well as IUE and HST.

1. Introduction

Observations with the IUE satellite over the last 16 years have permitted great strides to be made in better understanding supernova remnants (SNRs) and their interaction with the interstellar medium (ISM). In particular, many filaments have been observed in the galactic SNRs Vela and the Cygnus Loop (Raymond et al. 1988; Raymond, Wallerstein, & Balick 1991; Hester, Raymond, & Blair 1993; and references therein), and a few studies have been made of bright remnants in the Magellanic Clouds (Vancura et al. 1992a; Blair et al. 1989). However, IUE (and even HST) is limited to wavelengths longer than about 1200 Å, and it is only in the last few years that significant inroads have been made at FUV wavelengths down to the Lyman limit at 912 Å. These observations have been made with the Ultraviolet Spectrometers (UVSs) onboard the *Voyager* interplanetary spacecraft, and the Hopkins Ultraviolet Telescope (HUT) onboard the Astro-1 space shuttle mission in December 1990. In separate sections below I will discuss some of the recent advances from each of these instruments.

2. Voyager UVS Results

The *Voyager* UVSs are low resolution ($\Delta\lambda \sim 35$ Å for extended sources) instruments with large fields of view ($0.1° \times 0.86°$) and no intrinsic spatial resolution capabilities (see Broadfoot et al. 1981). They were, of course, mainly intended to observe the atmospheres of the outer planets, with wavelength coverage from 500 – 1700 Å. Even so, with very low background rates these small spectrographs have been able to detect three galactic SNRs in the sub-Ly α spectral region. These observations show the 912 – 1200 Å spectrum to be dominated by two peaks at 980 and 1035 Å, due mainly to C III λ 977 and O VI $\lambda\lambda$ 1032,1038. These peaks vary in relative intensity from object to object and from place to place within the individual objects, indicating differences in the types and velocities of shocks within the large *Voyager* FOV at any given position.

For galactic SNRs with large angular size, the *Voyager* UVSs can provide some crude spatial information by summing individual (short integration) spectra as a function of position on the sky. Blair et al. (1991a) used over 15,000 *Voyager* spectra to produce FUV "maps" of the Cygnus Loop in C III and O VI, sampling optical and X-ray data in the same manner for comparison. Considerable line intensity variations were detected as a function of position, and a globally-averaged O VI:C III ratio near 2 was found. The luminosity of the Cygnus Loop in O VI was found to be 4.6×10^{36} ergs s^{-1}, roughly 4 times the 0.1–4.5 keV X-ray luminosity reported by Ku et al. (1984). Rasmussen & Martin

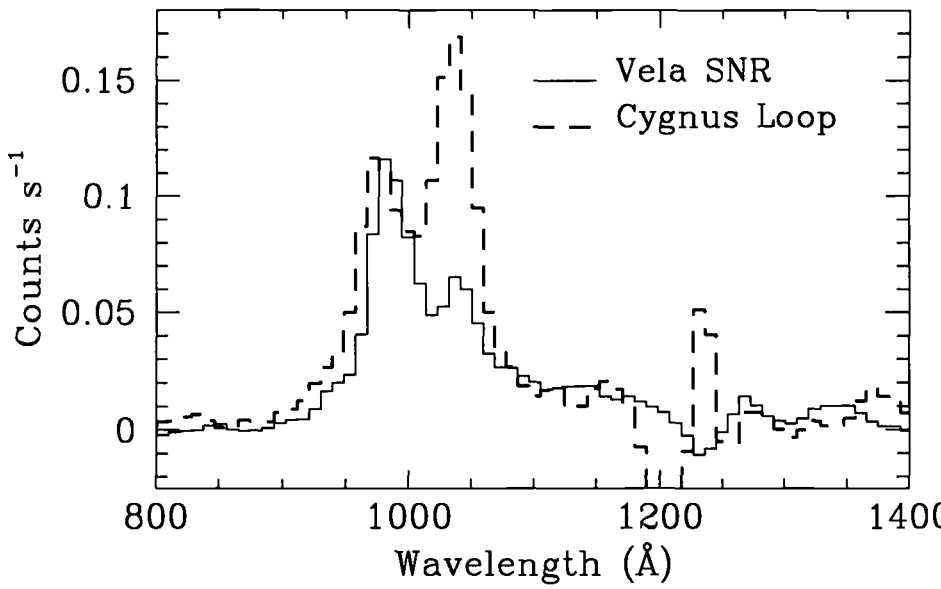

FIGURE 1. A comparison of *Voyager* UVS spectra of the Vela (solid line) and Cygnus Loop (dashed line) SNRs. Note the change in relative intensity of the two peaks, which are attributed to C III λ 977 and O VI λ 1035.

(1992) found a lower O VI luminosity roughly comparable to the soft X-ray luminosity using a rocket experiment. While reasons for this discrepancy are not understood, it remains clear that the luminosities of individual UV (and by analogy, optical) lines are roughly on a par with the total soft X-ray luminosity. This global perspective of the Cygnus Loop's UV emission was only obtainable with the *Voyager* spacecraft.

Voyager has also been used to perform more detailed studies of selected regions in the Cygnus Loop. In a recent paper, Vancura et al. (1993) report selected *Voyager* observations stepping across the main blast wave in the Cygnus Loop. They estimate that the main blast wave accounts for 10–15% of the total O VI flux observed by Blair et al. (1991a). The remainder arises from radiative shocks more closely associated with the bright optical filaments.

The Vela SNR also has a large angular size and low reddening, making it available to *Voyager* FUV observations. Blair, Vancura, & Long (1993) report observation of a filament in the extreme SE portion of Vela that corresponds to a "breakout" from the X-ray shell. The optical filaments at this location are quite reminiscent of Cygnus Loop filaments, appearing to be a large sheet of material viewed approximately edge-on. The *Voyager* spectrum at this position in Vela is compared with the global Cygnus Loop spectrum in Figure 1.1. The sub-Ly α spectrum of Vela is dominated by the same two peaks seen in the Cygnus Loop, but the relative intensity of O VI is much weaker than in the Cygnus Loop. An ongoing effort to map a section of the northern rim of Vela (Blair et al., in preparation) indicates that this weaker O VI emission is apparently a general feature of Vela and not restricted to the SE filaments. This implies a smaller filling factor of $\geq 160\,\mathrm{km\,s^{-1}}$ shocks in Vela than in the Cygnus Loop.

A third galactic SNR has recently been detected with *Voyager*. G65.3+5.7 is a large diameter SNR with relatively faint optical and X-ray emission. In particular, the optical filaments are peculiar, consisting of large smooth arcs of emission relatively strong in [O III] λ 5007 (Fesen, Gull, & Ketelson 1983). The *Voyager* spectrum of one of these

filaments (Fesen & Blair, in preparation) shows an O VI:C III ratio of unity, intermediate to the Vela and Cygnus Loop results.

Hence, while the strong [O III] optical emission could only indicate the presence of shocks with velocity ≥ 100 km s^{-1}, the presence of strong O VI indicates shocks of ≥ 160 km s^{-1} must be occurring in this old SNR.

X-ray data for the Cygnus Loop (Ku et al. 1984) indicate a velocity of ~ 400 km s^{-1} for the main blast wave, while optical and IUE results have pointed toward shocks with velocities near 100 km s^{-1} in the bright optical filaments (cf. Raymond et al. 1988, and references therein). The presence of strong and ubiquitous O VI emission in these objects provides widespread evidence for shocks with intermediate velocities in excess of 160 km s^{-1} in the bright filamentary structures of galactic SNRs. This may indicate thermally unstable cooling, evaporative processes, or a more extensive intermediate density component of the ISM than has been recognized previously.

3. HUT Results

The Hopkins Ultraviolet Telescope was flown on the space shuttle Columbia for 9 days in December 1990 as part of the Astro-1 mission. HUT consists of a 0.9 m telescope and a prime focus FUV spectrograph with a microchannel–plate intensifier and reticon readout. The spectrograph provided coverage from 830 – 1860 Å at about 3 Å resolution. Seven selectable apertures provide some flexibility in matching the needs of individual observations, but no intrinsic spatial resolution was available. Further details on the instrument and its performance can be found in Davidsen et al. (1992). The excellent sensitivity, good resolution, and wavelength coverage of HUT make it an ideal instrument for studying interstellar shocks. Unfortunately, the brevity of the mission meant that only a few key observations of SNRs could be made.

The HUT observations allowed a much more detailed look at individual filaments in the Cygnus Loop (see Figure 1.2). Blair et al. (1991b) used a 9.4" x 116" aperture with HUT to isolate emission from a bright radiative filament in the eastern portion of the remnant. This was the first spectrum to resolve the full sub-Ly α spectrum of an interstellar shock wave, and showed without a doubt that the peaks seen with *Voyager* corresponded mainly to C III λ 977 and O VI $\lambda\lambda$ 1032,1038, with other lines at a much lower level. The O VI doublet was observed in the 2:1 ratio indicative of optically thin conditions, and the O VI:N V and O VI:C IV ratios were both consistent with the expectations from a 170 km s^{-1} shock wave. However, contrary to the optical appearance of this filament (which indicates extreme incompleteness of the cooling and recombination zone), the intermediate ionization lines in the UV were stronger that predicted by a single, steady–flow shock model. Hence, the possibilities of thermal instabilities (cf. Innes 1992) and/or multiple shock velocities within the aperture were indicated.

Subsequent work on this region of the Cygnus Loop is in progress.

We are using IUE data, longslit optical spectra, and optical imagery to investigate spatial variations within the HUT aperture location. A preliminary analysis of these data indicates that the agreement of the O VI:N V and O VI:C IV ratios with a 170 km s^{-1} may have been fortuitous. Both N V and C IV are apparently affected by resonance line scattering at some positions along the HUT aperture (an effect also indicated by UV imaging observations from Astro–1, see Cornett et al. 1992). Multiple shock velocities are almost certainly present, and the peak velocity in the HUT aperture may be considerably higher than the previous estimate of 170 km s^{-1}.

A second position observed by HUT was the "nonradiative" filament in the NE Cygnus Loop previously observed with IUE by Raymond et al. (1983). Long et al. (1992)

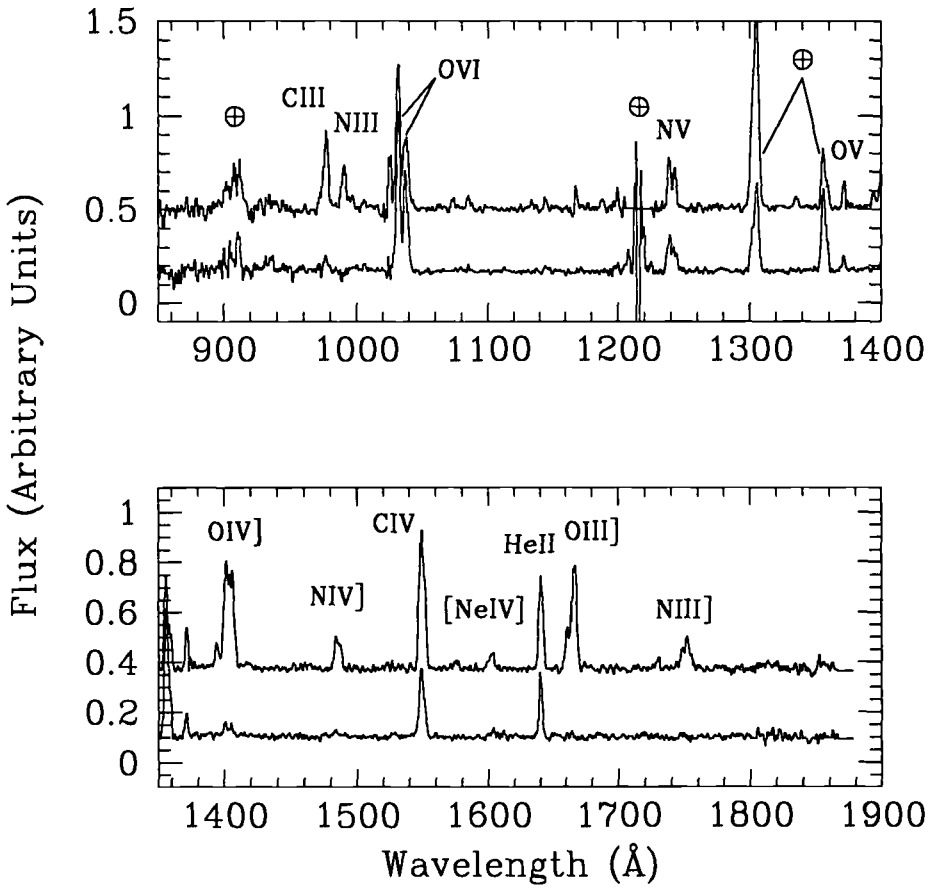

FIGURE 2. A comparison of HUT spectra of two filaments in the Cygnus Loop. The top line in each panel shows the spectrum of a radiative filament while the bottom line shows a noradiative filament. Strong lines are identified, and and earth symbol denotes regions affected by airglow emissions. Only the highest ionization lines are present at the nonradiative position.

report a spectrum very similar to the high ionization portion of the HUT radiative filament mentioned above, but with much weaker intermediate and low ionization lines (see Figure 1.2). These authors estimate a shock velocity of about 180 km s^{-1} from the HUT data. This filament represents a very recent encounter between the blast wave and an interstellar cloud, and may represent an earlier stage of the evolution that is taking place at the HUT radiative position. Long et al. (1992) find some support for the idea that this shock is rapidly decelerating as it encounters a density step in the ISM, which is consistent with the velocity width of the filament and the fact that it may already be undergoing the transition from nonradiative to radiative conditions (cf. Hester, Raymond, & Blair 1993). Long et al. (1992) find that a below solar carbon abundance is necessary to match the spectrum at this position, which could indicate that grain destruction has occurred at the HUT radiative position (which was matched with cosmic abundances).

Other HUT SNR observations include the Crab Nebula (Blair et al. 1992) and the bright LMC remnant N49 (Vancura et al. 1992; discussed in the next section). Although the HUT observation of the Crab Nebula failed to detect any new emission lines in the sub-Ly α region, it did detect variations of the C IV:He II ratio in the Crab for the first

time. Interpretation of these variations is model dependent, but fairly extreme carbon abundances and abundance variations are allowed by the models. This sheds a different light on the possible precursors of this unique object. The relatively normal carbon abundance inferred previously from IUE observations (Davidson et al. 1982) has been used to constrain the mass range of the precursor to 8–10 $M_{\odot}$ (cf. Nomoto et al. 1982). A higher carbon abundance would permit the precursor mass to be above 10 $M_{\odot}$.

4. IUE/HST Results

The IUE spacecraft has continued to demonstrate its versatility for SNR/ISM observations over the years, and is largely responsible for many of the advances in our understanding of interstellar shocks. As our understanding has improved, the observations have become more comprehensive, combining optical spectroscopy and imagery and/or X-ray data with the IUE spectra to better determine physical conditions and constrain models. Raymond et al. (1988) performed such a study of the "spur" filament in the eastern Cygnus Loop, inferring the geometry and physical parameters in unprecedented detail and demonstrating for the first time that thermal support was not the dominant source of pressure in this filament.

Recently Hester, Raymond, & Blair (1993) have published a similar tome on the NE nonradiative filaments in the Cygnus Loop, inferring that the blast wave in this region is decelerating and finding that this entire region is on the verge of becoming radiative. Also, Raymond, Wallerstein, & Balick (1991) have used high dispersion IUE and optical data of a star behind the Vela SNR in conjunction with low resolution IUE spectra of nearby Vela filaments to provide the strongest evidence to date of thermal instabilities in fast shocks predicted theoretically (cf. Innes 1992; Gaetz, Edgar, & Chevalier 1988).

IUE and optical data have also provided a powerful tool for investigating a few bright extragalactic SNRs. Vancura et al. (1992a,b) performed an extensive analysis of N49 in the LMC, including a HUT observation that detected the O VI lines. By investigating the spatial variations in optical/UV line intensities, it is clear that a wide range of shock velocities are present, indicating a complex preshock medium of relatively high density (to account for the optical and UV luminosity).

Oxygen-rich SNRs are thought to arise from the explosions of massive stars (Type II or Type Ib SNe). Unfortunately, the galactic examples of this class are heavily reddened, which negates UV observations. We have recently obtained IUE spectra of two positions in the LMC remnant N132D (Blair, Raymond, & Long 1993), which show strong lines of carbon, oxygen, neon, magnesium, and at one position silicon and helium (the first detection of these elements in an oxygen-rich SNR). This combination of elements may indicate significant mixing of the ejecta have taken place in this object. General characteristics of the spectrum, including especially the relative strength of the UV and optical emission lines, point toward photoionization as the dominant emission mechanism as opposed to shock heating, which is similar to the conclusion reached for E0102–7219, the oxygen-rich SNR in the SMC (Blair et al. 1989). Even so, model fits have been unacceptable, partially because emission from various knots gets blended in the IUE spectra.

The power of the Hubble Space Telescope has yet to be turned effectively toward many SNRs. HST is not a very efficient telescope for faint, extended sources, but there are certainly places where it can make significant contributions to our understanding. We have requested time to observe N132D to resolve the structures blended in the IUE spectra and to obtain accurate relative UV/optical line intensities at the same positions; this will greatly improve the comparison to models. It is somewhat frightening to realize

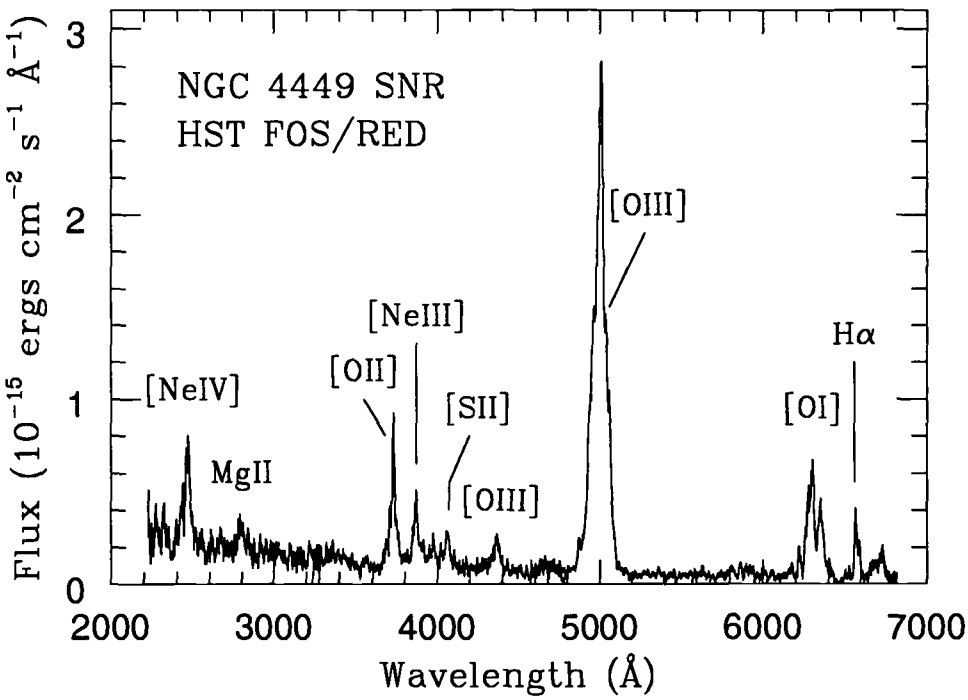

FIGURE 3. A collage of HST/FOS red side spectra of the O-rich SNR in NGC 4449. None of the lines below 3600 Å have been seen previously, and many of the longer wavelength lines are seen more clearly than in ground-based data.The data have been smoothed and combined for presentation here.

how few SNRs have actually been observed successfully in the ultraviolet. Extragalactic SNRs are often better UV targets than galactic SNRs, and HST/FOS has the sensitivity to expand the sample. Figure 1.3 shows FOS/RED spectra of the oxygen-rich remnant in the irregular galaxy NGC 4449 from an FOS/GTO observation. This object is 5 Mpc away and yet is readily detected in reasonable exposure times with FOS. New lines of neon, magnesium, and carbon have been detected in this object for the first time, which should lead to improved estimates of the mass of the precursor star (cf. Blair et al. 1984).

Acknowledgements

Special thanks go to Jay Holberg for continued assistance with *Voyager* data reductions, and to the many scientists, engineers, and technical staff people at Johns Hopkins and NASA who worked hard to make HUT and Astro–1 a success. I would like to thank my collaborators for their sound advice and continued support on various aspects of these projects. This work has been supported by the Center for Astrophysical Sciences at the Johns Hopkins University and through various NASA grants and contracts, including NAG 5-1276, NAG 5-1793, NAG 5-1630, NAS 5-27000, and NAS 5-29293.

REFERENCES

Blair, W. P., Long, K. S., Vancura, O., & Holberg, J. B. 1991a, *ApJ*, **374**, 202.

Blair, W. P., et al. 1991b, *ApJ*, **379**, L33.

Blair, W. P., et al. 1992, *ApJ*, **399**, 611.

Blair, W. P., Raymond, J. C., Danziger, I. J., & Matteucci, F. 1989, *ApJ*, **338**, 812.

Blair, W. P., Raymond, J. C., Fesen, R. A. & Gull, T. R. 1984, *ApJ*, **279**, 708.

Blair, W. P., Raymond, J. C., & Long, K. S. 1993, *ApJ*, **423**, 334.

Blair, W. P., Vancura, O., & Long, K. S. 1993, *ApJL*, submitted.

Broadfoot, L., et al. 1981, *J. Geo. Res.*, **86**, 8259.

Cornett, R. H., et al. 1992, *ApJ*, **395**, L9.

Davidsen, A. F., et al. 1992, *ApJ*, **392**, 264.

Davidson, K., et al. 1982, *ApJ*, **253**, 696.

Fesen, R. A., Gull, T. R., & Ketelson, D. A. 1983, *ApJS*, **51**, 337.

Gaetz, T. J., Edgar, R. J., & Chevalier, R. A. 1988, *ApJ*, **329**, 927.

Hester, J. J., Raymond, J. C., & Blair, W. P. 1993, *ApJ*, **420**, 721.

Innes, D. E. 1992, *A&A*, **256**, 660.

Ku, W. H.-M., Kahn, S. M., Pisarski, R., & Long, K. S. 1984, *ApJ*, **278**, 615.

Long, K. S., Blair, W. P., Vancura, O., Bowers, C. W., Davidsen, A. F., & Raymond, J. C. 1992, *ApJ*, **400**, 214.

Nomoto, K., et al. 1982, *Nature*, **299**, 803.

Rasmussen, A., & Martin, C. 1992, *ApJ*, **396**, L103.

Raymond, J. C., Blair, W. P., Fesen, R. A., & Gull, T. R. 1983, *ApJ*, **275**, 636.

Raymond, J. C., et al. 1988, *ApJ*, **324**, 869.

Raymond, J. C., Wallerstein, G., & Balick, B. 1991, *ApJ*, **383**, 226.

Vancura, O., Blair, W. P., Long, K. S., & Raymond, J. C. 1992a, *ApJ*, **394**, 158.

Vancura, O., et al. 1992b, *ApJ*, **401**, 220.

Vancura, O., Blair, W. P., Long, K. S., Raymond, J. C., & Holberg, J. B. 1993, *ApJ*, **417**, 663

Compact Objects in Supernova Remnants

By ROGER A. CHEVALIER

University of Virginia, Charlottesville, VA 22903-3818, USA

Core collapse in very massive stars can lead to a central black hole that swallows the rest of the star and in less massive stars to a central neutron star and explosion. There is probably an intermediate mass range that gives an explosion and a central black hole; supernova remnants with no observable central object are candidates. The association of pulsars with Type II supernovae gives an estimate of the pulsar power to be expected in a supernova, but the uncertainty in the initial pulsar periods gives a wide range in possible powers. The relativistic wind bubble model for the Crab Nebula has steadily developed and there are now predictions regarding particle acceleration in the optical wisps. The bubble model with expansion into supernova gas can also be applied to other young pulsar nebulae.

1. Introduction

The study of compact objects in supernova remnants has long been troubled by the lack of evidence for such objects. For many years, the Crab and Vela pulsars were the only compact objects observed in remnants. More recently, the number of pulsar/remnant associations has increased to 9 or 10 (Kaspi et al. 1992; Kulkarni et al. 1993). In other cases, the presence of a pulsar is inferred from a centrally condensed, flat radio spectrum nebula thought to be created by a pulsar. The study of these objects, as well as more detailed study of the Crab Nebula, has led to a general theoretical picture, although many basic uncertainties remain.

In section 2, I describe the possibilities for forming neutron stars or black holes in core collapse supernovae. Section 3 discusses the implications of observed pulsars for supernovae. The Crab Nebula and its evolution are described in section 4 and recent investigations of other pulsar nebulae are described in section 5.

2. The Nature of the Compact Objects

Core collapse is thought to occur at the end of the lives of stars with an initial mass $\gtrsim 8\ M_\odot$, although there may be a high mass range ($\gtrsim 100\ M_\odot$) where oxygen burning can lead to the complete destruction of the star. The Fe core mass ranges from $\sim 1.4\ M_\odot$ for the $\lesssim 18\ M_\odot$ star to $\sim 2\ M_\odot$ for the more massive stars (S. Woosley, this volume); the core mass is not necessarily a monotonic function of initial mass. The maximum mass of a neutron star, M_{cr}, is not well-determined, but probably lies in the range 1.5–2.0 $M_\odot$. Thus, in the more massive stars, core collapse can lead directly to black hole formation. The generation of a supernova shock by any plausible mechanism requires the initial formation of a neutron star, so the star remains bound to the black hole and is accreted by it. This is thought to be the origin of massive black holes like Cygnus X-1.

The timescale to launch the supernova shock may be $\sim$1 second. There are two ways to form a black hole after this time. One is by the fall-back of matter that was initially ejected by the supernova shock. Colgate (1971) and Chevalier (1989) discussed how this could happen as a result of pressure waves or reverse shock waves during the initial expansion of the supernova. Chevalier (1989, 1991) estimated that 0.1 $M_\odot$ could fall back on a timescale of hours after the explosion. Brown, Bruenn, & Wheeler (1992)

estimated a similar amount of fall-back (up to 1 $M_\odot$) during the hot bubble phase on a timescale of 10^3 seconds. They also estimated that M_{cr} is fairly low, about 1.5 $M_\odot$. If these estimates are reliable, there should be an initial core mass range just below M_{cr} where the fall-back can give a black hole with an explosion. We do not know the relevant parameters sufficiently well to estimate the initial mass range.

Another way to achieve a black hole with explosion is to form a hot neutron star that can remain stable above M_{cr} that then cools on a >1 second timescale and forms a black hole (e.g. Brown & Bethe 1993). Again, the mass range is very uncertain, although Brown and Bethe suggest that it is large.

If a black hole does form at the center, the compact object is likely to be difficult to observe. Chevalier (1989) estimated that the late fall-back rate for SN 1987A was $\dot{M} \sim 10^{-4} t_{\rm yr}^{-5/3} M_\odot$ yr^{-1}, where $t_{\rm yr}$ is the age in years. The $t^{-5/3}$ factor is generally expected for late fall back (see also Michel 1988), but the coefficient may vary with the details of the supernova. In spherically symmetric accretion, the radiation field becomes trapped in the inflow so that the only luminosity is due to compression outside the radiation trapping radius. The resulting luminosity is low, about $5 \times 10^{35} t_{\rm yr}^{-1.4}$ ergs s^{-1} for the above accretion rate. If angular momentum of the material causes a disk to form, the radiative efficiency may be considerably higher.

The possible low radiative output of black holes has led to the suggestion that they are present in supernova remnants that should have a central compact object but show no sign of one, such as SN 1987A and Cas A. In the case of SN 1987A, the observed neutrino burst directly implies that a neutron star or black hole is present, but the luminosity from a pulsar was $\lesssim 8 \times 10^{36}$ ergs s^{-1} on day 1500 (Suntzeff et al. 1992). However, a neutron star with a low power output could be present. The minimum luminosity is thermal emission from the hot neutron star surface soon after formation. At an age of 1 year, the expected temperature of 3×10^6 K gives a luminosity of $\sim 10^{35}$ ergs s^{-1} (Nomoto & Tsuruta 1987). Unfortunately, in the case of SN1987A, the longer lived radioactive nuclides, such as ^{44}Ti, can dominate this emission for decades (Woosley, Hartmann & Pinto 1989). In the case of Cas A, thermal emission from the hot gas impedes the detection of a central soft X-ray source.

3. Pulsars and Supernovae

Observations of supernovae during the first few years after the explosion have not given any information on the nature of central compact objects. However, it has long been held that there is a correspondence between Type II supernovae and pulsar formation so that an analysis of pulsar properties can tell us what to expect inside of these supernovae. There are basically three reasons supporting this correspondence. First, the rate of pulsar formation in our Galaxy is comparable to the Type II supernovae rate, both are about 1 per 50 years, within a factor of 2 (Gunn & Ostriker 1970; Narayan & Ostriker 1990; van den Bergh & Tammann 1991). The second is that although the pulsar dispersion in the z direction (galactic altitude) is large, the dispersion can be attributed to the high space velocity of pulsars and the data are consistent with pulsar birth in a narrow region close to the galactic plane, as expected for a massive star origin (Gunn & Ostriker 1970; Chevalier & Emmering 1986). However, Narayan & Ostriker (1990) have claimed that there are two populations of pulsars with roughly equal birthrates, one born with a large scale height ($\gtrsim$ 350 pc) and the other born with a small scale height ($\sim$ 120 pc). This claim needs further confirmation, but it is certainly possible that Type II supernovae should be identified with a subset of the pulsars. Finally, the association of the Crab

TABLE 1. Observed Pulsars in Nebulae

	PSR 0531+21	PSR 0540–69	PSR 1509–58
P(s)	0.0333	0.0503	0.150
$\dot{P}$	4.21×10^{-13}	4.77×10^{-13}	1.54×10^{-12}
n	2.509	2.01	2.83
$\dot{E}$(erg s^{-1})	4.5×10^{38}	1.5×10^{38}	1.8×10^{37}
$t+\tau$(yr)	1660	3310	1690
t(yr)	930	830	1660
τ(yr)	730	2480	30
$\dot{E}_i$(erg s^{-1})	3.0×10^{39}	3.5×10^{38}	8.3×10^{40}
P_i(s)	0.019	0.038	0.017
$B_s(10^{12}$ G)	3.8	5.0	15.4

pulsar with SN 1054 has provided a direct link of pulsar formation with a supernova explosion.

The study of pulsars can thus lead to information on the properties of neutron stars to be expected in supernovae. The power output from the neutron star is a fundamental property and in the magnetic dipole theory for pulsar spindown, the power output is

$$\dot{E} = 5 \times 10^{38} \left(\frac{B_s}{10^{12.5}\mathrm{G}}\right)^2 \left(\frac{P}{30 \text{ msec}}\right)^{-4} \text{ergs s}^{-1}, \quad (1)$$

where it has been assumed that the magnetic axis is perpendicular to the rotation axis, B_s is the surface magnetic field and P is the pulsar spin period. Analyses of pulsar statistics have led to estimates of the initial values of B_s and P for pulsars. There is general agreement that the initial values of B_s fall in a fairly narrow range – $10^{12.5\pm0.3}$ G (Gunn & Ostriker 1970; Stollman 1987) and any magnetic decay occurs on a timescale that is longer than the ages of supernova remnants. An increase in B_s on a timescale smaller than the typical pulsar ages is possible (Blandford, Applegate, & Hernquist 1983). The initial periods of pulsars have not been well-determined from pulsar statistics because of the small number of young, rapidly spinning pulsars and uncertainties in the selection effects. Initial periods for most pulsars from ~10 msec to ~0.7 sec have been suggested (Chevalier & Emmering 1986; Narayan 1987; Stollman 1987; Emmering & Chevalier 1989; Narayan & Ostriker 1990). The difference in initial power output is large: for $B_s = 10^{12.5}$ G, the power of a 10 msec period pulsar is 4×10^{40} ergs s^{-1}, while that of a 0.7 sec period pulsar is 1.6×10^{33} ergs s^{-1}.

Some information can be obtained from the 3 youngest known pulsars, which have ages of $\sim 10^3$ years. The basic data on these pulsars is given in Table 1 (for references to the observations, see Chevalier & Fransson 1992), which includes the period P, first period derivative $\dot{P}$, and braking index $n = \Omega\ddot{\Omega}/\dot{\Omega}^2$, where $\Omega = 2\pi/P$ is the spin rate. The current spin-down power is $\dot{E} = I\Omega\dot{\Omega}$, where I is the neutron star moment of inertia and is taken to be 10^{45} g cm^2 in Table 1. If the pulsar spin evolves with constant braking index n, the initial spin rate is $\Omega_i = \Omega(1+t/\tau)^{1/(n-1)}$, where τ is a constant and t is the age. We also have that $P/2\dot{P} = (\tau + t)(n-1)/2$. The age of the Crab pulsar is known and that of 0540–69 can be deduced from the expansion age of the nebula (Kirshner et al. 1989), with some correction for acceleration of the nebula (Reynolds 1985; Chevalier & Fransson 1992). The age of 1509–58 is determined if it was born in SN 185 (Thorsett

1992) but the values of t and τ given here are based on a speculative model described in section 5. The result of an initial period for 1509–58 comparable to that of the Crab pulsar is thus speculative. The high initial power of this pulsar is due to its unusually high magnetic field.

These results use the observed braking index, which, in every case, is less than the value expected for pure magnetic dipole spindown, n=3. The lower value may be due to a particle wind from the neutron star. The use of n=3 to extrapolate back to the initial values would not greatly change the results. In the magnetic dipole model, $\tau = 3Ic^3/4B_s^2R_N^6\Omega_i^2$, where c is the speed of light and R_N is the neutron star radius.

These three pulsars lead to the best estimates for the original periods of individual pulsars. It is not clear whether their fairly fast initial spin rates are representative because there is a selection effect to observe the brightest pulsars and pulsar nebulae. Srinivasan, Bhattacharya, & Dwarakanath (1984) estimated the galactic rate of formation of pulsar nebulae like the Crab Nebula to be 1 per 240 years, only ~20% of the estimated Type II supernova or pulsar formation rate. From radio observations of the galaxy M33, Reynolds & Fix (1987) deduced a similarly low rate of Crab-type nebula formation in that galaxy as an upper limit. Srinivasan et al. concluded that most Galactic pulsars are probably formed with $P_i \gtrsim 35 - 70$ msec.

Another piece of evidence for a long initial period is the general lack of observed pulsars in shell supernova remnants. Although this problem is influenced by selection effects, Narayan & Schaudt (1988) found that the implication is either that there are no pulsars in these supernova remnants or that the pulsars are unusually weak. A solution to the problem is that pulsars are born with periods $\gtrsim$ 0.7 sec. However, one uncertainty is the beaming function for young pulsars. Narayan and Schaudt argue that young pulsars have fan radio beams and are thus always observable, but this result remains controversial (Frail & Moffett 1993). Also, at the time of the Narayan & Schaudt paper, there were 4 pulsar/supernova remnant associations, but that number has now grown to 9 or 10.

Chevalier & Fransson (1992) addressed the question if a Crab-like pulsar does form in a Type II supernova, what are the effects on the supernova emission during the first decade after the explosion. The magnetic field and relativistic particles powered by the spin-down of the pulsar create a bubble that drives a shock front into the supernova gas. The shock front is initially radiative and the radiative luminosity is ~1.5% of $\dot{E}$. A higher radiative efficiency (30% in the case of the Crab) is possible if the pulsar bubble is a significant source of synchrotron emission; there is evidence that pulsars with higher values of $\dot{E}$ have nebulae with higher efficiencies of synchrotron emission (Seward & Wang 1988). The ionizing radiation can create an ionized region from which optical lines like those of [OIII] are prominent; these lines are from more highly ionized atoms than those expected from radioactive power input. The lines tend to start out narrow and broaden with time as more of the supernova matter is ionized. Chevalier & Fransson (1992) examined observations of supernovae over the age range up to 10 years and found that none of them clearly show evidence for pulsar-powered emission; the supernovae in question are generally radio emitters and have strong circumstellar interaction that powers the observed luminosity. The continued observation of Type II supernovae to faint luminosity levels is important for the discovery of very young pulsars. In the meantime, we can examine the properties of pulsars and their nebulae with ages $\sim 10^3$ years.

4. The Crab Nebula and its Evolution

The observed kinetic energy of the Crab Nebula is only $\sim 3 \times 10^{49}$ ergs, which is far short of the 10^{51} ergs typically thought to be associated with Type II supernovae.

The problem is aggravated by the evidence for acceleration of the Crab Nebula filaments (Trimble 1968), which suggests that some of the kinetic energy has been derived from the pulsar spin-down power. Partly for this reason, Chevalier (1977) and Chevalier & Fransson (1992) proposed that the observed Crab Nebula is just the inner part of a typical Type II supernova that has been swept up by the pulsar bubble. If a pulsar with the properties described in Table 1 for PSR 0531+21 is placed inside of a typical Type II supernova, the average shell velocity (1400 km s^{-1}), shell mass ($1 - 2\ M_\odot$), acceleration ($t - R/V \sim 100$ years), and bubble pressure ($\sim 10^{-8}$ dynes cm^{-2}) of the Crab Nebula can be roughly reproduced. The filamentary structure of the nebula can be the result of Rayleigh–Taylor instabilities in the acceleration process.

Although this model has a number of attractive features, it does predict that an energetic supernova lies outside the presently observed Crab, and no such object has been clearly observed. The interaction of the rapidly moving gas with the surrounding medium might be most sensitively seen as a shell radio supernova remnant, but no radio shell has been observed to a low level (Velusamy 1985). The implication is that the surrounding density must be low, as might be expected if the main sequence progenitor star cleared a hole with its wind. A low surrounding density implies that much of the supernova gas is in free expansion and is cool. The gas is ionized by the nebular radiation and is expected to be a source of line emission. Murdin & Clark (1981) did in fact find evidence for a halo around the Crab, but this observation has not yet been confirmed; the problem is the very low emission measure of the expected halo.

Although there is no clear evidence for the interaction of the Crab Nebula with an external medium, there have been recent claims that the bays seen in the synchrotron emission are related to the circumstellar medium around the progenitor star. Fesen, Martin, & Shull (1992) studied the bays on either side of the pulsar in the east-west direction and found that they are long-lived features that are expanding with the nebula. The bays line up with a band of He-rich filaments that cross the nebula. Fesen et al. (1992) suggest that the filaments came from a disk surrounding the progenitor star outside of which was a magnetic torus. A somewhat different model for the bays was proposed by Li & Begelman (1992), who suggest that the Crab Nebula is interacting with a slow progenitor wind that is 5 times denser in the equatorial plane than along the poles.

If these circumstellar interaction models have validity, there is a problem with the normal Type II scenario discussed above because the energetic supernova gas would disrupt the nearby circumstellar medium. However, there are possible problems with circumstellar interaction. Images of the outer line emission from the Crab Nebula (e.g. Chevalier & Gull 1975) show no evidence for an indentation at the position of the bays, as would be expected for current circumstellar interaction with an asymmetric medium. The asymmetric interaction could have occurred at an earlier time. Also, if the filaments lying across the bays had a partial circumstellar origin, they would be expected to have less He than the average for the Crab Nebula rather than more. The previous explanation for the Crab bays is that they are related to the complex interaction of the pulsar magnetic field with the filaments and this may still be a viable model (cf. Michel et al. 1991).

The standard model for the internal structure of the Crab Nebula is a bubble created by a relativistic, particle dominated wind that is shocked and fills most of the volume (Kennel & Coroniti 1984a,b and references therein). The shock front is at about 1/20 the nebular radius at the position of optical filaments in the synchrotron emission. In the model of Kennel & Coroniti, the observed synchrotron emission at optical and higher frequencies can be explained if the Lorentz factor in the wind is $\gamma \sim 10^6$. This model predicts a toroidal magnetic field structure and at X-ray wavelengths there is evidence for

a toroidal structure at the position of suspected wind shock (Aschenbach & Brinkmann 1975). The position of the structure implies that the rotation axis of the pulsar is aligned in the NW–SE direction (projected against the sky). The outer contours of the Crab Nebula are elongated in the same direction. Begelman & Li (1992) extended the theory of Kennel and Coroniti to allow for an asymmetry in the nebula. The effect of the tension in the toroidal magnetic field is to reduce the pressure in the equatorial direction, while the polar pressure is not affected. The result is that the wind bubble extends further along the rotation axis, as observed. Begelman & Li (1992) found that for the wind magnetization parameter deduced by Kennel and Coroniti, the expected degree of asymmetry in the nebula is close to that observed. A problem with this picture is that the polarization of the optical synchrotron nebula clearly shows a toroidal field structure, but with the axis in the N–S direction (Michel et al. 1991). Michel et al. (1991) suggest that the misalignment is related to precession of the pulsar axis. Another possibility is that the magnetic structure is subject to instabilities.

In the Kennel and Coroniti model, particle acceleration occurs at the termination shock of the relativistic pulsar wind, but they did not address the details of the acceleration mechanism. The problem with the usual diffusive shock acceleration mechanism is that it does not operate for a perpendicular shock (magnetic field perpendicular to the shock normal), as expected here. Hoshino et al. (1992) have carried out plasma simulations of a relativistic perpendicular shock to investigate the microphysics of acceleration. A pure electron/positron wind, as is often assumed for pulsars, gives rise to a thermal particle distribution (Gallant et al. 1992), which is not observed. However, if most of the energy flux is in ions, the ions experience reflections at the shock and the magnetic field overshoots its final downstream value, leading to oscillations on the scale of the ion Larmor radius. The ions transfer energy to a nonthermal distribution of positrons and electrons on this scale. For a $\gamma = 10^6$ wind, the ion Larmor radius is ~ 0.01 pc, or $\sim$ 1 arcsec at the distance of the Crab Nebula. Hoshino et al. identify the wisp structure seen in a high resolution optical image of the Crab Nebula (van den Bergh & Pritchet 1989) with the acceleration region and predict that the synchrotron spectrum should systematically change with distance from the pulsar. Although the theory does not yet explain the radio synchrotron emission, Bietenholz & Kronberg (1992) found that the radio spectral index shows changes on a scale comparable to that of the optical wisps, supporting the hypothesis of particle acceleration on this scale.

5. Other Pulsar Nebulae

The properties of PSR 0540–69 in the Large Magellanic Cloud are given in Table 1. As with the Crab Nebula, when a pulsar with these properties is placed inside of a normal Type II supernova, the resulting nebula does have characteristics like those of the 0540–69 nebula (Reynolds 1985; Chevalier & Fransson 1992). A difference with the Crab is that a cooling shock is expected at the edge of the bubble if the gas is enriched in oxygen and the radiative shock power can explain the optical line emission from the nebula. Kirshner et al. (1989) found that the high temperature derived from the [OIII] lines is indicative of shock emission in 0540–69, as opposed to photoionization in the Crab Nebula. Imaging of the nebula in the [OIII] line shows a larger extent than in the continuum or other lines (Caraveo et al. 1992), which would also appear to be consistent with a shock origin. The Hα image of Caraveo et al. (1992) shows a curious hourglass structure, which does not have a straightforward explanation. The model of a pulsar bubble inside of a Type II supernova has been strengthened for 0540–69 by the detection of a radio shell that has

similar properties to those of a shell supernova remnant (Manchester, Staveley-Smith, & Kesteven 1993).

The properties of PSR 1509–58 are also given in Table 1. Chevalier & Fransson (1992) chose a value of τ for this pulsar that is quite small for two reasons. First, a small τ implies that the pulsar had a large initial power, which is needed to create an X-ray synchrotron nebula as large as that observed (Seward et al. 1984). Second, it implies a large value for t, which is needed to reduce the average velocity of the MSH 15-52 nebula (Seward et al. 1983) to $\sim 10,600$ km s^{-1}; this value is high, but is perhaps plausible if the supernova has been expanding into a mass loss wind bubble. More recently, Thorsett (1992) has identified the birth of PSR 1509–58 with SN 185. This implies an age that again requires minimizing the contribution of τ to the value of $\tau + t$.

Finally, I consider the nebula 3C 58, the likely remnant of SN 1181, which does not have an observed radio pulsar, but is believed to be powered by a pulsar based on the radio morphology and the presence of an X-ray point source (Becker et al. 1982). Frail & Moffett (1993) have recently undertaken a high spatial resolution radio study of 3C 58 and have found no evidence for a radio pulsar, suggesting that the pulsar is not beamed toward us despite the youth of the object. Frail and Moffett did observe a narrow filament near the X-ray point source and they identify the filament with the toroidal termination shock of the pulsar wind, analogous to the optical wisps near the Crab pulsar. The axis of the torus is along the long axis of the radio synchrotron nebula (Reynolds & Aller 1988), as expected in the models of asymmetric expansion discussed for the Crab Nebula. The position of the termination shock, together with the pressure in the nebula, gives an estimate of the spin-down power of the pulsar, $\dot{E} = 1.5 \times 10^{36}$ ergs s^{-1}, which approximately agrees with that deduced from the X-ray luminosity of the synchrotron nebula (Seward & Wang 1988). Frail and Moffett take $P/2\dot{P} \approx t$ (i.e. τ is small and the pulsar is substantially spun down) to derive $P = 730$ msec and $\dot{P} = 15,000 \times 10^{-15}$ s s^{-1}. In the magnetic dipole theory, these values yield the extraordinarily high magnetic field strength of 1×10^{14} G. An alternate hypothesis is that τ makes a major contribution to $P/2\dot{P}$ and the pulsar has not spun down much from its birth. If the magnetic field has the typical value of $10^{12.5}$ G, the current period is 100 msec, which is close to the initial period. The problem with this hypothesis is that it fails by a factor $\gtrsim 10^2$ in accounting for the energy content of the nebula. Either the methods used to estimate $\dot{E}$ are flawed or this pulsar has a very unusual magnetic field.

Acknowledgements

This work was supported in part by NSF grant AST-9016687.

REFERENCES

Aschenbach, B. & Brinkmann, W. (1975). A&A, 41, 147

Becker, R. H., Helfand, D. J., & Szymkowiak, A. E. (1982). ApJ, 255, 557

Begelman, M. C. & Li, Z.-Y. (1992). ApJ, 397, 187

Bietenholz, M. F. & Kronberg, P. P. (1992). ApJ, 393, 206

Blandford, R. D., Applegate, J. H., & Hernquist, L. (1983). MNRAS, 204, 1025.

Brown, G. E. & Bethe, H. (1993), preprint

Brown, G. E., Bruenn, S. W., & Wheeler, J. C. (1992). Comm. Ap., 16, 152

Caraveo, P. A., Bignami, G. F., Mereghetti, S., & Mombelli, M. (1992). ApJ, 395, L103

Chevalier, R. A. (1977). *Supernovae*, ed. D. N. Schramm, Dordrecht, Reidel, p. 53

Chevalier, R. A. (1989). ApJ, 346, 847

Chevalier, R. A. (1991). *SN 1987A and Other Supernovae*, ed. I. J. Danziger, Garching, ESO, p. 511

Chevalier, R. A. & Emmering, R. T. (1986). ApJ, 304, 140

Chevalier, R. A. & Fransson, C. (1992). ApJ, 395, 540

Chevalier, R. A. & Gull, T. R. (1975). ApJ, 200, 399

Colgate, S. A. (1971). ApJ, 163, 221

Emmering, R. T. & Chevalier, R. A. (1989). ApJ, 345, 931

Fesen, R. A., Martin, C. L., & Shull, J. M. (1992). ApJ, 399, 599

Frail, D. A. & Moffett, D. A. (1993). ApJ, 408, 637

Gallant, Y. A., Hoshino, M., Langdon, A. B., Arons, J., & Max, C. E. (1992). ApJ, 391, 73

Gunn, J. E. & Ostriker, J. P. (1970). ApJ, 160, 979

Hoshino, M., Arons, J., Gallant, Y. A., & Langdon, A. B. (1992). ApJ, 390, 454

Kaspi, V. M., Manchester, R. N., Johnston, S., Lyne, A. G., & D'Amico, N. (1992). ApJ, 399, L155

Kennel, C. F. & Coroniti, F. V. (1984a). ApJ, 283, 694

Kennel, C. F. & Coroniti, F. V. (1984b). ApJ, 283, 710

Kirshner, R. P., Morse, J. A., Winkler, P. F., & Blair, W. P. (1989). ApJ, 342, 260

Kulkarni, S. R., Predehl, P., Hasinger, G., & Aschenbach, B. (1993). Nature, 362, 135

Li, Z.-Y. & Begelman, M. C. (1992). ApJ, 400, 186

Manchester, R. N., Staveley-Smith, L., & Kesteven, M. J. (1993). ApJ, 411, 756

Michel, F. C. (1988). Nature, 333, 644

Michel, F. C., Scowen, P. A., Dufour, R. J., & Hester, J. J. (1991). ApJ, 368, 463

Murdin, P. & Clark, D. H. (1981). Nature, 294, 543

Narayan, R. (1987). ApJ, 319, 162

Narayan, R. & Schaudt, K. J. (1988). ApJ, 325, L43

Narayan, R. & Ostriker, J. P. (1990). ApJ, 352, 222

Nomoto, K. & Tsuruta, S. (1987). ApJ, 312, 711

Reynolds, S. P. (1985). ApJ, 291, 152

Reynolds, S. P. & Fix, J. D. (1987). ApJ, 322, 673

Reynolds, S. P. & Aller, H. D. (1988). ApJ, 327, 845

Seward, F. D., & Wang, Z. (1988). ApJ, 332, 199

Seward, F. D., Harnden, F. R., Jr., Murdin, P., & Clark, D. H. (1983). ApJ, 281, 650

Seward, F. D., Harnden, F. R., Jr., Szymkowiak, A., & Swank, J. (1984). ApJ, 267, 698

Srinivasan, G., Bhattacharya, D., & Dwarakanath, K. S. (1984). J. Ap. Astr., 5, 403

Stollman, G. M. (1987). A&A, 178, 143

Suntzeff, N. B., Phillips, M. M., Elias, J. H., DePoy, D. L., & Walker, A. R. (1992). ApJ, 384, L33

Trimble, V. L. (1968). AJ, 73, 535

Thorsett, S. E. (1992). Nature, 356, 690

van den Bergh, S. & Pritchet, C. J. (1989). ApJ, 338, L69

van den Bergh, S. & Tammann, G. (1991). ARA&A, 29, 363

Velusamy, T. (1985). *The Crab Nebula and Related Supernova Remnants*, ed. M. C. Kafatos & R. C. B. Henry, Cambridge, CUP, p. 115

Woosley, S. E., Pinto, P. A., & Hartmann, D. (1989). ApJ, 346, 395

A List of Supernovae Discovered Between 1989 January 1 and 1993 April 1

By SIDNEY VAN DEN BERGH

Dominion Astrophysical Observatory, National Research Council, 5071 West Saanich Road, Victoria, British Columbia, V8X 4M6, Canada

A catalog of all supernovae discovered between 1885 and 1988 December 31 has been published by Barbon, Cappellaro & Turatto (1989). In Table 1 a similar listing is given for all 203 supernovae found between 1989 January 1 and 1993 April 1. A statistical discussion of these new data, and references to original sources, will be given in van den Bergh (1994). The main results of that paper are the following: (1) The most recently discovered supernovae, almost all of which were found during systematic search programs, show no evidence for the inclination effect. If no inclination corrections need to be applied then supernova rates in spirals are only half as large as previously believed (van den Bergh & Tammann 1989, Cappellaro *et al.* 1993). (2) The data for supernovae of type II (SNe II) show clear evidence for the Shaw (1979) effect. However, no evidence for such an effect (which is due to the fact that some supernovae are not discovered when they appear projected on the bright nuclear bulges of distant galaxies) is seen for the more luminous supernovae of Type Ia (SNe Ia). (3) Due to more intensive surveillance of bright galaxies supernovae with m (discovery) < 16 are frequently found before maximum light, whereas fainter supernovae are more often discovered at a later phase.

REFERENCES

Barbon, R., Cappellaro, E., & Turatto, M. 1989 A&AS, 81, 421

Cappellaro, E., Turatto, M., Benetti, S., Tsvetkov, D. Yu., Bartunov, O. S., & Markova, I. N. 1993, A&A, 273, 383

Shaw, R. L. 1979, A&A, 76, 188

van den Bergh, S. 1994, Ap. J. Suppl., 92, 219

van den Bergh, S., & Tammann, G. A. 1991, ARAA, 29, 363

TABLE 1. List of Recent Supernovae

SN	Galaxy (Type)	α(1950 ^{h,m,s}) V (km/s)	δ(1950 $^{\circ}$ $'$ $''$) m (disc.)	Offsets ($''$) Type
1989A	N3687	11 25 21.4	+29 47 11	21W,18S
	Sb II-III:	2377	15.3	Ia
1989B	N3627	11 17 38.4	+13 15 55	15W,50N
	Sb II	703	13.0 V	Ia
1989C	...	09 45 10.0	+02 51 33	0:E,0:N
	Sc	...	14.5 B	IIpec
1989D	N2963	09 43 15.0	+73 11 46	2E,23N
	SBab	6538	16.0 B	Ia
1989E	M	13 35 19.5	+29 03 24	5E,0N
	...	7900	18.6 B	Ib
1989F	U8084	12 55 49.1	+03 03 49	18:E,18:N
	SB IV-V	2768	16.5	IIpec
1989G	...	11 11 12.0	+09 52 00	18E,18S
	M	8758	20.0	I
1989H	...	13 36 24.0	+32 32 00	4E,16S
	M	...	20.0 B	...
1989I	...	14 34 16.0	+14 53 14	3W,4S
	...	...	19.0 B	...
1989J	...	13 38 42.1	+32 43 55	4E,5S
	...	...	18.5 B	...
1989K	N5375	13 54 35.0	+29 25 00	65E,10N
	SBab	2270	17.5 R	II
1989L	N7339	22 35 24.0	+23 31 00	38E,1N
	S(B)bc:	1256	16.0	II
1989M	N4579	12 35 12.0	+12 05 36	39W,27N
	Sab II	1627	12.2 V	Ia
1989N	N3646	11 19 05.0	+20 26 42	29W,45S
	Sbc II	4261	14.5	II
1989O	M	00 18 27.2	+34 14 17	16E,9N
	...	19000	18.0 R	IIpec
1989P	N6636	18 22 00.0	+66 36 00	9W,47S
	S?	4226	16.5 R	Ia
1989Q	...	01 42 49.1	+21 50 12	2W,4N
	...	17000	19.5	Ia
1989R	U2912	03 56 06.8	+42 28 31	9W,9N
	S0/a	5000	15.0 R	IIpec
1989S	I226	02 24 50.9	+27 59 09	11E,30S
	S?	10894	19.0 R	Ia
1989T	...	01 44 28.5	+01 44 27	6W,5N
	...	...	18.0	...
1989U	U5295	09 49 47.3	+43 05 03	20W,47N
	S(B)b	4805	17.0 R	II

TABLE 1. List of Recent Supernovae (continued)

SN	Galaxy (Type)	α (1950 ^{h,m,s}) V (km/s)	δ (1950 $^{\circ}$ $'$ $''$) m (disc.)	Offsets ($''$) Type
1989V	...	01 29 18.9	+11 56 31	1W,2S
	...	18000	18.5	Ia
1989W	...	13 42 41.3	+30 01 07	4E,8N
	...	...	18.0 R	...
1989X	...	07 23 35.1	+64 00 34	4:S,4:W
	...	...	17.5	...
1989Y	E	21 14 46.7	-46 30 41	0E,31S
	SBb	4156	18.9 B	...
1989Z	N4013	11 55 57.6	+44 13 40	10E,4N
	Sbc:	694	K	...
1989aa	...	01 16 33.5	+13 00 26	2W,4N
	...	...	19.5	...
1990A	N500	01 20 03.4	+05 07 35	10E,7N
	E	...	19.5 J	...
1990B	N4568	12 34 02.6	+11 30 50	6W,10N
	Sc II-III	2260	16.0	Ib
1990C		Not a supernova		
1990D	...	13 41 07.8	+29 21 41	6E,1N
	...	...	20.0 J	...
1990E	N1035	02 37 01.7	-08 20 54	3W,9S
	Sc: III	1250	16.7	II
1990F	...	13 36 46.9	+32 24 34	6W,1S
	S	...	18.7 V	Ia
1990G	I2735	11 18 22.1	+34 37 05	35W,13N
	Sab	10970	15.0 B	Ia
1990H	N3294	10 33 23.7	+37 35 01	12W,1S
	Sc I-II	1436	16.0	II
1990I	N4650A	12 42 04.6	-40 26 27	13E,45S
	S0/a:pec	2837	16.7 B	Ib
1990J	...	12 13 48.2	+12 48 18	7W,10N
	...	...	18.0 B	Ia
1990K	N150	00 31 46.8	-28 04 45	18W,27N
	Sbc II	1523	14.0 V	II
1990L	U9927	15 34 12.0	+22 40 00	20E,2S
	SB0	...	19.0 B	Ia
1990M	N5493	14 08 52.6	-04 48 35	15W,4N
	E7/S0	2627	13.5 V	Ia
1990N	N4639	12 40 21.4	+13 31 50	65E,1S
	SBb II	898	15.5	Ia
1990O	M	17 13 18.0	+16 22 00	20E,3S
	...	...	17.0 B	Ia
1990P	...	16 12 16.3	-15 28 28	4W,6N
	...	...	19.0 R	...

TABLE 1. List of Recent Supernovae (continued)

SN	Galaxy (Type)	α (1950 ^{h,m,s}) V (km/s)	δ (1950 $^{\circ\,\prime\,\prime\prime}$) m (disc.)	Offsets ($''$) Type
1990Q	N5917	15 18 52.2	-07 11 54	11E,11N
	Sb?pec	1904	18.0 V	II
1990R	U11699	21 09 54.0	+12 24 00	10E,0N
	SBd:	4812	17.5 B	Ia
1990S	M	12 02 59.0	-29 53 03	7W,5N
	S	8000	15.5 B	II:
1990T	...	19 54 58.0	-56 23 38	25E,2S
	S0?	12000	16.5 B	Ia
1990U	N7479	23 02 26.0	+12 03 06	22W,54S
	SBbc I-II	2394	16.0	Ic
1990V	N7564	23 13 00.1	+07 01 00	11E,16S
	...	10252	18.0 B	II
1990W	N6221	16 48 25.6	-59 08 02	7E,5N
	Sbc II-III	1350	15.0 V	Ic
1990X	U12565	23 20 15.8	+22 56 07	12W,20S
	S?	8534	19.0 B	II
1990Y	...	03 35 24.1	-33 12 16	1E,5S
	E	11000	18.0 B	Ia
1990Z	U12133	22 37 00.0	+08 22 00	26W,30S
	Scd:	7422	19.0 R	II
1990aa	U540	00 50 16.0	+28 45 40	12E,8S
	S?	5096	17.0	Ibc
1990ab	...	21 51 00.1	-40 18 19	4E,9S
	...	10000	18.0 R	Ia
1990ac	...	03 51 08.1	-29 53 34	1W,6N
	...	19000	18.0 R	Ia
1990ad	...	22 40 05.9	+01 02 22	5W,3N
	...	...	19.5 J	II:
1990ae	...	00 20 18.0	+06 33 00	13E,0N
	...	7680	18.0 R	II
1990af	...	21 31 08.7	-62 57 30	7W,7N
	...	14000	17.0 B	Ia
1990ag	...	07 29 35.7	+33 00 48	0E,5S
	S	16000	19.0	IIpec
1990ah	U249	00 23 34.7	+13 22 52	3E,8N
	Sdm:	5242	18.0	II
1990ai	...	07 17 11.3	+21 59 57	...
	...	...	19.5	Ibc
1990aj	N1640	04 40 04.3	-20 31 43	10E,47N
	SBbc I-II	1643	18.0	Ib

TABLE 1. List of Recent Supernovae (continued)

SN	Galaxy (Type)	α(1950 ^{h,m,s}) V (km/s)	δ(1950 $^{\circ}\,'\,''$) m (disc.)	Offsets ($''$) Type
1990ak	...	13 22 06.2	-32 09 39	1W,11S
	E	...	18.0	...
1991A	I2973	11 51 15.5	+33 38 35	28E,10S
	SBd:	3199	17.0	Ic
1991B	N5426	14 00 47.0	-05 49 52	10W,20S
	Sct	2371	16.0 V	Ia
1991C	...	11 30 06.0	+05 37 30	5E,5S
	...	...	18.0 B	II
1991D	...	13 38 32.5	-14 23 39	13E,8S
	S	...	16.5 V	Ib
1991E	...	06 34 13.9	-65 30 44	6E,5N
	...	7000	19.0 R	II
1991F	N3458	10 52 58.0	+57 23 00	13E,12S
	SB0	1818	18.0 B	I
1991G	N4088	12 03 00.7	+50 49 07	37W,13S
	S(B)c II-III	723	17.0 R	II
1991H	...	12 56 17.4	-10 27 40	2W,11S
	...	...	17.5 R	II
1991I	...	05 25 17.2	-52 16 03	0W,1N
	...	11000	18.5 R	II
1991J	N5020	13 10 11.0	+12 51 53	34W,56S
	S(B)bc	3359	17.0 R	II
1991K	N2851	09 18 09.0	-16 16 57	5E,19S
	S0	5000	18.0 R	Ib
1991L	M	16 39 32.9	+39 23 05	2W,8N
	...	9000	18.0 R	Ibc
1991M	I1151	15 56 16.5	+17 35 03	60N,36E
	SBc	2083	17.5	Ia
1991N	N3310	10 35 40.3	+53 45 45	5E,7S
	Sbc pec	1018	15.0 V	Ibc
1991O	...	14 23 32.3	+65 59 02	10E,5N
	...	...	18.0 R	Ia
1991P	...	13 15 24.3	-15 02 19	8E,9S
	S	11000	20.0 R	II
1991Q	N4926A	12 59 43.5	+27 55 01	6W,2N
	S0 pec?	...	18.0 V	...
1991R	...	15 52 39.8	+19 09 37	6W,9S
	...	10500	18.0 J	Ibc
1991S	U5691	10 26 43.1	+22 15 48	5E,18N
	...	16000	17.5 B	Iapec?
1991T	N4527	12 31 34.9	+02 55 47	26E,44N
	Sb II	1727	15.0 V	Iapec?

TABLE 1. List of Recent Supernovae (continued)

SN	Galaxy (Type)	α(1950 ^{h,m,s}) V (km/s)	δ(1950 $^{\circ}$ $'$ $''$) m (disc.)	Offsets ($''$) Type
1991U	I4232	13 20 37.0	-25 51 00	3W,6N
	Sbc:pec	9000	16.0 B	Ia
1991V	I4508	14 45 42.0	+31 59 00	0E,14S
	...	...	18.5 R	...
1991W		Not a supernova		
1991X	N4902	12 58 21.6	-14 14 40	14E,11N
	...	2625	13.8 V	Ia
1991Y	...	17 13 42.0	+57 22 00	0E,7N
	...	...	19.0 B	...
1991Z	...	10 52 07.4	-03 56 33	10E,4N
	...	...	20.0 R	...
1991aa	...	12 42 33.8	-06 02 33	13E,5S
	...	3280	16.0 R	Ia
1991ab	...	13 56 59.3	+19 55 27	8E,11N
	...	19000	19.5	Ia
1991ac	...	12 58 55.5	+29 27 06	4W,1N
	...	...	18.5	...
1991ad	...	16 17 09.7	+17 45 56	11E,2N
	...	20900	18.5 B	Ia
1991ae	M	15 48 24.0	+68 15 00	2W,8N
	...	...	18.0 B	IIpec
1991af	...	17 25 06.0	+29 31 00	7E,3S
	...	...	19.0 B	Ia
1991ag	I4919	19 56 11.0	-55 30 42	3W,22N
	SBdm pec	4286	15.0 B	Ia
1991ah	...	22 07 01.7	-46 34 10	5W,6N
	...	11000	18.5 B	II
1991ai	I4434	14 25 32.6	+16 25 49	7E,5S
	...	...	18.5	Ia
1991aj	M	16 28 06.0	+41 53 09	5E,2N
	S	9600	18.0	Ia
1991ak	N5378	13 54 42.0	+38 02 37	28W,19S
	SB0	3017	15.5 B	Ia
1991al	...	19 38 18.0	-55 13 00	17E,7S
	S	3000	16.0 B	II
1991am	M	16 40 05.4	+37 49 44	6E,5N
	S	...	18.0 R	Ia:
1991an	...	17 39 19.0	+67 43 56	33W,4N
	...	...	20.3	...
1991ao	U270	00 25 18.7	+32 29 56	18W,11N
	S?	4923	17.8	II
1991ap		Not a supernova		

TABLE 1. List of Recent Supernovae (continued)

SN	Galaxy (Type)	α(1950 ^{h,m,s}) V (km/s)	δ(1950 $^{\circ}$ $'$ $''$) m (disc.)	Offsets ($''$) Type
1991aq	...	01 53 42.1	-81 52 57	5W,11S
	S	...	18.0 R	...
1991ar	I49	00 41 22.0	+01 34 36	8E,12N
	S(B)c	4571	17.0 J	Ib
1991as	...	22 46 10.0	+07 54 36	9E,13S
	...	...	18.0 B	Ia
1991at	U733	01 08 00.0	+16 20 00	20E,34N
	SBb	12307	18.0 B	Ia
1991au	U11616	20 40 00.3	+63 19 00	14W,2S
	Scd:	2612	18.5 R	II:
1991av	...	21 53 28.0	+00 45 33	7E,5N
	...	...	18.0 R	IIpec.
1991aw	...	17 42 20.8	+67 30 20	2W,9N
	S	...	15.4 B	...
1991ax	...	03 03 22.6	-41 57 46	11W,1N
	...	...	16.5 B	II
1991ay	...	00 44 33.9	+40 16 11	0W,5S
	...	15000	18.5 B	Ia
1991az	M	02 22 24.0	+24 02 00	10W,3S
	S?	9711	18.0 B	II
1991ba	E	01 28 36.7	-42 43 10	1W,11N
	Ir	7341	18.5 V	II
1991bb	U2892	03 50 00.7	+18 57 00	9E,2N
	SBbc	7963	18.0 R	Ia
1991bc	U2691	03 18 12.9	-01 13 27	5E,6S
	S	6401	16.0 J	Ia
1991bd	U2936	04 00 12.4	+01 49 33	21E,30N
	SBd	3812	17.0 V	Ia
1991be	...	21 30 04.5	-42 26 04	7W,1S
	...	...	18.5 J	...
1991bf	E	23 49 41.0	-29 43 34	12W,23N
	S0	...	17.5 I	Ia
1991bg	N4374	12 22 31.0	+13 09 48	57S,1E
	E1	1029	14.3 V	Iapec
1991bh	...	02 42 16.2	+14 57 13	5E,17S
	...	...	18.0 B	Ia
1991bi	N5127	13 21 44.0	+31 49 36	13W,6S
	E pec	4782	18.5 J	Ia
1991bj	I344	03 39 00.3	-04 49 31	14E,8N
	...	5450	18.8	Ia
1992A	N1380	03 34 31.8	-35 08 24	3W,62N
	S0/Sa	1861	12.8	Ia

TABLE 1. List of Recent Supernovae (continued)

SN	Galaxy (Type)	α (1950 ^{h,m,s}) V (km/s)	δ (1950 $^{\circ}$ $'$ $''$) m (disc.)	Offsets ($''$) Type
1992B	...	11 13 15.5	+55 45 48	13E,4N
	S	16000	17.8 V	Ia
1992C	N3367	10 43 54.7	+14 00 58	27E,28S
	SBc II	3037	16.5 B	II
1992D	...	05 58 51.0	-20 22 02	1W,7S
	...	15000	19.0 R	IIpec
1992E	...	06 34 37.4	-59 53 31	8W,2S
	...	17000	20.0 R	Ia
1992F	...	11 22 34.6	+56 52 28	3W,4N
	...	...	19.0	...
1992G	N3294	10 33 23.9	+37 34 58	27E,10S
	Sc I-II	1571	14.0 V	Ia
1992H	N5377	13 54 18.0	+47 29 00	57E,19N
	S(B)a	1796	15.0 V	II-L
1992I	N2565	08 16 52.2	+22 11 21	28W,7N
	SBbc:	3675	18.0	...
1992J	...	10 06 43.0	-26 24 00	11W,13N
	S	13000	18.4 V	Ia
1992K	E	13 07 10.0	-46 10 12	2W,14S
	S(B)ab	3080	16.2 V	Ia
1992L	...	07 34 09.3	-47 10 13	6W,5S
	...	...	20.0 R	...
1992M	...	07 11 31.7	+45 31 12	3W,7S
	...	...	18.2 I	Ia
1992N	I4831	19 10 09.2	-62 21 31	94E,43S
	Sab	4314	19.0 B	II
1992O	...	19 19 07.3	-62 55 19	7W,1N
	...	12000	17.8 V	Ia
1992P	I3690	12 40 17.8	+10 37 51	6W,11N
	S?	7617	16.8 B	Ia
1992Q	...	12 08 28.1	-01 35 58	5W,11S
	...	...	18.5 B	...
1992R	M	16 36 15.7	+58 15 55	13E,4S
	S	15687	18.0 B	I
1992S	...	14 15 30.2	+31 16 49	15E,0N
	S	...	18.5 B	...
1992T	...	13 40 10.0	-31 38 24	4E,6S
	S	...	18.0 B	II
1992U	E	20 35 42.0	-70 52 21	18E,9N
	SB	3000	18.5 B	II
1992V	...	12 32 13.7	+14 49 58	10E,8N
	S	...	18.0 B	Ia

TABLE 1. List of Recent Supernovae (continued)

SN	Galaxy (Type)	α (1950 ^{h,m,s}) V (km/s)	δ (1950 $^{\circ}$ $'$ $''$) m (disc.)	Offsets ($''$) Type
1992W		Not a Supernova		
1992X		Not a Supernova		
1992Y	N3527	11 04 36.1	+28 47 50	13E,6S
	SBa:	10093	18.8 B	...
1992Z	...	13 26 09.0	-29 45 17	3E,4N
	...	...	19.0 B	II
1992aa	N6464	17 45 12.0	+60 55 00	0E,11S
	S	...	18.0 R	II
1992ab	N6389	17 30 25.9	+16 26 16	80E,20S
	Sbc	3081	17.0 R	II
1992ac	M	16 36 15.7	+58 15 55	...
		15687	...	Ia
1992ad	N4411B	12 24 15.0	+09 09 42	35E,26S
	S(B)cd	1250	13.5 V	II
1992ae	...	21 24 26.8	-61 46 12	3E,5N
	...	20000	18.0 B	Ia
1992af	E	20 27 17.0	-42 28 39	10E,3S
	S	6000	17.5 B	II
1992ag	E	13 21 26.0	-23 37 06	4W,0N
	S?	7000	16.5 B	Ia
1992ah	...	17 35 26.2	+12 56 00	25W,8S
	...	...	17.0 R	Ia
1992ai	...	01 26 50.4	-32 31 52	2W,7S
	S	...	17.5 B	Ia
1992aj	...	23 45 12.5	-35 28 39	9E,5N
	S	...	17.0	II
1992ak	U3862	07 24 51.1	+20 29 54	...
	S?	8151	16.0	...
1992al	E	20 42 17.4	-51 34 26	18E,12S
	SBc:	4362	16.0 R	Ia
1992am	...	01 22 32.0	-04 54 36	19W,1S
	S	14000	18.5 B	II
1992an	...	13 34 59.0	-30 26 12	6E,6N
	S	15000	18.0 B	IIpec
1992ao	N7637	23 22 10.6	-82 10 15	54E,57N
	...	3679	17.0 R	II
1992ap	U10430	16 28 47.6	+41 35 25	7E,16N
	SBbc	9072	18.0 B	Ia
1992aq	...	23 01 49.0	-37 36 48	2E,7S
	...	29000	19.0 B	Ia
1992ar	...	23 14 42.0	-44 55 18	2W,5S
	...	40000	19.0 B	Ic

TABLE 1. List of Recent Supernovae (continued)

SN	Galaxy (Type)	α (1950 ^{h,m,s}) V (km/s)	δ (1950 $^{\circ}$ $'$ $''$) m (disc.)	Offsets ($''$) Type
1992as	...	21 00 36.0	-44 50 48	3W,4S
	...	7000	18.5 B	II
1992at	...	21 24 03.4	-37 12 51	6E,11S
	SB	...	18.0 B	Ia
1992au	...	00 08 08.0	-50 13 36	21E,9N
	...	18000	17.0 B	Ia
1992av	...	17 43 12.6	+67 50 16	11E,5N
	...	...	20.0 V	...
1992aw	...	19 05 39.4	+50 58 06	13E,7N
	...	11000	18.0 R	II
1992ax	...	22 08 24.0	+44 47 04	0W,20S
	...	...	18.5 B	I
1992ay	...	04 28 50.2	-46 30 32	6E,6N
	...	18000	18.5 B	IIpec
1992az	N818	02 05 42.6	+38 32 26	28E,16S
	S(B)c:	4457	18.0	II
1992ba	N2082	05 41 35.3	-64 19 21	60W,0N
	Sc II-III	1241	14.0 V	II
1992bb	...	21 15 36.5	-07 47 46	19W,4N
	S	...	17.5 B	Ia
1992bc	E	03 03 22.2	-39 45 15	15E,5N
	S	6000	15.0 B	Ia
1992bd	N1097	02 44 11.0	-30 29 06	2E,9S
	SBbc I-II	1274	15.0 V	II
1992be	...	03 59 28.7	+27 38 47	3W,10N
	...	...	17.0 R	II
1992bf	N930	02 25 06.1	+20 06 32	9E,11S
	Sa	4086	17.0 B	I
1992bg	...	07 41 19.0	-62 24 06	3W,6N
	S	10000	17.8 B	Ia
1992bh	...	04 58 40.0	-58 54 10	1E,2S
	...	13000	17.3 B	Ia
1992bi	...	16 08 28.3	+39 54 57	2E,0N
	...	108000	22.0 R	...
1992bj	...	23 19 21.8	+24 53 02	0W,5N
	...	16000	19.8	II
1992bk	E	03 41 43.4	-53 46 55	12E,21N
	E	17000	18.0 B	Ia
1992bl	E	23 12 25.0	-45 00 36	15E,22S
	SBa:	13000	17.0 B	Ia
1992bm	...	07 29 30.4	+50 34 52	0W,11S
	...	15000	18.0 B	II

TABLE 1. List of Recent Supernovae (continued)

SN	Galaxy (Type)	α (1950 ^{h,m,s}) V (km/s)	δ (1950 $^{\circ}$ $'$ $''$) m (disc.)	Offsets ($''$) Type
1992bn	...	01 26 20.6	+08 53 32	1W,7S
	...	...	19.0	...
1992bo	E	01 19 44.1	-34 27 29	48W,55S
	Sa	6000	17.0 B	Ia
1992bp	...	03 34 22.3	-18 31 04	6W,2S
	S	23000	18.0 B	Ia
1992bq	...	10 14 43.6	-34 30 08	15E,1S
	S	...	17.0 B	...
1992br	...	01 43 55.4	-56 20 57	2E,7S
	...	25000	18.5 B	Ia
1992bs	...	03 27 37.2	-37 26 38	9W,4N
	S	19000	18.0 B	Ia
1993A	...	07 38 38.4	-61 56 11	6W,4S
	...	...	18.5 B	II-P
1993B	...	10 32 35.1	-34 11 03	1E,5N
	S	20000	18.0 B	Ia
1993C	...	09 37 40.6	+15 08 58	5W,50N
	E	3821	18.7 B	Ia
1993D	E	11 26 29.7	-22 12 27	11W,7S
	SB0	8190	18.0 R	Ia
1993E	...	09 40 27.4	+49 31 34	11W,8N
	...	...	19.0	II
1993F	...	07 54 26.4	+20 13 06	1E,2S
	...	...	18.5	...
1993G	N3690	11 25 44.2	+58 50 23	2W,15S
	IBm pec	3033	16.6 R	II
1993H	E	13 49 58.0	-30 27 54	1E,12N
	SBab	7265	16.5 B	Ia
1993I	M	12 32 11.4	+09 16 48	14W,8S
	...	...	18.0	Ia
1993J	N3031	09 51 27.7	+69 18 13	45W,167S
	Sb I-II	-49	12.0 V	IIb
1993K	N2223	06 22 30.0	-22 48 36	30E,31N
	SBbc I-II	2722	14.5	II

A Catalogue of Galactic Supernova Remnants

By D. A. GREEN

Mullard Radio Astronomy Observatory, Cavendish Laboratory, Madingley Road, Cambridge CB3 0HE, UNITED KINGDOM

1. The Catalogue

This catalogue of Galactic supernova remnants (SNRs) is an updated version of those presented in detail in Green (1984, 1988) and in summary form in Green (1991). The basic parameters of the 182 SNRs included in this (1993 May) version of the catalogue are presented below. Notes on how these parameters are derived from observational data are given in Green (1988). It should be noted that there are serious selection effects which apply to the identification of Galactic SNRs (see Green 1991), so that great care should be taken if these data are used in statistical studies. There are many objects that have been identified as SNRs and are listed in the catalogue, although they have been barely resolved in the available observations, or are faint, and have not been well separated from confusing background or nearby thermal emission. The identification of these objects as SNRs, or at least their parameters remain uncertain (see Green 1988).

2. Revisions

Since Green (1991) the following eight SNRs have been added to the catalogue:

- Three new remnants (G59.5+0.1, G67.7+1.8 and G84.9+0.5) of the the eleven possible SNRs reported by Taylor, Wallace & Goss (1992).
- G156.2+5.7, which was first identified from X-ray observations by ROSAT (Pfeffermann, Aschenbach & Predehl 1991).
- G318.9+0.4, a complex of radio arcs reported by Whiteoak (1990).
- G322.5−0.1, reported by Whiteoak (1992).
- G343.1−2.3, an incomplete radio shell, with an associated pulsar (McAdam, Osborne & Parkinson 1993).
- G348.5−0.0, a radio arc near G348.5+0.1 (=CTB 37A), revealed by Kassim, Baum & Weiler (1991).

Also note that G308.7+0.0 has been renamed G308.8−0.1 because of improved observations revealing its extent more fully (see Caswell et al. 1992).

A detailed version of the catalogue, in the format of Green (1988), complete with references for each object, and notes on possible remnants not included and questionable SNRs listed in the catalogue is available from me on request. The summary data presented in the table below are also available in computer readable form (either by e-mail, or by ''ftp'').

REFERENCES

Caswell J.L., Kesteven M.J., Stewart R.T., Milne D.K., Haynes R.F., 1992, ApJ, 399, L151

Green D.A., 1984, MNRAS, 209, 449

Green D.A., 1988, Ap&SS, 148, 3

Green D.A., 1991, PASP, 103, 209

Kassim N., Baum S.A., Weiler K.W., 1991, ApJ, 374, 212

McAdam W.B., Osborne J.L., Parkinson M.L., 1993, Nat, 361, 516

Pfeffermann E., Aschenbach B., Predehl P., 1991, A&A, 246, L28

Taylor A.R., Wallace B.J., Goss W.M., 1992, AJ, 103, 931

Whiteoak J.B.Z., 1990, Nat, 347, 157

Whiteoak J.B.Z., 1992, MNRAS, 256, 121

Galactic SNRs

l	b	RA (1950.0) (h m s)	Dec (° ′)	size (arcmin)	type	Flux at 1 GHz (Jy)	spectral index	other names
0.0	+0.0	17 42 33	−28 59	3.5 × 2.5	S	100?	0.8?	Sg r A East
0.9	+0.1	17 44 12	−28 08	8	C	18?	varies	
1.9	+0.3	17 45 37	−27 09	1.2	S	0.6	0.7	
4.2	−3.5	18 05 45	−27 04	28	S	3.2?	0.6?	
4.5	+6.8	17 27 42	−21 27	3	S	19	0.64	Kepler, SN1604, 3C358
5.2	−2.6	18 04 25	−25 45	18	S	2.6?	0.6?	
5.4	−1.2	17 59 00	−24 55	35	C?	35?	0.2?	Milne 56
5.9	+3.1	17 44 20	−22 15	20	S	3.3?	0.4?	
6.1	+1.2	17 51 55	−23 05	30 × 26	F	4.0?	0.3?	
6.4	−0.1	17 57 30	−23 25	42	C	310	varies	W28
6.4	+4.0	17 42 10	−21 20	31	S	1.3?	0.4?	
7.7	−3.7	18 14 20	−24 05	18	S	10	0.32	1814−24
8.7	−5.0	18 21 05	−23 50	26	S	4.4	0.3	
8.7	−0.1	18 02 35	−21 25	45	S?	80	0.5	(W30)
9.8	+0.6	18 02 10	−20 14	12	S	3.9	0.5	

Galactic SNRs (continued)

l	b	RA (1950.0) (h m s)	Dec (° ′)	size (arcmin)	type	Flux at 1 GHz (Jy)	spectral index	other names
10.0	−0.3	18 05 40	−20 26	8?	S?	2.9	0.8	
11.2	−0.3	18 08 30	−19 26	4	S	22	0.49	
11.4	−0.1	18 07 50	−19 06	8	S?	6	0.5	
12.0	−0.1	18 09 15	−18 38	5?	?	3.5	0.7	
13.5	+0.2	18 11 20	−17 13	5 × 4	S	3.5?	1.0?	
15.1	−1.6	18 21 05	−16 36	30 × 24	S	5.5?	0.8?	
15.9	+0.2	18 16 00	−15 03	7 × 5	S?	4.5?	0.7?	
16.7	+0.1	18 18 05	−14 21	4	C	3.0	0.6	
16.8	−1.1	18 22 30	−14 48	30 × 24?	?	2?	?	
17.4	−2.3	18 28 05	−14 54	24?	S	4.8?	0.8?	
17.8	−2.6	18 30 00	−14 41	24	S	4.0?	0.3?	
18.8	+0.3	18 21 10	−12 25	18 × 13	S	27	0.5	Kes 67
18.9	−1.1	18 27 00	−13 00	33	C?	37	varies	
20.0	−0.2	18 25 20	−11 37	10	F	10	0.0	
21.5	−0.9	18 30 47	−10 37	1.2	F	6	0.0	
21.8	−0.6	18 30 00	−10 10	20	S	69	0.5	Kes 69
22.7	−0.2	18 30 30	−09 15	26	S?	33	0.6	
23.3	−0.3	18 32 00	−08 50	27	S	70	0.5	W41
23.6	+0.3	18 30 20	−08 15	10?	?	8?	0.3	
24.7	−0.6	18 36 00	−07 35	15?	S?	8	0.5	
24.7	+0.6	18 31 30	−07 07	30 × 15	C?	20?	0.2?	
27.4	+0.0	18 38 40	−04 59	4	S	6	0.68	4C−04.71
27.8	+0.6	18 37 06	−04 28	50 × 30	F	30	varies	
29.7	−0.3	18 43 48	−03 02	3	C?	10	0.7	Kes 75
30.7	−2.0	18 51 50	−02 58	16	?	0.5?	0.7?	
30.7	+1.0	18 42 10	−01 35	24 × 18	S?	6	0.4	
31.5	−0.6	18 48 35	−01 35	18?	S?	2?	?	
31.9	+0.0	18 46 50	−00 59	5	S	24	0.55	3C391
32.0	−4.9	19 03 00	−03 00	60?	S?	22?	0.5?	3C396.1
32.8	−0.1	18 48 50	−00 12	17	S?	11?	0.2?	Kes 78
33.2	−0.6	18 51 12	−00 05	18	S	5?	varies	
33.6	+0.1	18 50 15	+00 37	10	S	22	0.5	Kes 79, 4C00.70, HC13
34.7	−0.4	18 53 30	+01 18	35 × 27	S	230	0.30	W44, 3C392
36.6	−0.7	18 58 05	+02 52	25?	S?	?	?	
36.6	+2.6	18 46 20	+04 23	17 × 13?	S	0.7?	0.5?	
39.2	−0.3	19 01 40	+05 23	8 × 6	S	18	0.6	3C396, HC24, NRAO 593
39.7	−2.0	19 10 00	+04 50	120 × 60	?	85?	0.7?	W50 , SS433
40.5	−0.5	19 04 45	+06 26	22	S	11	0.5	
41.1	−0.3	19 05 08	+07 03	4.5 × 2.5	S	22	0.48	3C3 97
42.8	+0.6	19 04 55	+09 00	24	S	3?	0.5?	
43.3	−0.2	19 08 44	+09 01	4 × 3	S	38	0.48	W49B
43.9	+1.6	19 03 30	+10 25	60?	F?	8.6?	0.0?	
45.7	−0.4	19 14 05	+11 04	22	S	4.2?	0.4?	
46.8	−0.3	19 15 50	+12 04	17 × 13	S	14	0.42	(HC30)
49.2	−0.7	19 21 30	+14 00	25?	S?	160?	0.3?	(W51)

Galactic SNRs (continued)

l	b	RA (1950.0) (h m s)	Dec (° ′)	size (arcmin)	type	Flux at 1 GHz (Jy)	spectral index	other names
53.6	−2.2	19 36 30	+17 08	28	S	8	0.6	3C400.2, NRAO 611
54.1	+0.3	19 28 28	+18 46	1.5	F?	0.5	0.1	
54.4	−0.3	19 31 10	+18 50	40	S	28	0.5	(HC40)
55.7	+3.4	19 19 10	+21 38	23	S	1.4	0.6	
57.2	+0.8	19 32 50	+21 50	12?	S?	1.8?	?	(4C21.53)
59.5	+0.1	19 40 25	+23 28	5	S	3?	?	
59.8	+1.2	19 36 50	+24 12	20 × 16?	?	1.6	0.5	
65.1	+0.6	19 52 30	+28 25	90 × 50	S	6	0.6	
65.3	+5.7	19 31 00	+31 05	310 × 240	S?	52?	0.6?	
65.7	+1.2	19 50 10	+29 18	18	?	5.1	0.6	DA 495
67.7	+1.8	19 52 34	+31 21	9	S	1.4	0.3	
68.6	−1.2	20 06 40	+30 28	28 × 25?	?	0.7?	0.0?	
69.0	+2.7	19 51 30	+32 45	80?	?	120?	varies	CTB 80
69.7	+1.0	20 00 45	+32 35	16	S	1.6	0.8	
73.9	+0.9	20 12 20	+36 03	22?	S?	9?	0.3?	
74.0	−8.5	20 49 00	+30 30	230 × 160	S	210	varies	Cygnus Loop
74.9	+1.2	20 14 10	+37 03	8 × 6	F	9	varies	CTB 87
78.2	+2.1	20 19 00	+40 15	60	S	340	0.5	DR4, γ Cygni
82.2	+5.3	20 17 30	+45 20	95 × 65	S	120?	0.5?	W63
84.2	−0.8	20 51 30	+43 16	20 × 16	S	11	0.5	
84.9	+0.5	20 48 45	+44 42	6	S	0.8	0.4	
89.0	+4.7	20 43 30	+50 25	120 × 90	S	220	0.40	HB2 1
93.3	+6.9	20 51 00	+55 10	27 × 20	S	9	0.54	DA 530, 4C(T)55.38.1
93.7	−0.2	21 27 45	+50 35	80	S	65	0.3	CTB 104A, DA 551
94.0	+1.0	21 23 10	+51 40	30 × 25	S	15	0.44	3C434 .1
109.1	−1.0	22 59 30	+58 37	28	S	20	0.50	CTB 109
111.7	−2.1	23 21 10	+58 32	5	S	2720	0.77	Cassiopeia A, 3C461
112.0	+1.2	23 13 40	+61 30	30?	S?	7?	0.6?	
114.3	+0.3	23 34 45	+61 38	90 × 55	S	6?	0.3?	
116.5	+1.1	23 51 20	+62 58	80 × 60	S	11?	0.8?	
116.9	+0.2	23 56 40	+62 10	34	S	9?	0.5?	CTB 1
117.4	+5.0	23 52 30	+67 30	60 × 80?	S?	30?	0.5?	
119.5	+10.2	00 04 00	+72 30	90?	S	36	0.3	CTA 1
120.1	+1.4	00 22 30	+63 52	8	S	56	0.61	Tycho, 3C10, SN1572
126.2	+1.6	01 18 30	+64 00	70	S?	7	varies	
127.1	+0.5	01 25 00	+62 55	45	S	13	0.6	R5
130.7	+3.1	02 01 55	+64 35	9 × 5	F	33	0.10	3C58, SN1181
132.7	+1.3	02 14 00	+62 30	80	S	45	0.6	HB3
152.2	−1.2	04 05 30	+48 24	110?	S?	16?	0.7?	
156.2	+5.7	04 54 40	+51 47	110	S	5	0.5	
160.9	+2.6	04 57 00	+46 36	140 × 120	S	110	0.6	HB 9
166.0	+4.3	05 23 00	+42 52	55 × 35	S	7?	0.4?	VRO 42.05.01
166.2	+2.5	05 15 30	+41 50	90 × 70	S	11	0.5	OA 184
179.0	+2.6	05 50 30	+31 05	70	S?	7	0.4	
180.0	−1.7	05 36 00	+27 50	180	S	65	varies	S147

Galactic SNRs (continued)

l	b	RA (1950.0) (h m s)	Dec (° ′)	size (arcmin)	type	Flux at 1 GHz (Jy)	spectral index	other names
184.6	−5.8	05 31 30	+21 59	7 × 5	F	1040	0.30	Crab Nebula, 3C144, SN1054
189.1	+3.0	06 14 00	+22 36	45	S	160	0.36	IC443, 3C157
192.8	−1.1	06 06 30	+17 20	78	S	20?	0.6?	PKS 0607+17
205.5	+0.5	06 36 00	+06 30	220	S	160	0.5	Monoceros Nebula
206.9	+2.3	06 46 00	+06 30	60 × 40	S?	6	0.5	PKS 0646+06
211.7	−1.1	06 43 10	+00 24	70?	S?	15?	0.5?	
240.9	−0.9	07 40 30	−25 06	95?	S?	24?	0.1?	
260.4	−3.4	08 20 30	−42 50	60 × 50	S	130	0.5	Pupp is A, MSH 08−*44*
261.9	+5.5	09 02 20	−38 30	40 × 30	S	10?	0.4?	
263.9	−3.3	08 32 30	−45 35	255	C	1750	varies	Vela (XYZ)
279.0	+1.1	09 56 00	−53 00	95	S	30?	0.6?	
284.3	−1.8	10 16 30	−58 45	24?	S	11?	0.3?	MSH 10−*53*
290.1	−0.8	11 01 00	−60 40	15 × 10	S	42	0.4	MSH 11−*61A*
291.0	−0.1	11 09 45	−60 22	10	F	16	0.29	(MSH 11−62)
292.0	+1.8	11 22 20	−59 00	12 × 8	C?	15	0.4	MSH 11−*54*
293.8	+0.6	11 32 40	−60 37	20	C	5.5?	0.6?	
296.1	−0.5	11 48 40	−62 17	33?	S	8?	0.6?	
296.5	+10.0	12 07 00	−52 10	90 × 65	S	48	0.5	PKS 1209−51/52
296.8	−0.3	11 56 00	−62 18	14	S	9	0.6	1156−62
298.5	−0.3	12 10 00	−62 35	5?	?	5	0.4	
298.6	−0.0	12 11 00	−62 20	12 × 8?	S	4.3	0.3	
299.0	+0.2	12 15 00	−62 12	11?	S?	9?	?	
302.3	+0.7	12 42 55	−61 52	15	S	5.5	0.4	
304.6	+0.1	13 02 50	−62 26	8?	S?	14	0.5	Kes 17
308.8	−0.1	13 39 00	−62 08	20 × 30?	C?	15?	0.4?	
309.2	−0.6	13 43 00	−62 39	17 × 13	S	7?	0.4?	
309.8	+0.0	13 47 00	−61 50	24	S	17	0.5	
311.5	−0.3	14 02 00	−61 44	3?	?	3.7	0.5	
312.4	−0.4	14 09 20	−61 29	36 × 27	S	44?	0.3?	
315.4	−2.3	14 39 00	−62 17	40	S	49	0.6	RCW 86, MSH 14−*63*
315.4	−0.3	14 32 10	−60 23	15 × 10	S	8	0.4	
316.3	−0.0	14 37 40	−59 47	25 × 15	S	24	0.4	(MSH 14−*57*)
318.9	+0.4	14 54 40	−58 17	30 × 20?	?	3.5?	0.1?	
320.4	−1.2	15 10 30	−58 58	30	C	60?	0.4?	MSH 15−*52*, RCW 89
321.9	−0.3	15 16 45	−57 23	30 × 20	S	13	0.3	
322.5	−0.1	15 19 30	−56 55	15	C	1.9	0.3?	
323.5	+0.1	15 24 50	−56 11	10?	S	3?	0.4?	
326.3	−1.8	15 49 00	−56 00	36	C	145	varies	MSH 15−*56*
327.1	−1.1	15 50 30	−55 00	14?	S?	8?	?	
327.4	+0.4	15 44 30	−53 40	20	S	34	0.6	Kes 27
327.6	+14.6	14 59 35	−41 44	30	S	19	0.6	SN1006, PKS 1459−41
328.0	+0.3	15 49 30	−53 20	6?	?	2.4?	0.6?	
328.4	+0.2	15 51 40	−53 08	6	F	16	0.2	(MSH 15−*57*)
330.0	+15.0	15 05 00	−39 30	180?	S	350?	0.5?	Lupus Loop
330.2	+1.0	15 57 20	−51 26	10	S?	7	0.3	

Galactic SNRs (continued)

l	b	RA (1950.0) (h m s)	Dec (° ′)	size (arcmin)	type	Flux at 1 GHz (Jy)	spectral index	other names
332.0	+0.2	16 09 30	−50 45	10	S	9	0.5	
332.4	−0.4	16 13 45	−50 55	9	S	28	0.5	RCW 103
332.4	+0.1	16 11 30	−50 35	15	S	26	0.5	MSH 16−51, Kes 32
335.2	+0.1	16 24 00	−48 40	19	S	18	0.5	
336.7	+0.5	16 28 30	−47 13	13 × 10	S	6	0.5	
337.0	−0.1	16 32 10	−47 27	14?	S?	17?	0.5?	(CTB 33)
337.2	−0.7	16 35 45	−47 45	4?	?	2.1	0.7	
337.3	+1.0	16 29 00	−46 30	11	S	16	0.5	Kes 40
337.8	−0.1	16 35 20	−46 53	7?	?	18	0.5	Kes 41
338.1	+0.4	16 34 20	−46 18	12	S	4.5	0.4	
338.3	−0.0	16 37 20	−46 28	8?	S?	15?	0.7?	
338.5	+0.1	16 37 30	−46 13	8?	?	28?	0.3?	
340.4	+0.4	16 42 55	−44 34	6	S	6	0.4	
340.6	+0.3	16 44 05	−44 29	5	S	5.1	0.4	
341.9	−0.3	16 51 25	−43 56	6	S	3.2	0.5	
342.0	−0.2	16 51 15	−43 48	11 × 7	S?	3.5?	0.4?	
343.1	−2.3	17 04 30	−44 15	44 × 32?	S	25?	0.5?	
344.7	−0.1	17 00 20	−41 38	8?	S?	3.0	0.5	
346.6	−0.2	17 06 50	−40 07	8	S	10	0.5	
348.5	−0.0	17 12 00	−38 25	10?	S?	10?	0.4?	
348.5	+0.1	17 10 40	−38 29	15	S	72	0.3	CTB 37A
348.7	+0.3	17 10 30	−38 08	10	S	26	0.3	CTB 37B
349.7	+0.2	17 14 35	−37 23	2.5 × 2	S?	20	0.5	
350.0	−1.8	17 23 40	−38 20	30?	S?	31	0.5	
351.2	+0.1	17 19 05	−36 08	7	C	5.8	0.4	
352.7	−0.1	17 24 20	−35 05	6 × 5	S?	6?	0.6?	
355.9	−2.5	17 42 35	−33 42	13	S	8	0.5	
357.7	−0.1	17 37 15	−30 56	3 × 8?	?	37	0.4	MSH 17−39
357.7	+0.3	17 35 20	−30 42	24	S	10	0.4?	
358.4	−1.9	17 46 05	−31 16	40 × 36	S	12.5?	0.5?	
359.0	−0.9	17 43 35	−30 15	23	S	23	0.5	
359.1	−0.5	17 42 20	−29 56	24	S	14	0.4?	

List of Contributed Papers

1. STATISTICS AND CLASSIFICATION OF SUPERNOVAE

Bias of Supernova Discoveries from the OCA Search
C. Pollas (Observatoire de la Cote d'Azur, France)

The Probability of Detecting Supernova Precursors in the Galaxy
O. A. Tsiopa (Pulkovo Observatory, St. Petersburg, Russia)

The Rate of Supernovae
E. Cappellaro, M. Turatto & S. Benetti (Osservatorio Astronomico di Padova, Italy)

A Numerical Parameter Study of Type II Supernovae
T. R. Young, E. Baron, & D. Branch (U. Oklahoma, USA)

Photometric Behavior of SN II
M. Turatto (Osservatorio Astronomico di Padova, Italy)

Sources of Color Dispersion in SNIa
P. Nugent, A. Fisher & D. Branch (U. Oklahoma, USA)

A revised classification scheme for SNII
R. Barbon, E. Cappellaro, F. Patat, & M. Turatto (Asiago Astrophysical Obs., Italy)

A Study of Multiple Supernovae in Spiral Galaxies
Li, Zongwei & Li, Weidong (Beijing Normal U., China)

The Relation between Supernovae and Spiral Structure
Song, Guo Xuan (Shanghai Observatory, China)

The Space Distribution of W-R Stars and HII Regions
Zhang, Xiangling (Beijing Normal University, China)

2. SUPERNOVA LIGHT CURVES AND DISTANCES

Model Photospheres for Type II Supernovae
M. Montes & R. V. Wagoner (Stanford University, USA)

The Absolute Magnitude Dispersion among Normal SNe Ia and the Value of H_0
D. Miller & D. Branch (U. Oklahoma, USA)

SN Ia Photometry and the Deceleration Parameter
T. E. Vaughan & D. Branch (U. Oklahoma, USA)

3. SN 1987A

Observations of SN 1987A
C. S. J. Pun & R. P. Kirshner (Harvard-Smithsonian Center for Astrophysics, USA)

Asymmetry in SN 1987A
V. Utrobin & N. Chugai (ITEP, Russia)

SN 1987A Observations at the Later Phases
P. Bouchet, I. J. Danziger, C. Gouiffes, M. Della Valle & A. Moneti (European Southern Observatory)

Simulation of Strong Emission Line Profiles in the Spectrum of SN 1987A
A. A.Andronova (Central Astron. Obs., St. Petersburg, Russia)

Spectral Line Changes of SN 1987A
Lin, Xianbin (Shanghai Jiaotong University, China)

Observations of the Radio Rebirth of SN 1987A
A. J. Turtle, D. F. Crawford & D. Campbell-Wilson (University of Sydney, Australia)

On the Nature of Radio Emission of SN 1987A
O. A. Tsiopa (Central Astron. Obs., St. Petersburg, Russia)

Formation of The Circumstellar Ring Around SN 1987A by Wind-Wind Interactions
T. Shigeyama (U. Tokyo, Japan)

The Line Emission from the Ring around SN 1987A
P. Lundqvist (Stockholm Obs., Sweden)

Problems in Using the Fluorescence Echo around SN 1987A as a Distance Indicator
J. E. Felten & E. Dwek (NASA Goddard Space Flight Center, USA)

X-ray Emission from SN 1987A due to Interaction with its Ring-Like Nebula
K. Masai (Service d'Astrophysique, CEN Saclay, France) & K. Nomoto (U. Tokyo, Japan)

UV Emission Lines from the Collision of SN 1987A with its Circumstellar Ring
D. Luo (U. Virginia, USA), R. McCray, & J. Slavin (JILA, U. Colorado, USA)

Circumstellar Echoes around SN 1987A and the Nature of the Progenitor Star
Arlin P.S. Crotts (Columbia U.), William E. Kunkel (Carnegie Obs.), Stephen R. Heathcote (Cerro Tololo InterAmerican Obs.), Elizabeth Bonar (Columbia U., USA)

Three Dimensional Mapping of Interstellar Structure – A New Probe by Light Echo
Jun Xu, & A. Crotts (Columbia U.), W. Kunkel (Carnegie Obs.), & S. Heathcote (Cerro Tololo InterAmerican Obs.)

4. SN 1993J

The Bright Supernova SN 1993J as Seen by Spanish Observers
G. Gomez (Inst. de Astrofisica de Canarias & U. de La Laguna, Tenerife, Spain)

The Early Light of SN 1993J
Lisa A. Wells (NOAO/KPNO), Thomas J. Balonek (Colgate U.), Richard Tweedy (Steward Obs.), Eric G. Hintz & Michael D. Joner (BYU), Alain C. Porter (NOAO/KPNO), William Neely (NF Obs., New Mexico), Christina A. Tremonti (Colgate U.), Jennifer L. Koch (St. Lawrence U.), Nicole Silvestri (Union College), Peter W. A. Roming & Kenneth A. Nelson (BYU), & Karen B. Kwitter (Williams College, USA)

Early-Time Spectroscopy of SN 1993J
T. Matheson & A. V. Filippenko (U. California, Berkeley, USA)

Spectroscopic and Photometric Observations of SN 1993J at Beijing Observatory
Hu, Jingyao (Beijing Obs., China)

Early Radio Light Curves for SN 1993J
Schuyler D. Van Dyk & Kurt W. Weiler (NRL, Washington, DC, USA), Richard A. Sramek, Michael P. Rupen (NRAO/VLA, Socorro, NM, USA), & Nino Panagia (StScI, Baltimore, MD, USA)

Interpretation of Early Spectra of SN 1993J
E. Baron, P. H. Hauschildt, M. Wagner, S. Austin, & D. Branch (U. Oklahoma, USA)

5. OTHER SUPERNOVAE

Spectral Evolution of Twin Supernovae in MCG 10 – 24 – 007
G. Gomez (Instituto de Astrofisica de Canarias & Universidad de La Laguna, Tenerife, Spain) & R. Lopez (Universitat de Barcelona & Centre d'Estudis Avançats de Blanes, Girona, Spain)

Reddening Correction and the Bolometric Light Curve of SN 1989B
Lisa A. Wells (NOAO/KPNO) & Nicholas B. Suntzeff (NOAO/CTIO)

6. SUPERNOVAE: RADIO AND X-RAY

SN 1988Z: The Most Distant and Luminous Radio Supernova
Schuyler D. Van Dyk & Kurt W. Weiler (NRL, Washington, DC, USA) Richard A. Sramek (NRAO/VLA, Socorro, NM, USA), & Nino Panagia (StScI, Baltimore, MD, USA)

SN 1978K – Another Serendipitously discovered Radio Supernova
Lister Staveley-Smith & Stuart Ryder (Australia Telescope National Facility, CSIRO, Australia)

X-Ray Emission from Supernovae
Eric M. Schlegel (NASA-Goddard Space Flight Center & USRA, USA)

7. SN Ia MODELS AND NUCLEOSYNTHESIS

^{57}Cu and Nucleosynthesis with $A > 56$
Chen Xueshi, Tian Jiaqi, Liang Yusheng,& Zhu Xiaodon (Shanghai Inst. of Nuclear Research, Academia Sinica, China)

The Evolution of SNIa Progenitors
J. Isern[1], E. Bravol, 2, R. Canal[3], I. Dominguez[1,4], M. Hernanz[1], J. Labay[3] ([1]Centre d'Estudis Avancats, C.S.I.C., [2]Departament de Fisica i Enginyeria Nuclear, U.P.C., [3]Departament d'Astronomia i Meteorologia, U.B., [4]Istituto di Astrofisica Spaziale, C.N.R., Spain)

Dynamics and Spectra of Type Ia Supernovae
C. Wheeler (U. of Texas)

Towards a Characterization of Deflagrations in Type Ia Supernovae
E. Bravo[1,2,3], D. Garcia[1,2], N. Serichol[1] ([1]Departament de Fisica i Enginyeria Nuclear U.P.C. Barcelona; [2]Laboratori d'Astrofisica, Institut d'Estudis Catalans, Barcelona; [3]Centre d'Estudis Avanats C.S.I.C., Cami Sta. Barbara s/n, Spain)

Constraints on SNIa Models and Nucleosynthesis
E. Bravo[1,2,3], J. Isern[2,3], R. Canal[3,4] ([1]Departament de Fisica i Enginyeria Nuclear, U.P.C., Barcelona; [2]Centre d'Estudis Avanats, C.S.I.C., Blanes (Girona); [3]Laboratori d'Astrofisica, Institut d'Estudis Catalans, Barcelona; [4]Departament d'Astronomia i Meteorologia, U.B., Barcelona, Spain)

Core Collapse vs. Thermonuclear Explosion in Mass-Accreting White Dwarfs
R. Canal[1], E. Bravo[2], D. Garcia[2], E. Garcia-Berro[3], J. Isern[4], & J. Labay[1] ([1]Departament d'Astronomia i Meteorologia, Universitat de Barcelona; [2]Departament de Fisica i Enginyeria Nuclear, Universitat Politecnica de Catalunya; [3]Departament de Fisica Aplicada, Universitat Politecnica de Catalunya; [4]Centre d'Estudis Avanccats de Blanes, CSIC, Spain)

SN Ia Diagnostics from Nebular Stages
P. Ruiz-Lapuente[1], R. Canal[2], P. M. Challis[1], A. V. Filippenko[3], D.vJ. Jeffery[1], R. P. Kirshner[1], & B. P. Schmidt[1] ([1]Harvard-Smithsonian Center for Astrophysics; [2]Dept. d'Astronomia i Meteorologia, U. Barcelona, Spain; [3]U. California, Berkeley, USA)

A Search for Double Degenerate Systems
Angela Bragaglia (Osservatorio Astronomico di Bologna, Italy)

8. SN II MODELS

Equation of State and Effect of General Relativity on Stellar Collapse
Wang Yi-ren[1], Zhang Suo-Chun[1], Xie Zuo-Heng[1], & Wang Wei-Zhong[2] ([1]Inst. of Applied Mathematics, Academica Sinica; [2]Computer Center, Beijing Medical University

The Formation and Propagation of a Shock Formed during the Gravitational Collapse of a Gaseous Polytrope
Zhu Luoding & Wang Jihai (Inst. Applied Physics and Computational Mathematics, Beijing, China)

Explosive and Hydrostatic Nucleosynthesis in Massive Stars
M. Hashimoto (Kyushu University, Japan)

SNe II Abundance Yields as a Function of Progenitor Mass: The Fe Group Composition
F.-K. Thielemann (Harvard-Smithsonian Center for Astrophysics), K. Nomoto (U. Tokyo), M. Hashimoto, & T. Tsujimoto (Kyushu U., Japan)

SN 1987A and Accretion Model
Yang, Lan Tian (Hua Zhong Normal U., China)

9. SUPERNOVA REMNANTS: RADIO

*G*76.9 + 1.0, *A Supernova Remnant with Unusual Properties*
T. L. Landecker, L. A. Higgs (Dominion Radio Astrophysical Observatory, Canada), & H.J. Wendker (Hamburger Sternwarte, Hamburg, Germany)

Radio Observations of Large Angular Diameter SNRs at 232 MHz
Zhu Jiang & Zhang Xizhen (Beijing Astronomical Observatory, Beijing, China)

Search for SNRs among the Extended Sources of the Kallas & Reich Survey
S.A. Trushkin (Special Astrophysical Observatory RAS, Russia)

Radio Investigations of SNRs with the RATAN-600 Radio Telescope
S.A. Trushkin (Special Astrophysical Observatory RAS, Russia)

Multi-Frequency Radio Observations of Peculiar SNRs
S.A. Trushkin (Special Astrophysical Observatory RAS, Russia)

SNRs in the Large Magellanic Cloud
D. K. Milne & John R Dickel (Australia Telescope National Facility)

Radio Polarization Observations of SNRs
D. Milne (Australia Telescope National Facility)

Search for Galactic Supernova Remnants at the Cygnus X Region
Zheng Yijia (Beijing Astronomical Observatory, China)

OH towards SNRs in the Gum Nebula Region
B. Woermann (Rhodes University, South Africa)

A New Method of Adding Short Spacing to Synthesis Maps for Observation of SNR's
Zhang Xizhen (Beijing Astronomical Observatory)

Dynamical Evolution of SNR VRO 42.05.01
S.-U. Choe & Bon-Chul Koo (Seoul National University, Korea)

Theoretical Model for SNR VRO 42.05.01
Chen, Yang (Nanjing U., China)

Radio flares of SS433 in 1986-1987: Multi-Frequency Monitoring
S.A. Trushkin (Special Astrophysical Observatory RAS, Russia)

Theoretical Models for SNR VRO 42.05.01
Chen, Y., Liu, N., & Wang, Zhenru (Nanjing U., China)

10. SUPERNOVA REMNANTS: OPTICAL, UV, & X-RAY

Iron Coronal lines in Old Supernova Remnants
Jean-Luc Sauvageot (CEN - Saclay, France)

Improved Dynamical Determination of the Mass Ejected by the Cas A Supernova
Wu, Xuebing & Yang, Pibo (Huazhong Normal U., Wuhan, China)

Correlated ROSAT and Radio Observations of SNRs
E. Fuerst, W. Reich, B. Aschenbach (Max-Planck-Institut f. Radioastronomie, Bonn, Germany)

ROSAT Observations of IC 443
J.-H. Rho (NASA/UMD), R. Petre (NASA), & J. J. Hester (Arizona State U.)

ROSAT Observation of the SNR VRO42.05.01
Zhiyu Guo & David N. Burrows (Pennsylvania State University)

High Spatial Resolution X-ray Studies of Kepler's SNR
P. Slane & J. P. Hughes (Harvard-Smithsonian Center for Astrophysics)

A Model of the X-Ray Emission of Kepler's Supernova Remnant
A. Decourchelle (CEN SACLAY Service d'Astrophysique, France)

Nonequilibrium Ionization in Supernova Remnants
Kuniaki MASAI (Service d'Astrophysique, CEN Saclay, France & National Institute for Fusion Science, Nagoya 464-01, Japan)

On the X-Ray Continuum of Type IA Supernova Remnants
Yu Wenfei & Yang Lantian (Huazhong Normal U., Wuhan, China)

The Role of Electric Currents in Saturated Thermal Conduction: Implications on the Evaporation of Knots in Young SNRs
R. Bandiera (Arcetri Astrophysical Observatory, Italy) & Y. Chen (Nanjing University, China)

Strong Thermal Conduction Process during Collective SN Explosions
Xu Wen (Beijing University, China)

Hot Gas in the Starburst Galaxy N3077
Bi Hongguan(Beijing Observatory), H. Arp (Carnegie Obs.), & H. U. Zimmermann

11. PULSARS

Evidence of Pulsed X-Ray Emission from Radio Pulsar in Supernova Remnant CTB80
Cheng Lingxiang, Li Tipei, Sun Xuejun, Ma Yuqian, & Wu Mei (Inst. of High Energy Physics, Beijing)

The Galactic Magnetic Field Derived from the RMs of Pulsars
Han Jin-Lin (Beijing Astronomical Observatory, Academia Sinica) & Qiao Guo-Jun Qiao (Department of Geophysics, Beijing University, China)

The Emission Beams of a Pulsar in the Inverse Compton Scattering Model
B. Zhang & Q. J. Qiao (Beijing University, China)

The Magnetic Evolution of X-Ray Binaries and Recycled Pulsars
Zhang Chengmin (Dept. of Physics, Hebei Inst. of Technology, Tianjin, and Inst. of Theor. Physics, Academia Sinica, Beijing) & Wu Xinji (Dept. of Geophysics, Beijing Univ., China)

Spin-Down of Hybrid Stars
Ma Feng & Pei Shouyang (Beijing Normal University, China)

The Acceleration Process of Particles in the Region Nearby the Magnetic Axes of Pulsars
Wu Xinji[1,3,4], Yi Tong[2,3], Chian, A. C.-L.[3,4] ([1]Geophysics Dept., Beijing University; [2]Beijing Normal University; [3]National Inst. for Space Research INPE So Jo dos Campos, S.P., Brazil; [4]Dept. of Applied Math. & Theor. Phys., U. of Cambridge, UK)

Theoretical Explanation of the Variation of $P/\dot{P}$ for Pulsars
Li X.-D. & Wang Zhenru (Nanjing U., China)

Statistical Analysis of Radio Pulsars
Zhang, Q. C., Li, X.-D., Wang Zhenru (Nanjing U., China)

The Evolution of Inclination in Binary X-ray and Radio Pulsars
Zhang, Chengmin (Hebei Technical Institute, Tianjin, China)

Accretion on White Dwarfs and the Overstability of Disk Models
Yu, Wenfei (Hua Zhong Normal U., China)

The Phenomenon of PSR 1951+32 in X-Ray
Chen, Lingxiang (Beijing High Energy Physics Institute)